

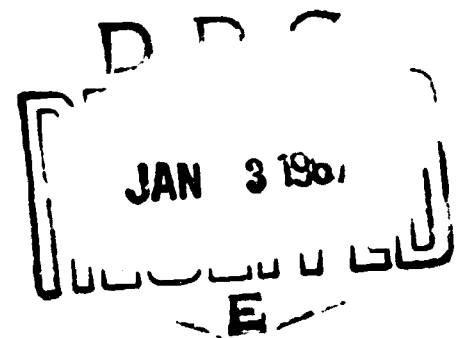
NAVORD REPORT 1488 (VOLUME 5)

0615-139-0050

AD 64421

HANDBOOK OF SUPERSONIC AERODYNAMICS SECTIONS 13 AND 14 VISCOSITY AND HEAT TRANSFER EFFECTS

CLEARINGHOUSE FOR FEDERAL SCIENTIFIC AND TECHNICAL INFORMATION			
Hardcopy	Microfiche		
\$ —	\$ 1.65	355 pp	7/2
1,24 ARCHIVE COPY			



PUBLISHED BY DIRECTION OF
COMMANDER, NAVAL ORDNANCE SYSTEMS COMMAND

NAVORD REPORT 1488 (VOLUME 5)

HANDBOOK OF SUPERSONIC AERODYNAMICS

SECTIONS 13 AND 14

VISCOSITY AND HEAT TRANSFER EFFECTS

By

R. E. WILSON

**Associate Technical Director, Aeroballistics
U. S. Naval Ordnance Laboratory
White Oak, Maryland**

**Produced and edited by the Aerodynamics Handbook Staff
of the Johns Hopkins University Applied Physics
Laboratory, Silver Spring, Maryland, operating under
Contract N0w 62-0604 -c, with the Bureau of Naval
Weapons, Department of the Navy.**

1 AUGUST 1966

SERIES CONTENTS

<u>Section</u>		<u>Status</u>
Volume 1		
1	Symbols and Nomenclature	Published 1950
2	Fundamental Equations and Formulae	1950
3	General Atmospheric Data	1950
4	Mechanics and Thermodynamics of Steady One-Dimensional Gas Flow	1950
Volume 2		
5	Compressible Flow Tables and Graphs	1953
Volume 3		
6	Two-Dimensional Airfoils	1957
7	Three-Dimensional Airfoils	1958
8	Bodies of Revolution	1961
Volume 4		
9	Mutual Interference Phenomena	Withdrawn
10	Stability and Control Analysis Techniques	Withdrawn
11	Stability and Control Parameters	Withdrawn
12	Aeroelastic Phenomena	1952
Volume 5		
13	Viscosity Effects	1966
14	Heat Transfer Effects	1966
15	Properties of Gases	1953
16	Mechanics of Rarefied Gases	1959
Volume 6		
17	Ducts, Nozzles and Diffusers	1964
18	Shock Tubes	1959
19	Wind Tunnel Design	Withdrawn
20	Wind Tunnel Instrumentation and Operation	1961

PREFACE

The preface appearing in Volume 1 of the Handbook of Supersonic Aerodynamics defines the Handbook's purpose and also traces the sequence of events leading to its undertaking. In accordance with the criteria established at that time, the subject matter of the Handbook is selected on the basis of anticipated usefulness to all who are actively concerned with the design and performance of supersonic vehicles. Essential to this subject matter are the properties of fluids in which a vehicle operates or is tested and the flight characteristics of the vehicle itself. Each section of the Handbook therefore presents appropriate theory and relevant data which are basic to supersonic aerodynamics and which conform to the above criteria.

On the opposite page appears a complete list of the sections originally intended to be included in the Handbook. Of these, fourteen have already been published, two are presented herein, and the remaining four have for various reasons been withdrawn.

Section 13 on Viscosity Effects and Section 14 on Heat Transfer Effects have been prepared by R. E. Wilson, Associate Technical Director, Aeroballistics, U.S. Naval Ordnance Laboratory, White Oak, Maryland. Since the effects of viscosity and heat transfer are so closely allied, it was decided that the subject matter would be more readily accessible to the reader if the two sections were combined to allow the pagination and decimal system numbering to be consecutive through the volume.

An Appendix to this volume gives some of the thermodynamic and transport properties of air at high temperatures. This material not only supplements that given in Section 15 of the Handbook, but corrects the errors that appeared there in gas properties at temperatures in excess of about 3000°K.

The Handbook is published and distributed by direction of the Bureau of Naval Weapons, Department of the Navy. It is available for public purchase (see Title Page) and is also distributed without charge to an approved list of facilities and institutions actively engaged in national defense research and development. Correspondence relating to the distribution of the Handbook should be directed to:

Chief, Bureau of Naval Weapons
Department of the Navy
Washington, D. C., 20360

Correspondence relating to the subject material should be directed to:

Editor, Handbook of Supersonic Aerodynamics
Applied Physics Laboratory
The Johns Hopkins University
8621 Georgia Avenue
Silver Spring, Maryland, 20910

The Handbook of Supersonic Aerodynamics is made ready for printing by the Handbook Staff; the justified typing and general layout work is done by Mrs. Doris McCeney; Mrs. Carol Dick prepared all sketches and figures in addition to many other tasks involved in processing a manuscript.

Ione D. V. Faro, Editor

CONTENTS

	<u>Page</u>
List of Tables	ix
List of Figures	xi
Symbols	xxi
1. Introduction	1
1.1 Scope of Contents	1
2. Boundary-Layer Equations	3
2.1 Continuity, Momentum, and Energy Equations in Viscous Flow	3
2.2 Two-Dimensional, Steady, Laminar Flow	6
2.3 Axisymmetric, Steady, Laminar Flow	7
2.4 Two-Dimensional, Steady, Laminar Flow in the (x, u) Plane .	8
2.5 The Momentum Integral Equation	10
2.5.1 Axisymmetric Compressible Steady Flow.	11
2.5.2 Two-Dimensional Flow	12
2.5.3 Transformations of the Integral Momentum Equation .	12
2.6 Two-Dimensional Turbulent Flow	13
2.6.1 Two-Dimensional Turbulent Flow in the (x, \bar{u}) Plane .	15
3. Solutions to the Flat Plate Boundary-Layer Equations	17
3.1 Laminar Boundary Layer on a Flat Plate--Perfect Gas	17
3.1.1 The Reference Temperature Method for Calculating Skin Friction	21
3.1.2 Comparison of Reference Temperature and Maximum Boundary-Layer Temperature	24
3.1.3 Boundary-Layer Thickness and Shape Parameter	24
3.2 Laminar Boundary Layer on a Flat Plate--Real Gas.	25
3.2.1 Skin Friction Coefficient.	27
3.2.2 Shape Parameter and Boundary-Layer Displacement .	28
3.3 Turbulent Boundary Layer on a Flat Plate--Perfect Gas . . .	29
3.3.1 A Reference Temperature Method for Turbulent Flows.	35
3.3.2 Theoretical and Experimental Skin Friction Co- efficients	37
3.3.3 Shape Parameter and Boundary-Layer Displacement Thickness	40
3.3.4 Laminar Sublayer Thickness	43
3.4 Turbulent Boundary Layer on a Flat Plate--Real Gas	45
3.5 Flat Plate with Transition	47

	<u>Page</u>
4. Boundary-Layer Growth on Two-Dimensional and Axisymmetric Bodies	77
4.1 Laminar Boundary Layer: Finite-Difference Methods	77
4.2 Laminar Boundary Layer: Approximate Method	79
4.2.1 Correlation Technique	80
4.2.2 Integration of the Momentum Equation for Two-Dimensional Bodies	83
4.2.2.1 Variable Wall Temperature	83
4.2.2.2 Constant Wall Temperature	84
4.2.3 Integration of the Momentum Equation for Axisymmetric Bodies	85
4.2.3.1 Variable Wall Temperature	85
4.2.3.2 Constant Wall Temperature	87
4.2.4 Local Shear Stress	88
4.2.5 Boundary-Layer Shape Parameter and Thickness	88
4.3 Turbulent Boundary Layer	89
4.4 Boundary Layer on Cones	89
4.4.1 Laminar Boundary Layer on Cones	91
4.4.2 Turbulent Boundary Layer on Cones	92
4.4.3 Boundary-Layer Transition on Cones	93
4.5 Laminar Boundary Layer on Spheres	94
4.6 Laminar Boundary Layer on Sphere-Cones	98
4.6.1 Boundary-Layer Parameters	99
4.6.2 Continuity Considerations	100
4.6.3 Expansion of the Flow Behind the Bow Shock	102
4.6.4 Calculation of the Mach Number Gradient	102
4.6.5 Integration of the Momentum Equation	102
4.6.6 Skin Friction and Friction Drag	105
4.6.7 Local Flow Conditions Far from the Tip	106
4.6.8 Numerical Example	107
4.6.9 Real Gas Effects	109
5. Boundary-Layer Transition	119
5.1 Effects of Mach Number and Surface Cooling	121
5.1.1 Cooled Surfaces	121
5.1.2 Insulated Surfaces	123
5.2 Effect of Body Angle of Attack	124
5.3 Effect of Bluntness	125
5.4 Transition Reynolds Number Based on Momentum Thickness	126
5.5 Effect of Sweep	127
5.6 Effect of Roughness	127
5.6.1 Minimum Transition Reynolds Number: Three-Dimensional Roughness	128
5.6.2 Maximum Three-Dimensional Roughness not Initiating Transition	131

	<u>Page</u>
5.6.3 Two-Dimensional Roughness	132
5.7 Effect of Stream Turbulence in a Wind Tunnel	132
5.8 Lateral Spreading of Turbulence	133
6. Effect of Roughness on the Flat Plate Turbulent Boundary Layer. .	159
6.1 Incompressible Flow over a Rough Insulated Plate	159
6.2 Compressible Flow over a Rough Insulated Plate	162
6.3 Compressible Flow over a Rough Plate with Heat Transfer . .	164
6.4 Transition from Laminar to Turbulent Flow on a Roughened Plate	165
6.5 Roughness Types	166
7. Heat Transfer.	189
7.1.1 Laminar Boundary Layer on a Flat Plate--Perfect Gas, Heat Transfer	189
7.1.2 Laminar Boundary Layer on a Flat Plate--Real Gas, Heat Transfer	191
7.1.3 Turbulent Boundary Layer on a Flat Plate--Perfect Gas, Heat Transfer	193
7.1.4 Turbulent Boundary Layer on a Flat Plate--Real Gas, Heat Transfer	195
7.2 Heat Transfer on Two-Dimensional and Axisymmetric Bodies. .	195
7.2.1 Laminar Boundary Layer	195
7.2.2 Turbulent Boundary Layer	199
7.2.3 Cones, Spheres, and Sphere-Cones	200
7.2.4 Bodies at Angle of Attack	200
7.3 Heat Transfer on Yawed Cylinders	203
7.4 Heat Transfer in the Transition Region	204
7.5 Turbulent Heat Transfer on Rough Surfaces	204
7.6 Heat Transfer in Separated Flows	206
7.7 Turbulent Heat Transfer Near Protuberances	209
Appendix	253
References	315
Index	331

LIST OF TABLES

<u>Table</u>		<u>Page</u>
3-1	Graphical Information Presented by Crocco in Ref. 4	53
3-2	Graphical Information Presented by Van Driest in Ref. 9 . .	54
4-1	Summary of Finite Difference Methods for Solving the Lam- inar Boundary-Layer Equations	111
7-1	Protuberance Configurations Tested by Wisniewski (Ref. 176).	211
7-2	Protuberance Configurations Tested by Burbank, Newlander, and Collins (Ref. 178)	212
7-3	Protuberance Configurations Tested by Bloom and Pallone (Ref. 179)	215
A-1	Some Sources of Thermodynamic Data	255
A-2	Thermodynamic Properties of Air	256
A-3	Transport Properties of Air	287
A-4	c_p/R vs T for Various Values of $\log \rho/\rho_0$	288

LIST OF FIGURES

Figure		Page
3-1	Flat plate laminar boundary layer; $(y/x) \sqrt{Re}$ vs u_* ; $T_w = T_e$ and T_1 ; $M_1 = 0, 4, 8, 12, 16$, and 20 ; $Pr = 0.75$; perfect gas, $\gamma = 1.4$; $\beta = 0.505$	55
3-2	Flat plate laminar boundary layer; $(y/x) \sqrt{Re}$ vs T_* ; $T_w = T_e$ and T_1 ; $M_1 = 4, 8, 12, 16$, and 20 ; $Pr = 0.75$; perfect gas, $\gamma = 1.4$; $\beta = 0.505$	56
3-3	Flat plate laminar boundary layer; comparison of theoretical values of $C_f \sqrt{Re}$ vs M_1 ; Van Driest and reference temperature methods; $M_1 = 0$ to 20 ; $T_{*w} = 0.25, 1, 2, 4$, and 6 and $T_w = T_e$; $Pr = 0.75$; perfect gas, $\gamma = 1.4$; $\beta = 0.505$	57
3-4	Flat plate laminar boundary layer; $C_f \sqrt{Re}$ vs T_* ; $\beta = 0, 0.5, 1.0, 1.5$, and 2.0 ; perfect gas, $\gamma = 1.4$	58
3-5	Flat plate laminar boundary layer; comparison of maximum temperature (Van Driest) and reference temperature as a function of M_1 ; $M_1 = 0$ to 20 ; $T_w = T_e$ and T_1 ; perfect gas, $\gamma = 1.4$; $Pr = 0.75$; $\beta = 0.505$	59
3-6	Flat plate laminar boundary layer; shape parameter, H , vs M_1 ; $M_1 = 0$ to 20 ; $T_{*w} = 0.25, 1, 2, 4$, and 6 ; perfect gas, $\gamma = 1.4$; $Pr = 0.75$; $T_1 = 392.4^\circ R$	59
3-7	Flat plate laminar boundary-layer thickness, δ/θ vs M_1 ; $M_1 = 0$ to 20 ; $T_{*w} = 0.25, 1, 2, 4$, and 6 ; perfect gas, $\gamma = 1.4$; $Pr = 0.75$; $T_1 = 392.4^\circ R$	60
3-8	Flat plate laminar boundary-layer thickness and shape parameter vs M_1 ; $M_1 = 0$ to 20 ; zero heat transfer; perfect gas, $\gamma = 1.4$; $Pr = 0.75$, $T_1 = 392.4^\circ R$	60
3-9	Flat plate laminar boundary layer: $(\delta/x) \sqrt{Re}$ and $(\delta^*/x) \sqrt{Re}$ vs M_1 ; $M_1 = 0$ to 20 ; $T_w = T_e$ and T_1 ; perfect gas, $\gamma = 1.4$; $Pr = 0.75$; $\beta = 0.505$	61
3-10	Variation of μ and Rk/c_v with Z for air; $Z = 1.0$ to 1.8 ; $\rho/\rho_0 = 0.01, 0.1$, and 1.0	62
3-11	Variation of a, b, c , and d with Z for use in Eqs. 3-25 and 3-26; $Z = 1.0$ to 1.8	63

Figure		Page
3-12	Variation of μ , k , c_p , ρ , and Pr with enthalpy for air at $p = 0.1$ atm	64
3-13	Real gas flat plate laminar boundary layer; comparison of exact and approximate values of $C_f \sqrt{Re}$ vs h_{*w} ; $h_{*w} = 0$ to 140; $u_1^2/2h_1 = 0, 10, 30$, and 80; $h_1 = 3000$ BTU/slug; $p_1 = 0.1$ atm	65
3-14	Real gas flat plate laminar boundary layer; comparison of exact and approximate values of $C_f \sqrt{Re}$ vs h_{*w} ; $h_{*w} = 0$ to 35; $u_1^2/2h_1 = 0, 10$, and 30; $h_1 = 15,000$ BTU/slug; $p_1 = 0.1$ atm	65
3-15	Real gas flat plate laminar boundary layer; comparison of exact and approximate values of $C_f \sqrt{Re}$ vs h_{*w} ; $h_{*w} = 0$ to 6; $u_1^2/2h_1 = 0$ and 10; $h_1 = 75,000$ BTU/slug; $p_1 = 0.1$ atm.	66
3-16	Real gas flat plate laminar boundary layer; comparison of exact and approximate values of $C_f \sqrt{Re}$ vs h_{*w} ; $h_{*w} = 0$ to 1; $u_1^2/2h_1 = 0$; $h_1 = 400,000$ BTU/slug; $p_1 = 0.1$ atm	66
3-17	Effect of heat transfer on laminar sublayer parameter, s	66
3-18	Flat plate turbulent boundary layer; C_F/C_{F_i} vs M_1 ; $M_1 = 0$ to 10; $(T_e - T_w)/T_e = 0, 0.2, 0.4, 0.6, 0.8, 0.9$, and 0.95; perfect gas, $\gamma = 1.4$; $Pr = 0.70$; $Re = 10^7$; $\beta = 0.505$	67
3-19	Flat plate turbulent boundary layer; $(C_f/C_{f_i})_{Re_\theta} / (C_F/C_{F_i})_{Re}$ vs $(C_F/C_{F_i})_{Re}$; $(C_F/C_{F_i})_{Re} = 0$ to 1.6; $\log Re_\theta = 2.5, 3.0, 3.5, 4.0$, and 4.5; perfect gas, $\gamma = 1.4$; $Pr = 0.70$	68
3-20	Flat plate turbulent boundary layer; comparison of experimental and theoretical incompressible skin friction; $1/\sqrt{C_f}$ vs $\log(C_f Re)$; perfect gas, $\gamma = 1.4$; $Pr = 0.70$; $Re = 10^5$ to 10^8	68
3-21	Flat plate turbulent boundary layer; C_F vs $\log Re$; theory and experiment; zero heat transfer; perfect gas, $\gamma = 1.4$; $Pr = 0.70$	69
3-22	Flat plate turbulent boundary layer; C_f vs $\log Re_\theta$; theory and experiment; zero heat transfer; perfect gas, $\gamma = 1.4$; $Pr = 0.70$	69
3-23	Flat plate turbulent boundary layer; C_f vs $\log Re$; theory and experiment; zero heat transfer; perfect gas, $\gamma = 1.4$; $Pr = 0.70$	70

<u>Figure</u>		<u>Page</u>
3-24	Flat plate turbulent boundary layer; C_F vs $\log Re$; theory and experiment; various heat-transfer ratios and Mach numbers; perfect gas, $\gamma = 1.4$; $Pr = 0.70$	70
3-25	Flat plate turbulent boundary layer; C_f vs $\log Re_\theta$; theory and experiment; $(T_e - T_w)/T_e = 0.075, 0.166, \text{ and } 0.352$; $M_1 = 5.2$; perfect gas, $\gamma = 1.4$; $Pr = 0.70$	71
3-26	Flat plate turbulent boundary layer; δ^*/δ vs M_1 ; $M_1 = 0$ to 10 ; $(T_e - T_w)/T_e = 0, 0.2, 0.4, 0.6, 0.8, \text{ and } 1.0$; perfect gas, $\gamma = 1.4$; $Pr = 0.70$	71
3-27	Flat plate turbulent boundary layer; shape parameter H vs M_1 ; $M_1 = 0$ to 10 ; $(T_e - T_w)/T_e = 0, 0.2, 0.4, 0.6, 0.8, \text{ and } 1.0$; perfect gas, $\gamma = 1.4$; $Pr = 0.70$	72
3-28	Flat plate turbulent boundary layer; thickness of the laminar sublayer, δ_l/x vs Re ; theory and experiment; $M_1 = 5.2$; $(T_e - T_w)/T_e = 0.075, 0.166, \text{ and } 0.352$; perfect gas, $\gamma = 1.4$; $Pr = 0.70$	73
3-29	Flat plate turbulent boundary layer; thickness of the laminar sublayer, δ_l/x vs M_1 ; $M_1 = 0$ to 10 ; $(T_e - T_w)/T_e = 0, 0.2, 0.4, 0.6, 0.8, 0.9, \text{ and } 0.95$; $Re = 10^7$; $\beta = 0.505$; perfect gas, $\gamma = 1.4$; $Pr = 0.70$	74
3-30	Perfect gas turbulent boundary layer; laminar sublayer thickness, δ_l/θ vs M_1 ; $M_1 = 0$ to 10 ; $(T_e - T_w)/T_e = 0, 0.2, 0.4, 0.6, 0.8, 0.9, \text{ and } 0.95$; $Re = 10^7$; $\beta = 0.505$; perfect gas, $\gamma = 1.4$; $Pr = 0.70$	75
3-31	Flat plate turbulent boundary layer; thickness of the laminar sublayer, δ_l/δ vs M_1 ; $M_1 = 0$ to 10 ; $(T_e - T_w)/T_e = 0, 0.2, 0.4, 0.6, 0.8, 0.9, \text{ and } 0.95$; $Re = 10^7$; $\beta = 0.505$; perfect gas, $\gamma = 1.4$; $Pr = 0.70$	76
4-1	Correlation of the momentum parameter, N , with the pressure gradient parameter, n	113
4-2	Effect of wall temperature on pressure gradient parameter, n	114
4-3	Effect of wall temperature on value of B ; $B = dN/dn$	114
4-4	Correlation of the shear parameter, l , and the pressure gradient parameter, n	115

Figure		Page
4-5	Correlation of \bar{H} or $\bar{\delta}/\bar{\theta}$ and the pressure gradient parameter, n	116
4-6	Behavior of integrand in Eq. 4-72; $M_\infty = 14.9$, $M_c = 10.0$; $\sigma = 8^\circ$; $T_w = T_\infty = 530^\circ R$	117
4-7	Effect of bluntness on momentum thickness Reynolds number; $M_\infty = 14.9$, $M_c = 10.0$; $\sigma = 8^\circ$; $T_\infty = T_w = 530^\circ R$	117
4-8	Effect of bluntness on local Mach number; $M_\infty = 14.9$, $M_c = 10.0$; $\sigma = 8^\circ$; $T_\infty = T_w = 530^\circ R$	118
4-9	Effect of bluntness on local skin friction coefficient; $M_\infty = 14.9$, $M_c = 10.0$; $\sigma = 8^\circ$; $T_\infty = T_w = 530^\circ R$	118
5-1	Effect of T_w/T_{e_1} and M_1 on the transition Re_{x_1} ; smooth, sharp cones; $\sigma = 5^\circ$; $\alpha \approx 0^\circ$	135
5-2	Effect of T_w/T_{e_1} and M_1 on the transition Re_{x_1} ; smooth, sharp flat plates and hollow cylinders; $\alpha = 0^\circ$	136
5-3	Effect of cooling on transition Re_{ℓ_∞} ; NACA RM-10 body; $\alpha = 0^\circ$; $M_\infty = 1.61$	137
5-4	Effect of M_1 on transition Re_{x_1} ; smooth, sharp cones; $\alpha = 0^\circ$; $T_e = T_w$; wind-tunnel tests	138
5-5	Effect of M_1 on transition Re_{x_1} ; smooth, sharp flat plates and hollow cylinders; $T_e = T_w$; wind-tunnel tests.	139
5-6	Effect of pressure gradient on transition Re_{ℓ_∞} ; $\alpha = 0^\circ$; $T_e = T_w$; wind-tunnel tests	140
5-7	Effect of α on transition Re_{x_∞} ; slender, smooth, sharp bodies; ballistics-range tests	141
5-8	Critical pressure rise coefficient as a function of transition Re_{x_∞} ; various models; $M_\infty = 0, 1.6$, and 3.5	142
5-9	Effect of bluntness on transition Re_{x_∞} ; cooled, smooth hollow cylinders; $M_\infty = 5.0$; roughness $= 8 \mu\text{in.}$; $Re_\infty/\text{ft} = 5.4 \times 10^6$; wind-tunnel data	142
5-10	Effect of semicircular bluntness and M_∞ on transition Re_{x_∞} ; smooth, flat plates and hollow cylinders; $T_e = T_w$; wind-tunnel tests	143

<u>Figure</u>		<u>Page</u>
5-11	Effect of bluntness on distance to end of transition as a function of $Re_\infty/in.$; smooth, hollow cylinder, $T_e = T_w$; $M_\infty = 3.1$; roughness = 10 $\mu in.$; wind-tunnel tests	144
5-12	Effect of tip radius, Re_{t_∞} , and M_∞ on Transition Re_{x_∞} ; smooth cones; $\alpha = 0^\circ$; $T_e = T_w$; wind-tunnel tests	145
5-13	Effect of bluntness on distance to end of transition; smooth cones; $2\sigma = 10^\circ$; $\alpha = 0^\circ$; $T_e = T_w$; $M_\infty = 3.1$; wind-tunnel tests	146
5-14	Effect of tip blunting on Re_{θ_1} at transition; smooth cone; $\alpha = 0^\circ$; $T_e = T_w$; wind-tunnel tests	147
5-15	Momentum thickness Reynolds number, Re_{θ_1} , at transition; smooth, blunt bodies; $\alpha \approx 0^\circ$; $T_w/T_t = 0.3$ to 0.56; $M_\infty = 2$ to 3.5; ballistics-range tests	150
5-16	Effect of sweep angle, leading edge thickness, and Mach number on transition location; flat plate; $T_e = T_w$	151
5-17	Effect of spherical roughness, Re_{k_1} , on transition Re_{x_1} ; sharp cone; $T_e = T_w$	152
5-18	Roughness location, x_k , as a function of the roughness height, k , normalized with respect to M_1 ; sharp cone; spherical roughness element; $T_e = T_w$	153
5-19	Displacement thickness, $Re_{\delta_1^*}$, as a function of the roughness size, (k/δ^*) , normalized with respect to M_1 ; cone and flat plate; spherical roughness element; $T_e = T_w$	153
5-20	Effect of roughness size, x_k/k or k/δ^* , on minimum transition Reynolds number, Re_{x_1} or $Re_{x_{k_1}}$; sharp cone; spherical roughness elements; $T_e = T_w$	154
5-21	Effect of M_1 on $(Re_{x_1} - Re_{x_{k_1}})$; cones and flat plate; spherical roughness elements; $T_e = T_w$	154
5-22	Relationship between roughness Reynolds numbers, Re_{k_1} and $Re_{k_{tr}}$	155
5-23	Critical Roughness Reynolds number, $Re_{k_{tr}}$; cones and flat plates; three-dimensional roughness elements; heat transfer	155

<u>Figure</u>		<u>Page</u>
5-24	Effect of single trip wire and heat transfer on Re_{x_1} at end of transition; sharp cones; $M_1 = 1.90, 2.70, \text{ and } 3.65$	156
5-25	Effect of supply stream turbulence and heat transfer on Re_{x_1} at end of transition; sharp cones; $M_1 = 1.90, 2.70, \text{ and } 3.65$.	157
6-1	Mean skin friction coefficients for a sand-roughened insulated plate; $M = 0$	167
6-2	Mean skin friction coefficients for a sand-roughened insulated plate; $M = 0.5$	168
6-3	Mean skin friction coefficients for a sand-roughened insulated plate; $M = 1.0$	169
6-4	Mean skin friction coefficients for a sand-roughened insulated plate; $M = 1.5$	170
6-5	Mean skin friction coefficients for a sand-roughened insulated plate; $M = 2.0$	171
6-6	Mean skin friction coefficients for a sand-roughened insulated plate; $M = 3.0$	172
6-7	Mean skin friction coefficients for a sand-roughened insulated plate; $M = 4.0$	173
6-8	Mean skin friction coefficients for a sand-roughened insulated plate; $M = 5.0$	174
6-9	Mean skin friction coefficients for a sand-roughened plate; $T_w = T_1$; $M = 0.5$	175
6-10	Mean skin friction coefficients for a sand-roughened plate; $T_w = T_1$; $M = 1.0$	176
6-11	Mean skin friction coefficients for a sand-roughened plate; $T_w = T_1$; $M = 1.5$	177
6-12	Mean skin friction coefficients for a sand-roughened plate; $T_w = T_1$; $M = 2.0$	178
6-13	Mean skin friction coefficients for a sand-roughened plate; $T_w = T_1$; $M = 3.0$	179
6-14	Mean skin friction coefficients for a sand-roughened plate; $T_w = T_1$; $M = 4.0$	180
6-15	Mean skin friction coefficients for a sand-roughened plate; $T_w = T_1$; $M = 5.0$	181

<u>Figure</u>		<u>Page</u>
6-16	Local skin friction coefficients for a sand-roughened plate; $T_w = T_1$; $M = 0.5$	182
6-17	Local skin friction coefficients for a sand-roughened plate; $T_w = T_1$; $M = 1.0$	183
6-18	Local skin friction coefficients for a sand-roughened plate; $T_w = T_1$; $M = 1.5$	184
6-19	Local skin friction coefficients for a sand-roughened plate; $T_w = T_1$; $M = 2.0$	185
6-20	Local skin friction coefficients for a sand-roughened plate; $T_w = T_1$; $M = 3.0$	186
6-21	Local skin friction coefficients for a sand-roughened plate; $T_w = T_1$; $M = 4.0$	187
6-22	Local skin friction coefficients for a sand-roughened plate; $T_w = T_1$; $M = 5.0$	188
7-1	Recovery factor and Reynolds analogy factor as a function of Prandtl number; flat plate, laminar flow, perfect gas . . .	217
7-2	Recovery factor vs Reynolds number; flat plate, turbulent flow, perfect gas; $M_1 = 0.87, 1.62, 2.06, 3.03, 3.90,$ and 5.05	218
7-3	Recovery factor as a function of distance from leading edge; transitional flow, perfect gas; $M_1 = 3.12$	219
7-4	St/C_f vs M_1 ; theoretical and experimental turbulent flow, flat plate, perfect gas	220
7-5	St/C_f vs Re ; theoretical and experimental turbulent flow, flat plate, perfect gas	220
7-6	Correlation of C_f/St with pressure gradient parameter, n , for $(T_w - T_{t1})/T_{t1} = -1.0, -0.8, -0.4, 0,$ and 1.0 ; lam- inar flow, perfect gas	221
7-7	Stagnation point heat transfer; laminar flow, perfect gas . . .	222
7-8	Stagnation point heat transfer rate at sub-orbital velocities; theory and experiment, laminar flow	223
7-9	Stagnation point heat transfer rate at super-orbital velocities; theory and experiment, laminar flow	224

<u>Figure</u>		<u>Page</u>
7-10	Mach number distribution at outer edge of boundary layer; flat plate with pressure gradient; turbulent flow	225
7-11	Wall temperature distributions along a flat plate with pressure gradient; turbulent flow	225
7-12	Reynolds analogy factor along a plate with pressure gradient; turbulent flow	226
7-13	Stanton number as a function of Reynolds number; theory and experiment; flow with transition on a 20° cone; $M_\infty = 4.95$; $\varphi = 0$; $\alpha = 0, 10$, and 20°	227
7-14	Stanton number as a function of Reynolds number; theory and experiment; turbulent flow on a 20° cone; $M_\infty = 4.95$; $\varphi = 0$; $\alpha = 0, 10$, and 20°	228
7-15	Laminar heat transfer on a sphere-cone most windward generator; $M_\infty = 3.2$, $\sigma = 13.3^\circ$, $b = 0.78$ in., $p_{t_\infty} = 980$ - 1210 mm Hg, $T_{t_\infty} = 318$ - 335°K	229
7-16	Laminar heat transfer on a sphere-cone most windward generator; $M_\infty = 4.8$, $\sigma = 13.3^\circ$, $b = 0.78$ in., $p_{t_\infty} = 2090$ - 2220 mm Hg, $T_{t_\infty} = 320^\circ\text{K}$	230
7-17	Laminar heat transfer on a sphere-cone, $\varphi = 45^\circ$; $M_\infty = 3.2$, $\sigma = 13.3^\circ$, $b = 0.78$ in., $p_{t_\infty} = 980$ - 1210 mm Hg, $T_{t_\infty} = 318^\circ\text{K}$	231
7-18	Laminar heat transfer on a sphere-cone, $\varphi = 45^\circ$; $M_\infty = 4.8$, $\sigma = 13.3^\circ$, $b = 0.78$ in., $p_{t_\infty} = 2090$ - 2220 mm Hg, $T_{t_\infty} = 320^\circ\text{K}$	232
7-19	Effect of angle of yaw on heat transfer rate on stagnation line of a cylinder; theory, laminar flow	233
7-20	Effect of angle of yaw on heat transfer rate on stagnation line of a cylinder; cool wall; laminar flow theory with real gas effects	234
7-21	Effect of angle of yaw on mean heat transfer rate to a cylinder; $M_\infty = 11$, $\rho_\infty u_\infty / \mu_t = 4.0 \times 10^4 / \text{ft}$, $T_t = 3660^\circ\text{R}$	235
7-22	Effect of angle of yaw on heat transfer rate along the stagnation line of a cylinder; theory and experiment; $M_\infty = 4.15$; $Re_\infty = \rho_\infty u_\infty D / \mu_\infty$	236
7-23	Local skin friction and heat transfer data for two-dimensional V-groove roughness; flat plate; turbulent boundary layer; $M_1 = 4.93$, $p_t = 255$ psia, $T_w = 555^\circ\text{R}$, $x = 12.5$ in. (11 in. from start of roughness)	237

<u>Figure</u>		<u>Page</u>
7-24	Effect of two-dimensional V-groove roughness on Reynolds analogy factor; flat plate; turbulent boundary layer; $M_1 = 4.93$	238
7-25	Effect of spike on heat transfer rate; hemisphere-cylinder; $M_\infty = 6.8$	239
7-26	Comparison of experimental and predicted heat transfer with and without separation; $M_\infty = 6.8$	240
7-27	Heat transfer on a flat plate with stringers; $M_\infty = 2$, $Re_\infty/ft = 15.2 \times 10^6$	241
7-28	Average values of the Stanton number; attached and separated flows; $M_1 = 2.6, 3.1$, and 4.0	242
7-29	Comparison of local heat transfer rates for attached and separated flows	242
7-30	Experimental data on the transition of separated laminar boundary layers; $0 < M_\infty < 5$	243
7-31	Effect on the total heat transfer of a cavity on a sharp cone; $M_\infty = 5.09$, $Re_\infty/ft = 1.2 \times 10^6$; $T_w/T_t = 0.25, 0.49$, and 0.72	244
7-32	Turbulent recovery factor distribution in the vicinity of a 90° cylindrical protuberance mounted on a cone-cylinder; $M_\infty = 3.12$	245
7-33	Local turbulent film coefficients in the vicinity of a 90° cylindrical protuberance mounted on a cone-cylinder; $M_\infty = 3.12$; $Re_\infty = 8 \times 10^6/ft$	245
7-34	Effect of boundary layer thickness on local film coefficients measured on the center line of a flat plate on which a cylindrical protuberance is mounted; turbulent flow; $M_\infty = 3.5$, $Re_\infty/ft = 2.9 \times 10^6$	246
7-35	Local turbulent film coefficients on a mounting plate in the vicinity of a 90° cylindrical protuberance; $\delta = 6.0$ in.	247
7-36	Local turbulent film coefficients on a mounting plate in the vicinity of a cylinder swept forward 45° ; $\delta = 6$ in.	248
7-37	Local turbulent film coefficients on a mounting plate in the vicinity of a cylinder swept back 45° ; $\delta = 6$ in.	249
7-38	Local turbulent film coefficients on a mounting plate in the vicinity of a rectangular stiffener $1 \times 2 \times 24$ in.; $\delta = 6$ in.	250
7-39	Local turbulent film coefficients on a mounting plate in the vicinity of a stiffener $2 \times 4 \times 24$ in.; $\delta = 6$ in.	251

Figure		Page
A-1	Log ρ as a function of T; p (atm) = 10^2 , 10^1 , 10^0 , 10^{-1} , 10^{-2} , 10^{-3} , and 10^{-4} ; cross-plot of data from Ref. 187 . . .	293
A-2	Z as a function of T; p (atm) = 10^2 , 10^1 , 10^0 , 10^{-1} , 10^{-2} , 10^{-3} , and 10^{-4} ; cross-plot of data from Ref. 187	294
A-3	Log h as a function of T; p (atm) = 10^2 , 10^1 , 10^0 , 10^{-1} , 10^{-2} , 10^{-3} , and 10^{-4} ; cross-plot of data from Ref. 187	295
A-4	Log ρ as a function of log h; p (atm) = 10^2 , 10^1 , 10^0 , 10^{-1} , 10^{-2} , 10^{-3} , and 10^{-4} ; cross-plot of data from Ref. 187 . . .	296
A-5	Coefficient of viscosity of air; $\rho/\rho_0 = 10^{+1}$	297
A-6	Coefficient of viscosity of air; $\rho/\rho_0 = 1$	298
A-7	Coefficient of viscosity of air; $\rho/\rho_0 = 10^{-1}$	299
A-8	Coefficient of viscosity of air; $\rho/\rho_0 = 10^{-2}$	300
A-9	Coefficient of viscosity of air; $\rho/\rho_0 = 10^{-3}$	301
A-10	Coefficient of viscosity of air; $\rho/\rho_0 = 10^{-4}$	302
A-11	Coefficient of viscosity of air; $\rho/\rho_0 = 10^{-5}$	303
A-12	Coefficient of viscosity of air; $\rho/\rho_0 = 10^{-6}$	304
A-13	Total coefficient of thermal conductivity of air; $\rho/\rho_0 = 10^{+1}$. . .	305
A-14	Total coefficient of thermal conductivity of air; $\rho/\rho_0 = 10^0$. . .	306
A-15	Total coefficient of thermal conductivity of air; $\rho/\rho_0 = 10^{-1}$. . .	307
A-16	Total coefficient of thermal conductivity of air; $\rho/\rho_0 = 10^{-2}$. . .	308
A-17	Total coefficient of thermal conductivity of air; $\rho/\rho_0 = 10^{-3}$. . .	309
A-18	Total coefficient of thermal conductivity of air; $\rho/\rho_0 = 10^{-4}$ and 10^{-5}	310
A-19	Total coefficient of thermal conductivity of air; $\rho/\rho_0 = 10^{+1}$, 10^0 , 10^{-1} , and 10^{-2}	311
A-20	Prandtl number of air; effects of chemical reaction not included; $\rho/\rho_0 = 10^{+1}$, 10^0 , 10^{-1} , 10^{-2} , 10^{-3} , 10^{-4} , and 10^{-5} . . .	312
A-21	Prandtl number of air including the effects of chemical reaction; $\rho/\rho_0 = 10^0$, 10^{-1} , 10^{-2} , 10^{-3} , 10^{-4} , and 10^{-5} . . .	313
A-22	c_p/R as a function of $T^\circ R$ and $\log \rho/\rho_0$; $\log \rho/\rho_0 = 1.4$ to $+1.6$; $\Delta \log \rho/\rho_0 = +0.2$	314

SYMBOLS

Only those symbols which are frequently used are defined here; all others are defined where they are used.

A	cross-sectional area
a	local velocity of sound; shock radius of curvature
b	radius of curvature of nose of a blunt body
C_F	mean skin friction coefficient
C_f	local skin friction coefficient, p. 11
C_p	pressure coefficient
c_p	specific heat at constant pressure
c_v	specific heat at constant volume
D	drag
g_*	$2\tau(x/p_1\mu_1u_1^3)^{\frac{1}{2}}$, p. 9
H	shape parameter, δ^*/θ
h	enthalpy
K	$\frac{3\gamma-1}{2(\gamma-1)}$, p. 81
k	coefficient of thermal conductivity; height (or characteristic dimension) of a roughness element
k_ϵ	eddy viscosity
ℓ	reference length; p. 7; mixing length, p. 29; shear parameter, p. 80
M	Mach number
m	velocity exponent, p. 80
N	momentum parameter, p. 81
n	pressure gradient parameter, p. 80; velocity exponent, p. 41
Pr	Prandtl number
p	pressure

q	heat conduction rate per unit area
R	universal gas constant (for air, 1715 ft ² /s · c ² °F)
Re	Reynolds number, $\rho u \ell / \mu$ (the characteristic dimension, ℓ , is often indicated by the subscript, e.g., Re_θ , Re_ℓ , Re_{x_k})
r	radius of the body measured normal to the axis of symmetry; recovery factor, p. 20
St	Stanton number, $h / c_p \rho_1 u_1$
s	non-dimensional thickness of the laminar sublayer
T	temperature
T_∞	Sutherland's constant (~198.6°R for air)
t	time; thickness of the leading edge
u	component of velocity in x-direction or along a surface
u_τ	friction velocity, p. 30
v	component of velocity in y-direction or normal to a surface
w	component of velocity in z-direction
x	distance measured along the surface
y	distance measured normal to the surface
Z	compressibility (pV/RT)
α	angle of attack, exponent of Pr, p. 196
β	T_k/T_1 , p. 18
γ	ratio of specific heats (c_p/c_v)
δ	boundary-layer thickness
δ_ℓ	thickness of the laminar sublayer
δ^*	boundary-layer displacement thickness, p. 11
η	non-dimensional form of y, p. 30
θ	boundary-layer momentum thickness, p. 11
Λ	sweep angle
μ	coefficient of viscosity

μ_e	eddy viscosity
ν	kinematic velocity
ξ	angle between center line and the normal to a curve
ρ	density
σ	normal stress; cone semi-angle; Mach number function, p. 30
τ	shear stress
τ_e	Reynolds stress, p. 14
Φ	dissipation function, p. 5
φ	u/u_τ , p. 30
ψ	stream function
ω_s	shock-wave angle

Subscripts

1	conditions at the outer edge of the boundary layer
o	sea-level values
∞	free-stream conditions
*	normalized with respect to conditions at the outer edge of the boundary layer
c	conditions along a sharp cone
e	equilibrium conditions
fr	fully rough surface
i	incompressible values
k	roughness
L	laminar flow
l	laminar sublayer
s	shock-wave conditions; smooth surface
sp	stagnation point of a blunt body
T	turbulent flow

t	total or stagnation value
tr	transition
w	conditions at the wall
ϵ	eddy conditions in turbulent flow

Superscripts

'	differentiation with respect to u_* ; reference value, p. 21; fluctuating value, p. 13
o	sharp cone conditions.

SECTIONS 13 and 14: VISCOSITY AND HEAT TRANSFER EFFECTS

1. Introduction

Although the equations of motion for compressible flows under the effects of friction were derived long ago, mathematical difficulties stand in the way of complete solution. In the last two decades, much intensive effort has been devoted to study of viscous effects in high-speed flows. Special cases and simplifying assumptions have allowed theoretical analyses to be made which have been favorably compared with experimental results. The technical literature contains a great many papers reporting the results of such theoretical and experimental investigations. Nearly two hundred papers are discussed in these sections and are listed at their conclusion. Within these referenced reports, further bibliographies may be found. In addition to these somewhat limited studies, several excellent reference books have been written which give a more comprehensive treatment of various aspects of the subject. Two of these books have already been used as Refs. 2 and 122, others are listed in the order of their publication as Refs. 199 through 203. Since such literature is readily available, no attempt is made in these sections of the Handbook to reproduce detailed theoretical treatments. Rather, the emphasis is placed on the presentation of theoretical and experimental results which can be used by the missile designer for the calculation of skin friction and heat transfer.

1.1 Scope of Contents

Although theoretical derivations have been kept to a minimum, various forms of the boundary-layer equations and momentum-integral equations are reproduced for ready reference. These equations form the basis of the various theoretical results which are presented and are included so that the assumptions underlying the specific cases considered in subsequent subsections may be readily apparent. Boundary-layer growth and skin friction is first treated for the case of smooth flat plates with laminar and turbulent flows of both real and perfect gases. The flow over two-dimensional and axisymmetric bodies is treated next. The results obtained from theoretical considerations are substantiated wherever possible by experimental data. Sample calculations are given in some instances.

Since the transition from laminar to turbulent flow has such marked effects on boundary-layer growth, skin friction, and heat transfer, an entire subsection is devoted to the current knowledge of transition. Since there is at present no theory which can predict the onset and termination of the transition process, the material presented is, of necessity, limited to empirical and experimental data. Due to the large number of parameters which influence transition, correlation of experimental results is difficult. However, an attempt has been made to classify the limited data which are available and thus make them as fruitful as possible. In many cases no conclusions can be drawn from the data, but they are presented not only to show the lack of conclusive evidence but also in order that they may be available for comparison with the results of future investigations. Methods are given for determining the mean skin friction on surfaces with mixed flows. It is shown that one of the factors which has a large effect on transition is surface roughness.

In addition to affecting the transition from laminar to turbulent flow, roughness can also have a marked effect on the characteristics of fully turbulent boundary layer. The effect of roughness on the growth of turbulent boundary layer is treated as fully as possible. Graphs are presented by which both the local and the total skin friction coefficient on sand roughened insulated flat plates may be determined for a wide range of Mach numbers and Reynolds numbers.

The somewhat detailed presentation of results on boundary-layer growth and skinfriction allow the subject of heat transfer to be more briefly treated. The cases for which the effects of heat transfer are presented parallel those for which skin friction effects were treated, i. e., the flat plate, two-dimensional, and axisymmetric bodies with laminar and turbulent flows of real and perfect gases. In addition, several subjects particularly significant with respect to heat transfer are discussed. Among these are the effect of body angle of attack and the effect of sweep on heat transfer, heat transfer rates in separated flows, and near protuberances.

The most recently available information on some of the thermodynamic and the transport properties of air at high temperatures has been compiled by the Handbook Staff and is presented in Appendix A (p. 253). The sources from which further data may be obtained are listed in Tables A-2 and A-3.

2. Boundary-Layer Equations

In this subsection the general equations of continuity, momentum, and energy are given for a compressible viscous fluid. These general equations may be re-expressed in many forms which either exhibit the flow properties under certain given conditions or are more amenable to certain required operations. The forms of the equations given in this subsection are those which will be used in the subsequent analyses of the boundary layer. By means of simplifying assumptions, the general equations may be reduced for the case of two-dimensional steady laminar flow over a flat or a simple curved surface. By means of suitable transformations of the variables they may be applied to flow along an axisymmetric surface or to flow in the (x, u) plane, or they may be reduced to a form which is independent of the compressibility. If each velocity component is assumed to be made up of a slowly varying average value and an instantaneous fluctuation from the mean, it is shown that the general equations may also be used to represent turbulent flow.

2.1 Continuity, Momentum, and Energy Equations in Viscous Flow

The equations of continuity, momentum, and energy which are presented here are based on the following assumptions or limitations:

1. The flow is unsteady, i.e., varies with time;
2. The gas is compressible;
3. It is Newtonian gas, i.e., the shear stress, τ , and the viscosity, μ , are related to the velocity field by Newton's friction law:

$$\tau = \mu \frac{du}{dy} \quad (2-1)$$

4. Body forces, i.e., forces such as gravity acting throughout the mass of the gas, are negligible;
5. The gas is everywhere in chemical equilibrium and the state variables are not affected by diffusion.

The continuity equation which expresses the conservation of mass is given by

$$\frac{D\rho}{Dt} + \rho \operatorname{div} W = 0 \quad (2-2)$$

where

W = the velocity vector whose axial components are u , v , and w

$$\frac{D}{Dt} = \frac{\partial}{\partial t} + u \frac{\partial}{\partial x} + v \frac{\partial}{\partial y} + w \frac{\partial}{\partial z}$$

and

$$\operatorname{div} W = \frac{\partial u}{\partial x} + \frac{\partial v}{\partial y} + \frac{\partial w}{\partial z}$$

The three equations of motion which express the conservation of momentum have been fully derived by Schlichting in Chapter III of Ref. 1. They are:

$$\left. \begin{aligned} \rho \frac{Du}{Dt} &= \frac{\partial}{\partial x} (\sigma_x) + \frac{\partial}{\partial y} (\tau_{xy}) + \frac{\partial}{\partial z} (\tau_{zx}) \\ \rho \frac{Dv}{Dt} &= \frac{\partial}{\partial y} (\sigma_y) + \frac{\partial}{\partial x} (\tau_{xy}) + \frac{\partial}{\partial z} (\tau_{yz}) \\ \rho \frac{Dw}{Dt} &= \frac{\partial}{\partial z} (\sigma_z) + \frac{\partial}{\partial x} (\tau_{zx}) + \frac{\partial}{\partial y} (\tau_{yz}) \end{aligned} \right\} \quad (2-3)$$

where

$\sigma_x, \sigma_y, \sigma_z$ = stresses normal to the $yz, zx,$ and xy planes, respectively

τ_{zx} = shearing stress in the xy plane, parallel to the x axis, etc.

The normal stresses are given by

$$\left. \begin{aligned} \sigma_x &= -p + 2\mu \frac{\partial u}{\partial x} - \frac{2}{3} \mu \operatorname{div} W \\ \sigma_y &= -p + 2\mu \frac{\partial v}{\partial y} - \frac{2}{3} \mu \operatorname{div} W \\ \sigma_z &= -p + 2\mu \frac{\partial w}{\partial z} - \frac{2}{3} \mu \operatorname{div} W \end{aligned} \right\} \quad (2-4)$$

and the shear stresses are

$$\left. \begin{aligned} \tau_{yx} = \tau_{xy} &= \mu \left(\frac{\partial u}{\partial y} + \frac{\partial v}{\partial x} \right) \\ \tau_{zy} = \tau_{yz} &= \mu \left(\frac{\partial v}{\partial z} + \frac{\partial w}{\partial y} \right) \\ \tau_{zx} = \tau_{xz} &= \mu \left(\frac{\partial w}{\partial x} + \frac{\partial u}{\partial z} \right) \end{aligned} \right\} \quad (2-5)$$

Substitution of the above expressions for the normal stresses and the shear stresses in Eq. 2-3 results in the following set of equations:

$$\left. \begin{aligned} \rho \frac{Du}{Dt} &= -\frac{\partial p}{\partial x} + \frac{\partial}{\partial x} \left[\mu \left(2 \frac{\partial u}{\partial x} - \frac{2}{3} \operatorname{div} W \right) \right] + \frac{\partial}{\partial y} \left[\mu \left(\frac{\partial u}{\partial y} + \frac{\partial v}{\partial x} \right) \right] + \frac{\partial}{\partial z} \left[\mu \left(\frac{\partial w}{\partial x} + \frac{\partial u}{\partial z} \right) \right] \\ \rho \frac{Dv}{Dt} &= -\frac{\partial p}{\partial y} + \frac{\partial}{\partial y} \left[\mu \left(2 \frac{\partial v}{\partial y} - \frac{2}{3} \operatorname{div} W \right) \right] + \frac{\partial}{\partial z} \left[\mu \left(\frac{\partial v}{\partial z} + \frac{\partial w}{\partial y} \right) \right] + \frac{\partial}{\partial x} \left[\mu \left(\frac{\partial u}{\partial y} + \frac{\partial v}{\partial x} \right) \right] \\ \rho \frac{Dw}{Dt} &= -\frac{\partial p}{\partial z} + \frac{\partial}{\partial z} \left[\mu \left(2 \frac{\partial w}{\partial z} - \frac{2}{3} \operatorname{div} W \right) \right] + \frac{\partial}{\partial x} \left[\mu \left(\frac{\partial w}{\partial x} + \frac{\partial u}{\partial z} \right) \right] + \frac{\partial}{\partial y} \left[\mu \left(\frac{\partial v}{\partial z} + \frac{\partial w}{\partial y} \right) \right] \end{aligned} \right\} \quad (2-6)$$

These equations, known as the Navier-Stokes equations, form the basis of the science of fluid mechanics. With Eq. 2-2 and the thermodynamic equation of state, they define all isothermal processes. Where the process is not isothermal, the energy equation must be added to the system.

Howarth in Ref. 2 (pp. 52-55) derives the energy equation, and presents it in several forms. In terms of the enthalpy (h), the heat-conduction rate per unit area (q), and the dissipation function (Φ), it may be written

$$\rho \frac{Dh}{Dt} = \frac{Dp}{Dt} + \frac{\partial}{\partial x} (q_x) + \frac{\partial}{\partial y} (q_y) + \frac{\partial}{\partial z} (q_z) + \Phi \quad (2-7)$$

where

$$q_x = k \frac{\partial T}{\partial x} ; \quad q_y = k \frac{\partial T}{\partial y} ; \quad q_z = k \frac{\partial T}{\partial z}$$

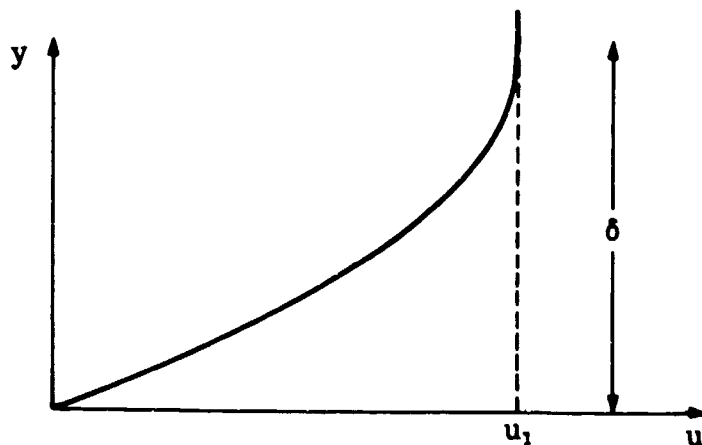
with

k = coefficient of thermal conductivity

and

$$\begin{aligned} \Phi &= (p + \sigma_x) \frac{\partial u}{\partial x} + (p + \sigma_y) \frac{\partial v}{\partial y} + (p + \sigma_z) \frac{\partial w}{\partial z} \\ &\quad + \tau_{yx} \frac{\partial u}{\partial y} + \tau_{xy} \frac{\partial v}{\partial x} + \tau_{zx} \frac{\partial u}{\partial z} + \tau_{xz} \frac{\partial w}{\partial x} + \tau_{zy} \frac{\partial v}{\partial z} + \tau_{yz} \frac{\partial w}{\partial y} \\ &= p \operatorname{div} W + \sigma_x \frac{\partial u}{\partial x} + \sigma_y \frac{\partial v}{\partial y} + \sigma_z \frac{\partial w}{\partial z} + \frac{1}{\mu} (\tau_{xy}^2 + \tau_{yz}^2 + \tau_{zx}^2) . \end{aligned}$$

Where the viscosity of a fluid is small its influence is virtually confined to a thin layer adjacent to a body immersed in the fluid. Beyond this boundary layer the flow may be considered nonviscous and, in the absence of shock waves, isentropic. The thickness, δ , of the boundary layer is in practice fairly easy to determine since the particle velocity rapidly approaches that of the free stream. However, in theory the approach is asymptotic and the limiting value of δ has to be arbitrarily defined. It is often taken in experimental work as the distance from the wall at which the particle velocity is 0.995 of its free-stream value.



In the two-dimensional case, shown in the previous sketch, y is the distance from the wall. When

$$y = 0; \quad u = 0 \quad \text{and} \quad \tau = \mu \frac{\partial u}{\partial y} \quad (\text{no slip at the wall})$$

and when

$$y = \delta; \quad \tau = 0 \quad \text{and} \quad u = u_1 \quad (\text{or } u = 0.995 u_1)$$

When these limiting conditions, together with those of surface shape, are applied to the general equations, specific equations for calculating the properties of the boundary layer may be derived. Several forms of these equations will be given in the following subsections and later they will be used in making boundary-layer calculations for specific types of flow and various surface properties.

2.2 Two-Dimensional, Steady, Laminar Flow

The simplest form of the compressible boundary-layer equations is that for two-dimensional, steady, laminar flow along either a plane or a curved wall where it is assumed that:

1. x is measured along and y normal to the surface.
2. The boundary-layer thickness, δ , is small in comparison with both x and the radius of curvature of the wall.

In this case the continuity equation, Eq. 2-2, reduces to

$$\frac{\partial(\rho u)}{\partial x} + \frac{\partial(\rho v)}{\partial y} = 0 \quad (2-8)$$

The relative magnitudes of the terms of Eq. 2-3 are then assessed. For a full discussion of this see Young (Ref. 2, pp. 379-381). When all but the terms of largest magnitude are rejected, the equations of motion reduce to:

$$\left. \begin{aligned} \rho \left(u \frac{\partial u}{\partial x} + v \frac{\partial u}{\partial y} \right) &= - \frac{\partial p}{\partial x} + \frac{\partial \tau}{\partial y} \\ \frac{\partial p}{\partial y} &= 0 \end{aligned} \right\} \quad (2-9)$$

and

where

$$\tau = \tau_{yx} = \tau_{xy} = \mu \frac{\partial u}{\partial y}$$

The energy equation, Eq. 2-7, becomes

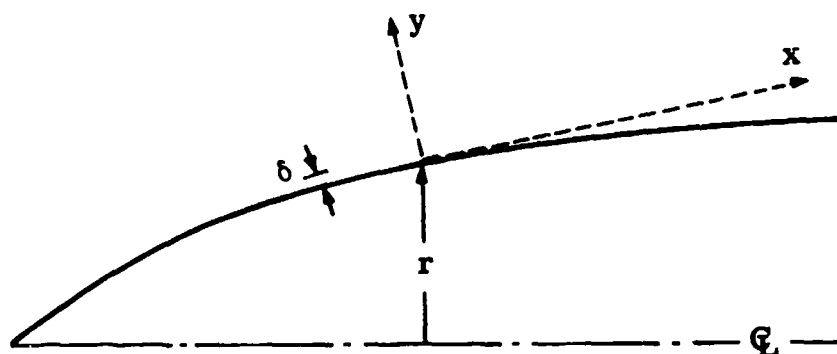
$$\rho \left(u \frac{\partial h}{\partial x} + v \frac{\partial h}{\partial y} \right) = u \frac{\partial p}{\partial x} + \frac{\partial q}{\partial y} + \tau \frac{\partial u}{\partial y} \quad (2-10)$$

where

$$q = q_y = k \frac{\partial T}{\partial y}$$

2.3 Axisymmetric, Steady, Laminar Flow

The boundary-layer equations for axisymmetric, steady, laminar flow over a body of revolution are of wide practical interest. The assumptions upon which they depend are the same as those of the preceding subsection with one additional limitation, i.e., δ is also small compared with r , the radius of the body measured normal to the axis of symmetry (see sketch below).



In axisymmetric flow the equations of motion and energy are identical to Eqs. 2-9 and 2-10, but the continuity equation (Eq. 2-8) becomes

$$\frac{\partial}{\partial x} (r\rho u) + \frac{\partial}{\partial y} (r\rho v) = 0 \quad (2-11a)$$

Since r is a function only of x this may be reduced to

$$\frac{\partial}{\partial x} (\rho u) + \frac{\partial}{\partial y} (\rho v) + \frac{\rho u}{r} \frac{\partial r}{\partial x} = 0 \quad (2-11b)$$

The presence of the last term in Eq. 2-11b makes the solution of this set of equations one step more difficult than that of the set of Eqs. 2-8 to 2-10. By means of a transformation of variables suggested by Mangler (Ref. 3), the axisymmetric set of equations may be reduced to a form identical with the two-dimensional set, thus permitting the use of the same solution.

The Mangler variables are

$$\tilde{x} = \int_0^x \frac{r^2}{l^2} dx, \quad \text{and} \quad \tilde{y} = \frac{r}{l} y$$

where l is a reference length. It follows that,

$$\tilde{p}(\tilde{x}) = p(x); \quad \tilde{h}(\tilde{x}, \tilde{y}) = h(x, y); \quad \tilde{T}(\tilde{x}, \tilde{y}) = T(x, y); \quad \tilde{\rho}(\tilde{x}, \tilde{y}) = \rho(x, y);$$

$$\tilde{\mu}(\tilde{x}, \tilde{y}) = \mu(x, y); \quad \tilde{k}(\tilde{x}, \tilde{y}) = k(x, y); \quad \tilde{\tau} = \tilde{\mu} \frac{\partial \tilde{u}}{\partial \tilde{y}}; \quad \tilde{q} = \tilde{k} \frac{\partial \tilde{T}}{\partial \tilde{y}}$$

Equations 2-9, 2-10, and 2-11b transform to

$$\frac{\partial}{\partial \tilde{x}} (\tilde{\rho} \tilde{u}) + \frac{\partial}{\partial \tilde{y}} (\tilde{\rho} \tilde{v}) = 0 \quad (2-12)$$

$$\left. \begin{aligned} \tilde{\rho} \left(\tilde{u} \frac{\partial \tilde{u}}{\partial \tilde{x}} + \tilde{v} \frac{\partial \tilde{u}}{\partial \tilde{y}} \right) &= - \frac{\partial \tilde{p}}{\partial \tilde{x}} + \frac{\partial \tilde{\tau}}{\partial \tilde{y}} \\ \frac{\partial \tilde{p}}{\partial \tilde{y}} &= 0 \end{aligned} \right\} \quad (2-13)$$

$$\tilde{\rho} \left(\tilde{u} \frac{\partial \tilde{h}}{\partial \tilde{x}} + \tilde{v} \frac{\partial \tilde{h}}{\partial \tilde{y}} \right) = \tilde{u} \frac{\partial \tilde{p}}{\partial \tilde{x}} + \frac{\partial \tilde{q}}{\partial \tilde{y}} + \tilde{\tau} \frac{\partial \tilde{u}}{\partial \tilde{y}} \quad (2-14)$$

which are of the same form as the two-dimensional equations (Eqs. 2-8 to 2-10) and therefore have a similar solution.

2.4 Two-Dimensional, Steady, Laminar Flow in the (x, u) Plane

For the case of two-dimensional, steady, laminar flow, Crocco in Ref. 4 reduced the equations of continuity, motion, and energy to two equations by taking x and u as the independent variables. With the transformation

$$\left. \begin{aligned} x &= x \\ u &= u(x, y) \end{aligned} \right\}$$

and making use of the relations

$$h = h(p, T)$$

and

$$c_p = \left(\frac{\partial h}{\partial T} \right)_{p=\text{const.}}$$

which hold both for a perfect gas and for a real gas in chemical equilibrium, Eqs. 2-8 to 2-10 reduce to

$$u \frac{\partial}{\partial x} \left(\frac{\mu \rho}{\tau} \right) + \frac{\partial^2 \tau}{\partial u^2} - \frac{\partial p}{\partial x} \cdot \frac{\partial}{\partial u} \left(\frac{\mu}{\tau} \right) = 0 \quad (2-15)$$

and

$$\frac{\partial}{\partial u} \left(\frac{1}{Pr} \tau \frac{\partial h}{\partial u} \right) - \frac{\partial \tau}{\partial u} \frac{\partial h}{\partial u} + \tau - \frac{\mu \rho u}{\tau} \frac{\partial h}{\partial x} + \frac{\mu}{\tau} \left(\frac{\partial h}{\partial u} + u \right) \frac{\partial p}{\partial x} = 0 \quad (2-16)$$

where

$$\text{Pr} = \frac{\mu c_p}{k} = \text{Prandtl number}$$

The method of transformation is presented in detail in Ref. 4.

For the case of the flat plate ($\partial p / \partial x = 0$) on which the enthalpy at the wall, h_w , is constant, the enthalpy profiles in the boundary layer and also the velocity profiles are similar for all values of x . Under these conditions

$$h = h(u); \quad \rho = \rho(h) = \rho(u); \quad \mu = \mu(h) = \mu(u);$$

and

$$\text{Pr} = \text{Pr}(h) = \text{Pr}(u)$$

Eqs. 2-15 and 2-16 then reduce to two ordinary differential equations (see Ref. 4). In non-dimensional form they are given by:

$$g_* g_*'' + 2u_* \rho_* \mu_* = 0 \quad (2-17)$$

and

$$\frac{d}{du_*} \left[\frac{1}{\text{Pr}} g_* h_*' \right] - g_*' h_*' + \frac{u_*^2}{h_1} g_* = 0 \quad (2-18)$$

where

$$g_* = 2\tau \sqrt{\frac{x}{\rho_1 \mu_1 u_1^3}}$$

and

$$u_* = u/u_1; \quad h_* = h/h_1; \quad \rho_* = \rho/\rho_1; \quad \mu_* = \mu/\mu_1$$

The subscript $_1$ denotes conditions at the outer edge of the boundary layer, and the primes denote differentiation with respect to u_* . The boundary conditions for Eqs. 2-17 and 2-18 are as follows:

$$\text{when } u_* = 0; \text{ then } g_*' = 0 \text{ and } h_* = h_w/h_1 = 0$$

$$\text{and when } u_* = 1; \text{ then } g_* = 0 \text{ and } h_* = 1$$

For the case of constant Prandtl number, Eq. 2-18 becomes

$$\left(h_*' + \text{Pr} \frac{u_*^2}{h_1} \right) g_* + (1 - \text{Pr}) g_*' h_*' = 0 \quad (2-19)$$

Given the thermodynamic and transport data for a gas (see Appendix A), Eq. 2-17 with either Eq. 2-18 or Eq. 2-19 can be integrated numerically. The numerical solutions will yield velocity profiles, enthalpy profiles, rates of heat transfer to the surface, and the shear stress on the surface.

When $Pr = 1$ and $g_* \neq 0$, Eq. 2-19 becomes

$$h_*'' + \frac{u_1^2}{h_1} = 0 \quad (2-20)$$

Equation 2-20 is independent of Eq. 2-17 and can be integrated at once to give the static enthalpy as a function of the velocity, i.e.,

$$h_* = h_{*w} - (h_{*w} - 1) u_* + \frac{u_1^2}{2h_1} (u_* - u_*^2) \quad (2-21)$$

where subscript w denotes conditions at the wall.

The total enthalpy is defined as

$$h_t = h + \frac{u^2}{2}$$

and thus

$$h_{t*} = h_t / h_{t_1} = \frac{h_* + \frac{u_1^2}{2h_1} u_*^2}{1 + \frac{u_1^2}{2h_1}}$$

In terms of the total enthalpy, Eq. 2-21 reduces to

$$h_{t*} = h_{t*w} + u_* \left(1 - h_{t*w} \right) \quad (2-22)$$

For a calorifically perfect gas, the enthalpy ratios in Eqs. 2-18 to 2-22 can be replaced by temperature ratios and in this case

$$\frac{u_1^2}{2h_1} = \frac{\gamma - 1}{2} M_1^2 \quad (2-23)$$

2.5 The Momentum Integral Equation

The boundary-layer equations so far derived have expressed the conditions that exist from point to point throughout the viscous region. Their solutions are cumbersome and time-consuming except under very special circumstances. On the other hand, the momentum equation or von Karman's integral condition as it is sometimes called, expresses an average effect of the particle flows and satisfies the conditions of the differential equations at the two boundaries of the viscous stratum, i.e., at the wall and at the transition to the external flow. While the integral method furnishes fairly accurate information on such properties as skin friction, heat transfer, and boundary-layer thickness, it is not able to give velocity or temperature profiles or to explain what happens within the friction layer itself. Since the momentum integral equation is developed without the necessity of assuming a relationship for the shear stress, the results may be applied to both laminar and turbulent flow.

At this point it is helpful to define two further quantities: the boundary-layer momentum thickness given by:

$$\theta = \int_0^{\delta} \frac{\rho u}{\rho_1 u_1} \left(1 - \frac{u}{u_1}\right) dy \quad (2-24)$$

and the boundary-layer displacement thickness given by:

$$\delta^* = \int_0^{\delta} \left(1 - \frac{\rho u}{\rho_1 u_1}\right) dy \quad (2-25)$$

The ratio δ^*/θ is called the shape parameter and is usually written as H.

2.5.1 Axisymmetric Compressible Steady Flow

The momentum integral equation for flow over axisymmetric bodies may be obtained easily from first principles or may be obtained by multiplying Eq. 2-11b by $(u_1 - u)$ and subtracting Eq. 2-9 from the product. Integration across the boundary layer results in

$$\frac{d\theta}{dx} + \frac{\theta}{\rho_1 u_1^2} \frac{d}{dx} (\rho_1 u_1^2) - \frac{1}{u_1} \frac{du_1}{dx} \int_0^{\delta} \frac{\rho u}{\rho_1 u_1} dy + \frac{\theta}{r} \frac{dr}{dx} - \frac{\delta}{\rho_1 u_1^2} \frac{dp}{dx} = \frac{C_f}{2} - \frac{\tau_1}{\rho_1 u_1^2} \quad (2-26)$$

where C_f is the local skin friction coefficient defined by:

$$C_f = \frac{\tau_w}{\frac{1}{2}(\rho_1 u_1^2)}$$

At $y = 0$: $u = 0$ and $\tau = \tau_w$;

at $y = \delta$: $u = u_1$ and $\tau = \tau_1$

Equation 2-26 is valid for both laminar and turbulent flow since it was unnecessary to assume a relation for the shear stress, τ .

When $\partial u / \partial y = 0$ at the outer edge of the boundary layer, then $\tau_1 = 0$ and Eq. 2-9 becomes

$$\rho_1 u_1 \frac{\partial u_1}{\partial x} = - \frac{\partial p}{\partial x} \quad (2-27)$$

and Eq. 2-26 may be written as

$$\frac{d\theta}{dx} - \frac{\theta}{\rho_1 u_1^2} \left[\left(2 + \frac{\delta^*}{\theta}\right) \frac{dp}{dx} - u_1^2 \frac{d\rho}{dx} \right] + \frac{\theta}{r} \frac{dr}{dx} = \frac{C_f}{2} \quad (2-28)$$

For an isentropic external flow of a calorifically perfect gas this becomes

$$\frac{d\theta}{dx} + \frac{\theta}{M_1} \left[\frac{H + 2 - M_1^2}{1 + \frac{\gamma - 1}{2} M_1^2} \right] \frac{dM_1}{dx} + \frac{\theta}{r} \frac{dr}{dx} = \frac{C_f}{2} \quad (2-29)$$

The boundary-layer flow over a slender, slightly blunted cone will be discussed in Subsec. 4 with the assumptions that the gas is calorifically perfect and adiabatic outside the boundary layer and also that $dp/dx = 0$. With these assumptions Eq. 2-26 becomes

$$\frac{d\theta}{dx} + \frac{\theta}{M_1} \left[2 - \frac{\delta/\theta - H}{1 + \frac{\gamma - 1}{2} M_1^2} \right] \frac{dM_1}{dx} + \frac{\theta}{r} \frac{dr}{dx} = \frac{C_f}{2} - \frac{\tau_1}{\rho_1 u_1^2} \quad (2-30)$$

Given the flow conditions outside the boundary layer and relations for C_f , H , and δ/θ , the above equations can be integrated along the surface to determine the boundary-layer growth.

2.5.2 Two-Dimensional Flow

The momentum integral equations for two-dimensional flow can be obtained immediately by putting $\frac{\theta}{r} \frac{dr}{dx} = 0$ in Eqs. 2-26, 2-28, 2-29, and 2-30.

2.5.3 Transformations of the Integral Momentum Equation

Two transformations of the momentum integral equation are frequently used. The first is the Mangler transformation (see Subsec. 2.3) by which the axisymmetric equation may be reduced to the form of a two-dimensional equation and thus more easily solved. The second is a transformation evolved by Stewartson (Ref. 6) by which the compressible two-dimensional momentum integral equation is transformed into one which is identical with its incompressible counterpart. Stewartson's method was modified by Cohen and Reshotko (Ref. 7) who used the following transformations:

$$\bar{x} = \int_0^x \lambda \frac{a_1}{a_{t_1}} \frac{p}{p_{t_1}} dx; \quad \bar{y} = \frac{a_1}{a_{t_1}} \int_0^y \frac{\rho}{\rho_{t_1}} dy;$$

$$\bar{u} = \frac{a_{t_1}}{a_1} u$$

where a = velocity of sound.

The assumed viscosity law is given by

$$\frac{\mu}{\mu_{t_1}} = \lambda \frac{T}{T_{t_1}} \quad (2-31)$$

The value of λ in any particular case is determined from the Sutherland formula in terms of T_w and T_{t_1} , i.e.,

$$\frac{\mu_w}{\mu_{t_1}} = \left(\frac{T_w}{T_{t_1}} \right)^{3/2} \left[\frac{T_{t_1} + T_k}{T_w + T_k} \right] = \lambda \frac{T_w}{T_{t_1}} \quad (2-32)$$

Here T_k = Sutherland's constant = 198.6°R for air. The transformed momentum integral equation which is identical in form to the incompressible flow equation becomes

$$\frac{d\bar{\theta}}{d\bar{x}} + \frac{\bar{\theta}}{\bar{u}_1} \frac{d\bar{u}}{d\bar{x}} (\bar{H} + 2) = \frac{\bar{C}_f}{2} \quad (2-33)$$

where

$$\bar{\theta} = \int_0^{\bar{\delta}} \frac{\bar{u}}{\bar{u}_1} \left(1 - \frac{\bar{u}}{\bar{u}_1} \right) d\bar{y} = \theta \left(\frac{T_1}{T_{t_1}} \right)^{\frac{\gamma+1}{2(\gamma-1)}}$$

$$\bar{\delta}^* = \int_0^{\bar{\delta}} \left(\frac{h_t}{h_{t_1}} - \frac{\bar{u}}{\bar{u}_1} \right) d\bar{y}$$

$$\bar{H} = \bar{\delta}^* / \bar{\theta}$$

$$\bar{C}_f = \frac{\mu_{t_1} \left(\frac{\partial \bar{u}}{\partial \bar{y}} \right)_w}{\frac{1}{2} \rho_{t_1} \bar{u}_1^2} = \frac{1}{\lambda} \left(\frac{T_{t_1}}{T_1} \right)^{\frac{2\gamma-1}{\gamma-1}} \cdot C_f$$

2.6 Two-Dimensional Turbulent Flow

Turbulent motion may be represented by assuming that each velocity component and each thermodynamic variable has a time-averaged value plus a fluctuation, i.e.,

$$u = \bar{u} + u', \quad v = \bar{v} + v', \quad p = \bar{p} + p', \quad \mu = \bar{\mu} + \mu', \text{ etc.} \quad (2-34)$$

where

$$\bar{u} = \frac{1}{\Delta t} \int_{t-\frac{\Delta t}{2}}^{t+\frac{\Delta t}{2}} u \, dt \quad (2-35)$$

and Δt is a time interval which is large compared with the period of fluctuation. It is further assumed that

1. The mean flow is steady, i.e., $\partial \bar{u} / \partial t = 0$
2. The averages of the fluctuations are zero, i.e., $\bar{u}' = 0$, etc.,
3. The boundary layer is thin, and
4. x is measured along the surface and y normal to it.

The values from Eqs. 2-34 are substituted in the following form of the equation for the momentum in the x -direction:

$$\frac{\partial}{\partial t} (\rho u) + \frac{\partial}{\partial x} (\rho u^2) + \frac{\partial}{\partial y} (\rho uv) = - \frac{\partial p}{\partial x} + \frac{\partial \tau}{\partial y}$$

The resulting equation reduces (see Ref. 1 or 5 for details) to the form

$$\bar{\rho u} \frac{\partial \bar{u}}{\partial x} + \bar{\rho v} \frac{\partial \bar{u}}{\partial y} = - \frac{\partial \bar{p}}{\partial x} + \frac{\partial \bar{\tau}}{\partial y} - \frac{\partial}{\partial y} \overline{(\rho v)' u'} \quad (2-36)$$

which may be seen to correspond to Eq. 2-9 if the viscous stress may be regarded as

$$\left(\bar{\tau} - \overline{(\rho v)' u'} \right)$$

The additional term, $-\overline{(\rho v)' u'}$, is known as the apparent stress or the virtual stress of turbulent flow or more simply as the Reynolds stress. Then

$$-\overline{(\rho v)' u'} = \tau_e = \mu_e \frac{\partial \bar{u}}{\partial y} \quad (2-37)$$

where

μ_e is known as the eddy viscosity which unlike μ is not a property of the fluid.

The Reynolds stresses far outweigh the viscous term, which is usually neglected, i.e.,

$$\bar{\mu} \frac{\partial \bar{u}}{\partial y} \approx 0$$

The momentum in the y -direction reduces as before to

$$\frac{\partial \bar{p}}{\partial y} = 0$$

The cumbersome transformation of the energy equation is given in detail in Ref. 8. By means of the transformation the time-mean equation becomes

$$\bar{\rho} \bar{u} \frac{\partial \bar{h}}{\partial x} + \bar{\rho} \bar{v} \frac{\partial \bar{h}}{\partial y} = \bar{u} \frac{\partial \bar{p}}{\partial x} + \frac{\partial}{\partial y} \left(\bar{k} \frac{\partial \bar{T}}{\partial y} \right) + \bar{\tau} \frac{\partial \bar{u}}{\partial y} + \frac{\partial}{\partial y} \left[- \overline{(\rho v)' h'} - \overline{(\rho v)' u'} \frac{\partial \bar{u}}{\partial y} \right] \quad (2-38)$$

and as before this is of the same form as the laminar equation if the heat flux is taken to be

$$\left(k \frac{\partial \bar{T}}{\partial y} - \overline{(\rho v)' h'} \right)$$

and the shear stress as $\tau = \overline{(\rho v)' u'}$. The latter has already been discussed; the former leads to the definition of the apparent heat flux, i.e.,

$$q_\epsilon = - \overline{(\rho v)' h'} = k_\epsilon \frac{\partial \bar{T}}{\partial y}$$

where q_ϵ is much larger than $k(\partial \bar{T}/\partial y)$, which term may then be neglected. The coefficient k_ϵ is known as the eddy conductivity.

The two-dimensional turbulent boundary-layer equations thus become

$$\frac{\partial}{\partial x} (\bar{\rho} \bar{u}) + \frac{\partial}{\partial y} (\bar{\rho} \bar{v}) = 0 \quad (2-39)$$

$$\bar{\rho} \bar{u} \frac{\partial \bar{u}}{\partial x} + \bar{\rho} \bar{v} \frac{\partial \bar{u}}{\partial y} = - \frac{\partial \bar{p}}{\partial x} + \frac{\partial}{\partial y} (\mu_\epsilon \frac{\partial \bar{u}}{\partial y}) \quad (2-40)$$

and

$$\bar{\rho} \bar{u} \frac{\partial \bar{h}}{\partial x} + \bar{\rho} \bar{v} \frac{\partial \bar{h}}{\partial y} = \bar{u} \frac{\partial \bar{p}}{\partial x} + \frac{\partial}{\partial y} (k_\epsilon \frac{\partial \bar{T}}{\partial y}) + \mu_\epsilon \left(\frac{\partial \bar{u}}{\partial y} \right)^2 \quad (2-41)$$

These equations are of the same form as the laminar equations. The solutions for the equations of the turbulent boundary layer on a flat plate will be discussed in Subsecs. 3.3 and 3.4 for the cases of a perfect gas and a real gas.

2.6.1 Two-Dimensional Turbulent Flow in the (x, \bar{u}) Plane

The Crocco transformation (see Subsec. 2.4) may also be applied to the turbulent boundary-layer equations. With the transformation

$$\left. \begin{aligned} x &= x \\ \bar{u} &= \bar{u}(x, y) \end{aligned} \right\}$$

Equations 2-39 and 2-40 reduce to

$$\frac{\partial}{\partial x} \left(\frac{\mu_\epsilon}{\tau_\epsilon} \bar{\rho} \bar{u} \right) + \frac{\partial^2}{\partial \bar{u}^2} (\tau_\epsilon) - \frac{\partial p}{\partial x} \cdot \frac{\partial}{\partial \bar{u}} \left(\frac{\mu_\epsilon}{\tau_\epsilon} \right) = 0 \quad (2-42)$$

and

$$\frac{\partial}{\partial \bar{u}} \left(\frac{\tau_\epsilon}{Pr_\epsilon} \frac{\partial \bar{h}}{\partial \bar{u}} \right) - \frac{\partial \tau_\epsilon}{\partial \bar{u}} \frac{\partial \bar{h}}{\partial \bar{u}} + \tau_\epsilon - \frac{\mu_\epsilon}{\tau_\epsilon} \bar{\rho} \bar{u} \frac{\partial \bar{h}}{\partial x} + \frac{\mu_\epsilon}{\tau_\epsilon} \left(\frac{\partial \bar{h}}{\partial \bar{u}} + \bar{u} \right) \frac{\partial p}{\partial x} = 0 \quad (2-43)$$

where

$$Pr_\epsilon = \frac{\mu_\epsilon c_p}{k_\epsilon}$$

Equations 2-42 and 2-43 have the same form as Eqs. 2-15 and 2-16. For isentropic flow over a flat plate, $\partial p / \partial x$ is zero and $\partial \bar{h} / \partial x$ nearly zero and hence Eq. 2-43 becomes

$$\tau_\epsilon \left[\frac{\partial}{\partial \bar{u}} \left(\frac{1}{Pr_\epsilon} \frac{\partial \bar{h}}{\partial \bar{u}} \right) + 1 \right] + \left(\frac{1 - Pr_\epsilon}{Pr_\epsilon} \right) \frac{\partial \bar{h}}{\partial \bar{u}} \frac{\partial \tau_\epsilon}{\partial \bar{u}} = 0 \quad (2-44)$$

For $Pr_\epsilon = 1$, this reduces to

$$\frac{\partial^2 \bar{h}}{\partial \bar{u}^2} + 1 = 0 \quad (2-45)$$

Integration of Eq. 2-45 gives the same variation of enthalpy with velocity as in the laminar boundary layer (see Eqs. 2-21 and 2-22).

3. Solutions to the Flat Plate Boundary-Layer Equations

Although solutions to the general boundary-layer equations present many difficulties, there are approximations and simplifications which reduce them to forms that may be solved. One frequent simplification is that of zero pressure and temperature gradients on the surface. For two-dimensional flow this is the flat plate. This subsection will discuss laminar and turbulent flows of both perfect and real gases over a flat plate.

The perfect gas is assumed to be both thermally and calorifically perfect. In addition, the Prandtl number is taken to be constant. The perfect gas assumptions hold only for a moderate range of temperatures. To be consistent, expressions for the transport properties need to be accurate only in the same temperature range. With the above assumptions, viscosity is the only transport property required for the solution of perfect gas flow equations. Many authors have assumed that viscosity varies linearly with temperature. Others have taken it to be proportional to some fractional power of the temperature. Since these representations are accurate only for narrow temperature ranges, still others have used Sutherland's viscosity law. For air, this law gives accurate values of viscosity over a somewhat wider range of temperatures than that for which the perfect gas assumptions remain valid. Sutherland's law is used for the perfect gas flat plate calculations discussed in this subsection.

For the real gas solutions, the gas is assumed to be in thermodynamic equilibrium. The values of any two state variables, therefore, define the thermodynamic state of the gas. However, no simple analytic equation of state exists. The thermodynamic data must be taken from tables, from a Mollier chart, or calculated from expressions which have been fitted to experimental data. Furthermore, there are no simple analytic expressions for the transport properties. These data must also be taken from tables or graphical presentations based on experimental data. In the solutions of the real gas boundary-layer equations, both viscosity and conductivity data are required. The values of two state variables are required to specify values of the transport properties. Tabulated values of the thermodynamic and transport properties of air at temperatures up to 9000°R are given in Section 15 of the Handbook (Ref. 39). Subsequent investigations have shown that the energy of dissociation used in these tables is too low; consequently, the data are doubtful at temperatures above about 3000°R. The gas properties are discussed further in Appendix A (p. 253) of this Section. They are evaluated not only at much higher temperatures than before but also in the light of recent experimental evidence.

3.1 Laminar Boundary Layer on a Flat Plate -- Perfect Gas

Crocco expressed the boundary-layer momentum and energy equations in the form given by Eqs. 2-17 and 2-19. They are

$$g_* g_*' + 2u_* \rho_* \mu_* = 0$$

$$\left(h_*' + \text{Pr} \frac{u_*^2}{h_*} \right) g_* + (1 - \text{Pr}) g_*' h_*' = 0$$

The Prandtl number must be assumed to be constant in order to write the energy equation in the foregoing form. For a perfect gas, h_* is of course identical to T_* . These equations were the basis of the theoretical and experimental investigations of the laminar flow of a perfect gas which are to be discussed in this subsection.

If viscosity is assumed to be directly proportional to temperature, then $\rho_* \mu_* = 1$. In this case, the momentum equation reduces to Blasius' equation and can be solved independently of the energy equation. However, it must be integrated numerically. Results are given by Blasius in Ref. 8. If $Pr = 1$, the energy equation is independent of the momentum equation and can be integrated at once to give the static enthalpy as in Eq. 2-21. For values of Pr other than 1, the energy equation is not independent of the momentum equation and must be integrated numerically. From his numerical calculations, Crocco (Ref. 4) obtained the useful result that the solution of the energy equation is essentially independent of the form of the viscosity-temperature relationship. The solution of Blasius' momentum equation can therefore always be used when integrating the energy equation. However, unlike that of the energy equation, the solution of the momentum equation is dependent on the form of the temperature-viscosity relationship. For cases other than $\rho_* \mu_* = 1$, the convenient method of solution is first to integrate the energy equation as above. The value of $\rho_* \mu_*$, which is required for the integration of the momentum equation, can be found when the temperature is known.

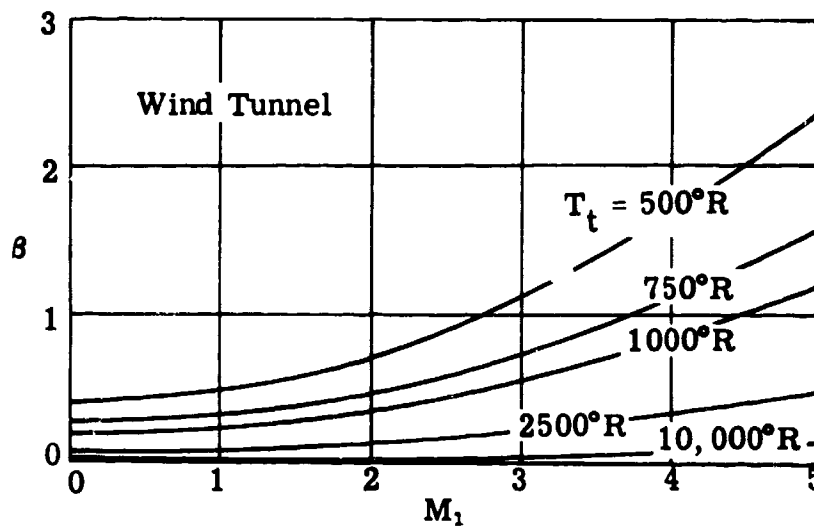
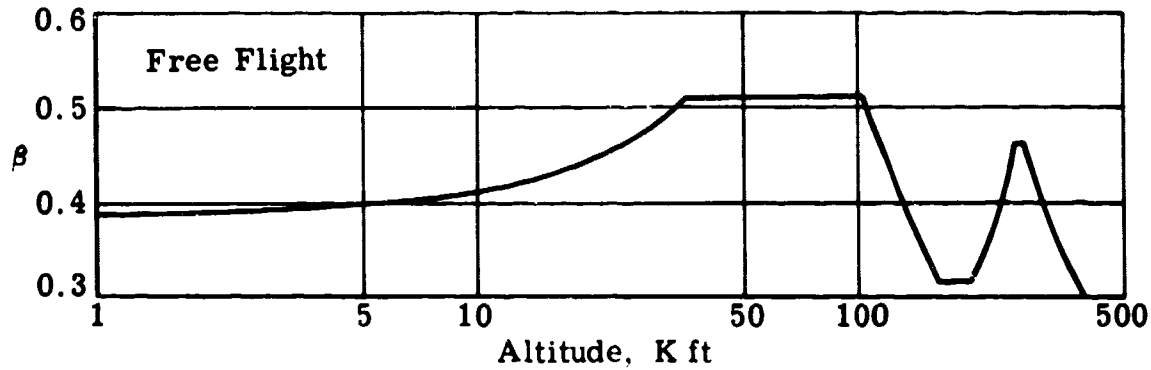
Crocco (Ref. 4) gives solutions to the equations for Pr from 0.5 to 2, and shows the effects of the variations in the dependence of viscosity on temperature. Table 3-1 (p. 53) lists the parameters of the figures which present the results of Crocco's calculations. Note that the ratio $\beta = T_k/T_1$ from the Sutherland law is used as a parameter, and the gas velocity is given in terms of u_1^2/h_1 ; the results are thus not limited to air, but apply to all gases for which the various parameters are realistic.

In 1952 Van Driest used the Crocco method for extensive calculations of the perfect-gas laminar boundary layer. His results, given graphically in Ref. 9, are the most complete that are available at the present time. The parameters of the figures given in Ref. 9 are listed in Table 3-2 (p. 54). Several of these figures have been reproduced herein and will be discussed later in this subsection. Van Driest used the Sutherland viscosity law by means of which the ratio, μ_* , may be written

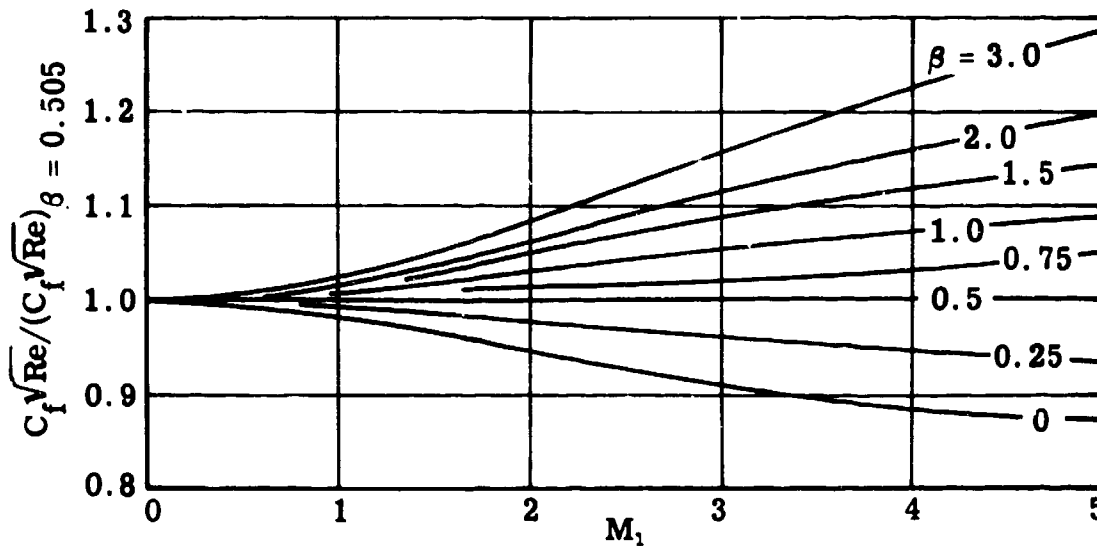
$$\mu_* = \left(\frac{T}{T_1}\right)^{\frac{1}{2}} \left[\frac{1 + (T_k/T_1)}{1 + (T_k/T)} \right] = T_*^{\frac{1}{2}} \left[\frac{1 + \beta}{1 + (\beta/T_*)} \right] \quad (3-1)$$

Van Driest uses $\beta = 0.505$ in his calculations. For air, which has $T_k = 198.7^\circ R$, this value of β corresponds to an ambient temperature of $392.4^\circ R$, which is the standard temperature of the isothermal layer between the altitudes of 35 and 105 K ft. For the free flight of slender configurations, where the temperature at the outer edge of the boundary layer is near the temperature of the atmosphere, this value of β will give reasonable results for all altitudes. The variation of β with altitude is from about 0.3 to 0.5 as shown on the first sketch on the following page. The second sketch shows that in a wind tunnel, β may

have a much wider variation.



Crocco determined the effect of β on the skin friction coefficient. The curves in the following sketch have been made from cross plots of his computations at $Pr = 0.725$. Since they give the skin friction for an insulated plate, they represent an upper limit to the effect of β . The curves show that the free-flight variation of β has a small effect on skin friction.



The assumptions of a perfect gas and the Sutherland viscosity law become less accurate as the Mach number and temperature are increased. Within the limits of the above basic assumptions, the errors in the skin friction coefficient will be moderate. The differences will be seen by comparing the perfect gas results, to be discussed in this subsection, with the real gas results to be given in the following subsection.

In examining the effect of wall temperature on the boundary-layer characteristics, one case of interest is the insulated plate. At the surface, $q_w = 0$ and hence $(\partial T / \partial y)_w = 0$. For this case the wall temperature is known as the equilibrium temperature, T_e , the adiabatic wall temperature, or the recovery temperature. The ratio of the dynamic temperature rise to that which would occur in frictionless adiabatic flow is called the recovery factor, r , i.e.,

$$r = (T_e - T_1) / (T_t - T_1) \quad (3-2)$$

or since in adiabatic flow

$$T_t / T_1 = 1 + \frac{\gamma - 1}{2} M_1^2$$

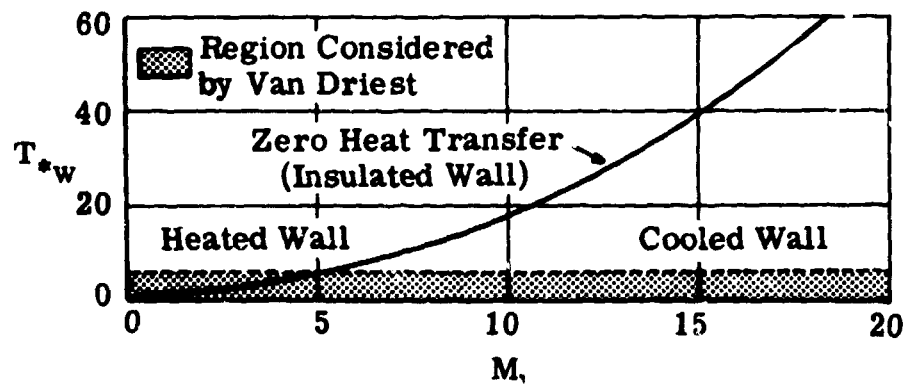
then

$$T_e / T_1 = 1 + r \cdot \frac{\gamma - 1}{2} \cdot M_1^2 = T_{*e} \quad (3-3)$$

Crocco shows in Ref. 4 that for $Pr = 0.5$ to 2.0 , the recovery factor is closely approximated by

$$r = Pr^{1/2} \quad (3-4)$$

In addition to the insulated wall case, calculations were made by Van Driest for $T_{*w} = 0.25, 1, 2, 4$, and 6 . The sketch below shows the relationship between these values and those for the insulated wall. It may be seen that the range of T_{*w} includes both heated and cooled walls up to $M_1 = 5$, beyond which only cooling is treated.



Some of the very useful contributions made in Ref. 9 are the graphs of the velocity and temperature distributions. After solving the momentum and energy equations, boundary-layer velocity profiles in non-dimensional form are readily obtained from the shear function, g_* , by the following integration:

$$\frac{y}{x} \sqrt{Re} = 2 \int_0^{u_*} \frac{\mu_* du_*}{g_*}$$

Figure 3-1 reproduces the velocity profiles of Ref. 9 for $M_1 = 0, 4, 8, 12, 16$, and 20, both for the insulated flat plate ($T_w = T_e$) and for $T_w = T_1$. The change in shape of the velocity profiles and the large reduction in boundary-layer thickness associated with the high cooling rate is immediately evident.

Having computed $(y/x) \sqrt{Re}$ in terms of u_* , the solution of the energy equation yields temperature profiles. Figure 3-2 shows the temperature profiles, T_* vs $(y/x) \sqrt{Re}$, in the laminar boundary layer for the same set of conditions as the preceding figure. This figure clearly demonstrates that, while boundary-layer temperatures at high Mach numbers are much greater than free-stream temperatures regardless of cooling rate, they are still greatly reduced when the wall is cooled. Thus, the cooler the wall, the higher the Mach number at which real gas effects may be neglected. This is further discussed in Subsec. 3.1.2.

The local skin friction coefficient may be determined directly from the solution, g_* , of Eqs. 2-17 and 2-19. It is given by

$$C_f \sqrt{Re} = (g_*)_w \quad (3-5)$$

The mean skin friction coefficient, C_F , is the average of C_f over the flat plate and in a laminar boundary layer is given by

$$C_F = 2C_f \quad (3-6)$$

The solid lines in Fig. 3-3 give the local skin friction coefficient as a function of Mach number for $T_{*w} = 0.25, 1, 2, 4$, and 6 and for an insulated surface.

3.1.1 The Reference Temperature Method for Calculating Skin Friction

In 1949 Rubesin and Johnson (Ref. 10) devised an approximate method for taking account of the effects of Mach number and heat transfer on laminar boundary-layer skin friction. They demonstrated that the incompressible, zero heat transfer result for skin friction could be used with good accuracy for compressible flow with heat transfer if the density and viscosity used in computing C_f and Re were those associated with a reference temperature, T' , computed from

$$T' = \frac{T'}{T_1} = 1 + 0.032 M_1^2 + 0.58 (T_{*w} - 1) \quad (3-7)$$

The method results in the following relation for the local skin friction coefficient

$$C_f \sqrt{Re} = \frac{\tau_w}{\frac{1}{2} \rho_1 u_1^2} \left(\frac{\rho_1 u_1 l}{\mu_1} \right)^{\frac{1}{2}} = C'_f \sqrt{Re'} \cdot \left(\frac{\rho'_1 \mu'_1}{\rho_1 \mu_1} \right)^{\frac{1}{2}} = 0.664 (\rho'_1 \mu'_1)^{\frac{1}{2}} \quad (3-8)$$

since T'_* was chosen to make $C'_f \sqrt{Re'}$ equal to the incompressible value, i.e., to 0.664. As ρ'_* and μ'_* may both be expressed in terms of T'_* , the skin friction is completely determined when T'_* is known.

Monaghan in Ref. 11 demonstrated that the constants in Eq. 3-7 are very close to values which appear in the equation ($Pr = 1$) for an average temperature computed in the following way:

$$\bar{T}_* = \bar{T}/T_1 = \int_0^1 T_* du_* \quad (3-9)$$

For a perfect gas Eq. 2-21, which holds for $Pr = 1$, may be written as

$$T_* = T_{*w} - (T_{*w} - 1) u_* + \frac{\gamma - 1}{2} M_1^2 (u_* - u_*^2) \quad (3-10)$$

from which one may easily obtain

$$\bar{T}_* = 1 + \frac{\gamma - 1}{12} M_1^2 + \frac{T_{*w} - 1}{2} \quad (3-11)$$

When $\gamma = 1.4$, Eq. 3-11 becomes

$$\bar{T}_* = 1 + 0.0333 M_1^2 + 0.5 (T_{*w} - 1) \quad (3-12)$$

It may be seen that this equation closely approximates Eq. 3-7 determined by Rubesin and Johnson.

Wilson in Ref. 12 used the results of Van Driest's work to determine the dependence of \bar{T}_* on the Prandtl number. It was found that \bar{T}_* could be closely approximated by

$$\bar{T}_* = 1 + \left[\frac{Pr^{\frac{1}{2}}}{2} - \frac{Pr^{\frac{1}{3}}}{3} \right] Pr^{\frac{1}{2}} \left[\frac{\gamma - 1}{2} M_1^2 \right] + \left[1 - \frac{Pr^{\frac{1}{2}}}{2} \right] (T_{*w} - 1) \quad (3-13)$$

A comparison of \bar{T}_* with T'_* computed from Eq. 3-8, by using Van Driest's skin friction results for $Pr = 0.75$, led Wilson to adjust the coefficients of Eq. 3-13 to give

$$T'_* = 1 + A M_1^2 + B(T_{*w} - 1) \quad (3-14)$$

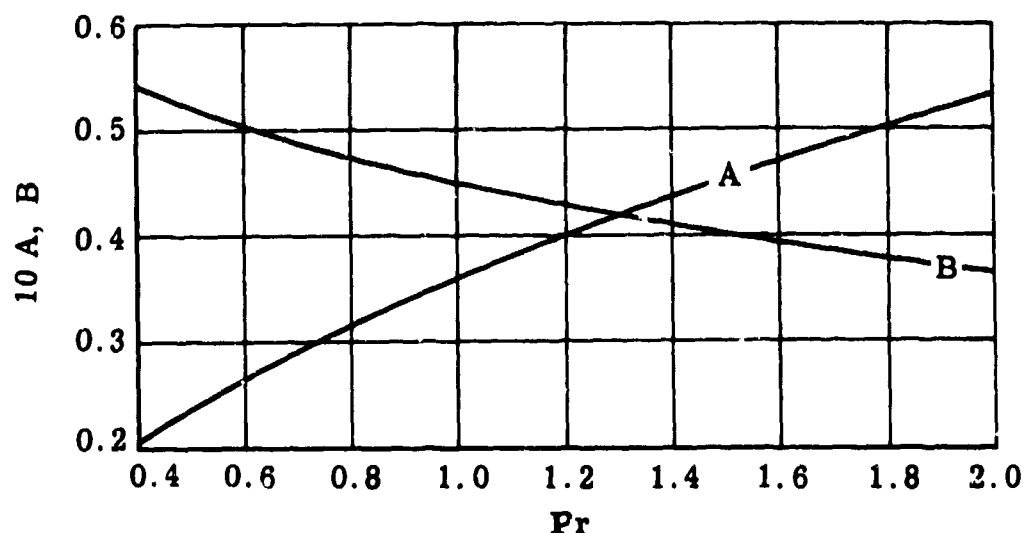
where

$$A = 1.08 \left[\frac{Pr^{\frac{1}{2}}}{2} - \frac{Pr^{\frac{1}{3}}}{3} \right] Pr^{\frac{1}{2}} \frac{\gamma - 1}{2} \quad (3-15)$$

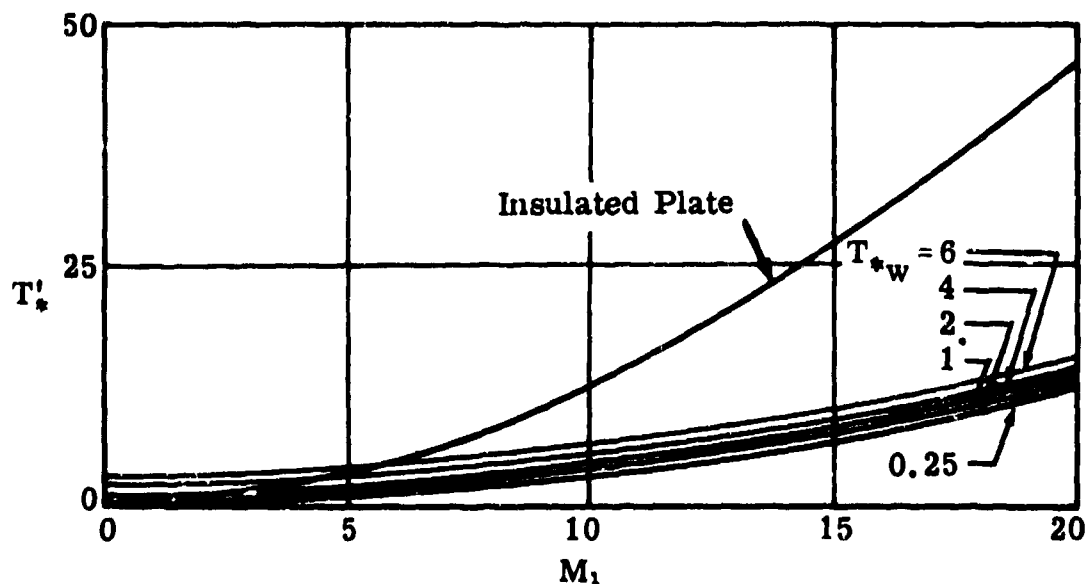
and

$$B = 0.90 \left[1 - \frac{\text{Pr}^{\frac{1}{2}}}{2} \right] \quad (3-16)$$

Values of A and B are shown in the sketch below. Equations 3-8 and 3-14 were used with $\text{Pr} = 0.75$, $\gamma = 1.4$, and $\beta = 0.505$ to compute the skin friction coefficients which are shown by dotted lines in Fig. 3-3. The agreement with Van Driest's results is generally better than 1.5%.



In order to estimate the effect on C_f of both T'_* and β , Eqs. 3-1 and 3-8 were used to calculate $C_f \sqrt{\text{Re}}$ for values of T'_* from 0 to 50 and for $\beta = 0, 0.5, 1.0, 1.5$, and 2.0 . The resultant curves are shown in Fig. 3-4. In order to use Fig. 3-4, it is necessary to relate β and T'_* to the physical properties of the flow. The values of β encountered in atmospheric flight and in wind tunnels are given in the sketches on page 19. The value of T'_* as a function of M_1 and T_{*w} is shown in the following sketch.



3.1.2 Comparison of Reference Temperature and Maximum Boundary-Layer Temperature

In order to examine more closely the validity of using perfect gas properties in calculations of high Mach number flows, it is necessary to determine the maximum temperature in the boundary layer under the given conditions. In Fig. 3-5 the reference temperature, T'_* , is shown as a function of Mach number for zero heat transfer and for the case of a wall cooled to give $T_{*w} = 1$. Also shown (by dashed lines) is the maximum boundary-layer temperature calculated by Van Driest (see Fig. 3-2). It may be seen that in the zero heat transfer case there is a large difference between the reference and the maximum temperatures, whereas the difference becomes less marked when the walls are cooled. The difference increases with Mach number. It is suggested that the reference temperature be used as a guide for determining the region of validity of perfect gas assumptions, i.e., the region where the reference temperature is low enough to assure that real gas effects are negligible.

3.1.3 Boundary-Layer Thickness and Shape Parameter

The boundary-layer displacement thickness, δ^* , is defined in Subsec. 2.5 as

$$\delta^* = \int_0^{\delta} (1 - \rho_* u_x) dy \quad (3-17)$$

The momentum thickness was given by

$$\theta = \int_0^{\delta} \rho_* u_x (1 - u_x) dy \quad (3-18)$$

For a flat plate, i.e., $dM_1/dx = 0$, it can be shown by integrating Eq. 2-28 with respect to x that

$$\frac{\theta}{x} = \frac{C_F}{2} \quad (3-19)$$

The shape parameter, H , is given by

$$H = \frac{\delta^*}{\theta} = \frac{2}{C_F \sqrt{Re}} \int_0^{\frac{\delta \sqrt{Re}}{x}} (1 - \rho_* u_x) d\left(\frac{y}{x} \sqrt{Re}\right) \quad (3-20)$$

Values of H have been obtained by evaluating the integral in Eq. 3-20 using the boundary-layer velocity and temperature profiles and the skin-friction results

of Ref. 9. It has been found in Ref. 13 that the shape parameter can be approximated by

$$H = \frac{\delta^*}{\theta} = 6.10 T'_* - 3.51 \quad (3-21)$$

where T'_* is given by Eq. 3-14. The results of Ref. 9 can also be used to obtain values of δ/θ . These values can be approximated (see Ref. 13) by

$$\frac{\delta}{\theta} = 6.10 T'_* + 2.90 \quad (3-22)$$

where δ is taken as the value of y when $u_* = 0.995$. Figures 3-6 and 3-7 show that Eqs. 3-21 and 3-22 are excellent fits to the values calculated from Ref. 9 for $0 \leq M_1 \leq 20$ and $0.25 \leq T_{*w} \leq 6.0$. Figure 3-8 shows that the agreement is not quite so good for the insulated flat plate case. Fortunately, the disagreement occurs at Mach numbers greater than 8 where the wall temperatures are much too high for practical interest. The above comparison was made with $Pr = 0.75$. For $Pr = 1$, Eqs. 3-21 and 3-22 are in reasonable agreement with the results of Ref. 7.

With Eqs. 3-6 and 3-19, the displacement thickness may be written

$$\frac{\delta^*}{x} \sqrt{Re} = H C_f \sqrt{Re} \quad (3-23)$$

and

$$\frac{\delta}{x} \sqrt{Re} = \frac{\delta}{\theta} C_f \sqrt{Re} \quad (3-24)$$

Then Eqs. 3-8, 3-14, and 3-21 to 3-24 may be used to calculate $(\delta^*/x)\sqrt{Re}$ and $(\delta/x)\sqrt{Re}$. Values obtained in this fashion are plotted in Fig. 3-9 as a function of Mach number for the insulated plate and for $T_{*w} = 1$. Figure 3-9 illustrates the strong dependence of the thicknesses, δ and δ^* , on the free-stream Mach number. Values of the boundary-layer thickness, $(\delta/x)\sqrt{Re}$, taken from Ref. 9 are shown in Fig. 3-9. At high Mach numbers it is evident that the displacement thickness approaches the total thickness of the boundary layer even at low surface temperatures.

3.2 Laminar Boundary Layer on a Flat Plate -- Real Gas

In the previous subsection, solutions of the boundary-layer equations were obtained for ideal gases, i.e., those for which c_p and Pr remain virtually constant and for which the viscosity may be found by Sutherland's formula. The current subsection presents and discusses solutions which take into account realistic variations of the thermodynamic and transport properties of the gas, assumed to be in chemical equilibrium at each point in the boundary layer.

Solutions to Eqs. 2-17 and 2-18 have been obtained by Romig and Dore (Ref. 14) and by Wilson (Ref. 12). In each case, the integration was carried out by high-speed computers. Wilson's work will be summarized here not only because it employs more recently evaluated air properties than those of Romig and Dore, but also because the form of the results allows easy comparison with those of the perfect gas case.

There are two important prerequisites to the integration of the equations. The first is the choice of values for the air properties, a decision which is by no means simple. From the best available information, which is presented in Appendix A, it may be seen that there is still a great deal of uncertainty and a wide discrepancy among the values calculated from different sets of basic assumptions. Once a set of values has been chosen, the second prerequisite is that the properties be expressed as functions of the enthalpy, with the pressure constant, in order that Eqs. 2-17 and 2-18 will contain only the two variables, g_* and h_* .

For his calculations, Wilson chose the following: values of μ and k at high temperatures computed by Green and Klein (optional values are given in Appendix A); values of the compressibility factor, Z , from Ref. 15; and values of c_p/R and c_v/R from Ref. 16. The value of R is based on the molecular weight of cold, undissociated air. At lower enthalpies the values of μ , k , and c_p were taken from Ref. 17. The density-enthalpy relationship was obtained from Refs. 15, 17, and 18.

Wilson found that expressing μ , Pr , and ρ in terms of h , while keeping the pressure constant, was a major part of his work. A summary of his method is given since it may be extended to a higher temperature regime or used for new data that may become available.

1. By means of curves such as those given in Figs. A-2 to A-8, plots of μ vs Z for $\rho/\rho_0 = 1.0, 0.1, \text{ and } 0.01$ were made (ρ_0 = density of the atmosphere at sea level). These plots are given in Fig. 3-10.

2. The coefficient of conductivity, k , could not be interpolated accurately by this method. A set of curves, much easier to work with, was obtained by plotting Rk/c_v vs Z for the same three values of ρ/ρ_0 . Results are also given in Fig. 3-10.

3. Since the relative concentration of the various constituents of air is essentially constant at constant Z , it was postulated that a formula of the Sutherland form could be used for μ and Rk/c_v at each value of Z . The equations used were

$$\mu = \frac{aT^{3/2}}{T + b} \quad (3-25)$$

and

$$\frac{Rk}{c_v} = \frac{cT^{3/2}}{T + d} \quad (3-26)$$

where a , b , c , and d are functions of Z only and were evaluated by taking a least squares fit to the data at various values of Z . The resulting values are shown in Fig. 3-11 for values of Z from 1.0 to 1.8. Within this range of Z , Eqs. 3-25 and 3-26 fit the original data to within 1%.

4. Since the interpolation of the Prandtl number proved impractical, it was determined by calculation. Values of μ and Rk/c_v were found by means of Eqs. 3-25 and 3-26; values of c_v/R and c_p/R were taken from Ref. 16.

5. Figure 3-12 gives the final plots of μ , k , c_p , Pr , and ρ as functions of the enthalpy for a constant pressure of 0.1 atmosphere.

An iterative procedure is required for the solution of Eqs. 2-17 and 2-18 since the boundary conditions are split. The conditions are:

$$\left. \begin{aligned} g'_* &= 0 \quad \text{and} \quad h_* = h_{*w} \quad \text{at} \quad u_* = 0 \\ g_* &= 0 \quad \text{and} \quad h_* = 1 \quad \text{at} \quad u_* = 1 \end{aligned} \right\} \quad (3-27)$$

A method which is convenient for machine computation is described in Ref. 12. The integration is started at the outer edge of the boundary layer ($u_* = 1$) and proceeds towards the wall. The method is such that iteration is required to satisfy only the condition $g'_* = 0$ at the wall. The wall enthalpy h_{*w} is not specified in advance but is obtained as a result of the computation. Where conditions related to a specific wall enthalpy are required, they may be determined easily by interpolation from a series of solutions giving a range of wall enthalpies.

3.2.1 Skin Friction Coefficient

In carrying out the solutions to Eqs. 2-17 and 2-18, the variation of g_* and h_* with u_* is obtained across the boundary layer. As in the perfect gas case, $C_f\sqrt{Re}$ is obtained immediately from the value of g_{*w} (Eq. 3-5). The values calculated by Wilson (Ref. 12) for $C_f\sqrt{Re}$ as a function of h_{*w} are shown in Figs. 3-13 to 3-16 by means of circles for $p_1 = 0.1$ atmosphere and the following values of the other parameters:

Figure	3-13	3-14	3-15	3-16
h_1 BTU/slug	3,000	15,000	75,000	400,000
$u_1^2/2h_1$	0, 10, 30, 80	0, 10, 30	0, 10	0

At low enthalpies the conditions represent those of a slender body traveling at speeds up to 25,000 ft/sec and the highest enthalpy is that which would be found on the nose of a blunt body at speeds up to 25,000 ft/sec.

The T' method discussed in Subsec. 3.1.1 may be extended logically to the real gas case by using a reference enthalpy, h' , in place of the reference temperature. Equation 3-14 thus becomes

$$h'_* = \frac{h'}{h_1} = 1 + 0.90 \left[1 - \frac{(Pr')^{\frac{1}{4}}}{2} \right] (h_{*w} - 1) + 1.08 (Pr')^{\frac{1}{2}} \left[\frac{(Pr')^{\frac{1}{4}}}{2} - \frac{(Pr')^{\frac{1}{3}}}{3} \right] \frac{u_1^2}{2h_1} \quad (3-28)$$

The Prandtl number, Pr' , in Eq. 3-28, and the reference enthalpy, h' , are interdependent (see Fig. 3-12) and hence an iterative process is required in the computation of h'_* . However, the coefficients in Eq. 3-28 are not very sensitive to the variation of Pr' and the iterative process converges rapidly. Once h'_* has been determined, the corresponding values of ρ' and μ' are read from Fig. 3-12 and the value of $C_f \sqrt{Re}$ computed from Eq. 3-8. The curves obtained by this method are shown as solid lines in Figs. 3-13 to 3-16. It may be seen that the agreement is, in general, very good between machine-computed values of the skin friction and those determined by means of the reference enthalpy. The agreement is not quite as good at high values of h_1 for very low air velocities over a cooled wall.

The real gas results of Figs. 3-13 to 3-16 may be compared easily with the perfect gas results of Fig. 3-3 since values of h_{*w} and $u_1^2/2h_1$ correspond to values of T_{*w} and $\frac{(\gamma-1)}{2} M_1^2$, respectively, in the perfect gas case. Curves showing the comparison are given in Ref. 12. The real gas values of $C_f \sqrt{Re}$ are greater than the corresponding perfect gas values, the difference in the present range of parameters being always less than 15%. It should, however, be noted that although the non-dimensionalized form of the skin friction does not appear to be changed greatly by real gas effects, the actual shear stress, τ_w , may be appreciably changed when real gas values for the density and viscosity are used.

3.2.2 Shape Parameter and Boundary-Layer Displacement

No velocity profiles were computed by Wilson (Ref. 12), and hence no values of the shape parameter, H , were obtained for the real gas case. However, it is suggested that the shape parameter may be estimated by rewriting Eq. 3-21 in the form

$$H = \frac{\delta^*}{\theta} = \frac{6.10}{\rho'_*} - 3.51 \quad (3-29)$$

The density ratio ρ'_* corresponds to the real gas enthalpy ratio, h'_* , which was obtained from Eq. 3-28. Having computed H from Eq. 3-29, the value of the displacement thickness can be estimated from Eq. 3-23 by using the value of $C_f \sqrt{Re}$ computed by the reference enthalpy method of the previous subsection.

In order to calculate δ/θ , it is suggested that Eq. 3-22 be rewritten as

$$\frac{\delta}{\theta} = \frac{6.10}{\rho'_*} + 2.90 \quad (3-30)$$

3.3 Turbulent Boundary Layer on a Flat Plate -- Perfect Gas

In Subsec. 2.6 it has been shown that the viscous stress in two-dimensional turbulent flow may be written as

$$\tau_{\epsilon} = -(\overline{\rho v})'u' = \mu_{\epsilon} \frac{\partial \bar{u}}{\partial y} \quad (\text{Eq. 2-37})$$

Prandtl in Ref. 19 (pp. 126-130) shows that this may be expressed as

$$\tau_{\epsilon} = \rho l^2 \left(\frac{du}{dy} \right)^2 \quad (3-31)$$

where l is known as a mixing length which is proportional to the distance from the wall, i.e.,

$$l = l_1 = \kappa y \quad (3-32)$$

In the similarity theory of von Karman, given in Ref. 19 as well as in Ref. 20, the value of l is given as

$$l = l_2 = -\kappa \frac{du}{dy} \frac{d^2 u}{dy^2} \quad (3-33)$$

Assuming that $\tau_{\epsilon} = \text{constant} = \tau_w$ in Eq. 3-31, these two mixing lengths result in the same boundary-layer velocity distribution for incompressible flow. κ is a universal constant whose value has been experimentally determined (taken herein to be 0.392). It is believed to be the same in both compressible and incompressible flow. When the density variation across the boundary layer is taken into account, the results of integrating Eq. 3-31 will depend on the choice between the use of Eqs. 3-32 and 3-33.

Although many analyses have been made for the turbulent boundary layer in the compressible flow of an ideal gas, only a few will be mentioned here. Frankl and Voishel (Ref. 21) were the first (1943) to solve Eq. 3-31 and they chose to represent the mixing length by means of Eq. 3-33. The numerical results which are given in Ref. 21 for the incompressible case and for high subsonic Mach numbers include the effects of heat transfer. However, if the method is extended to higher Mach numbers, the accuracy decreases due to the mathematical approximations employed. In 1950 Wilson also used the von Karman mixing length with Eq. 3-31 to derive skin friction relations for compressible flow with zero heat transfer and obtained good agreement with experimentally determined values over a moderate range of Mach numbers (1.5 to 2.2). Van Driest in 1951 (Ref. 45) chose to use the Prandtl mixing length in his solution of Eq. 3-31 but in 1954 he obtained a solution using the von Karman expression and extended Wilson's results to include the effects of heat transfer. Studies of von Karman's similarity theory made by Lin and Shen (Ref. 22) and by Li and Nagamatsu (Ref. 23) indicate that the use of the von Karman mixing length expression is preferable to that of Prandtl for compressible flow analyses.

Wilson's method of solution will be outlined briefly. Assuming that $\tau_\epsilon = \text{constant} = \tau_w$, Eqs. 3-31 and 3-33 combine to give

$$(\tau_w/\rho)^{\frac{1}{2}} = -\kappa \left[\left(\frac{du}{dy} \right)^2 \frac{d^2u}{dy^2} \right] \quad (3-34)$$

In order to determine a value of ρ to be used in the solution of Eq. 3-34, it is assumed that $Pr_\epsilon = 1$. Equation 3-10 then holds true for turbulent flow and $1/\rho_*$ is substituted for T_* . It may be seen from Eq. 3-31 that $(\tau_w/\rho)^{\frac{1}{2}}$ has the dimensions of a velocity. When $\rho = \rho_w$, this is sometimes referred to as the friction velocity and represented by u_τ , i.e.,

$$(\tau_w/\rho_w)^{\frac{1}{2}} = u_\tau \quad (3-35)$$

If

$$u/u_\tau = \phi \quad \text{and} \quad \frac{\rho_w u_\tau y}{\mu_w} = \eta \quad (3-36)$$

where ϕ and η are non-dimensional forms of u and y , then Eq. 3-31 may be written as

$$\frac{d}{d\phi} [\log (d\phi/d\eta)] = -\kappa \left[1 - \left(1 - \frac{T_{t1}}{T_w} \right) \frac{\phi}{\phi_1} - \sigma \left(\frac{T_{t1}}{T_w} \right) \left(\frac{\phi}{\phi_1} \right)^2 \right]^{-\frac{1}{2}} \quad (3-37)$$

where

$$\sigma = \frac{\frac{\gamma-1}{2} M_1^2}{1 + \frac{\gamma-1}{2} M_1^2} \quad (3-38)$$

Equation 3-37 may be integrated twice to give the relationship between ϕ and η in terms of two constants of integration. In order to evaluate the constants of integration it is necessary to examine the structure of the turbulent boundary layer. A rational assumption, and one that is borne out by experimental data, is that adjacent to the wall is a thin layer of laminar flow in which the viscous stress ($\mu du/dy$) is large and the Reynolds stress [$\rho l^2 (du/dy)^2$] is negligible. Above this is a turbulent layer in which the viscous stress is negligible and the Reynolds stress is large. Between these two layers is a transition layer (often neglected in mathematical analyses) in which the two stresses are of the same order of magnitude.

Assuming that $\tau = \text{constant} = \tau_w$ and $\mu = \text{constant} = \mu_w$ in the laminar region, Eqs. 2-1 and 3-35 give

$$\tau_w = \mu_w \frac{du}{dy} = \rho_w u_\tau^2$$

and after integration

$$\frac{u}{u_\tau} = \frac{\rho_w u_\tau y}{\mu_w} \quad (3-39)$$

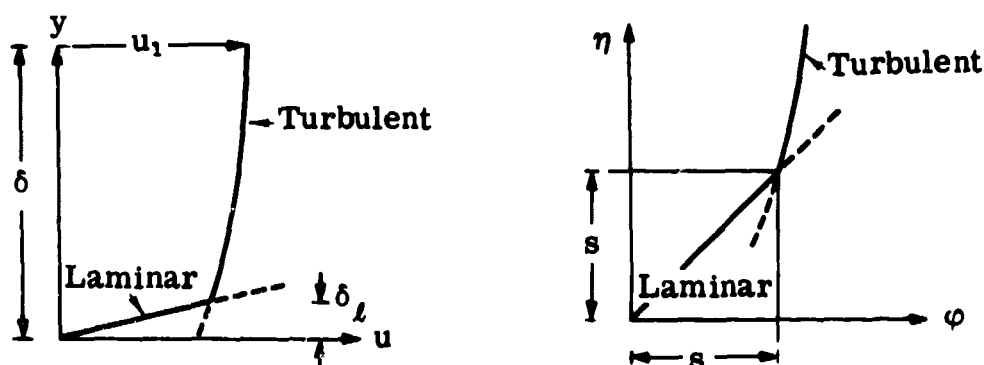
From this it follows that at the edge of the laminar sublayer (see sketches below)

$$\eta = \varphi = s \quad (3-40)$$

Assuming that Eq. 3-32 holds true near the laminar sublayer and that in this region $\rho = \text{constant} = \rho_w$, it can be shown that

$$\left(\frac{d\varphi}{d\eta} \right)_{\eta=s} = 1/\kappa s \quad (3-41)$$

These two equations will be used as the boundary conditions in the solution of Eq. 3-37. A model of the turbulent boundary layer (in terms of the physical coordinates y and u as well as in the non-dimensional η and φ) is shown by the sketches below.



Equations 3-39 to 3-41 are strictly true only for incompressible laminar flow with no heat transfer, but they are not greatly in error for compressible turbulent flow in which the sublayer is very thin. The non-dimensional thickness of the sublayer, s , is usually considered invariant. However, Harkness has shown (Ref. 25) that its value varies with the heat-transfer rate and has obtained the following relationship from the experimental data which is shown on Fig. 3-17:

$$s = 11.5 + 6.6 \left(\frac{T_e - T_w}{T_e} \right) \quad (3-42)$$

where T_e is defined by Eq. 3-3. When there is no heat transfer, Eq. 3-42 reduces to the better known value of s (i.e., 11.5) quoted by von Karman and derived from incompressible flow data. Harkness derived skin friction relations based on Eq. 3-34 and used the above result. His equations differ slightly from those which will be given here due to the fact that somewhat different mathematical approximations were made.

A single integration of Eq. 3-37 was used to obtain $\partial\varphi/\partial\eta$ which yielded du/dy and hence an integral expression for the momentum thickness, θ . For a flat plate the momentum integral equation, Eq. 2-26, reduces to

$$C_f/2 = \frac{d\theta}{dx}$$

which may be written as

$$C_f/2 = \frac{dRe_\theta}{dRe_x} \quad (3-43)$$

Equation 3-43 may be integrated and the constant of integration evaluated at the leading edge of the plate where $Re = 0$ and $C_f = \infty$. After several mathematical approximations the final result is

$$\left(\sin^{-1} \xi - \sin^{-1} \xi_f \right) \frac{1}{\sqrt{\sigma \frac{T_e}{T_1} C_f}} = -6.43 + 4.15 \log_{10} \left(\frac{11.5}{s} \frac{\mu_1}{\mu_w} C_f Re \right) \quad (3-44)$$

where

$$\xi = \frac{2\sigma - \frac{T_e - T_w}{T_e}}{\sqrt{4\sigma \left(1 - \frac{T_e - T_w}{T_e} \right) + \left(\frac{T_e - T_w}{T_e} \right)^2}} \quad (3-45)$$

$$\xi_f = \frac{2\sigma s \sqrt{\frac{T_w}{T_1} C_f} - \frac{T_e - T_w}{T_e}}{\sqrt{4\sigma \left(1 - \frac{T_e - T_w}{T_e} \right) + \left(\frac{T_e - T_w}{T_e} \right)^2}} \quad (3-46)$$

It should be noted that the temperature distribution in the boundary layer was based on the assumption of $Pr = 1$. However, in the subsequent development it was assumed that the Prandtl number could be varied and hence that T_e (defined by Eq. 3-3) has now replaced T_t . Experimental evidence indicates that in turbulent flow the recovery factor may be expressed as

$$r = (Pr)_w^{\frac{1}{3}} \quad (3-47)$$

For incompressible flow with no heat transfer, Eq. 3-44 reduces to von Karman's equation, i.e.,

$$\left(C_{f_i} \right)^{-\frac{1}{2}} = 1.7 + 4.15 \log_{10} \left(C_{f_i} Re \right) \quad (3-48)$$

The mean, or total, skin friction coefficient, C_F , is given by

$$C_F = \frac{D}{\frac{1}{2} \rho_1 u_1^2 x} \quad (3-49)$$

and may be obtained from the local coefficient by means of

$$C_F = \frac{1}{Re} \int_0^{Re} C_f dRe \quad (3-50)$$

In incompressible flow, according to Schoenherr (Ref. 26), the equation for the mean skin friction coefficient can be written in a form identical to that for the local skin friction coefficient with the constants adjusted. This holds true in compressible flow in which case C_F for turbulent flow on a flat plate is given by

$$\left(\sin^{-1} \xi - \sin^{-1} \xi_F \right) \frac{0.242}{\sqrt{\sigma} \frac{T_e}{T_1} C_F} = -1.968 + \log_{10} \left(\frac{11.5 \mu_1}{s \mu_w} C_F Re \right) \quad (3-51)$$

where

$$\xi_F = \frac{2\sigma s \sqrt{\frac{T_w}{T_1} \frac{C_F}{2}} - \frac{T_e - T_w}{T_e}}{\sqrt{4\sigma \left(1 - \frac{T_e - T_w}{T_e} \right) + \left(\frac{T_e - T_w}{T_e} \right)^2}} \quad (3-52)$$

For incompressible flow with no heat transfer, Eq. 3-51 reduces to the result given by Schoenherr in Ref. 26, i.e.,

$$0.242 \left(C_{F_i} \right)^{\frac{1}{2}} = \log_{10} \left(C_{F_i} Re \right) \quad (3-53)$$

Equation 3-53 is comparable to von Karman's equation, Eq. 3-48, for C_{f_i} .

Many authors present skin friction results in terms of the ratios C_F/C_{F_i} and C_f/C_{f_i} . The mean skin friction coefficient, C_F , has been computed from Eq. 3-51 at $Re = 10^7$, for a range of Mach numbers of 0 to 10, for $(T_e - T_w)/T_e$ from 0 to 0.95, using Eq. 3-1 for μ_1/μ_w . A value of C_{F_i} was computed from Eq. 3-53 for $Re = 10^7$. The ratio C_F/C_{F_i} so obtained is shown as a function of Mach number in Fig. 3-18. Since the value of β in the viscosity law was taken as 0.505, the conditions outside the boundary layer are those in the standard isothermal altitude range from 35,322 to 104,987 feet. When the value of Re is varied, C_F/C_{F_i} increases slowly with decreasing Re .

If Eqs. 3-44 and 3-48 are used to compute C_f/C_{f_i} it may be shown that for a wide range of M and Re , $C_f/C_{f_i} \approx C_F/C_{F_i}$. It follows that Fig. 3-18 may be used for either mean or local skin friction coefficient ratios at $Re = 10^7$.

It is sometimes necessary to compute the Reynolds number of the flow with the momentum thickness, θ , as the characteristic dimension rather than the more usual length, x , from the leading edge of the plate to the point in question. For a flat plate the mean skin friction coefficient is given by

$$C_F = 2 \frac{\theta}{x} = 2 \frac{Re_\theta}{Re_x} \quad (3-54)$$

Therefore C_F as a function of Re_θ comes directly from Eqs. 3-51 and 3-52, i.e.,

$$\left(\sin^{-1} \xi - \sin^{-1} \xi_F \right) \frac{0.242}{\sqrt{\sigma \frac{T_e}{T_1} C_F}} = -1.968 + \log_{10} \left(\frac{23}{s} \frac{\mu_1}{\mu_w} Re_\theta \right) \quad (3-55)$$

For a given Re_θ , a value of C_f can be calculated by the following tedious process. Calculate C_F from Eq. 3-55, then calculate the corresponding Re from Eq. 3-54, and finally calculate the corresponding value of C_f from Eq. 3-44. A simpler method can be derived as follows: the local skin friction coefficient for a flat plate can be written

$$C_f = \frac{d(C_F Re)}{dRe} = C_F + Re \frac{dC_F}{dRe} \quad (3-56)$$

After differentiating Eq. 3-51 to obtain dC_F/dRe and making use of Eqs. 3-55 and 3-56, C_f is given by

$$C_f = C_F (-1.968 + \Omega) / (-1.099 + \Omega) \quad (3-57)$$

where

$$\Omega = \log_{10} \left(\frac{23}{s} \frac{\mu_1}{\mu_w} Re_\theta \right) + 0.242 s \left\{ \frac{2\sigma \left(1 - \frac{T_e - T_w}{T_e} \right)}{\left(1 - \xi_F^2 \right) \left[4\sigma \left(1 - \frac{T_e - T_w}{T_e} \right) + \left(\frac{T_e - T_w}{T_e} \right)^2 \right]} \right\}^{\frac{1}{2}} \quad (3-58)$$

For a given value of Re_θ , Eq. 3-55 is used to calculate C_F and Eq. 3-57 will give a corresponding value of C_{f_i} .

It should be noted that care must be taken to specify which Reynolds number is held constant, Re or Re_θ , when giving skin friction ratios. This will be demonstrated by estimating $(C_f/C_{f_i})_{Re_\theta}$ from $(C_F/C_{F_i})_{Re}$ or $(C_f/C_{f_i})_{Re}$. The subscripts Re_θ and Re indicate the Reynolds number which is held constant. Equation 3-53 can be written

$$\frac{0.242}{\sqrt{C_F}} \sqrt{\left(\frac{C_F}{C_{F_i}}\right)_{Re}} = \log_{10} (C_F Re) - \log_{10} \left(\frac{C_F}{C_{F_i}}\right)_{Re} \quad (3-59)$$

Now since $(C_F/C_{F_i})_{Re}$ varies slowly with Re , assume that $(C_F/C_{F_i})_{Re}$ is constant and differentiate Eq. 3-59 with respect to Re . Making use of Eqs. 3-54 and 3-56 leads to

$$C_{f_i} = \frac{(0.242)^2 (C_F/C_{F_i})_{Re}}{\left\{ 0.869 + \log_{10} \left[2Re_\theta \left(\frac{C_{F_i}}{C_F}\right)_{Re} \right] \right\} \log_{10} \left[2Re_\theta \left(\frac{C_{F_i}}{C_F}\right)_{Re} \right]} \quad (3-60)$$

Equations 3-54 and 3-56 are also valid for the incompressible case. Differentiating Eq. 3-53 to obtain dC_{F_i}/dRe , they give

$$C_{f_i} = \frac{(0.242)^2}{(0.869 + \log_{10} 2Re_\theta) \log_{10} 2Re_\theta} \quad (3-61)$$

From Eqs. 3-60 and 3-61

$$\left(\frac{C_f}{C_{f_i}}\right)_{Re_\theta} \left(\frac{C_F}{C_{F_i}}\right)_{Re} = \frac{(0.869 + \log_{10} 2Re_\theta) \log_{10} 2Re_\theta}{\left\{ 0.869 + \log_{10} \left[2Re_\theta \left(\frac{C_F}{C_{F_i}}\right)_{Re} \right] \right\} \log_{10} \left[2Re_\theta \left(\frac{C_F}{C_{F_i}}\right)_{Re} \right]} \quad (3-62)$$

The ratio $(C_f/C_{f_i})_{Re_\theta} / (C_F/C_{F_i})_{Re}$ is plotted on Fig. 3-19 as a function of $(C_F/C_{F_i})_{Re}$ for several values of $\log_{10} Re_\theta$.

3.3.1 A Reference Temperature Method for Turbulent Flows

Sommer and Short (Ref. 27) proposed that Eq. 3-53 be used to compute mean skin friction coefficients for compressible flow with heat transfer

by means of values of C_F and Re based on a reference temperature. For turbulent flows they proposed a relation for reference temperature with the same form as that given by Rubesin and Johnson (Eq. 3-7) for laminar flows but with slightly different coefficients. When values of C_F/C_{F_i} derived from the equations of Sommer and Short are compared with those on Fig. 3-19, there is good agreement at zero heat transfer ($T_w = T_e$) and at some of the higher values of $(T_e - T_w)/T_e$ but the agreement is not good at moderate values of this parameter.

For the T' method, Eq. 3-53 is written as

$$\frac{0.242}{\sqrt{C'_F}} = \log_{10} (C'_F Re') \quad (3-63)$$

where

$$C'_F = \frac{\rho_1}{\rho'} C_F = \frac{T'}{T_1} C_F$$

$$Re' = \frac{\rho'}{\rho_1} \frac{\mu_1}{\mu'} Re = \frac{T_1}{T'} \frac{\mu_1}{\mu'} Re$$

With these relationships, Eq. 3-63 becomes

$$0.242 \left(\frac{T'}{T_1} C_F \right)^{-\frac{1}{2}} = \log_{10} \left(\frac{\mu_1}{\mu'} C_F Re \right) \quad (3-64)$$

where C_F and Re are based on the density and viscosity at the outer edge of the boundary layer. To fit a reference temperature method to Wilson's results, it is necessary to find a relation for T'/T_1 such that values of skin friction computed from Eq. 3-64 will agree with those computed from Eq. 3-51. Expressions for T'/T_1 have been found at $Re = 10^7$ and $\beta = 0.505$ such that the agreement is good in two cases: 1) over a range of Mach numbers at zero heat transfer, $(T_e - T_w)/T_e = 0$, and 2) over a range of temperature ratios at zero Mach number. The expressions for T'/T_1 found for the two cases are:

For zero heat transfer:

$$\left(\frac{T'}{T_1} \right)_e = 1 + 0.100 M_1^2 \quad (3-65)$$

and

For zero Mach number:

$$\left(\frac{T'}{T_1} \right)_0 = 1 - 0.134 \left(\frac{T_e - T_w}{T_e} \right) - 0.372 \left(\frac{T_e - T_w}{T_e} \right)^3 \quad (3-66)$$

where the subscripts e and o denote zero heat transfer and zero Mach number, respectively. Sommer and Short give the following relation for T'/T_1 for all combinations of Mach number and temperature ratio:

$$\frac{T'}{T_1} = 1 + 0.035 M_1^2 + 0.45 \left(\frac{T_w}{T_1} - 1 \right) \quad (3-67)$$

For $Pr_w = 0.7$ and $\gamma = 1.4$, Eq. 3-3 becomes

$$\frac{T_e}{T_1} = 1 + 0.178 M_1^2 \quad (3-68)$$

Using Eq. 3-68, the Sommer and Short relation gives the following results for zero heat transfer and zero Mach number:

$$\left(\frac{T'}{T_1} \right)_e = 1 + 0.115 M_1^2 \quad (3-69)$$

and

$$\left(\frac{T'}{T_1} \right)_o = 1 - 0.45 \left(\frac{T_e - T_w}{T_e} \right) \quad (3-70)$$

Equation 3-69 is in reasonable agreement with Eq. 3-65. However, Eq. 3-70 is quite different from Eq. 3-66 and gives different numerical results at low and moderate values of $(T_e - T_w)/T_e$: at $(T_e - T_w)/T_e = 0.92$, they give the same results.

It has not been found possible to obtain an expression for T'/T_1 such that Eq. 3-64 would agree with Eq. 3-51 for all combinations of Mach number and temperature ratio and at all Reynolds numbers. It is therefore recommended that Eqs. 3-44, 3-51, 3-55, and 3-57 be used in calculating local and mean skin friction coefficients.

3.3.2 Theoretical and Experimental Skin Friction Coefficients

Experimental measurements of skin friction have been made in many ways. Boundary-layer profiles have been surveyed to obtain velocity and temperature distributions from which the momentum boundary-layer thickness and the mean skin friction coefficient may be computed. For the case of a flat plate it has been shown (Eq. 3-19) that

$$C_F = \frac{2\theta}{x}$$

Total drag measurements have been made in ballistic ranges and in wind tunnels. The friction drag is then computed as the difference between measured

total drag and a computed pressure drag, i.e.,

$$D_F = D_t - D_p \quad (3-71)$$

The mean skin friction may then be obtained from

$$C_F = \frac{D_F}{\frac{1}{2}(\rho_1 u_1^2 A)} \quad (3-72)$$

where A is the total surface area. The local shear stress, τ_w , has been obtained experimentally by means of a skin-friction balance which measured the drag on a small isolated surface element. Details of the design, construction, and operation of skin friction balances may be found in Refs. 28 and 29. The experimental local skin friction coefficient is then obtained by definition from

$$C_f = \frac{\tau_w}{\frac{1}{2}(\rho_1 u_1^2)}$$

At high Mach numbers it is possible to measure the velocity in the laminar sublayer and thus determine the velocity gradient at the wall $(du/dy)_w$. The local shear stress is then determined from Eq. 2-1, i.e.,

$$\tau_w = \mu_w \left(\frac{du}{dy} \right)_w$$

The local skin friction is then computed from τ_w . Measurements of the temperature at the walls have been made to determine the temperature gradient in the wall at the surface, thus giving the heat-transfer rate and the heat transfer coefficient, h . The non-dimensional form of h is known as the local Stanton number, defined as

$$St = \frac{h}{c_p \rho_1 u_1} \quad (3-73)$$

The local skin friction coefficient may then be deduced from the heat transfer using the modified Reynolds analogy

$$C_f = 2(\text{Pr})_w^{\frac{2}{3}} St \quad (3-74)$$

It is not easy to substantiate or compare the various theories by means of experimental data. Skin friction and heat transfer measurements are difficult to make with a high degree of accuracy and hence there is a considerable scatter between different sets of data. Experimentally determined skin friction coefficients have been selected from a few sources in an attempt to

cover ranges of Mach number and temperature ratio as wide as possible. In some cases good agreement is found between theory and experiment, in some cases the theoretical values are higher, and in others they are lower than those obtained by measurement. Although comparisons are often made in terms of C_F/C_{F_i} , they are presented here in terms of the absolute values of C_f or C_F

in order that the actual test parameters may be included in the computed values of the coefficients.

von Karman's equation (Eq. 3-48) for the local skin friction in incompressible flow was derived by fitting a straight line to six experimental values obtained by Kempf (see Ref. 30). Recently Kozlov (Ref. 31) obtained fifteen measurements by means of a floating skin friction sensing device in flow at Mach numbers from 0.32 to 0.58 and T_w/T_e from 0.94 to 0.98. His empirical formula is

$$C_f = 0.085 \text{Re}^{-0.29 + 0.01 \log_{10} \text{Re}} \quad (3-75)$$

Within the range of the Reynolds numbers of the test points, i.e., from 10^6 to 10^9 , Eqs. 3-48 and 3-75 agree to within 1%. The experimental data and the fitted curves are shown in Fig. 3-20 in terms of $C_f^{-1/2}$ vs $\log(C_f \text{Re})$.

The next experimental results to be discussed are three sets of supersonic data obtained at zero heat transfer. Wilson obtained mean skin friction coefficients from boundary-layer surveys over a Mach number range from 1.72 to 2.47 (Ref. 24). Jackson et al (Ref. 46) used both skin friction balances and boundary-layer momentum surveys to obtain skin friction coefficients at Mach numbers of 1.61 and 2.20. The Reynolds numbers in this investigation were considerably higher than those of Wilson's tests. As shown on Fig. 3-21, both sets of data are in good agreement with the theoretical results given by Eq. 3-51. The trend with Reynolds number variation follows that of the theory more closely than does that with Mach number variation. Coles (Ref. 32) made local measurements of shear stress by means of a skin friction balance and also surveyed the boundary layer to obtain the momentum thickness. The resultant data in terms of C_f and Re_θ are plotted on Fig. 3-22 for Mach numbers from 1.98 to 4.53. For comparison C_f is calculated from Eq. 3-44 in terms of Re and expressed in terms of Re_θ by means of Eqs. 3-51 and 3-54. The agreement between the theory and Coles' data is very good. Korkegi (Ref. 33), using the same techniques as Coles, made measurements at $M = 5.79$. These data are also compared with the theory on Fig. 3-22 where it may be seen that the experimental values are somewhat higher than those of theory. Matting, Chapman, Nyholm and Thomas (Ref. 34) also measured the local shear stress by means of a skin friction balance. Their data, in terms of C_f and $\log \text{Re}$, are shown in Fig. 3-23 together with the theoretical curve from Eq. 3-44. Matting, et al, made the measurements in air at Mach numbers of 2.95 and 4.20 and in helium at Mach numbers of 5.21 and 7.70. The latter data are comparable to those taken in air at $M = 6.7$ and 9.9, respectively. In contrast to Coles' results which agree with theory and those of Korkegi which are higher than theory, the results of Matting are in every case lower

than the theoretical values. In addition to the measurements with a skin friction balance, Matting made boundary-layer surveys which gave a surface shear stress gradient higher than that measured with the balance. The discrepancy increased with increasing Mach number. Although the authors of Ref. 34 caution against using the velocity profile data, the values of the skin friction coefficient obtained from them would be above the curves shown on Fig. 3-23.

The skin friction measurements made under conditions of the highest heat transfer rates are those reported by Sommer and Short (Ref. 27). Their models were fired in a ballistics range and the skin friction drag was obtained by subtracting the calculated pressure drag from the measured total drag. They obtained the data over a Mach number range of 2.81 to 7.00 and a range of temperature ratios, $(T_e - T_w)/T_e$, from 0.572 to 0.820. Their results shown in Fig. 3-24 indicate reasonable agreement with the theoretical values computed from Eq. 3-51. Also shown on Fig. 3-24 are measured values obtained by Kozlov (Ref. 31) at $M = 2.9$ with high Re and low heat transfer. The agreement with the theory of Eq. 3-51 is very good.

The next data discussed also include the effects of heat transfer. Winkler and Cha (Ref. 35) determined the local skin friction coefficient from measurements of the velocity gradient at the surface and also using the Reynolds analogy, deduced the skin friction from measurements of the heat transfer. The measurements were made at a Mach number of 5.2 with $(T_e - T_w)/T_e$ varying from 0.075 to 0.352. The data, in terms of experimentally determined values of Re_θ , are plotted in Fig. 3-25 in which it may be seen that the two sets of data are in agreement with each other as well as in reasonable agreement with the theoretical curve obtained from Eqs. 3-44 and 3-51.

3.3.3 Shape Parameter and Boundary-Layer Displacement Thickness

The boundary-layer displacement thickness and the momentum thickness which were defined by Eqs. 3-17 and 3-18 may be expressed in non-dimensional form by

$$\frac{\delta^*}{\delta} = \int_0^1 (1 - \rho_* u_*) d(y/\delta) \quad (3-76)$$

and

$$\frac{\theta}{\delta} = \int_0^1 \rho_* u_* (1 - u_*) d(y/\delta) \quad (3-77)$$

Assuming that the Prandtl number is unity, Eq. 3-10 may be used to give the following expression for ρ_* :

$$\frac{1}{\rho_*} = \left(1 + \frac{\gamma - 1}{2} M_i^2\right) \left[\frac{T_w}{T_t} + \frac{(T_t - T_w)}{T_t} u_* - \sigma u_*^2 \right] \quad (3-78)$$

Although it is possible to derive a theoretical velocity distribution by integrating Eq. 3-37, it has been found that the simple expression,

$$u_* = (y/\delta)^{1/n} \quad (3-79)$$

not only gives a better approximation to experimentally determined velocity distributions over a wide range of Mach numbers and heat transfer ratios but also gives rise to more usable forms of the boundary-layer thickness equations. Using Eq. 3-79 to change the variable of integration to u_* , Eqs. 3-76, 3-77, and 3-78 give

$$\frac{\delta^*}{\delta} = n \int_0^1 \left\{ u_*^{n-1} - \frac{u_*^n}{\left(1 + \frac{\gamma-1}{2} M_1^2\right) \left(\frac{T_w}{T_t} + \frac{T_t - T_w}{T_t} u_* - \sigma u_*^2\right)} \right\} du_* \quad (3-80)$$

and

$$\frac{\theta}{\delta} = n \int_0^1 \frac{u_*^n (1 - u_*) du_*}{\left(1 + \frac{\gamma-1}{2} M_1^2\right) \left(\frac{T_w}{T_t} + \frac{T_t - T_w}{T_t} u_* - \sigma u_*^2\right)} \quad (3-81)$$

The above integrals may be evaluated for any combination of M_1 and T_w/T_t . It has been found from experiment that the index, n , increases slowly with increasing Reynolds number. However, there are insufficient data to show the effect of Re on n over a wide range of Mach numbers and temperature ratios. Tucker in Ref. 36 derives the following empirical relationship for n at the outer edge of the boundary layer:

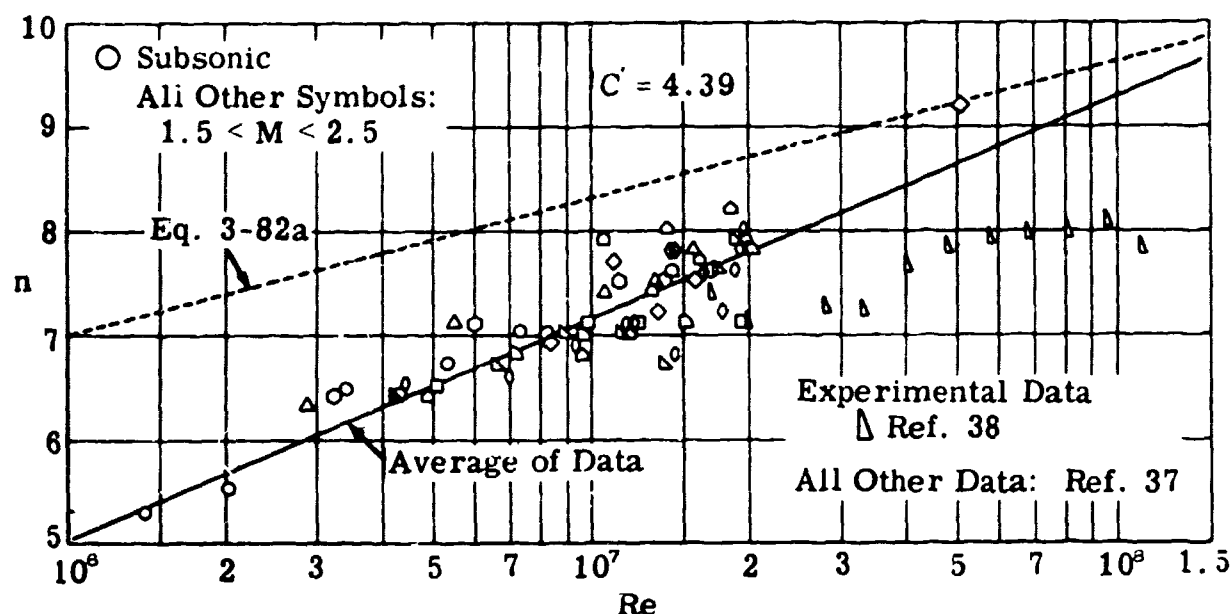
$$n = 2.6 (Re_{1,w})^{1/14} \quad (3-82)$$

where the subscript 1,w indicates that the Reynolds number may be evaluated at the wall or in the free stream. It is evident that for $M > 1$ the constant should be adjusted to account for the difference in Re_1 and Re_w at any point.

Wilson in Ref. 37 discusses at some length the relationship between n and Re and derives the following semi-empirical formula:

$$Re = (n + 2)^2 \frac{C^2}{4} e^{0.2774(n+2)C-0.943} \quad (3-82a)$$

from boundary-layer measurements in the Mach number range from 1.5 to 2.5. Winter, et al (Ref. 38), made measurements at $M = 2.2$ but at higher Reynolds numbers. The next sketch compares the experimental results of both Wilson and Winter with the above empirical equations. It may be seen that neither of the latter compare well with the data over this range of Re . A nominal value of $n = 7$ is satisfactory for most purposes.



Wilson evaluated the integrals in Eqs. 3-80 and 3-81 and from his results derived the following empirical formulas for δ/θ and H :

$$\delta/\theta = \frac{(n+1)(n+2)}{n \left[1 + \frac{2}{n} \frac{T_e - T_w}{T_e} \right]} + \frac{\gamma - 1}{2} M_1^2 (1.34 + 1.38 T_w/T_e) \quad (3-83)$$

and

$$H = \frac{\delta^*/\delta}{\theta/\delta} = \frac{n+2}{n} \cdot \frac{T_w}{T_e} + \frac{\gamma - 1}{2} M_1^2 (1 + 1.20 T_w/T_e) \quad (3-84)$$

The temperature ratio, T_w/T_e , has been used in place of T_w/T_t for convenience in the calculations. For $n = 7$, a range of values of M_1^2 from 0 to 95 and of T_w/T_e from 0 to 1, the results of the numerical integration of Eqs. 3-80 and 3-81 agree with values obtained from Eq. 3-83 within 3% and from Eq. 3-84 within 1.5%.

Values of the displacement thickness, δ^*/δ , obtained from Eqs. 3-83 and 3-84 are shown in Fig. 3-26, and values of the shape parameter, H , derived from Eq. 3-84 are plotted in Fig. 3-27.

Persh (Ref. 43), using Crocco's form of the temperature distribution rather than Eq. 3-10, has computed and tabulated values of δ^*/δ , θ/δ , and H for M_1 from 0 to 20, $(T_w - T_e)/T_t$ from +10 to -10, and for $n = 5, 7, 9$, and 11. These tables are presented in Section 17 of the Handbook (Ref. 44). In the limited region of overlap the agreement is good between the calculations of Wilson and Persh.

It should be noted that the laminar sublayer is neglected in both calculations, i.e., it is assumed that the whole boundary layer is turbulent.

3.3.4 Laminar Sublayer Thickness

The thickness, δ_l , of the laminar sublayer is of interest for several reasons. In the first place, the theoretical calculations in this subsection are dependent upon the assumption that the laminar layer is thin compared with the total boundary-layer thickness. It is therefore necessary to examine the variation of δ_l/δ with Mach number, Reynolds number and heat transfer in order to determine the range wherein the preceding theory is valid. It is also of interest to compare the thickness of the laminar layer with the mean height of the surface roughness since it will be shown in Subsec. 5. that the surface roughness has very little effect on the turbulent skin friction as long as the mean height does not exceed the thickness of the laminar sublayer. The absolute thickness of the laminar sublayer is of practical importance, since in some flow regimes it may be sufficiently thick to permit investigation by means of probes. It is of interest to define the Mach number, Reynolds number, and heat transfer ranges in which such investigations may be possible.

In order to estimate the thickness, δ_l , of the laminar sublayer, Eqs. 3-35, 3-36, 3-40, and 3-42 may be combined to yield

$$\delta_l = \frac{\mu_w \left[11.5 + 6.6 \left(\frac{T_e - T_w}{T_e} \right) \right]}{\sqrt{r_w \tau_w}} \quad (3-85)$$

Then Eq. 3-85 may be written as

$$\frac{\delta_l}{x} = \mu_{*w} \sqrt{T_{*w}} \left[11.5 + 6.6 \left(\frac{T_e - T_w}{T_e} \right) \right] \sqrt{\frac{2}{C_f}} \cdot \frac{1}{Re} \quad (3-86)$$

Since

$$\left(\frac{C_f}{C_{fi}} \right)_{Re} \approx \left(\frac{C_F}{C_{Fi}} \right)_{Re}$$

this may be expressed as

$$\frac{\delta_l}{x} = \frac{\mu_{*w} \sqrt{T_{*w}} \left[11.5 + 6.6 \left(\frac{T_e - T_w}{T_e} \right) \right]}{Re \sqrt{\frac{0.247}{(\log Re)^{2.53}} \left(1 - \frac{1.142}{\log Re} \right) \left(C_F/C_{Fi} \right)_{Re}}} \quad (3-87)$$

From numerical calculations it has been found that the following equation approximates Eq. 3-87 with good accuracy:

$$\frac{\delta_l}{x} = 8.27 \operatorname{Re}^{-0.224} \mu_{*w} \sqrt{T_{*w}} \left[11.5 + 6.6 \left(\frac{T_e - T_w}{T_e} \right) \right] \left(\frac{C_F}{C_{F_i}} \right)^{-\frac{1}{2}} \quad (3-88)$$

Values of δ_l/x calculated from Eq. 3-88 for $M = 5.2$, Re from 10^6 to 6×10^7 , and heat transfer ratios of 0.075, 0.166, and 0.352 are compared in Fig. 3-28 with the experimental data of Ref. 35. In the calculations, the value of C_F/C_{F_i}

is taken from Fig. 3-18 (i.e., at $\operatorname{Re} = 10^7$), since it is considered to be relatively constant for small variations of Re . The agreement between the experimental data and theoretical values is reasonably good. The length, x , in the experimental data is measured from an "effective" leading edge at which the flow becomes fully turbulent. The location of the effective leading edge was determined by extrapolating to zero the measured values of the momentum thickness in the turbulent portion of the flow.

Figure 3-29 shows the calculated value of δ_l/x at $\operatorname{Re} = 10^7$ for Mach numbers from 0 to 10 and $(T_e - T_w)/T_e$ from 0 to 0.95. From this figure it may be noted that the thickness of the laminar sublayer increases with Mach number but decreases with increasing heat transfer. At low Mach numbers and high values of $(T_e - T_w)/T_e$ it becomes extremely small. This condition corresponds in free flight to the flow over blunt bodies at high flight velocities. It is evident from Fig. 3-29 that in considering the effect of roughness on skin friction (see Subsec. 5.6.1) both heat transfer and Mach number have a marked influence on the allowable surface roughness.

If values of δ_l/θ are required, the use of

$$C_F = \frac{2\theta}{x} = \left(\frac{C_F}{C_{F_i}} \right) C_{F_i}$$

allows Eq. 3-87 to be written as

$$\frac{\delta_l}{\theta} = \frac{\mu_{*w} \sqrt{T_{*w}} \left[11.5 + 6.6 \left(\frac{T_e - T_w}{T_e} \right) \right]}{\operatorname{Re} \left[\frac{0.247}{(\log \operatorname{Re})^{2.83}} \right]^{3/2} \sqrt{1 - \frac{1.142}{\log \operatorname{Re}} \left(\frac{C_F}{C_{F_i}} \right)^{3/2}}} \quad (3-89)$$

It has been found from numerical calculations that Eq. 3-89 may be approximated by

$$\frac{\delta_l}{\theta} = 391 \operatorname{Re}^{-0.760} \mu_{*w} \sqrt{T_{*w}} \left[11.5 + 6.6 \left(\frac{T_e - T_w}{T_e} \right) \right] \left(\frac{C_F}{C_{F_i}/\operatorname{Re}} \right)^{-3/2} \quad (3-90)$$

Values of δ_l/δ may be obtained directly from Eq. 3-90 by multiplying by θ/δ obtained from Eq. 3-83. Values of δ_l/θ and δ_l/δ computed from Eqs. 3-83 and 3-90 are shown in Figs. 3-30 and 3-31 for $\operatorname{Re} = 10^7$, M_1 from 0 to 10, and $(T_e - T_w)/T_e$ from 0 to 0.95.

3.4 Turbulent Boundary Layer on Flat Plate -- Real Gas

In Subsec. 3.1.1 it was shown that for laminar boundary layer a reference temperature method could be used for calculating skin friction on a flat plate in the flow of a perfect gas. It was shown in Subsec. 3.1.3 that this temperature could be used in approximate expressions for the boundary-layer displacement thickness and its total thickness. Real gas effects are taken into account by replacing the reference temperature with a reference enthalpy (see Subsec. 3.2). The method for calculating skin friction for the flow of such a gas over a flat plate is discussed in Subsec. 3.2.1. In Subsec. 3.2.2 it is suggested that expressions for the boundary-layer thicknesses be based on a density which corresponds to the reference enthalpy.

It was concluded in Subsec. 3.3.1 that the reference temperature method was not readily applicable for a turbulent boundary layer caused by the flow of a perfect gas over a flat plate. Therefore, the technique of replacing the reference temperature by the reference enthalpy is impractical for the real gas case. The following rigorous procedure could be used to account for real gas effects. Equation 3-34 is a second order differential equation for the velocity profile in a turbulent boundary layer. The density used in Eq. 3-34 must be expressed in terms of the velocity in order to integrate the equation. This is accomplished in the perfect gas case by applying the equation of state and then relating temperature to velocity by means of Eq. 3-10. For the real gas case, the temperature can be replaced by enthalpy in Eq. 3-10. However, the density must then be related to enthalpy by means of a Mollier chart rather than by the equation of state. This is theoretically straightforward; its execution is more complex. Equation 3-34 could then be integrated numerically; the remainder of the calculations could be performed as outlined in Subsec. 3.3. This procedure would be laborious since it would have to be repeated every time there was a change in any of the following parameters: the wall enthalpy, the static pressure, and the velocity or ambient enthalpy outside the boundary layer.

It is shown in Ref. 12 that the values of the laminar skin friction coefficients for a perfect gas can easily be made to agree within 15% with those for a real gas. This agreement can be accomplished without resorting to a reference enthalpy. It is necessary only to present perfect gas results in terms of the wall enthalpy ratio instead of the wall temperature ratio and then to replace $[(\gamma - 1)/2] M_1^2$ by $u_1^2/2h_1$. It is suggested that this procedure be used to estimate turbulent boundary-layer skin friction with real gas effects. In this procedure Eq. 3-42 and Eqs. 3-44 through 3-47, which were

used for calculating the local skin friction coefficient in terms of the Reynolds number (based on x), will now be replaced by:

$$s = 11.5 + 6.6 \left(\frac{h_e - h_w}{h_e} \right) \quad (3-91)$$

and

$$(\sin^{-1} \xi - \sin^{-1} \xi_f) \left(\sigma \frac{h_e}{h_1} C_f \right)^{-\frac{1}{2}} = -6.43 + 4.15 \log_{10} \left(\frac{11.5}{s} \frac{\mu_1}{\mu_w} C_f \text{Re} \right) \quad (3-92)$$

where

$$\xi = \frac{2\sigma - \frac{h_e - h_w}{h_e}}{\left[4\sigma \left(1 - \frac{h_e - h_w}{h_e} \right) + \left(\frac{h_e - h_w}{h_e} \right)^2 \right]^{\frac{1}{2}}} \quad (3-93)$$

$$\xi_f = \frac{2\sigma s \left(\frac{h_w}{h_1} \frac{C_f}{2} \right)^{\frac{1}{2}} - \frac{h_e - h_w}{h_e}}{\left[4\sigma \left(1 - \frac{h_e - h_w}{h_e} \right) + \left(\frac{h_e - h_w}{h_e} \right)^2 \right]^{\frac{1}{2}}} \quad (3-94)$$

$$\sigma = \frac{u_1^2}{2h_1} \left/ \left(1 + \frac{u_1^2}{2h_1} \right) \right. \quad (3-95)$$

$$h_e = \left(1 + r \frac{u_1^2}{2h_1} \right) h_1 \quad (3-96)$$

and

$$r = (\text{Pr}_w)^{\frac{1}{3}} \quad (3-97)$$

Equations 3-51 and 3-52 for calculating the mean skin friction coefficient become

$$(\sin^{-1} \xi - \sin^{-1} \xi_F) 0.242 \left(\sigma \frac{h_e}{h_1} C_F \right)^{-\frac{1}{2}} = -1.968 + \log_{10} \left(\frac{11.5}{s} \frac{\mu_1}{\mu_w} C_F \text{Re} \right) \quad (3-98)$$

where

$$\xi_F = \frac{2\sigma s \left(\frac{h_w}{h_1} \frac{C_F}{2} \right)^{\frac{1}{2}} - \frac{h_e - h_w}{h_e}}{\left[4\sigma \left(1 - \frac{h_e - h_w}{h_e} \right) + \left(\frac{h_e - h_w}{h_e} \right)^2 \right]^{\frac{1}{2}}} \quad (3-99)$$

If a method for calculating the local skin friction coefficient in terms of the momentum thickness Reynolds number, Re_θ , is required, Eqs. 3-55 and 3-57 may be replaced by the following:

$$(\sin^{-1} \xi - \sin^{-1} \xi_F) 0.242 \left(\sigma \frac{h_e}{h_i} C_F \right)^{-\frac{1}{2}} = -1.968 + \log_{10} \left(\frac{23}{s} \frac{\mu_1}{\mu_w} Re_\theta \right) \quad (3-100)$$

and

$$C_f = C_F (-1.968 + \Omega) / (-1.099 + \Omega) \quad (3-101)$$

where

$$\Omega = \log_{10} \left(\frac{23}{s} \frac{\mu_1}{\mu_w} Re_\theta \right) + 0.242 s \left\{ \frac{2\sigma \left(1 - \frac{h_e - h_w}{h_e} \right)}{\left((1 - \xi_F^2) \left[4\sigma \left(1 - \frac{h_e - h_w}{h_e} \right) + \left(\frac{h_e - h_w}{h_e} \right)^2 \right] \right)^{\frac{1}{2}}} \right\} \quad (3-102)$$

As before, C_F in Eqs. 3-100 and 3-101 is used merely as a parameter which is eliminated during the process of numerical calculation.

It is possible to estimate the total thickness and the displacement thickness of the boundary layer by replacing $(T_e - T_w)/T_e$ and $[(\gamma - 1)/2] M_1^2$ by $(h_e - h_w)/h_e$ and $u_1^2/2h_1$, respectively, in Eqs. 3-83 and 3-84. In order to determine the accuracy of these estimates, Eqs. 3-76 and 3-77 should be integrated numerically, taking due account of real gas effects.

3.5 Flat Plate with Transition

The laminar boundary layer on a flat plate has been discussed in Subsecs. 3.1 and 3.2, and the turbulent boundary layer in Subsecs. 3.3 and 3.4. In practice, the entire boundary layer over the plate is laminar only if the Reynolds number is less than some critical value. A turbulent boundary layer, when it exists, develops at some distance downstream of the leading edge with an ill-defined region of transition separating it from the laminar flow. The skin friction on such a plate will be found by a consideration of both the laminar and the turbulent conditions. The Reynolds number at which transition occurs will be treated in detail in Subsec. 5, where it is shown that transition takes place over a finite distance or region, whose length or extent is also discussed. In computing boundary-layer characteristics, it is often satisfactory to assume that transition takes place at some station along the plate and is thus associated with a single transition Reynolds number. This assumption will be used here to compute the skin friction on a flat plate with transitional flow.

Relationships derived from the momentum integral equation will be valid for both laminar and turbulent boundary layers. For the flat plate, the momentum integral equation (Eq. 2-26), reduces to

$$d\theta/dx = C_f/2 \quad (3-103)$$

Since conditions at the outer edge of the boundary layer are constant over the plate, this equation can be written as

$$\frac{dRe_{\theta}}{dRe} = \frac{C_f}{2} \quad (3-104)$$

At the leading edge of the plate both Re and Re_{θ} are zero and hence Eq. 3-104 can be written as

$$Re_{\theta} = \frac{1}{2} \int_0^{Re} C_f dRe \quad (3-105)$$

The mean skin friction coefficient is given by

$$C_F = \frac{1}{x} \int_0^x C_f dx = \frac{1}{Re} \int_0^{Re} C_f dRe \quad (3-106)$$

Equations 3-105 and 3-106 can be combined to yield

$$C_F = 2 \frac{Re_{\theta}}{Re} = 2 \frac{\theta}{x} \quad (3-107)$$

which is independent of the character of the boundary layer.

In the laminar portion of the flow, the local skin friction coefficient may be defined as

$$C_f \sqrt{Re} = K_L \quad (3-108)$$

where K_L depends on whether the gas is perfect or real as well as on such properties as the Mach number and the surface temperature. Various methods for calculating $C_f \sqrt{Re}$ are given in Subsecs. 3.1 and 3.2 and values of K_L may be read from figures such as Fig. 3-3. Equations 3-106 and 3-108 may be combined to give the mean skin friction coefficient in laminar flow as

$$C_F \sqrt{Re} = 2K_L \quad (3-109)$$

Integration of Eq. 3-105 after substituting C_f from Eq. 3-108 leads to the following relationship between Re_{θ} and Re :

$$Re_{\theta} = K_L \sqrt{Re} \quad (3-110)$$

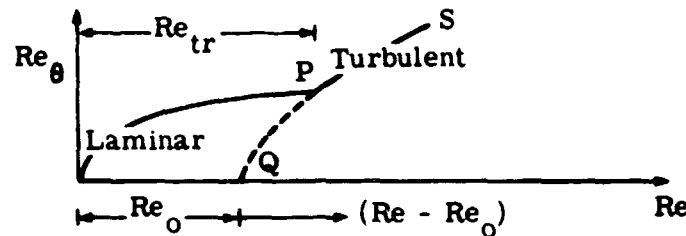
The local and mean laminar skin friction coefficients in terms of Re_{θ} are then

$$C_f Re_\theta = K_L^2 \quad (3-111)$$

and

$$C_F Re_\theta = 2K_L^2 \quad (3-112)$$

When transition is assumed to occur at a point, the shear stress makes a discontinuous change from a laminar value to a turbulent value. The local skin friction coefficient is also discontinuous. Re_θ derived from the integral form of the momentum equation is a continuous function of Re with an abrupt change in slope at the point of transition. The momentum thickness, θ , is a continuous function of x . The sketch below shows the relationship between Re_θ and Re in flow where transition occurs.



Given a value of Re_{tr} , a value of $Re_{\theta tr}$ can be calculated from Eq. 3-110, i.e.,

$$Re_{\theta tr} = K_L \sqrt{Re_{tr}} \quad (3-113)$$

Downstream of the transition point, P , the boundary layer will grow according to the laws of turbulent flow. This growth is identical to that which would exist on a plate having a fully developed turbulent boundary layer originating at point Q (see sketch above). The Reynolds number of this effective leading edge, Q , is Re_0 . The value of Re for this hypothetical fully turbulent flow is $(Re - Re_0)$ whereas $Re_\theta(P)$ has the same value for both cases. Since Re_{tr} is assumed to be known, Re_0 can be calculated. The required relation between Re_θ and Re can be obtained by putting $C_F = 2Re_\theta/Re$ in the perfect gas relation given by Eq. 3-51. For the real gas case, Eq. 3-98 should be used.

When $Re \geq Re_{tr}$ and the Reynolds number in Eqs. 3-44 and 3-51 is replaced by $(Re - Re_0)$, the skin friction coefficients for a plate with its leading edge located at $Re = Re_0$ (i.e., at Q on the previous sketch) will be obtained. These coefficients will be denoted by C_{f_0} and C_{F_0} . Although the values of C_{f_0} may be applied directly to the plate with transitional flow, the mean skin friction coefficient must be corrected, i.e.,

$$C_F = \frac{Re - Re_0}{Re} C_{F_0} \quad (3-114)$$

The procedure indicated previously may be used for the real gas case when Eqs. 3-92 and 3-98 replace Eqs. 3-44 and 3-51. If it is possible to express the turbulent skin friction as a simple function of the Reynolds number, a relationship between C_f and C_F can be obtained for mixed flow in terms of the skin friction coefficients for fully laminar and fully turbulent flows. In Ref. 30, Prandtl and von Karman obtained the following expression for fully turbulent incompressible flow:

$$C_f Re^{1/5} = \text{constant} \quad (3-115)$$

This equation is valid for a moderate range of Reynolds numbers. The exponent $1/5$ indicates that for the turbulent case the skin friction coefficient varies slowly with Reynolds number. Curves of C_f vs Re , calculated by such equations as 3-44 and 3-92, are almost linear in log-log scales, and hence a specific value of the exponent used in the Prandtl approximation may be chosen for the Reynolds number range of interest. For compressible flow, it has also been shown that the turbulent skin friction coefficient changes slowly with Reynolds number. It is therefore reasonable to assume that Eq. 3-115 may be modified to apply to compressible flow. Here the constant has been replaced by K_T , which is a function of such variables as the Mach number and surface temperature as well as the state of the gas (real or perfect), i.e., for a fully turbulent compressible flow over a flat plate, let

$$C_f Re^{1/5} = K_T \quad (3-116)$$

From Eqs. 3-106 and 3-116

$$C_F Re^{1/5} = \frac{5}{4} K_T \quad (3-117)$$

Using Eqs. 3-105 and 3-116, one obtains

$$Re_\theta^{1/4} = \left(\frac{5}{8} K_T \right)^{1/4} Re^{1/5} \quad (3-118)$$

This equation allows both C_f and C_F to be expressed in terms of Re_θ and K_T , i.e.,

$$C_f Re_\theta^{1/4} = \frac{8}{5} \left(\frac{5}{8} K_T \right)^{5/4} \quad (3-119)$$

and

$$C_F Re_\theta^{1/4} = 2 \left(\frac{5}{8} K_T \right)^{5/4} \quad (3-120)$$

It should be noted that Eq. 3-119 for the local skin friction coefficient is valid for any region where the flow is turbulent. However, the mean skin friction coefficient given by Eq. 3-120 is valid only where the flow over the entire plate

is turbulent, i.e., the hypothetical plate shown in the last sketch. Substituting Eq. 3-119 in 3-104 and integrating the result gives

$$Re_{\theta}^{5/4} = \left(\frac{5}{8} K_T \right)^{5/4} Re + \text{constant} \quad (3-121)$$

This equation is valid in any turbulent region. At the transition point ($Re = Re_{tr}$ and $Re_{\theta} = Re_{\theta tr}$), Eqs. 3-112 and 3-121 combine to give

$$Re_{\theta}^{5/4} = \left(K_L \sqrt{Re_{tr}} \right)^{5/4} + \left(\frac{5}{8} K_T \right)^{5/4} (Re - Re_{tr}) \quad (3-122)$$

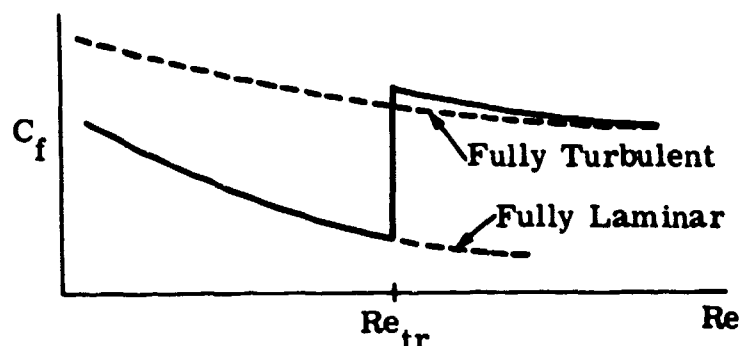
Substituting Re_{θ} from Eq. 3-122 in Eq. 3-119 and making use of Eqs. 3-108 and 3-116, one obtains

$$C_f = \frac{C_{fT}}{\left\{ 1 - \frac{Re_{tr}}{Re} + \left(\frac{8}{5} \frac{C_{fL}}{C_{fT}} \right)^{5/4} \left(\frac{Re_{tr}}{Re} \right)^{5/8} \right\}^{1/5}} \quad (3-123)$$

A combination of Eqs. 3-107, 3-109, 3-117, and 3-122 yields

$$C_F = C_{FT} \left\{ 1 - \frac{Re_{tr}}{Re} + \left(\frac{C_{FL}}{C_{FT}} \right)^{5/4} \left(\frac{Re_{tr}}{Re} \right)^{5/8} \right\}^{4/5} \quad (3-124)$$

The subscripts L and T indicate values of the coefficients associated with a particular Re for a plate with fully laminar or fully turbulent flow. Equations 3-123 and 3-124 are valid for $Re \geq Re_{tr}$. The values of the laminar coefficients can be obtained by the methods given in Subsecs. 3.1 and 3.2. Although simplified relationships between the skin friction coefficients and the Reynolds number in turbulent flow were used in the above derivation, the turbulent skin friction coefficients given in Subsecs. 3.3 and 3.4 can now be used in Eqs. 3-123 and 3-124. These equations are approximations which can be used for a quick determination of the effect of varying Re_{tr} . It is of interest to note that, at the transition point, there is a single discontinuity in C_f ; its value jumps, immediately becomes larger than that for fully turbulent flow and then rapidly approaches the turbulent curve from above. This is illustrated below.



On the other hand the mean skin friction coefficient makes an abrupt change at the transition point and then gradually approaches the turbulent curve from below as shown in the next sketch.

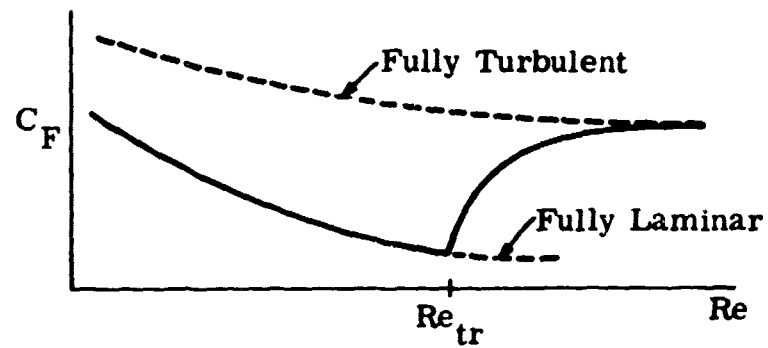


Table 3-1

Graphical Information Presented by Crocco in Ref. 4

Dependent Variable	Independent Variable	Primary Parameter	Secondary Parameter
$C_f \sqrt{Re}$	u_1^2/h_1 or M	h_{*w}	$\left(\frac{\partial h}{\partial u_*}\right)_w = 0$
$C_f \sqrt{Re}$	β	u^2/h_1	h_{*w}
$C_f \sqrt{Re}$	h_{*w}	u^2/h_1	$\beta, \left(\frac{\partial h}{\partial u_*}\right)_w = 0$
h_*	u_*	$Pr = 1$ $Pr = 0.725$ } $(\rho u = \text{const})$ $Pr = 0.725^\dagger$	$u_1^2/h_1 = 0$ and 10 $h_{*w} \approx 0.3, 2.1$ and 5.3
$\left(\frac{\partial h}{\partial u_*}\right)_w$	$h_{*w} = 0$ to 6	$u_1^2/h_1 = 0$ to 10	$Pr = 1$ $Pr = 0.725 (\rho u = \text{const})$ $Pr = 0.725^\dagger$
$g_*, y/\delta, h_*$	u_*	$\beta = 0$	$u_1^2/h_1 = 0$ and 10

Ranges of Variables

$$u_1^2/h_1 = 0, 0.4, 1.6, 3.6, 6.4, 10$$

$$M = 1 \text{ to } 5$$

$$\beta = 0, 1/3, 1.3$$

$$h_{*w} = 0.25, 0.5, 1, 1.5, 2$$

[†] Sutherland's law used for viscosity

Table 3-2

Graphical Information Presented by Van Driest in Ref. 9

Dependent Variable	Independent Variable	Primary Parameter	Secondary Parameter
$C_F \sqrt{Re}$ $C_h \sqrt{Re}$ $(\delta/x) \sqrt{Re}$	M_1	T_{*w}	
g_*	u_*	M_1	T_{*w}
u_*, T_*, M_*	$\frac{y}{x} \sqrt{Re}$	M_1	T_{*w}
u_*, T_*	$\frac{y}{x} \sqrt{Re}$	T_{*w}	M_1
M_*	y/δ	T_{*w}	M_1
u_*, T_*, M_*	$\frac{y}{x} \sqrt{Re}$	M_1	$Pr = 1.0,$ <u>Insulated Plate</u>
h_{*t}	$\frac{y}{x} \sqrt{Re}$	M_1	

Range of Variables $Pr = 0.75$ or 1.0 $\gamma = 1.4$ $T_1 = -67.6^\circ F$ $\beta = 0.505$ $y = \delta$ at $u_* = 0.995$ $M_1 = 0$ to 20 $T_{*w} = 0.25, 1, 2, 4, 6$

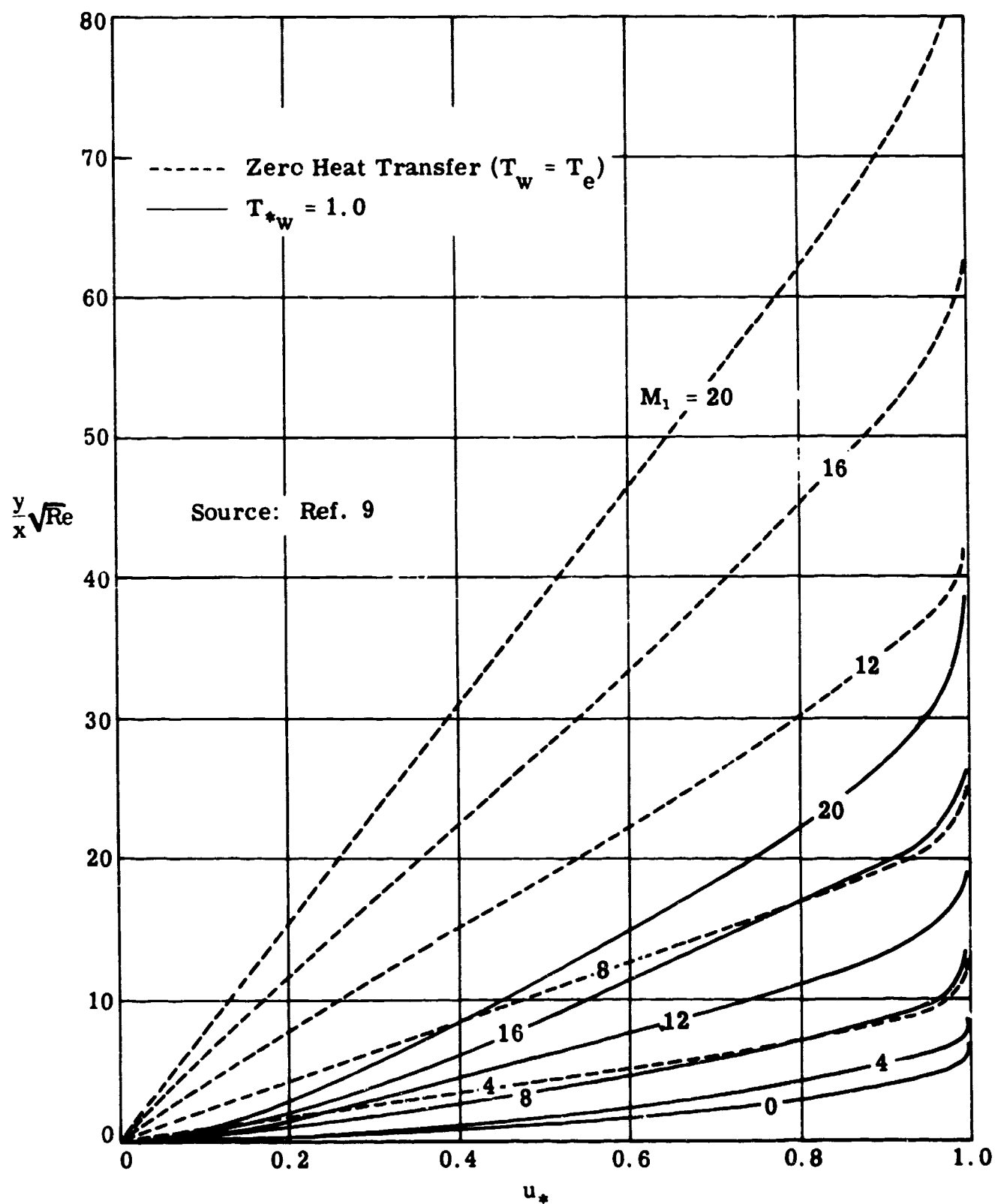


Fig. 3-1. Flat plate laminar boundary layer; $(y/x)\sqrt{Re}$ vs u_* ; $T_w = T_e$ and T_1 ; $M_1 = 0, 4, 8, 12, 16$, and 20 ; $Pr = 0.75$; perfect gas, $\gamma = 1.4$; $\beta = 0.505$.

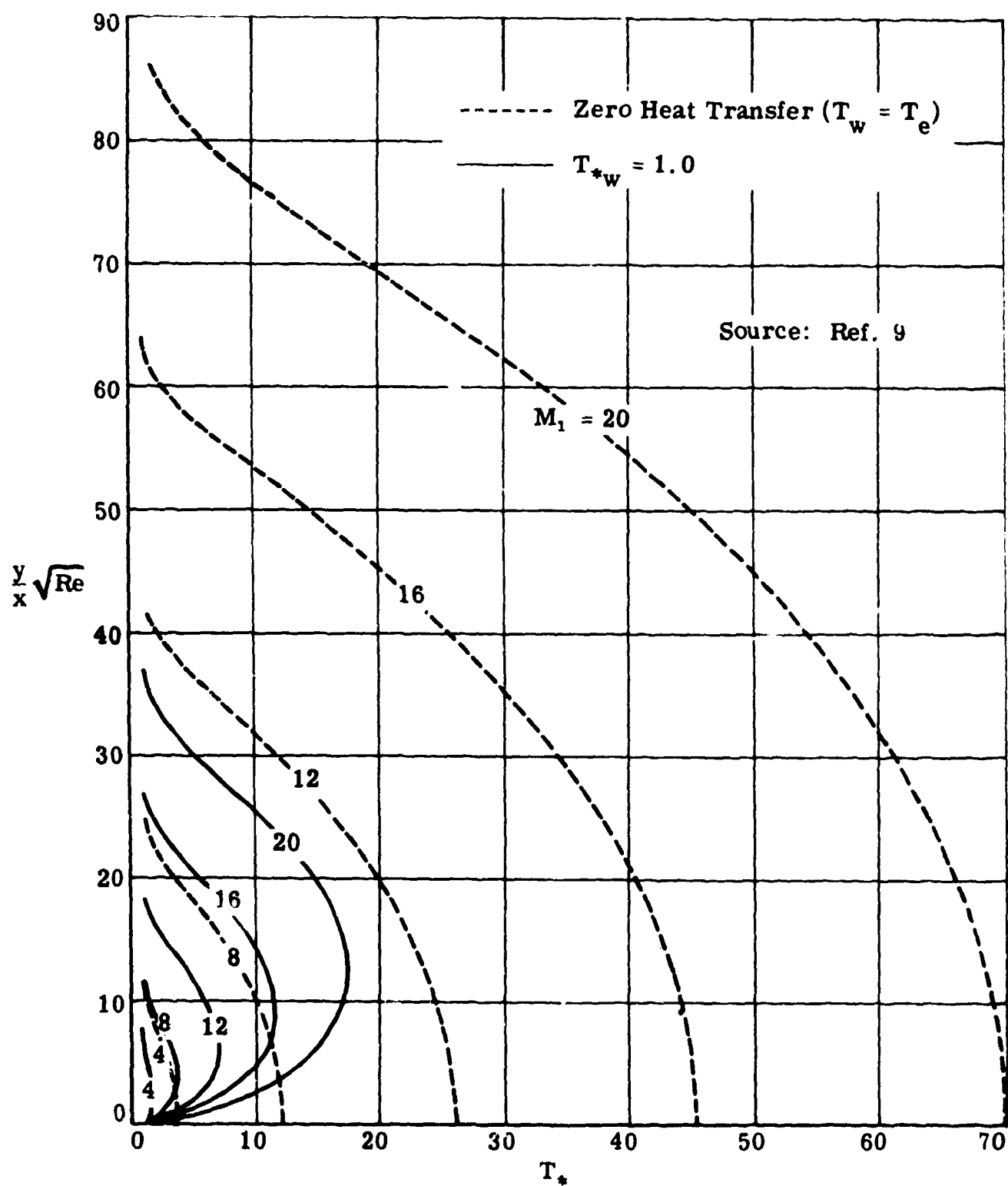


Fig. 3-2. Flat plate laminar boundary layer; $(y/x) \sqrt{Re}$ vs T_* ; $T_w = T_e$ and T_1 , $M_1 = 4, 8, 12, 16$, and 20 ; $Pr = 0.75$; perfect gas, $\gamma = 1.4$; $\beta = 0.505$.

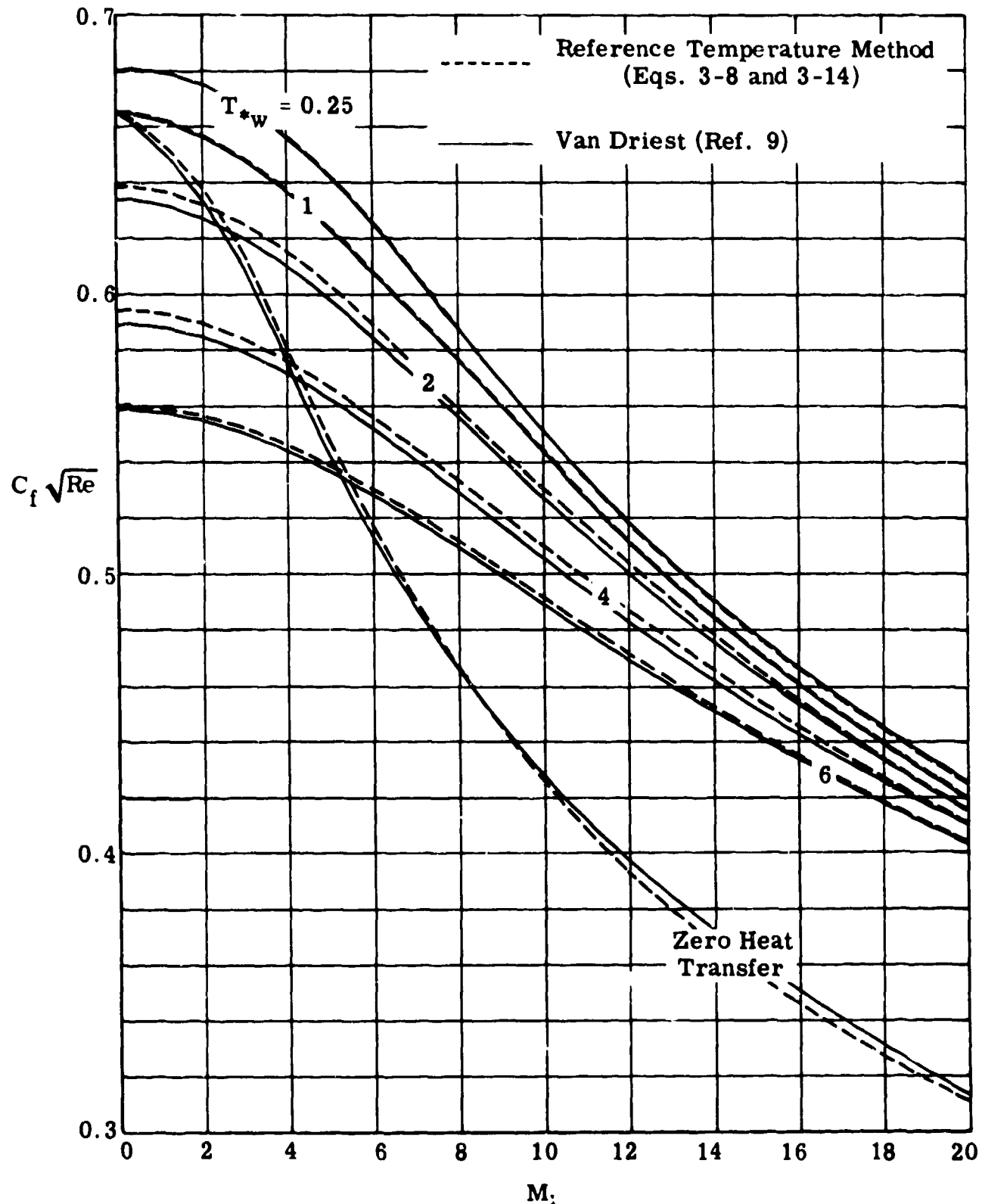


Fig. 3-3. Flat plate laminar boundary layer; comparison of theoretical values of $C_f \sqrt{Re}$ vs M_1 ; Van Driest and reference temperature methods; $M_1 = 0$ to 20; $T_{*w} = 0.25, 1, 2, 4$, and 6 and $T_w = T_e$; $Pr = 0.75$; perfect gas, $\gamma = 1.4$; $\beta = 0.505$.

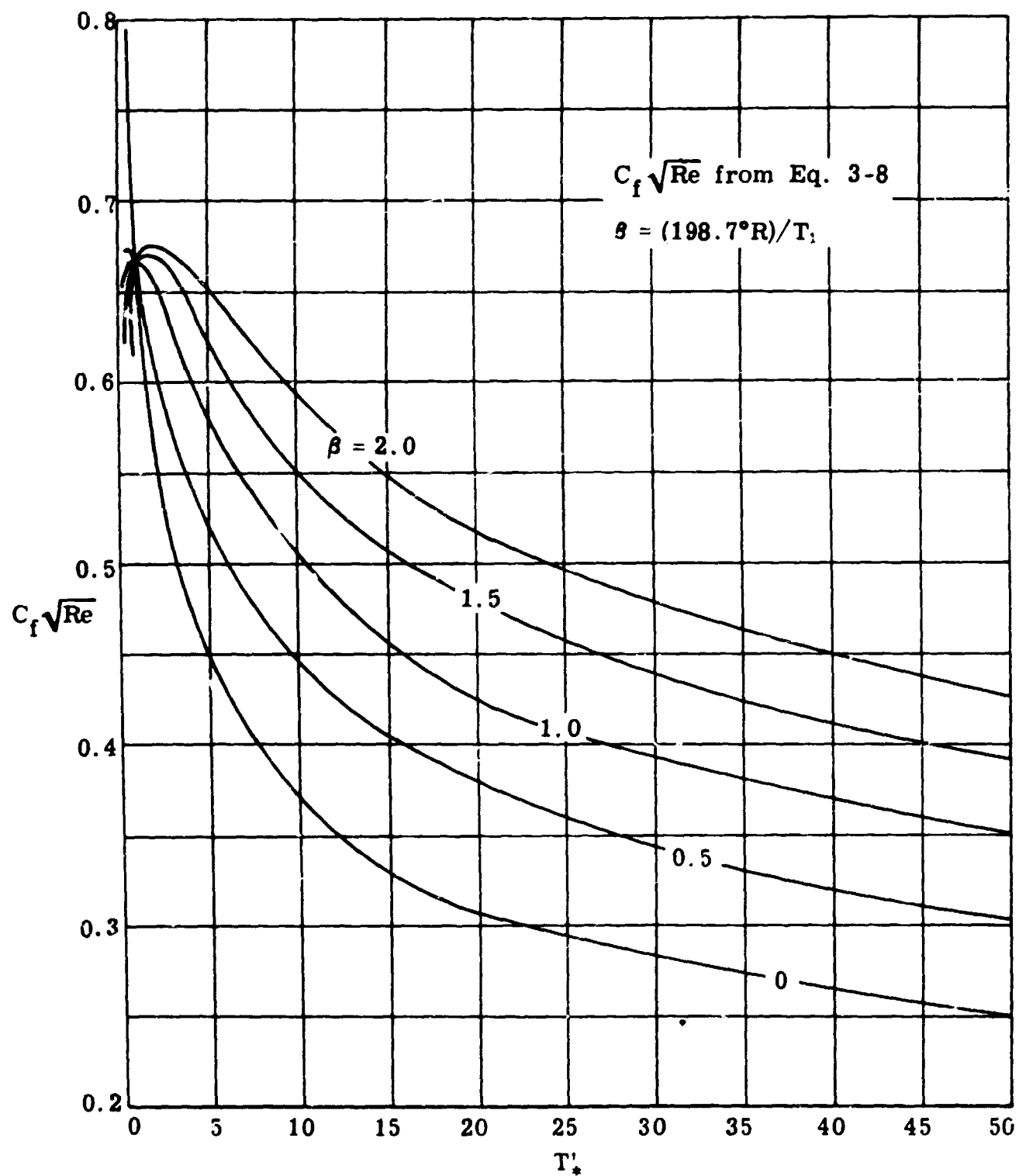


Fig. 3-4. Flat plate laminar boundary layer; $C_f \sqrt{Re}$ vs T'_* ; $\beta = 0, 0.5, 1.0, 1.5$, and 2.0 ; perfect gas, $\gamma = 1.4$.

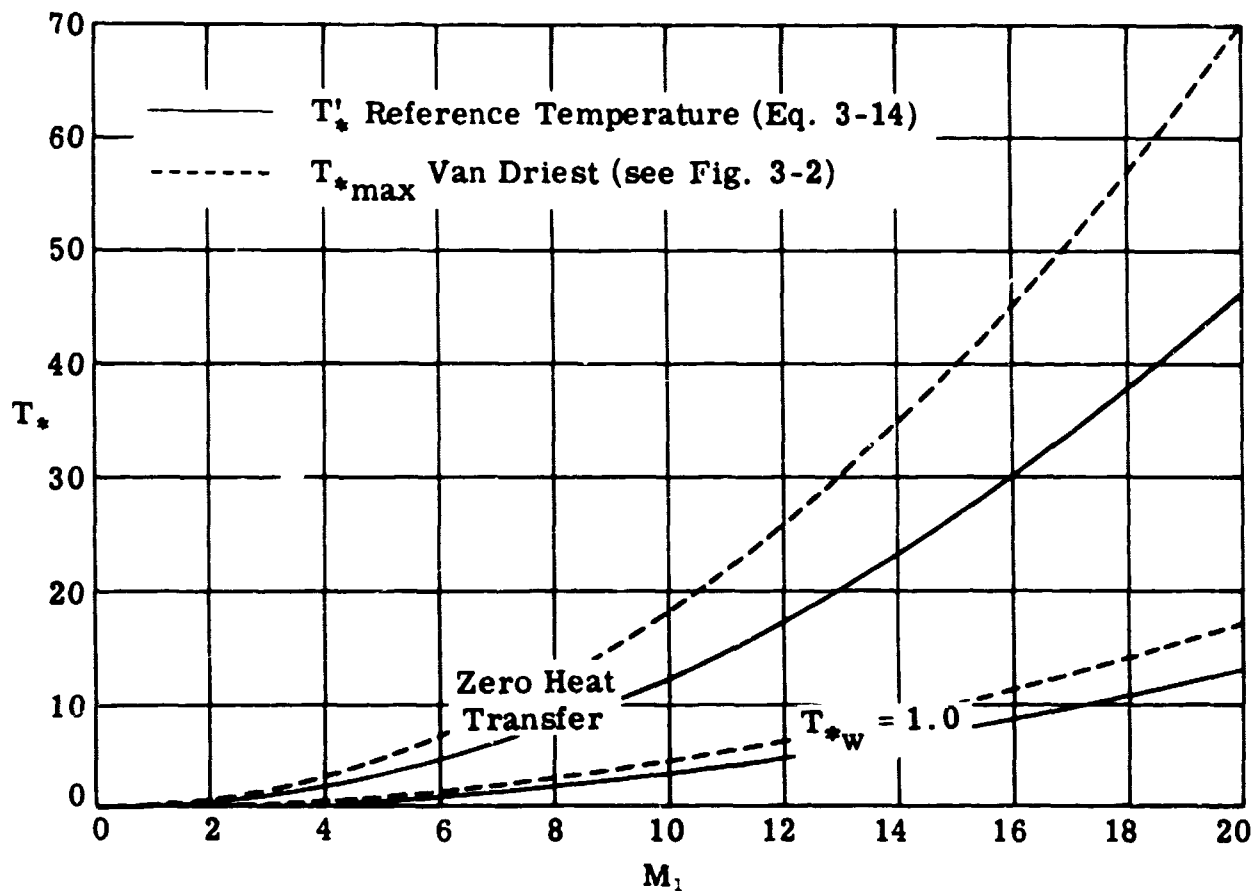


Fig. 3-5. Flat plate laminar boundary layer; comparison of maximum temperature (Van Driest) and reference temperature as a function of M_1 ; $M_1 = 0$ to 20; $T_w = T_e$ and T_1 ; perfect gas, $\gamma = 1.4$; $Pr = 0.75$; $\beta = 0.505$.

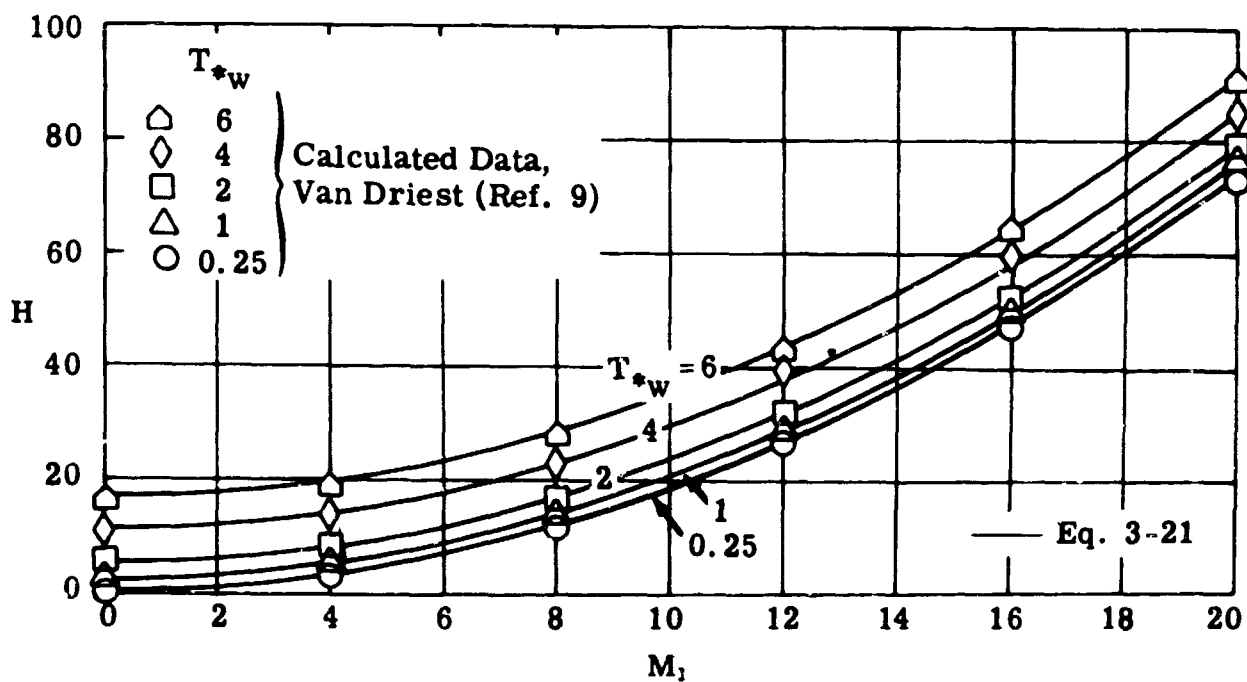


Fig. 3-6. Flat plate laminar boundary layer; shape parameter, H , vs M_1 ; $M_1 = 0$ to 20; $T_{*w} = 0.25, 1, 2, 4$, and 6; perfect gas, $\gamma = 1.4$; $Pr = 0.75$; $T_1 = 392.4^\circ R$.

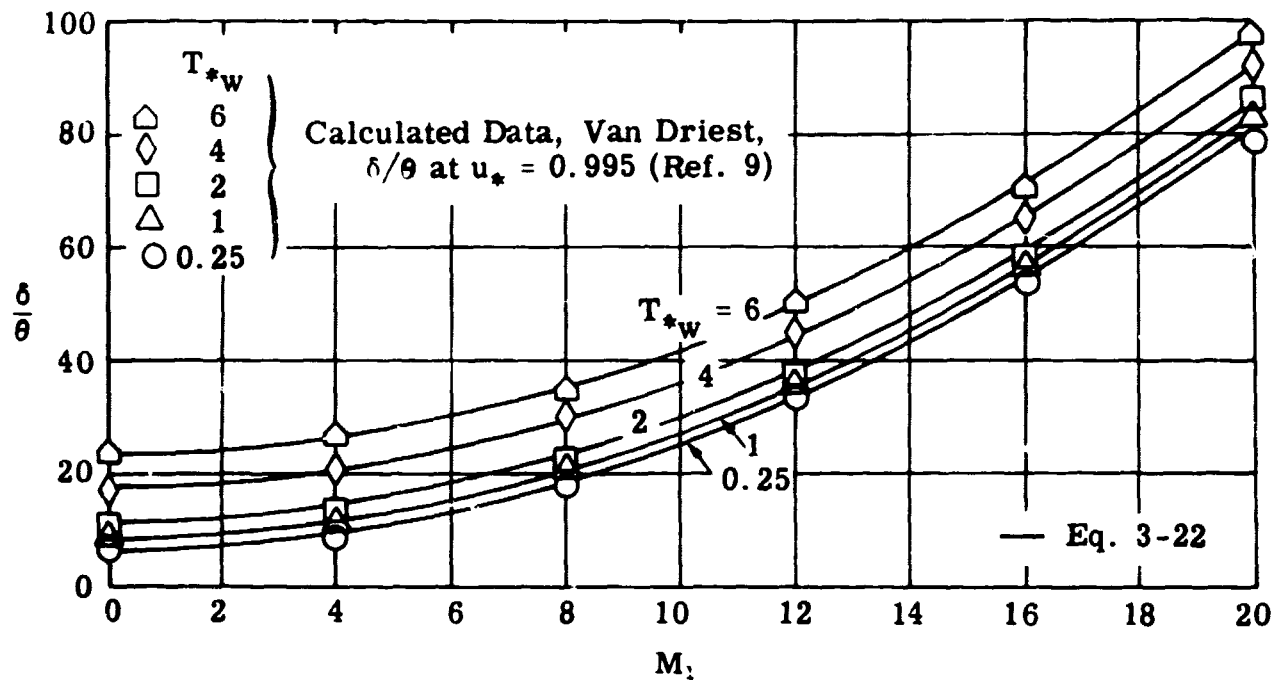


Fig. 3-7. Flat plate laminar boundary-layer thickness, δ/θ vs M_1 ; $M_1 = 0$ to 20; $T^*_{w} = 0.25, 1, 2, 4,$ and 6; perfect gas, $\gamma = 1.4$; $Pr = 0.75$; $T_1 = 392.4^\circ R$.

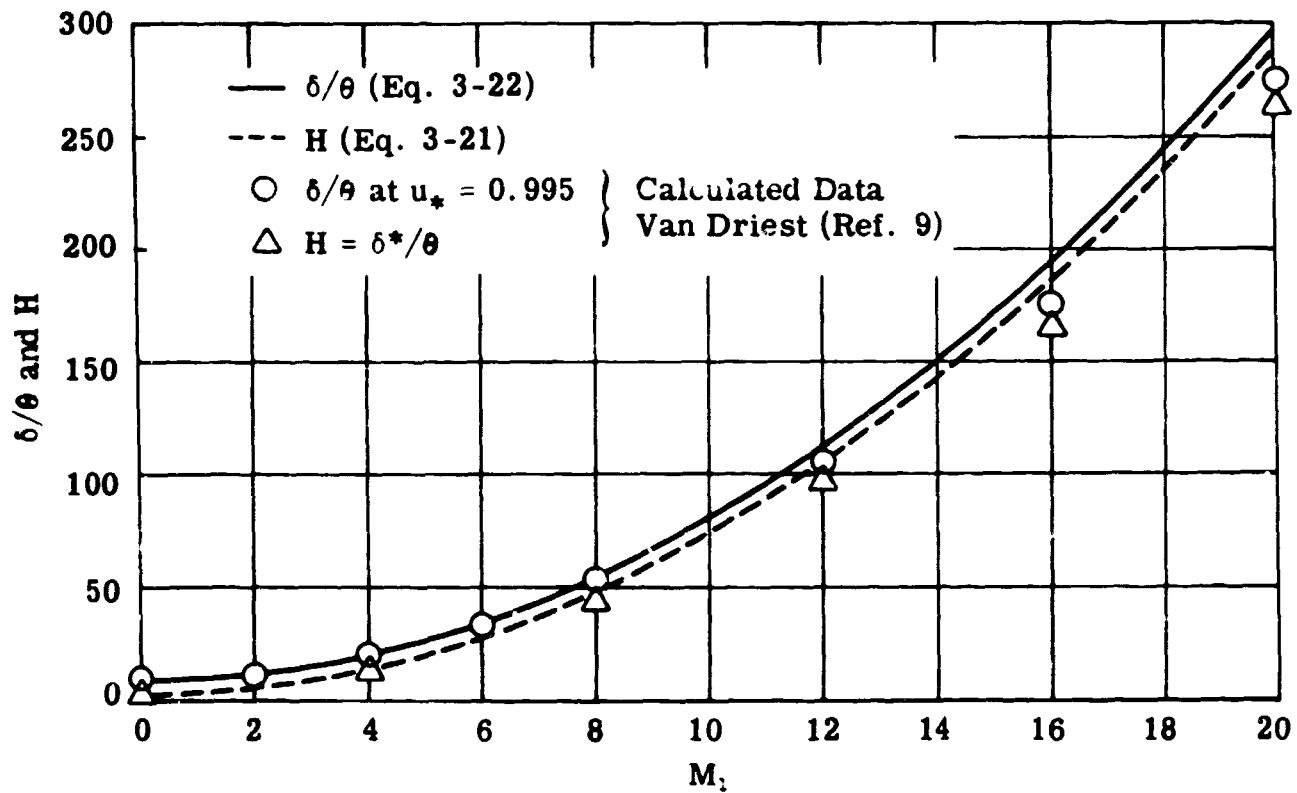


Fig. 3-8. Flat plate laminar boundary-layer thickness and shape parameter vs M_1 ; $M_1 = 0$ to 20; zero heat transfer; perfect gas, $\gamma = 1.4$; $Pr = 0.75$; $T_1 = 392.4^\circ R$.

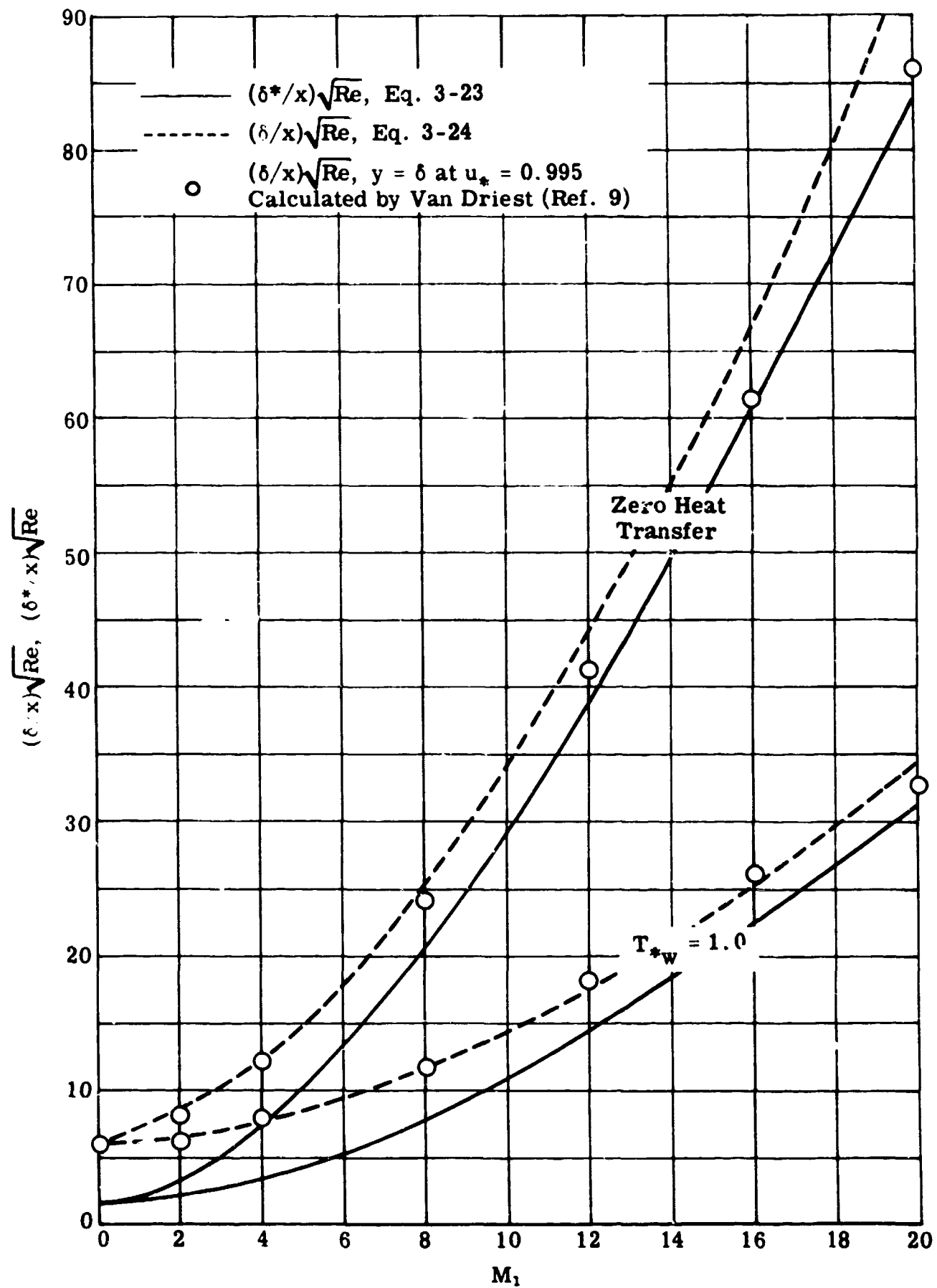


Fig. 3-9. Flat plate laminar boundary layer: $(\delta/x)\sqrt{Re}$ and $(\delta^*/x)\sqrt{Re}$ vs M_1 ; $M_1 = 0$ to 20 ; $T_w = T_e$ and T_1 ; perfect gas, $\gamma = 1.4$; $Pr = 0.75$; $\beta = 0.505$.

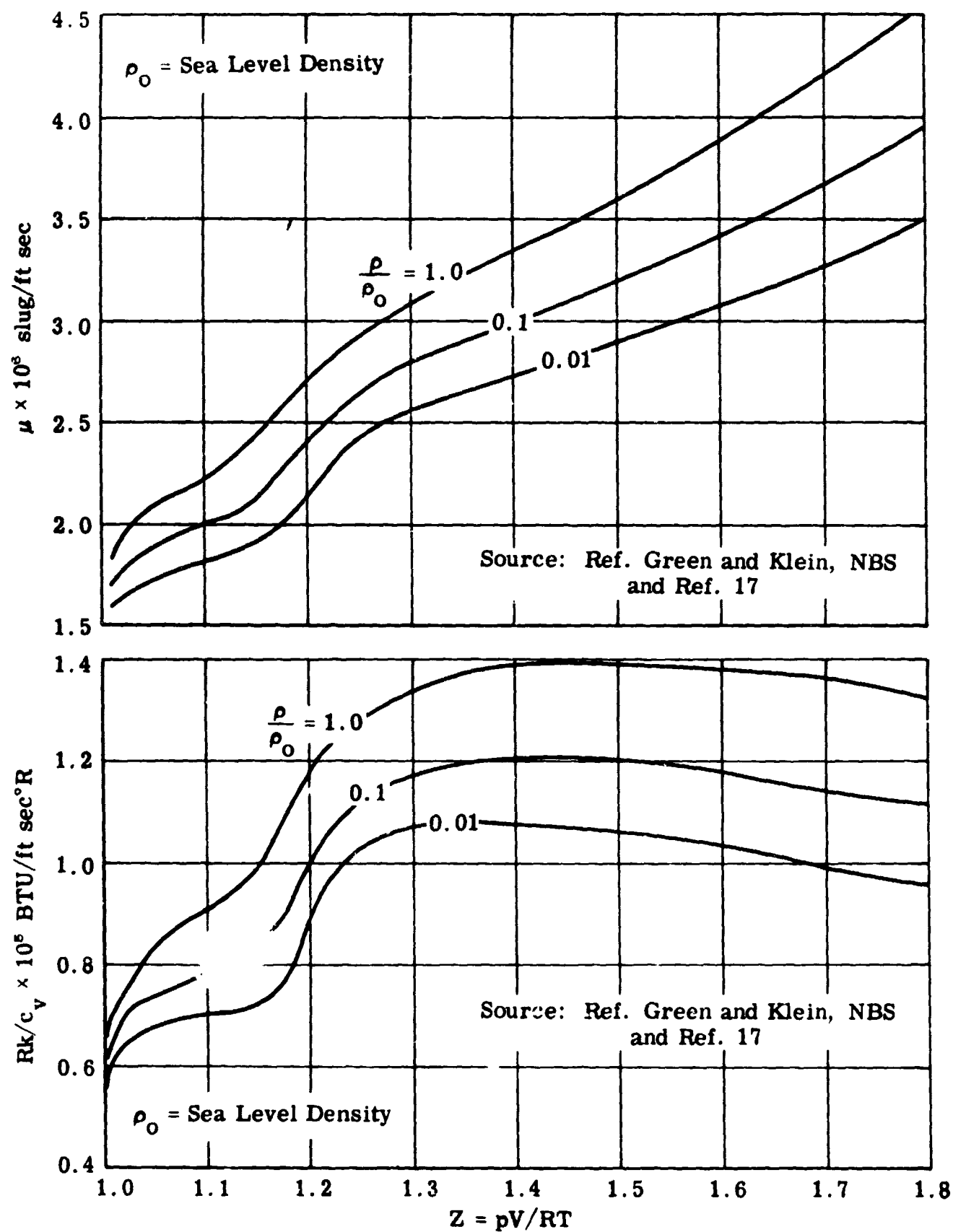


Fig. 3-10. Variation of μ and Rk/c_v with Z for air; $Z = 1.0$ to 1.8 ;
 $\rho/\rho_0 = 0.01, 0.1$, and 1.0 .

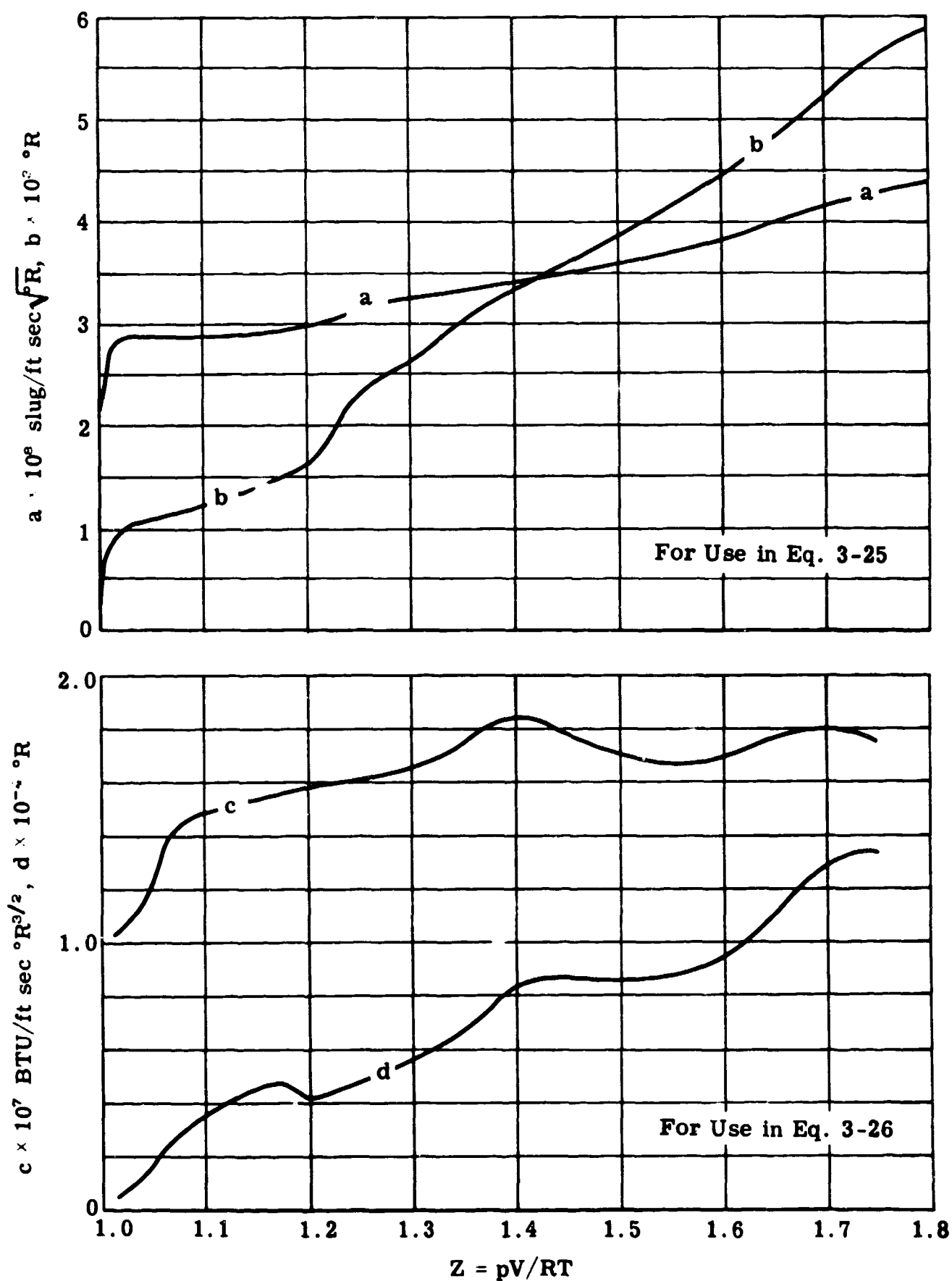


Fig. 3-11. Variation of a , b , c , and d with Z for use in Eqs. 3-25 and 3-26; $Z = 1.0$ to 1.8 .

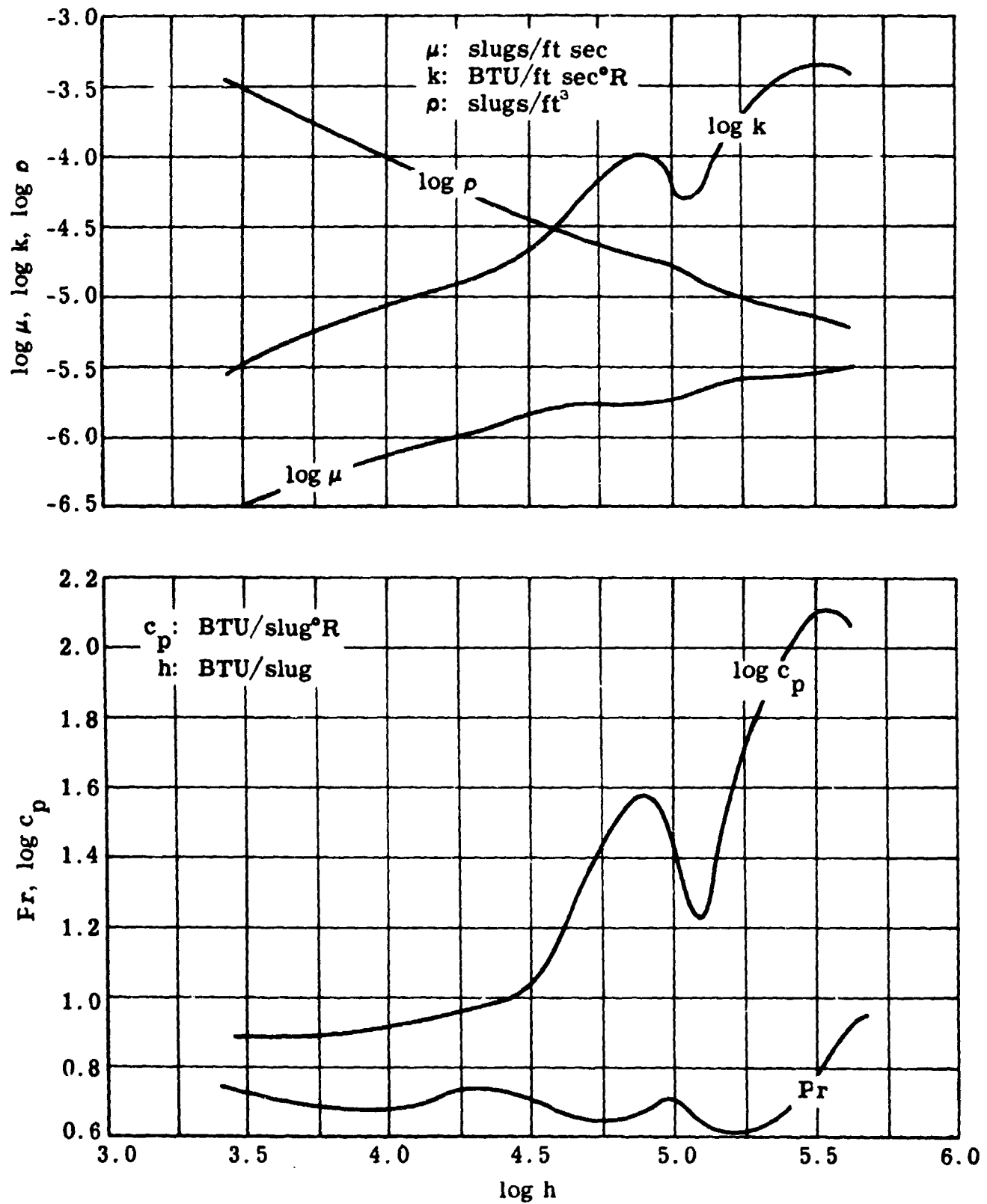


Fig. 3-12. Variation of μ , k , c_p , ρ , and Pr with enthalpy for air at $p = 0.1$ atm.

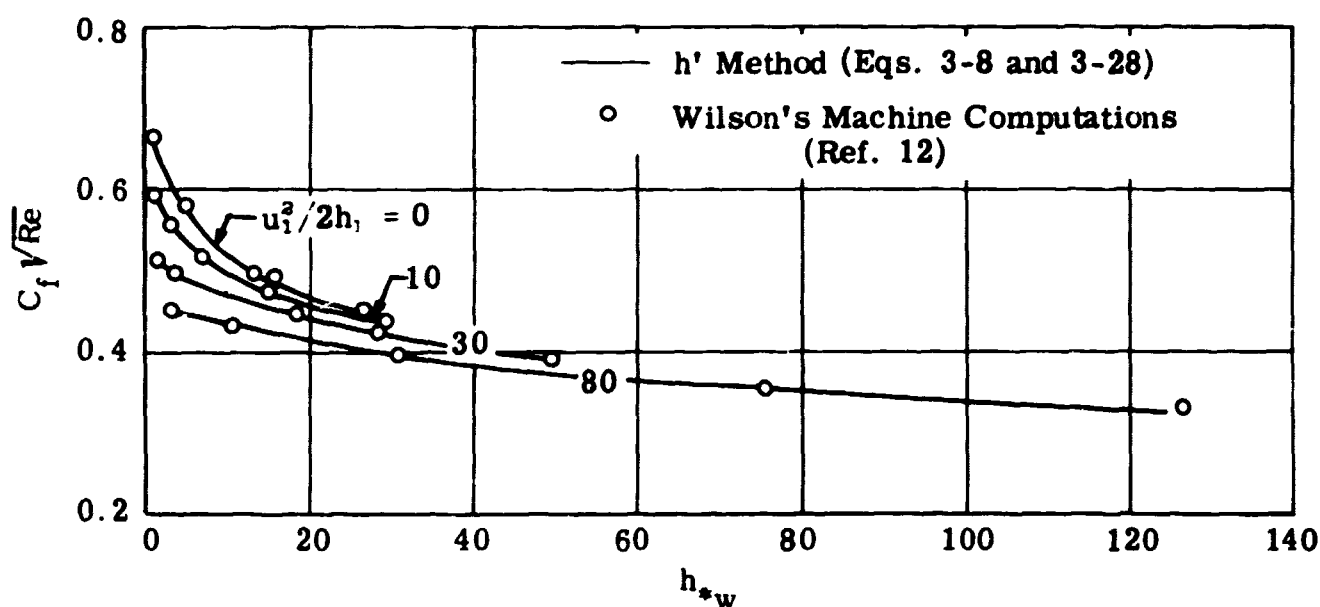


Fig. 3-13. Real gas flat plate laminar boundary layer; comparison of exact and approximate values of $C_f \sqrt{Re}$ vs h_{*w} ; $h_{*w} = 0$ to 140; $u_1^2/2h_1 = 0, 10, 30$, and 80; $h_1 = 3000$ BTU/slug; $p_1 = 0.1$ atm.

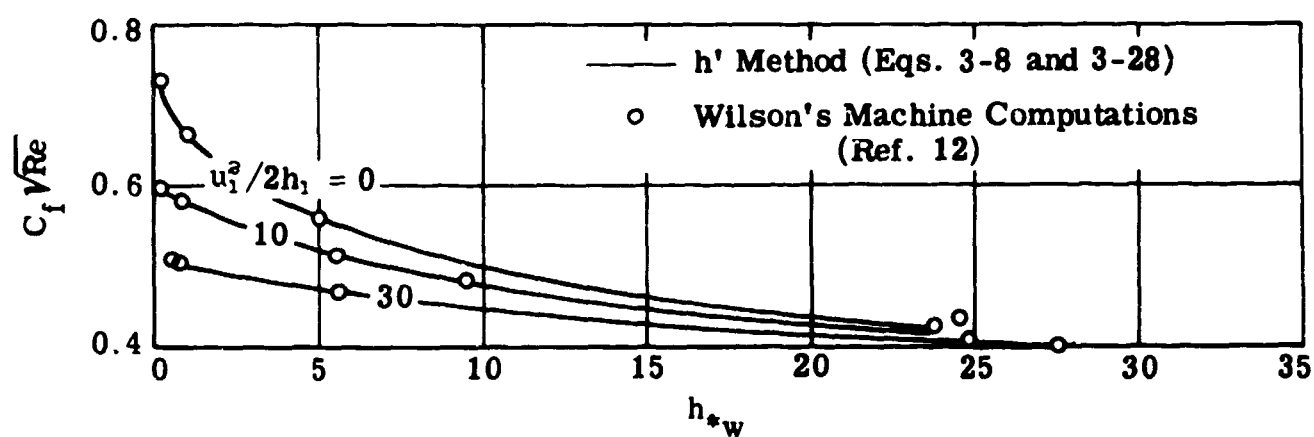


Fig. 3-14. Real gas flat plate laminar boundary layer; comparison of exact and approximate values of $C_f \sqrt{Re}$ vs h_{*w} ; $h_{*w} = 0$ to 35; $u_1^2/2h_1 = 0, 10$, and 30; $h_1 = 15,000$ BTU/slug; $p_1 = 0.1$ atm.

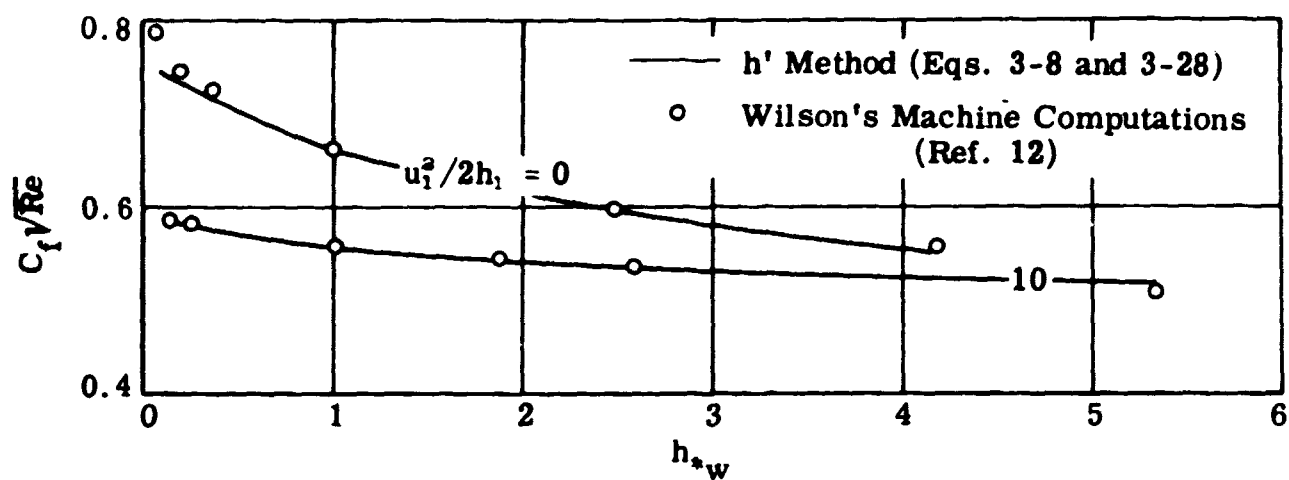


Fig. 3-15. Real gas flat plate laminar boundary layer; comparison of exact and approximate values of $C_f \sqrt{Re}$ vs h_{*w} ; $h_{*w} = 0$ to 6; $u_1^2/2h_1 = 0$ and 10; $h_1 = 75,000$ BTU/slug; $p_1 = 0.1$ atm.

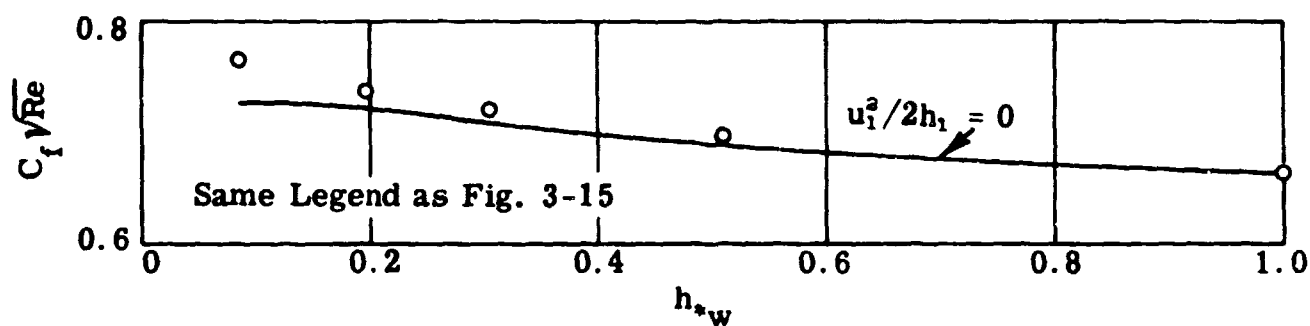


Fig. 3-16. Real gas flat plate laminar boundary layer; comparison of exact and approximate values of $C_f \sqrt{Re}$ vs h_{*w} ; $h_{*w} = 0$ to 1; $u_1^2/2h_1 = 0$; $h_1 = 400,000$ BTU/slug; $p_1 = 0.1$ atm.

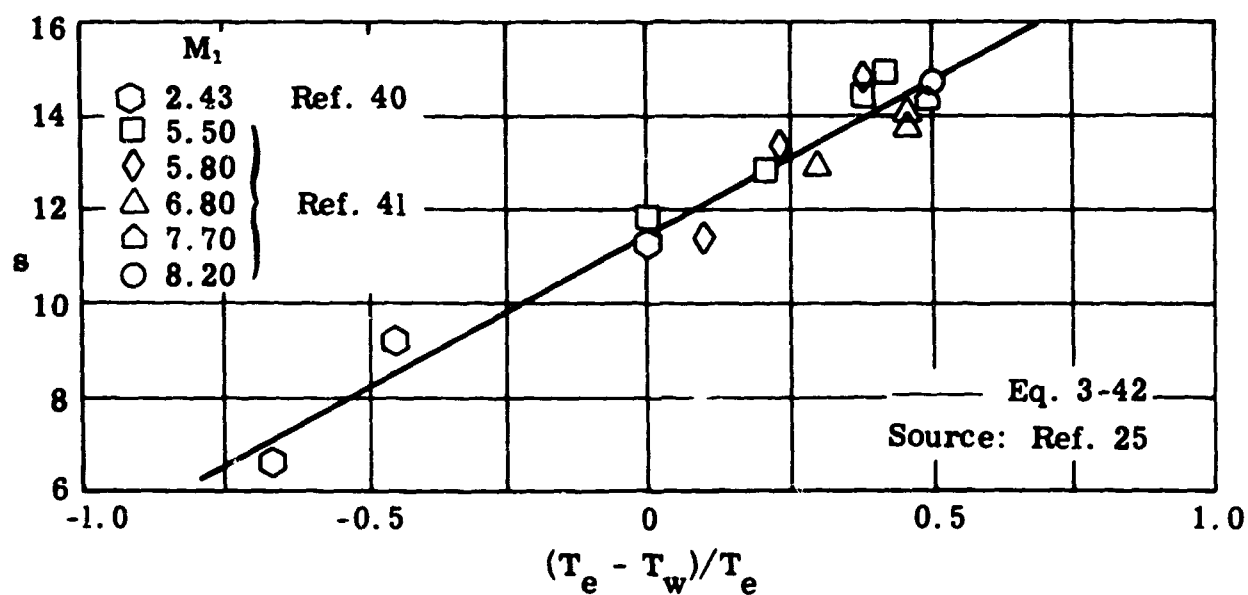


Fig. 3-17. Effect of heat transfer on laminar sublayer parameter, s .

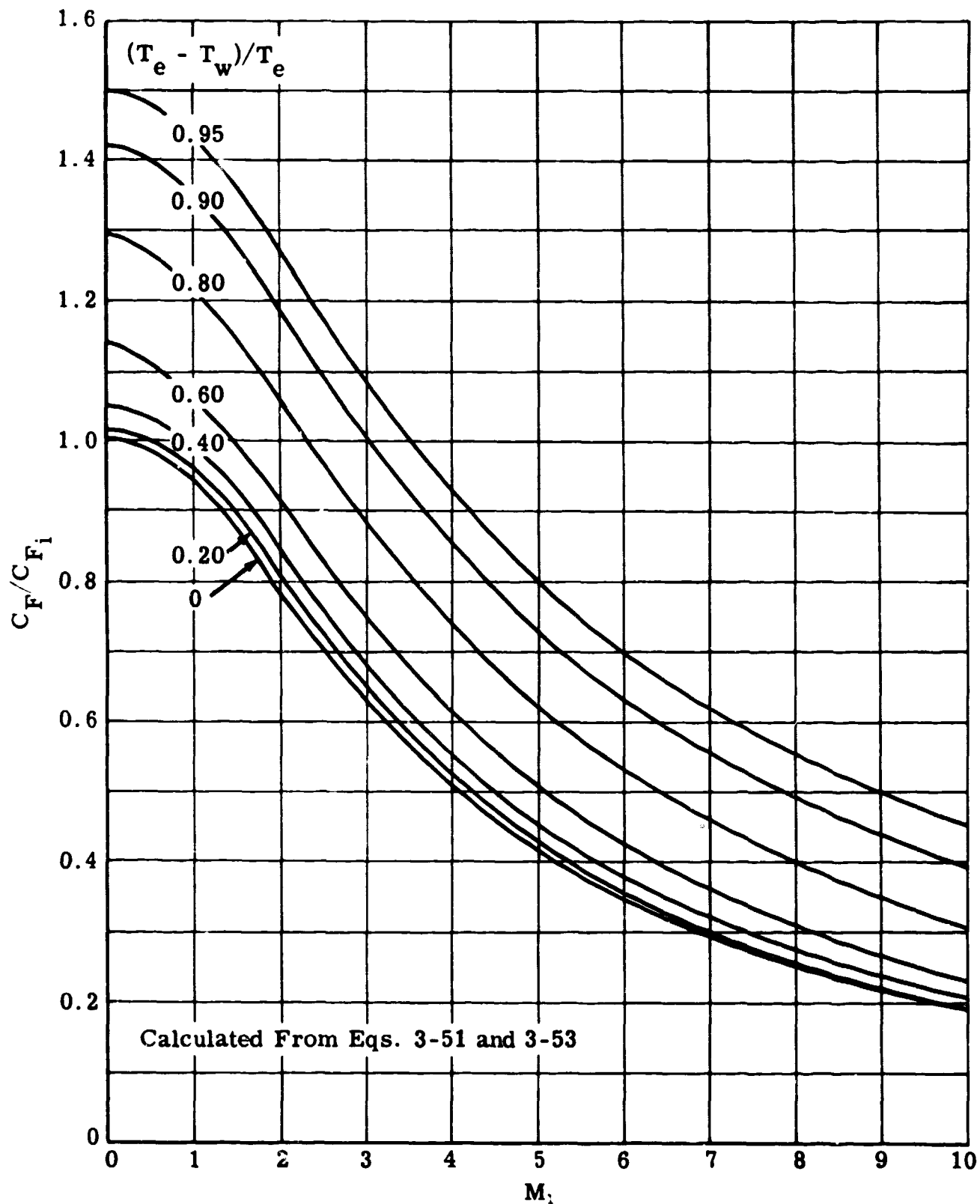


Fig. 3-18. Flat plate turbulent boundary layer; C_F/C_{F_i} vs M_1 ; $M_1 = 0$ to 10; $(T_e - T_w)/T_e = 0, 0.2, 0.4, 0.6, 0.8, 0.9$, and 0.95 ; perfect gas, $\gamma = 1.4$; $Pr = 0.70$; $Re = 10^7$; $\beta = 0.505$.

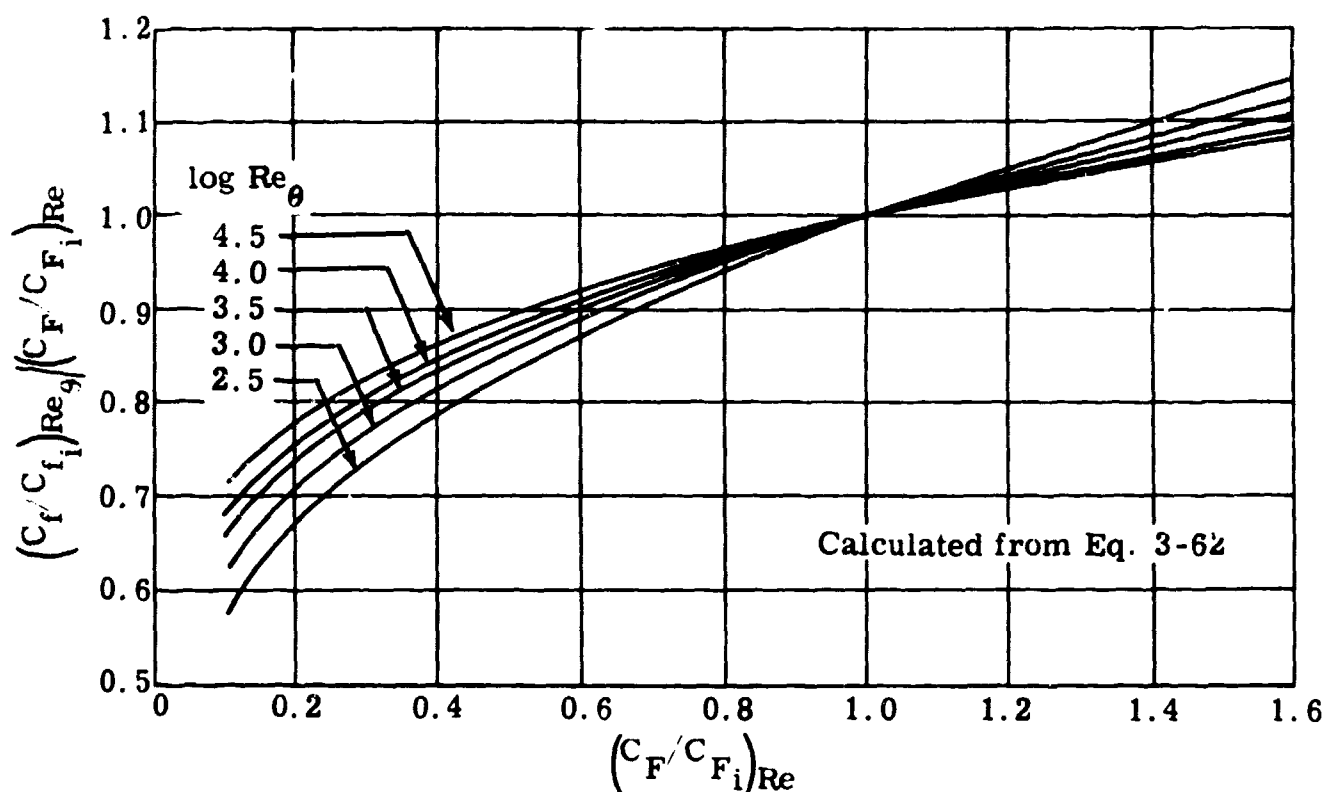


Fig. 3-19. Flat plate turbulent boundary layer; $(C_f/C_{f_i})_{Re_\theta} / (C_f/C_{f_i})_{Re}$ vs $(C_f/C_{f_i})_{Re}$; $(C_f/C_{f_i})_{Re} = 0$ to 1.6 ; $\log Re_\theta = 2.5, 3.0, 3.5, 4.0$, and 4.5 ; perfect gas, $\gamma = 1.4$; $Pr = 0.70$.

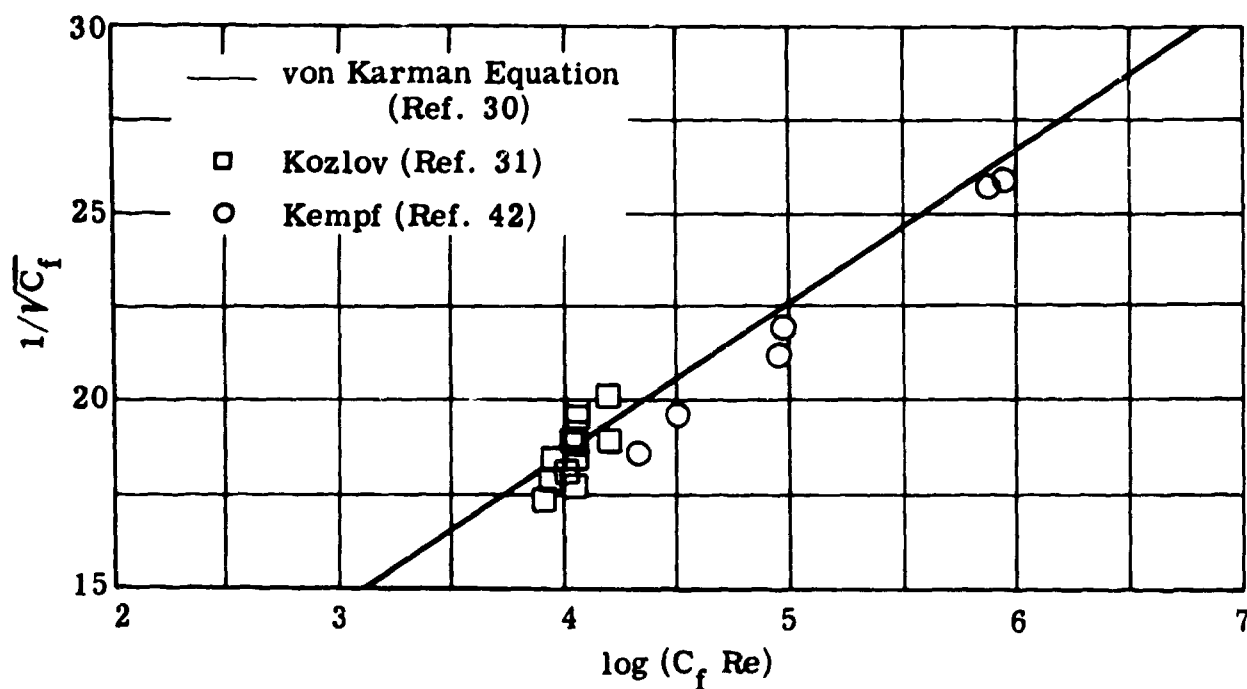


Fig. 3-20. Flat plate turbulent boundary layer; comparison of experimental and theoretical incompressible skin friction; $1/\sqrt{C_f}$ vs $\log(C_f Re)$; perfect gas, $\gamma = 1.4$; $Pr = 0.70$; $Re = 10^5$ to 10^6 .

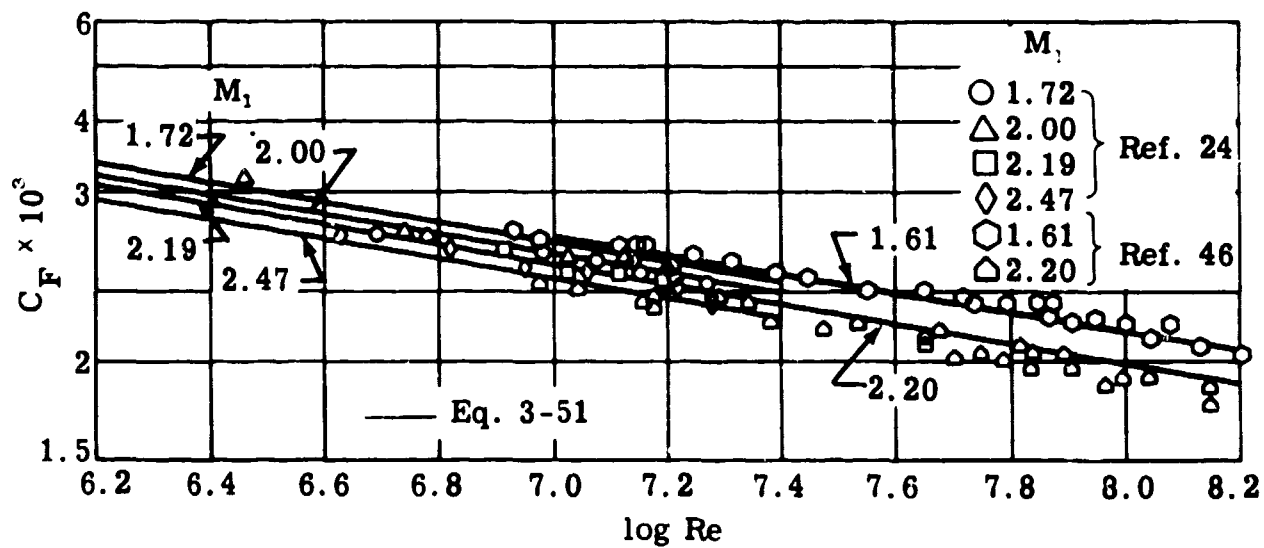


Fig. 3-21. Flat plate turbulent boundary layer; C_F vs $\log Re$; theory and experiment; zero heat transfer; perfect gas, $\gamma = 1.4$; $Pr = 0.70$.

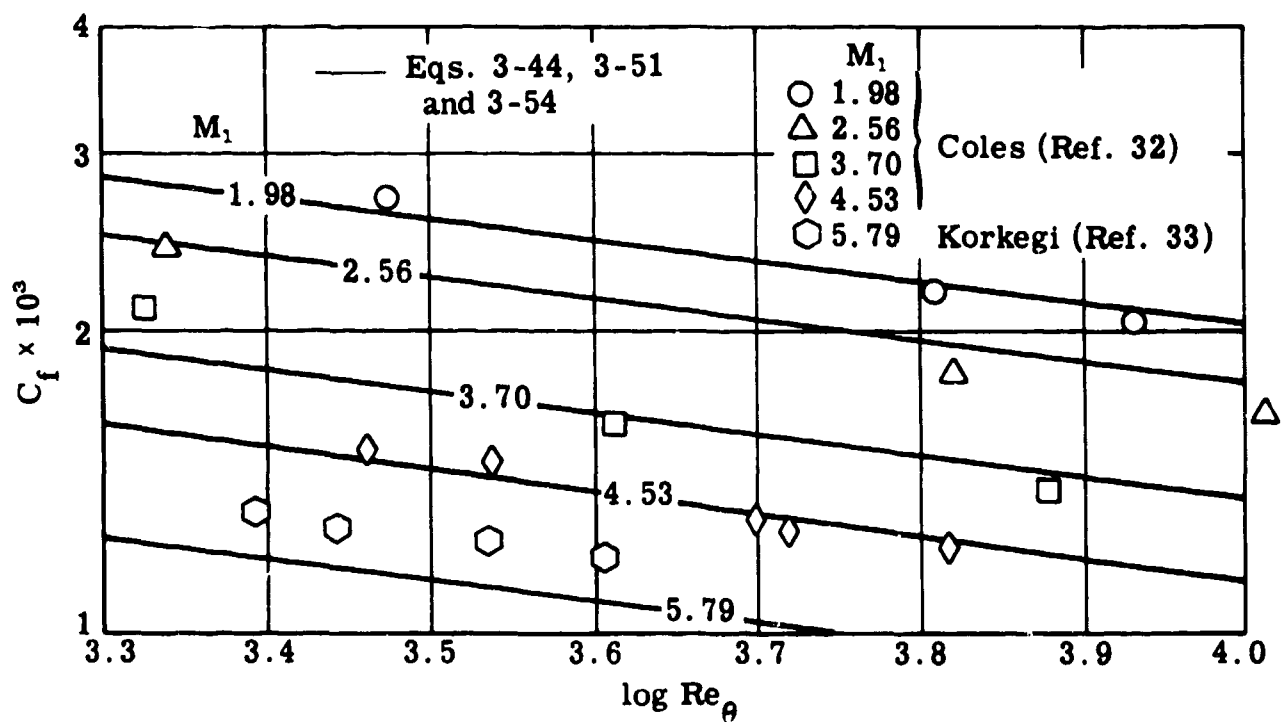


Fig. 3-22. Flat plate turbulent boundary layer; C_f vs $\log Re_\theta$; theory and experiment; zero heat transfer; perfect gas, $\gamma = 1.4$; $Pr = 0.70$.

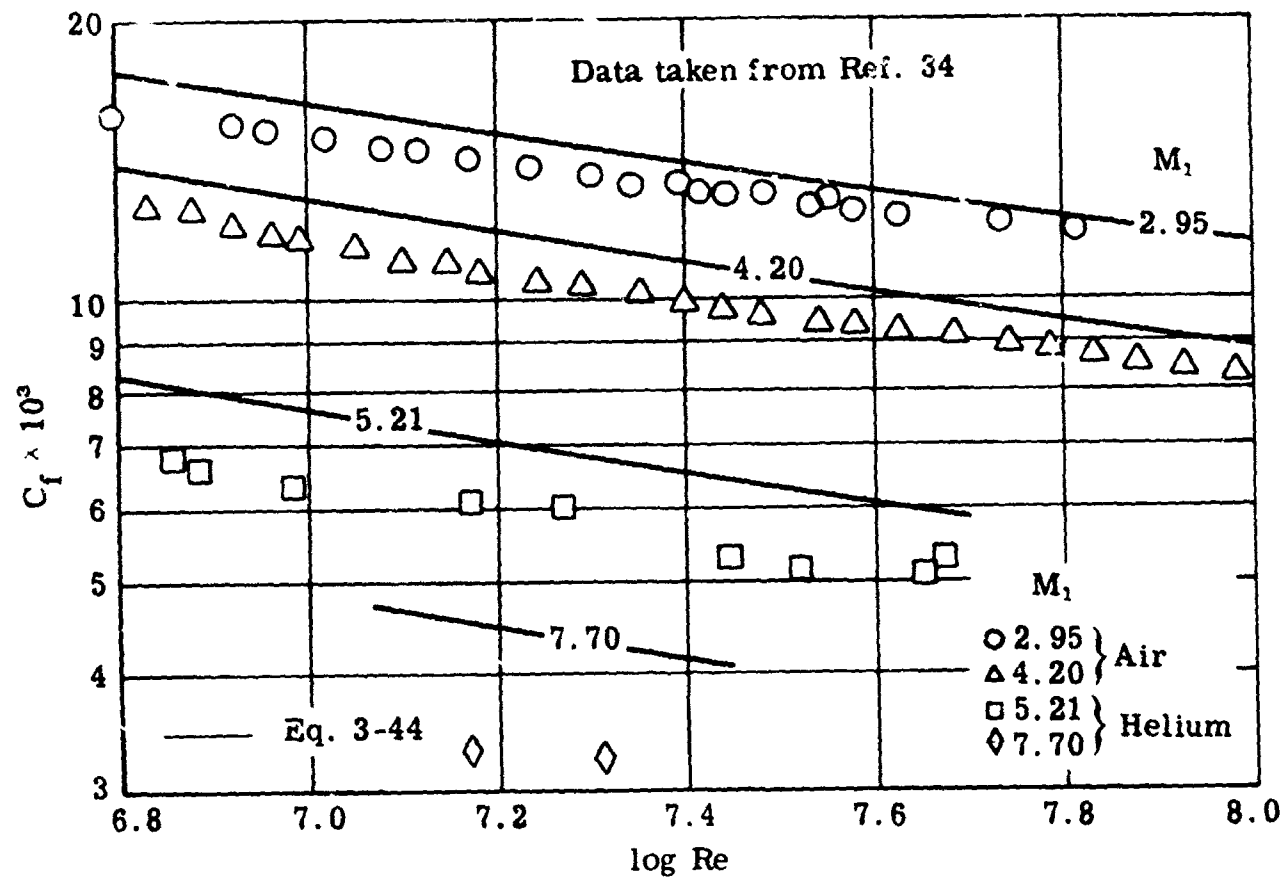


Fig. 3-23. Flat plate turbulent boundary layer; C_f vs $\log Re$; theory and experiment; zero heat transfer; perfect gas, $\gamma = 1.4$; $Pr = 0.70$.

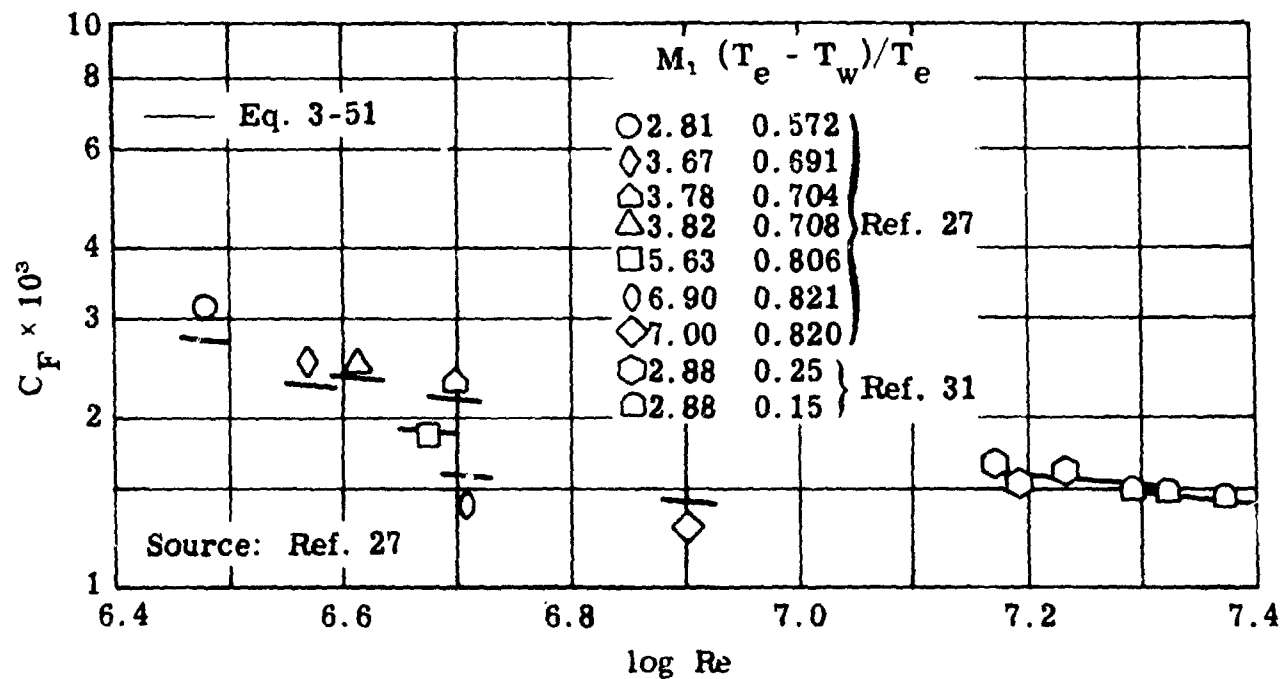


Fig. 3-24. Flat plate turbulent boundary layer; C_F vs $\log Re$; theory and experiment; various heat-transfer ratios and Mach numbers; perfect gas, $\gamma = 1.4$; $Pr = 0.70$.

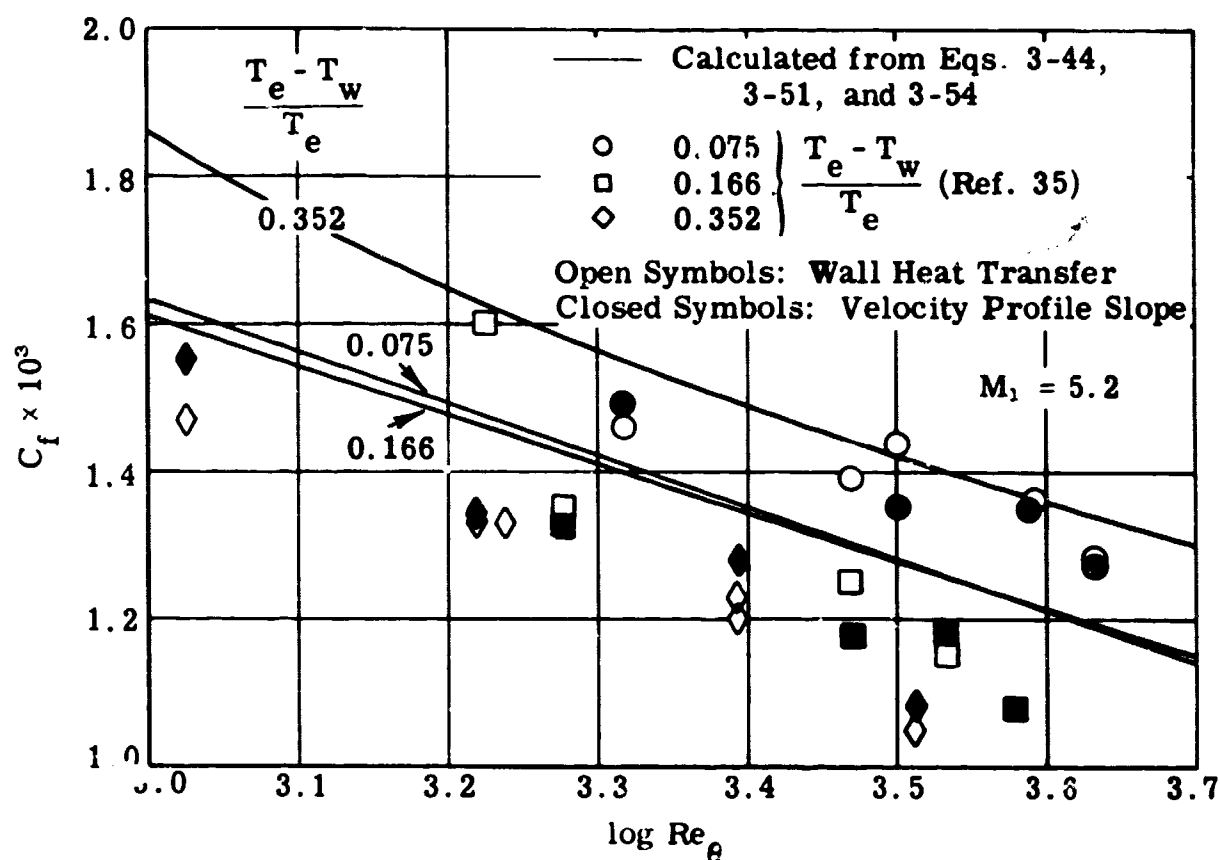


Fig. 3-25. Flat plate turbulent boundary layer; C_f vs $\log Re$; theory and experiment; $(T_e - T_w)/T_e = 0.075, 0.166$, and 0.352 ; $M_1 = 5.2$; perfect gas, $\gamma = 1.4$; $Pr = 0.70$.

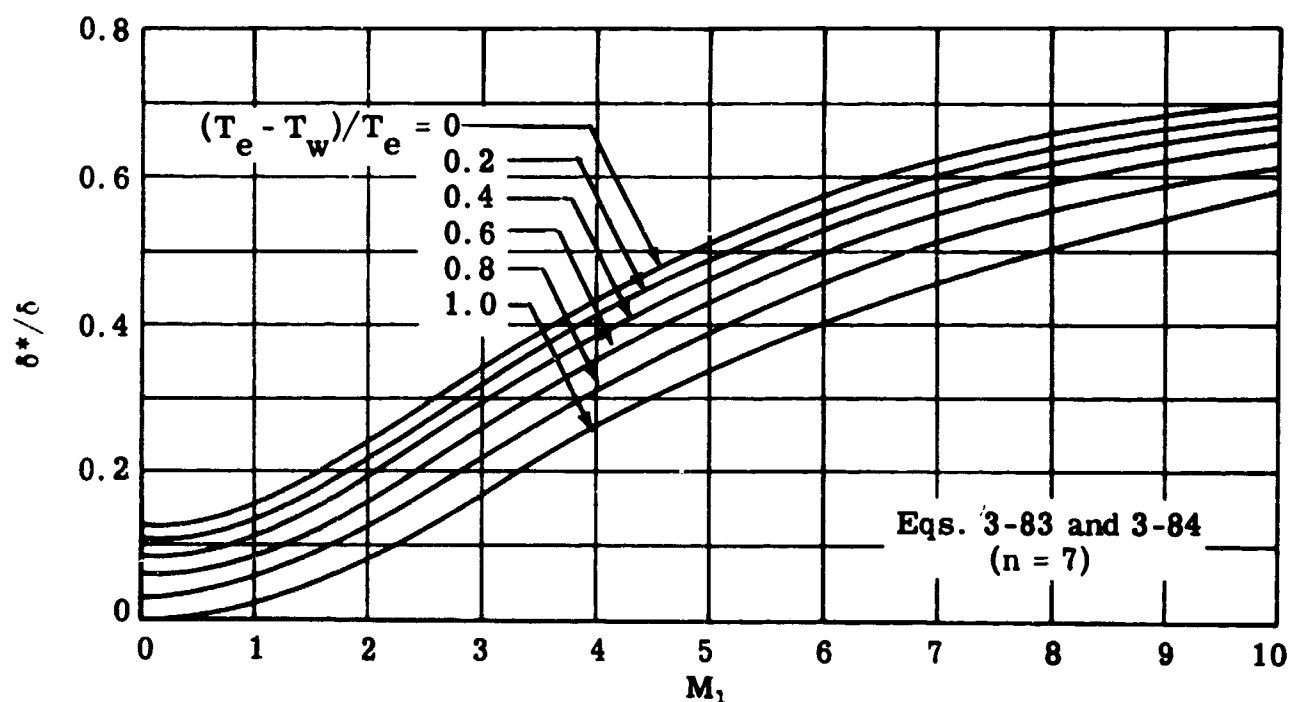


Fig. 3-26. Flat plate turbulent boundary layer; δ^*/δ vs M_1 ; $M_1 = 0$ to 10 ; $(T_e - T_w)/T_e = 0, 0.2, 0.4, 0.6, 0.8$, and 1.0 ; perfect gas, $\gamma = 1.4$; $Pr = 0.70$.

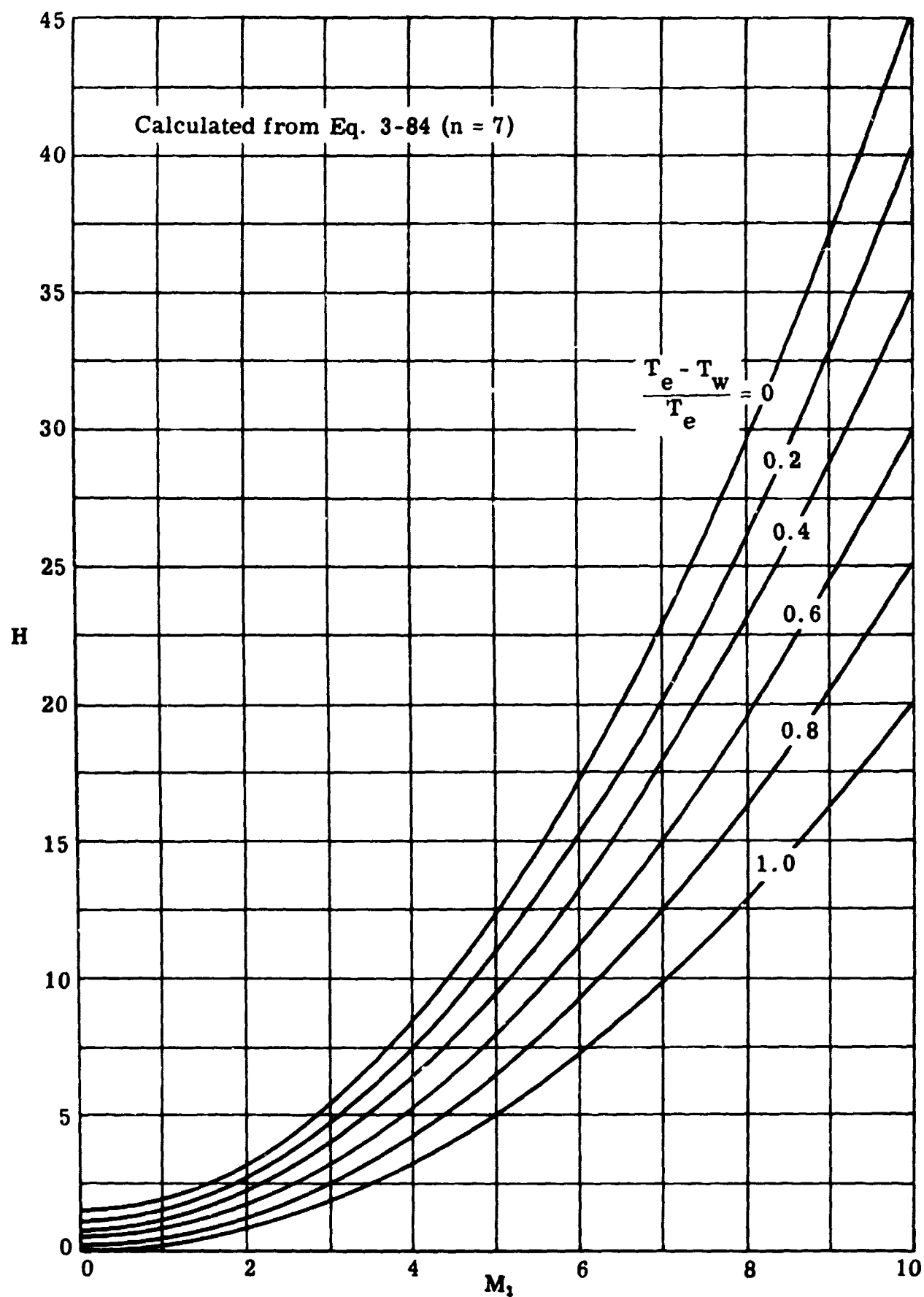


Fig. 3-27. Flat plate turbulent boundary layer; shape parameter H vs M_1 ; $M_1 = 0$ to 10; $(T_e - T_w)/T_e = 0, 0.2, 0.4, 0.6, 0.8$, and 1.0; perfect gas, $\gamma = 1.4$; $Pr = 0.70$.

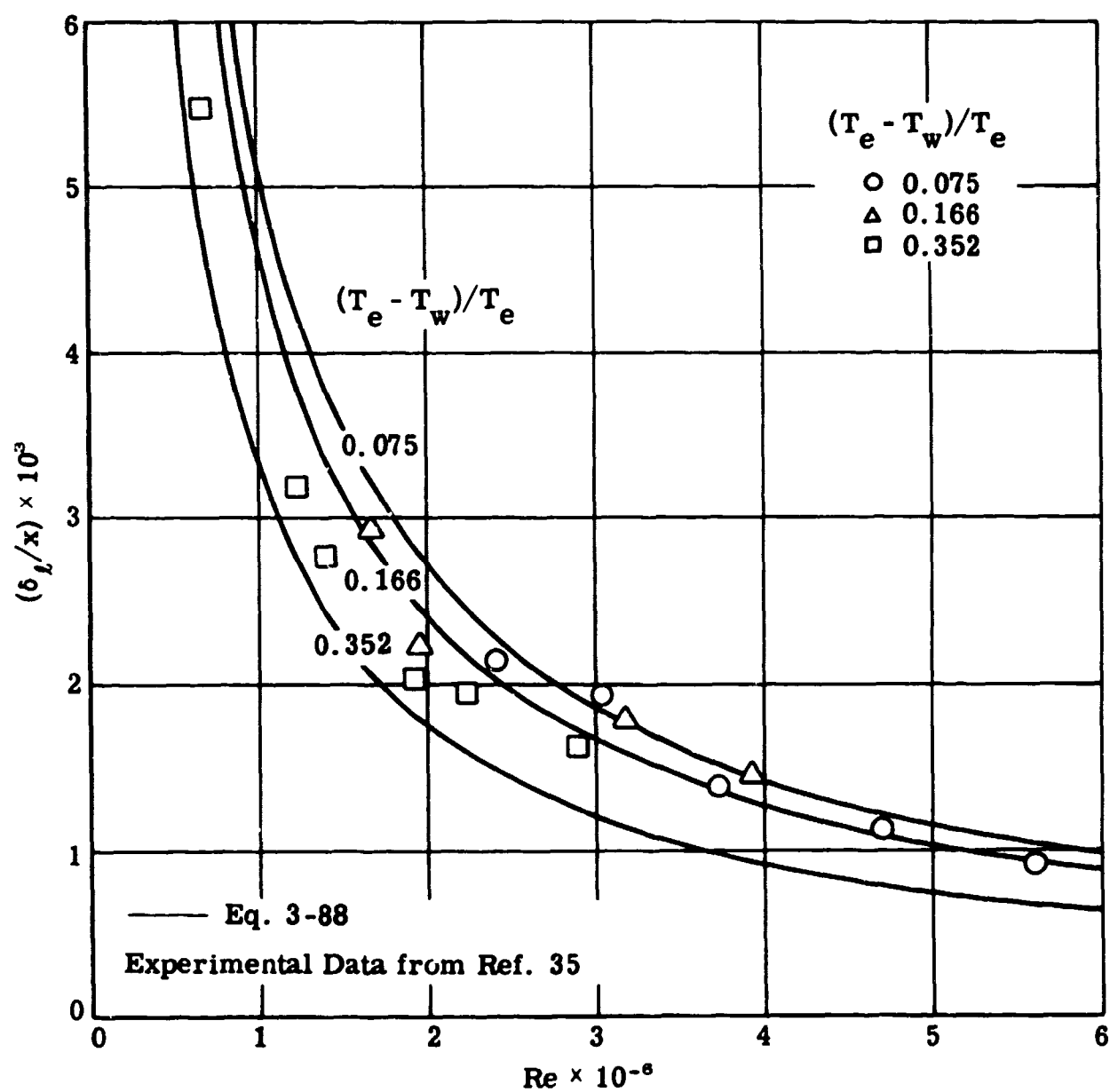


Fig. 3-28. Flat plate turbulent boundary layer; thickness of the laminar sublayer, δ_l/x vs Re ; theory and experiment; $M_1 = 5.2$; $(T_e - T_w)/T_e = 0.075, 0.166, \text{ and } 0.352$; perfect gas, $\gamma = 1.4$; $Pr = 0.70$.

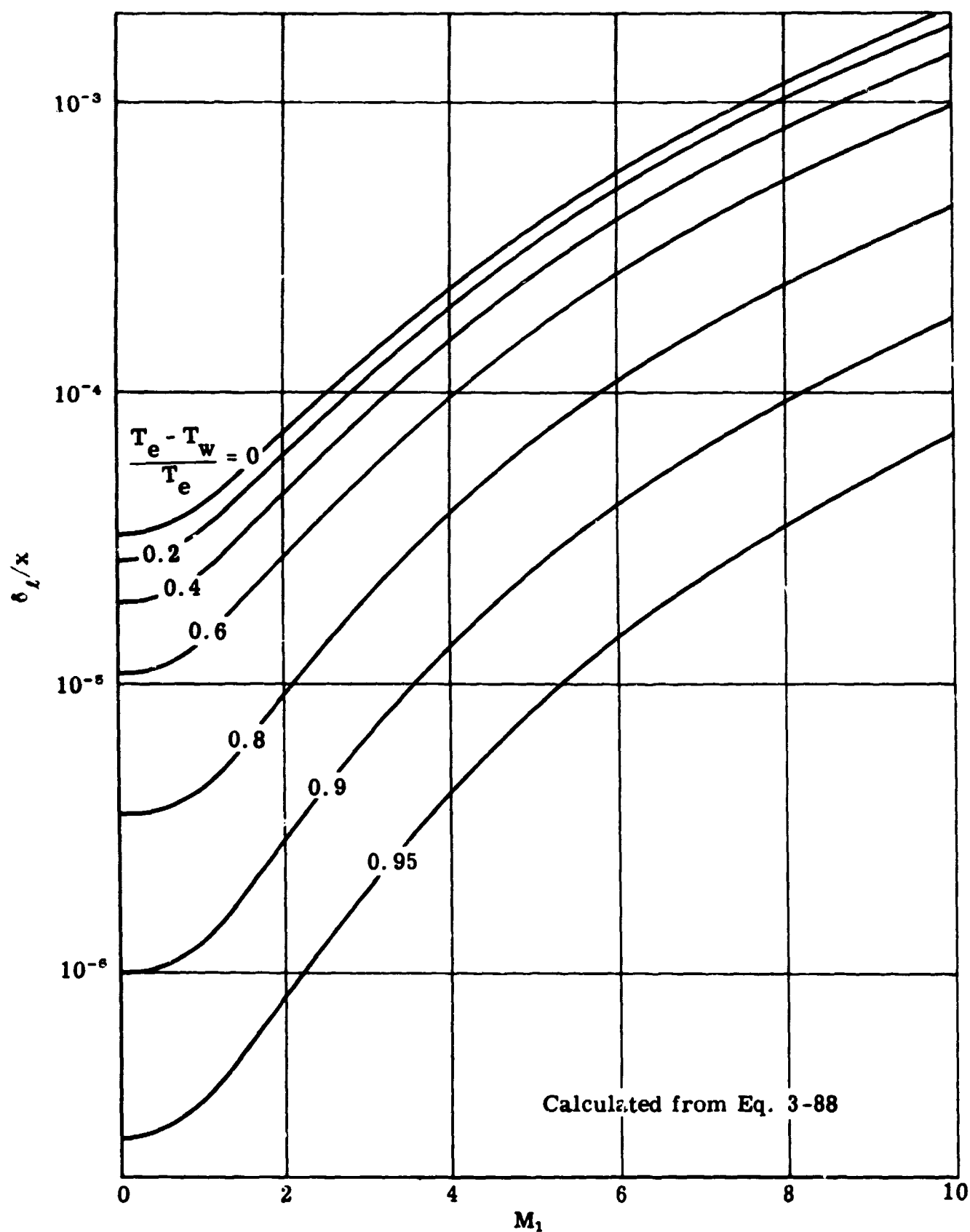


Fig. 3-29. Flat plate turbulent boundary layer; thickness of the laminar sublayer, δ_L/x vs M_1 ; $M_1 = 0$ to 10; $(T_e - T_w)/T_e = 0, 0.2, 0.4, 0.6, 0.8, 0.9$, and 0.95 ; $Re = 10^7$; $\beta = 0.505$; perfect gas, $\gamma = 1.4$; $Pr = 0.70$.

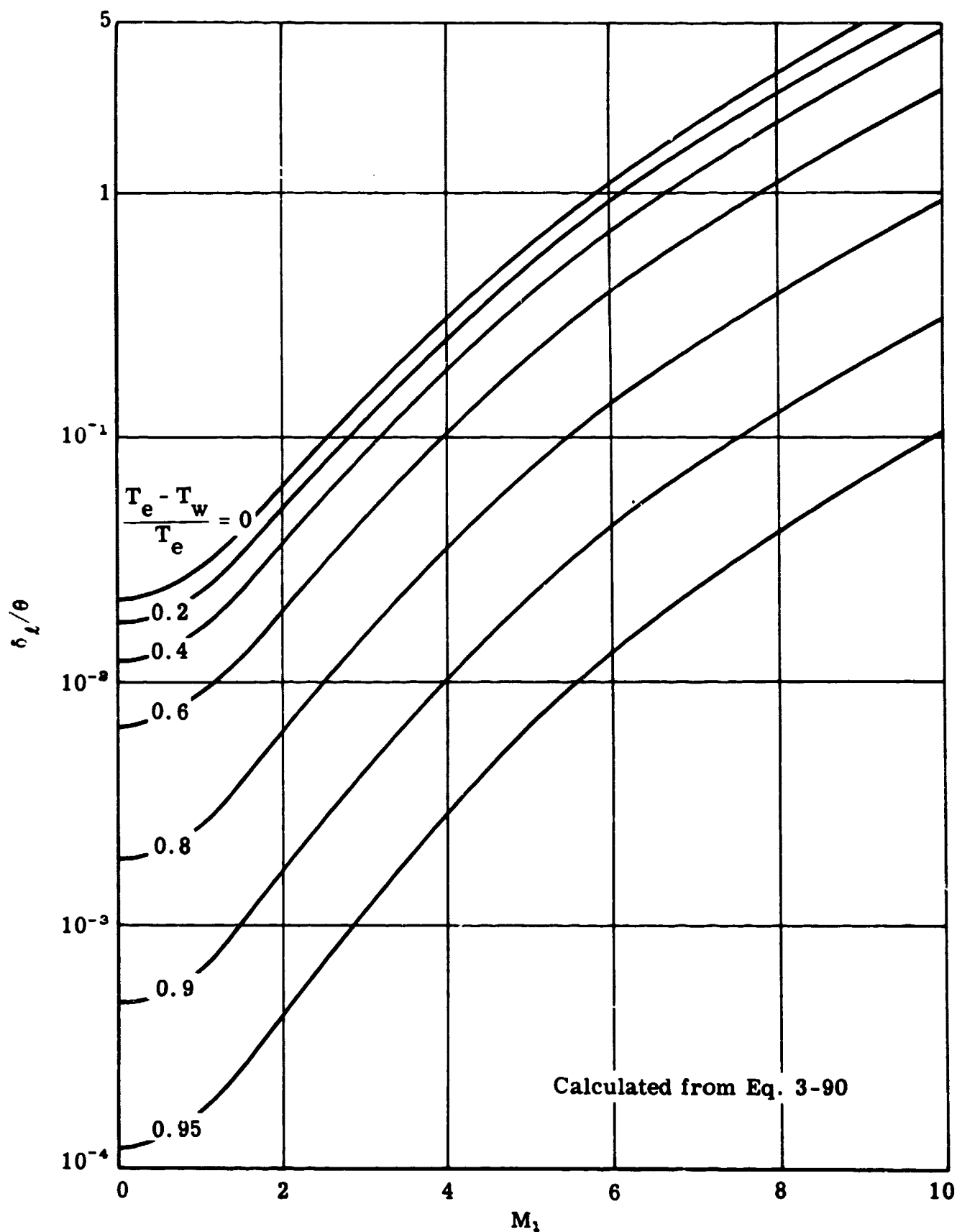


Fig. 3-30. Perfect gas turbulent boundary layer; laminar sublayer thickness, δ_l/θ vs M_1 ; $M_1 = 0$ to 10; $(T_e - T_w)/T_e = 0, 0.2, 0.4, 0.6, 0.8, 0.9$, and 0.95; $Re = 10^7$; $\beta = 0.505$; perfect gas, $\gamma = 1.4$; $Pr = 0.70$.

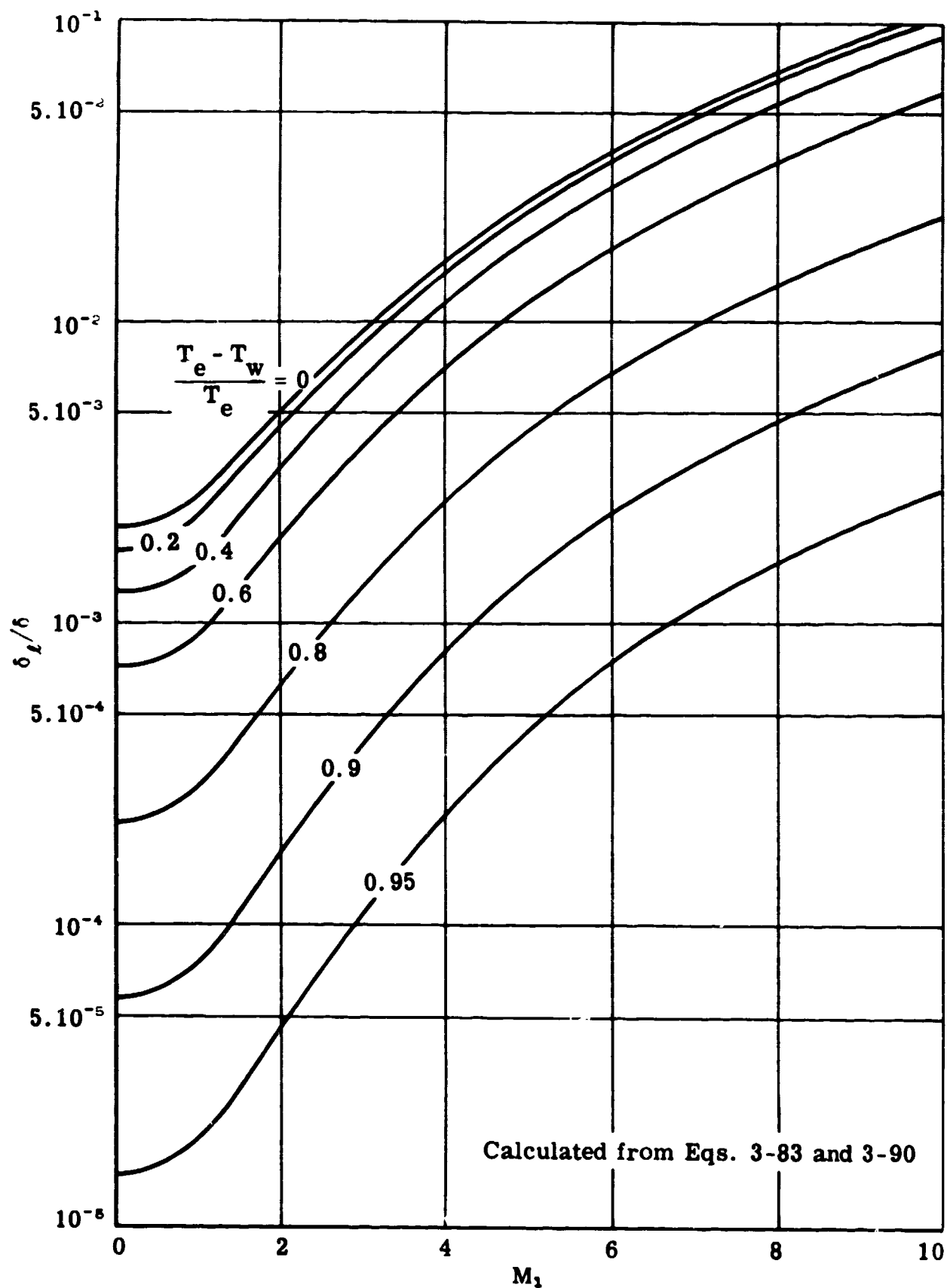


Fig. 3-31. Flat plate turbulent boundary layer; thickness of the laminar sublayer, δ_L/δ vs M_1 ; $M_1 = 0$ to 10; $(T_e - T_w)/T_e = 0, 0.2, 0.4, 0.6, 0.8, 0.9$, and 0.95 ; $Re = 10^7$; $\beta = 0.505$; perfect gas, $\gamma = 1.4$; $Pr = 0.70$.

4. Boundary-Layer Growth on Two-Dimensional & Axisymmetric Bodies

The boundary-layer growth on such two-dimensional bodies as wings and on axisymmetric missiles or fuselages is of great practical importance to the aerodynamicist. Methods of obtaining solutions to the partial differential equations for the laminar boundary layer in the presence of either adverse or favorable pressure gradients are discussed in this subsection. The associated heat-transfer effects are included in the discussions. A step-by-step technique is given (Subsec. 4.3) for computing the growth of turbulent boundary layer on two-dimensional and axisymmetric bodies. The special cases of cones, spheres, and cone-spheres are discussed in Subsecs. 4.4 to 4.6.

4.1 Laminar Boundary Layer: Finite-Difference Methods

Large, high-speed, digital computers make it feasible to calculate the laminar boundary-layer growth using finite-difference forms of the appropriate partial differential equations. In recent years, the boundary layers on two-dimensional and axisymmetric bodies have been investigated by several authors. These investigations are significant since finite-difference methods account exactly (or at least to the accuracy of the numerical methods) for the effects of pressure and temperature distributions along the surface. Thus, the boundary-layer characteristics determined at any station reflect the complete upstream history.

A complete description of finite-difference methods would be too long for this volume; however, the status of several current investigations will be discussed briefly and the reader directed to the references from which details of the methods may be obtained. Smith and Clutter in Ref. 47 give an excellent summary of the principal methods of solving the laminar boundary-layer equations. They discuss the relative advantages of each method, the working form of the equation upon which it is based, as well as the accuracy with which the values of the shear stress may be determined. All investigators assume constant entropy in the flow field outside the boundary layer. From this summary the four techniques which employ the method of finite differences have been extracted and are shown in Table 4-1 (p. 111). For their own solutions to the partial differential equations, Smith and Clutter (Refs. 47a, 47b, 47c, and 48) chose the Hartree-Womersley method (Refs. 51a, 51b, and 52) which can, in a reasonably short time, produce results of high accuracy. The solutions can be started simply and correctly and do not involve any problems of numerical stability.

For axisymmetric flow of thin boundary layers in thermal equilibrium, the method of Smith, et al, is based on the boundary-layer equations (Eqs. 2-9, 2-10, and 2-11b). The continuity and momentum equations (Eqs. 2-9 and 2-11b) can be written as

$$\frac{1}{r} \frac{\partial}{\partial x} (r \rho u) + \frac{\partial}{\partial y} (\rho v) = 0 \quad (4-1)$$

$$\rho \left(u \frac{\partial u}{\partial x} + v \frac{\partial u}{\partial y} \right) = - \frac{\partial p}{\partial x} + \frac{\partial}{\partial y} \left(\mu \frac{\partial u}{\partial y} \right) \quad (4-2)$$

Taking $\partial p / \partial y = 0$ and $\partial h / \partial y = c_p \partial T / \partial y$, and denoting the total enthalpy by h_t , where $h_t = h + u^2/2$, Eqs. 2-9 and 2-10 may be combined to yield the following energy equation:

$$\rho u \frac{\partial}{\partial x} (h_t) + \rho v \frac{\partial}{\partial y} (h_t) = \frac{\partial}{\partial y} \left[\frac{\mu}{Pr} \frac{\partial}{\partial y} (h_t) + u \left(1 - \frac{1}{Pr} \right) u \frac{\partial u}{\partial y} \right] \quad (4-3)$$

The boundary-layer equations may be transformed by using

$$\left. \begin{aligned} \eta &= \left[\frac{u_1}{\rho_\infty \mu_\infty x} \right]^{\frac{1}{2}} \int_0^y \rho \, dy \\ x &= x \end{aligned} \right\}$$

It is also helpful to define a stream function, ψ , and a dimensionless stream function, f , such that

$$\rho u = \frac{\partial \psi}{\partial y}, \quad \rho r v = - \frac{\partial}{\partial x} (\psi r), \quad \text{and} \quad \psi = [\rho_\infty \mu_\infty u_1 x]^{\frac{1}{2}} f$$

An enthalpy ratio, g , may be defined as

$$g = \frac{h_t}{h_{t_1}}$$

By means of these transformations, the momentum and energy equations can be written as

$$\frac{1}{C_\infty} \frac{\partial}{\partial \eta} (C f'') + Q \left(\frac{\rho_1}{\rho} - f'^2 \right) + \left(\frac{Q+1}{2} + R \right) f f' - x \left(f' \frac{\partial f'}{\partial x} + f'' \frac{\partial f}{\partial x} \right) = 0 \quad (4-4)$$

and

$$\frac{1}{C_\infty} \frac{\partial}{\partial \eta} \left[\frac{C}{Pr} g' + \frac{u_1^2}{h_{t_1}} C (1 - Pr) f' f'' \right] = - \left[\frac{Q+1}{2} + R \right] f g' + x \left[f' \frac{\partial g}{\partial x} - g' \frac{\partial f}{\partial x} \right] \quad (4-5)$$

The primes in Eqs. 4-4 and 4-5 denote differentiation with respect to η . The other parameters are defined as follows:

$$C = \frac{\rho \mu}{\rho_1 \mu_1}; \quad C_\infty = \frac{\rho_\infty \mu_\infty}{\rho_1 \mu_1}$$

$$Q = \frac{x}{u_1} \frac{du_1}{dx}; \quad R = \frac{x}{r} \frac{dr}{dx}$$

The continuity equation is satisfied by the definition of ψ . The definition of the dimensionless stream function, f , is such that

$$f' = \frac{u}{u_1}$$

For impermeable walls on which the surface enthalpy distribution is specified, the boundary conditions to Eqs. 4-4 and 4-5 are

$$\text{when } \eta = 0: \quad f(0) = 0, \quad f'(0) = 0, \quad \text{and } g(0) = g_w$$

$$\text{and at } \eta \rightarrow \infty: \quad f'(\eta) \rightarrow 1, \quad f''(\eta) \rightarrow 0, \quad \text{and } g(\eta) \rightarrow 1$$

When the x -derivatives in both the momentum and energy equations are replaced by finite differences, Eqs. 4-4 and 4-5 take the form of ordinary differential equations. This pair of equations is then solved simultaneously by numerical methods for each station of interest along the surface. Since the boundary conditions are split, an iterative procedure is necessary. The numerical method used by Smith et al has several advantages. Being an implicit formulation, there is no stability problem in the x direction. The integration of the ordinary differential equations across the boundary layer can be accomplished by well-proven numerical methods. A disadvantage of this technique is that the interval of integration across the boundary layer is unbounded. Baxter and Flügge-Lotz (Ref. 54) as well as Kramer and Lieberstein (Ref. 55) circumvented this disadvantage by using the Crocco transformation discussed in Subsec. 2.4 (see columns 2 and 3 in Table 4-1). In this case, the boundary-layer equations are transformed to the x, u variables and since u lies between 0 and u_1 , it is always finite. The use of the Crocco equations presents a numerical difficulty in that the velocity profile can exhibit an overshoot, i.e., u_* becomes > 1 . This can occur when the boundary layer is first heated by the surface and then accelerated. The shear stress can then become a double-valued function of u . For most high-speed problems of interest, the heat is transferred from the boundary layer to the surface, rather than from the surface to the boundary layer, in which case the velocity overshoot should not occur.

Blottner and Flügge-Lotz (Ref. 56), Parr (Ref. 57) and several other investigators solved the equations by replacing all partial derivatives by finite differences.

4.2 Laminar Boundary Layer: Approximate Method

Using a correlation technique, Cohen and Reshotko (Ref. 7) derived an approximate method for calculating the growth of a compressible boundary layer with arbitrary pressure and temperature distribution along the surface. The method, which employs the momentum integral equation, has been widely used and gives good agreement with experiment. Lewis and Whitfield (Ref. 58) recently have applied the method most successfully to the analysis of hypersonic viscous effects.

The transformation of the two-dimensional momentum integral equation, derived by Cohen and Reshotko, is given in Subsec. 2.5.3. The resulting equation, Eq. 2-33, is based on the following assumptions:

1. The gas is thermally and calorifically perfect.
2. The flow outside the boundary layer has constant entropy.
3. The Prandtl number is unity.
4. The viscosity is a linear function of the temperature.

Cohen and Reshotko define a shear parameter, ℓ , and a correlation number or pressure gradient parameter, n . The following equations define n and ℓ :

$$n = - \frac{\rho_{t_1} \bar{\theta}^2}{\mu_{t_1}} \frac{d\bar{u}_1}{d\bar{x}} = - \frac{\rho_{t_1} \theta^2}{\lambda \mu_{t_1}} \left(\frac{T_{t_1}}{T_1} \right)^{\frac{2\gamma-3}{\gamma-1}} \frac{du_1}{dx} = - \frac{\rho_{t_1} a_{t_1} \theta^2}{\lambda \mu_{t_1}} \left(\frac{T_{t_1}}{T_1} \right)^{\frac{\gamma-3}{2(\gamma-1)}} \frac{dM_1}{dx} \quad (4-6)$$

$$\ell = \frac{\rho_{t_1} \bar{u}_1 \bar{\theta}}{\mu_{t_1}} \frac{\bar{C}_f}{2} = \frac{\rho_{t_1} u_1 \theta}{\lambda \mu_{t_1}} \left(\frac{T_{t_1}}{T_1} \right)^{\frac{\gamma-2}{\gamma-1}} \frac{C_f}{2} = \frac{\rho_{t_1} a_{t_1} \theta}{\lambda \mu_{t_1}} \left(\frac{T_{t_1}}{T_1} \right)^{\frac{\gamma-3}{2(\gamma-1)}} M_1 \frac{C_f}{2} \quad (4-7)$$

These equations, together with the preceding assumptions and definitions, allow Eq. 2-33 to be written as:

$$-\bar{u}_1 \frac{d}{d\bar{x}} \left(\frac{n}{d\bar{u}_1/d\bar{x}} \right) = 2 \left[n(\bar{H} + 2) + \ell \right] \quad (4-8)$$

If the variations of n and ℓ over a surface can be determined by solving the momentum integral equation, the variations of θ and C_f over the surface can then be obtained from Eqs. 4-6 and 4-7.

4.2.1 Correlation Technique

For the case of incompressible flow with zero heat transfer, Eq. 2-33 can be integrated by the well-known Pohlhausen technique. It is assumed that the boundary-layer profiles can be correlated in terms of a single parameter involving only the local pressure gradient, i.e., the correlation is independent of the history of the boundary-layer development. When the effects of heat transfer are being considered, a second parameter related to the local wall temperature must be included.

The correlation technique used by Cohen and Reshotko is based on a Falkner-Skan type flow defined by

$$\bar{u}_1 = \text{const } (\bar{x})^m \quad (4-9)$$

For the case of constant wall temperature, the boundary-layer velocity and temperature profiles are similar at all points along a surface over which the velocity distribution is described by Eq. 4-9. The boundary layers thus form a two-parameter family allowing n , ℓ , and \bar{H} to be written:

$$\left. \begin{aligned} n &= n \left(m, \frac{T_w - T_{t_1}}{T_{t_1}} \right) \\ \ell &= \ell \left(m, \frac{T_w - T_{t_1}}{T_{t_1}} \right) \\ \bar{H} &= \bar{H} \left(m, \frac{T_w - T_{t_1}}{T_{t_1}} \right) \end{aligned} \right\}$$

From the above three relations it is clear that

$$\ell = \ell \left(n, \frac{T_w - T_{t_1}}{T_{t_1}} \right) \quad \text{and} \quad \bar{H} = \bar{H} \left(n, \frac{T_w - T_{t_1}}{T_{t_1}} \right)$$

Assuming that this correlation will hold at any point along a surface with arbitrary pressure and temperature distributions regardless of the history of the boundary layer, Eq. 4-8 can be written as

$$-\bar{u}_1 \frac{d}{d\bar{x}} \left(\frac{n}{d\bar{u}_1/d\bar{x}} \right) = N \left(n, \frac{T_w - T_{t_1}}{T_{t_1}} \right) \quad (4-10)$$

where N , a momentum parameter, is defined by

$$N \left(n, \frac{T_w - T_{t_1}}{T_{t_1}} \right) = 2 \left[n (\bar{H} + 2) + \ell \right]$$

When integrating Eq. 4-10 it is unnecessary to use transformed coordinates. In physical coordinates it can be written as

$$-M_1 \left(\frac{T_{t_1}}{T_1} \right)^K \frac{d}{dx} \left\{ n \left[\left(\frac{T_{t_1}}{T_1} \right)^K \frac{dM_1}{dx} \right]^{-1} \right\} = N \left(n, \frac{T_w - T_{t_1}}{T_{t_1}} \right) \quad (4-11)$$

where

$$K = \frac{3\gamma - 1}{2(\gamma - 1)} \quad (4-12)$$

It is more convenient to use the Mach number in Eq. 4-11 than to use the velocity.

To integrate Eq. 4-11 along a surface, it is necessary to specify M_1 and $(T_w - T_{t_1})/T_{t_1}$ as functions of x . In addition, it is necessary to have initial values of n and N and to specify N as a function of n and $(T_w - T_{t_1})/T_{t_1}$. To accomplish this, Cohen and Reshotko make use of the solutions to the Falkner-Skan flow (see Ref. 59).

Figure 4-1 (taken from Ref. 7) presents the momentum parameter, N , as a function of the pressure gradient parameter, n , for four values of m (see Eq. 4-9) and five values of $(T_w - T_{t_1})/T_{t_1}$. The four values of m are 0, 1/3, 1, and ∞ , corresponding to a flat plate, the stagnation point of an axisymmetric blunt body, the stagnation edge of a blunt two-dimensional leading edge, and the limiting case of an infinite velocity. It may be seen from Fig. 4-1 that for all values of $(T_w - T_{t_1})/T_{t_1}$, $N = 0.44$ when $n = 0$. This fact gives an initial value of N that may be used for bodies with sharp tips or sharp leading edges.

Initial values of n corresponding to the stagnation point of blunt two-dimensional or axisymmetric bodies can be obtained from Fig. 4-2 (also taken from Ref. 7). The initial value of n (determined from Eq. 4-6) for a sharp leading edge or tip is zero since $\theta = 0$ at $x = 0$. The relationship between N and m at the stagnation point of blunt bodies is as follows:

$$N_{sp} = \frac{m-1}{m} n_{sp} \quad (4-13)$$

For two-dimensional flow at a stagnation edge ($m = 1$), the initial value of N from Eq. 4-13 is zero. For flow at the stagnation point of an axisymmetric body ($m = 1/3$), Eq. 4-13 gives $N_{sp} = -2n_{sp}$.

As the integration proceeds over the surface, the variation of N with n and $(T_w - T_{t_1})/T_{t_1}$ is obtained from Fig. 4-1. Figure 4-2 shows n as a function of $(T_w - T_{t_1})/T_{t_1}$ with m as a parameter. Noting that the constant temperature lines are almost linear on Fig. 4-1, Cohen and Reshotko suggested that the relationship between N and n for isothermal walls is of the form:

$$N = A + Bn \quad (4-14)$$

Since all lines pass through $n = 0$ and $N = 0.44$, this equation becomes

$$N = 0.44 + Bn \quad (4-15)$$

The value of B as a function of $(T_w - T_{t_1})/T_{t_1}$ is given in Ref. 7 and reproduced here as Fig. 4-3.

The four curves of B were derived from Fig. 4-1 by considering the slopes of the following line segments of $N = 0.44 + Bn$ for each value of the heat transfer, $(T_w - T_{t_1})/T_{t_1}$:

1. For flow with a favorable pressure gradient over a two-dimensional body, use the segments between $P(0, 0.44)$ and the intersections with the line $m = 1$.
2. For a favorable pressure gradient over an axisymmetric blunt body, use the segments between P and the intersections with the line $m = \frac{1}{3}$.
3. For flow with small pressure gradients, use the slope of the lines in the vicinity of P .
4. For flow with an adverse pressure gradient, use the slopes of the line segments with small positive values of n .

4.2.2 Integration of the Momentum Equation for Two-Dimensional Bodies

4.2.2.1 Variable Wall Temperature

Equation 4-11 can be written in integral form as follows:

$$n = \left(\frac{T_{t_1}}{T_1}\right)^K \frac{dM_1}{dx} \left\{ n_i \left(\frac{T_{t_1}}{T_1}\right)_i^{-K} \left(\frac{dM_1}{dx}\right)_i^{-1} - \int_0^x \frac{1}{M_1} \left(\frac{T_{t_1}}{T_1}\right)^{-K} \cdot N dx \right\} \quad (4-16)$$

The initial conditions, denoted by subscript i , are:

1. For a sharp leading edge:

$$x = 0, \quad N = N_i = 0.44, \quad n = n_i = 0$$

2. For a blunt leading edge:

$$x = 0, \quad N = N_i = 0, \quad n = n_i$$

where n_i is read from Fig. 4-2 for $m = 1$ and the appropriate value of $(T_w - T_{t_1})/T_{t_1}$.

Starting with these initial conditions, the integration is carried out making use at each step of the values of N determined as a function of n and $(T_w - T_{t_1})/T_{t_1}$ from Fig. 4-1.

Cohen and Reshotko (Ref. 7) point out that it is sometimes useful to have analytical relations to check the initial values of dn/dx . It can be shown that

1. For a sharp leading edge:

$$\left(\frac{dn}{dx}\right)_i = - \frac{0.44}{(M_1)_i} \left(\frac{dM_1}{dx}\right)_i$$

2. For a blunt leading edge:

$$\left(\frac{dn}{dx}\right)_i = \frac{n_i}{1 + (dN/dn)_i} \frac{(d^2 M_1 / dx^2)_i}{(dM_1 / dx)_i}$$

where $(dN/dn)_i$ is evaluated for the instantaneous constant wall temperature, i.e., $T_w = T_{wi}$.

4.2.2.2 Constant Wall Temperature

When the wall temperature is constant, N is approximated by Eq. 4-15 and the integral form of Eq. 4-11 becomes

$$n = - 0.44 \left(\frac{T_{t_1}}{T_1}\right)^K \frac{1}{M_1^B} \frac{dM_1}{dx} \int_0^x M_1^{B-1} \left(\frac{T_{t_1}}{T_1}\right)^{-K} dx \quad (4-17)$$

The appropriate initial values of n are given by Eq. 4-17 as $x \rightarrow 0$, and the initial values of N can be obtained from Eq. 4-15. These initial values are:

1. For a sharp leading edge:

$$x = 0, \quad N = N_i = 0.44, \quad n = n_i = 0$$

2. For a blunt leading edge:

$$x = 0, \quad N = N_i = 0, \quad n = n_i = - \frac{0.44}{B}$$

where B may be read from Fig. 4-3 as a function of $(T_w - T_{t_1})/T_{t_1}$.

Since B (given by Fig. 4-3) is constant for any particular application, evaluation of n along the surface is given by the straightforward integration of Eq. 4-17. Analytical expressions for $(dn/dx)_i$ are:

1. For a sharp leading edge:

$$\left(\frac{dn}{dx}\right)_i = -\frac{0.44}{M_1} \left(\frac{dM_1}{dx}\right)_i$$

2. For a blunt leading edge:

$$\left(\frac{dn}{dx}\right)_i = -\frac{0.44}{B(1+B)} \frac{(d^2 M_1 / dx^2)_i}{(dM_1 / dx)_i}$$

4.2.3 Integration of the Momentum Equation for Axisymmetric Bodies

Application of the Mangler transformation yields the following equation for axisymmetric flows:

$$-\frac{\bar{u}_1}{r^2} \frac{d}{d\bar{x}} \left(\frac{nr^2}{d\bar{u}/d\bar{x}} \right) = N \left(n, \frac{T_w - T_{t_1}}{T_{t_1}} \right) \quad (4-18)$$

This equation corresponds to Eq. 4-10 used in the two-dimensional case. In physical coordinates, Eq. 4-18 becomes

$$-\frac{M_1}{r^2} \left(\frac{T_{t_1}}{T_1} \right)^K \frac{d}{dx} \left\{ nr^2 \left(\frac{T_{t_1}}{T_1} \right)^{-K} \left(\frac{dM_1}{dx} \right)^{-1} \right\} = N \left(n, \frac{T_w - T_{t_1}}{T_{t_1}} \right) \quad (4-19)$$

4.2.3.1 Variable Wall Temperature

For variable wall temperature, Eq. 4-19 will have two integral forms: one for ducted bodies and one for solid-nosed bodies.

For the ducted body case, the integral form is

$$n = \left(\frac{T_{t_1}}{T_1} \right)^K \frac{1}{r^2} \frac{dM_1}{dx} \left\{ n_i r_i^2 \left(\frac{T_{t_1}}{T_1} \right)_i^{-K} \left(\frac{dM_1}{dx} \right)_i^{-1} - \int_0^x \frac{Nr^2}{M_1} \left(\frac{T_{t_1}}{T_1} \right)^{-K} dx \right\} \quad (4-20)$$

The initial conditions for the open body correspond to those of the two-dimensional case. They are

1. For a sharp lip:

$$x = 0, \quad r = r_i, \quad N = N_i = 0.44, \quad n = n_i = 0,$$

2. For a blunt lip:

$$x = 0, \quad r = r_i, \quad N = N_i = 0, \quad n = n_i$$

where n_i may be read from Fig. 4-2 for $m = 1$ and the appropriate value of $(T_w - T_{t_1})/T_{t_1}$.

As the integration proceeds downstream from the lip, values of N for use in Eq. 4-20 are taken from Fig. 4-1. Initial values of dn/dx are given by

1. For a sharp lip:

$$\left(\frac{dn}{dx}\right)_i = - \frac{0.44}{(M_1)_i} \left(\frac{dM_1}{dx}\right)_i$$

2. For a blunt lip:

$$\left(\frac{dn}{dx}\right)_i = \frac{n_i}{1 + (dN/dn)_i} \left[\frac{(d^2 M_1 / dx^2)_i}{(dM_1 / dx)_i} - \frac{2}{r_i} \left(\frac{dr}{dx}\right)_i \right]$$

where $(dN/dn)_i$ is evaluated for constant $T_w = T_{w_i}$.

For the closed body case with variable wall temperature, the integral form of Eq. 4-19 is

$$n = - \left(\frac{T_{t_1}}{T_1}\right)^K \frac{1}{r^2} \frac{dM_1}{dx} \int_0^x \frac{Nr^2}{M_1} \left(\frac{T_{t_1}}{T_1}\right)^{-K} dx \quad (4-21)$$

The appropriate initial values of n are given by Eq. 4-21 as $x \rightarrow 0$. The initial values of n and N are

1. For a sharp nose:

$$x = 0, \quad r_i = 0, \quad N = N_i = 0.44, \quad n = n_i = 0$$

2. For a blunt nose:

$$x = 0, \quad r_i = 0, \quad N = N_i = -2n_i, \quad n = n_i$$

(read from Fig. 4-2 for $m = 1/3$ and required $(T_w - T_{t_1})/T_{t_1}$)

As the integration proceeds downstream from the nose, values of N for use in Eq. 4-21 are taken from Fig. 4-1. Initial values of $(dn/dx)_i$ are given by

1. For a sharp nose:

$$\left(\frac{dn}{dx}\right)_i = - \frac{0.147}{(M_1)_i} \left(\frac{dM_1}{dx}\right)_i$$

2. For a blunt nose:

$$\left(\frac{dn}{dx}\right)_i = \frac{n_i}{3 + (dN/dn)_i} \left[2 \frac{(d^2 M_1/dx^2)_i}{(dM_1/dx)_i} - \frac{(d^2 r/dx^2)_i}{(dr/dx)_i} \right]$$

where $(dN/dn)_i$ is evaluated for constant $T_w = T_{w_i}$.

4.2.3.2 Constant Wall Temperature

For constant wall temperature, N is approximated by Eq. 4-15 and the integral form of Eq. 4-19 becomes

$$n = -A \left(\frac{T_{t_1}}{T_1}\right)^K (r^2 M_1^B)^{-1} \frac{dM_1}{dx} \int_0^x r^2 M_1^{B-1} \left(\frac{T_{t_1}}{T_1}\right)^{-K} dx \quad (4-22)$$

Equation 4-22 is valid for both open and closed bodies with values of B given by Fig. 4-3.

For an open body the initial conditions are

1. For a sharp lip:

$$x = 0, \quad r = r_i, \quad N = N_i = 0.44, \quad n = n_i = 0$$

2. For a blunt lip:

$$x = 0, \quad r = r_i, \quad N = N_i = 0, \quad n = n_i = -\frac{0.44}{B}$$

Analytic expressions for $(dn/dx)_i$ are

1. For a sharp lip:

$$\left(\frac{dn}{dx}\right)_i = -\frac{0.44}{(M_1)_i} \left(\frac{dM_1}{dx}\right)_i$$

2. For a blunt lip:

$$\left(\frac{dn}{dx}\right)_i = -\frac{0.44}{B(1+B)} \left[\frac{(d^2 M_1/dx^2)_i}{(dM_1/dx)_i} - \frac{2}{r_i} \left(\frac{dr}{dx}\right)_i \right]$$

For the closed body the initial conditions are

1. For a sharp nose:

$$x = 0, \quad r = 0, \quad N = N_i = 0.44, \quad n = n_i = 0$$

2. For a blunt nose:

$$x = 0, \quad r = 0, \quad N = N_i = -2n_i, \quad n = n_i = -\frac{0.44}{B+2}$$

Analytic expressions for $(dn/dx)_i$ are

1. For a sharp nose:

$$\left(\frac{dn}{dx}\right)_i = -\frac{0.147}{(M_1)_i} \left(\frac{dM_1}{dx}\right)_i$$

2. For a blunt nose:

$$\left(\frac{dn}{dx}\right)_i = -\frac{0.44}{(3+B)(B+2)} \left[2 \frac{(d^2 M_1 / dx^2)_i}{(dM_1 / dx)_i} - \frac{(d^2 r / dx^2)_i}{(dr / dx)_i} \right]$$

4.2.4 Local Shear Stress

After integrating the momentum equation to obtain values of n , the momentum thickness, θ , can be computed from Eq. 4-6; the shear parameter, l , can be read directly from Fig. 4-4 (taken from Ref. 7). Using these values of θ and l , the local skin friction coefficient, C_f , can be computed from Eq. 4-7.

The friction drag can, of course, be obtained by integrating the wall shear stress, $\tau_w = \frac{1}{2} \rho_1 u_1^2 C_f$, over the surface.

4.2.5 Boundary-Layer Shape Parameter and Thickness

The transformed shape parameter is given on Fig. 4-5 (from Ref. 7) as a function of $(T_w - T_{t_1})/T_{t_1}$ and n . Cohen and Reshotko give the following expression for the shape parameter in the physical plane:

$$H = \frac{\delta^*}{\theta} = \bar{H} + \frac{\gamma - 1}{2} M_1^2 (\bar{H} + 1) \quad (4-23)$$

The transformed total boundary-layer thickness is also shown on Fig. 4-5. Reference 7 also gives the following expression for δ in the physical plane:

$$\frac{\delta}{\theta} = \frac{\bar{\delta}}{\bar{\theta}} + \frac{\gamma - 1}{2} M_1^2 (\bar{H} + 1) \quad (4-24)$$

The above calculations are based on the assumption that when $y = \delta$, $u = 0.995 u_1$.

4.3 Turbulent Boundary Layer

The momentum integral equation (Eq. 2-29) holds true for both laminar and turbulent boundary-layer flow over axisymmetric bodies. This equation assumes that the gas is thermally and calorifically perfect and that the flow outside the boundary layer has constant entropy.

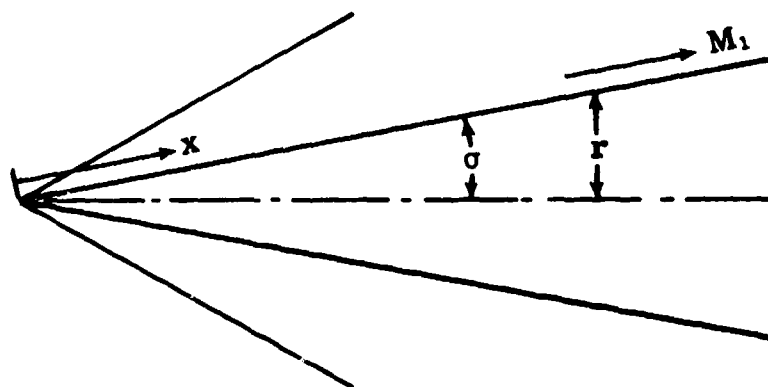
There are no experimentally verified compressible turbulent boundary-layer theories that give the effect of surface pressure and temperature gradients on the shape parameter, H , and on the skin friction coefficient, C_f . In order to integrate Eq. 2-29, assume that H and C_f are given by flat-plate results and evaluated at the local flow conditions at each point along the surface. An expression which gives C_f as a function of Re_θ is necessary and may be obtained by combining Eqs. 3-55 and 3-57. The shape parameter can be computed from Eq. 3-84.

For specified pressure and temperature distributions over a surface, numerical integration of Eq. 2-29 will give the variation of C_f , H , and θ along the surface. This method should give reasonable results for small pressure gradients, especially for favorable gradients.

The equation for flow over two-dimensional surfaces is given by putting $(\theta/r)(dr/dx) = 0$ in Eq. 2-29.

4.4 Boundary Layer on Cones

When the bow wave is attached to a sharp cone at supersonic speeds, local conditions at the outer edge of a thin boundary layer can be assumed to be constant and equal to those for inviscid flow over the same cone. When the surface temperature is constant, certain of the skin friction values for a flat plate can be applied to the cone. Three cases will be considered: fully laminar flow, fully turbulent flow, and flow with transition. As in Subsec. 3.5, the momentum integral equation will be used to derive relationships which will be valid for all three types of flow. The following sketch defines the coordinate system.



Since for a cone,

$$r = x \sin \sigma,$$

the momentum integral equation (Eq. 2-26) reduces to

$$\frac{d\theta}{dx} + \frac{\theta}{x} = \frac{C_f}{2} \quad (4-25)$$

As conditions at the outer edge of the boundary layer are constant over the cone, this equation can be written

$$\frac{dRe_\theta}{dRe} + \frac{Re_\theta}{Re} = \frac{C_f}{2} \quad (4-26)$$

or

$$\frac{d}{dRe} (Re Re_\theta) = \frac{C_f}{2} Re \quad (4-27)$$

Since both Re and Re_θ are zero at the tip of the cone, this equation can be integrated to give

$$Re_\theta = \frac{1}{2Re} \int_0^{Re} C_f Re dRe \quad (4-28)$$

The mean skin friction coefficient for a cone will be defined as

$$C_F = \frac{1}{\pi r x} \int_0^x C_f 2\pi r dx$$

or

$$C_F = \frac{2}{x^2} \int_0^x C_f x dx = \frac{2}{Re^2} \int_0^{Re} C_f Re dRe \quad (4-29)$$

With this definition of C_F , the friction drag of a cone is given by

$$D = \frac{1}{2} \rho_1 u_1^2 C_F A \cos \sigma \quad (4-30)$$

where $A = \pi r x$. From Eqs. 4-28 and 4-29

$$C_F = 4 \frac{Re_\theta}{Re} = 4 \frac{\theta}{x} \quad (4-31)$$

Equation 4-31 is valid for both laminar and turbulent flows. This equation for a cone is comparable to Eq. 3-107 for a flat plate, differing only by a factor of 2.

4.4.1 Laminar Boundary Layer on Cones

The Mangler transformation described in Subsec. 2.3 may be conveniently applied to the case of a cone with constant surface temperature. For laminar flow along a cone, the non-dimensional forms of the velocity profiles, temperature profiles, etc., are identical to those on a flat plate. Although the Mangler transformation could have been used to determine the skin friction on a cone, the momentum integral equation was chosen for this derivation since it can also be applied to turbulent flow.

Since both C_f and Re_θ depend on local boundary-layer profiles which are identical for a cone and a flat plate, it follows that the relations between C_f and Re_θ in the two cases are identical. Therefore,

$$C_f Re_\theta = K_L^2 \quad (\text{Eq. 3-111})$$

is also valid for conical flow where K_L has the flat plate value calculated by the methods of Subsecs. 3.1 and 3.2 or read from graphs such as Fig. 3-3 (see Subsec. 3.5).

Equations 3-111 and 4-27 combined and integrated yield

$$Re_\theta = K_L \sqrt{Re/3} \quad (4-32)$$

The constant of integration is zero since $Re_\theta = Re = 0$ at the tip of the cone. Combining Eqs. 3-111 and 4-32 gives the local skin friction coefficient for a cone as

$$C_f \sqrt{Re} = \sqrt{3} K_L \quad (4-33)$$

Comparing this equation with Eq. 3-108, it may be seen that for the same value of Re ,

$$C_{f_{\text{cone}}} = \sqrt{3} C_{f_{\text{plate}}}$$

Equations 4-31 and 4-32 lead to the following expression for the mean skin friction coefficient:

$$C_F \sqrt{Re} = \frac{4}{\sqrt{3}} K_L = \frac{2}{3} \sqrt{3} (2K_L) \quad (4-34)$$

This equation may be compared with Eq. 3-109 for the same value of Re to show

$$C_{F_{\text{cone}}} = \frac{2\sqrt{3}}{3} C_{F_{\text{plate}}}$$

Thus laminar skin friction coefficients calculated for a flat plate can be used directly to obtain corresponding values on a cone. It is of interest to note from Eqs. 3-110 and 4-32 that the boundary-layer momentum thickness on a cone will be the same as that on a plate whose length is one-third that of the cone.

4.4.2 Turbulent Boundary Layer on Cones

In order to express the characteristics of turbulent flow in a form which is adaptable to a boundary layer with transition, it has been assumed that C_f and Re_θ on the cone bear the same relationship as on a fully turbulent flat plate (see Subsec. 3.5), i.e.,

$$C_f Re_\theta^{1/4} = \frac{8}{5} \left(\frac{5}{8} K_T \right)^{5/4} \quad (\text{Eq. 3-119})$$

When C_f from this equation is substituted in Eq. 4-27, integration of the latter gives

$$(Re_\theta Re)^{5/4} = \frac{4}{9} \left(\frac{5}{8} K_T \right)^{5/4} Re^{9/4} + \text{constant} \quad (4-35)$$

Since $Re = Re_\theta = 0$ at the tip of the cone, the constant of integration is zero and Eq. 4-35 may be written as

$$Re_\theta^{1/4} = \left(\frac{5}{8} K_T \right)^{1/4} \left(\frac{4}{9} Re \right)^{1/5} \quad (4-36)$$

If the exponent of the Reynolds number in the basic equation (Eq. 3-116) is taken as $1/n$ rather than $1/5$, then as $n \rightarrow \infty$ the factor $4/9$ in Eq. 4-36 becomes $1/2$, giving the same result as Van Driest obtained in Ref. 60. It may be seen from Eqs. 4-36 and 3-118 that the boundary-layer thickness on a cone is equal to that on a flat plate whose length is $4/9$ of the cone's length.

An expression for the local skin friction coefficient obtained from Eqs. 4-36 and 3-119 is

$$C_f \left(\frac{4}{9} Re \right)^{1/5} = K_T \quad (4-37)$$

Comparing this equation with Eq. 3-116, it may be seen that for fully turbulent flow,

when $Re_{\text{cone}} = (9/4) Re_{\text{plate}}$, then $C_{f_{\text{cone}}} = C_{f_{\text{plate}}}$.

Thus the flat plate skin friction coefficients given in Subsecs. 3.3 and 3.4 can be applied to cones by replacing Re by $4/9 Re$.

The mean skin friction coefficient for a cone, obtained from Eqs. 4-31 and 4-36, is

$$\frac{9}{8} C_F \left(\frac{4}{9} Re \right)^{1/5} = \frac{5}{4} K_T \quad (4-38)$$

This equation, together with Eq. 3-117, shows that $4/9$ of the flat plate Re and $9/8$ of the flat plate C_F should be used to obtain the cone C_F . The flat plate relations for C_F in Subsecs. 3.3 and 3.4 can thus be applied to cones.

4.4.3 Boundary-Layer Transition on Cones

The laminar relations given in Subsec. 4.4.1 are valid up to the transition point, i.e., up to

$$Re = Re_{tr}, \quad Re_{\theta} = Re_{\theta tr}$$

The relation between $Re_{\theta tr}$ and Re_{tr} is given by substituting these values in Eq. 4-32, i.e.,

$$Re_{\theta tr} = K_L \left(\frac{Re_{tr}}{3} \right)^{1/2} \quad (4-39)$$

For $Re \geq Re_{tr}$, the constant of integration in Eq. 4-35 may be evaluated for the region between Re_{tr} and any other Re by eliminating $Re_{\theta tr}$ from Eqs. 4-35 and 4-39. The result is

$$(Re_{\theta} Re)^{5/4} = \left(\frac{K_L}{\sqrt{3}} \right)^{5/4} (Re_{tr})^{15/8} + \frac{4}{9} \left(\frac{5}{8} K_T \right)^{5/4} (Re^{9/4} - Re_{tr}^{9/4}) \quad (4-40)$$

Equations 3-119, 4-33, 4-37, and 4-40 may be combined to give the local skin friction coefficient for $Re \geq Re_{tr}$ on a cone, i.e.,

$$C_f = \frac{C_{fT}}{\left[1 - \left(\frac{Re_{tr}}{Re} \right)^{9/4} + \left(\frac{6}{5} \frac{C_{fL}}{C_{fT}} \right)^{5/4} \left(\frac{Re_{tr}}{Re} \right)^{15/8} \right]^{1/5}} \quad (4-41)$$

Similarly the mean skin friction coefficient is obtained from Eqs. 4-31, 4-34, 4-38, and 4-40. For $Re \geq Re_{tr}$, it is

$$C_F = C_{F_T} \left\{ 1 - \left(\frac{Re_{tr}}{Re} \right)^{9/4} + \left(\frac{C_{F_L}}{C_{F_T}} \right)^{5/4} \left(\frac{Re_{tr}}{Re} \right)^{15/8} \right\}^{4/5} \quad (4-42)$$

The subscripts L and T in these equations have the same meaning as before (see Subsec. 3.5), i.e., C_{f_L} , C_{F_L} , C_{f_T} , and C_{F_T} are the cone values for

laminar and turbulent, local and mean skin friction coefficients. Methods of determining these from the flat plate values have been given in Subsecs. 4.4.1 and 4.4.2.

It should be noted that these derivations, as in the flat plate case of Subsec. 3.5, are based on the assumption that the transition takes place at a discrete point along each streamline. The variations of C_f and C_F along the cone will follow the same pattern as those of the flat plate which were illustrated on p. 51, i.e., at the transition point, P, C_f is discontinuous while C_F makes only an abrupt change.

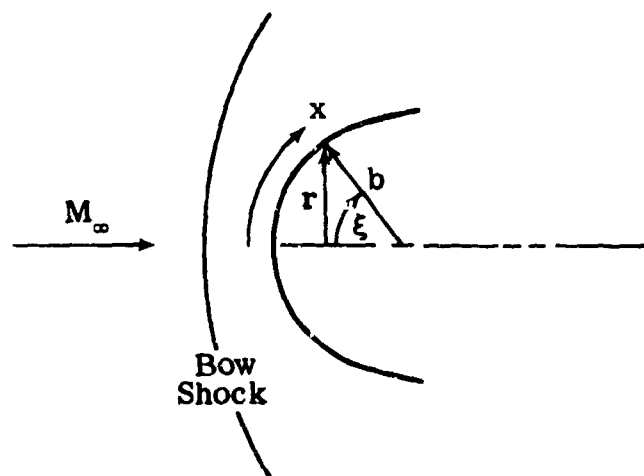
4 5 Laminar Boundary Layer on Spheres

The perfect gas laminar boundary-layer growth on any blunt body can be computed using the approximate method described in Subsec. 4.2. The method will now be applied to boundary-layer growth on the windward side of a sphere with constant surface temperature. This case is of particular interest, since bodies of many practical shapes are blunted by adding spherical tips.

The pressure gradient parameter, n , for a closed axisymmetric body is given by Eq. 4-22 with $A = 0.44$. For a spherical body,

$$r = b \sin \xi \quad \text{and} \quad x = b\xi$$

as shown in the sketch below.



Using these expressions, Eq. 4-22 becomes

$$n = -0.44 \left(\frac{T_{t_1}}{T_1} \right)^K (M_1^B \sin^2 \xi)^{-1} \frac{dM_1}{d\xi} \int_0^\xi M_1^{B-1} \left(\frac{T_{t_1}}{T_1} \right)^{-K} \sin^2 \xi d\xi \quad (4-43)$$

In order to compute n from this equation, it is necessary to express M_1 and T_{t_1}/T_1 as functions of ξ . The modified Newtonian theory gives a realistic pressure distribution over a sphere, i.e., the pressure coefficient may be written as

$$C_p = C_{p_{\max}} \cos^2 \xi \quad (4-44)$$

where

$$C_p = \frac{p_1 - p_\infty}{\frac{1}{2} \rho_\infty u_\infty^2} = \frac{(p_1/p_\infty) - 1}{\frac{1}{2} \gamma M_\infty^2}$$

and

$$C_{p_{\max}} = \frac{(p_{t_1}/p_\infty) - 1}{\frac{1}{2} \gamma M_\infty^2}$$

The pressure, p_{t_1} , at the stagnation point is given by the Rayleigh pitot equation. Assuming that the flow at the outer edge of the boundary layer is isentropic, the local Mach number is given by

$$M_1 = \left(\frac{2}{\gamma - 1} \right)^{\frac{1}{2}} \left[\left(\frac{p_{t_1}}{p_1} \right)^{\frac{\gamma-1}{\gamma}} - 1 \right]^{\frac{1}{2}} \quad (4-45)$$

which, in terms of $C_{p_{\max}}$, is

$$M_1 = \left(\frac{2}{\gamma - 1} \right)^{\frac{1}{2}} \left[\left(\frac{1 + \frac{\gamma}{2} M_\infty^2 C_{p_{\max}}}{1 + \frac{\gamma}{2} M_\infty^2 C_{p_{\max}} \cos^2 \xi} \right)^{\frac{\gamma-1}{\gamma}} - 1 \right]^{\frac{1}{2}} \quad (4-46)$$

Thus, from this equation, the local Mach number, M_1 , may be found in terms of ξ for specified values of M_∞ . Using the isentropic temperature ratio

$$\frac{T_{t_1}}{T_1} = 1 + \frac{\gamma - 1}{2} M_1^2$$

and Eqs. 4-43 and 4-46, n may be computed as a function of ξ , M_∞ , and B . The value of the exponent B may be taken from Fig. 4-3 for an axisymmetric

body with a favorable pressure gradient. The exponent K is given by Eq. 4-12, i.e.,

$$K = \frac{3\gamma - 1}{2(\gamma - 1)}$$

The momentum thickness, θ , may then be expressed in terms of the local parameters by combining Eqs. 4-6 and 4-43, i.e.,

$$\frac{\rho_{t_1} a_{t_1} b}{\lambda \mu_{t_1}} \left(\frac{\theta}{b}\right)^2 = 0.44 \left(\frac{T_{t_1}}{T_1}\right)^{\frac{\gamma+1}{\gamma-1}} (M_1^B \sin^2 \xi)^{-1} \int_0^\xi M_1^{B-1} \left(\frac{T_{t_1}}{T_1}\right)^{-K} \sin^2 \xi d\xi \quad (4-47)$$

where λ is defined by Eq. 2-32. Evaluating Eq. 4-6 at the stagnation point where $x = \xi = 0$ and hence $n = -0.44/(B+2)$ (see Subsec. 4.2.3.2, closed body) one obtains

$$\frac{\rho_{t_1} a_{t_1} b}{\lambda \mu_{t_1}} \left(\frac{\theta}{b}\right)^2 = 0.44 \left[(B+2) \left(\frac{dM_1}{d\xi}\right)_{\xi=0} \right]^{-1} \quad (4-48)$$

Equation 4-47 may be readily integrated if the flow regime is restricted to high Mach numbers and the zone of interest limited to the neighborhood of the stagnation point. The first restriction limits M_∞ to such values that make $(\gamma/2) M_\infty^2 C_{p_{\max}} \gg 1$. The second restriction specifies that ξ be small enough that $(\gamma/2) M_\infty^2 C_{p_{\max}} \cos^2 \xi \gg 1$. With these restrictions, Eq. 4-46 may then be reduced to

$$M_1 \approx \left(\frac{2}{\gamma-1}\right)^{\frac{1}{2}} \left[(\cos \xi)^{\frac{-2(\gamma-1)}{\gamma}} - 1 \right]^{\frac{1}{2}} \quad (4-49)$$

and

$$\left(\frac{dM_1}{d\xi}\right)_{\xi=0} = (2/\gamma)^{\frac{1}{2}} \quad (4-50)$$

The value of B given by Fig. 4-3 depends on the wall temperature. As the Mach number increases, a high cooling rate at the nose will be necessary from a practical standpoint, i.e., $B = 3$ may be considered as a representative value for a high Mach number flow. At the nose ($\xi = 0$), Eqs. 4-48 and 4-50 combine to give

$$\frac{\rho_{t_1} a_{t_1} b}{\lambda \mu_{t_1}} \left(\frac{\theta}{b}\right)^2 = 0.088 (\gamma/2)^{\frac{1}{2}} \quad (4-51)$$

Using the Reynolds number defined by

$$Re_{\theta t} = \frac{\rho_{t_1} a_{t_1} \theta}{\lambda \mu_{t_1}} \quad \text{and} \quad Re_{bt} = \frac{\rho_{t_1} a_{t_1} b}{\lambda \mu_{t_1}} \quad (4-52)$$

one has

$$\frac{Re_{\theta t}}{(Re_{bt})^{\frac{1}{2}}} = \left(\frac{\rho_{t_1} a_{t_1} b}{\lambda \mu_{t_1}} \right)^{\frac{1}{2}} \frac{\theta}{b} \quad (4-53)$$

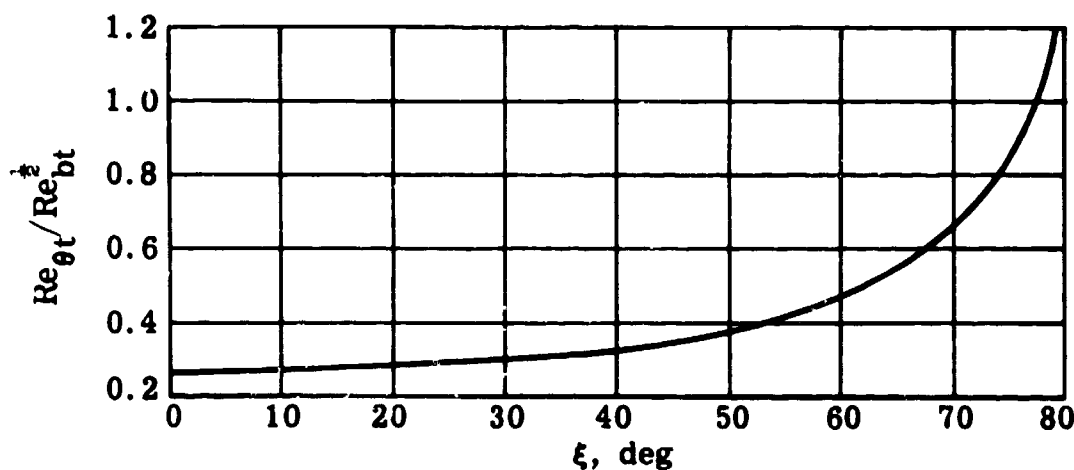
i. e., at the nose

$$\frac{Re_{\theta t}}{(Re_{bt})^{\frac{1}{2}}} = (0.088)^{\frac{1}{2}} (\gamma/2)^{\frac{1}{4}} = 0.2713$$

For small values of ξ , when $B = 3$, Eq. 4-47 becomes

$$\frac{\rho_{t_1} a_{t_1} b}{\lambda \mu_{t_1}} \left(\frac{\theta}{b} \right)^2 = 0.44 \left(\frac{T_{t_1}}{T_1} \right)^{\frac{\gamma+1}{\gamma-1}} (M_1^2 \sin^2 \xi)^{-1} \int_0^{\xi} M_1^2 \left(\frac{T_{t_1}}{T_1} \right)^{-K} \sin^2 \xi \, d\xi \quad (4-54)$$

The ratio, $Re_{\theta t}/(Re_{bt})^{1/2}$, has been computed as a function of ξ from Eq. 4-54 and is shown on the sketch below.



Knowing the variation of $Re_{\theta t}/(Re_{bt})^{1/2}$ over a portion of the sphere, values of n can be computed using the definition of n (Eq. 4-6), since T_{t_1}/T_1 and M_1 may easily be expressed in terms of ξ . Other parameters such as the local skin friction coefficient, the shape parameter, and the total boundary-layer thickness can then be computed by the methods described in Subsecs. 4.2.4 and 4.2.5.

The method described above will be used to compute the boundary-layer growth over the tips of the sphere-cones in Subsec. 4.6. For the numerical results given there, Eq. 4-46 was used to determine the Mach number

distribution over the tip. The boundary-layer parameters given in the next subsection have been expressed in terms of the wall slope rather than ξ . The conversion from the form given in Eq. 4-53 is easily made.

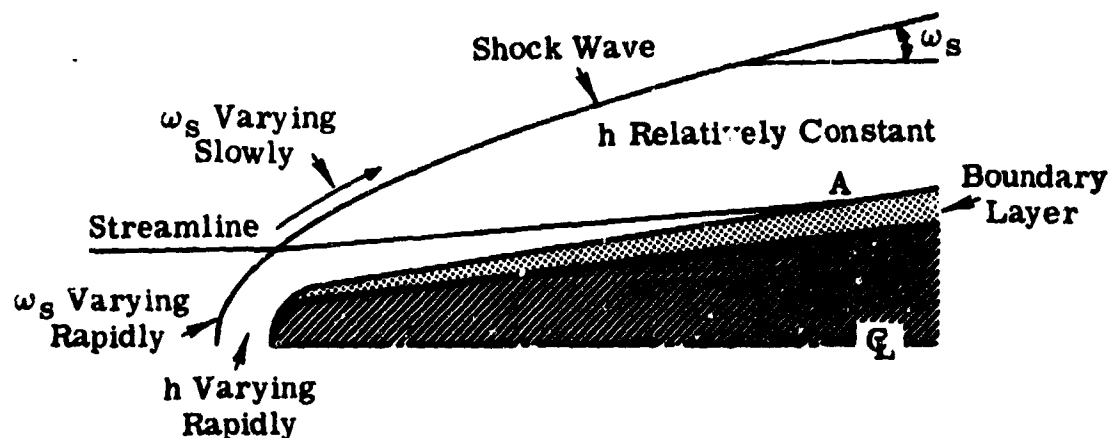
4.6 Laminar Boundary Layer on Sphere-Cones

The momentum integral equation for an axisymmetric body is given by Eq. 2-27. Wilson, in Ref. 13, has simplified this equation for a thermally and calorifically perfect gas flowing over slightly blunted cones by assuming:

1. A constant pressure on the conical surface which is equal to that on a sharp cone in inviscid flow.
2. Adiabatic flow outside the boundary layer.
3. $\tau_1/\rho_1 u_1^2 \ll C_f/2$.

The experimental results of Lewis (Ref. 61) show that, for hypersonic flow over slender cones, the first assumption is reasonably accurate for points more than five nose radii from the tip. The second assumption implies that the heat conduction and shear stress terms in the energy equation may be neglected in the flow outside the boundary layer. The third assumption is shown by Ferri in Ref. 62 to be valid for the relatively high Reynolds numbers at which the boundary layer is thin. In that case the velocity gradient at the wall is high compared to the velocity gradient in the variable entropy regime outside the boundary layer, i.e., $\tau_1 \ll \tau_w$.

With the above assumptions, Eq. 2-27, the momentum integral equation, is expressed by Eq. 2-30. In this equation it may be noted that in spite of the assumption of constant pressure along the surface, a term with Mach number gradient appears. This term takes into account the variation of the entropy normal to the streamline in the flow above the boundary layer. It will be finite until the variable entropy layer has been completely swallowed or absorbed (point A) by the growing boundary layer, as shown in the sketch below.



In order to integrate Eq. 2-30, expressions must be found for the boundary-layer parameters (C_f , δ/θ , and H), for the Mach number (M_1), and for the Mach number gradient (dM_1/dx). The method developed by Wilson in Ref. 13 will be followed.

4.6.1 Boundary-Layer Parameters

The expressions for C_f , δ/θ , and H will be taken from flat plate results (Subsecs. 3.1 and 3.2) and evaluated at the local flow conditions which must be determined at each point along the body. The momentum integral equation for the flat plate, obtained by putting $(\theta/r)(dr/dx) = 0$ in Eq. 2-29, may be combined with the Rubesin-Johnson skin friction relation given by Eq. 3-8 to give

$$C_f = \frac{\tau_w}{\frac{1}{2} \rho_1 u_1^2} = \frac{(0.664)^2}{Re_{\theta_1}} \frac{T_1}{T'_*} \frac{\mu'_*}{\mu_1} = \frac{(0.664)^2}{Re_{\theta_1}} \frac{\mu'_*}{T'_*} \quad (4-55)$$

where

$$Re_{\theta_1} = \frac{\rho_1 u_1 \theta}{\mu_1}$$

A Prandtl number of 0.75 will be used for the sample calculations, in which case Eq. 3-14 becomes

$$T'_* = 1 + 0.076 (\gamma - 1) M_1^2 + 0.481 (T_{*w} - 1) \quad (4-56)$$

The ratio μ'_* in Eq. 4-55 can be obtained from Sutherland's viscosity law given by Eq. 3-1 and re-written as:

$$\mu'_* = (T'_*)^{3/2} \left(1 + \frac{198.7^\circ R}{T_1} \right) \left/ \left(T'_* + \frac{198.7^\circ R}{T_1} \right) \right. \quad (4-57)$$

where T_1 is in degrees Rankine. With the assumptions of a perfect gas and adiabatic flow outside the boundary layer, T_1 can be computed from the energy equation

$$\frac{T_{t_1}}{T_1} = 1 + \frac{\gamma - 1}{2} M_1^2$$

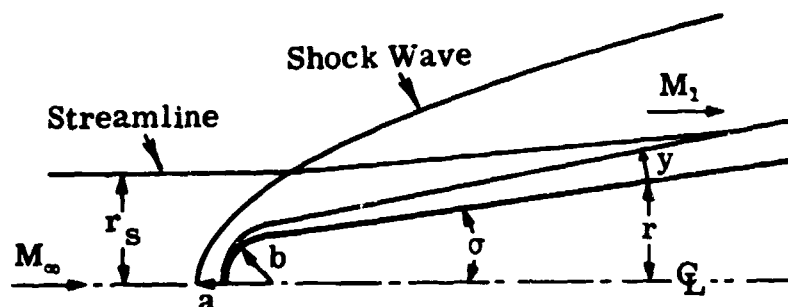
The difference between δ/θ and H , which is required in the solution of Eq. 2-30, is obtained from Eqs. 3-21 and 3-22, i.e.,

$$\frac{\delta}{\theta} - H = \text{constant} = 6.41 \quad (4-58)$$

Mangler's transformation (see Subsec. 2.3), demonstrates that the velocity and temperature distributions through the boundary layer are the same for a flat plate as for a sharp cone. It follows that Eqs. 4-55, 4-56, and 4-58, which apply to the flat plate, will also apply to the sharp cone with constant pressure gradient and wall temperature. It is now assumed that for a blunt-nosed cone the above equations will apply if the flow conditions are evaluated from point to point along the surface.

4.6.2 Continuity Considerations

Expressions for M_1 and dM_1/dx to be used in the integration of Eq. 2-30, are derived from two relations between M_1 and the local shock-wave angle, ω_s . The first relation is obtained from a consideration of the continuity of mass flow. Referring to the sketch below, it may be seen that the mass



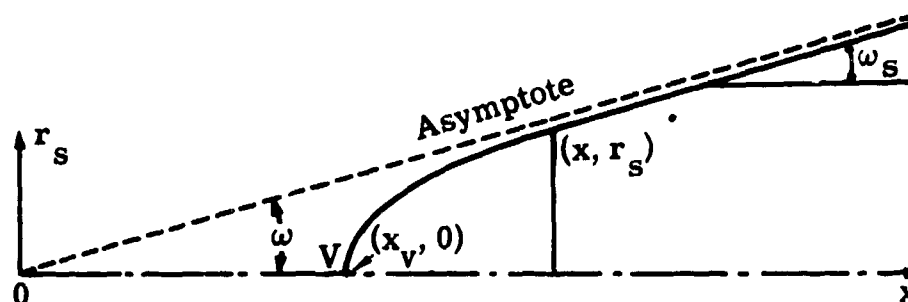
flow through the thin boundary layer in the annulus (of depth y and distance r from the axis) is equal to the flow through the associated stream tube of radius r_s , i.e.,

$$2\pi r \int_0^\delta \rho u \, dy = \rho_\infty u_\infty \pi r_s^2 \quad (4-59)$$

In the evaluation of ω_s , where experimental data are inadequate or non-existent, elaborate flow calculations must be carried out. For the present calculations, it has been assumed that the shape of the detached shock is the hyperbola suggested by Moeckel (Ref. 63) and defined by

$$r_s = \pm \tan \omega (x^2 - x_v^2)^{1/2}$$

where the coordinate system is shown in the following sketch.



The shock-wave angle, ω_s , approaches the sharp cone shock angle, ω , as $r_s \rightarrow \infty$. Heybey in Ref. 64 gives an expression for the shock radius of curvature, a , at $r_s = 0$. The values of a and ω define the shape of the hyperbola. The relation between r_s and ω_s can be shown to be:

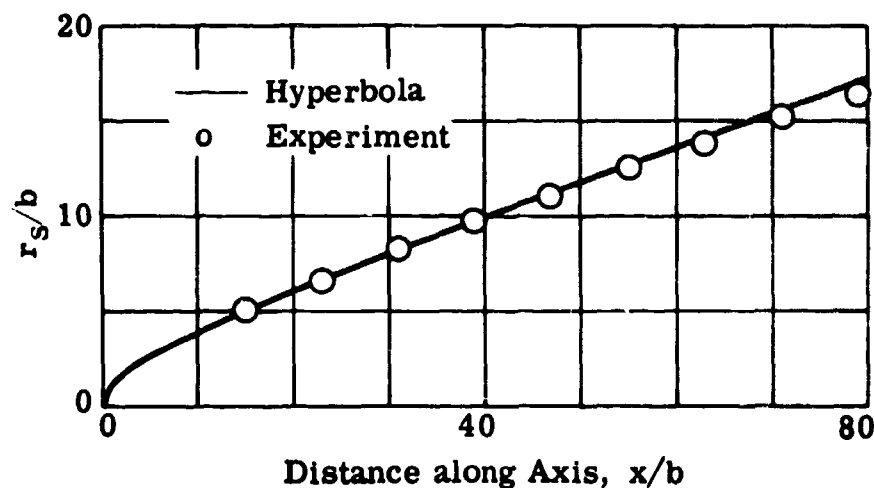
$$\frac{a^2}{r_s^2} = \tan^2 \omega_s - \tan^2 \omega \quad (4-60)$$

At high Mach numbers, the equations of Heybey indicate a constant ratio between a and the radius of curvature, b , of the blunt-body nose. It is expressed by

$$a \approx 1.5b \quad (4-61)$$

This result holds for free-stream Mach numbers higher than about 4. It agrees with experimental data and appears to be nearly independent of γ and real gas effects.

The sketch below compares the experimentally determined shock-wave shape for a slender blunt-tipped cone ($\sigma = 6^\circ$) with that derived from Eq. 4-60. The hyperbola is seen to be an excellent fit to the data for a large



portion of the shock wave. With the assumptions of a perfect gas and adiabatic flow outside the boundary layer, Eqs. 4-59 and 4-60 may be used to obtain the following relationship between M_1 and ω_s :

$$\frac{p_\infty}{p_1} \frac{M_\infty}{M_1} \left(\frac{2 + (\gamma - 1) M_\infty^2}{2 + (\gamma - 1) M_1^2} \right)^{\frac{1}{2}} \left(\frac{a^2}{\tan^2 \omega_s - \tan^2 \omega} \right) = 2r\theta \left(\frac{\delta}{\theta} - H \right) \quad (4-62)$$

where, as before, p_1 and M_1 are measured along the cone surface, just outside the boundary layer.

Zakkay and Krause (Ref. 65) give a method similar to the above for relating the mass flow in the boundary layer to the flow through a stream tube ahead of the shock. Their method assumes local similarity and makes use of a mass-flow function given by Lees (Ref. 66). This mass-flow function includes a parameter representing the boundary-layer growth along the surface. In the present method the growth along the surface is obtained from the momentum

integral equation (Eq. 2-30). The shock wave shapes assumed in the present work and in Ref. 65 are somewhat different.

4.6.3 Expansion of the Flow Behind the Bow Shock

Although the layers immediately above the boundary layer may have variable entropy, isentropic flow is assumed along each streamline from the bow shock to the outer edge of the boundary layer (see sketch on p. 98). This assumption, together with the oblique shock equations for a perfect gas, yields the second required relationship between M_1 and ω_s , i.e.,

$$\left(\frac{p_1}{p_\infty}\right)^{\frac{\gamma-1}{\gamma}} \left[1 + \frac{\gamma-1}{2} M_1^2\right] = \left[\frac{\gamma+1}{2\gamma M_\infty^2 \sin^2 \omega_s} - (\gamma-1)\right]^{1/\gamma} \quad (4-63)$$

$$\left\{ \frac{(\gamma+1) M_\infty^2 \sin^2 \omega_s [2 + (\gamma-1) M_\infty^2]}{2 [2 + (\gamma-1) M_\infty^2 \sin^2 \omega_s]} \right\}$$

4.6.4 Calculation of the Mach Number Gradient

Equations 4-62 and 4-63 can be used to calculate dM_1/dx . Although these equations do not require $p_1 = \text{constant}$, this assumption will now be used. Taking into account Eq. 4-58 and differentiating Eqs. 4-62 and 4-63 with respect to x , the result, after eliminating $d\omega_s/dx$, is

$$\frac{2\theta}{M_1 [2 + (\gamma-1) M_1^2]} \left\{ \frac{[2 + (\gamma-1) M_1^2] - 6.41}{F_1} \right\} \frac{dM_1}{dx} = \frac{d\theta}{dx} + \frac{\theta dr}{r dx} \quad (4-64)$$

where

$$F_1 = \frac{2 + (\gamma-1) M_1^2 - 6.41}{\frac{M_1^2 \tan^2 \omega_s \sec^2 \omega_s}{2 (\tan^2 \omega_s - \tan^2 \omega)} \frac{[2\gamma M_\infty^2 \sin^2 \omega_s - (\gamma-1)] [2 + (\gamma-1) M_\infty^2 \sin^2 \omega_s]}{(M_\infty^2 \sin^2 \omega_s - 1)^2} - [1 + (\gamma-1) M_1^2]} \quad (4-65)$$

4.6.5 Integration of the Momentum Equation

Making use of Eq. 4-58 and taking dM_1/dx from Eq. 4-64, Eq. 2-30 can be written in the following form:

$$\frac{d\theta}{dx} + \frac{\theta dr}{r dx} = \frac{C_f}{2} \frac{1}{(1 + F_1)} \quad (4-66)$$

When $F_1 = 0$, Eq. 4-66 applies to an axisymmetric body with zero pressure gradient and constant flow conditions outside the boundary layer. For the conical

portion of the blunted cone, $dr/dx = r/x$. With this relationship and Eq. 4-55, Eq. 4-66 can be written as

$$2 \left(\frac{Re_{x_c} Re_{\theta_c}}{Re_{x_c}^2} \right) dRe_{x_c} (Re_{x_c} Re_{\theta_c}) = F_2 \quad (4-67)$$

where

$$Re_{x_c} = \frac{\rho_c u_c x}{\mu_c} \quad \text{and} \quad Re_{\theta_c} = \frac{\rho_c u_c \theta}{\mu_c}$$

$$F_2 = (0.664)^2 \frac{\rho_c u_c}{\rho_1 u_1} \frac{\mu_1}{\mu_c} \frac{T_1}{T_c} \frac{u'}{\mu_1} \left(\frac{1}{1 + F_1} \right) \quad (4-68)$$

$$\frac{\rho_c u_c}{\rho_1 u_1} \frac{\mu_1}{\mu_c} = \frac{M_c}{M_1} \left(\frac{T_1}{T_c} \right)^2 \left(\frac{T_c}{T_1} + \frac{198.7^\circ R}{T_1} \right) \left/ \left(1 + \frac{198.7^\circ R}{T_1} \right) \right. \quad (4-69)$$

and

$$\frac{T_c}{T_1} = \frac{2 + (\gamma - 1) M_c^2}{2 + (\gamma - 1) M_1^2} \quad (4-70)$$

The values of x and θ in the Reynolds numbers Re_{x_c} and Re_{θ_c} are local values along the surface of the blunted cone; all parameters with the subscript c are associated with the flow conditions on a sharp cone.

Starting the integration at the tangent point of the spherical segment and conical section, Eq. 4-67 can be written

$$\frac{1}{3} (Re_{x_c}^3 - Re_{n_c}^3) = \int_{(Re_{x_c} Re_{\theta_c})_n}^{(Re_{x_c} Re_{\theta_c})} \frac{2}{F_2} (Re_{x_c} Re_{\theta_c}) d(Re_{x_c} Re_{\theta_c}) \quad (4-71)$$

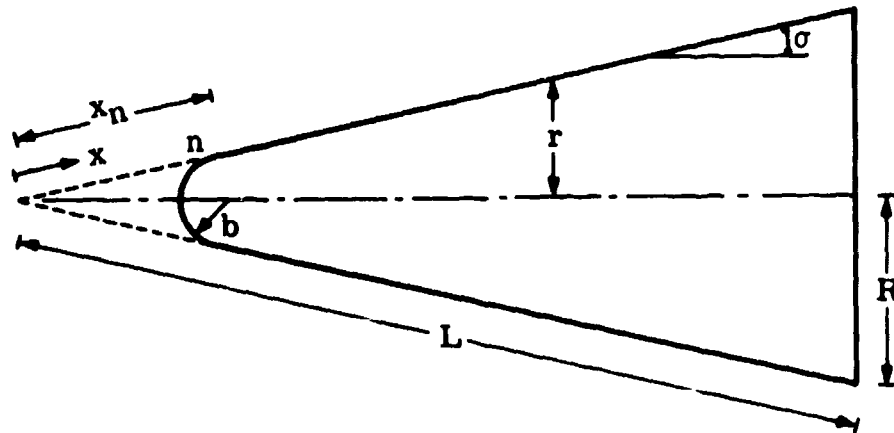
where the subscript r denotes values at the tangent point. Equation 4-71 can be put into a form convenient to integrate by dividing both sides by $Re_{b_c}^4$, where $Re_{b_c} = \rho_c u_c b / \mu_c$, and noting that $Re_{n_c} / Re_{b_c} = x_n / b = \cot \sigma$. Equation 4-71 thus becomes

$$\frac{1}{3 Re_{b_c}} \left\{ \left(\frac{Re_{x_c}}{Re_{b_c}} \right)^3 - \cot^3 \sigma \right\} = \int_{\Lambda_n}^{\Lambda} \frac{2}{F_2} \Lambda d\Lambda \quad (4-72)$$

where

$$\Lambda = \frac{Re_{x_c} Re_{\theta_c}}{Re_{b_c}^2}$$

The nomenclature is illustrated by the following sketch.



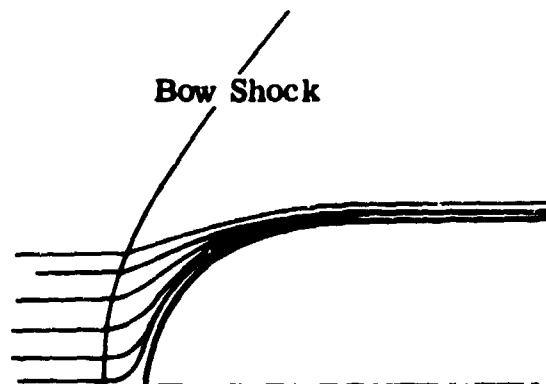
For known flight conditions, cone angle, and surface temperature, the parameters F_2 and Λ in Eq. 4-72 are functions of M_1 and ω_s only.

Making use of Eqs. 4-58 and 4-61, Eq. 4-62 may be written as

$$\Lambda = \frac{1.125 \frac{P_\infty}{p_1} \frac{M_\infty}{M_1} \left(\frac{2 + (\gamma - 1) M_\infty^2}{2 + (\gamma - 1) M_1^2} \right)^{\frac{1}{2}}}{6.41 (\tan^2 \omega_s - \tan^2 \omega)} \quad (4-73)$$

The integral in Eq. 4-72 can now be evaluated as follows. Equation 4-63 is used to compute M_1 as a function of ω_s . The value of ω_s ranges from $\pi/2$ on the axis to ω . Pairs of values of ω_s and M_1 derived from Eq. 4-63 are then used to compute F_2 and Λ from Eqs. 4-65, 4-68, and 4-73. Values of M_c can be found in cone tables such as Refs. 67, 68, and 69.

It can be seen from the above equations that the integrand of Eq. 4-72 is independent of Re_{b_c} , i.e., independent of the nose radius, b . However, Re_{b_c} does appear in the lower limit, Λ_n , to the integral in Eq. 4-72. The value of this lower limit can be obtained by integrating the boundary-layer momentum equation over the spherical segment at the nose. For cases of most general interest, the entropy outside the nose boundary layer can be assumed to be constant since the streamlines near the cap all emanate from the normal portion of the shock as shown in the sketch below.



Given the flight conditions, cone angle, and surface temperature, Cohen and Reshotko (see Ref. 7 and Subsec. 4.5) show that

$$\Lambda_n = \text{constant} \left(\text{Re}_{b_c} \right)^{-\frac{1}{2}} \quad (4-74)$$

Equations 4-72 and 4-74, with a given value of Re_{b_c} , can be used to obtain Re_{θ_c} as a function of Re_{x_c} . Having obtained a solution for one value of Re_{b_c} , results for additional values are easily obtained since the parameters under the integral in Eq. 4-72 will be unchanged. The evaluation of the integral, however, will start at a different lower limit associated with each value of Re_{b_c} .

Having determined the values of Re_{θ_c} , the momentum thickness based on local flow conditions is found from

$$\text{Re}_{\theta_1} = \frac{\rho_1 u_1}{\rho_c u_c} \frac{\mu_c}{\mu_1} \text{Re}_{\theta_c} \quad (4-75)$$

where $\frac{\rho_1 u_1}{\rho_c u_c} \frac{\mu_c}{\mu_1}$ is given by Eq. 4-69.

For a sharp cone (superscript o), where $T_1 = T_c$ and $F_1 = 0$, Eq. 4-68 becomes

$$F_2^o = (0.664)^2 \frac{T_c}{T'} \frac{\mu'}{\mu_c} = \text{constant} \quad (4-76)$$

where T'/T_c and μ'/μ_c are given by Eqs. 4-56 and 4-57 with $T_1 = T_c$ and $M_1 = M_c$. The boundary-layer growth over a sharp cone can be obtained by putting Re_{n_c} and $\left(\text{Re}_{x_c} \text{Re}_{\theta_c} \right)_n$ equal to zero in Eq. 4-71 which then reduces to

$$\text{Re}_{\theta_c}^o = \left(\frac{F_2^o \text{Re}_{x_c}}{3} \right)^{\frac{1}{2}} \quad (4-77)$$

4.6.6 Skin Friction and Friction Drag

After integrating Eq. 4-72 and determining values of Re_{θ_1} from Eq. 4-75, values of the local skin friction coefficient may be computed from Eq. 4-55. In order to compare the results with those of a sharp cone, it is convenient to define the local skin friction coefficient of a blunt cone as follows:

$$C_{f_c} = \frac{\tau_w}{\frac{1}{2} \rho_c u_c^2} = \frac{\rho_1 u_1^2}{\rho_c u_c^2} C_{f_1} \quad (4-78)$$

where C_{f_1} is given by Eq. 4-55 and

$$\frac{\rho_1 u_1^2}{\rho_c u_c^2} = \frac{M_1^2}{M_c^2}$$

The local skin friction coefficient on a sharp cone is obtained by re-writing Eq. 4-55 as

$$C_{f_c}^0 = \frac{(0.664)^2}{Re_{\theta_c}^0} \frac{T_c \mu'}{T' \mu_c} \quad (4-79)$$

where $Re_{\theta_c}^0$ is given by Eq. 4-77. A comparison of C_{f_c} and $C_{f_c}^0$ will show the effect of tip blunting on the local shear stress, since both coefficients are referenced to the same flow conditions.

If the skin friction on the nose is neglected, the friction drag on the conical frustum is given by

$$D = \int_{x_n}^L 2\pi \cos \sigma \tau_w r dx \quad (4-80)$$

By definition, the skin friction drag coefficient is

$$C_{D_F} = \frac{D}{\frac{1}{2} \rho_\infty u_\infty^2 \pi R^2} \quad (4-81)$$

where R is the radius at the end of a finite cone. Equations 4-78, 4-80, and 4-81 combine to give

$$C_{D_F} = \frac{\rho_c u_c^2}{\rho_\infty u_\infty^2} \sin 2\sigma \int_{\frac{b}{R} \cot \sigma}^{\csc \sigma} C_{f_c} \frac{x}{R} d\left(\frac{x}{R}\right) \quad (4-82)$$

4.6.7 Local Flow Conditions Far from the Tip

Far from the tip both Re_{θ_c} and Re_{θ_1} approach $Re_{\theta_c}^0$. The numerical example of the next subsection shows that Re_{θ_1} approaches $Re_{\theta_c}^0$ faster than Re_{θ_c} . Therefore, taking the value of $Re_{\theta_c}^0$ from Eq. 4-77, far from the tip

$$Re_{\theta_1} \approx \left(\frac{F_2^0 Re_{x_c}}{3} \right)^{\frac{1}{2}}$$

With this result and Eq. 4-75, the value of Re_{θ_c} for the blunt cone is given by

$$Re_{\theta_c} \approx \frac{\rho_c u_c \mu_1}{\rho_1 u_1 \mu_c} \left(\frac{F_2^0 Re_{x_c}}{3} \right)^{\frac{1}{2}}$$

This may be re-written as

$$Re_{x_c} / Re_{b_c}^{4/3} \approx \left(\frac{\rho_1 u_1 \mu_c}{\rho_c u_c \mu_1} \frac{Re_{x_c} Re_{\theta_c}}{Re_{b_c}^2} \sqrt{3/F_2^0} \right)^{\frac{2}{3}} \quad (4-83)$$

When the flight conditions, cone angle, and surface temperature are known, the value of $Re_{x_c} / (Re_{b_c}^{4/3})$ far from the tip may be determined as a function of M_1 only by means of Eqs. 4-63, 4-69, 4-73, 4-76, and 4-83. This parameter makes it possible to estimate the effect of nose bluntness on the value of M_1 far from the tip without integrating the momentum equation. If the point at which the boundary layer swallows the variable entropy layer can be defined by some value of $M_1 < M_c$, then Eq. 4-83 indicates that Re_{x_c} at this point will be directly proportional to $Re_{b_c}^{4/3}$.

4.6.8 Numerical Example

The example presented here may also be found in Ref. 13. These calculations apply to free-stream flow at $M_\infty = 14.9$ over a blunted cone ($\sigma = 8^\circ$). The temperature of the surface is assumed to be the static temperature of the free stream ($530^\circ R$). Three values of the Reynolds number at the nose are considered:

$$Re_{b_c} = 5 \times 10^3, \quad 5 \times 10^4, \quad \text{and} \quad 5 \times 10^5$$

When $M_\infty = 14.9$ the local Mach number, M_c , on a sharp cone is 10.0. For inviscid flow the Mach number at the tangent point on the blunted cone can be shown, by a modified Newtonian theory, to be 3.02.

The behavior of $(2\Lambda/F_2)$, the integrand in Eq. 4-72, is shown on Fig. 4-6. It may be noted that Eq. 4-65 gives $F_1 = 0$ for $\omega_s = \pi/2$ and $\omega_s = \omega$. It is of interest to note that, for the case considered, F_1 reached a maximum value of 0.6 at $\omega_s \approx 30^\circ$. It can be seen from Eq. 4-66 that F_1 , and thus the Mach number gradient dM_1/dx will have a significant effect on the boundary-layer growth. Near the tangent point, F_2 given by Eq. 4-68 can be approximated by taking $M_1 = 3.02$ and $F_1 = 0$. Far from the nose, F_2 can be approximated by taking $M_1 = 10.0$ and $F_1 = 0$. Each of these limiting values of F_2 gives a linear variation of the integrand with the variable of integration (dashed lines in Fig. 4-6). It can be seen from this figure that there can be three flow regimes. Near the nose, the Mach number and the entropy outside the boundary layer are almost constant and correspond to the flow through the normal portion of the shock. Next there is the swallowing regime in which the Mach number

and entropy are changing fairly rapidly. Finally, far from the nose, when the variable entropy layer has been completely swallowed, the Mach number and entropy are again almost constant and correspond to the flow through the conical portion of the shock.

It is necessary to define the lower limits in order to evaluate the integral in Eq. 4-72. A modified Newtonian pressure distribution was assumed and boundary-layer growth over the nose calculated by the method of Ref. 7. The result, in the same form as Eq. 4-74, is

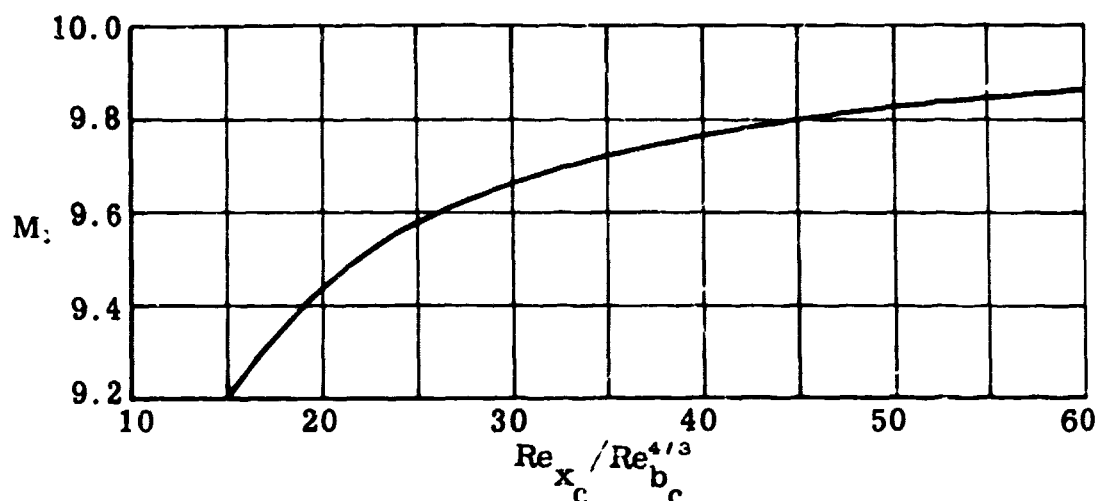
$$\Lambda_n = 56 \text{Re}_{bc}^{-\frac{1}{2}} \quad (4-84)$$

The lower limits for each of the three nose Reynolds numbers are indicated on Fig. 4-6. It has already been stated that the integrand represented by the solid curve in Fig. 4-6 is independent of Re_b , but the integration will begin at points A, B, or C depending on which of the three nose radii is being used. A small enough portion of the variable entropy layer is swallowed by the nose boundary layer so that conditions corresponding to flow through a normal shock may be assumed without much loss of accuracy. The effects of errors in these limits (shown by the distances of points A, B, or C from the dashed curve for $M = 3.02$) quickly become negligible as the boundary layer grows along the conical section.

Curves of Re_{θ_c} and Re_{θ_1} vs Re_{x_c} obtained from Eqs. 4-71 and 4-72 are plotted on Fig. 4-7. These curves are compared with the sharp cone results obtained from Eq. 4-77. Since the blunt cone Re_{θ_c} values are based on sharp cone local flow properties, the comparison shows the effect of blunting on θ . These curves show that blunting can increase the value of θ by an order of magnitude. However, when the Reynolds number is based on local flow conditions outside the boundary layer (Re_{θ_1}), the trend is reversed, i.e., the bluntness reduces the momentum thickness Reynolds number.

Curves of M_1 vs Re_{x_c} , generated in solving Eq. 4-72, are plotted on Fig. 4-8. As the bluntness is increased, its effect on the local Mach number is felt farther from the tip. For a cone of finite length, the bluntness ratio (nose radius to base radius) must be very small before $M_1 \approx M_c$ near the base. For example, Fig. 4-8 shows that for the smallest value of Re_{bc} , i.e., 5×10^3 , M_1 does not approximate M_c (10.0) until $\text{Re}_{x_c} = 10^7$. The bluntness ratio given by $\text{Re}_{bc}/(\text{Re}_{x_c} \sin \sigma)$, for this case is only 0.0036.

For given flight conditions, cone angle, and surface temperature, Eq. 4-83 can be used to obtain a curve of M_1 vs $\text{Re}_{x_c}/\text{Re}_{bc}^{4/3}$ for the regime far from the tip. The curve obtained from the present example is plotted on the sketch opposite. For any value of Re_{bc} , the curve can be used to determine the value of Re_{x_c} at which a particular value of M_1 will be reached.



Values of C_{f_c} and $C_{f_c}^0$ were computed from Eqs. 4-78 and 4-79 respectively and their ratio is plotted on Fig. 4-9 as a function of Re_{x_c} . It can be seen that bluntness significantly reduces the local shear stress. For a slender cone at hypersonic speeds, a large fraction of the total drag is due to friction. A slight bluntness will therefore significantly decrease the total drag. The method given here for computing skin friction was used by Lyons, et al (Ref. 70), in calculating the total drag of slightly blunted cones. Their results were in excellent agreement with measurements obtained in a ballistics range.

4.6.9 Real Gas Effects

Real gas data for equilibrium air can be used directly in the blunt cone computations. Rubin in Ref. 71 reworks the calculations of Ref. 65 introducing real gas effects. In order to include such data in the method given here, the solution to the inviscid flow over a sharp cone in equilibrium air is required. From this solution one may obtain the pressure on the blunt cone, the asymptotic value of the bow shock-wave angle, and the flow conditions at the outer edge of the boundary layer far from the tip. Equation 2-27 holds for the real gas case. However, without the assumption of a perfect gas, Eq. 2-30 must be re-written as

$$\frac{d\theta}{dx} + \frac{29}{u_1} \left[1 + \frac{u_1}{2\rho_1} \frac{d\rho_1}{du_1} - \frac{1}{2} \left(\frac{\delta}{\theta} - H \right) \right] \frac{du_1}{dx} + \frac{\theta}{r} \frac{dr}{dx} = \frac{C_f}{2} \quad (4-85)$$

The density, ρ_1 , and the velocity, u_1 , are related by the assumptions of constant pressure and adiabatic flow outside the boundary layer. The reference temperature method for calculating C_f from Eq. 4-55 must be replaced by the reference enthalpy method (see Subsec. 3.2.1). Equation 4-55 must be re-written as

$$C_f = \frac{(0.664)^2}{Re_{\theta_1}} \frac{\rho' \mu'}{\rho_1 \mu_1} \quad (4-86)$$

where ρ' and μ' correspond to the reference enthalpy given by Eq. 3-28. The values of t/θ and H may be computed from Eqs. 3-29 and 3-30. The difference, $[(\delta/\theta) - H]$, given by Eq. 4-58, will be unchanged. Equation 4-62 must be replaced by

$$\frac{\rho_{\infty}}{\rho_1} \frac{u_{\infty}}{u_1} \left(\frac{a^2}{\tan^2 \omega_s - \tan^2 \omega} \right) = 2r\theta \left(\frac{\delta}{\theta} - H \right) \quad (4-87)$$

Differentiating this equation with respect to x yields

$$\frac{d\theta}{dx} + \frac{\theta}{r} \frac{dr}{dx} + \frac{\theta}{u_1} \left(1 + \frac{u_1}{\rho_1} \frac{d\rho_1}{du_1} + \frac{2 \tan \omega_s \sec^2 \omega_s}{\tan^2 \omega_s - \tan^2 \omega} u_1 \frac{d\omega_s}{du_1} \right) \frac{du_1}{dx} = 0 \quad (4-88)$$

Equations 4-85 and 4-88 can be combined to obtain an integral equation of the same form as Eq. 4-72. A second equation relating u_1 and ω_s can be obtained in the same manner as Eq. 4-63, but the inclusion of real gas data precludes the expression of the relationship in an implicit analytical form.

Table 4-1
Summary of Finite Difference Methods for Solving the Laminar Boundary-Layer Equations

	Explicit		Implicit	
	(1)	(2)	(3)	(4)
Working Form of Equation	Unmodified momentum and energy equations.	Crocco's transformed equation, in which x, u are independent variables.	Crocco's transformed equation, in which x, u are independent variables.	Simple transformation of momentum equation in which x, y remain essentially as independent variables.
Important Contributors & References	Wu (Ref. 49) Görtler (Ref. 50)	Baxter and Flüggelotz (Ref. 54) Raetz (Ref. 53)	Kramer and Lieberstein (Ref. 55)	Hartree (Refs. 51a, 51b, and 52) Smith and Clutter (Ref. 47a)
Accuracy of τ in Terms of Computing Time	Theoretically exact, but insufficient work has been done to establish the accuracy-computing time relation.	Theoretically exact. Accuracy high (3 to 5 figure). Computing time is long.	Theoretically exact, but insufficient work has been done to establish accuracy-computing time relation. Computing time should be short.	Theoretically exact. Accuracy high (3 to 5 figure). Computing time now medium, but could be reduced greatly.
Advantages	Simple and sufficiently fast for low accuracy. Theoretically can handle any boundary-layer problem exactly in limit.	Theoretically exact and convenient formulations, because boundaries are at $u = 0$, $u = 1$, and Crocco's equation is second order.	Same as No. 2 plus rapid computing time. Computing is fast because a "rick" good for second order equations has been used. No numerical stability problem.	Theoretically can handle any boundary-layer problem, exactly in limit. Computing time is good. Has best starting procedure of any exact method. No numerical stability problem.
Criticisms	Boundary-layer thickness in this system varies greatly, causing computing complications. Computing time excessive where high accuracy demanded. Has numerical stability problem.	Computing time great where high accuracy demanded. Crocco's equation not suitable for problems involving "overshoot." Has numerical stability problem.	Crocco's equation not suitable for problems involving "overshoot."	Probably slower than No. 3 in cases where No. 3 can handle the problem.

Taken from Ref. 47a.

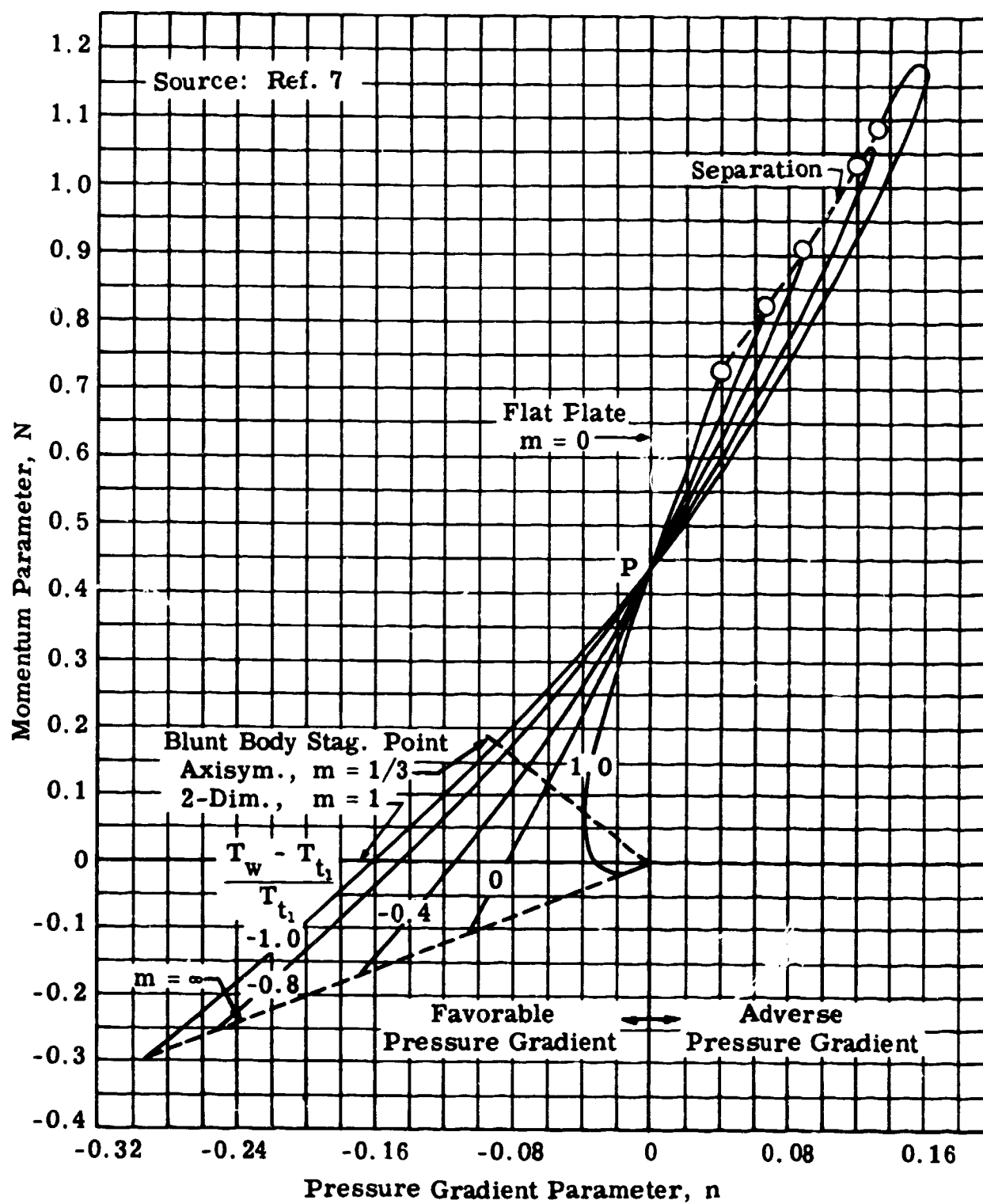
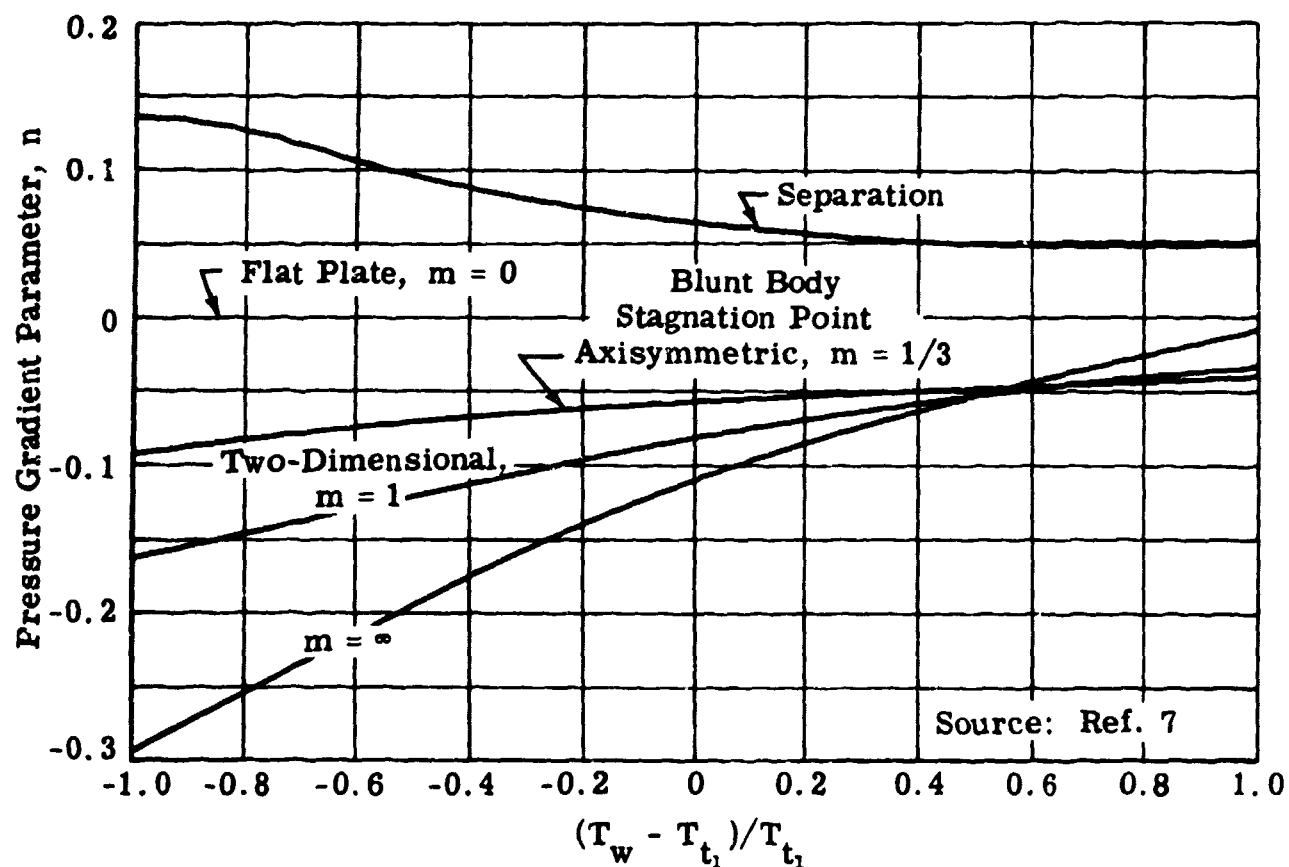
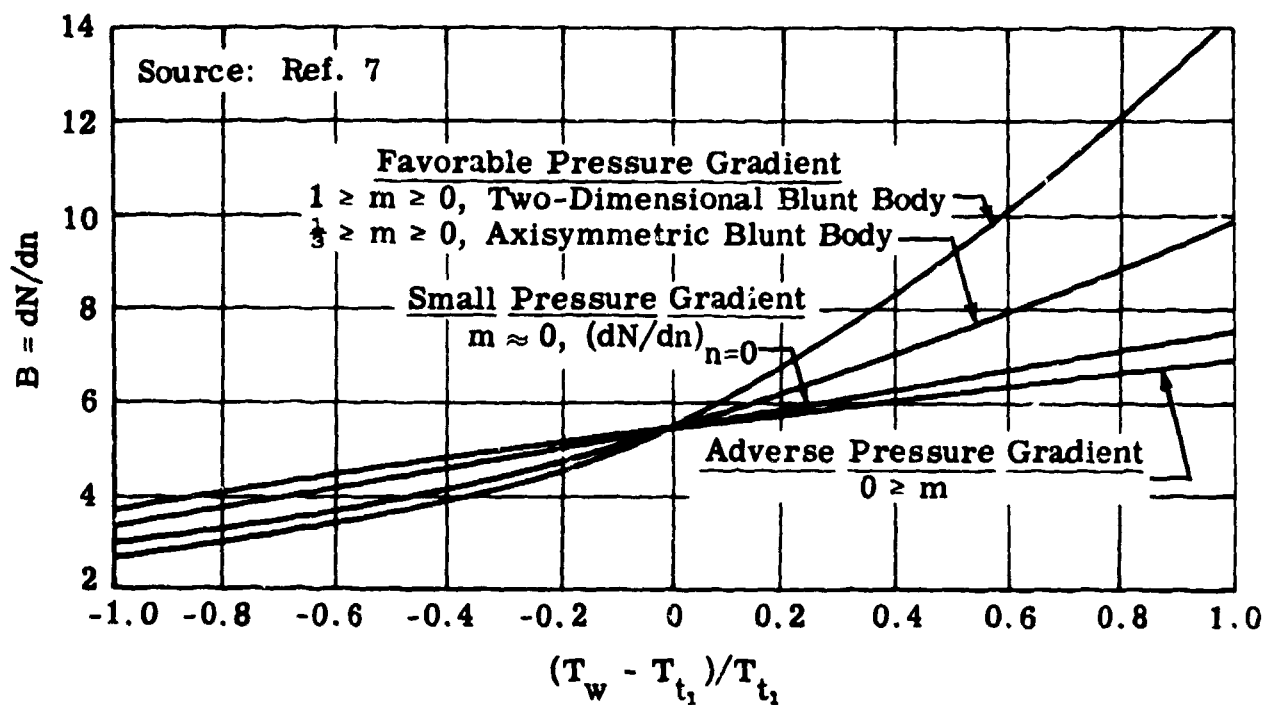


Fig. 4-1. Correlation of the momentum parameter, N , with the pressure gradient parameter, n .

Fig. 4-2. Effect of wall temperature on pressure gradient parameter, n .Fig. 4-3. Effect of wall temperature on value of B ; $B = dN/dn$

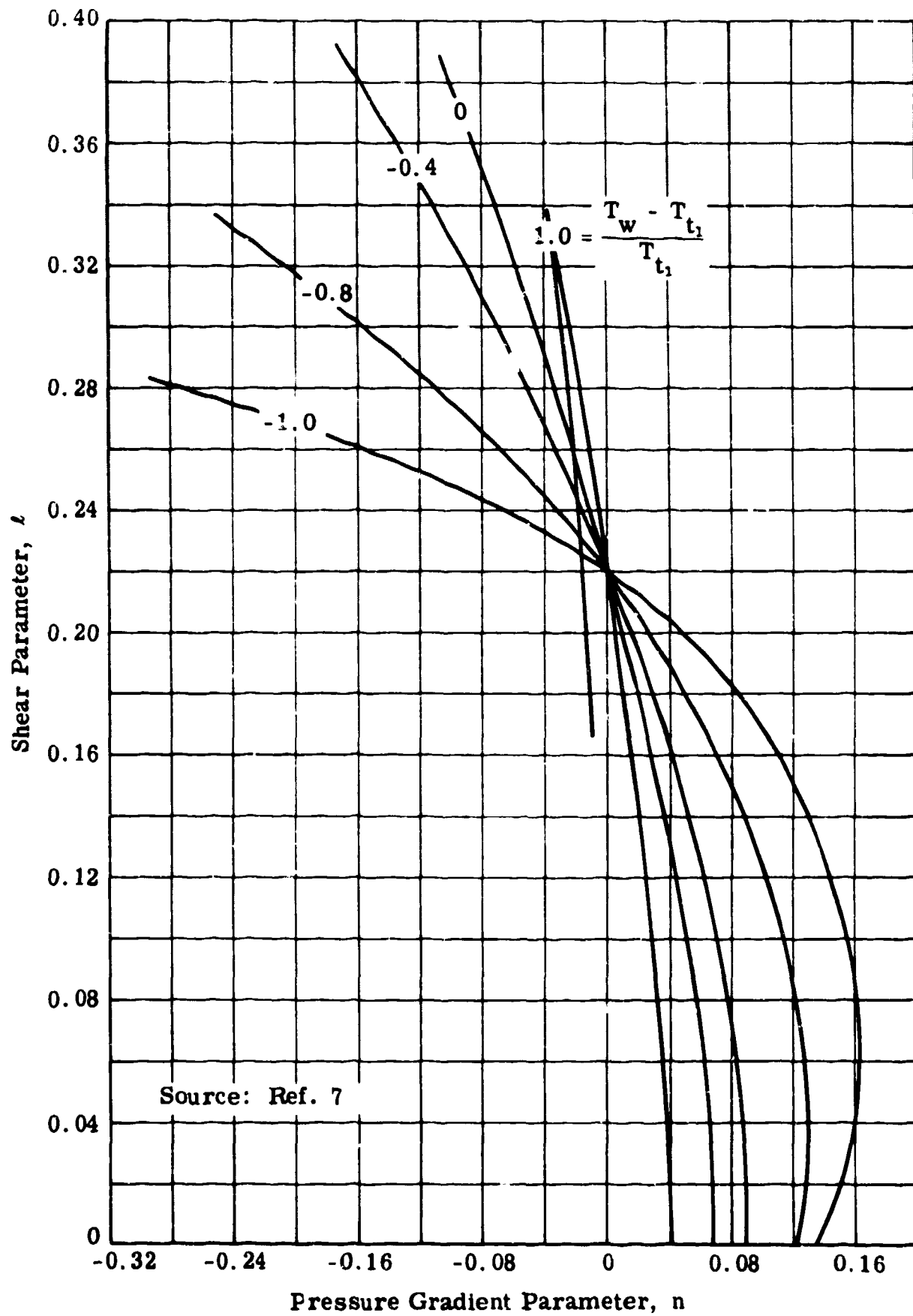


Fig. 4-4. Correlation of the shear parameter, l , and the pressure gradient parameter, n .

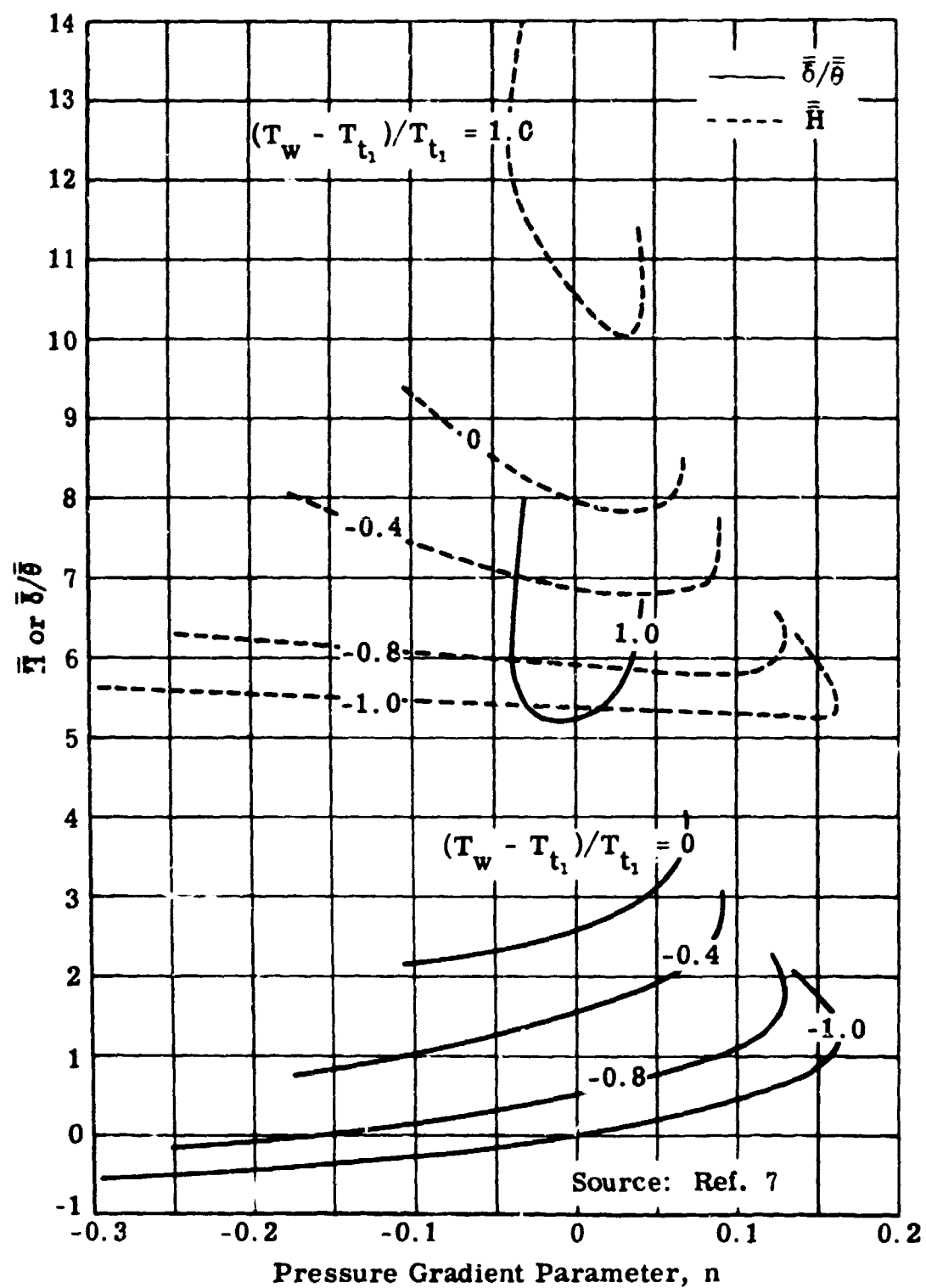


Fig. 4-5. Correlation of \bar{H} or $\bar{\delta}/\bar{\theta}$ and the pressure gradient parameter, n .

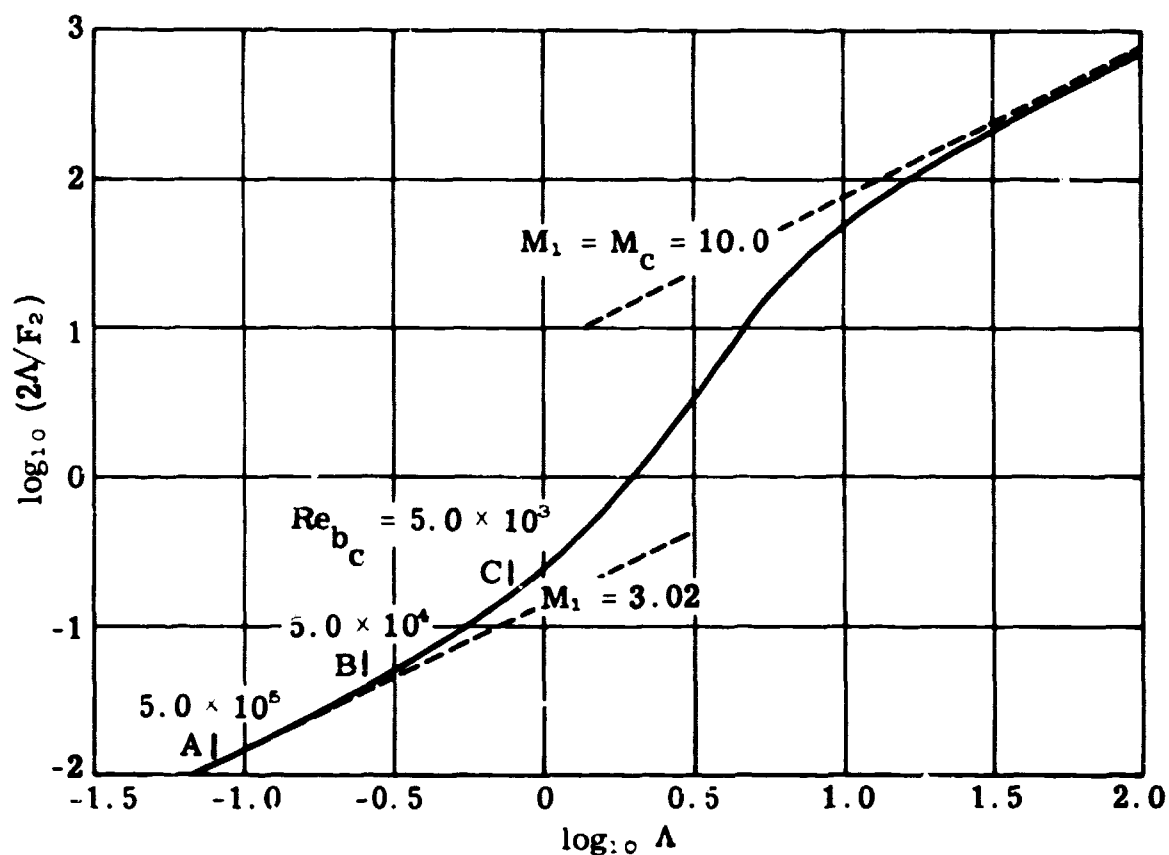


Fig. 4-6. Behavior of integrand in Eq. 4-72; $M_\infty = 14.9$, $M_c = 10.0$; $\sigma = 8^\circ$; $T_w = T_\infty = 530^\circ\text{R}$.

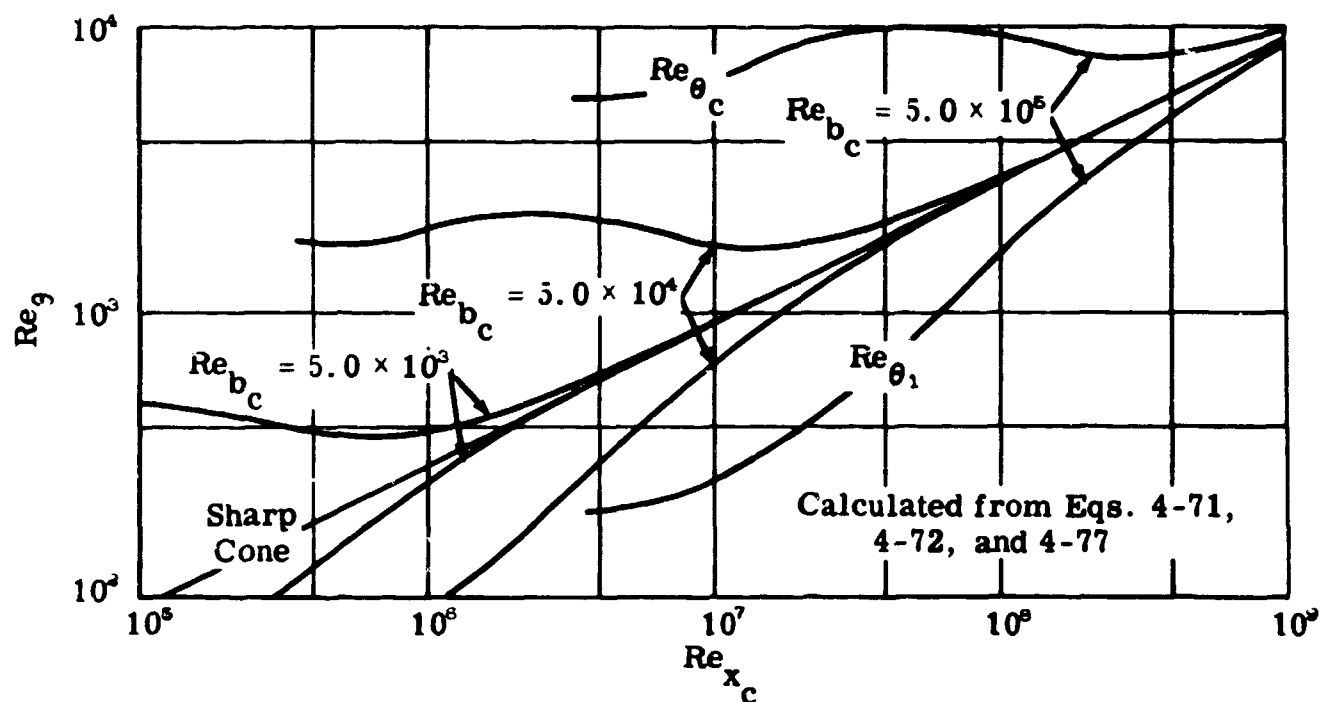


Fig. 4-7. Effect of bluntness on momentum thickness Reynolds number; $M_\infty = 14.9$, $M_c = 10.0$; $\sigma = 8^\circ$; $T_\infty = T_w = 530^\circ\text{R}$.

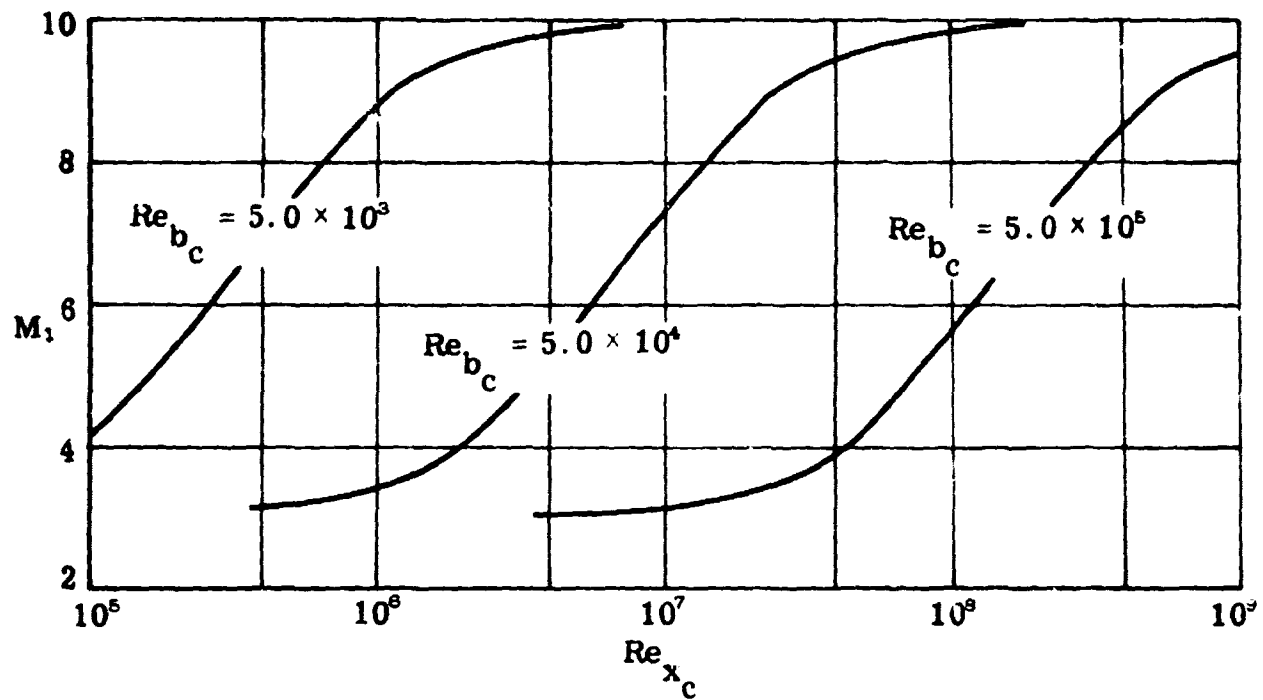


Fig. 4-8. Effect of bluntness on local Mach number; $M_\infty = 14.9$, $M_c = 10.0$; $\sigma = 8^\circ$; $T_\infty = T_w = 530^\circ R$.

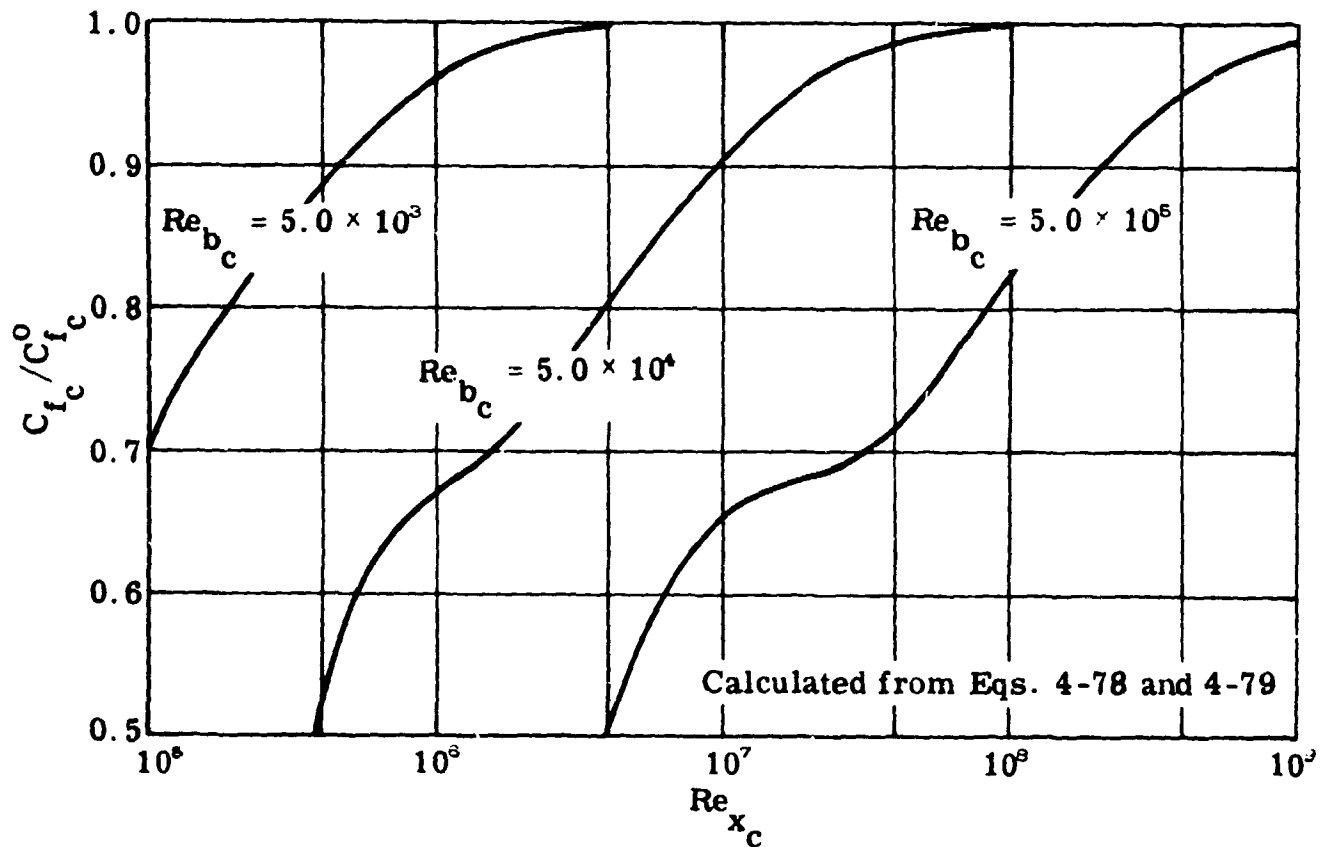


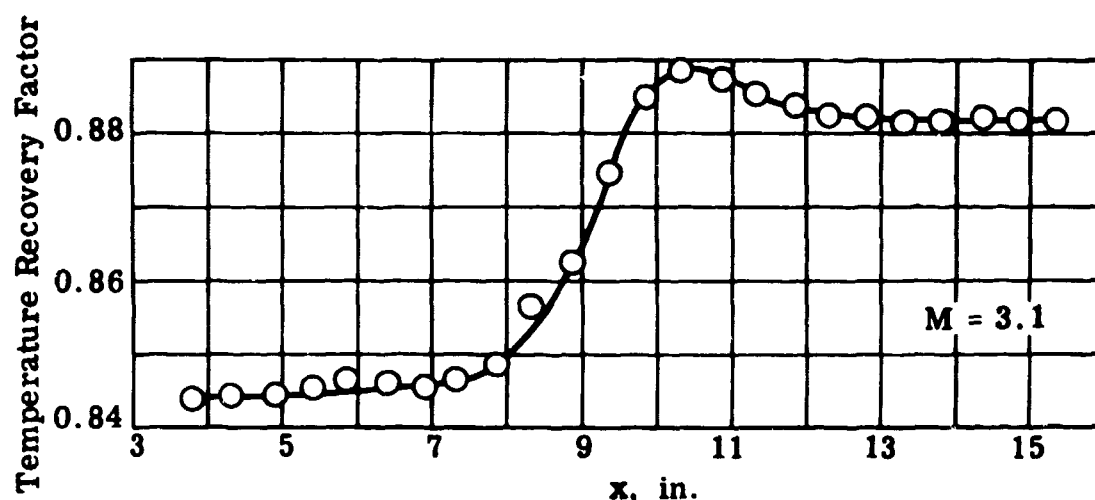
Fig. 4-9. Effect of bluntness on local skin friction coefficient; $M_\infty = 14.9$, $M_c = 10.0$; $\sigma = 8^\circ$; $T_\infty = T_w = 530^\circ R$.

5. Boundary-Layer Transition

Transition from laminar to turbulent flow is of great practical importance because of large changes which occur in the friction drag, heat transfer rate, and flow separation. The stability of the laminar boundary layer in the presence of small disturbances has been investigated theoretically by a number of authors. In spite of the multiplicity of these investigations, it is still impossible to make an accurate prediction of the point at which laminar flow breaks down and a turbulent flow begins, nor is it possible to predict the point at which the turbulence is said to be fully developed.

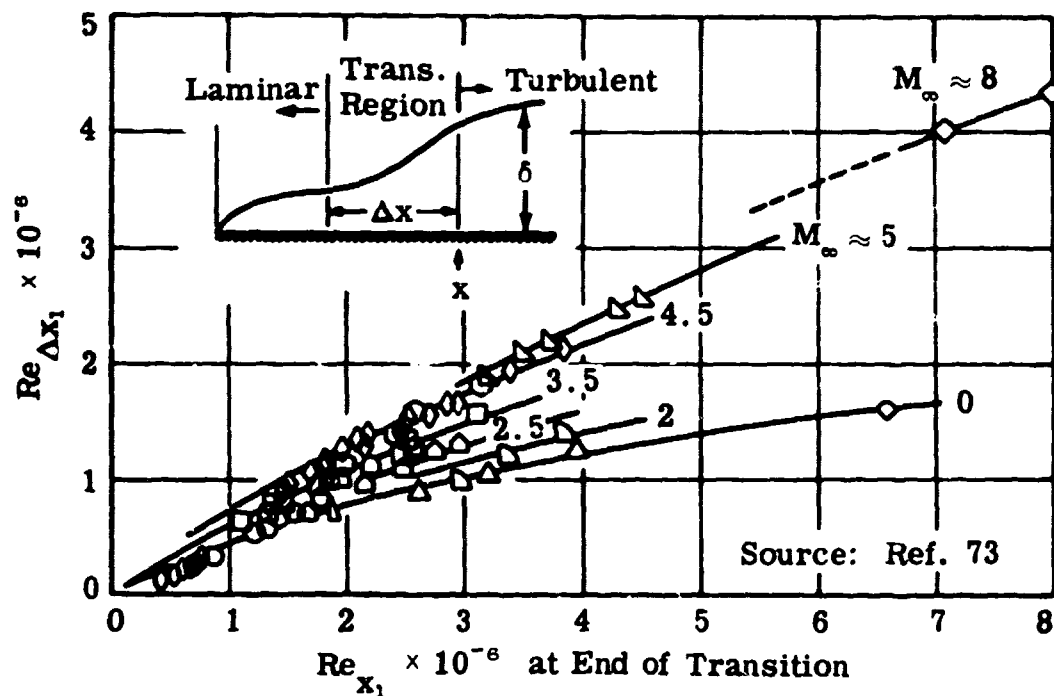
An understanding of the transition process depends heavily on experimental data which, unfortunately, do not form a well-ordered body of information. The ambiguity arises from two principal causes. First, transition depends on a great many parameters including Mach number, surface temperature, pressure gradient, angle of attack, nose bluntness, sweep angle, surface roughness, stream turbulence, and unit Reynolds number. Some of these parameters are interdependent. The second reason for this disparity is associated with the fact that different investigators have limited their measurements to different portions of the transition region.

Transition does not occur abruptly at a well-defined point on any surface but takes place over an extended region. If the flow along a smooth surface is investigated as a function of time, the extent of the laminar region is found to be nearly constant along the surface. However, at some point in the transition region, the flow may change character with time, e.g., the steady laminar motion may become motion in which disturbances with a particular frequency predominate, or it may change to motion in which random bursts of turbulence appear. Farther downstream, the bursts of turbulence will occur more frequently until, at some point, a fully developed turbulent flow exists. The existence of a finite region of transition is demonstrated by the experimental measurements of the temperature recovery factor made by Brinich and Sands (Ref. 72), and is shown in the sketch below. At the onset of transition the recovery factor begins to increase from the lower value associated with laminar



flow. Transition is probably complete when the temperature reaches its peak or perhaps at a point just downstream of the peak temperature. It can be seen

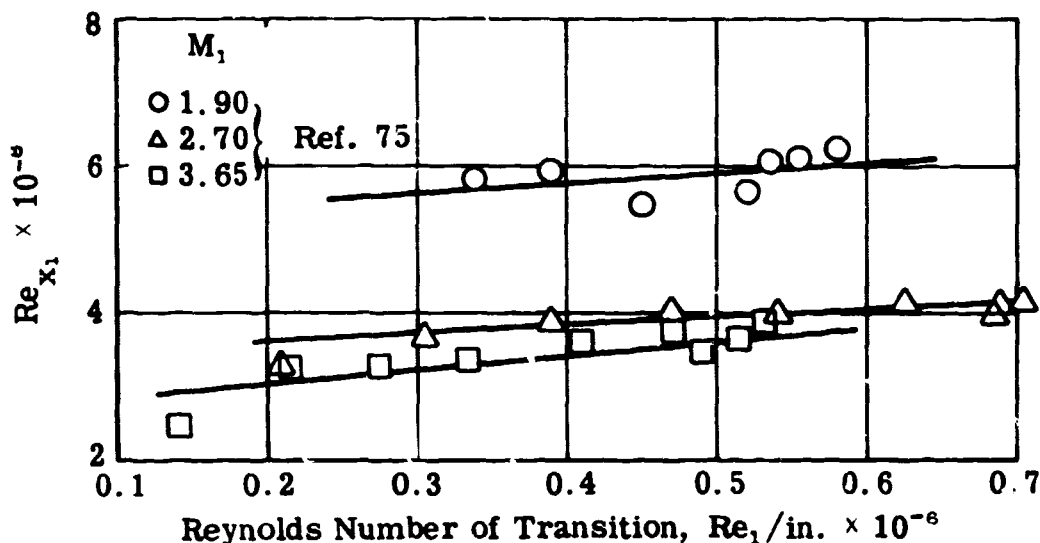
that the transition region is extensive when compared to the laminar region which starts at $x = 0$. It has been shown by Potter and Whitfield (see sketch below) that the Reynolds number based on the length of the transition region, Δx , is greatly affected by both the transition Reynolds number and the Mach number. The Reynolds number of transition should be clearly defined in each instance since it could depend on the properties at the starting point, some mean point, or the end of the transition region.



Many techniques are used to detect the presence of transition. They include the measurement of surface parameters such as the temperature along insulated models or the rate of heat transfer to or from a surface, and the pitot pressure at a small fixed distance from a surface. The local friction drag may be found by means of a floating skin friction balance or the total drag may be determined by means of a balance support arm. Optical techniques such as schlieren and shadowgraph may be used or the sublimation of a surface film may be observed. Hot wire anemometry may also be used. (Details of these techniques may be found in Section 20 of the Handbook, Ref. 74.) Whenever transition data are presented, it will be noted whether the start or the end of transition was measured. Two techniques which are most frequently used are the measurement of the recovery factor (on insulated models) and the use of schlieren or shadowgraph pictures. It appears, from experimental work reported by Potter and Whitfield in Ref. 73, that both the peak recovery factor and also the detectable change in the boundary-layer growth (shown on a schlieren or shadowgraph) occur just upstream of the fully developed turbulent flow. These techniques as well as sublimation methods are assumed to indicate the end of the transition region.

The effects on transition of the various parameters will be discussed in the following subsections. In many cases it is impossible to separate the effects of several parameters. However, it is hoped that the experimental information presented here will give sufficient basis for estimating the transition Reynolds number in many cases of practical interest.

It may be noted that the unit Reynolds number will not be considered as a primary parameter mainly because there is no unambiguous correlation of data from the various facilities. In some cases the unit Reynolds number has little effect, while in other cases the transition Reynolds number increases with unit Reynolds number, and in still other cases the trend is in the opposite direction. However, it is possible to state that in most cases the transition Reynolds number increases with increasing unit Reynolds number. Some typical data given by Van Driest and Boison in Ref. 75 are shown in the sketch below. In flow at Mach numbers of 1.90, 2.70, and 3.65 along a 10 degree cone, the transition Reynolds number increases slightly with the unit Reynolds number as the stagnation pressure is stepped up. The model was insulated and the tunnel turbulence was 0.4%.



5.1 Effects of Mach Number and Surface Cooling

The effects of Mach number and surface cooling are discussed in Subsec. 5.1.1. Subsection 5.1.2 considers surfaces with zero heat transfer since there is a large body of data in this category.

5.1.1 Cooled Surfaces

In an attempt to isolate the effects of Mach number and surface cooling, data have been collected for flow over smooth sharp models, including cones near zero angle of attack, plates and hollow cylinders, and in one case a body with a variable surface pressure.

Figure 5-1 presents transition data for cones obtained from wind tunnels (Refs. 75 and 76), ballistics ranges (Refs. 77, 78, and 79), and free-flight tests (Ref. 80). The Reynolds numbers are all based on conditions at the outer edge of the boundary layer (subscript 1) and the characteristic distance is measured along the surface. At the higher wall temperature ratios, the wind-tunnel data (open symbols) show that for constant T_w/T_{e_1} , the transition Reynolds number decreases with increasing Mach number, at least for Mach numbers up to 3.7. It will be shown later that this trend is substantiated by additional data for $T_w/T_{e_1} = 1.0$, but that the trend is reversed at higher

Mach numbers. The data given by Van Driest and Boison (Ref. 75) should serve as a standard for wind-tunnel results since they were obtained in a tunnel with highly uniform flow and a known low level of turbulence. The difference between the $M_1 = 3.0$ data from Jack, et al (Ref. 76) and the $M_1 = 2.7$ data from Ref. 75 may be due to the fact that the Reynolds number of one set is based on the start of transition and the other on the end. At the higher temperature ratios, a decrease in the wall temperature results in a marked increase in the transition Reynolds number. For the experiments at $M_1 = 3.0$, the temperature was decreased until the flow over the cone was completely laminar. This situation existed until the temperature ratio was decreased to about 0.25, at which time transition was once more observed near the end of the cone. With a further decrease in the temperature, the transition moved forward along the cone. There has been no satisfactory explanation for this phenomenon. However, there is some speculation that it might be caused by the increased roughness due to cooling but this seems unlikely.

The ballistics range data (solid symbols) were obtained at angles of attack of less than one degree. The purpose of the experiments of Lyons and Sheetz (Ref. 77) was to investigate this transition reversal. In the neighborhood of $T_w/T_{e_1} = 0.25$ the range and wind-tunnel data at $M_1 = 3.0$ are in remarkable agreement. For the range data at $M_1 = 4.5$, given by Sheetz in Ref. 78, the transition reversal takes place at a lower T_w/T_{e_1} and transition moves forward until a temperature ratio of about 0.13 is reached. At this point a second reversal takes place and transition moves aft once more. This occurrence of a second reversal should definitely exclude roughness as the cause of the first. It will be shown later that flat plate data also exhibit a second reversal. Witt (Ref. 79) gives one test point from a ballistics range at $M_1 = 3.0$, where the flow was completely laminar at a Reynolds number of 21.6×10^6 and $T_w/T_{e_1} = 0.42$. The data of Refs. 76 and 77 indicate that high transition Reynolds numbers can occur at such a temperature ratio.

The individual points for $M_1 = 1.6$ to 3.4 from the free-flight data (half-closed symbols) given by Rumsey and Lee (Ref. 80) are in the same Reynolds number range as the wind-tunnel tests. However, their free-flight data at $M_1 = 3.7$ appear high with respect to those of the wind tunnel. It should be noted that the free-flight data points are obtained in the order of increasing wall temperature. The symbols with arrows pointing down indicate that the flow was turbulent at the measuring station. Later in time, the flow near the tip became laminar with transition moving aft as the wall became warmer. Reference 80 shows that still later the flow again became fully turbulent. This may be due to some unknown variation in the angle of attack with time, in which case the four $M_1 = 3.7$ transition points could be on the windward side and thus be higher than they would be at zero angle of attack (see Subsec. 5.2).

It may be concluded that the data on Fig. 5-1 are reasonably consistent. As cooling begins, transition Reynolds numbers increase until quite high values are obtained. The maximum transition Reynolds number which can be reached has not been established as yet. However, as cooling continues, the transition reverses and quite low values can be obtained.

Figure 5-2 presents data for flat plates and hollow cylinders. The Mach number effect in this case is not as well defined as for the cones. Wind-tunnel data of Brinich (Ref. 81) at $M_1 = 5$, and of Deem and Murphy (Ref. 82) at $M_1 = 10.2$, show essentially no effect of wall temperature. This is not in agreement with the cone data, nor is it in agreement with the flat-plate gun-tunnel data taken by Richards and Stollery (Ref. 83) at $M_1 = 8.2$. The gas in the gun tunnel is pressurized in a shock tube, released by a gun-operated piston and expanded through a nozzle which produces uniform flow. The data of Ref. 83 can therefore be compared with wind-tunnel data. It is interesting to note that these data exhibit the double reversal found for the cone data. Three points obtained on gun-launched hollow cylinders have been taken from Ref. 84 by James. The two points at $M_1 = 3.9$ and the point at $M_1 = 7.0$ may lie on one of the very steep lines which occur during reversals.

Results from Refs. 85 and 86 for a body with variable surface pressure are shown on Fig. 5-3. In this case the data are based on conditions in the free stream rather than just outside the boundary layer. The points indicate the maximum Reynolds number at which the boundary layer was completely laminar over the entire model. It will be noted that here the transition is very sensitive to surface cooling. These data at $M_\infty = 1.61$ are consistent with the cone data from Ref. 75 plotted on Fig. 5-1. The cone data at the lowest Mach number ($M_1 = 1.9$) have a slope only slightly less than that of the data on Fig. 5-3.

5.1.2 Insulated Surfaces

Figures 5-4, 5-5, and 5-6 show how the transition Reynolds number on smooth sharp models with zero heat transfer is affected by Mach number. The data are all from wind-tunnel tests.

Figure 5-4 presents data for cones at zero angle of attack. It will be noted that the data from Refs. 72, 75, 87, and 88 are in quite good agreement. It was pointed out previously that the data from Ref. 75 were taken in a wind tunnel with smooth, uniform flow and a turbulence level known to be low. The Re_{tr} from Refs. 89 and 90 appears to be low in comparison with that of Ref. 75. This may be due in part to flow irregularities and high turbulence levels. Furthermore, the unit Reynolds number used in Ref. 90 was based on the properties of the flow at a point near the start of transition. The over-all conclusion that may be drawn from this figure is that the transition Reynolds number decreases with increasing Mach number, at least up to Mach numbers of about four.

Figure 5-5 presents data for flat plates and hollow cylinders. In this category, data are available at both high and low Mach numbers. Although the data do not really present a consistent quantitative picture, there appear to be two distinctive trends. At Mach numbers below about four, the transition Reynolds number decreases with Mach number; at the higher Mach numbers, the trend is reversed.

Limited data for bodies with variable surface pressure are given on Fig. 5-6. Each point indicates the maximum unit Reynolds number at which the flow was laminar over the entire model. The points for the three bodies, A, B, and C, at $M_\infty = 1.6$ are in the expected order. The cone-cylinder body,

A, has an adverse pressure gradient aft of the shoulder and has the lowest transition Reynolds number. The ogive-cylinder, B, has a slight adverse pressure gradient aft of the ogive and is next. The third, C, is an NACA RM-10 body and has a favorable pressure gradient for the first 80% of its length. It has by far the highest transition Reynolds number. Each of these three bodies had some adverse pressure gradient. It is possible to determine the increase in pressure coefficient which occurred on each before transition took place. This increase, termed the critical pressure rise coefficient, is compared in Subsec. 5.2 with subsonic data and with data obtained on supersonic bodies at angles of attack. At $M_\infty = 3.1$, the data points for the other two bodies, D and E, are in the expected order. Both models D and E have approximately constant favorable pressure gradients over the greater part of the bodies. Model D has a change in pressure coefficient, $\Delta C_p = (p_1 - p_\infty) / \frac{1}{2} \rho_\infty u_\infty^2$, of about 0.12 from tip to base, which is about the same as for the RM-10 body, C, tested at $M_\infty = 1.6$. Model E has about twice the change in pressure coefficient, i.e., $\Delta C_p = 0.24$. The transition points for C and D exhibit the expected trend with Mach number.

5.2 Effect of Body Angle of Attack

From a study of the bodies shown on Fig. 5-6, it was found that transition at supersonic speeds is sensitive to the pressure gradient. This general observation is consistent with subsonic experience. Since adverse pressure gradients promote early transition, the onset of transition should move forward on the sheltered side of slender bodies as the angle of attack increases. Data from Witt (Ref. 79) and Jedlicka, et al (Ref. 97) plotted on Fig. 5-7, demonstrate this effect. Although the transition on both the cone and the slender ogive-cylinder is extremely sensitive to angle of attack, that on the cone is the more sensitive. This may be expected since the cone pressure at zero angle of attack is constant, and at small angles of attack each streamline within any meridian plane from the tip to the base will be subject to an adverse pressure gradient. On the other hand at zero angle of attack, the ogive-cylinder has a favorable pressure gradient on the nose, which will remain favorable for small angles of attack and thus assist in stabilizing the boundary layer. Although adverse pressure gradients aft of the nose promote transition, the nose gradients should counteract this effect to some extent and reduce the sensitivity to angles of attack.

The authors of Ref. 97 have calculated the patterns of the streamlines and the pressure distributions along them near the surface of the ogive cylinder at angles of attack of 1, 2, and 3 degrees. At several stations along the body the streamline was found which had the maximum pressure difference from the minimum upstream pressure on the same streamline. When transition occurred at a particular station, the pressure coefficient associated with the maximum pressure rise, $\Delta p / \frac{1}{2} \rho_\infty u_\infty^2$, was termed the critical pressure rise coefficient. A correlation of this coefficient with the transition Reynolds number assumes that transition is caused by local laminar separation. The results obtained from analyzing the angle of attack data at $M_\infty = 3.5$ are compared with subsonic data on Fig. 5-8. In addition, the pressure rise from the minimum pressure point to the base has been computed for each of the three bodies tested at $M_\infty = 1.6$ and these values are also shown on Fig. 5-8. Additional supersonic data, with and without heat transfer, are needed to substantiate the scanty supersonic data in Fig. 5-8 since the $M_\infty = 1.6$ data and that at $M_\infty = 3.5$ show

considerable difference in the sensitivity of the transition Reynolds number to the pressure rise.

5.3 Effect of Bluntness

A number of investigators have found that the transition Reynolds number is quite sensitive to the relative bluntness of the body tip or of the leading edge. Despite the fact that this effect is known to be significant, few data are available for blunted models with heat transfer. Limited data presented by Brinich (Ref. 81) for hollow cylinders at $M_\infty = 5$ are shown on Fig. 5-9. The data are based on free-stream conditions since local conditions at the outer edge of the boundary layer along the surface vary with the bluntness (see Subsec. 4.6). The data for the sharp cylinder are also shown on Fig. 5-2 and were discussed in Subsec. 5.1.1, where it was pointed out that these data do not exhibit the more general effect of wall cooling. It is interesting to note that the blunted cylinder data on Fig. 5-9 follow the general trend and show increasing transition Reynolds number with decreasing wall temperature. It can be seen that even a slight blunting causes a large increase in the transition Reynolds number based on free-stream conditions. Several effects are involved. First, there is a decrease in the local unit Reynolds number as a result of the flow having passed through the bow shock. If the transition Reynolds number based on local conditions were constant, blunting the tip would cause an aft movement of transition. Secondly, nose blunting lowers the local Mach number which, depending on the Mach number range, might increase or decrease the transition Reynolds number. Finally, the bluntness produces pressure gradients which might have an appreciable effect on transition aft of the tip or the leading edge.

Figure 5-10 presents the effect of leading-edge bluntness and Mach number on the transition Reynolds number for smooth flat plates and hollow cylinders with zero heat transfer. The data, taken from Refs. 72, 73, 82, and 92, are in good agreement. As the bluntness increases, the transition Reynolds number increases steadily at first and then appears to remain constant as might be expected. For small bluntness, the local conditions change continuously as the entropy layer, due to the curved bow shock, is swallowed by the boundary layer (see sketch on p. 98). As the bluntness increases, less and less of the entropy layer is swallowed before transition takes place. When the bluntness exceeds some critical value, transition will always occur close enough to the leading edge that the local conditions are those of the flow through the normal part of the bow shock. The onset of transition might then be expected to remain fixed. However, at still larger bluntnesses, the adverse pressure gradient which occurs just aft of the tip may cause a forward movement of transition. This may explain the behavior (see Fig. 5-10) of the data at $M_\infty = 2.0$ as the bluntness increases beyond the critical value.

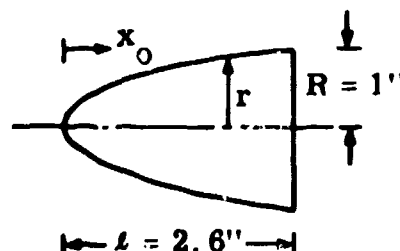
Brinich and Sands (Ref. 72) covered a wide range of unit Reynolds numbers in their investigations of flat as well as semicircular leading edges. A few of their results are given on Fig. 5-11 in which it may be noted that some of the transition Reynolds numbers for the flat leading edge at $M_\infty = 3.1$ exhibit the same characteristics as those of the semicircular leading edge at $M_\infty = 2.0$ which are shown on Fig. 5-10. Increasing the leading edge thickness displaces the transition point downstream, but beyond a critical thickness the trend is reversed.

Figure 5-12 shows limited data of the effect which changing the tip radius of conical bodies has on the transition Reynolds number. These data are not as consistent as those of the flat plate and hollow cylinder shown on Fig. 5-10. However, it is interesting to note that the data obtained by Czarnecki and Jackson (Ref. 98), for large bluntness, show decreasing transition Reynolds numbers with increasing bluntness. Brinich and Sands in Ref. 72 give results for flat as well as rounded tips over a wide range of unit Reynolds numbers. These results are given on Fig. 5-13. The authors investigated many other tip configurations such as blunt cones, rounded flats, spikes, cylindrical extensions, as well as step changes in the body diameter.

5.4 Transition Reynolds Number Based on Momentum Thickness

In calculating boundary-layer growth over bodies with variable surface pressure and temperature, it is necessary to specify values of the Reynolds number, Re_{θ_1} , using the momentum thickness and the local flow properties at transition. For the sharp cone, flat plate, and hollow cylinder data given so far, it is a simple matter to compute values of Re_{θ_1} from the values of Re_{x_1} at transition. It is also possible to calculate the laminar boundary-layer growth over blunted bodies and bodies with pressure gradients to determine values of Re_{θ_1} at the transition point. The authors of Ref. 98, using this method to get Re_{θ_1} at transition, have analyzed zero heat transfer experimental results for sharp and blunted cones at four Mach numbers and three cone angles. The cone blunting was accomplished by means of spherical, hyperbolic, and parabolic tips. Their results are presented on Fig. 5-14 where the values of Re_{θ_1} are plotted as a function of the local unit Reynolds number. Transition in all cases occurred downstream of the nose section so that the local Mach number can be estimated from the ratio of the stagnation pressure and the static pressure on a sharp cone. The stagnation pressure is taken to be that behind the normal-shock portion of the bow wave. The tip radius in each case is assumed to be large enough to ensure that transition occurs before the swallowing of the variable entropy layer begins. It will be noted from Fig. 5-14 that neither the unit Reynolds number nor the nose radius has, in general, a marked effect upon the transition Reynolds number. This is to be expected since the bluntness Reynolds number which is a product of the nose radius and the unit Reynolds number is shown in Fig. 5-10 to have little effect on Re_{t_1} . The nose radius and unit Reynolds number have the most significant effects when the Mach number is low and the nose radius is large. The effect of very large radii is evidenced up to a Mach number as high as 2.2 (see the third part of Fig. 5-14). In most of the cases investigated in Ref. 98, the value of Re_{θ_1} at the end of transition lies between 900 and 1100.

Witt and Persh (Ref. 99) conducted tests on blunted cones and power bodies described by $r/R = (x_0/\ell)^n$ (see following sketch) on a ballistics range. Their results are presented in Fig. 5-15. Transition on the cones always occurred after the blunted tip, i.e., on the conical section where the pressure gradient may be taken to be zero. However, transition on the power bodies always occurred where the pressure gradient was still favorable. Witt and



Persh, therefore, plotted Re_{θ_1} at the end of transition as a function of the local velocity (or pressure) gradient parameter, $Re_{\theta_1} \frac{\theta}{u_1} \frac{du_1}{dx}$, to detect any effect of pressure gradient. Over the range of test Mach numbers ($M_1 = 1.5$ to 2.2), the value of Re_{θ_1} varied from 315 to 750. There seems to be little correlation with pressure gradient. These tests also showed very little correlation between Re_{θ_1} and any of the other parameters, M_∞ , M_1 , and T_w/T_{e_1} (see Ref. 87). The maximum transition Re_{θ_1} on the cones, 750, is less than the maximum cone value reported by Czarnecki and Jackson in Ref. 98 and shown on Fig. 5-14.

Buglia (Ref. 100) analyzes free-flight data on a cone ($2\sigma = 29^\circ$) with a rounded tip at free-stream Mach numbers of 2.3 to 3.1. These data were obtained at high heating rates and are therefore comparable to those for the ballistics-range tests. Values of Re_{θ_1} , measured along the cone at the beginning of transition, were found to be about 2000, whereas when transition occurred on the rounded tip, Re_{θ_1} varied from about 1300 to 800.

5.5 Effect of Sweep

Dunning and Ulmann in Ref. 101 present photographs of transition on swept wings in supersonic flow. The luminescent lacquer technique was used to reveal the fact that transition always occurred along a front parallel to the leading edge, making it unnecessary to measure transition at more than one spanwise station in order to determine the effect of sweep angle. In Ref. 102, Chapman analyzed data from tests at $M_\infty = 3$ and 4; his results are shown on Fig. 5-16. The Mach 8 data of Deem and Murphy (Ref. 82) have been added to this figure. It can be seen that as the sweep angle increases, the distance from the leading edge to transition (measured in the streamwise direction) is greatly reduced. Blunting the leading edge augments this effect.

5.6 Effect of Roughness

Transition data on smooth models were presented in Subsecs. 5.1 to 5.5. When it was known, the surface roughness was given for each model since roughness can greatly reduce the transition Reynolds number. Even on a highly polished surface, a certain random roughness remains. The data given were usually in terms of a root-mean-square roughness and were obtained with a profilometer. In this subsection the discussion is limited to those tests in which the roughness size was controlled. The size will be given in terms of the actual height, k , of either a three-dimensional or two-dimensional roughness element. Since three-dimensional elements have the greater effect on transition, they will be treated in more detail.

5.6.1 Minimum Transition Reynolds Number: Three-Dimensional Roughness

Consider the effect of three-dimensional roughness elements located at a particular station along a surface. Let the station be upstream of the natural transition point. Elements which are less than a critical size will not affect the location of transition. However, increasing the element size beyond the critical value will cause transition to move forward. This effect will continue until a second critical size is reached, beyond which the forward movement will cease, and transition will be stabilized downstream of this element for a wide range of roughness size. This will define the minimum transition Reynolds number for roughness located at that particular station. It has been noted that after the first critical size is reached, a relatively small increase will bring the transition Reynolds number to its minimum value. For a particular station, there are then these two critical roughness sizes: (1) the maximum size which will not affect transition, and (2) the size which will bring the transition Reynolds number to its minimum value.

The roughness associated with the minimum transition Reynolds number will be discussed first. Van Driest and Blumer in Ref. 103 present and analyze an excellent set of data obtained for spherical roughness elements on a cone. For each experiment the roughness elements, with diameter k , were located at one station along the cone. They were spaced at intervals of $4k$ on a single line around the periphery. The wind-tunnel tests were conducted with an insulated model. A typical set of data is reproduced in Fig. 5-17 and will be used to illustrate the test procedure. With elements located at one station, x_k , the unit Reynolds number was varied by changing the supply pressure. This varied the roughness Reynolds number, $Re_{k_1} = \frac{\rho_1 u_1 k}{\mu_1}$, and caused the variation in the transition Reynolds number, $Re_{x_1} = \rho_1 u_1 x / \mu_1$, shown by the data points on Fig. 5-17. The Reynolds number based on the distance from the tip of the cone to the roughness element, $Re_{x_{k_1}} = \rho_1 u_1 x_k / \mu_1$, varied linearly with

Re_{k_1} as shown on Fig. 5-17. What appears to be a variation with Re_{k_1} for the smooth wall is actually a variation with unit Reynolds number. The smooth wall curve in this figure shows an increase in the transition Reynolds number with increasing unit Reynolds number as shown in the sketch on p. 121. The first data point with roughness is the only point which actually falls on the smooth wall curve. This point corresponds to the maximum value of Re_{k_1} which does not affect transition and will be discussed later. Just after the data points depart from the smooth wall curve, they drop rapidly to a minimum Re_{x_1} . The value of $(Re_{x_1} - Re_{x_{k_1}})$ then remains essentially constant as Re_{k_1} increases.

Tests for the same x_k/k , but different x_k and k , give the same results. Except for small values of x_k/k , experimental data at constant Mach number show that $(Re_{x_1} - Re_{x_{k_1}})$ is independent of x_k/k after the minimum transition Reynolds number is reached. The minimum transition Reynolds number will move to a smaller or larger Re_{k_1} as x_k/k is decreased or increased. The data thus show that, for constant Mach number, the minimum transition Reynolds number

for roughness located at x_k can be written

$$Re_{x_1} = Re_{x_{k_1}} + \text{constant} \quad (5-1)$$

The constant may be expressed as a function of the Mach number; thus Eq. 5-1 becomes

$$Re_{x_1} = Re_{x_{k_1}} + f(M_1) \quad (5-2)$$

Van Driest and Blumer then derived an expression for $Re_{x_{k_1}}$ in Eq. 5-2 in terms of Re_{k_1} at the minimum transition Reynolds number. It is assumed that the roughness Reynolds number required to bring the transition Reynolds number to its minimum value is a constant, i.e.,

$$\frac{\rho u_k k}{\mu} = \text{constant} \quad (5-3)$$

where u_k is the velocity in the boundary layer at the top of the roughness element. The density, ρ , and the viscosity, μ , are associated with some points, not yet specified. Assume that the roughness element is contained within that portion of the boundary layer characterized by a linear velocity profile. Then

$$u_k = k \left(\frac{du}{dy} \right)_w = \frac{\tau_w k}{\mu_w} = \frac{\frac{1}{2} \rho_1 u_1^2 C_f k}{\mu_w} \quad (5-4)$$

Now, from Eq. 3-8 and Mangler's results for a cone

$$C_f (Re_{x_{k_1}})^{\frac{1}{2}} = 1.15 \left(\frac{\rho' \mu'}{\rho_1 \mu_1} \right)^{\frac{1}{2}} \quad (5-5)$$

From Eqs. 5-3, 5-4, and 5-5 one obtains

$$\frac{\rho}{\rho_1} \frac{\mu_1^2}{\mu \mu_w} \left(\frac{\rho' \mu'}{\rho_1 \mu_1} \right)^{\frac{1}{2}} (Re_{k_1})^2 (Re_{x_{k_1}})^{-\frac{1}{2}} = \text{constant} \quad (5-6)$$

When it was assumed that $Pr = 1$ and $\rho\mu = \text{constant}$, the experimental variation with Mach number could be matched to that derived from Eq. 5-6 by evaluating ρ at the outer edge of the boundary layer and μ at the wall. Equation 5-6 then becomes

$$Re_{k_1} = \text{constant} \left(1 + \frac{\gamma - 1}{2} M_1^2 \right) Re_{x_{k_1}}^{1/4} \quad (5-7)$$

By fitting the data on a cone at $M_1 = 2.71$ to Eq. 5-7, the constant was determined to be 32.8. This constant was found to hold for the data at $M_1 = 1.90$

and $M_1 = 3.67$. The excellent agreement between Eq. 5-7 and the data is shown on Fig. 5-18.

From Mangler's results, the equation for a flat plate is given by multiplying the constant in the cone equation by $3^{\frac{1}{2}}$. Thus for the flat plate

$$Re_{k_1} = 43.2 \left(1 + \frac{\gamma - 1}{2} M_1^2 \right) Re_{x_{k_1}}^{1/2} \quad (5-8)$$

The constant in Eq. 5-3 may now be evaluated by putting $\rho = \rho_1$ and $\mu = \mu_w$, taking $\rho\mu = \text{constant}$ and $Pr = 1$. Using Eqs. 5-4, 5-5, and 5-7 one obtains

$$\frac{\rho_1 u_k k}{\mu_w} = 619 \quad (5-9)$$

For some unknown reason, this differs slightly from the value of 588 given in Ref. 103, i.e., the roughness Reynolds number for a minimum Re_{tr} is ~ 600 .

In order to facilitate the comparison of flat plate and conical data, Van Driest and Blumer derived an expression for the Reynolds number of the displacement thickness, $Re_{\delta_1^*}$, in terms of the Reynolds number of the local length, Re_{x_1} . For a flat plate with zero heat transfer,

$$Re_{\delta_1^*} = 1.73 \left(1 + \frac{\gamma - 1}{2} M_1^2 \right) Re_{x_1}^{1/2} \quad (5-10)$$

This equation and the data of Ref. 103 agree within 5% for $0 \leq M_1 \leq 5$. A combination of Eqs. 5-8 and 5-10 yields

$$Re_{\delta_1^*} = 1025 \left(1 + \frac{\gamma - 1}{2} M_1^2 \right) (k/\delta^*)^{-2} \quad (5-11)$$

Equation 5-11 applies to any flow with zero pressure gradient as is demonstrated by Fig. 5-19.

By means of Eq. 5-7 or 5-8, the transition Reynolds number, Re_{tr} , for cones or for flat plates can now be calculated from Eq. 5-2 if $f(M_1)$ is given. The data presented on Fig. 5-20 show that $f(M_1)$ is constant and equal to 0.5×10^6 when $M_1 = 2.71$. In the region where $x_k/k \leq 200$, the roughness element emerges from the linear portion of the boundary layer and thus $f(M_1)$ is no longer constant since one of the basic assumptions (Eq. 5-4) of the theory has been violated. Ignoring the region where (x_k/k) is small, this technique can be applied to each set of data to obtain a unique value of $f(M_1)$ for each value of M_1 . Figure 5-21 shows a curve of $f(M_1)$ vs M_1 for several sets of comparable data covering Mach numbers from 0 to 6.

It should be emphasized that all of the above data apply to the case of zero heat transfer and zero pressure gradient. An investigation of the effects

of various wall temperatures and pressure gradients is needed to extend these results.

5.6.2 Maximum Three-Dimensional Roughness not Initiating Transition

In the preceding discussion, a constant value of a roughness Reynolds number defined as $\rho_1 u_k k / \mu_w$, was used to correlate the data for a minimum Re_{tr} . A similar Reynolds number has not yet been found to correlate the onset of transition with the three-dimensional roughness size. The limited data available will be presented in terms of a critical roughness Reynolds number, defined as

$$Re_{ktr} = \frac{\rho_k u_k k}{\mu_k} \quad (5-12)$$

where subscript k denotes the flow properties at the top of a roughness element of height k. The term critical is applied to Re_{ktr} to denote the value at which transition is first affected by the roughness. Before presenting the data, expressions for calculating values of Re_{k_1} from given values of Re_{ktr} will be derived for surfaces with a zero pressure gradient. Equation 5-12 may be written as

$$Re_{ktr} = \frac{T_1}{T_k} \frac{\mu_1}{\mu_k} \frac{u_k}{u_1} Re_{k_1} \quad (5-13)$$

Assuming, as before, that the roughness element is submerged in that portion of the boundary layer in which the velocity profile is linear

$$\frac{u_k}{u_1} = \frac{\mu_1}{\mu_w} \frac{C_f}{2} Re_{k_1} \quad (5-14)$$

where $C_f = \tau_w / \frac{1}{2} \rho_1 u_1^2$. Equations 5-13 and 5-14 yield

$$\frac{C_f}{2} Re_{ktr} = \frac{T_1}{T_k} \frac{\mu_1}{\mu_k} \frac{\mu_1}{\mu_w} \left(\frac{C_f}{2} Re_{k_1} \right)^2 \quad (5-15)$$

The ratio T_k/T_1 may be approximated by using the temperature distribution when $Pr = 1$, i.e., Eq. 3-10 may be expressed as

$$\frac{T_k}{T_1} = \frac{T_w}{T_1} - \left(\frac{T_w}{T_1} - 1 \right) \frac{u_k}{u_1} - \frac{\gamma - 1}{2} M_1^2 \left[\left(\frac{u_k}{u_1} \right)^2 - \frac{u_k}{u_1} \right] \quad (5-16)$$

Incorporating Sutherland's viscosity law, Eqs. 5-14, 5-15, and 5-16 have been used to compute $(C_f/2) Re_{k_1}$ as a function of $(C_f/2) Re_{ktr}$ and the results are plotted in Fig. 5-22. For given values of Re_{ktr} and C_f , these curves or the

above equations can be used to compute Re_{k_1} and finally to determine the roughness size. Although the expressions were derived for flows with zero pressure gradient, they should give a good approximation when there is a small pressure gradient if the appropriate values of C_f are used, i.e., those associated with the local flow properties.

It was noted in Subsec. 5.6.1 that the first data point on Fig. 5-17 gives the minimum value of Re_{k_1} associated with transition. Several such values of Re_{k_1} were read from the graphs of Ref. 103 and used to calculate the critical roughness Reynolds numbers. The results, which are shown on Fig. 5-23, are plotted in terms of $Re_{ktr}^{1/2}$ so as to be compatible with the results of Braslow and Knox (Ref. 106). The latter data, also shown on Fig. 5-23, were obtained by use of a hot wire anemometer mounted near the model surface slightly downstream of the roughness element. As the unit Reynolds number of the test was increased, the bursts of turbulence indicated when the critical value of Re_{ktr} had been reached. It may be noted that any effect of moderate cooling is masked by the scatter of the data. The supersonic Re_{ktr} are, in general, well below the constant subsonic value.

Lyons and Levensteins (Ref. 107) give an extensive set of graphs for calculating roughness sizes. The boundary-layer profiles that they used include a pressure gradient parameter. From an examination of available data they conclude that a representative value of Re_{ktr} is 700. The data of Refs. 103 and 106 indicate that this value of Re_{ktr} may be too high.

5.6.3 Two-Dimensional Roughness

The investigations of Van Driest and Boison (Ref. 75) included transition caused by a single trip wire on a sharp cone. These results are shown on Fig. 5-24 for three Mach numbers and several wall temperature ratios. The transition Reynolds number, Re_{x_1} , has been normalized by the use of $(Re_{x_1})_0$, the transition Reynolds number in the absence of the trip wire. Values of $(Re_{x_1})_0$ are those from Ref. 75, plotted on Fig. 5-1. It can be seen from Fig. 5-24 that, in terms of k/δ_k^* , the trip-wire effect decreases with increasing Mach number and decreases more rapidly with wall cooling. However, it should be remembered that the ratio of δ^* to the total boundary-layer thickness, δ , increases rapidly with Mach number. The curves would look quite different if k/δ_k were plotted on the abscissa.

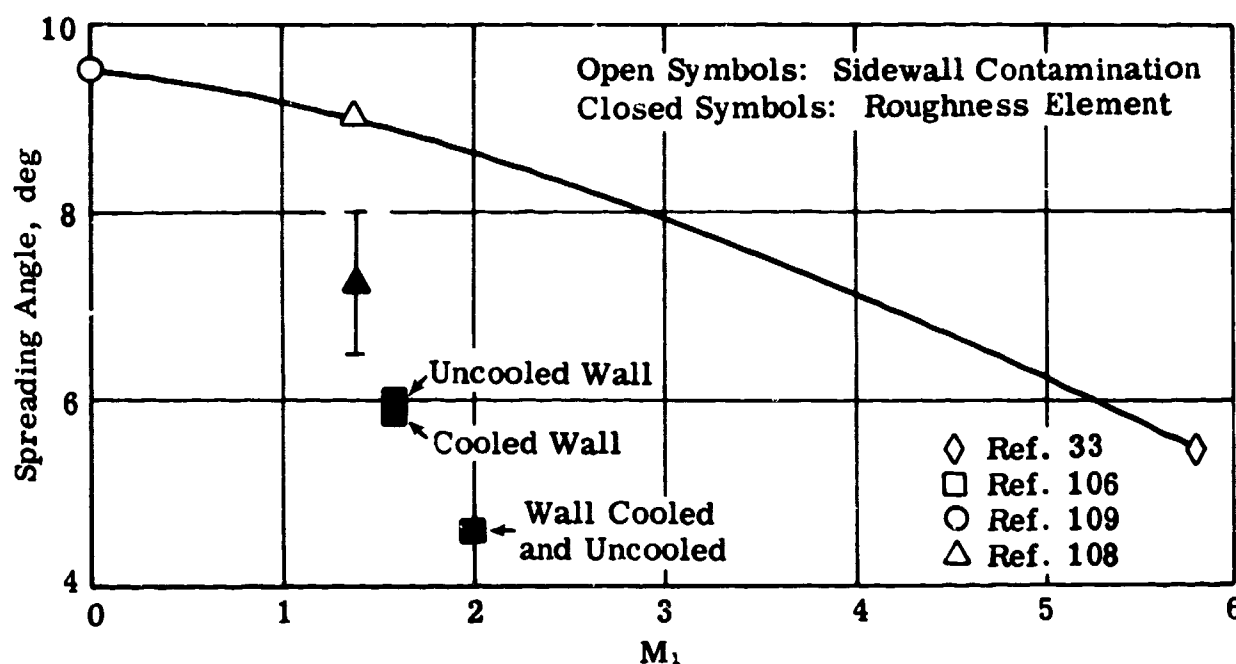
5.7 Effect of Stream Turbulence in a Wind Tunnel

Very few data are available concerning the effect on transition of supersonic wind-tunnel turbulence. Van Driest and Boison investigated widely varying turbulence levels in the supply stream. Their results are shown on Fig. 5-25 for three Mach numbers and several wall temperature ratios. The values of $(Re_{x_1})_0$ are the transition Reynolds numbers for the lowest turbulence

level (see data from Ref. 75 plotted on Fig. 5-1). The transition Reynolds number is inversely proportional to both the supply stream turbulence and the wall temperature ratio. Both these effects decrease markedly as the Mach number is increased. It would be of great interest to determine the effect of varying the level of the supply air turbulence on the turbulence level in the presence of a model, as well as the turbulence associated with the sound field reflected from the boundary layer on the tunnel wall.

5.8 Lateral Spreading of Turbulence

Two types of lateral spreading will be considered: that due to contamination from any surface to which a model is attached, and that in the wake of a discrete roughness element. The effect of the former is of particular interest at a wing-fuselage or tail-fuselage juncture. The limited amount of supersonic data available indicates that the angle at which turbulence will spread decreases with increasing Mach number, as shown on the sketch below.



At low speeds, this lateral contamination starts at the leading edge and spreads at an angle of about 9 degrees. At high speeds, however, it will start some distance from the leading edge and spread at a smaller angle. The last data point on Fig. 5-21 gives the transition Reynolds number on a plate supported from the tunnel wall in flow at $M_1 = 5.8$ and represents the distance from the leading edge at which the turbulent side-wall contamination begins to spread on to the plate (see Ref. 33). Since this point appears to correlate with the rest of the data on the above sketch, it is suggested that Fig. 5-21 be used to determine the lag at other Mach numbers from 0 to 5.8. In other words, the Reynolds number at which spreading starts is given by $(Re_{x_1} - Re_{x_{k_1}})$ in Fig. 5-21.

In Ref. 106 the data on lateral spreading were obtained by measuring the angle of the turbulent wedge behind a single roughness element mounted on a flat plate. Two sets of data were obtained at Mach numbers of 1.61 and 2.01.

In one case the plate was cooled and in the other it was at the adiabatic recovery temperature. The cooling had very little effect on the spreading angle of the turbulence. Wedges of spreading turbulence on a flat plate (Ref. 108) were caused by small nicks on the leading edge. The semi-angle of the spreading due to these imperfections should be comparable to those from the single roughness elements of Ref. 106. Accordingly, these data are also shown on the above sketch. These few data, obtained under different circumstances, suggest that side-wall contamination is less affected by Mach number than is the spread in the wake of a single roughness element.

Symbol	Facility	Ref.	$Re_{x_1}/ft \times 10^{-6}$	Temperature	Rough.	Trans.
\triangle	Wind Tunnel	76	4.3-7.7	$T_t = 50-100^\circ F$	12 $\mu in.$	Start
\circ		75	6.4	$T_t = 50-100^\circ F$	10 $\mu in.$	End*
\triangle			8.0			
\square			6.0			
\blacktriangle	Ballistics	77	12.3-17.2	$T_w = 75-610^\circ F$	6 $\mu in.$	End
\blacksquare	Range	78	18.9-31.4		6 $\mu in.$	
\bullet		79	47		3 $\mu in.$	
\odot	Free Flight	80	7.8-16.6	$T_w = 100-900^\circ F$	4 $\mu in.$	Start

*Supply Air Turbulence = 0.4%

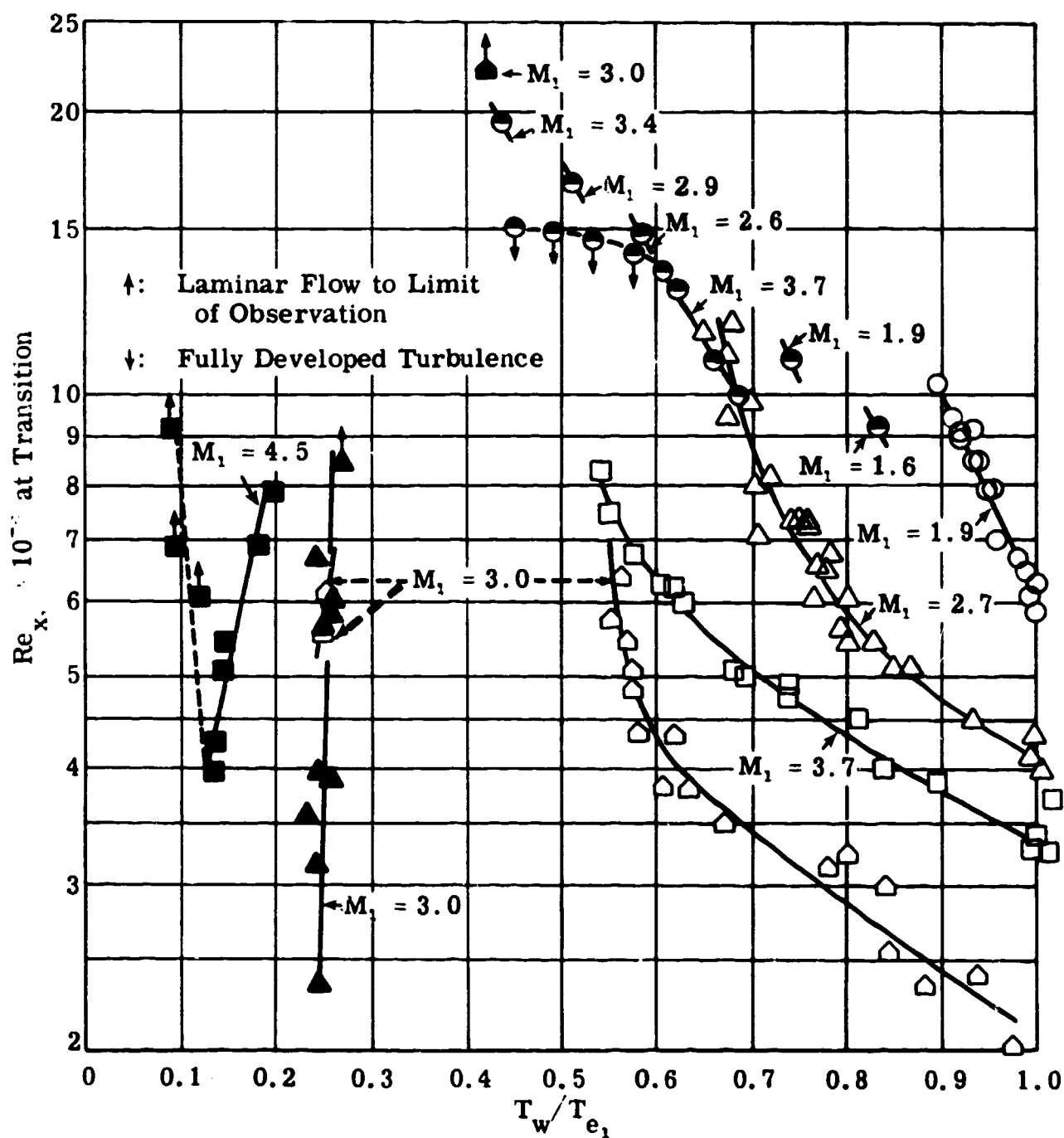


Fig. 5-1. Effect of T_w/T_{e_1} and M_1 on the transition Re_{x_1} ; smooth, sharp cones; $\sigma = 5^\circ$; $\alpha \approx 0^\circ$.

Symbol	Facility	Ref.	Re_x/ft ($\times 10^{-6}$)	T_t , °F	Roughness
○	Wind Tunnel	81	5.4	250	8 μ in.
○		82	2.2		10 μ in.
◇	Gun Tunnel	83	6.7	746-935	16 μ in.
△			7.5		
△			8.5		
□	Gun Launched into M-2 Tunnel	84	33.6	--	25 μ in.
■	Bal. Range	84	33.6	--	25 μ in.

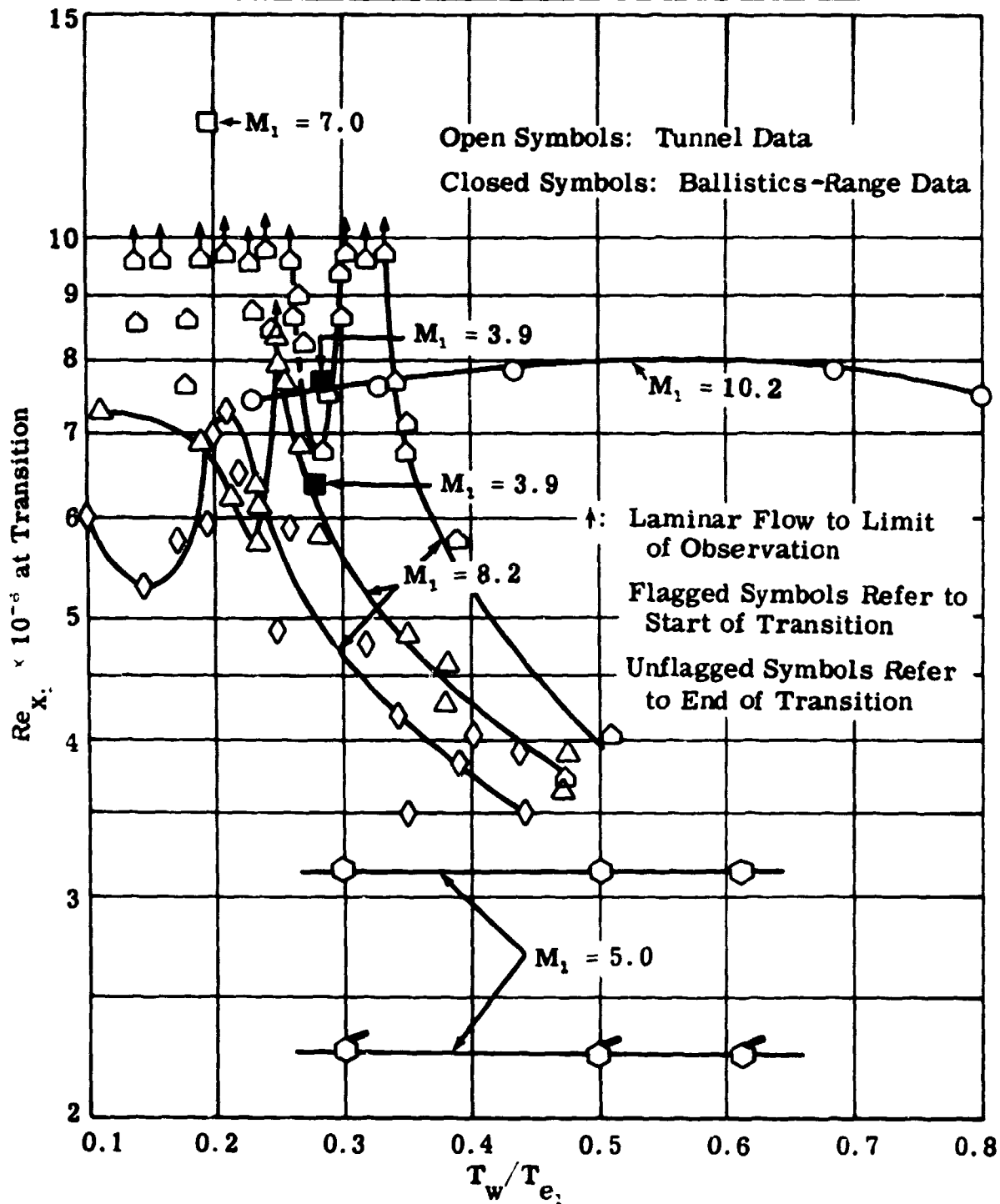


Fig. 5-2. Effect of T_w/T_e and M_1 on the transition Re_{x_1} ; smooth, sharp flat plates and hollow cylinders; $\alpha = 0^\circ$.

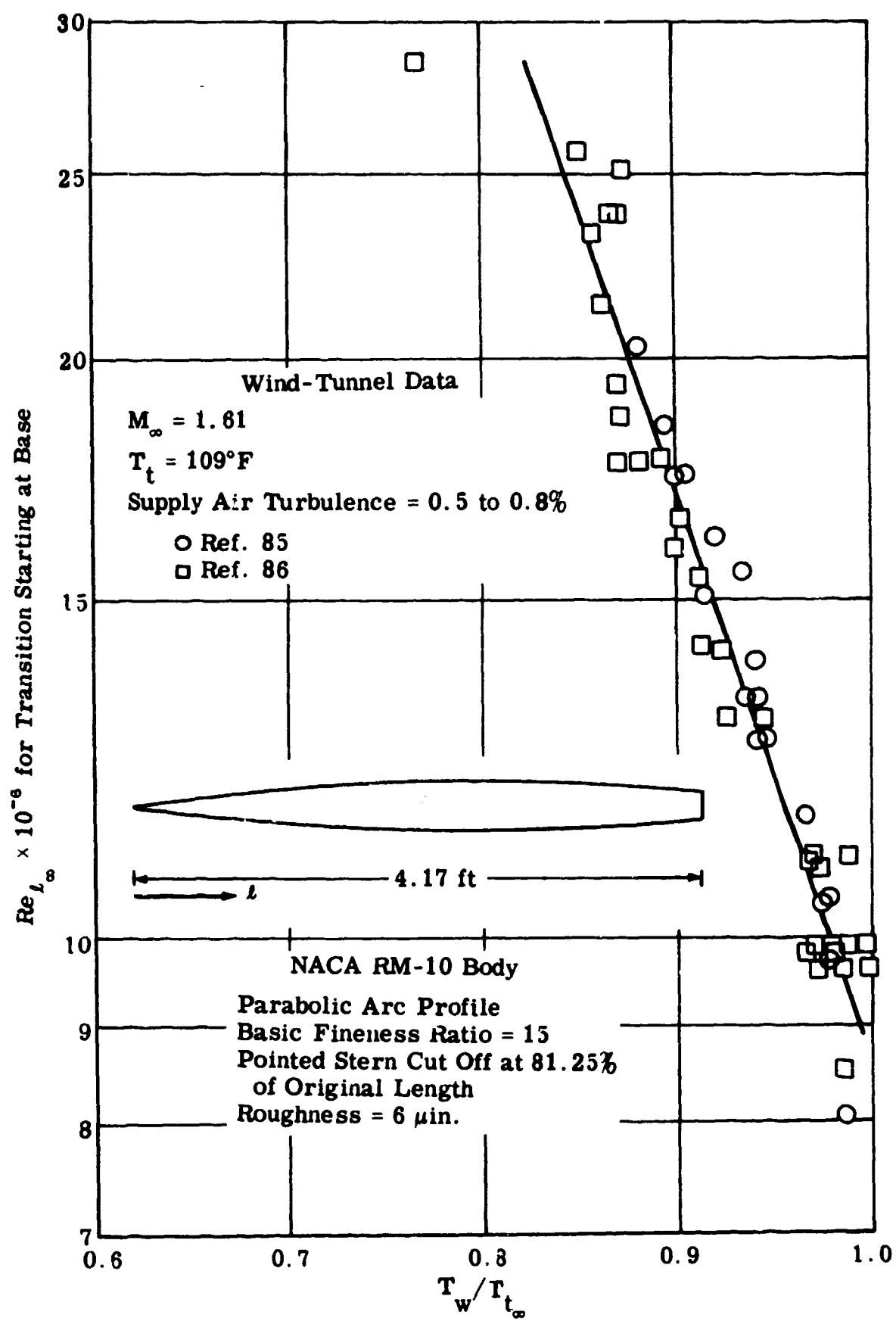


Fig. 5-3. Effect of cooling on transition Re_l ; NACA RM-10 body;
 $\alpha = 0^\circ$; $M_\infty = 1.61$.

Symbol	Ref.	$Re_1/ft \times 10^{-6}$	2σ	Roughness	Transition
○	75	6.0 - 8.0	10°	10 μ in.	End*
□	89	0.6 - 2	5°	--	End
△	90	2 - 8.7	10°	--	Start
◇	87	3.4 - 9.3	10°	6 μ in.	End
○	72	1.1 - 8.1	10°	8 μ in.	End
□	88	1.5 - 7.7	10°	5 μ in.	End
◇		3.0 - 8.4	27°		
○		2.0 - 8.1	45°		
◇		4.1 - 8.4	60°		

*Supply air turbulence = 0.4%

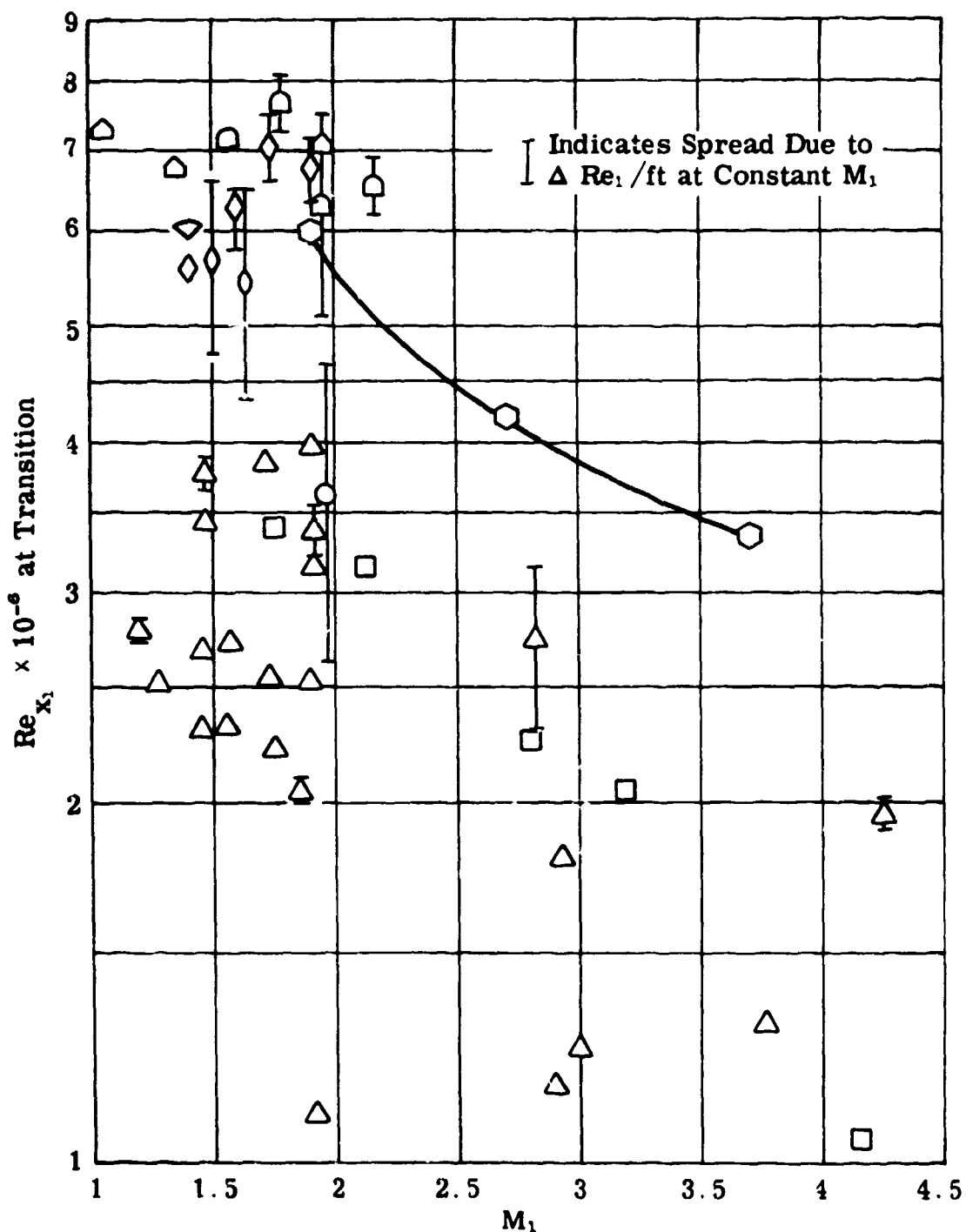


Fig. 5-4. Effect of M_1 on transition Re_{x_1} ; smooth, sharp cones; $\alpha = 0^\circ$; $T_e = T_w$; wind-tunnel tests.

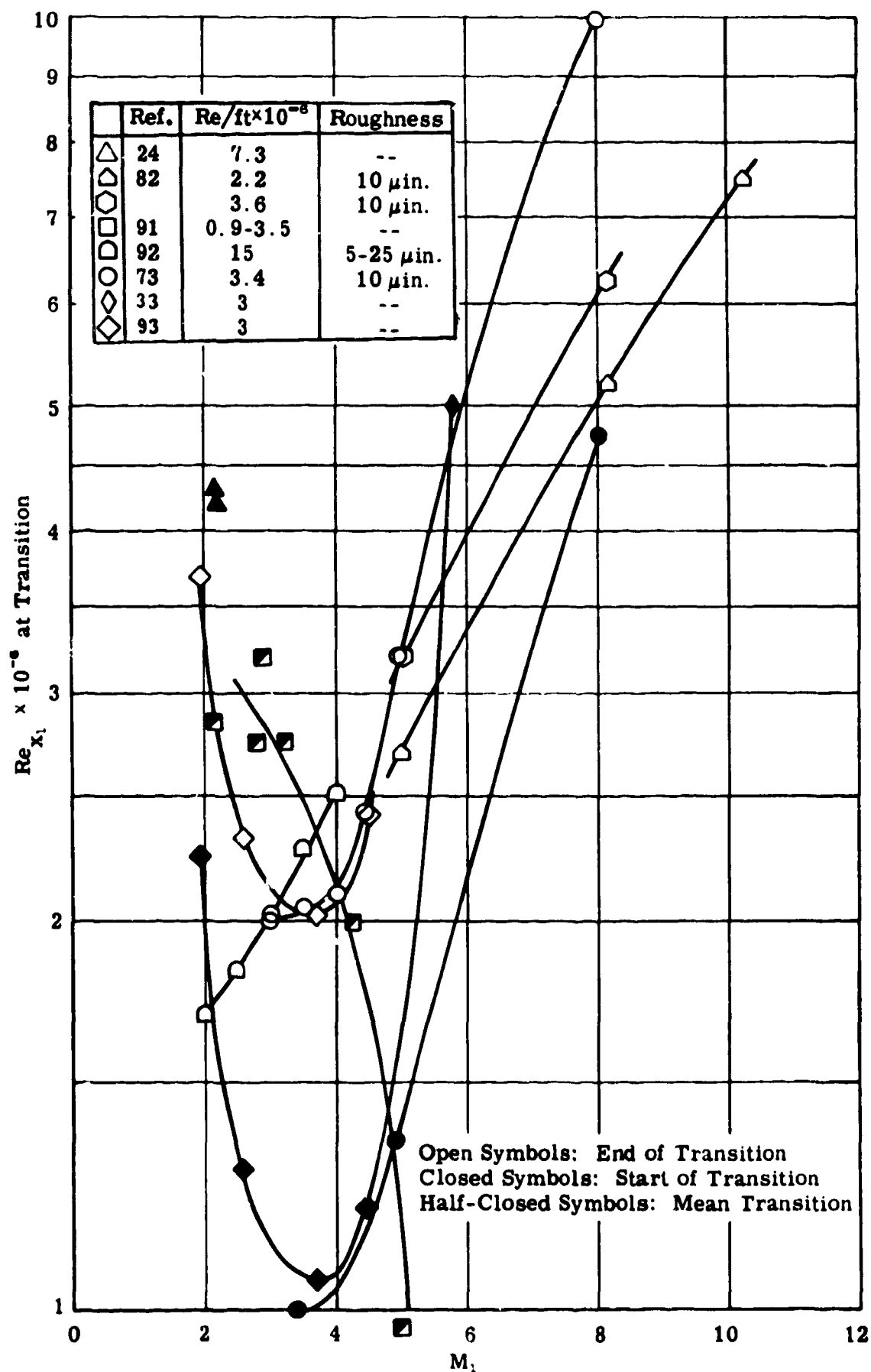


Fig. 5-5. Effect of M_1 on transition Re_{x_1} ; smooth, sharp flat plates and hollow cylinders; $T_e = T_w$; wind-tunnel tests.

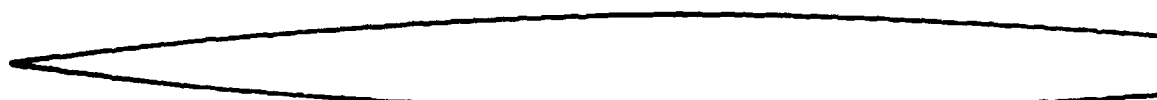
(All Models are Approximately to Scale)



Model A: Cone-Cylinder



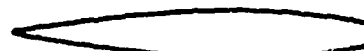
Model B: Ogive-Cylinder



Model C: NACA RM-10 Body



Model D: $dp/dx = -0.05$



Model E: $dp/dx = -0.10$

Constant Pressure Gradient Bodies

Model	$Re_{l_{\infty}} \times 10^{-6} *$	M_{∞}	Length, l , ft	Re_1 /ft	Roughness (μ in.)	Ref.
A	2.6	1.61	4.17	6×10^5	23 ± 5	95
B	4.8	1.61	4.17	to	6 - 12	95
C	11.5	1.61	4.17	8.9×10^5	6 - 12	95
D	3.99	3.12	1.58	0.83×10^5	6	96
E	59.2	3.12	1.33	to 10^5	6	96

* For transition starting at base of model.

Fig. 5-6. Effect of pressure gradient on transition $Re_{l_{\infty}}$; $\alpha = 0^\circ$;

$T_e = T_w$; wind-tunnel tests (see Subsec. 5.1.2).

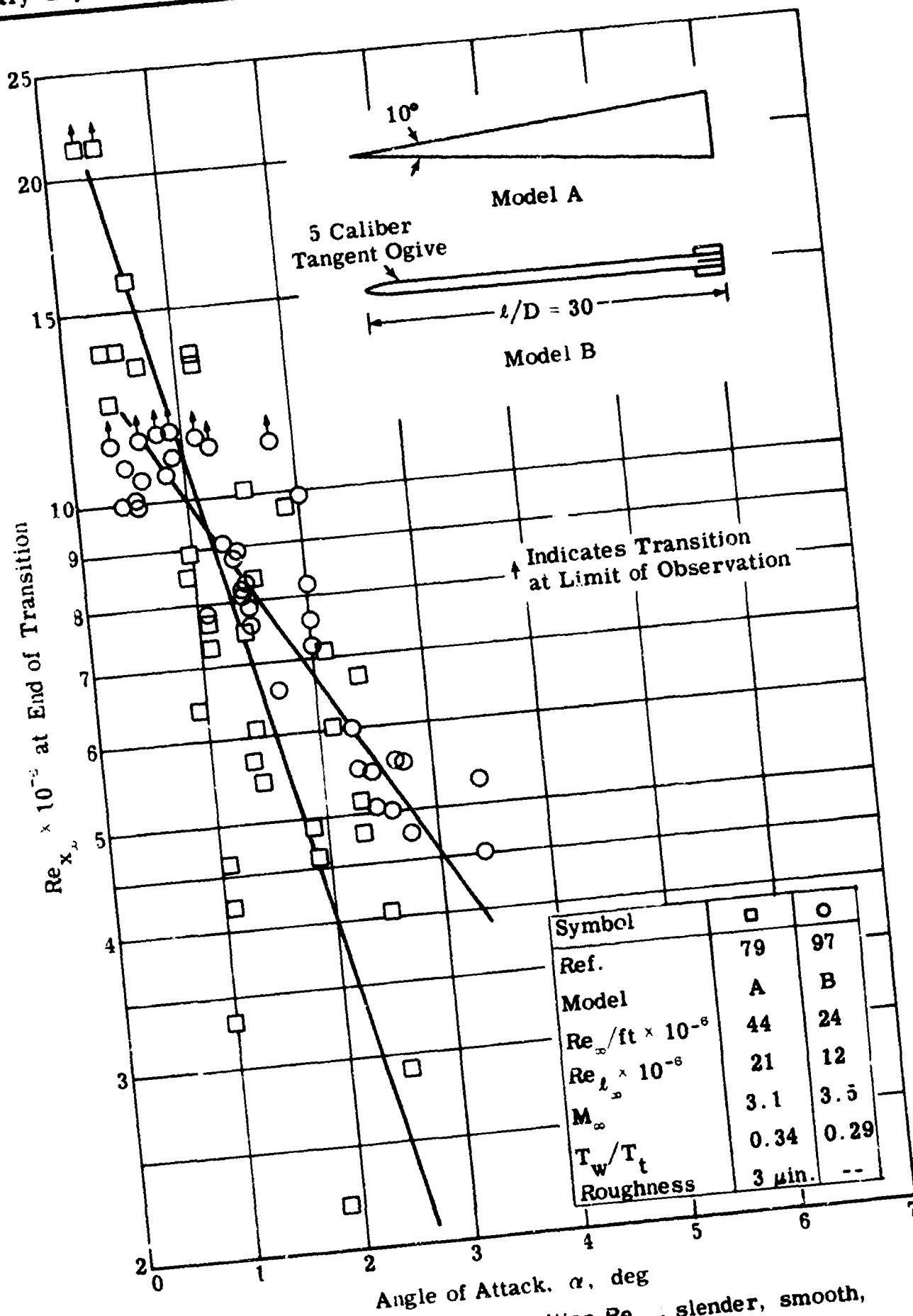


Fig. 5-7. Effect of α on transition $Re_{x_{\infty}}$, slender, smooth, sharp bodies; ballistics-range tests.

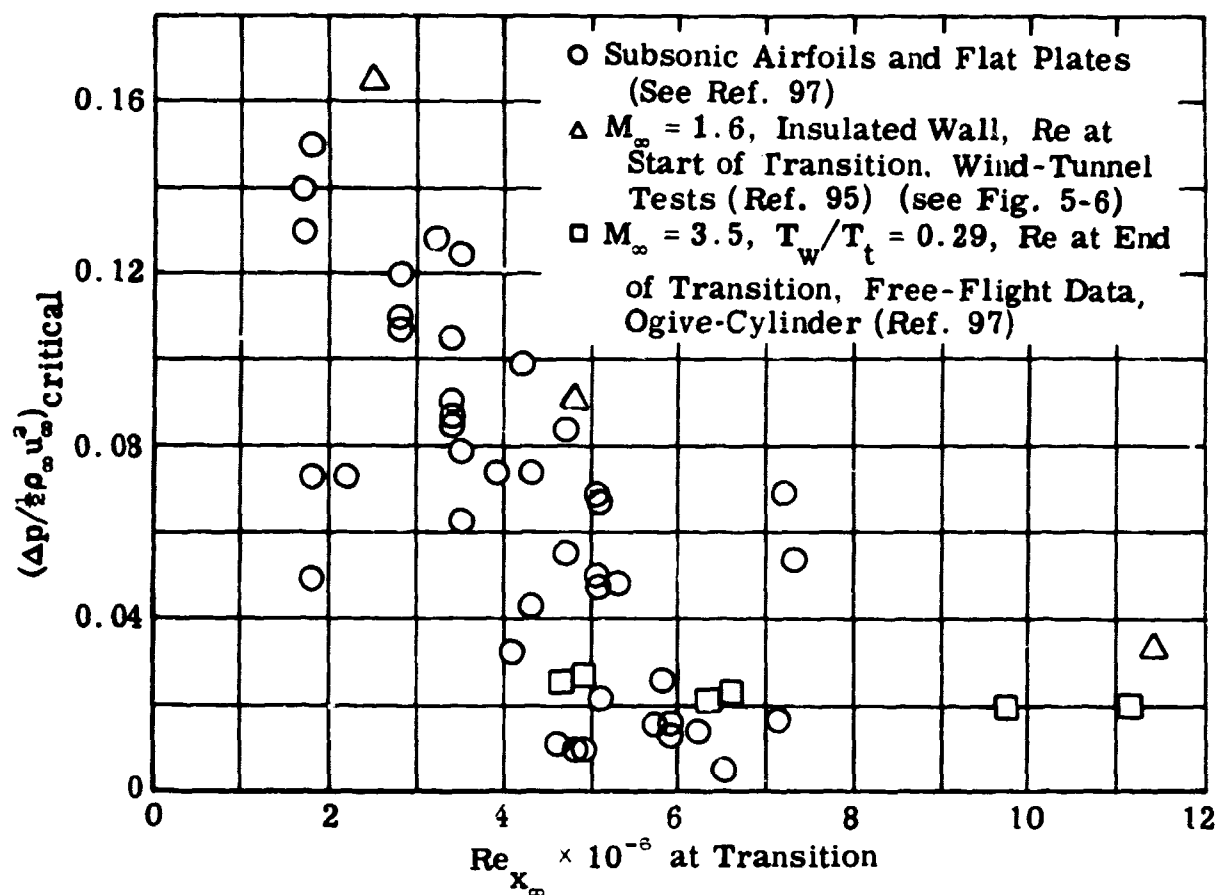


Fig. 5-8. Critical pressure rise coefficient as a function of transition Re_{x_∞} ; various models; $M_\infty = 0, 1.6$, and 3.5 .

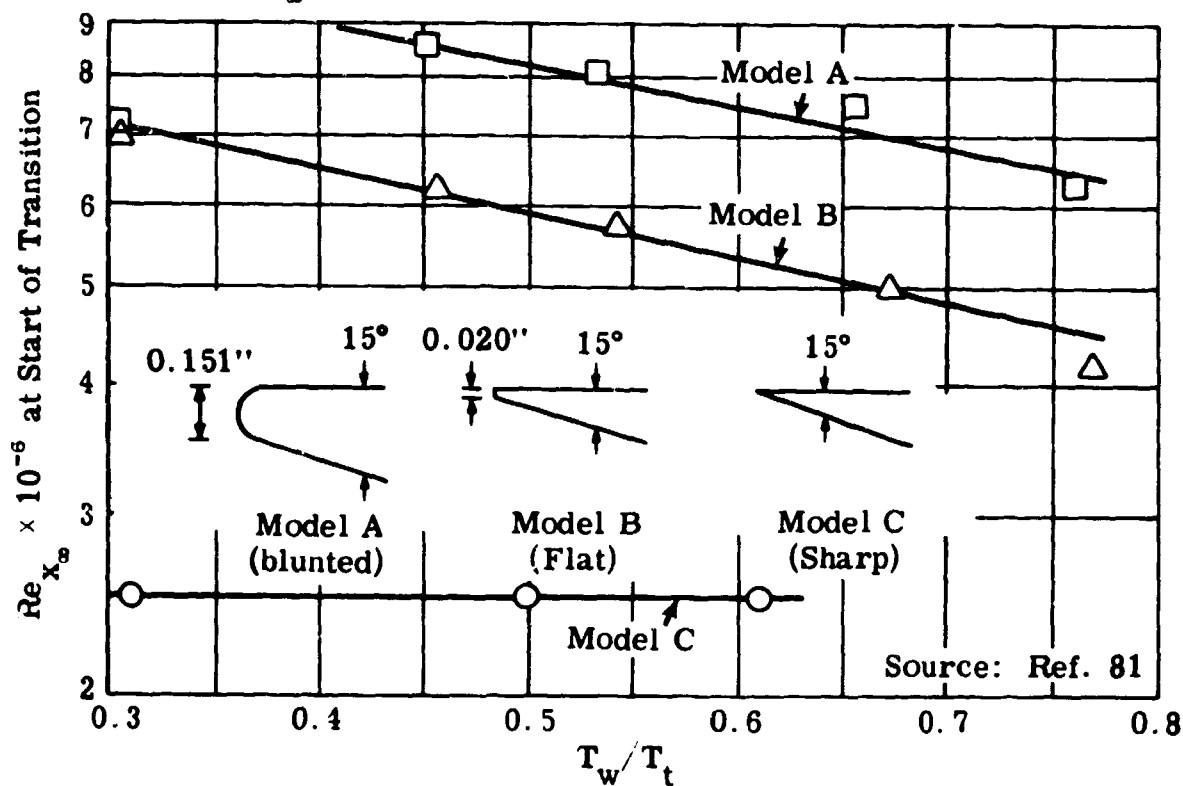


Fig. 5-9. Effect of bluntness on transition Re_{x_∞} ; cooled, smooth hollow cylinders; $M_\infty = 5.0$; roughness = $8 \mu\text{in.}$; $Re_\infty/\text{ft} = 5.4 \times 10^5$; wind-tunnel data.

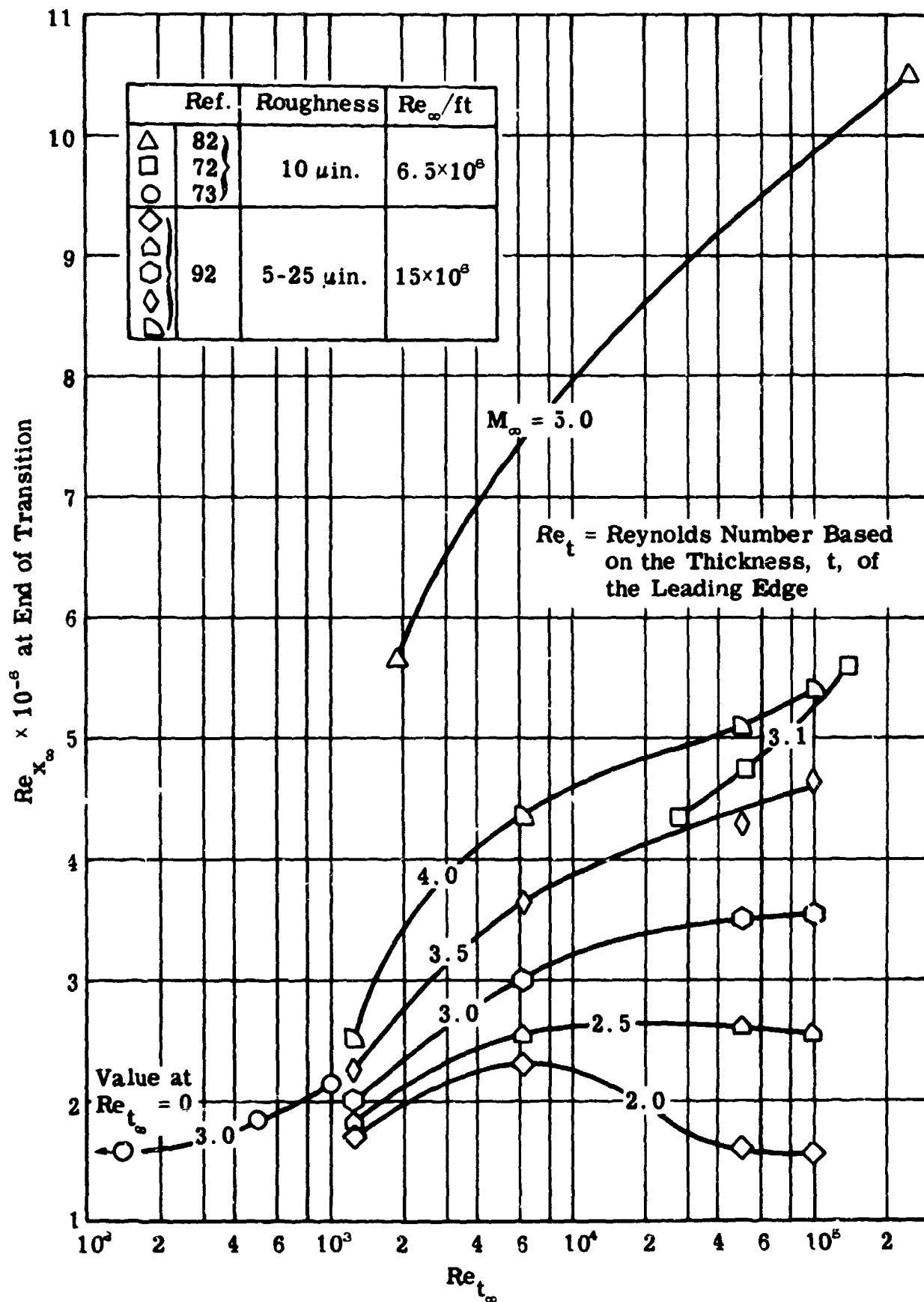


Fig. 5-10. Effect of semicircular bluntness and M_{∞} on transition $Re_{x_{\infty}}$; smooth, flat plates and hollow cylinders; $T_e = T_w$, wind-tunnel tests.

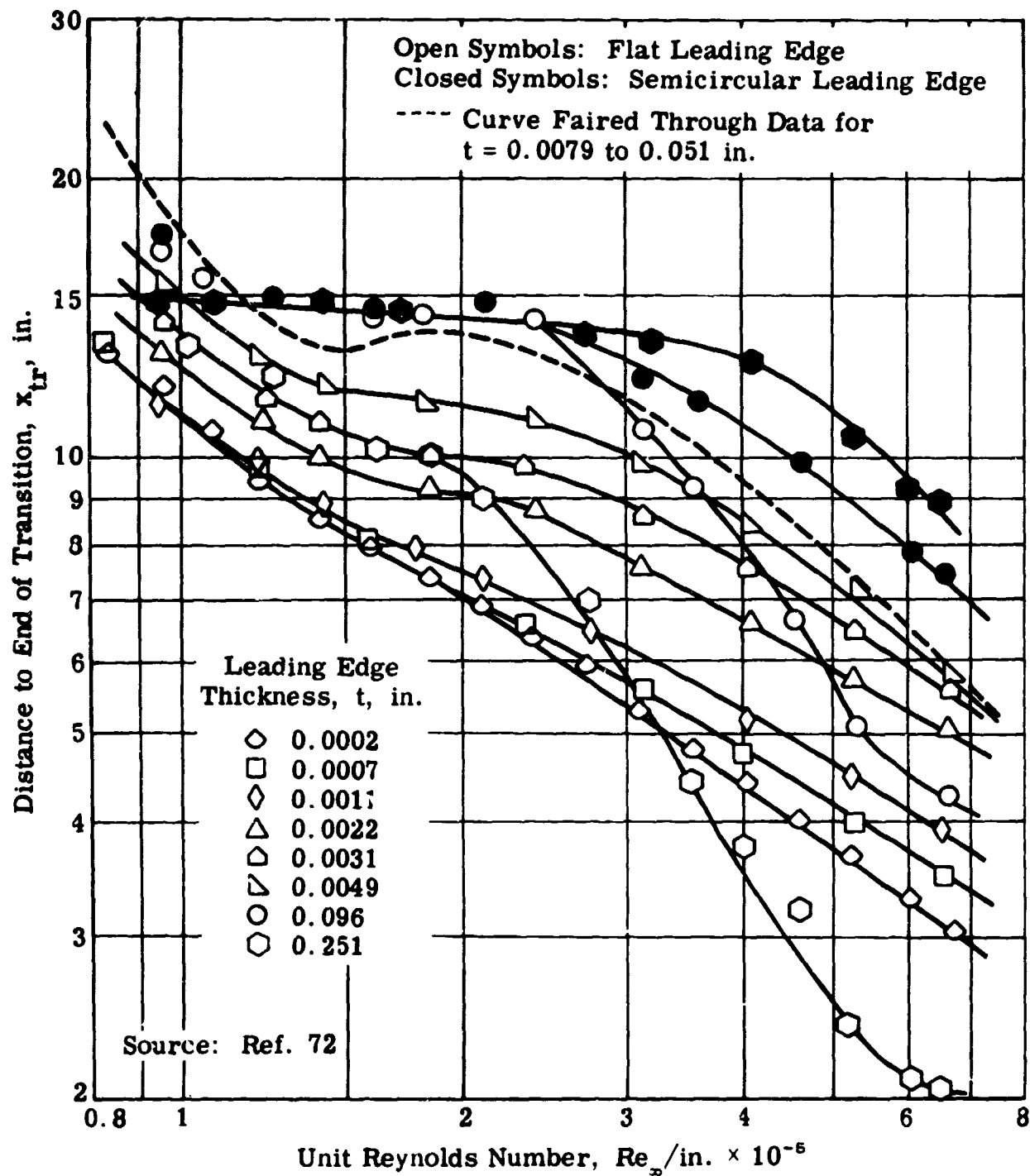


Fig. 5-11. Effect of bluntness on distance to end of transition as a function of $Re_\infty/\text{in.}$; smooth, hollow cylinder, $T_e = T_w$, $M_\infty = 3.1$, roughness = $10 \mu\text{in.}$; wind-tunnel tests.

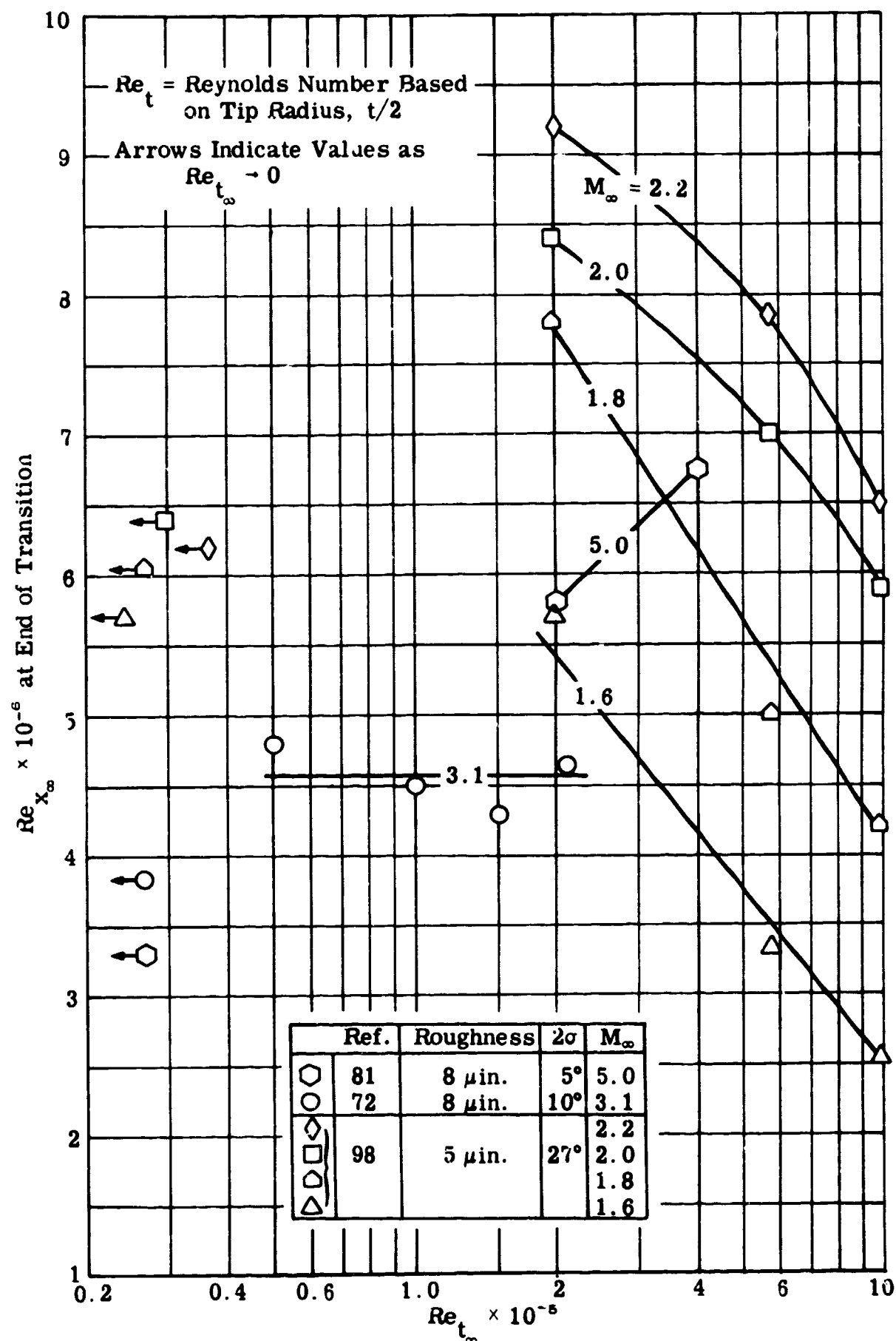


Fig. 5-12. Effect of tip radius, Re_t , and M_∞ on transition Re_x ; smooth cones; $\alpha = 0^\circ$, $T_{e1} = T_w$; wind-tunnel tests.

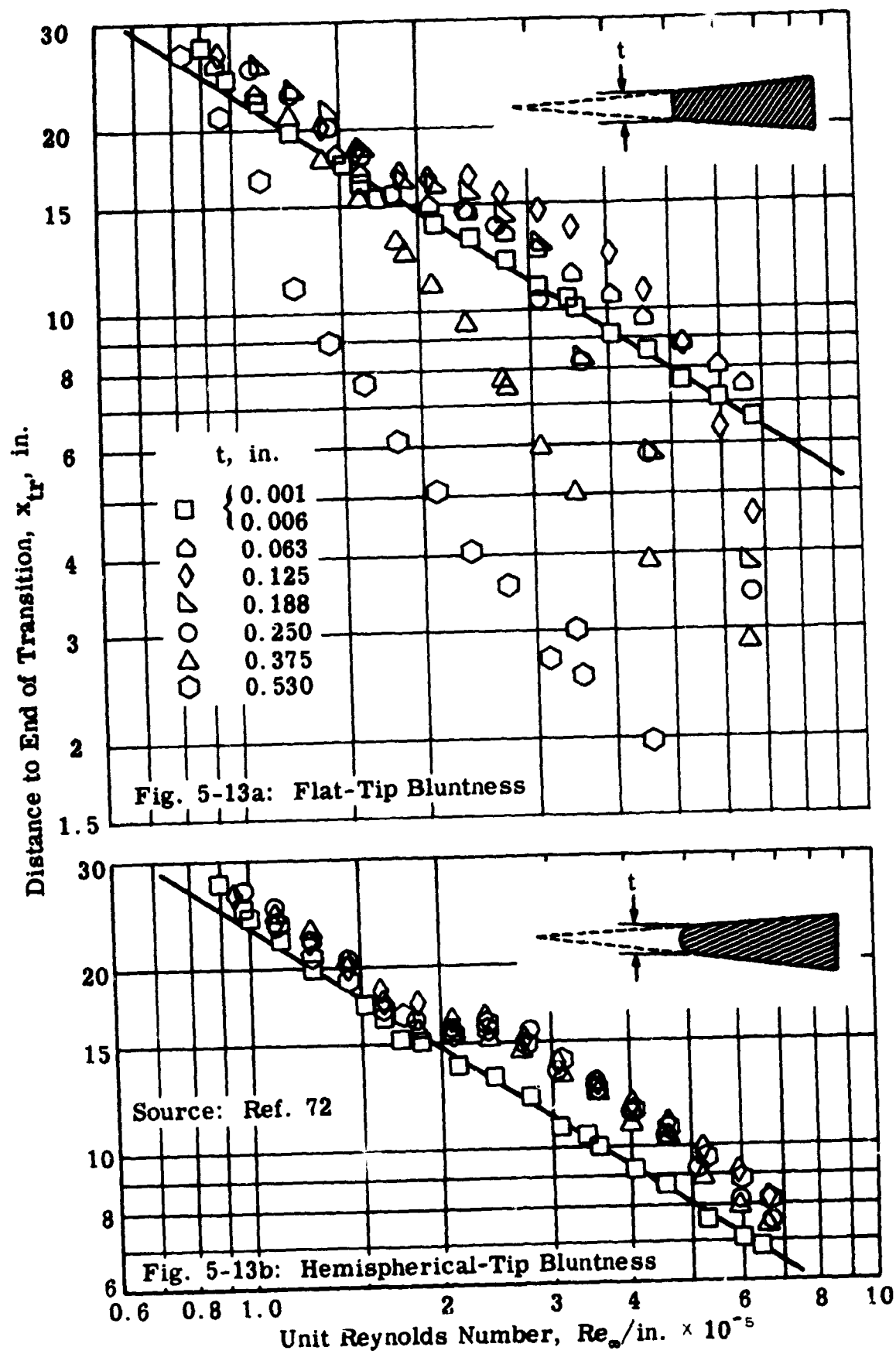


Fig. 5-13. Effect of bluntness on distance to end of transition; smooth cones; $2\sigma = 10^\circ$; $\alpha = 0^\circ$; $T_{e1} = T_w$; $M_\infty = 3.1$; roughness = $8 \mu\text{in.}$; wind-tunnel tests.

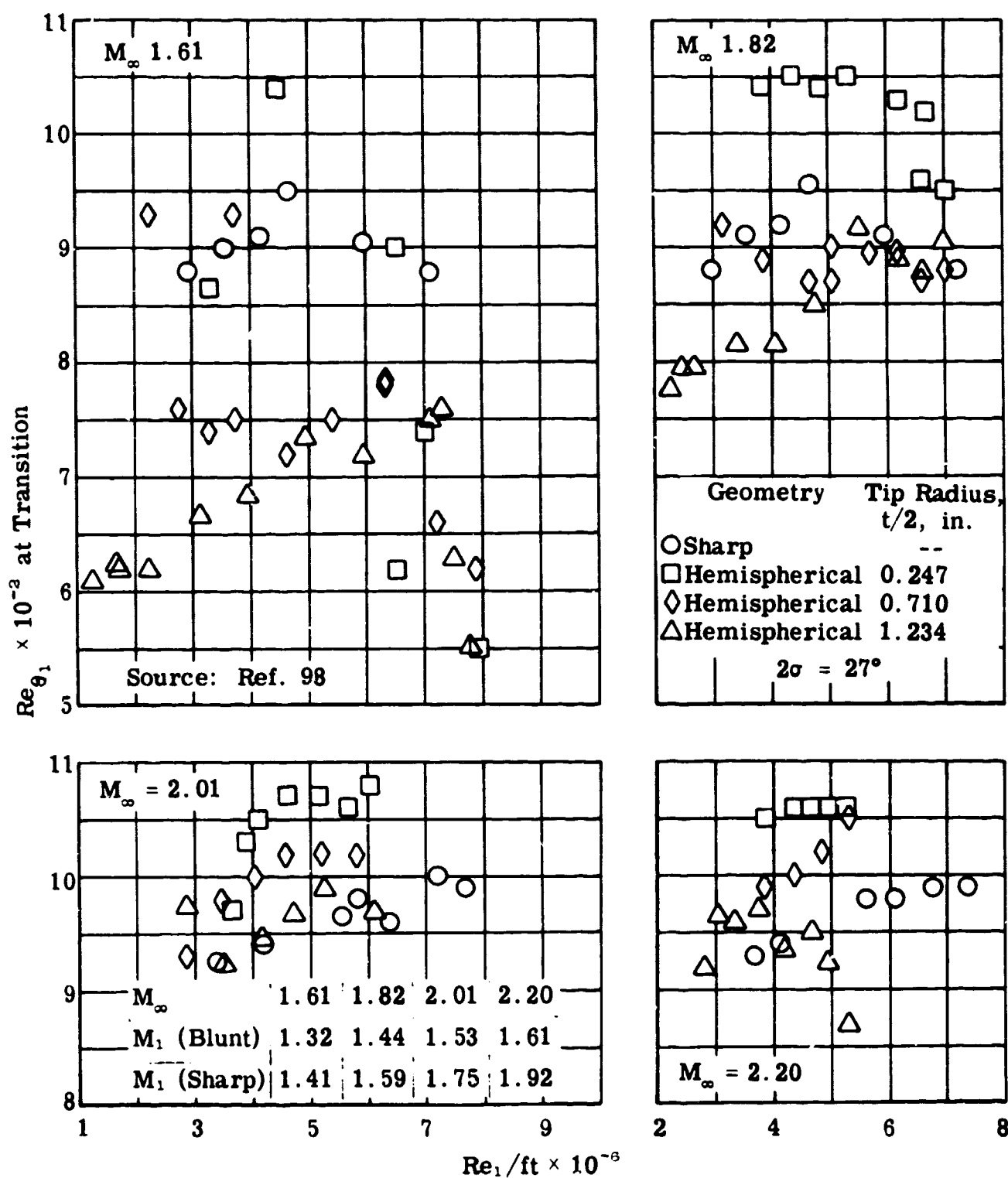


Fig. 5-14. Effect of tip blunting on Re_{θ_1} at transition; smooth cone; $\alpha = 0^\circ$; $T_{e1} = T_w$; wind-tunnel tests.

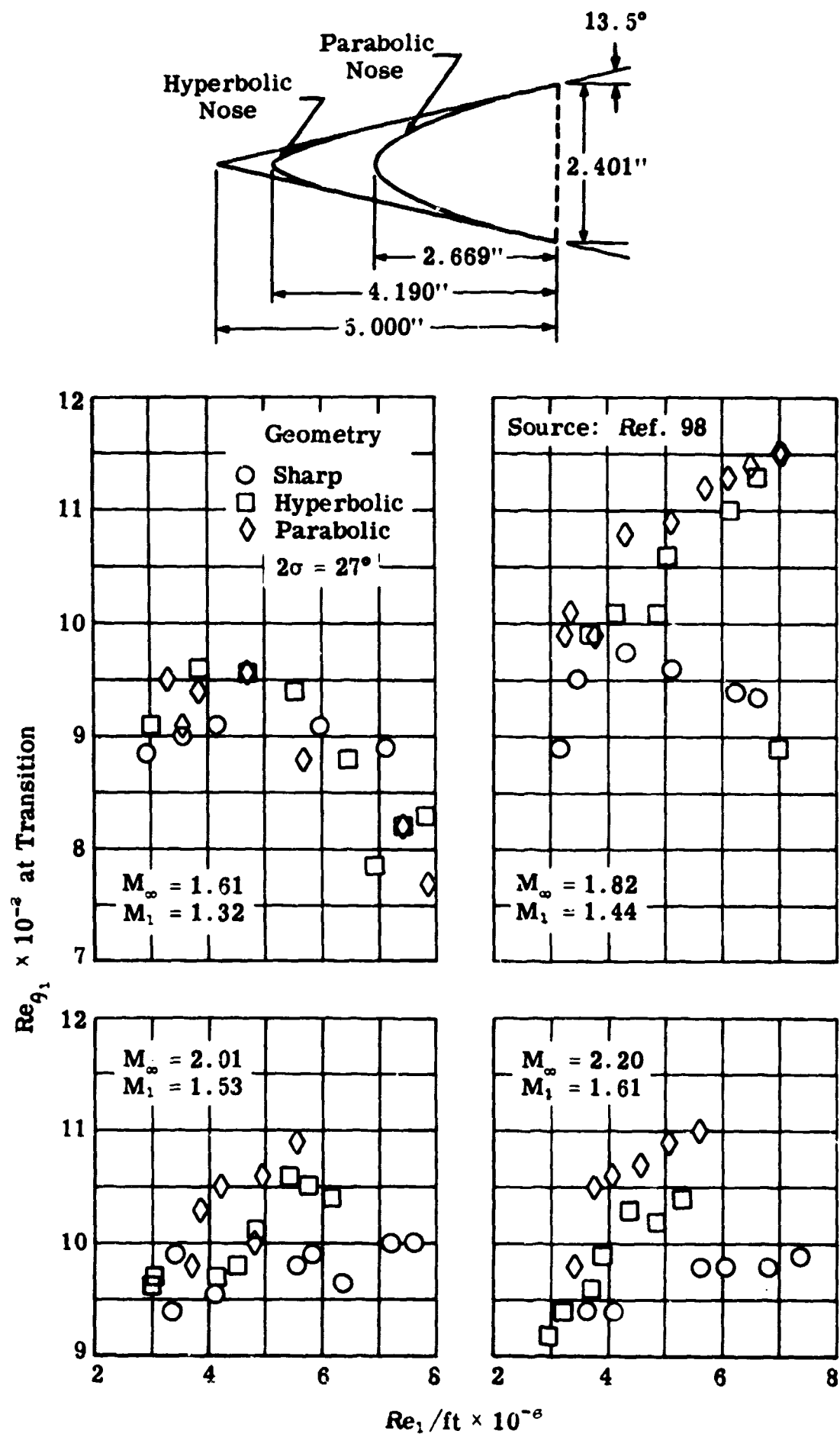


Fig. 5-14 (cont'd)

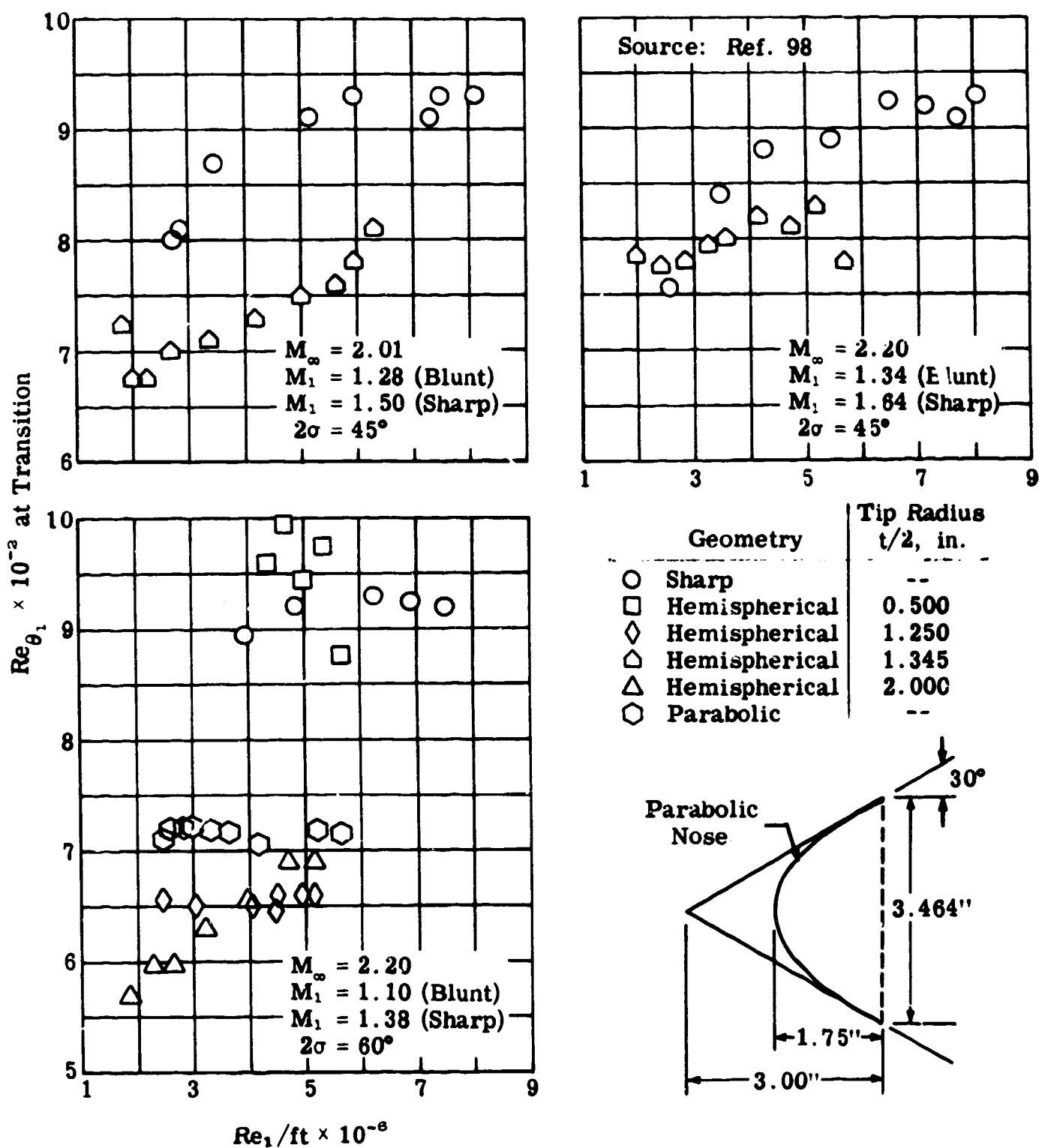


Fig. 5-14 (cont'd)

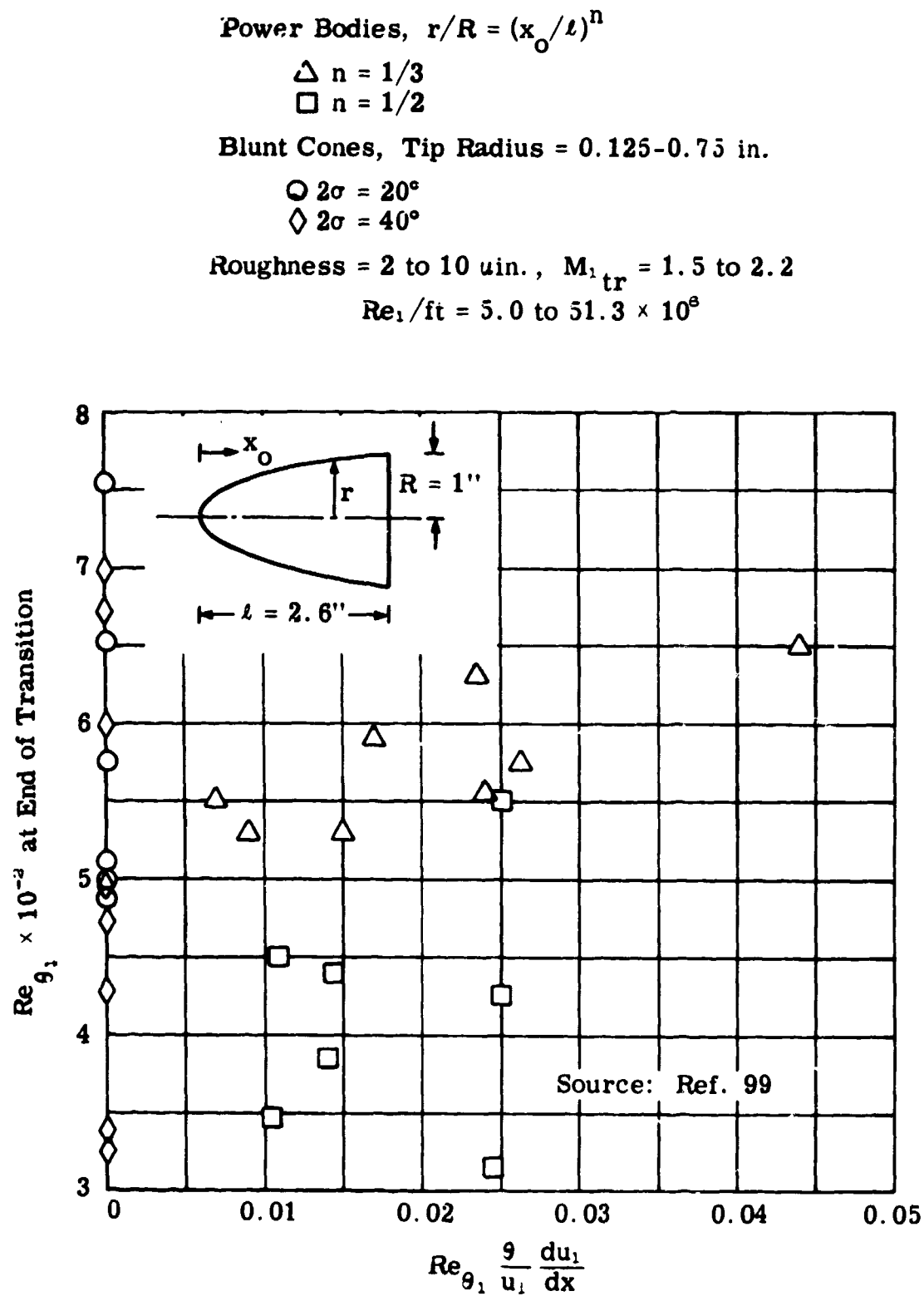


Fig. 5-15. Momentum thickness Reynolds number, Re_{θ_1} , at transition; smooth, blunt bodies, $\alpha \approx 0^\circ$; $T_w/T_t = 0.3$ to 0.56 ; $M_\infty = 2$ to 3.5 ; ballistics-range tests.

Leading Edge	Thickness, in.	M_∞	Re_1 /ft	Roughness	$x_{\Lambda=0}$, in.	Ref.
○ Semicircular	0.001	3	15×10^6	5-25 μ in.	1.61	102*
● "	0.001	4	15×10^6	5-25 μ in.	2.09	92
◻ "	0.002	8	$3-3.7 \times 10^6$	10 μ in.	20.5-21.6	82
● Flat	0.002	4	19.3×10^6	5-25 μ in.	2.70	101
● "	0.003					
△ Semicircular	0.005	3	15×10^6	5-25 μ in.	2.42	102*
▲ "	0.005	4	15×10^6	5-25 μ in.	3.52	92
◇ "	0.040	3	15×10^6	5-25 μ in.	3.19	102*
◆ "	0.040	4	15×10^6	5-25 μ in.	3.99	92

* Analysis of data from Ref. 92.

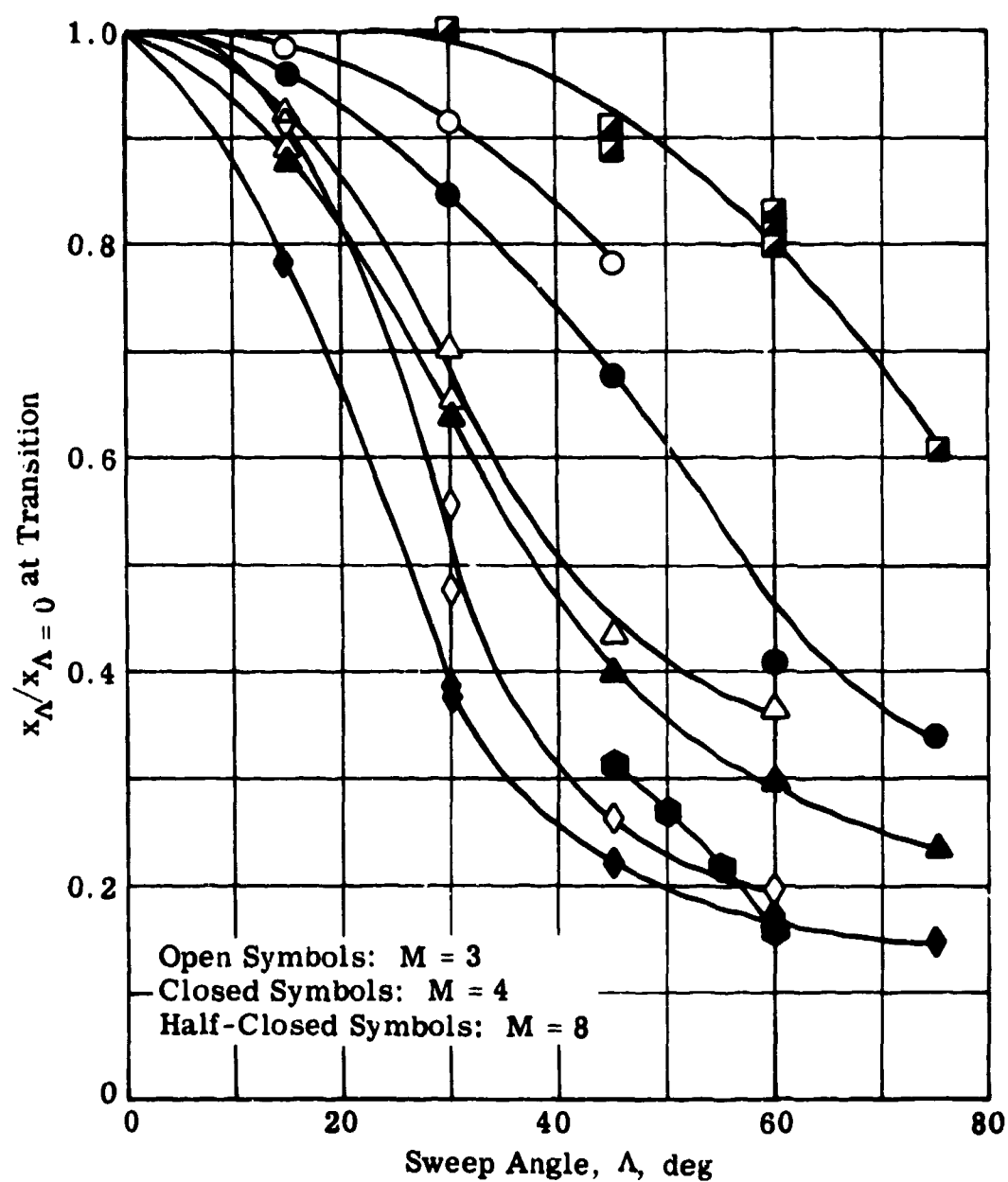


Fig. 5-16. Effect of sweep angle, leading edge thickness, and Mach number on transition location; flat plate; $T_e = T_w$.

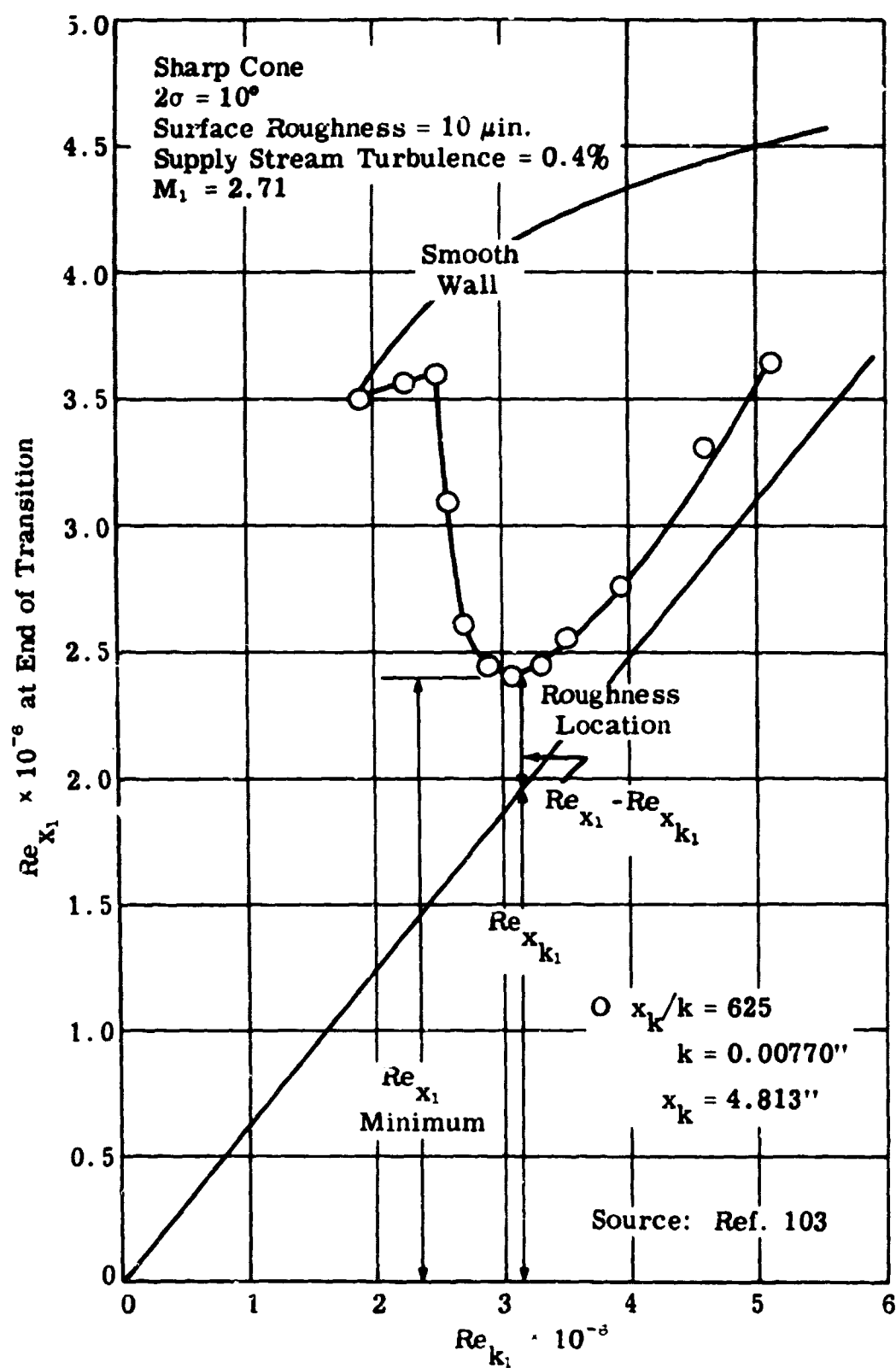


Fig. 5-17. Effect of spherical roughness, Re_{k_1} , on transition Re_{x_1} ; sharp cone; $T_{e_1} = T_w$ (see Subsec. 5.6.1).

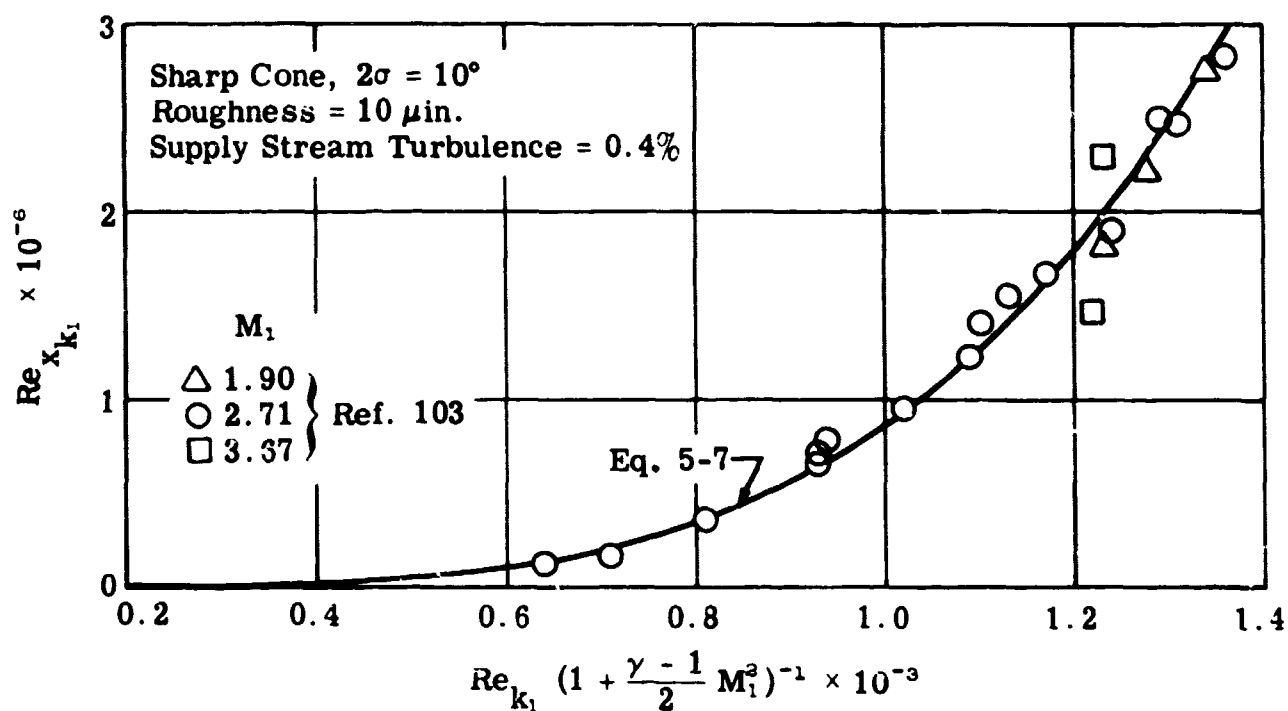


Fig. 5-18. Roughness location, x_k , as a function of the roughness height, k , normalized with respect to M_1 ; sharp cone; spherical roughness element; $T_{e1} = T_w$.

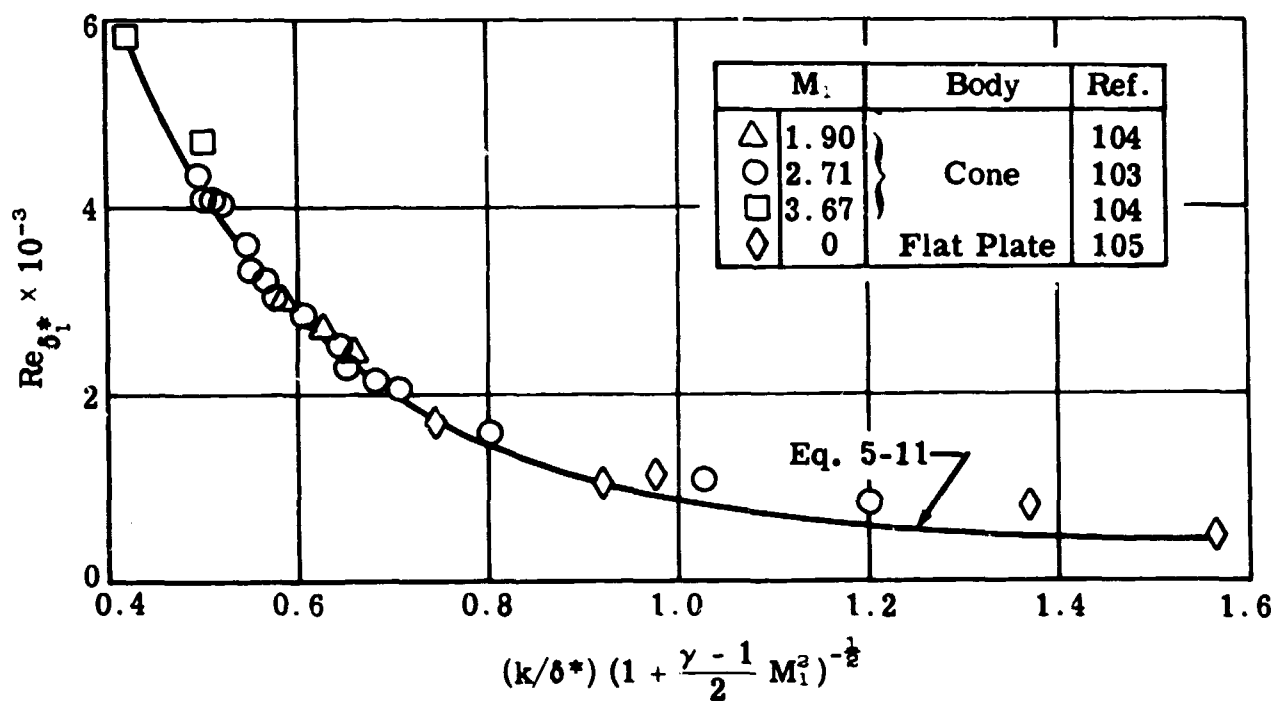


Fig. 5-19. Displacement thickness, $Re_{\delta_1^*}$, as a function of the roughness size, (k/δ^*) , normalized with respect to M_1 ; cone and flat plate; spherical roughness element; $T_{e1} = T_w$.

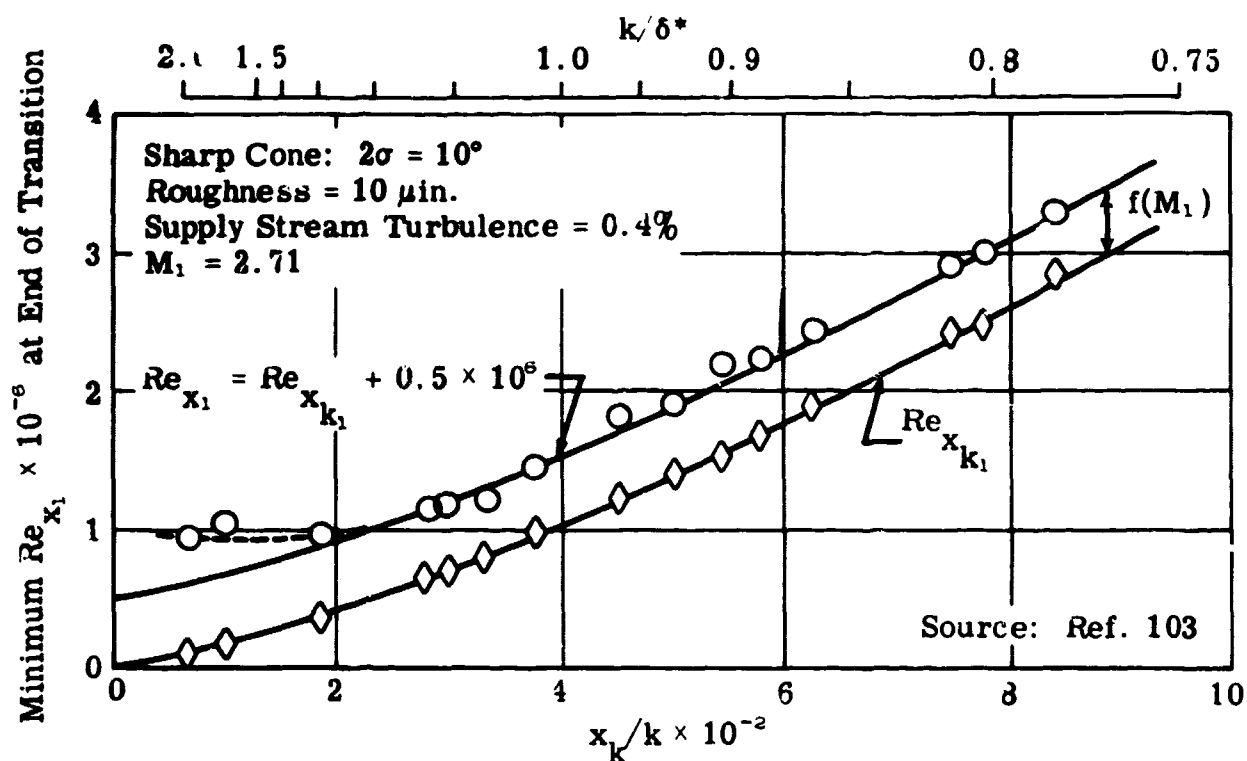


Fig. 5-20. Effect of roughness size, x_k/k or k/δ^* , on minimum transition Reynolds number, Re_{x_1} or $Re_{x_{k_1}}$; sharp cone, spherical roughness elements; $T_{e_1} = T_w$.

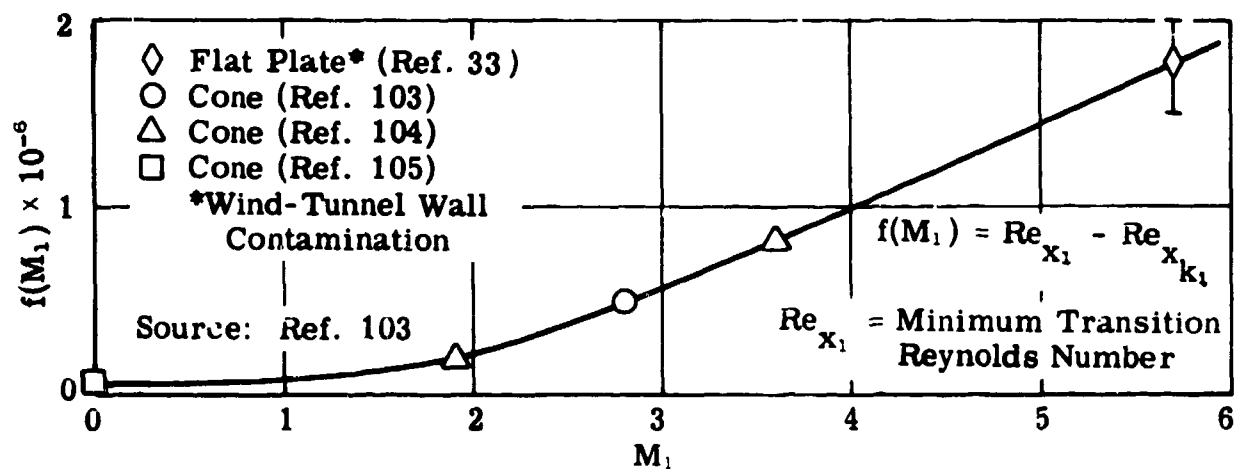


Fig. 5-21. Effect of M_1 on $(Re_{x_1} - Re_{x_{k_1}})$; cones and flat plate; spherical roughness elements; $T_{e_1} = T_w$.

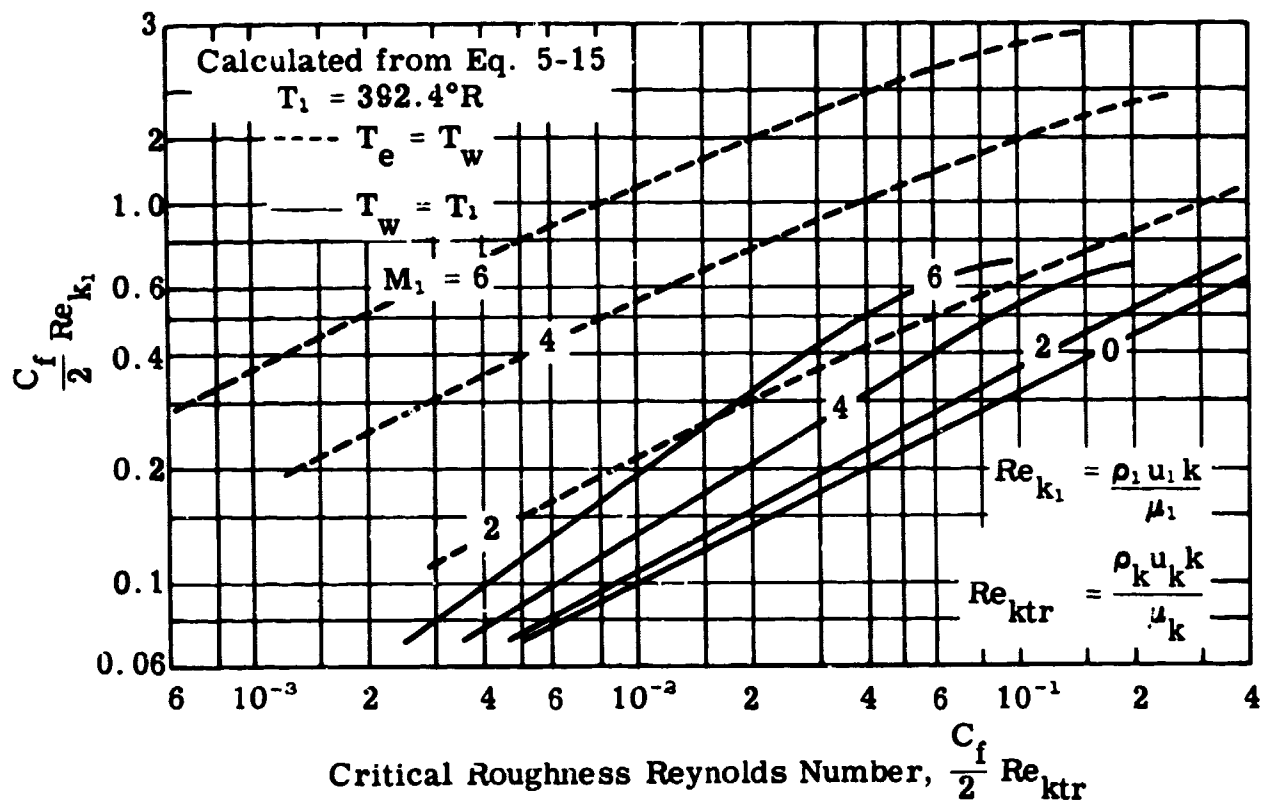


Fig. 5-22. Relationship between roughness Reynolds numbers, Re_{k1} and Re_{ktr} .

	Ref.	M_1	Configuration	
○	103	2.71	Cone, $2\sigma = 10^\circ$	Insulated
□	106	1.56	Cone, $2\sigma = 10^\circ$	Insulated
■	"	1.56	Cone, $2\sigma = 10^\circ$	$T_w/T_1 = 1.29$
△	"	1.94	Cone, $2\sigma = 10^\circ$	Insulated
▲	"	1.94	Cone, $2\sigma = 10^\circ$	$T_w/T_1 = 1.47$
◇	"	1.61	Flat Plate	Insulated
○	"	2.01	Flat Plate	Insulated

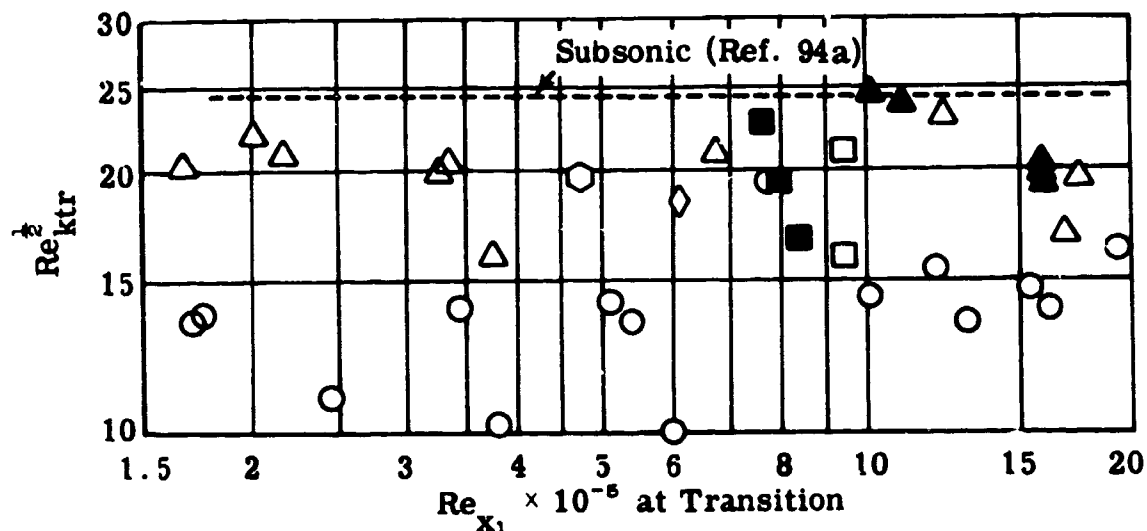


Fig. 5-23. Critical roughness Reynolds number, Re_{ktr} ; cones and flat plates; three-dimensional roughness elements; heat transfer.

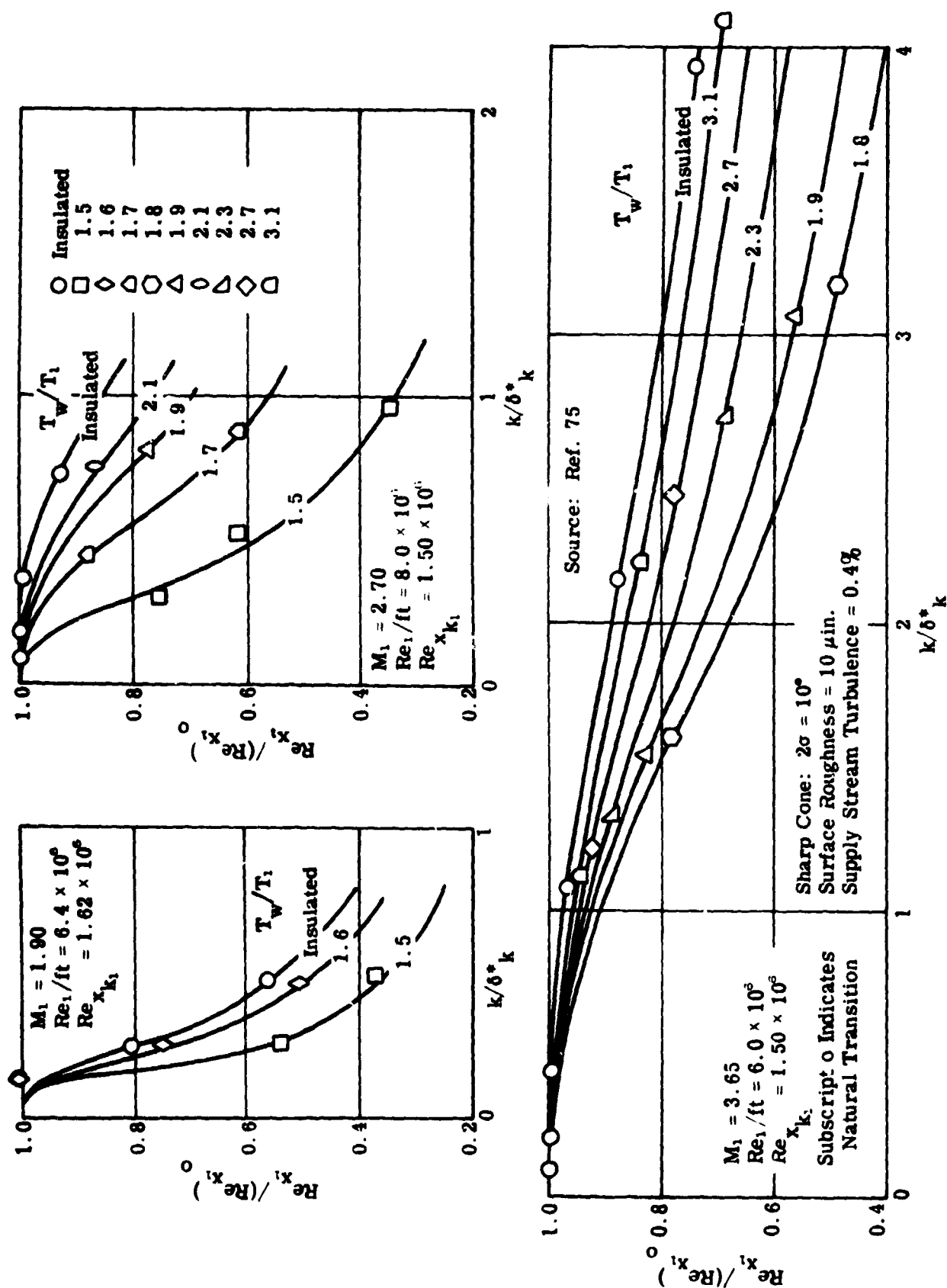


Fig. 5-24. Effect of single trip wire and heat transfer on Re_{x_1} at end of transition, sharp cones, $M_1 = 1.90$, 2.70 , and 3.65 .

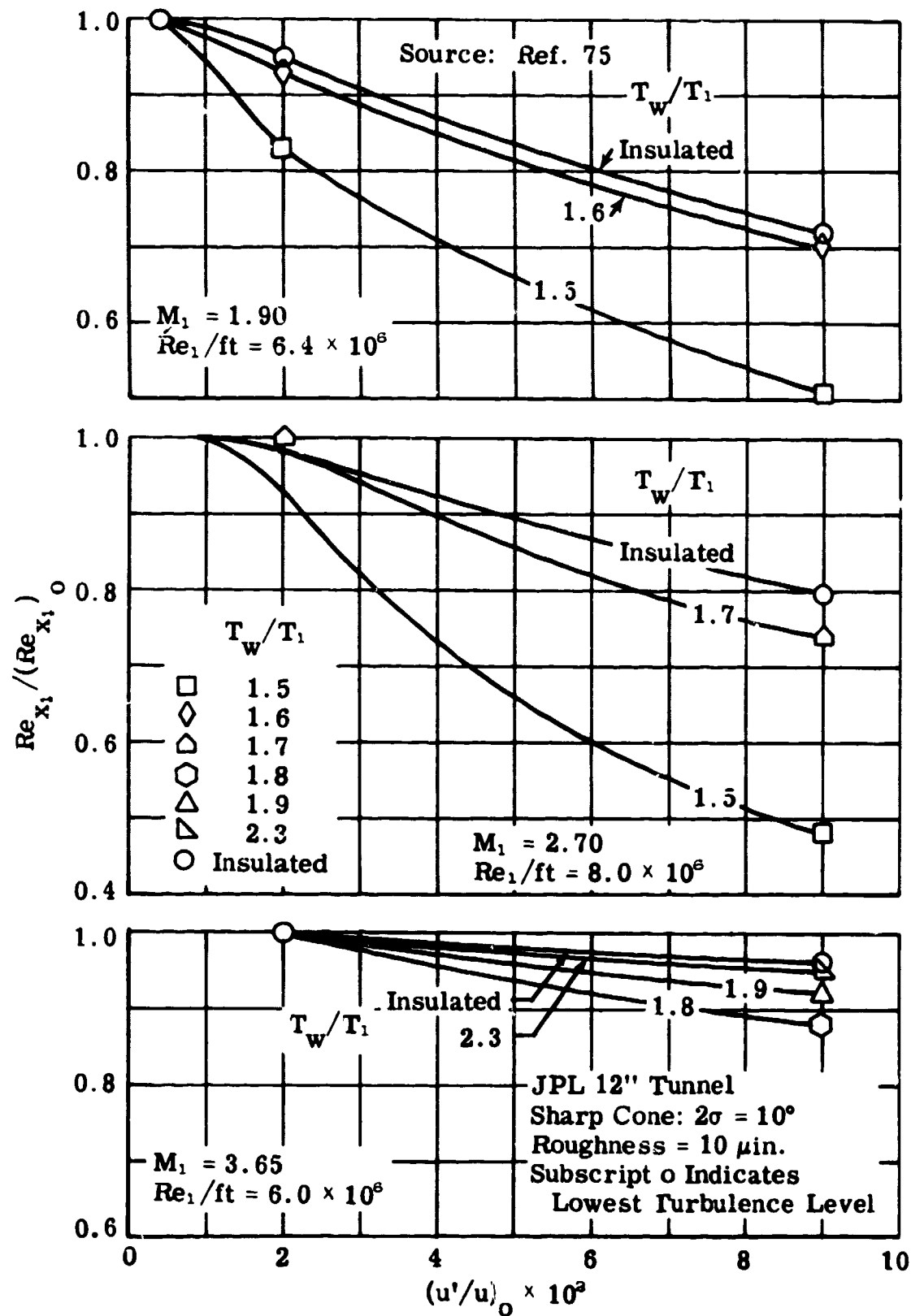


Fig. 5-25. Effect of supply stream turbulence and heat transfer on Re_{x_1} at end of transition; sharp cones; $M_1 = 1.90, 2.70, \text{ and } 3.65$.

6. Effect of Roughness on the Flat Plate Turbulent Boundary Layer

During recent years several studies have been conducted on the effect of roughness on the characteristics of supersonic turbulent boundary layers. Roughness created by sand grains is treated in Refs. 110 to 113, and two-dimensional V-groove roughness is treated in Refs. 113 to 115. Clutter, Ref. 112, gives an excellent review of the theoretical and experimental results available for computing the effects of sand roughness on turbulent skin friction. He carried out a number of skin friction calculations and presented his results in the form of useful charts. His work provides the basis for this subsection.

6.1 Incompressible Flow over a Rough Insulated Plate

The skin friction coefficient on a roughened plane surface with incompressible turbulent flow was determined theoretically by Prandtl and Schlichting (Ref. 116). Details of the method may also be found in Ref. 1 (Ch. 21) and Ref. 19 (pp. 135-155). The turbulent velocity profile was represented by

$$\frac{u}{u_\tau} = A \log y/k + B \quad (6-1)$$

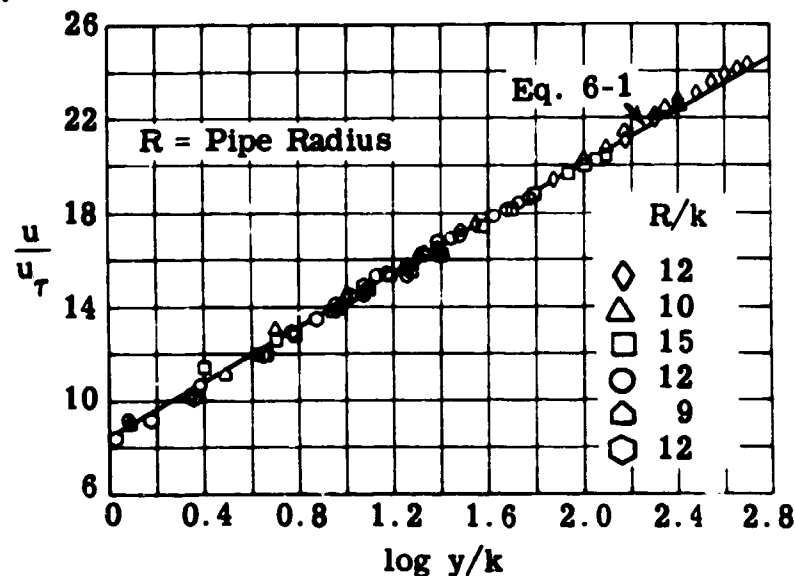
where

u_τ = the friction velocity (defined by Eq. 3-35)

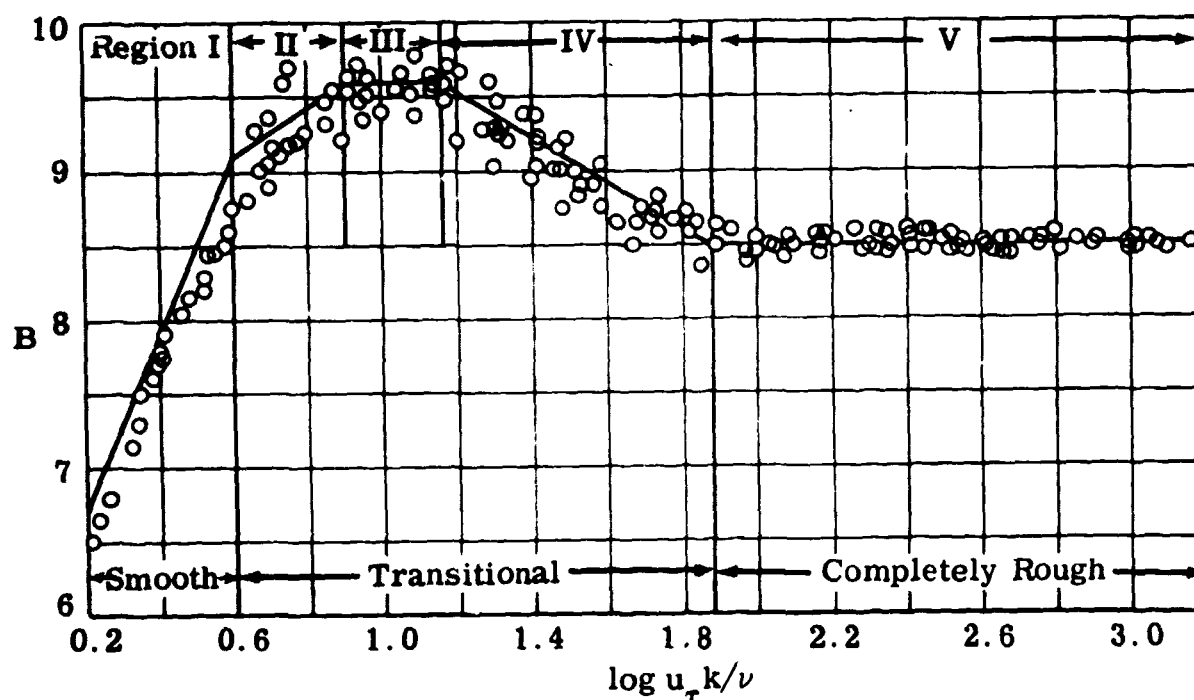
and

k = the roughness height (or characteristic dimension)

The values of A and B were determined by comparison with the experimental data obtained by Nikuradse for flow through rough pipes. The data for fully rough flow are shown in the sketch below. From this sketch it may be seen that the slope of the curve, i.e., the value of A , is about 5.75. It has been found that if A is taken as 5.85 the calculated values of C_F fit the experimental results over a wide range of Reynolds numbers. The discrepancy in values of the slope is attributed to the difference in the velocity profiles inside a pipe and over a flat plate.



The value of B as a function of $\log u_{\tau} k/\nu$ (where $u_{\tau} k/\nu$ is often called the roughness Reynolds number) has been plotted for the Nikuradse data and is shown in the next sketch. These data were used by Prandtl and Schlichting in making their flat plate calculations (Ref. 116). Before making calculations for the supersonic boundary layer, Clutter (Ref. 112) recalculated the incompressible case. He fitted straight lines to Nikuradse's data as shown on the sketch and considered the transitional region as being composed of three sections rather than a single region. It is interesting to note that the value of $u_{\tau} y/\nu$ is about 11.5 at the edge of the laminar sublayer for a smooth plate (see Subsec. 3.3). Nikuradse's data show that the boundary-layer profile begins to depart from the smooth case when $u_{\tau} k/\nu > 4$, i.e., when the diameter of the roughness grains is about 35% of the sublayer thickness.



The parameters of the equations derived by Clutter to represent the data in the different regimes are given in the following table:

Region	Limits of $u_{\tau} k/\nu$	Value of B
Smooth - I	$0 < u_{\tau} k/\nu < 4$	$5.56 + 5.85 \log u_{\tau} k/\nu$
Transition - II	$4 < u_{\tau} k/\nu < 7.95$	$8.076 + 1.672 \log u_{\tau} k/\nu$
- III	$7.95 < u_{\tau} k/\nu < 14.46$	9.58
- IV	$14.46 < u_{\tau} k/\nu < 75.9$	$11.32 - 1.50 \log u_{\tau} k/\nu$
Fully Rough - V	$75.9 < u_{\tau} k/\nu$	8.5

The values of B from the above table are substituted in Eq. 6-1 together with $A = 5.85$. After some manipulation the equation for each of the five regions may be written in the form

$$\frac{u}{u_{\tau}} = a \ln b (y u_{\tau} / \nu) = a \ln b \eta \quad (6-2)$$

where

$$\eta = y u_\tau / \nu \text{ (see Eq. 3-36)}$$

$$a = 2.54 \text{ in all cases}$$

and

b has the values shown in the following table:

Region	b	$u_\tau k / \nu$
Smooth - I	8.92	$0 < u_\tau k / \nu < 4$
Transition - II	$24.02 (u_\tau k / \nu)^{-0.7142}$	$4 < u_\tau k / \nu < 7.95$
- III	$43.41 (u_\tau k / \nu)^{-1}$	$7.95 < u_\tau k / \nu < 14.46$
- IV	$86.11 (u_\tau k / \nu)^{-1.2564}$	$14.46 < u_\tau k / \nu < 75.9$
Fully Rough - V	$23.38 (u_\tau k / \nu)^{-1}$	$u_\tau k / \nu > 75.9$

In order to make $u = 0$ when $y = 0$, Eq. 6-2 is written as

$$\frac{u}{u_\tau} = a \ln(1 + b\eta) \quad (6-3)$$

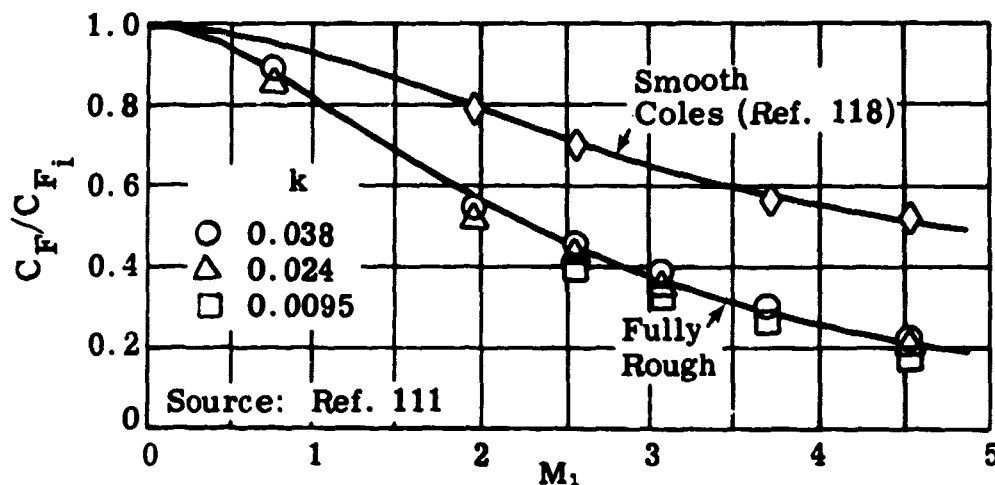
Since the values of $b\eta$ are very large over most of the boundary layer, i.e., greater than 200, Eq. 6-3 is a close approximation to Eq. 6-2.

Using the velocity profiles given by Eq. 6-3 with values of a and b from the above table, the local and mean skin friction coefficients can be calculated as functions of the Reynolds number. The method given in Ref. 116 makes use of the boundary-layer momentum integral equation. The application of this method using the boundary-layer profiles for the regions I - V, described above, is given in Ref. 112. The calculations are carried out by considering a flat plate covered with uniform roughness grains. The momentum integral equation is integrated along the surface starting from the leading edge. Care must be taken that the appropriate boundary-layer velocity profile is used at each point along the plate. At the leading edge the value of $u_\tau k / \nu$ is large and the boundary layer is fully rough; the equations of Region V then apply. As the boundary layer grows along the plate, the value of $u_\tau k / \nu$ becomes smaller until the transitional regime is reached. Regions IV, III, and II will then apply successively until Region I, with its aerodynamically smooth flow, is reached. In Region I the roughness elements are well within the laminar sublayer and no longer affect the boundary-layer profile. This is evidenced by the fact that the value of b in Eq. 6-2 for the smooth case is independent of k .

Clutter's mean skin friction coefficients, calculated for the incompressible case, are shown in Fig. 6-1. The dotted curve on Fig. 6-1 indicates the boundary between fully rough and transitional flow.

6.2 Compressible Flow over a Rough Insulated Plate

For compressible flow on an insulated plate, Goddard (Ref. 111) found experimentally that, just as in the incompressible case, the value of the skin friction is first affected by the roughness when $u_\tau k / \nu_w$ is between 4 and 10. This agrees with the experimental results of Lobb, Winkler, and Persh (Ref. 117) which show that compressibility does affect the value of $u_\tau y / \nu_w$ at the edge of the laminar sublayer on an insulated surface. Goddard found that the effect of compressibility on the mean skin friction coefficient was greater for fully rough flow than for smooth flow. This is shown on the following sketch taken from Ref. 111. The subscript "i" indicates incompressible flow over both a rough and a smooth surface.



In analyzing his results, Goddard followed the suggestion made by Liepmann (Ref. 119) that the drag must be directly proportional to $\frac{1}{2} \rho u_i^2$. This is implied by the fact that for incompressible flow and constant l/k , the mean skin friction coefficient is constant in the fully rough regime (see Fig. 6-1). To extend this reasoning to the compressible case, the density should be evaluated at the wall. Thus,

$$C_{F_i} = C_D n k^{\frac{1}{2}} \rho_i u_k^2 / \frac{1}{2} \rho_i u_i^2 \quad (6-4)$$

and

$$C_F = C_D n k^{\frac{1}{2}} \rho_w u_k^2 / \frac{1}{2} \rho_i u_i^2 \quad (6-5)$$

where

C_D = the drag coefficient of a single sand grain and is virtually independent of both Re and M since the grain may be considered as a bluff body

n = number of sand grains per unit area

u_k = velocity at $y = k$

and hence from Eqs. 6-4 and 6-5

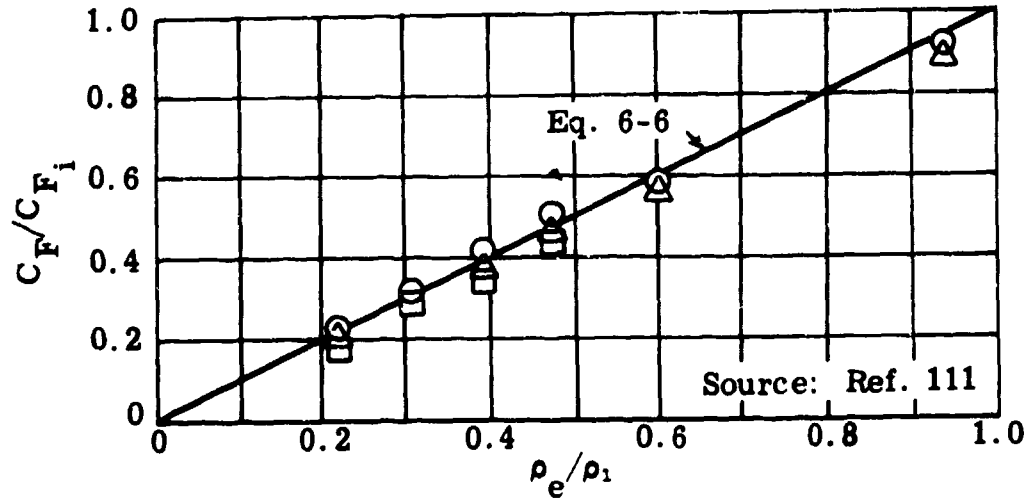
$$C_F/C_{F_i} = \rho_w/\rho_1 \quad (6-6)$$

$$= \rho_e/\rho_1 \text{ for an insulated plate}$$

The ratio ρ_e/ρ_1 is given by

$$\frac{\rho_e}{\rho_1} = \frac{T_1}{T_e} = \left(1 + r \cdot \frac{\gamma - 1}{2} M_1^2\right)^{-1} \quad (6-7)$$

Goddard replotted his data as a function of ρ_e/ρ_1 as shown in the following sketch. It can be seen that Eq. 6-6 is an excellent fit to the data for an insulated surface.



Clutter used Eq. 6-6 and the results given on Fig. 6-1 to compute mean skin friction coefficients for fully rough flow on insulated plates. To calculate skin friction coefficients for transitional and smooth flow, he used the following interpolation formula:

$$\frac{C_F}{C_{F_i}} = \left(\frac{C_F}{C_{F_i}}\right)_s - \left[\frac{\log u_\tau k/\nu_w - \log (u_\tau k/\nu_w)_s}{\log (u_\tau k/\nu_w)_{fr} - \log (u_\tau k/\nu_w)_s} \right] \left[\left(\frac{C_F}{C_{F_i}}\right) - \left(\frac{C_F}{C_{F_i}}\right)_{fr} \right] \quad (6-8)$$

He assumed that the regions of smooth, transitional, and fully rough flow were defined by the same values of $u_\tau k/\nu$ as in the incompressible case. Taking the values of $u_\tau k/\nu$ appropriate to the transitional region, Eq. 6-8 becomes

$$\frac{C_F}{C_{F_i}} = \left(\frac{C_F}{C_{F_i}}\right)_s - \left[\frac{\log u_\tau k/\nu_w - \log 4}{\log 75.9 - \log 4} \right] \left[\left(\frac{C_F}{C_{F_i}}\right) - \left(\frac{C_F}{C_{F_i}}\right)_{fr} \right] \quad (6-9)$$

where

s = smooth values

fr = fully rough values

The application of Eq. 6-9 to compute values of C_F using C_{F_i} from Fig. 6-1 is complicated by the necessity of evaluating $u_\tau k/\nu_w$. Clutter in Ref. 112 describes a method for obtaining these values. The values of $(C_F/C_{F_i})_s$ incorporate Van Driest's calculations (Ref. 120) which are in reasonable agreement with Wilson's smooth plate results given in Subsecs. 3.3 and 3.4 and Ref. 24. Clutter's mean skin friction coefficients for an insulated flat plate are given on Figs. 6-2 through 6-8 for Mach numbers from 0.5 to 5.0 and Reynolds numbers of 10^5 to 10^9 .

6.3 Compressible Flow over a Rough Plate with Heat Transfer

Clutter assumed that Eq. 6-6, using ρ_w instead of ρ_e , is valid for fully rough flow with heat transfer. He calculated the mean skin friction coefficient using the method given in Subsec. 6.2. For flow calculations in the transitional regime, the ratio $(C_F/C_{F_i})_s$ which appears in Eq. 6-9 was obtained from Ref. 120 which gives the coefficients in the presence of heat transfer. It is further assumed that the values of $u_\tau k/\nu_w$ which define the smooth, transitional, and fully rough regions are unaffected by both heat transfer and compressibility. Clutter admits that this assumption is open to question since the experimental results of Ref. 117 indicate that heat transfer does have some effect on the laminar sublayer thickness for a smooth plate. The first assumption, i.e., that Eq. 6-6 remains valid even in the presence of heat transfer, certainly is also open to question. When there is no heat transfer the density is nearly constant near the surface and is thus virtually equal to the wall value. This is no longer true for the heat transfer case in which the temperature and density gradients at the surface are large. However, Clutter's method, in spite of its uncertainties, may be used to indicate the effects of roughness with heat transfer. Additional experimental work is needed to validate this extension into the heat transfer regime.

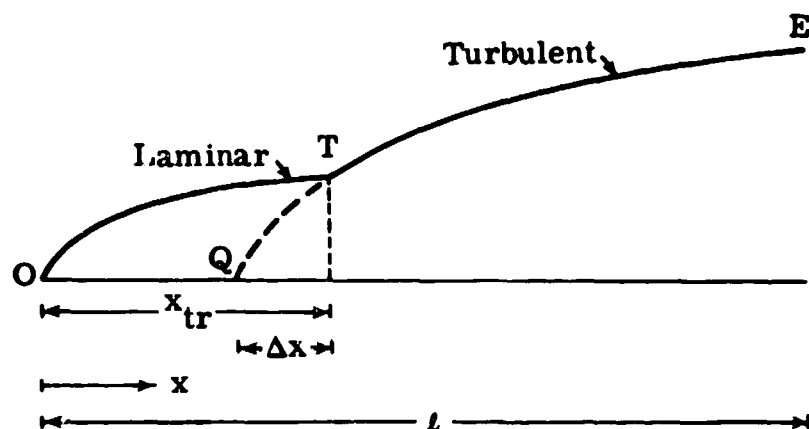
Equation 6-6 can also be assumed to hold if C_F/C_{F_i} is replaced by C_f/C_{f_i} in the fully rough region. Clutter apparently used this assumption together with an interpolation formula similar to Eq. 6-9 to calculate the local skin friction coefficients in the transitional region.

Curves for mean skin friction coefficients for $T_w = T_1$ are given on Figs. 6-9 to 6-15, and the local skin friction coefficients are plotted on Figs. 6-16 to 6-22. The figures cover the Mach number range from 0.5 to 5.0 and Reynolds numbers from 10^5 to 10^9 .

6.4 Transition from Laminar to Turbulent Flow on a Roughened Plate

In the preceding subsections it has been assumed that turbulent flow originates at the leading edge. In practical cases a region of laminar flow may exist ahead of the turbulent region even on roughened plates. Some idea of the extent of this region can be obtained for most cases of practical interest from the data of Subsec. 5.6. When the location of transition is known, the laminar skin friction coefficient may be obtained and combined with the fully turbulent values derived by the methods of this subsection. Clutter has made calculations for various assumed transition locations; his method will be outlined here.

In order to obtain the mean skin friction coefficient over the entire plate, it is assumed that the turbulent boundary layer behaves as if it started at the point Q as shown in the sketch below.



Since $C_F = 2\theta/x$ whether the flow is laminar or turbulent, at the point of transition, T,

$$2\theta_{tr} = C_{F_L} x_{tr} = C_{F_T} \Delta x \quad (6-10)$$

and

$$C_{F_L} \frac{x_{tr} u_1}{\nu} = C_{F_T} \frac{\Delta x u_1}{\nu} \quad (6-11)$$

If the values of Re_l and x_{tr}/l (where l is the total length of the plate) are known, then $Re_{x_{tr}}$ and hence C_{F_L} can be determined. For a given roughness size, l/k , $u_1 k/\nu$ can be calculated, and thus from Fig. 6-1 the required Reynolds numbers $\Delta x u_1/\nu$ can be found to satisfy Eq. 6-11. The mean skin friction coefficient for the turbulent section (TE) can be read from Fig. 6-1 for the known value of ku_1/ν , where

$$Re_{l_T} = \left[\frac{\Delta x}{l} + \frac{l - x_{tr}}{l} \right] Re_l \quad (6-12)$$

Finally the value of C_F over the whole plate is given by

$$C_F = \left[\frac{\Delta x}{l} + \frac{l - x_{tr}}{l} \right] C_{F_T} \quad (6-13)$$

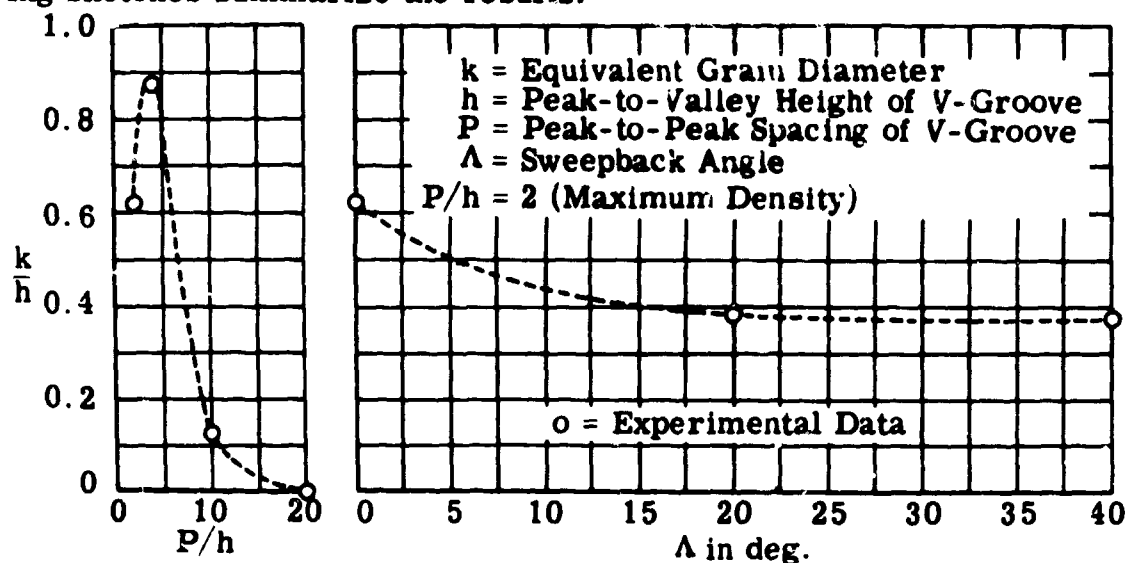
Values of C_F obtained from Eq. 6-13 are given in Ref. 112 for $x_{tr}/L = 0.1$, 0.2, 0.3, 0.4, and 0.5 and Mach numbers from 0 to 5 and Reynolds numbers from 10^5 to 10^9 .

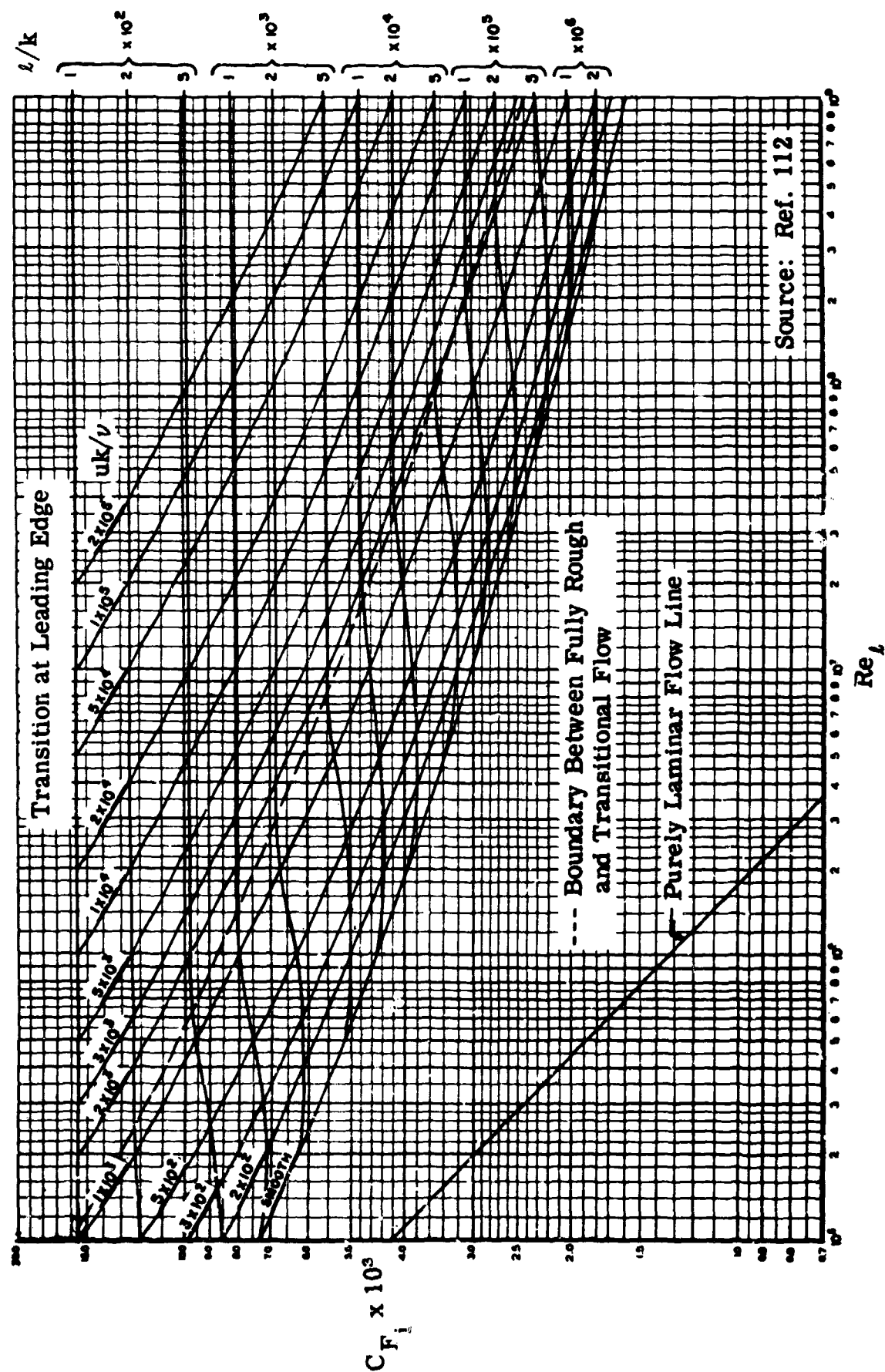
6.5 Roughness Types

The graphs and calculations that have been presented in this subsection have assumed a sand-type roughness composed of spherical grains with diameter k . In actual practice the surface roughness could be of many types and of varying degrees of uniformity. If the roughness of any surface is uniformly distributed and can be expressed in terms of an equivalent grain roughness, then the extensive experimental results may be used to predict the skin friction for that surface. Some experimentally determined values of the equivalent sand roughness for a few types of rough surfaces are given in the following table taken from Ref. 112.

Type of Surface	Equivalent Sand Roughness k (i.n.)
Aerodynamically smooth	0
Polished metal or wood	$0.02 - 0.08 \times 10^{-3}$
Natural sheet metal	0.16×10^{-3}
Smooth matte paint, carefully applied	0.25×10^{-3}
Standard camouflage paint, average application	0.40×10^{-3}
Camouflage paint, mass-production spray	1.20×10^{-3}
Dip-galvanized metal surface	6×10^{-3}
Natural surface of cast iron	10×10^{-3}

Young, in Ref. 115, gives several suggestions for the experimental determination of the equivalent sand grain roughness of a surface, all of which require a confidence in the existing relations among the properties associated with sand roughness. Fenter (Ref. 113) describes a systematic test of V-grooves in which, unfortunately, the height and width of the groove were maintained constant. The following sketches summarize the results.



Fig. 6-1. Mean skin friction coefficients for a sand-roughened insulated plate; $M = 0$.

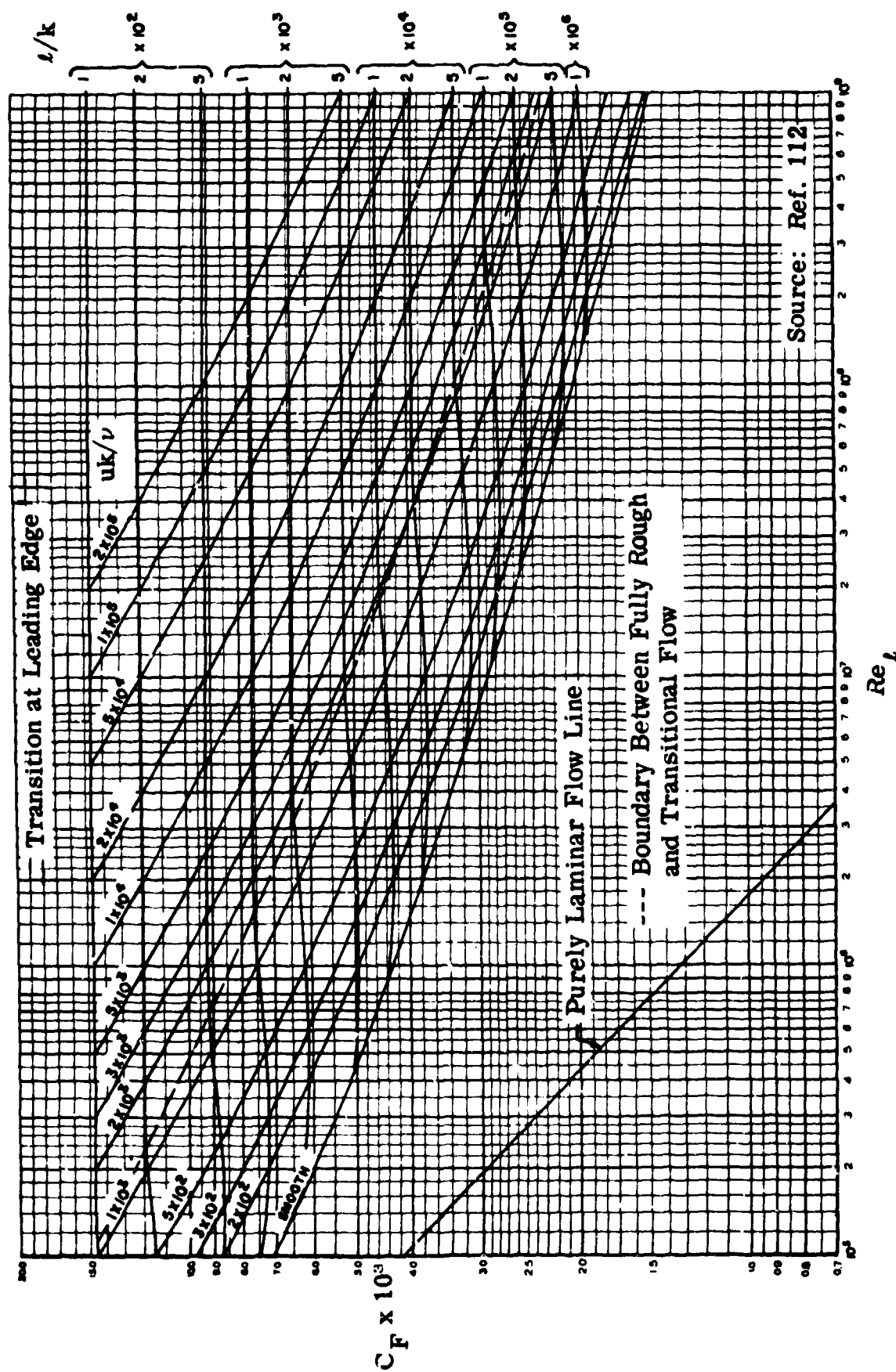


Fig. 6-2. Mean skin friction coefficients for a sand-roughened insulated plate;
 $M = 0.5$.

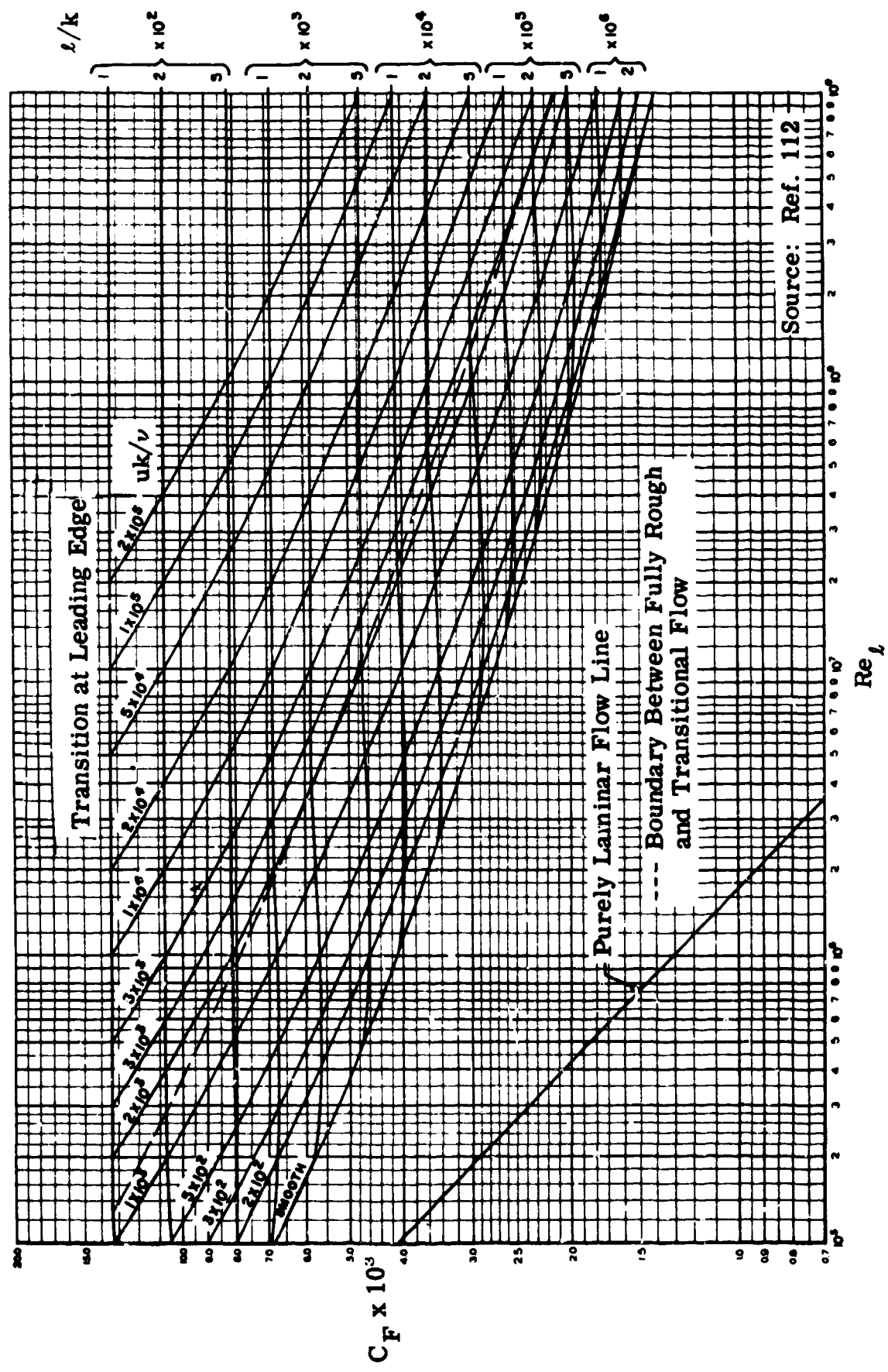


Fig. 6-3. Mean skin friction coefficients for a sand-roughened insulated plate;
 $M = 1.0$.

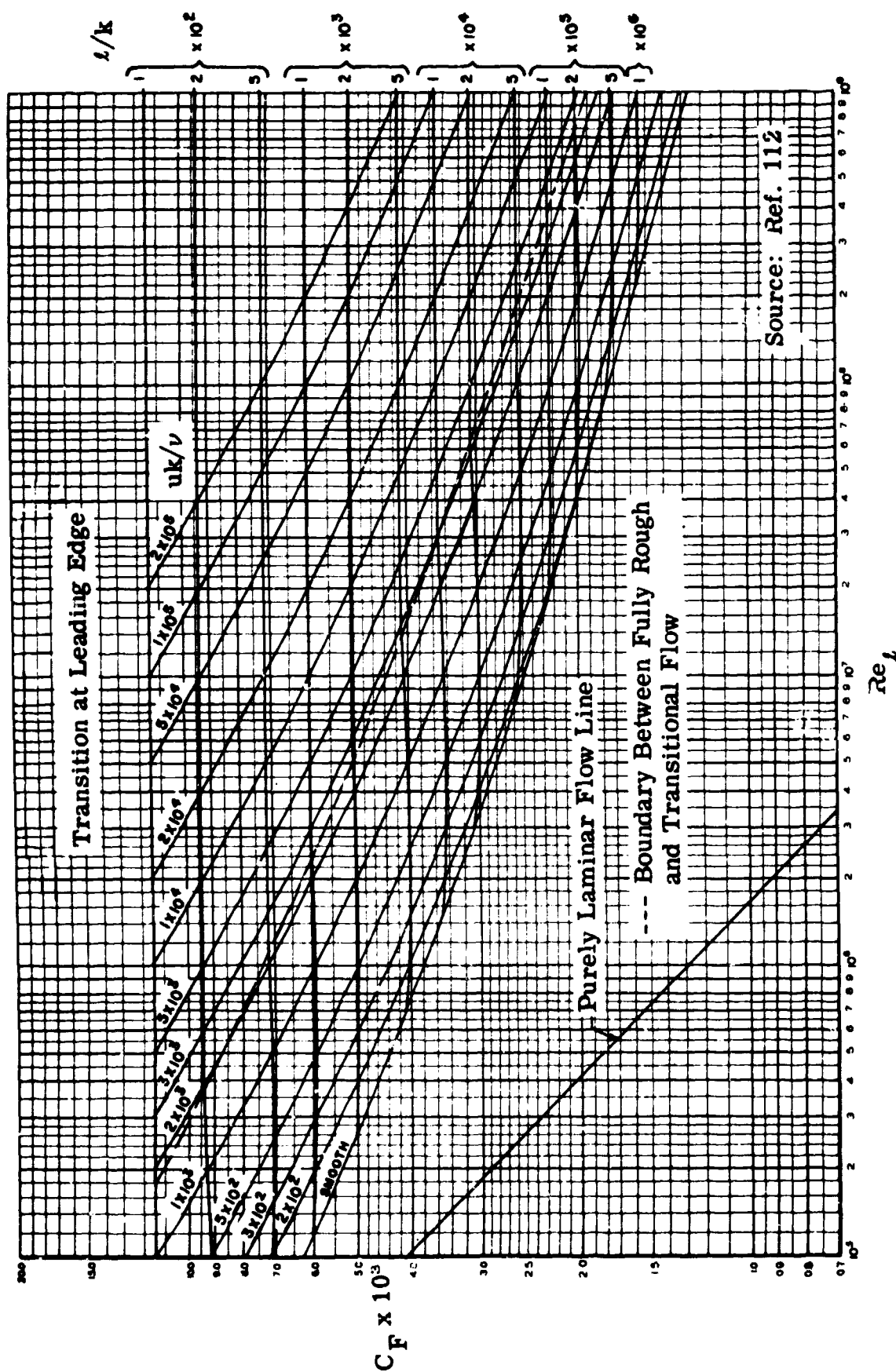


Fig. 6-4. Mean skin friction coefficients for a sand-roughened insulated plate; $M = 1.5$.

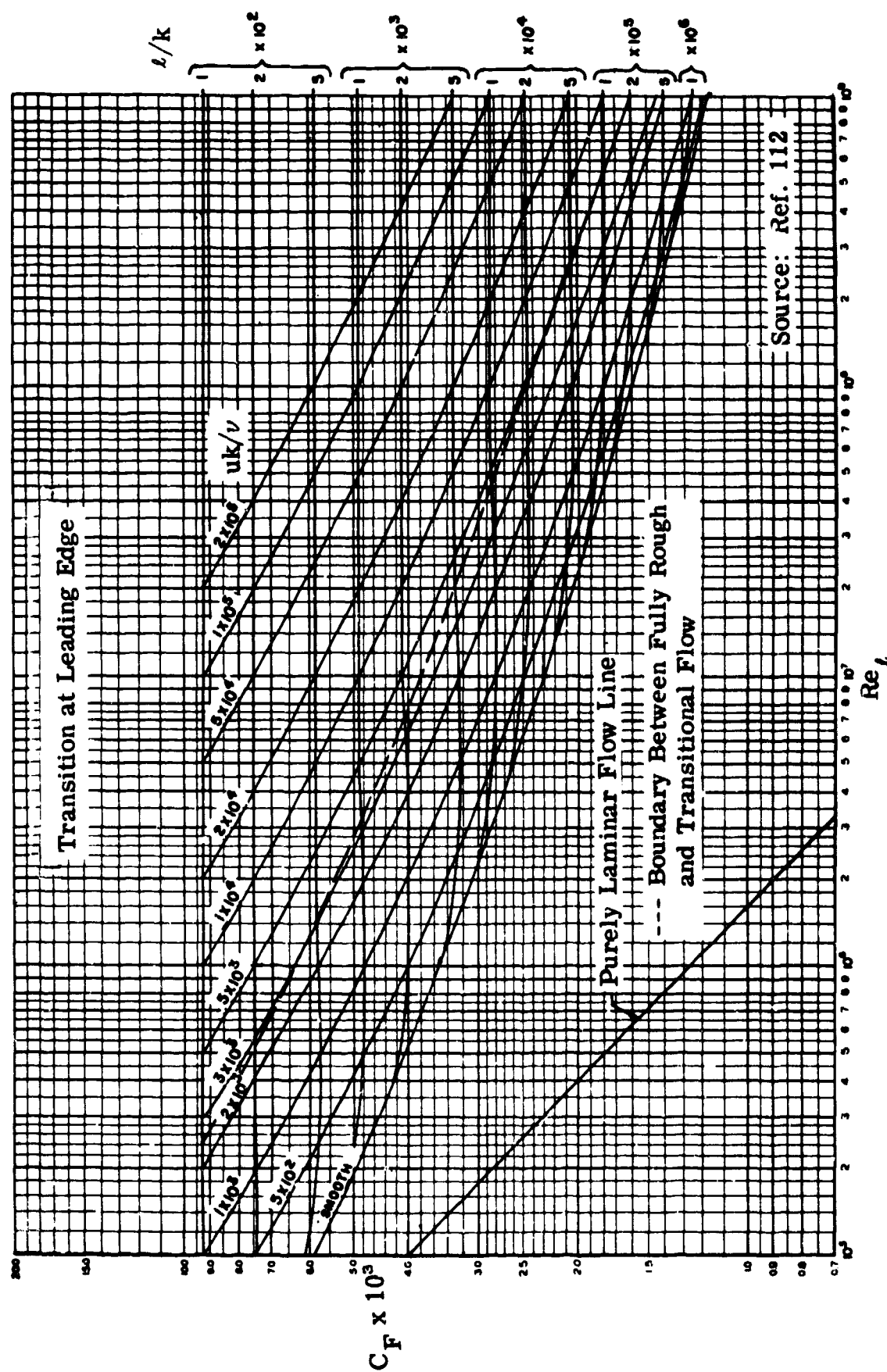
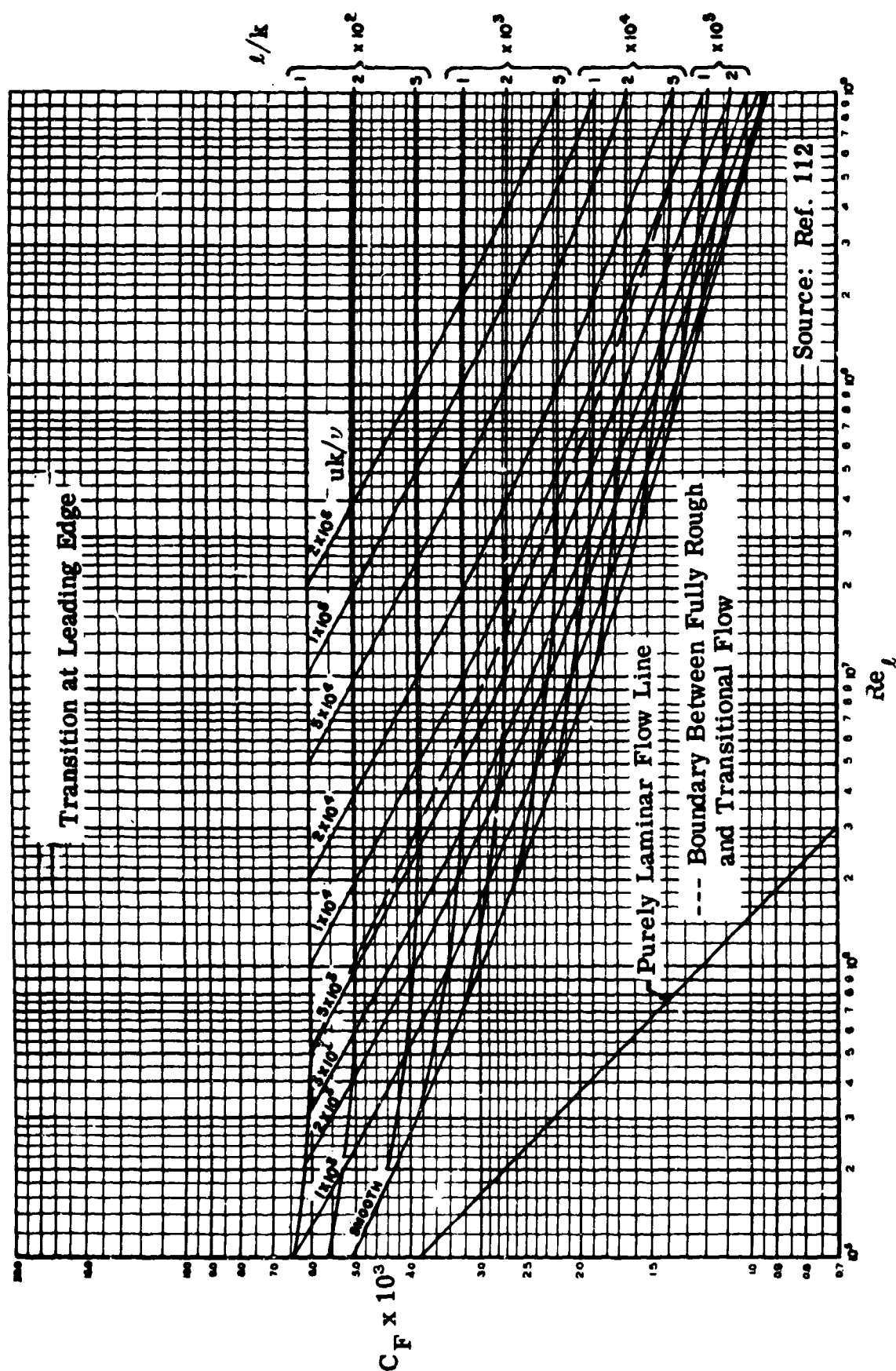


Fig. 6-5. Mean skin friction coefficients for a sand-roughened insulated plate; $M = 2.0$.

Fig. 6-6. Mean skin friction coefficients for a sand-roughened insulated plate; $M = 3.0$.

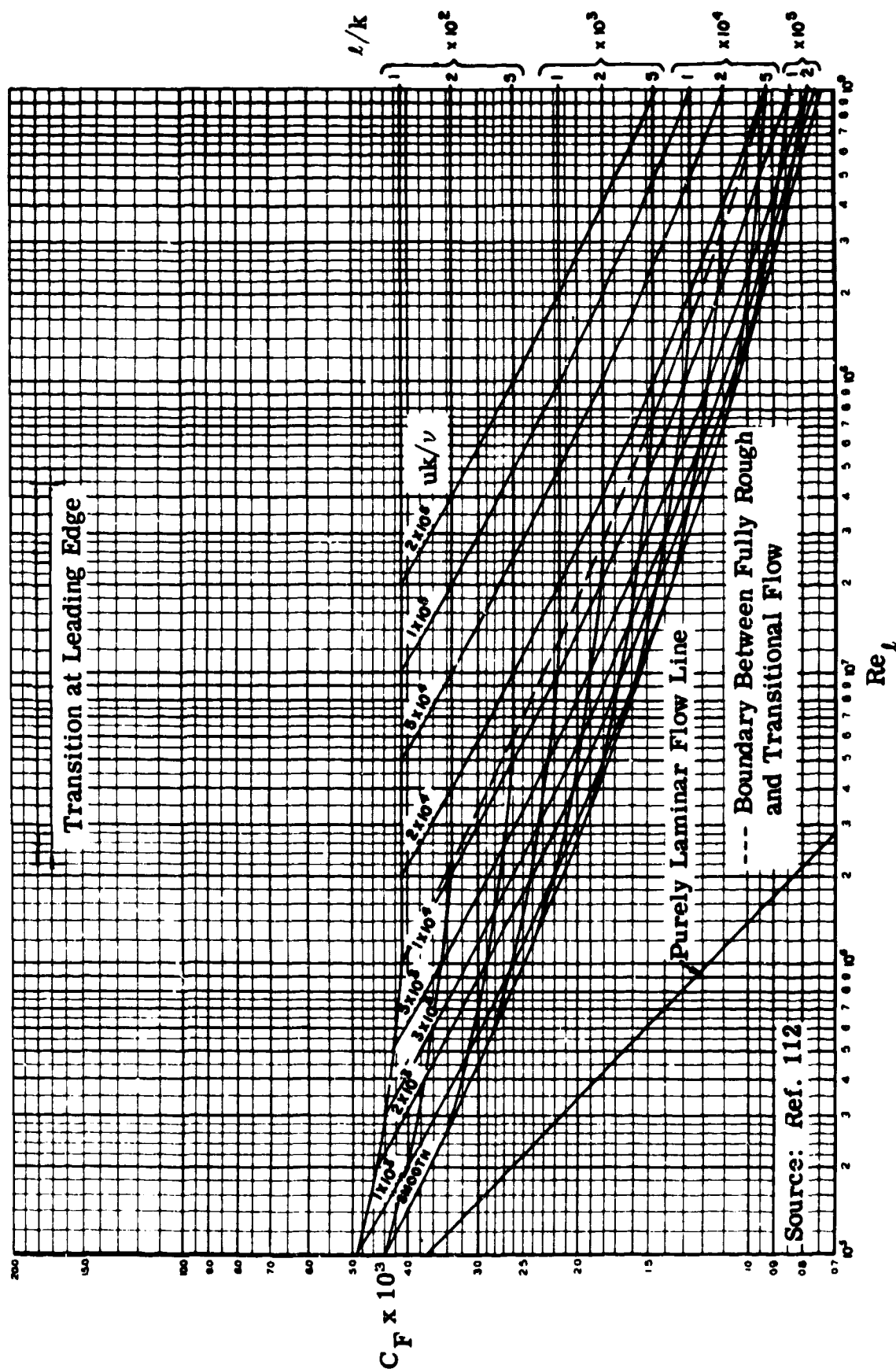


Fig. 6-7. Mean skin friction coefficients for a sand-roughened insulated plate; $M = 4.0$.

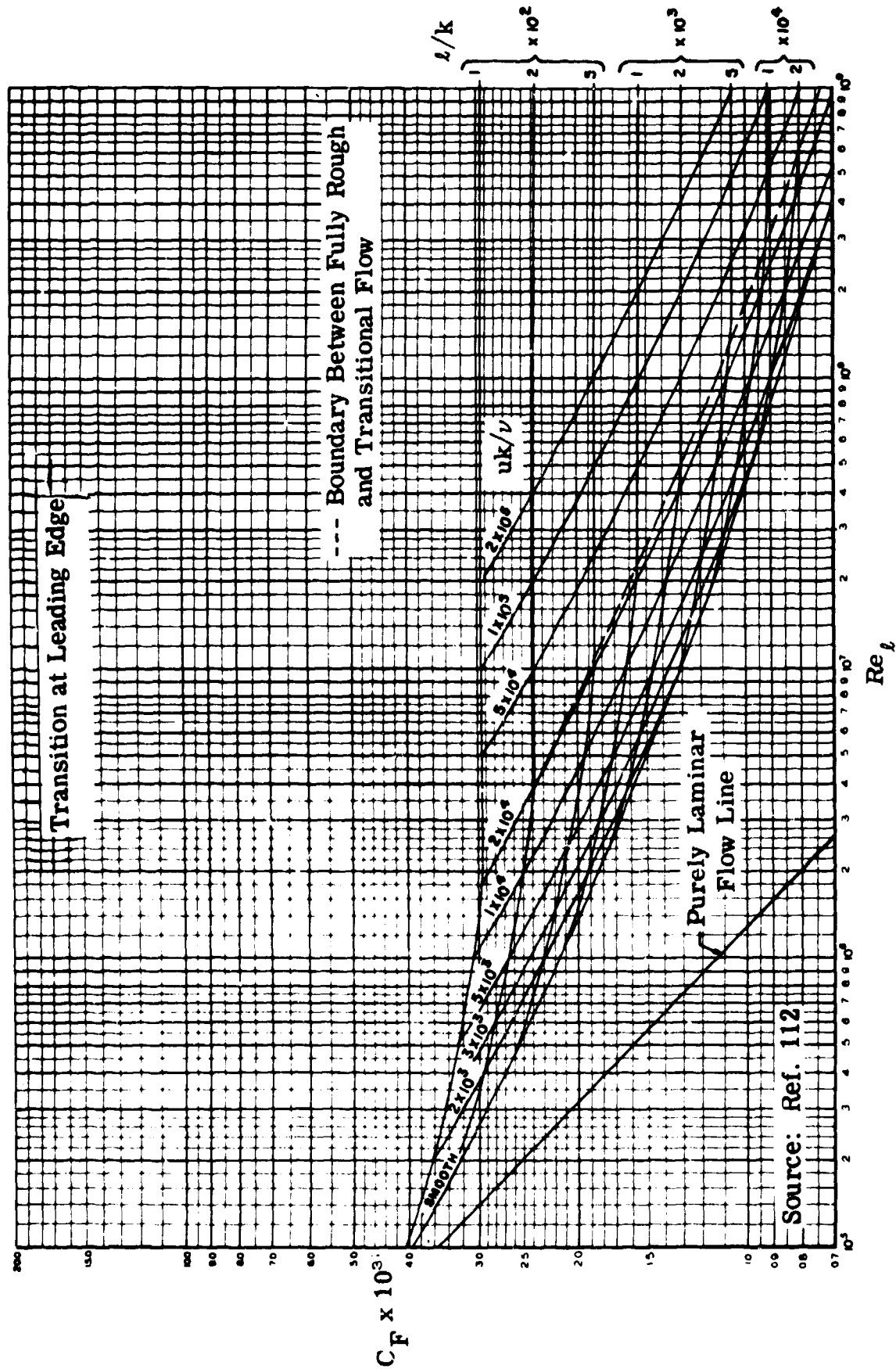


Fig. 6-8. Mean skin friction coefficients for a sand-roughened insulated plate; $M = 5.0$.

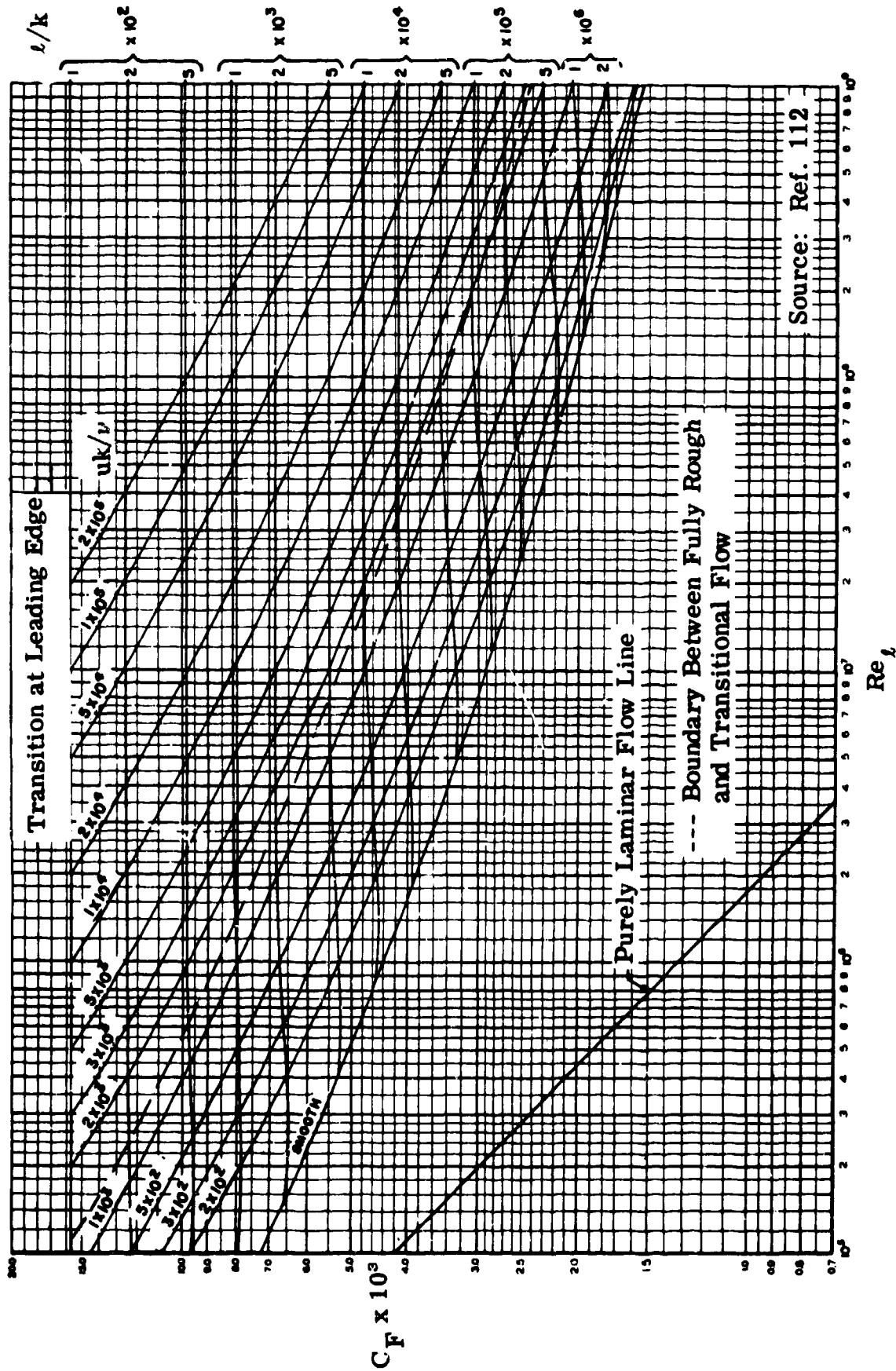


Fig. 6-9. Mean skin friction coefficients for a sand-roughened plate;

$$T_w = T_1; M = 0.5.$$

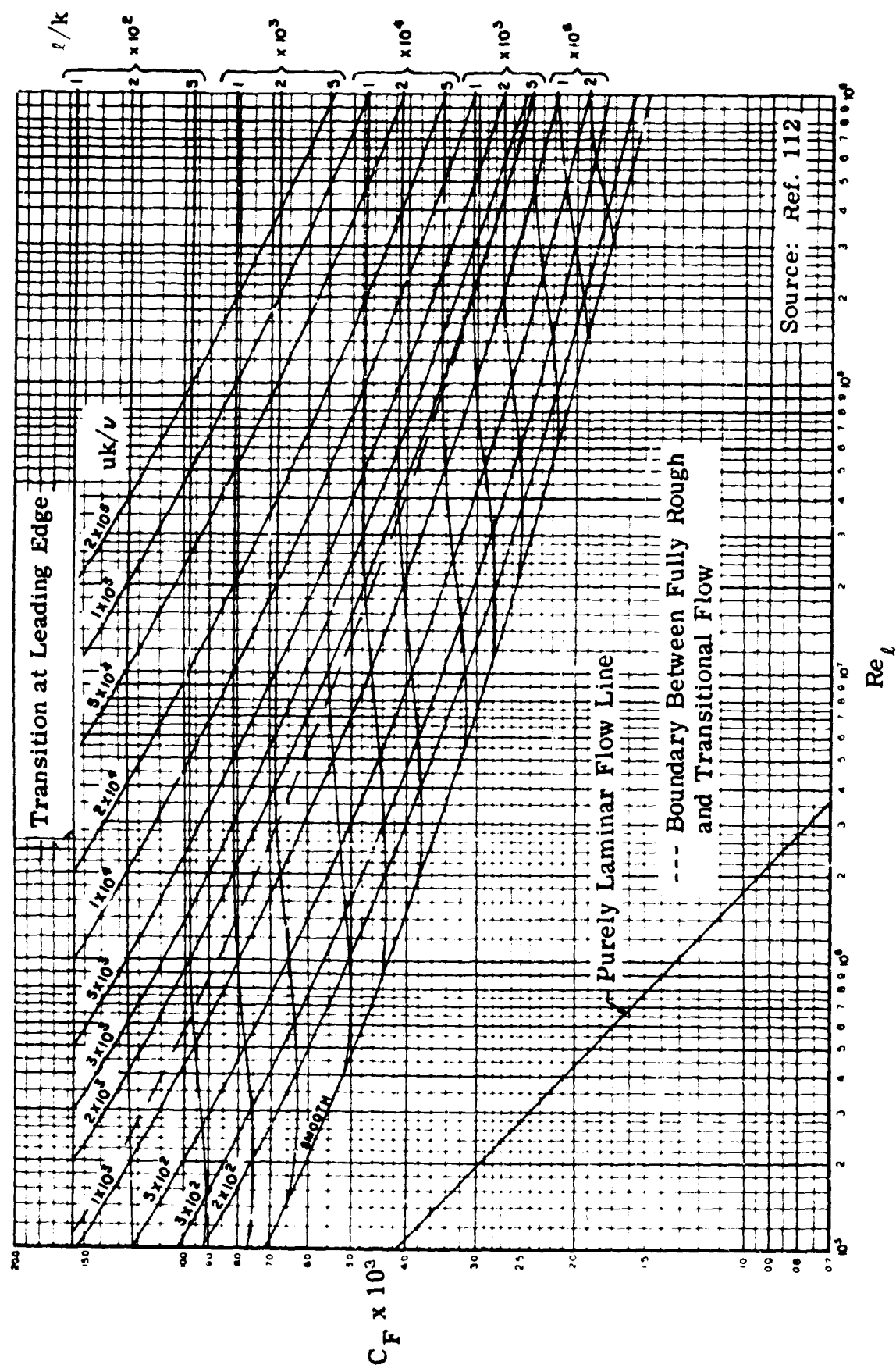


Fig. 6-10. Mean skin friction coefficients for a sand-roughened plate;
 $T_w = T_1$; $M = 1.0$.

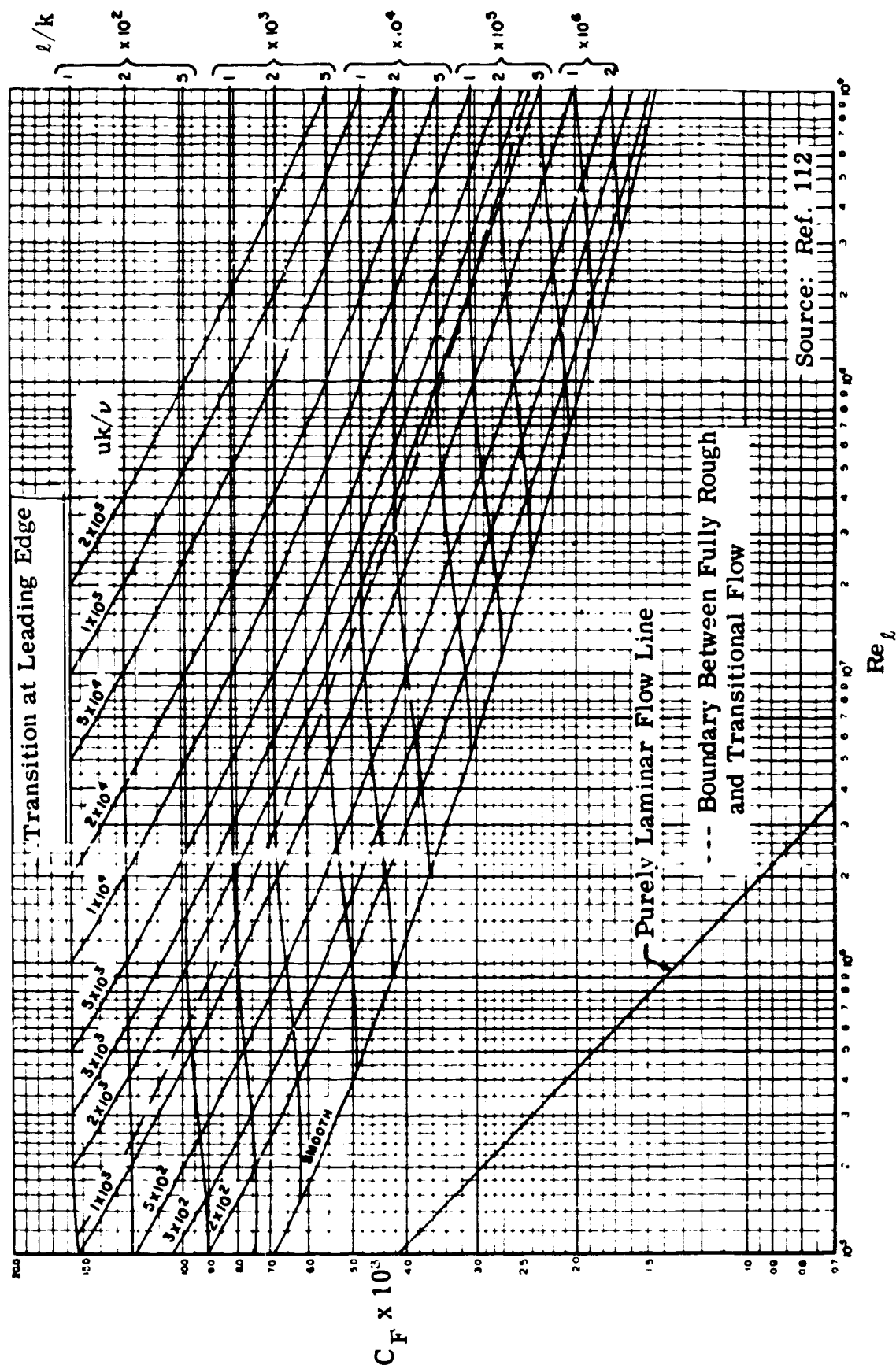


Fig. 6-11. Mean skin friction coefficients for a sand-roughened plate;
 $T_w = T_1$; $M = 1.5$.

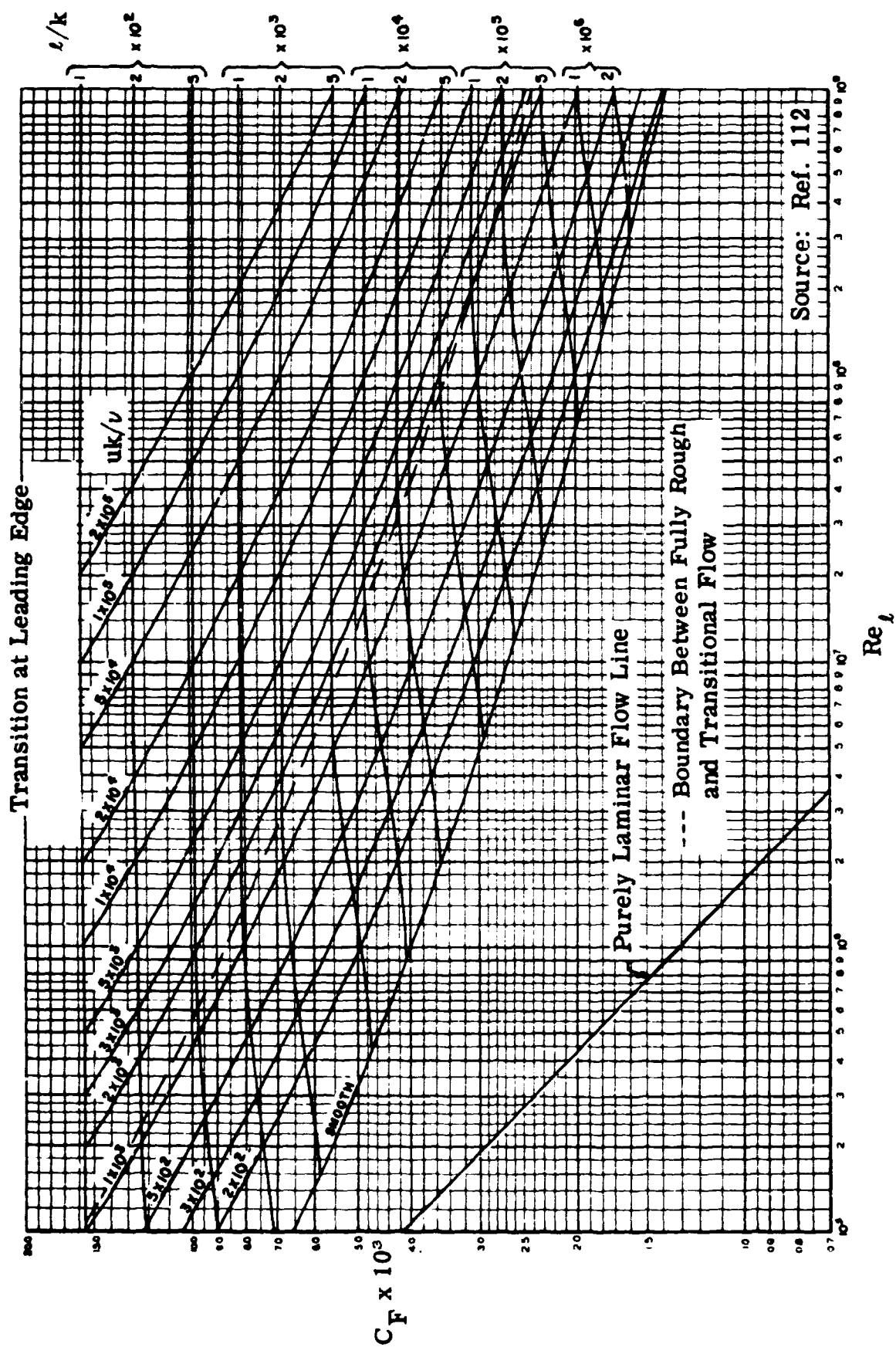


Fig. 6-12. Mean skin friction coefficients for a sand-roughened plate;

$$T_w = T_1; M = 2.0.$$

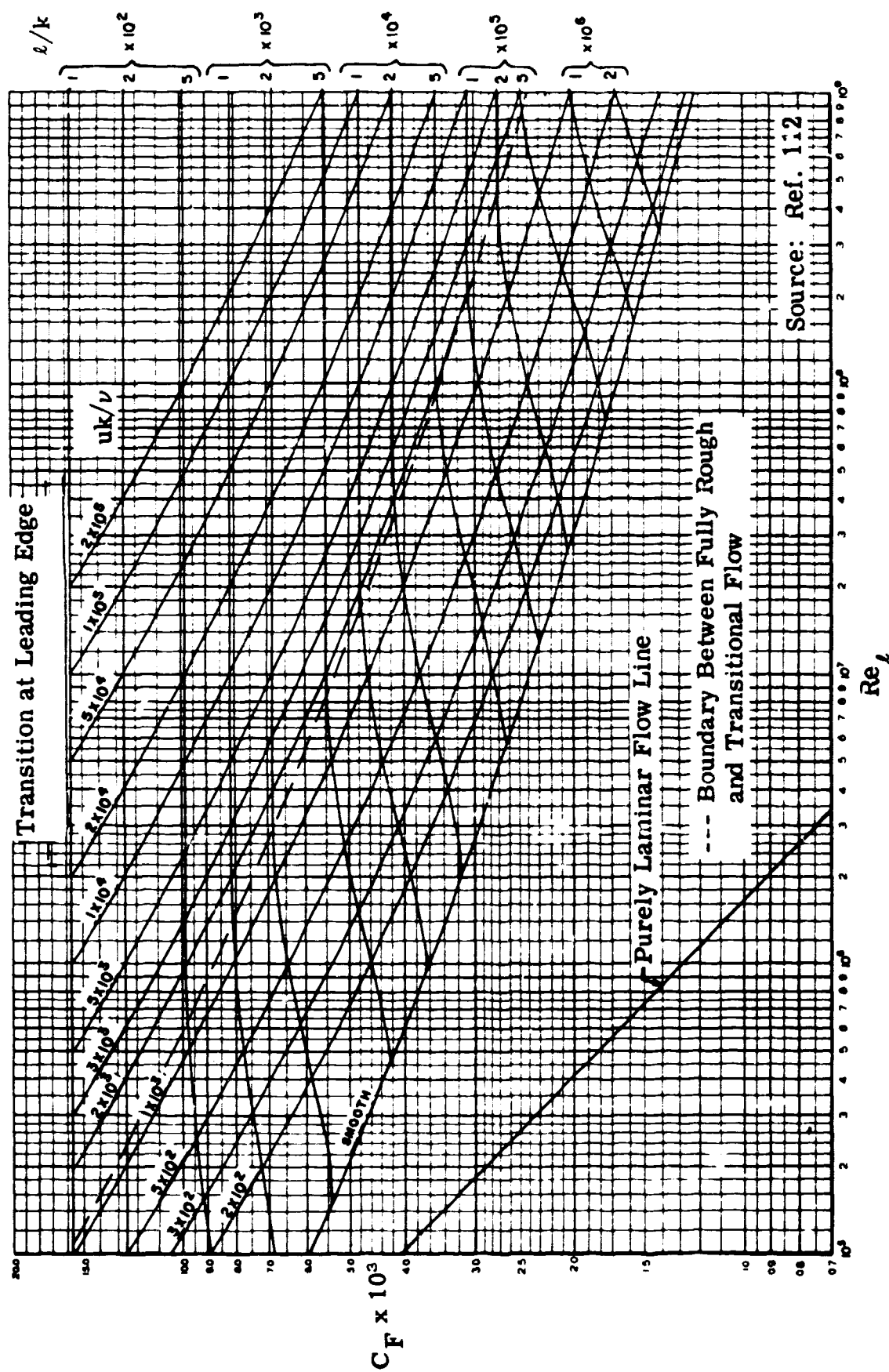


Fig. 6-13. Mean skin friction coefficients for a sand-roughened plate;
 $T_w = T_1$; $M = 3.0$.

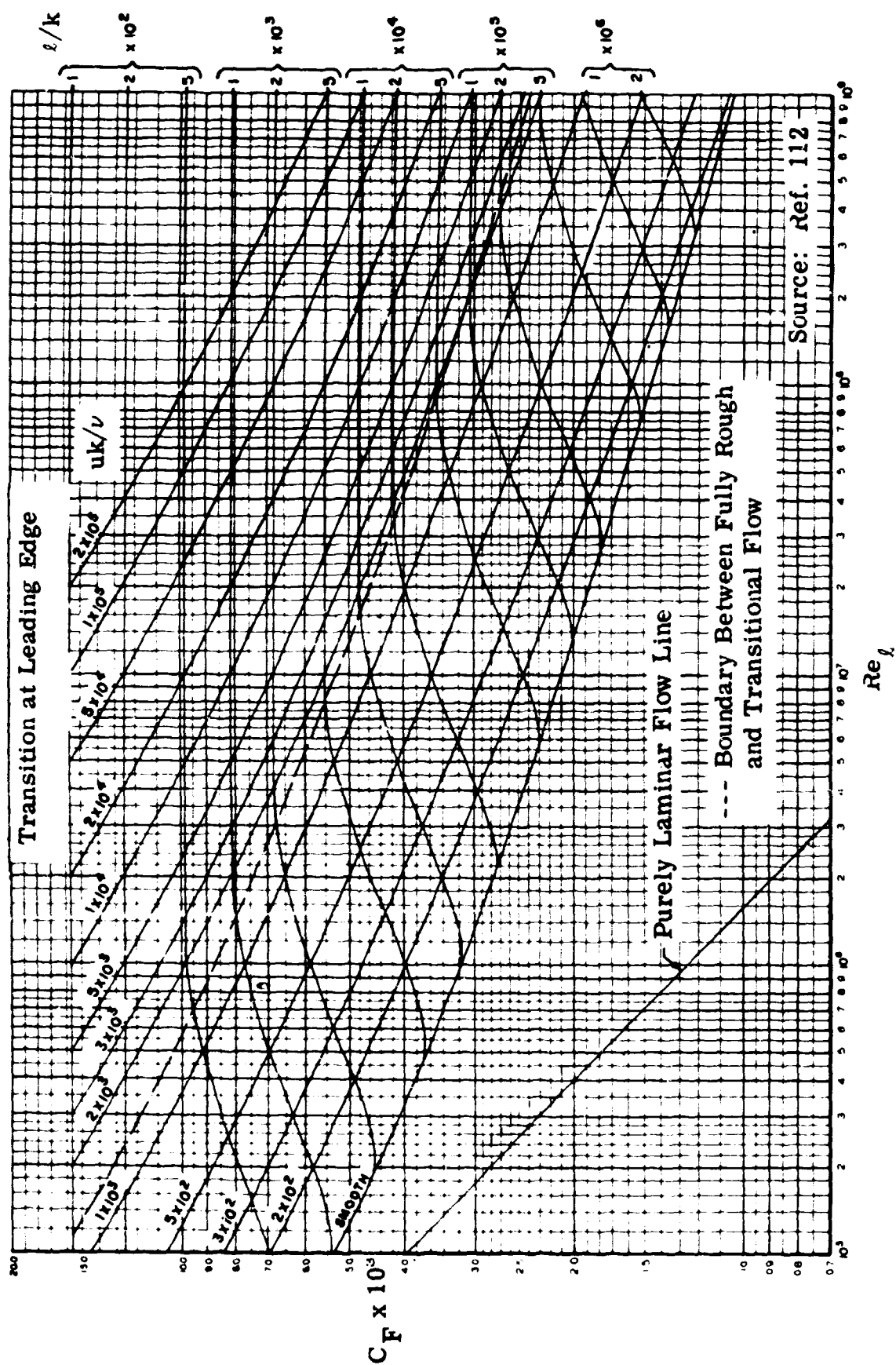


Fig. 6-14. Mean skin friction coefficients for a sand-roughened plate;
 $T_w = T_1$; $M = 4.0$.

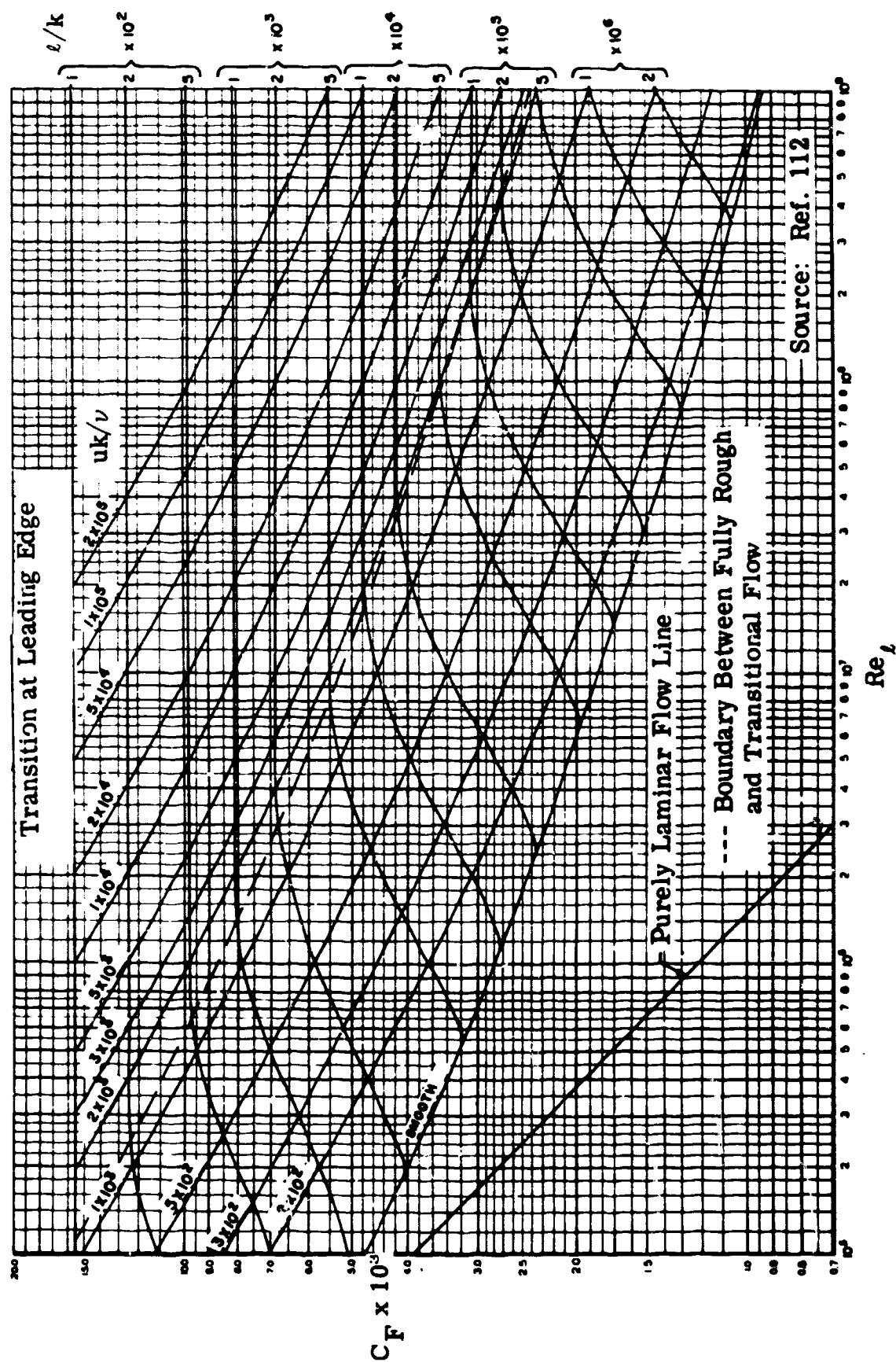


Fig. 6-15. Mean skin friction coefficients for a sand-roughened plate;
 $T_w = T_1$; $M = 5.0$.

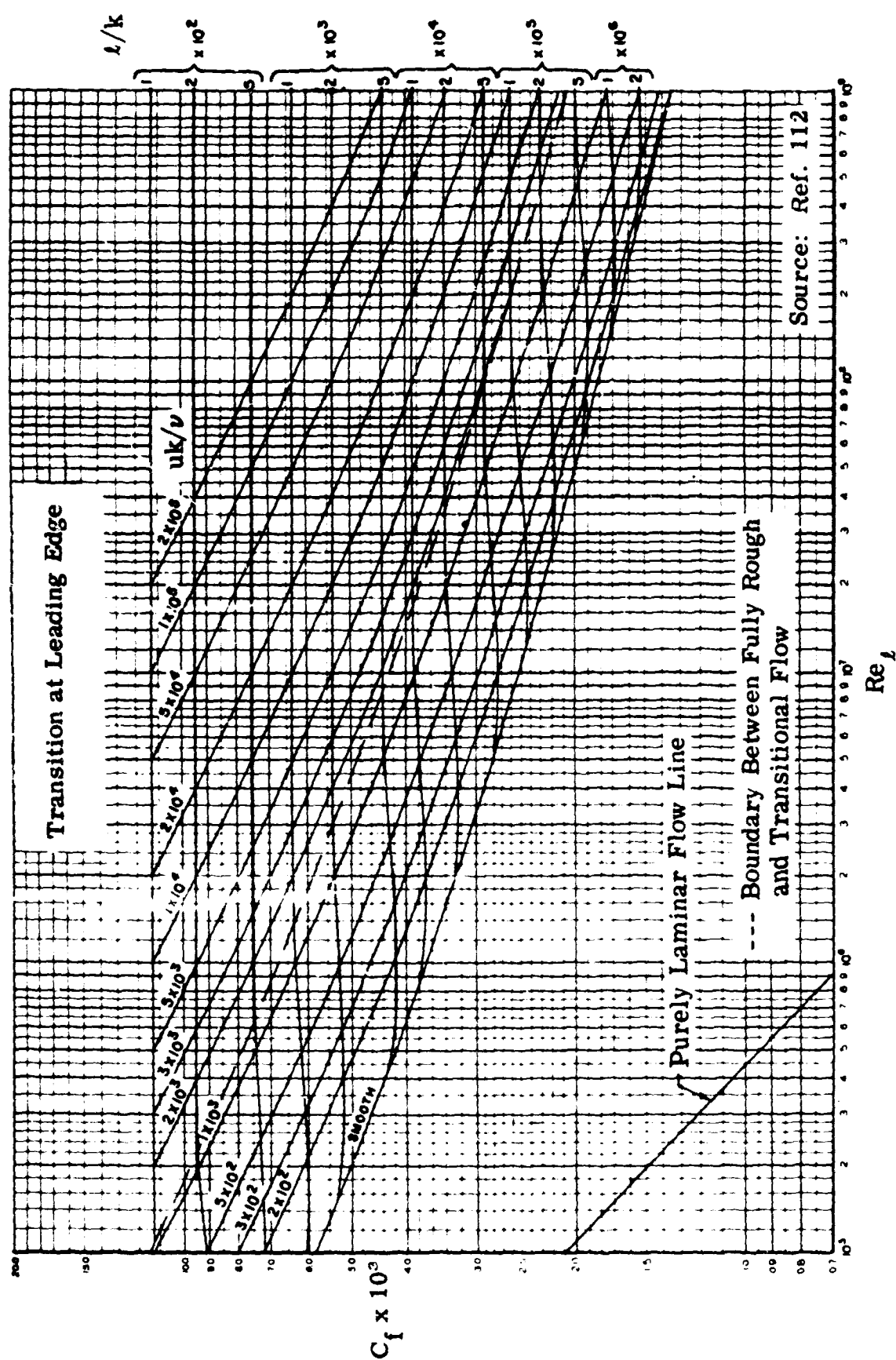


Fig. 6-16. Local skin friction coefficients for a sand-roughened plate;
 $T_w = T_1$; $M = 0.5$.

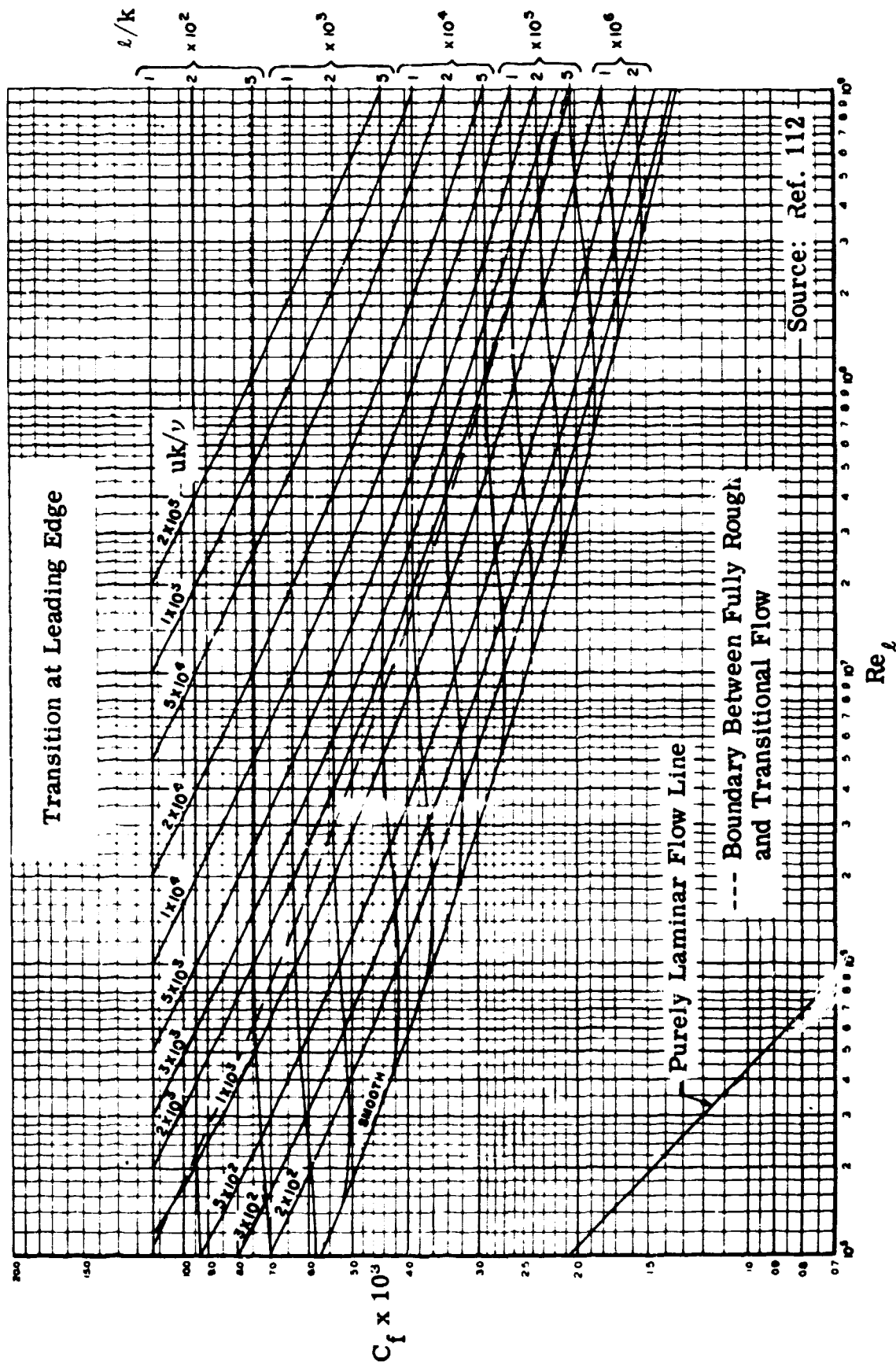


Fig. 6-17. Local skin friction coefficients for a sand-roughened plate;
 $T_w = T_1$; $M = 1.0$.

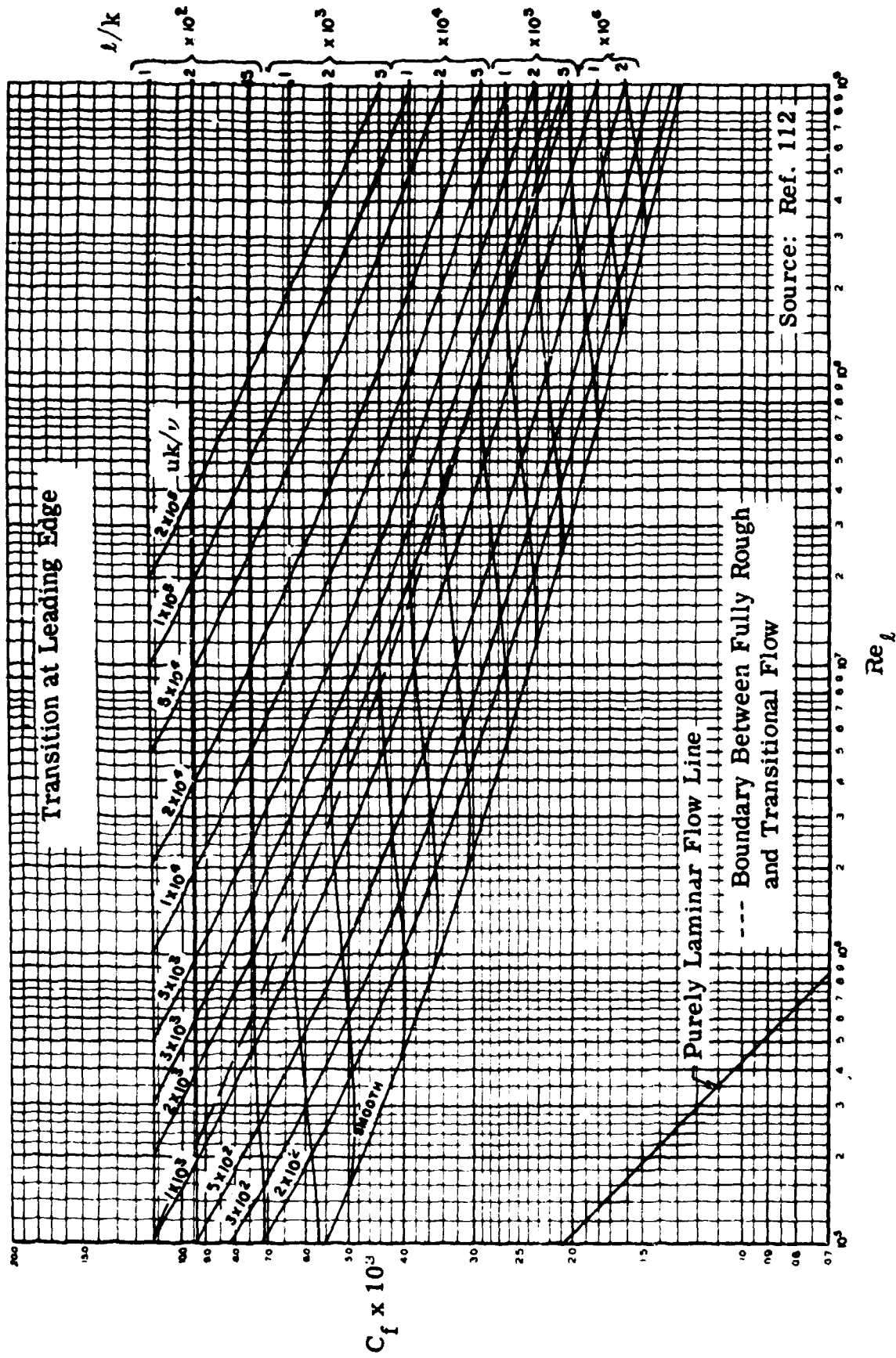


Fig. 6-18. Local skin friction coefficients for a sand-roughened plate;
 $T_w = T_1$; $M = 1.5$.

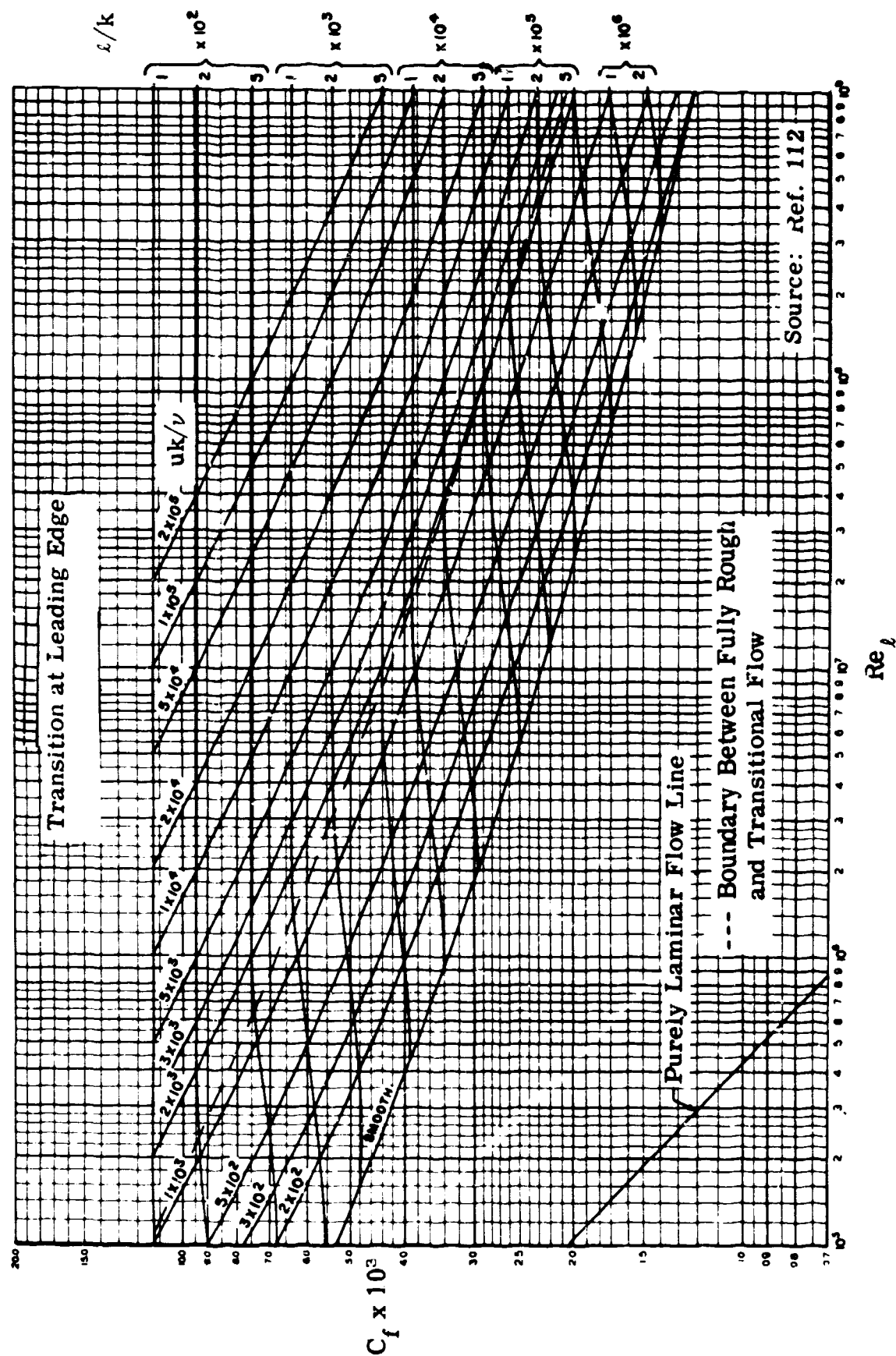


Fig. 6-19. Local skin friction coefficients for a sand-roughened plate;
 $T_w = T_1$; $M = 2.0$.

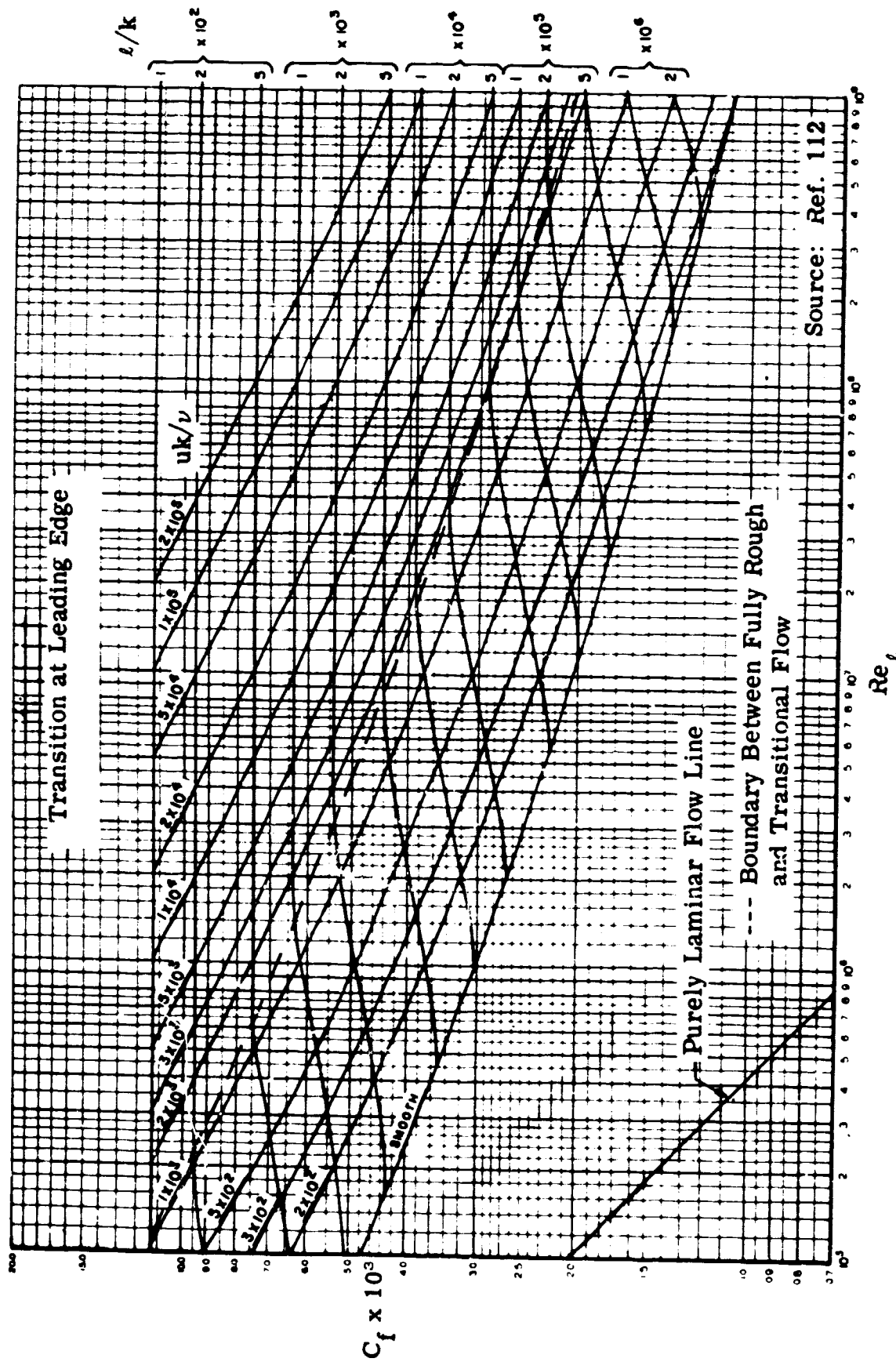


Fig. 6-20. Local skin friction coefficients for a sand-roughened plate;
 $T_w = T_1$; $M = 3.0$.

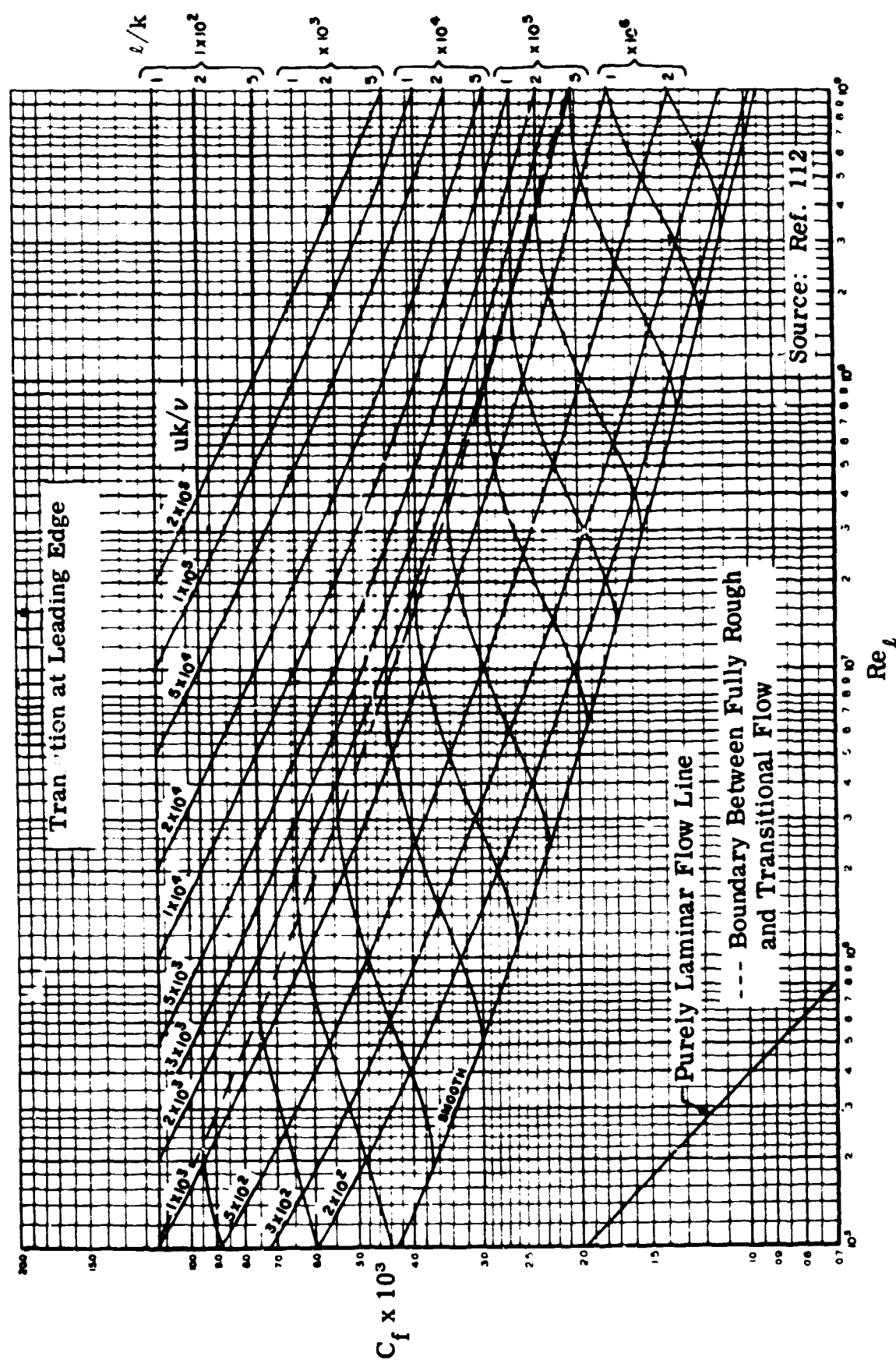


Fig. 6-21. Local skin friction coefficients for a sand-roughened plate;
 $T_w = T_1$; $M = 4.0$.

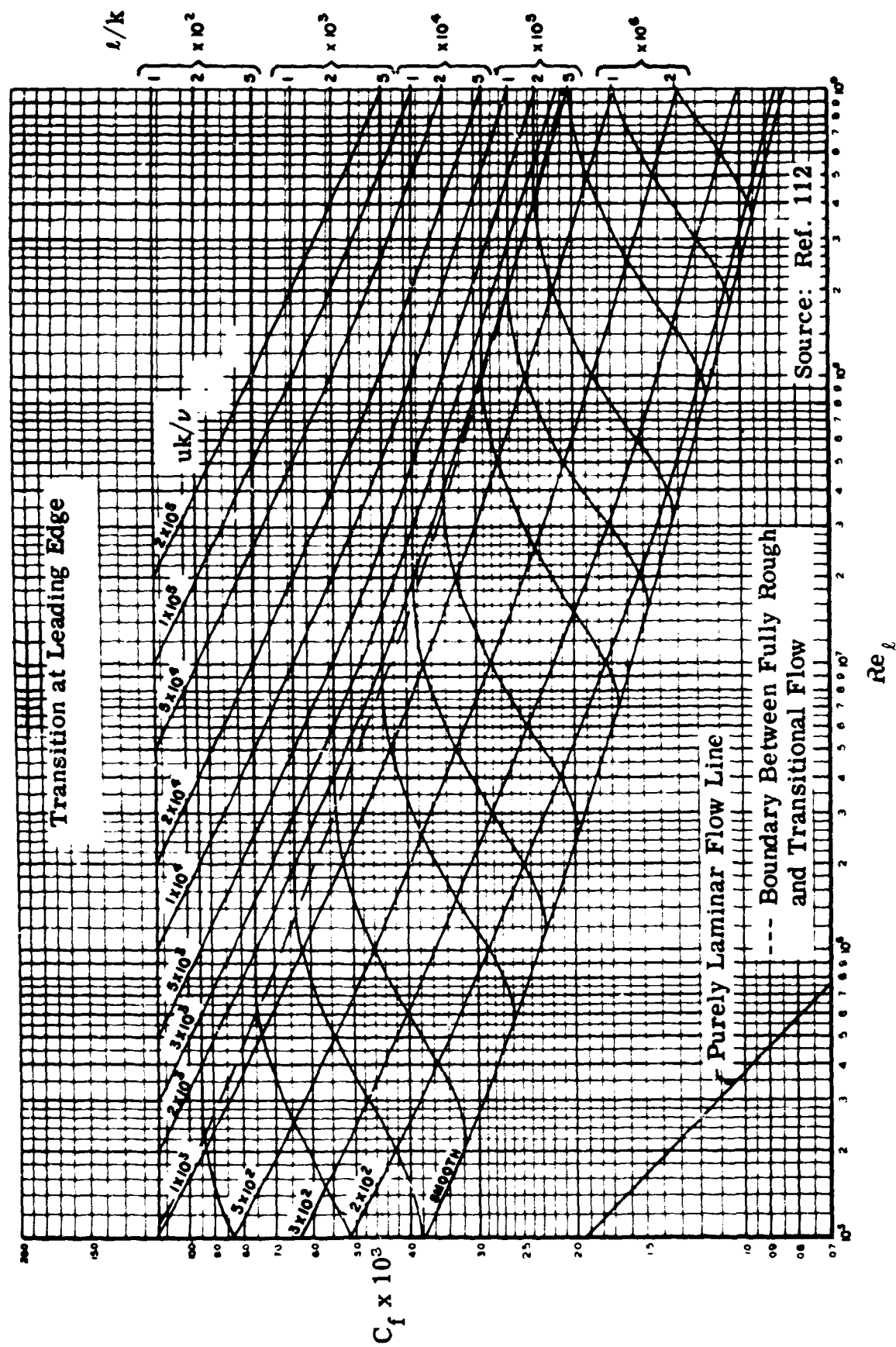


Fig. 6-22. Local skin friction coefficients for a sand-roughened plate;
 $T_w = T_1$; $M = 5.0$.

7. Heat Transfer

Methods are given in considerable detail in Subsecs. 3, 4, 5, and 6 for calculating boundary-layer growth and skin friction for both laminar and turbulent flows. It is therefore relatively simple to extend these results to provide methods for calculating the rate of heat transfer to the wall.

7.1.1 Laminar Boundary Layer on a Flat Plate--Perfect Gas, Heat Transfer

Equations by means of which skin friction coefficients may be calculated for a perfect gas laminar boundary layer on a flat plate are given in Subsec. 3.1. Heat transfer rates can be computed from these equations by the introduction of Reynolds' analogy. This analogy between heat transfer and skin friction is developed as follows. The local heat transfer rate, q , is given by

$$q = \left(k \frac{\partial T}{\partial y} \right)_w \quad (7-1)$$

In the laminar boundary layer, the temperature and the velocity profiles each have similar shapes at every point on a plate which has a uniform surface temperature, i.e., both T and u may be considered as functions of y only. In which case

$$\left(\frac{\partial T}{\partial y} \right)_w = \left(\frac{dT}{du} \right)_w \left(\frac{\partial u}{\partial y} \right)_w \quad (7-2)$$

Since $\tau_w = \left(\mu \frac{\partial u}{\partial y} \right)_w$, Eqs. 7-1 and 7-2 can be combined to give

$$q = \tau_w \left(\frac{k}{\mu} \right)_w \left(\frac{dT}{du} \right)_w \quad (7-3)$$

The heat transfer rate is expressed non-dimensionally by the Stanton number defined by

$$St = \frac{q}{\rho_1 u_1 c_p (T_e - T_w)} \quad (7-4)$$

By means of Eq. 7-3 the local Stanton number may be written in terms of T_* , T'_* , and the local skin friction coefficient, i.e.,

$$St = \frac{C_f}{2Pr_w} \frac{T'_{*w}}{(T_{*e} - T_{*w})} \quad (7-5)$$

where

$$C_f = \tau_w / \frac{1}{2} \rho_1 u_1^2$$

$$Pr = c_p \mu / k$$

$$T_* = T/T_1, u_* = u/u_1, \text{ etc.}$$

and

$$T'_* = dT_*/du_*$$

Appropriate values of the variables in Eq. 7-5 are determined as follows: For the perfect gas case with constant Prandtl number, $Pr_w = Pr$. Integration of the momentum and energy equations, Eqs. 2-17 and 2-19, gives the shear function, g_* , and enthalpy, h_* , as functions of u_* . For the perfect gas case where c_p is constant, the temperature T_* may then be obtained directly. Methods of determining the skin friction coefficient for laminar flow over a flat plate are outlined in Subsec. 3.1 and numerical values are given in Fig. 3-1 as a function of Mach number, Reynolds number and the temperature ratio T_{*w} . The recovery temperature, T_e , is defined as the value of T_w when $q = 0$. From Eq. 7-1, this requires $(\partial T/\partial y)_w = 0$. Equation 7-2 shows that $(\partial T/\partial y)_w = 0$ when $(dT/du)_w = 0$ or, in non-dimensional form, when $(T'_*)_w = 0$. The ratio T_{*e} can be expressed in terms of the recovery factor, r , i.e., by

$$\frac{T_e}{T_1} = T_{*e} = 1 + \frac{r(\gamma - 1)}{2} M_1^2 \quad (7-6)$$

Crocco (Ref. 4) solved Eq. 2-19 numerically holding Pr constant. For values of Pr from 0.5 to 2.0, his results showed that the relationship between the recovery factor and the Prandtl number can be closely approximated by

$$r = Pr^{\frac{1}{2}} \quad (7-7)$$

The results of Crocco's calculations also give a good approximation to Eq. 7-5, i.e.,

$$St = \frac{C_f}{2Pr^{\frac{3}{4}}} \quad (7-8)$$

Figure 7-1 gives Crocco's values of $2St/C_f$ and r as a function of Pr and demonstrates how good the approximations are in the range of $0.5 < Pr < 2.0$.

The simple empirical formulas (Eqs. 7-7 and 7-8), together with values of C_f given by the relationships of Subsec. 3.1, may be used with the definition of the Stanton number (Eq. 7-4) to obtain the heat transfer rate, q , when the wall temperature and the flow characteristics just outside the laminar boundary layer are known.

If the local skin friction coefficient, C_f , in Eq. 7-8 is replaced by the mean value, C_{F} , a mean Stanton number is obtained. Using this mean Stanton number in Eq. 7-4 will give a mean value of q which, when multiplied by the length of the plate, x , will give the total heat transfer rate.

7.1.2 Laminar Boundary Layer on a Flat Plate--Real Gas, Heat Transfer

Where real gas properties must be included in the calculations, it is more convenient to use the enthalpy as the variable rather than the temperature. Since the pressure is constant across the boundary layer, it can be shown that

$$\frac{\partial T}{\partial y} = \frac{1}{c_p} \frac{\partial h}{\partial y} \quad (7-9)$$

Equation 7-9 remains valid even for the case of variable c_p and can be used with Eq. 7-1 to give

$$q = \left(\frac{k}{c_p} \frac{\partial h}{\partial y} \right)_w \quad (7-10)$$

The enthalpy gradient can be written

$$\left(\frac{\partial h}{\partial y} \right)_w = \left(\frac{dh}{du} \right)_w \left(\frac{\partial u}{\partial y} \right)_w \quad (7-11)$$

Using enthalpy as a variable instead of temperature, Eqs. 7-3, 7-4, 7-5, and 7-6 now become

$$q = \frac{\tau_w}{Pr_w} \left(\frac{dh}{du} \right)_w \quad (7-12)$$

$$St = \frac{q}{\rho_1 u_1 (h_e - h_w)} \quad (7-13)$$

$$St = \frac{C_f}{2Pr_w} \frac{(h'_*)_w}{(h_{*e} - h_{*w})} \quad (7-14)$$

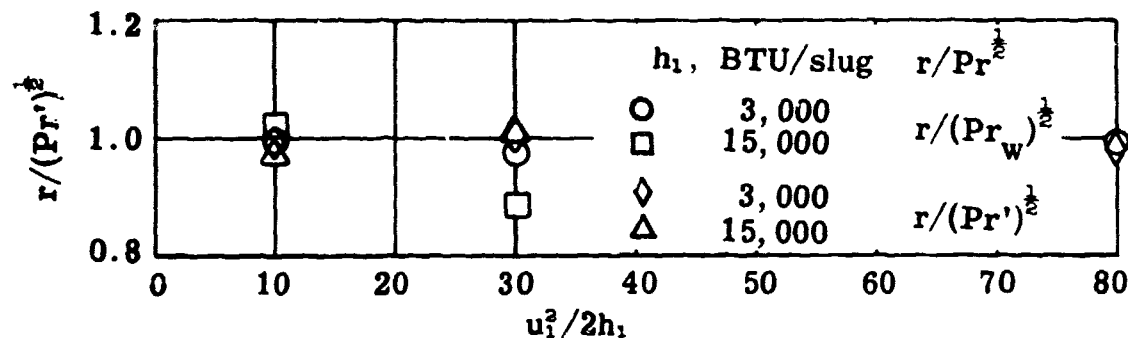
and

$$\frac{h_e}{h_1} = h_{*e} = 1 + r (u_1^2/2h_1) \quad (7-15)$$

By integrating the momentum and energy equations (Eqs. 2-17 and 2-18) for the real gas case, Wilson has obtained skin friction and heat transfer results as a function of $u_1^2/2h_1$ for a wide range of wall enthalpies and of gas properties just outside the boundary layer. He found that these skin friction coefficients are in good agreement with those computed using a reference enthalpy method (see Subsec. 3.2). Wilson in Ref. 12 shows that the recovery factor can be approximated by

$$r = (Pr')^{\frac{1}{2}} \quad (7-16)$$

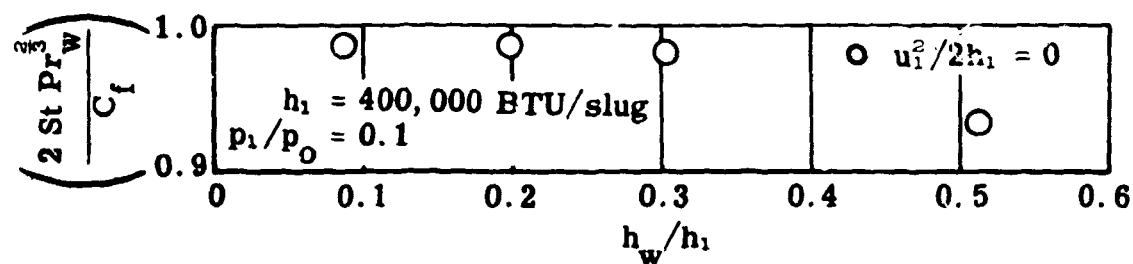
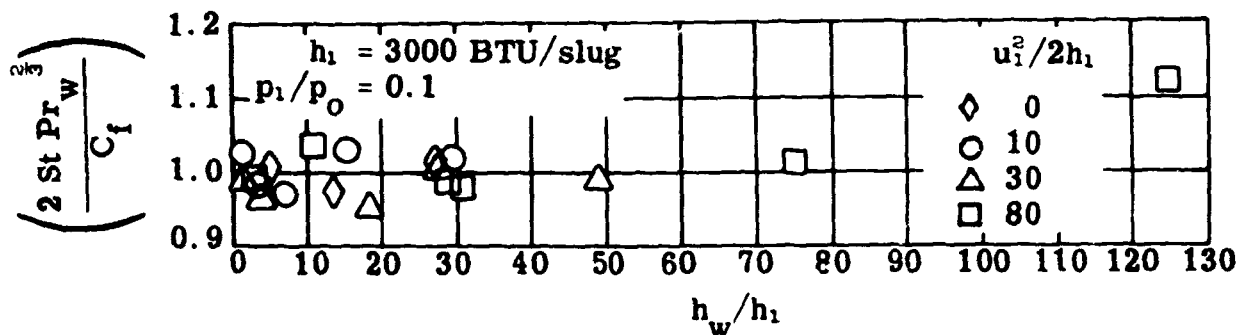
when the prime in this case denotes the Prandtl number corresponding to the reference enthalpy given by Eq. 3-28. As an alternative value of Prandtl number, one might consider Pr_w . However, the following sketch from Ref. 12 shows that at least for the cases calculated, Pr' is a somewhat better value.



In attempting to find a simple approximation for Eq. 7-14, Wilson found that the Crocco relationship gave reasonable results, but in this case the agreement is better when the Prandtl number is evaluated at the wall rather than at the reference conditions (Pr'). Thus

$$St = C_f / 2(Pr_w)^{1/2} \quad (7-17)$$

The following sketches show that, except for a few cases, the simple relationship, Eq. 7-17, agrees with the exact calculations to within five percent.



It should be pointed out that the Prandtl number fluctuates with enthalpy (see Fig. 3-12) and therefore it fluctuates across the boundary layer. Perhaps better agreement between Eq. 7-17 and the exact calculations could be obtained if the Prandtl number were averaged in some way across the boundary layer. However, since such a procedure would be extremely laborious it is suggested that Eqs. 7-16 and 7-17 be used.

Given the wall enthalpy and the flow conditions just outside the laminar boundary layer, the heat transfer is calculated as follows:

1. The reference enthalpy and the reference Prandtl number are calculated from Eq. 3-28 by iteration.
2. Using Eq. 7-16 the recovery factor is then computed from the reference Prandtl number.
3. The Stanton number is computed from Eq. 7-17 using the skin friction results of Subsec. 3.2 and the Prandtl number based on flow properties at the wall.
4. The heat transfer rate is then calculated from Eqs. 7-13 and 7-15.

7.1.3 Turbulent Boundary Layer on a Flat Plate--Perfect Gas, Heat Transfer

The definitions given by Eqs. 7-4 and 7-6 for the local Stanton number and the recovery factor are valid for both laminar and turbulent flow. Since the turbulent boundary layer has a laminar sublayer, the heat transfer rate to the wall is given by Eq. 7-1 and the shear stress is given by $\tau_w = (\mu \partial u / \partial y)_w$. It follows that the relationship between St and C_f given by Eq. 7-5 is also valid for both laminar and turbulent flow. In both cases, Pr_w must be computed using molecular transport properties. Therefore, calculation of the heat transfer rate for the turbulent case will differ from that of the laminar case only in the expression for the recovery factor and the appropriate approximation for Eq. 7-5. For low-speed turbulent flow, Squire (Ref. 121) deduced the relationship

$$r = Pr^{\frac{1}{3}} \quad (7-18)$$

where Pr is based on molecular transport properties of the gas as before and, in this case, is taken as constant. Van Driest (Ref. 122) has derived an elaborate expression for r containing the molecular Prandtl number and also a turbulent Prandtl number based on the eddy viscosity and the eddy conductivity (see Subsec. 2.6). Actually, Van Driest uses experimentally determined values of the recovery factor to determine the turbulent Prandtl number since no reliable data exist for the latter. He then assumes that this turbulent Prandtl number is constant and uses it to calculate recovery factors at Mach numbers and Reynolds numbers where no experimental data exist. Since Squire's result for low speeds agrees within one or two percent with experimental results for air over a wide range of Mach numbers, it is recommended that the recovery factor in turbulent flow be computed from

$$r = Pr_w^{\frac{1}{3}} \quad (7-18a)$$

where Pr_w is the molecular Prandtl number corresponding to the wall temperature. The wall value is recommended since the molecular transport properties can be the only significant properties in the laminar sublayer. Equation 7-18a is compared with the experimental results of Brevoort and Arabian (Ref. 123) on Fig. 7-2. The agreement is reasonably good over the Mach number range from 0.87 to 5.05. In general, the values of r derived from Eq. 7-18a are a little higher than those derived from the test data. It is of interest to note that the test data appear to show a slight downward trend as well as a greater spread with increasing Reynolds number.

When transition from laminar to turbulent flow occurs, the recovery factor rises from $Pr^{1/2}$ to approximately $Pr^{1/3}$. In experimental data taken in the transition region, a slight overshoot occurs. This is demonstrated by Fig. 7-3 which gives the recovery factor derived from the experiments of Brinich (Ref. 124) at a Mach number of 3.12. The recovery factors given here for the turbulent region confirm the downward trend with Reynolds number shown by Fig. 7-2. The data on Figs. 7-2 and 7-3 are considered to be typical examples of recovery factors, selected from the many papers dealing with the subject.

In addition to the relationship for recovery factor, Van Driest (Ref. 122) derives an expression for a Reynolds analogy factor. This expression contains both the molecular Prandtl number and the turbulent Prandtl number which was determined from the experimental recovery factors as described above. Since Eq. 7-5 is valid for both laminar and turbulent flow when Pr_w has the molecular value corresponding to the wall temperature, it may be compared with Eq. 7-8. Hence, for the laminar case with constant Prandtl number

$$(T'_*)_w / (T_{*e} - T_{*w}) = Pr^{1/3} \quad (7-19)$$

An evaluation of $(T'_*)_w / (T_{*e} - T_{*w})$ for the turbulent case is necessary to determine the turbulent Reynolds analogy factor. If it is assumed that Eq. 7-19 also holds for the turbulent case when the wall molecular Prandtl number is used, then Eq. 7-5 for the turbulent case is

$$St = C_f / 2 Pr_w^{1/3} \quad (7-20)$$

Figures 7-4 and 7-5 compare St/C_f (computed from Eq. 7-20) with Seiff's experimental values (taken from Ref. 125). The agreement of the empirical value with the experimental is good enough to allow Eq. 7-20 to be used rather than the more elaborate expression derived by Van Driest in Ref. 122. The ratio, St/C_f , is plotted as a function of Mach number in Fig. 7-4 and as a function of Reynolds number in Fig. 7-5. If Pr_w is assumed to be constant, then by Eq. 7-20 the ratio St/C_f must also be constant. On both Figs. 7-4 and 7-5 there is one set of data points (Fisher and Norris - Station M) which are appreciably lower than the rest. From the position of these points on Fig. 7-5 it might be concluded that St/C_f decreases as the Reynolds number increases. However, this trend is not

substantiated elsewhere. Since these data are associated with a favorable pressure gradient, the drop in St/C_f might be attributed to this fact. However, it is shown in Subsec. 7.2 that a moderate pressure gradient does not affect this ratio.

In summary, the turbulent heat transfer rates may be calculated as follows:

1. Skin friction coefficients are obtained from the equations given in Subsec. 3.3.
2. The recovery factor and the Stanton number are then calculated from Eqs. 7-18a and 7-20.
3. The value of q may then be calculated from Eqs. 7-4 and 7-6.

7.1.4 Turbulent Boundary Layer on a Flat Plate--Real Gas, Heat Transfer

A method for calculating turbulent skin friction for the real gas case is given in Subsec. 3.4. To calculate turbulent heat transfer it is recommended that the skin friction coefficients thus obtained be used with Eqs. 7-13, 7-15, 7-18a, and 7-20. This makes use of the enthalpy rather than the temperature. The recovery factor and Reynolds analogy factor given by Eqs. 7-18a and 7-20 are recommended for both the perfect and real gas cases, since the molecular Prandtl number is the significant one in the laminar sublayer in either case. Thus, the wall value which appears in Eqs. 7-18a and 7-20 would be appropriate.

7.2 Heat Transfer on Two-Dimensional and Axisymmetric Bodies

7.2.1 Laminar Boundary Layer

Subsection 4.2 presents the method of Cohen and Reshotko (Ref. 7) for calculating boundary-layer growth and skin friction over two-dimensional and axisymmetric bodies with arbitrary pressure and temperature distributions over the surface. The method is based on the following assumptions:

1. The gas is perfect.
2. The flow outside the boundary layer is isentropic.
3. The viscosity is linearly proportional to temperature.
4. The Prandtl number has a value of unity.

When the constant in the linear viscosity relation is adjusted to give the correct viscosity at the wall temperature, skin friction coefficients are obtained which agree with experimental values at moderate Mach numbers. Using the same assumptions, Cohen and Reshotko also derived a method of calculating heat transfer rates which compared favorably with experimental data in the moderate Mach number range. They derived a Reynolds analogy factor which is a function of both wall temperature and surface pressure gradient. Their analogy factor can be reduced to $(C_f/St)_{Pr=1}$. From the work of Tifford and Chu (Ref. 126), it has been

found that when the Prandtl number is not unity, a good approximation is

$$\left(\frac{C_f}{St}\right)_{Pr=1} = \frac{C_f Pr^{\alpha-1}}{St} \quad (7-21)$$

where both α and the ratio $(C_f/St)_{Pr=1}$ are functions of the pressure gradient. Values of α recommended by Ref. 126 are listed below. The value for stagnation point flows is taken from Squire (Ref. 127).

Pressure Gradient	α
Large, favorable	0.5
Stagnation point flows	0.4
Small	0.3
Large, adverse	0.25

The values of $(C_f/St)_{Pr=1}$, from Cohen and Reshotko, have been substituted in Eq. 7-21 and the resulting analogy factor of Tifford and Chu is plotted on Fig. 7-6 as a function of the pressure gradient parameter, n , with $(T_w - T_{t1})/T_{t1}$ as a secondary parameter.

The heat transfer rate is calculated as follows:

1. The skin friction coefficient is determined by the method given in Subsec. 4.2.
2. The Stanton number is determined from Fig. 7-6. If the Pr is not constant, the wall value should be used.
3. The heat transfer is then calculated using Eqs. 7-4, 7-6, and 7-7.

It should be noted that the calculations of Cohen and Reshotko for $Pr = 1$ give no information on the appropriate value of the recovery factor, r . They recommend that Eq. 7-7 be used until definitive experimental data are available on the effect of pressure gradient.

A special technique is required for calculating the heat transfer rate at the stagnation point, i.e., where the velocity is zero. For the case of $Pr = 1$, Cohen and Reshotko determined values of a stagnation point parameter which can be expressed as $q(h_{t1} - h_w)^{-1}(\rho_w \mu_w \beta)^{-\frac{1}{2}}$. In order to evaluate this parameter at values of Pr other than unity, following the findings of Ref. 126, an equation similar in form to Eq. 7-21 may be written as

$$\left[\frac{q}{(h_{t1} - h_w)(\rho_w \mu_w \beta)^{\frac{1}{2}}} \right]_{Pr=1} = \frac{q Pr^{1-\alpha}}{(h_{t1} - h_w)(\rho_w \mu_w \beta)^{\frac{1}{2}}} \quad (7-22)$$

where

$$\beta = \left(\frac{du_1}{dx} \right)_{x=0} \quad (7-23)$$

Equation 7-22 may be used to calculate stagnation point heat transfer rates when $Pr \neq 1$. The values calculated by Cohen and Reshotko for the left-hand side of this equation are plotted in Fig. 7-7 as a function of the wall temperature for both two-dimensional and axisymmetric stagnation point flows. Values of the right-hand side of Eq. 7-22 when $Pr = 0.7$ are also plotted on Fig. 7-7. It can be seen that Eq. 7-22 is a good approximation to the more exact calculations. When the flow conditions and wall temperature are known, the stagnation point heat transfer rate can be calculated with the use of Fig. 7-7. It is also necessary to evaluate the parameter, β .

For axisymmetric bodies a good approximation to β can be obtained by assuming Newtonian flow, i.e., a pressure distribution given by

$$C_p = C_{p_{\max}} \cos^2 \xi$$

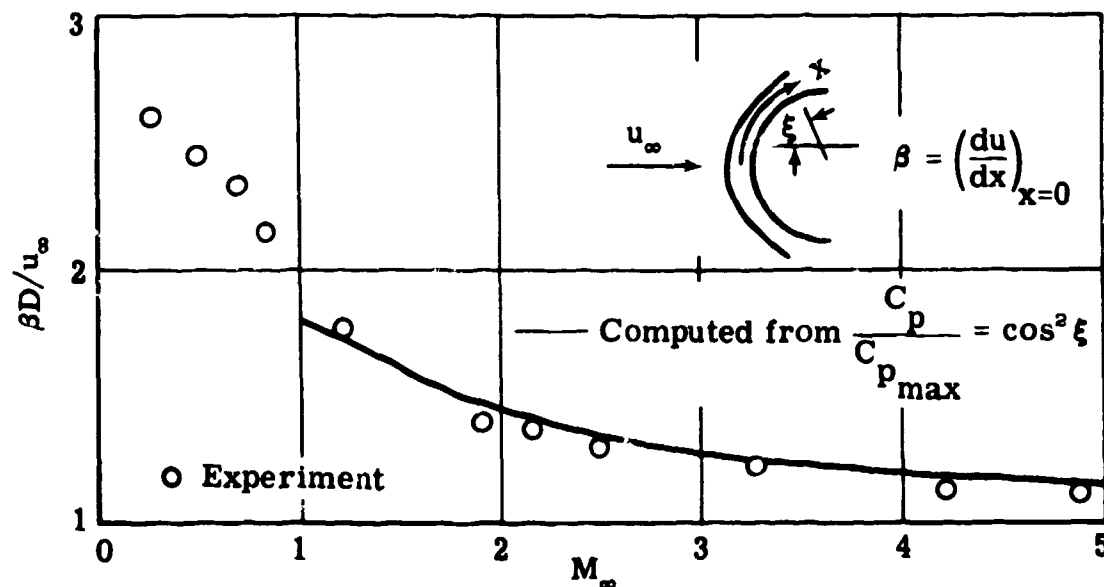
where ξ is the angle between the flow direction and the normal to the point in question. For a spherical tip this will yield

$$\beta D = 2 \left[\left(\frac{p_\infty}{\rho_\infty} \right)^2 \left(\frac{p_{t1}}{\rho_\infty - 1} \right) \frac{\rho_\infty}{\rho_{t1}} \right]^{\frac{1}{2}} \quad (7-24)$$

where

D = the tip diameter and the subscript ∞ refers to conditions ahead of the bow shock.

Equation 7-24 holds true for both perfect gases and real gases if the correct values of stagnation pressure, p_{t1} , and stagnation density, ρ_{t1} , are used. If the equation is divided by u_∞ , $\beta D/u_\infty$ is a function of Mach number for a perfect gas. A comparison of the calculations with the experimental results from Ref. 128 is shown on the following sketch. The agreement is excellent.



The foregoing relationships between the parameters for bodies of several shapes and for stagnation point flows give results in good agreement with test measurements for moderate Mach numbers. High Mach number data for stagnation point flows show that these simplified theories are not adequate to account for the effects of real gas flows. Heat transfer rates obtained at stagnation points by means of shock-tube tests made by Rose and Stark (Ref. 129) and by Rose and Stankevics (Ref. 130) are shown on Figs. 7-8 and 7-9, respectively. The flight velocities shown correspond to the total enthalpy in the shock tube. It can be seen on Fig. 7-8 that the stagnation point theory of Fay and Riddell (Ref. 131) is in excellent agreement with the data. The theory given here approaches the experimental data as the shock Mach number is decreased. It is interesting to note that the perfect gas calculations give values which are too high. These calculations were made using Fig. 7-7 and Eq. 7-24. The real gas values of p_{t_1} and ρ_{t_1} were used in Eq. 7-24. The data on Fig. 7-9 are compared with the theory of Fay and Kemp (Ref. 132). At the very high velocities, even the real gas calculations are above the experimental values. The perfect gas calculations can be expected to give even higher results. For free-flight data, the agreement between theory and experiment will improve with distance from the stagnation point and will be still better where there is no stagnation flow.

The experimental heat transfer rates at a stagnation point show that the perfect gas calculations of Cohen and Reshotko do not give satisfactory values at high stagnation enthalpies. This will also be true though to a lesser extent at other body stations at which the enthalpy is high. There are several theoretical investigations which can be applied satisfactorily not only to flow over the stagnation area but also to entire bodies at hypersonic speeds. For high stagnation enthalpies and highly cooled walls, Lees (Ref. 133) neglected the pressure gradient term in the momentum equation, took $\rho\mu$ constant through the boundary layer, and assumed local similarity for the boundary-layer profiles. Probstein (Ref. 134) proposed that the pressure gradient term in the momentum equation be retained but that ρh be taken as constant through the boundary layer. Eckert and Tewfik in Ref. 135 evaluated the product, $\rho\mu$, in Lees' theory at a reference enthalpy which, for the flat plate (Subsec. 3.2), takes account of the variation in $\rho\mu$ through the boundary layer. Kemp, Rose, and Detra (Ref. 136) assumed local similarity for velocity and temperature profiles and solved the boundary-layer equations for a fluid with variable thermodynamic and transport properties. Solomon (Ref. 137) extended the method of Cohen and Reshotko, taking into account the effect of high stagnation enthalpies by evaluating the gas properties at Eckert's reference enthalpy. The expression given by Eckert in Ref. 138 for reference enthalpy results in values which approximate those given by Eq. 3-28. Solomon's calculated heat transfer parameters are in good agreement with the stagnation point calculations of Fay and Riddell (Ref. 131) and also agree with the calculations and data for heat transfer over a hemisphere-cylinder and a flat-faced cylinder given by Kemp, Rose, and Detra in Ref. 136. Since the results of Solomon's empirical method are in good agreement with those of more complicated theories and also with experimental data, it is recommended that the method outlined in Ref. 137 be used for calculations involving high stagnation enthalpies.

An approximate analysis by Eggers, Hansen, and Cunningham (Ref. 139) appears to give excellent agreement with experimental data at velocities up to 27,000 ft/sec. It should be noted that the analysis is limited to stagnation point heat transfer.

7.2.2 Turbulent Boundary Layer

In Subsec. 4.3 it is suggested that for small surface pressure gradients, reasonably accurate values for the turbulent boundary-layer growth and skin friction coefficients can be obtained by integrating Eq. 2-29 after substituting the flat plate boundary-layer characteristics associated with the point under consideration. The same method could also be used to take into account small arbitrary temperature gradients. Once the local skin friction coefficient has been computed as described in Subsec. 4.3, the heat transfer can then be computed using flat plate flow characteristics. The recovery factor and Stanton number are calculated from Eqs. 7-18a and 7-19, respectively, and q is then calculated using Eqs. 7-4 and 7-6.

The use of the flat plate Reynolds analogy, Eq. 7-19, is justified by at least one set of experimental data. Pasiuk, et al (Ref. 140), describe experiments in which heat transfer rates, as well as velocity and temperature profiles, are measured in the boundary layer on a flat plate on which there is a favorable pressure gradient. The plate extends from the throat to the test section in a two-dimensional wind-tunnel nozzle contoured to generate on the plate a turbulent boundary layer with a constant Polhausen parameter. Figure 7-10 shows the Mach number distribution at the outer edge of the boundary layer on the plate. Figure 7-11 shows the distribution of temperature ratio, T_w/T_{t_1} along the plate for two heat transfer rates which were achieved by cooling the plate surface. The data were used to determine the Reynolds analogy factor in a turbulent boundary layer on a surface with both temperature and pressure gradients. No skin friction coefficients were measured. However, values of Σ_1 were determined from the boundary-layer surveys by integrating the momentum integral equation where

$$\Sigma_1 = \int_{x_1}^x \frac{C_f}{2} dx$$

Values of Σ_2 were determined from measurements of the local heat transfer rate where

$$\Sigma_2 = \int_{x_1}^x \text{Pr}^{\frac{2}{3}} \text{St} dx$$

The resultant values of these two integrals are given as a function of distance along the plate in Fig. 7-12 for both the high and low heat transfer cases. In reducing the heat transfer data to obtain the Stanton number, a recovery factor, r , approximately equal to $\text{Pr}^{\frac{1}{3}}$ was used. The value of x_1 is arbitrary, taken as 1.28 ft in this case. It may be noted from Fig. 7-12 that the two integrals have essentially the same values. Thus the flat plate Reynolds analogy given by Eq. 7-19 is apparently satisfactory for Mach number and temperature gradients of this test, i.e., those shown on Figs. 7-10 and 7-11. Three other definitions of Reynolds analogy factors (proposed by various authors) are also compared with the experimental data in Ref. 140. With one exception, i.e., that of Rubesin (Ref. 141), the values were not as good as the flat plate values. Cohen (Ref. 142) discusses briefly the

various theories which have been proposed for predicting the heat transfer rate in a turbulent boundary layer on a surface with a pressure gradient. Cohen derives a method for computing the turbulent heat transfer to two-dimensional and axisymmetric bodies in high-speed flow. His method utilizes a Stewartson-type transformation and the integration of the boundary-layer equations. He gives an exact solution for certain arbitrary initial conditions and an approximate solution requiring fully developed turbulent flow from the stagnation point or leading edge. The techniques of Ref. 142 are recommended for bodies with large pressure gradients.

7.2.3 Cones, Spheres, and Sphere-Cones

Subsection 4.4 gives equations for finding the skin friction coefficients for cones at zero angle of attack and constant wall temperature. Both laminar and turbulent boundary layers are considered. The cone values are obtained from the results of flat plate theories. Therefore, once the skin friction coefficients are determined, the heat transfer rates can be computed using the methods given in Subsecs. 7.1.1 and 7.1.2 (laminar boundary layer) and Subsecs. 7.1.3 and 7.1.4 (turbulent boundary layer).

In Subsec. 4.5, the approximate method of Cohen and Reshotko (Ref. 7) is applied to the calculation of laminar boundary-layer growth on spheres. Although skin friction coefficients are not actually derived, they can be obtained by the technique outlined in Subsec. 4.2.4. Heat transfer rates can then be calculated using the method described in Subsec. 7.2.1.

When the tip radius of a sphere-cone is small compared to the length of the conical section and the angle of attack is zero, the laminar skin friction coefficient can be computed using the method of Wilson (Ref. 13) which is given in Subsec. 4.6. This method has been extended to include the calculation of the turbulent shear stress (Ref. 143). For both the laminar and turbulent boundary-layer calculations, it is assumed that the pressure on the conical section is constant and that the surface may be considered as a flat plate. However, local flow conditions at each point along the surface must be used since, even with a slight bluntness, the boundary layer on the conical section is in the process of swallowing the variable entropy layer consequent upon the bow shock curvature. The heat transfer rates can be calculated from the skin friction results using the flat plate formulas given in Subsecs. 7.1, 7.2.1, and 7.2.2.

When the bluntness of the sphere-cones is large, there are two departures from the simple flow pattern just described. The first is that the blunting of the tip will affect the pressures over a large part, perhaps all, of the conical portion. Secondly, the conditions at the outer edge of the boundary layer are associated with the flow which has passed through the normal portion of the bow shock, i.e., the variable entropy layer will extend further down the body. In this case the flow at the outer edge of the boundary layer is isentropic. The heat transfer characteristics for these large bluntnesses can be computed by the methods described in Subsecs. 7.2.1 and 7.2.2.

7.2.4 Bodies at Angle of Attack

When a body is at an angle of attack, an approximate method for calculating the boundary-layer growth and skin friction coefficients can be devised by integrating the momentum integral equation along streamlines. If it is assumed

that the flow direction in the boundary layer corresponds to the flow direction at the boundary-layer edge, the streamline pattern can then be obtained by considering only the inviscid flow. A method of calculation such as that described in Ref. 144 may then be employed. The momentum integral equation for the axisymmetric case given by Eq. 2-28 can be altered slightly and applied to the body at angle of attack. It is necessary to replace the term $\frac{\theta}{r} \frac{dr}{dx}$ by a term $\frac{\theta}{\Delta n} \frac{d\Delta n}{dx}$ where Δn is the distance between two adjacent streamlines as shown in the sketch below.



The distance x is measured along a streamline. If the flow at the outer edge of the boundary layer is isentropic, then Eq. 2-29 is used after replacing the term $\frac{\theta}{r} \frac{dr}{dx}$ as described above. For the isentropic case, after replacing r by Δn , the methods for calculating skinfriction given in Subsecs. 4.2 and 4.3 can be applied. The heat transfer rate can then be computed by the methods of Subsecs. 7.2.1 and 7.2.2.

Several investigations of heat transfer on bodies at angle of attack are reported in the literature. Julius (Ref. 145) gives the experimentally determined Stanton number on a 20 deg cone in both laminar and turbulent flow. The values of the Stanton number, based on local conditions at the outer edge of the boundary layer, are plotted as a function of Reynolds number on Fig. 7-13 for the models on which transition occurred. The cone tip was then roughened to give fully turbulent flow; results for these models are shown on Fig. 7-14. The data shown on Figs. 7-13 and 7-14 are for angles of attack of 0, 10, and 20 deg and measured on the most windward surface generator, i.e., $\phi = 0$ deg. It can be seen from these figures that the theories of Braun (Ref. 146) and Brunk (Ref. 147) for the turbulent and laminar heat transfer, respectively, are in excellent agreement with experimental results. The theory of Van Driest (Ref. 120) is shown for both laminar and turbulent flow with $\alpha = 0$ deg. Using local values of the flow characteristics in both St and Re tends to bring the curves together at all angles of attack. It can be seen from the figures that there is some increase in Stanton number with angle of attack for both laminar and turbulent flow. This increase is associated with the thinning of the boundary layer at increasing angle of attack. Reference 145 also presents data on generators at 30, 60, 90, and 180 deg from the most windward generator. When the boundary layer is completely laminar or completely turbulent, the maximum heat transfer rate is found on the most windward generator. When transition occurs, the generator along which the maximum heat transfer occurs, moves around the cone and usually lies between the 30 and 60 deg generators.

The measurements just discussed were made by Julius at Mach 4.95. Burbank and Hodge (Ref. 148) present experimental data for a 10 deg cone at Mach numbers of 2.49, 2.98, 3.51, 3.96, and 4.65. Heat transfer rates were measured with the cone at 0, 7.5, and 15 deg angle of attack. Data were obtained with fully laminar flow and with transition.

Heat transfer data on sphere-cone configurations have been given by several investigators. For each experimental study which will be discussed here, the bluntness was relatively large. The entropy at the outer edge of the boundary layer is then constant and equal to the value on the stagnation streamline. Laminar heat transfer data from wind-tunnel tests are given by Pasiuk in Ref. 149. The ratio of the radii of the conical frustum of the sphere-cone was 0.19 and the cone angle was 26.6 deg. Heat transfer data for the most windward generator are shown on Figs. 7-15 and 7-16. The tests were run at Mach numbers of 3.2 and 4.8 and at three angles of attack: 0, 6, and 8 deg. The data are given in terms of the ratio of local film coefficient, \bar{h} , to the stagnation point film coefficient, \bar{h}_{sp} . The film coefficient is defined by

$$\bar{h} = q / (T_e - T_w) .$$

Data for the generator which is 45 deg from the most windward generator are shown on Figs. 7-17 and 7-18. Pasiuk shows that the theory of Beckwith (Ref. 150) is in reasonable agreement with the experimental results. In addition to the results shown here, Ref. 149 gives data at several stations around the body on generators up to 150 deg from the most windward generator. The ratio T_w/T_{t_1} varied from 0.7 to 0.8 during these tests.

Data on a 20 deg sphere-cone with fully laminar flow and also with transition are given by Van Camp in Ref. 151. These wind-tunnel results were obtained at Mach numbers of 2.47, 3.58, and 4.53 with the model at angles of attack of 0, 5, 10, 14, and 16 deg. Measurements of turbulent heat transfer on a 60 deg sphere-cone are given by Aeillo in Ref. 152. Aeillo used the shrouded model technique of Ferri and Libby (Ref. 153) in which the shroud is designed to give a Newtonian pressure distribution over the model at zero angle of attack. The tests were then run with the model at a geometric angle of attack to provide a three-dimensional flow. Although this technique does not precisely simulate that of a model at angle of attack in an unconfined flow, high local Reynolds numbers can be obtained. The turbulent heat transfer data with three-dimensional flow can be compared with theory. Aeillo found that the flatplate reference enthalpy method, based on local flow conditions at the outer edge of the boundary layer, gave good agreement with measured values. The Reynolds number used in the calculations was based on the distance along an inviscid streamline measured from the stagnation point. Since the skin friction coefficient and the Stanton number for turbulent flow are relatively insensitive to Reynolds number, some uncertainty in choosing the proper Reynolds number will not greatly affect the calculations. These results tend to confirm the suggestion made in Subsec. 7.2.2 that flat plate characteristics be used for the turbulent boundary layer in the presence of small pressure gradients.

In addition to the cone and sphere-cone results, heat transfer data on other bodies at angles of attack can be found in the literature. Feller, for example (Ref. 154), gives data for a modified Karman nose shape at a Mach number of 3.69 for angles of attack from 0 to 25 deg. These tests were conducted in a wind tunnel with a smooth model which showed natural transition. The model was also roughened to obtain fully turbulent flow. In Ref. 155, Sands and Jack give wind-tunnel results for cylindrical bodies with cone tips and with parabolic noses. The models were tested at a Mach number of 3.12 and angles of attack up to 18 deg.

7.3 Heat Transfer on Yawed Cylinders

Wing leading edges are often blunted in order to reduce the heat transfer rate at high flight velocities. Although the drag increase consequent upon the blunting may at times be unacceptably high, it may be reduced by sweeping the leading edge. The sweep can, in some cases, further reduce the leading-edge heat transfer rate. A number of theoretical and experimental studies on yawed cylinders have been carried out to investigate the effect on heat transfer of the various parameters. The results of a few of these studies will be presented here.

Cunningham and Kraus (Ref. 156) compared several methods of calculating the heat transfer rate on the laminar stagnation line of a yawed cylinder. The comparison is shown on Fig. 7-19 in terms of the angle of yaw or sweep, λ . It can be seen that the theories of Eggers, et al (Ref. 157), Reshotko and Beckwith (Ref. 158), and Goodwin, et al (Ref. 159), give heat transfer rates that are in reasonable agreement with one another. The ratio of the heat transfer rate at λ to that at $\lambda = 0$ is approximated by the curve of

$$q_{\lambda}/q_{\lambda=0} = \cos^{3/2}\lambda \quad (7-25)$$

At $\lambda = 60$ deg, this yields a value of q_{λ} that is only 40% of the zero sweep value. Eggers, Hansen, and Cunningham (Ref. 139) have derived an approximate theory for calculating laminar heat transfer in the stagnation region. This theory takes into account real gas effects. It was shown in Subsec. 7.2.1 that the theory when applied to blunt bodies is in excellent agreement with measured heat transfer rates in the stagnation region. Calculations given in Ref. 139 for yawed cylinders moving at satellite velocities are shown on Fig. 7-20. These calculations demonstrate that, even with real gas effects, the trend of heat transfer rate with angle of yaw is approximated by Eq. 7-25.

Figure 7-21 shows experimental results at $M_{\infty} = 11$ which were obtained by Cunningham and Kraus (Ref. 156) for yawed circular cylinders. The data are given in terms of an average heat transfer rate, Q , defined by

$$Q = \frac{rc\rho}{2} \frac{dT}{dt}$$

where, for the cylinder

r = radius

c = specific heat per unit mass

ρ = density

and

T = temperature

It may be seen from Fig. 7-21 that the effect of sweep angle is in good agreement with Eq. 7-25. It should be noted that the Reynolds numbers of these data are quite small and that the flow over the cylinders was therefore undoubtedly laminar. Experimental results at $M_{\infty} = 9.8$, given in Ref. 157, show a similar trend at sweep angles up to 45 deg. At $\lambda = 70$ deg the data in Ref. 157 fall above the curve of

Eq. 7-25. The authors of Ref. 156 suggest that this discrepancy may be due to interference from the model support.

Beckwith and Gallagher (Ref. 160) present experimental data taken at much higher Reynolds numbers (1×10^6 to 4×10^6). These measurements, made at $M_\infty = 4.15$ are shown on Fig. 7-22. It may readily be seen that the effect of yaw on the heat transfer rate is in sharp contrast with that of the low Reynolds number data shown on Fig. 7-21. As the cylinder was yawed from 0 to 40 deg, the stagnation line heat transfer rates increased by 100 to 180%. However, a further increase in yaw angle from 40 to 60 deg resulted in a 40% reduction in heat transfer rate. At zero yaw angle, the heat transfer rate agrees with the laminar flow theory of Beckwith (Ref. 161). This is also true at 10 deg yaw for the lower test Reynolds numbers. However, as the Reynolds number is increased, the heat transfer at 10 deg yaw becomes considerably greater than that predicted by laminar flow theory, indicating transition to turbulent flow. At yaw angles greater than 10 deg, the heat transfer is always much higher than laminar predictions. It may be seen that the 40 and 60 deg yaw angle results of Fig. 7-22 are in good agreement with the turbulent flow theory of Ref. 160. Although this theory predicts zero heat transfer at $\lambda = 0$ and must therefore be in error at very small angles of yaw, it still gives a reasonable qualitative prediction of the behavior of the heat transfer at low angles of yaw. The heat transfer is predicted to rise to a maximum value at $\lambda \approx 30$ deg and then decrease with further increase in λ . This is in contrast to the behavior of the laminar heat transfer rate which has its maximum at $\lambda = 0$ deg. As the authors of Ref. 160 point out, the test Reynolds numbers of the data shown on Fig. 7-22 are larger than typical values of full-scale leading edge Reynolds numbers for most hypersonic vehicles. In view of this they suggest that the data may be more profitably applied to bodies at reasonable angles of attack than to wings of large sweep.

7.4 Heat Transfer in the Transition Region

Although no comment was made at the time, Fig. 7-13, discussed in Subsec. 7.2.4, shows clearly the behavior of the local Stanton number in the region of transition from laminar to turbulent flow. The Stanton number is well-behaved in the transition region and increases in the same way that the local skin friction coefficient increases in that region. Figure 7-13 also shows that the values of St overshoot slightly the curves for the fully turbulent flow. This overshoot corresponds to the overshoot of the local skin friction coefficient which was discussed in Subsec. 3.5. In calculating the heat transfer rate, a conservative estimate can always be obtained by assuming that transition occurs abruptly at a point and, furthermore, that the point corresponds to the onset of transition rather than its termination.

7.5 Turbulent Heat Transfer on Rough Surfaces

The effect of roughness on turbulent boundary-layer skin friction is discussed in Subsec. 6. The method used by Clutter (Ref. 112) for computing both the local and mean skin friction coefficients is described. For fully rough flow, Clutter makes use of the experimental results of Goddard (Ref. 111) who found that for zero heat transfer, the ratio of compressible to incompressible skin friction coefficients was equal to the ratio of wall to free-stream densities. Clutter assumed that this relationship could also be used to calculate the skin friction coefficient when there was heat transfer to the plate. He recognized that some error

might be introduced since, with heat transfer, the wall density does not represent the average density of the flow to which the roughness is exposed. To compute the skin friction coefficient for flows in the region between the smooth plate and the fully rough one, Clutter makes use of the smooth flat plate theory of Van Driest (Ref. 120) and derives an empirical interpolation formula. To calculate heat transfer coefficients, Clutter suggests the use of smooth plate values of the temperature recovery factor and the Reynolds analogy factor.

In Ref. 115, Young reports the results of simultaneous measurements of the local skin friction and the heat transfer rate on a flat plate in turbulent flow. The experiments were run at a Mach number of 4.93 with two-dimensional V-grooves as the roughness elements. Measurements were made at a single station on the plate with constant tunnel supply pressure, $p_{t\infty}$, and constant plate surface temperature, T_w . The ratio of wall to free-stream temperatures, T_w/T_1 , was varied by changing the tunnel supply temperature. Values of the local skin friction coefficient and the local Stanton number are plotted on Fig. 7-23. The three V-groove heights tested ($h = 0.0025, 0.005$, and 0.015 in.) were respectively about 0.6, 1.2, and 4.0 times the thickness of the laminar sublayers. The values of C_f on Fig. 7-23 show that when $h = 0.0025$ in., the plate is essentially smooth; when $h = 0.005$ in., there is a small increase in C_f , and when $h = 0.015$ in., there is a large increase in C_f . It may also be seen from this figure that Van Driest's theoretical values of C_f are in reasonable agreement with the data. One calculated curve using Clutter's method is shown for the case of sand roughness with a grain size, k , of 0.015 in. The data point for $h = 0.015$ in. at $T_w/T_1 = 5.1$ (i.e., corresponding to zero heat transfer), is seen to be above the Clutter curve. Young concludes from this that the values of h and k are not equivalent but rather that $k = 1.82 h$. This relationship contrasts sharply with the results of Fenter (discussed in Subsec. 6.5) which give $k = 0.6 h$. At low values of T_w/T_1 , the Clutter curve is above the experimental data, and Young concludes from this that the ratio of wall to free-stream densities should not be used in calculating skin friction coefficients for a plate with heat transfer. When heat is transferred to the wall, the average density of the flow to which the roughness is exposed is less than the wall density. This is borne out by the differences between Clutter's calculations and the test data.

The experimental values of Stanton number, St , plotted on Fig. 7-23 are well below the values of C_f . Although there is a marked increase in St when $h = 0.015$ in., it appears smaller than the corresponding increase in C_f . Values of $C_f/2St$ have been computed from corresponding values of C_f and St plotted on Fig. 7-23, and the results are plotted on Fig. 7-24. The smooth plate Reynolds analogy factor, $Pr_w^{2/3}$, is shown for comparison. Essentially all the experimental values, even those on the smooth plate, fall above $Pr_w^{2/3}$. Although the experimental values appear to increase with increasing roughness, it can be seen that all the data fall between $C_f/2St = Pr_w^{2/3}$ and $C_f/2St = 1.0$. It should be noted that Young used the smooth-plate recovery factor in reducing the heat-transfer data since

this value appears to be valid for the rough surfaces and the flow conditions under which they were investigated.

In Ref. 162, Jones gives experimental turbulent heat transfer rates on cones (10° half-angle) with several surface finishes. The tests were conducted at a free-stream Mach number of 4.95. The largest roughness investigated was about two or three times the height of the laminar sublayer. Very little effect of roughness on the heat transfer rate was measured. This is in agreement with the results of Young shown on Fig. 7-24.

In view of the test results discussed above and the scarcity of additional data, it is recommended that heat transfer calculations for surfaces with sand roughness be based on the skin friction calculations of Clutter given in Subsec. 6. It is further recommended that the temperature recovery factor and the Reynolds analogy factor for rough plates be computed as described in Subsec. 7.1.3 for smooth plates. It appears that this method should yield conservative results.

7.6 Heat Transfer in Separated Flows

Heat transfer in separated flows can be either greater or less than that in attached flows. If the flow conditions at the leading edge of a separated region are the same as those for an attached flow and both flows are laminar, the heat transfer can be reduced by separation. This is also true if both flows are turbulent. However, if the attached flow is laminar and the separated flow undergoes transition to turbulence, the separated flow may produce higher heating rates. High local heating rates may be produced by high pressures which occur at the reattachment point. With separated flows, the occurrence of several oblique shocks produces higher pressures on reattachment and thus higher heat transfer rates than if there is a single strong shock. Even if the pressure at reattachment is the same in both cases, the flow downstream of the reattachment may have a lower entropy when there are several oblique shocks and thus produce higher heat transfer rates than in the case of a single strong shock.

Chapman (Ref. 163) predicts heat transfer rates to a surface which forms the boundary of a separated region. He took as a model a two-dimensional cavity and assumed that the region of recompression through the reattachment zone was small. The pressure was thus taken to be essentially constant over the separated region. It was further assumed that the boundary-layer thickness at the onset of separation was zero and that the mixing zone was thin compared to the depth of the region of separation. With laminar flow and $Pr = 0.72$, Chapman found that the heat transfer rate for the separated flow was 56% of that for an equivalent attached flow. An equivalent attached flow is defined as one which has the same Mach number and Reynolds number at the outer edge of the boundary layer as those at the outer edge of the mixing region of the separated flow. The wall to free-stream temperature ratio is also the same in each case. Chapman estimates the heat transfer rates for the case of turbulent flow and concludes that at low Mach numbers separation causes heat transfer rates to be several times as great as the values for attached flow. However, this increase becomes less with increasing Mach number. Measured heat transfer rates agree with Chapman's laminar predictions but disagree with the turbulent values. This will be discussed later.

Tests on nose spikes used to reduce the drag of hemisphere-cylinders showed that the flow which became turbulent after separation caused higher heat-transfer rates than an attached laminar flow. Stalder and Nielsen (Ref. 164) give experimental results which show that, although the drag of a hemisphere-cylinder is reduced by a nose spike, the total heat transfer rate to the hemisphere is doubled. This was shown to be true for all spike lengths tested at the three test Mach numbers of 1.75, 2.67, and 5.04. Crawford and Rumsey (Ref. 165) showed, however, that the Reynolds number had a marked effect on the heat transfer rates. Data for a Mach number of 6.8 are given in Fig. 7-25 which shows that at a high Reynolds number the heat transfer over most of the hemisphere and all of the cylinder is greater for the model with a spike. Schlieren photographs of the spiked nose indicate that the flow in the separated region is turbulent. The total heat transfer to the hemisphere is doubled by the addition of the spike. At the lower Reynolds number, the heat transfer rate over the hemisphere is decreased. The total heat transfer is roughly one-half of the total heat transfer on the hemisphere without a spike. The heat transfer on the cylinder is relatively unchanged. The flow in this case was laminar in the separated region and also laminar over the entire body. Crawford (Ref. 166) gives further information on the effect of spikes on the heat transferred to a hemisphere-cylinder at the same Mach number (6.8). The Reynolds number, $Re_{\infty d}$, based on free-stream conditions and cylinder diameter was varied from 0.12×10^6 to 1.5×10^6 . Spikes up to four cylinder diameters in length were tested. The effects of spike length and Reynolds number on the shape of the separated region and on the location of transition within it were determined. Heat transfer and pressure distributions were correlated with the separation point, the reattachment point, and the start of transition.

Crawford and Rumsey (Ref. 165) give interesting experimental results for an ogive-cylinder with a stabilizing flare. The data are plotted on Fig. 7-26 which shows two cases: One with a high Reynolds number producing transition on the body and attached flow at the cylinder-flare junction, the other with a low Reynolds number giving laminar separation on the cylinder. Where there is no separation, the laminar prediction agrees with the data. The predicted heat transfer rate for the flare was computed on the assumption that a turbulent boundary layer started at the beginning of the flare. Where there is separation, the predicted heat transfer rate for the laminar portion ahead of the separation point agrees with the test data. The curve labeled "attached laminar flow" (Fig. 7-26) which lies above the data points taken in the separation region was computed for an attached flow with an increased pressure corresponding to the separated flow. The curve labeled "separated laminar flow" was obtained by taking 56% of the values along the attached laminar flow curve in accordance with Chapman's theory (see Ref. 163). The separated curve so obtained is in reasonable agreement with the test data in the separated region ahead of transition. The turbulent prediction on the flare was made by assuming that a turbulent boundary layer started at the reattachment point. To check Chapman's estimate of the effect of separation on the heat transfer with turbulent flow, Crawford and Rumsey obtained data for a flat plate with transverse stringers. The results are shown on Fig. 7-27. The turbulent theory shown on the figure is in agreement with measurements made on the plate without the stringers. Although there are high heat transfer rates on the upstream faces of the stringers where the pressure is high, the heat transfer in the region of separation behind each stringer is always lower than the smooth plate value. This is in contrast to Chapman's prediction of an increase.

Larson (Ref. 167) gives experimental results which are in agreement with Crawford and Rumsey, i.e., the heat transfer in both laminar and turbulent separated flows are lower than the equivalent attached flows. Sketches of the two electrically heated, axisymmetric models are shown on Fig. 7-28 where values of the average Stanton number, \bar{St} are plotted. The heat transfer coefficient in \bar{St} is an average of the measured values in the cross-hatched sections shown in the sketches; the flow properties in \bar{St} are those at the outer edge of the separated region. The Reynolds number, Re_{1L} , is based on the length L shown on the sketch and conditions at the outer edge of the separated region. In the separated laminar flow, \bar{St} is proportional to $Re_{1L}^{-1/2}$ just as it is in the attached laminar flow. Chapman's figure of 56% closely predicts the reduction in level due to separation. It can be seen that in turbulent flow also, separation causes a large reduction in the heat transfer. For the attached turbulent flow, the Stanton number is proportional to $Re_{1L}^{-1/5}$. For the separated flow the Stanton number is much more sensitive to Reynolds number, being proportional to $Re_{1L}^{-2/5}$. At a constant Reynolds number, the reduction in heat transfer for the turbulent case was found to be essentially independent of Mach number for values of M_1 from 0.3 to 4.0. Although for both the laminar and turbulent cases separation reduced the average heat transfer, Larson made measurements which showed that the local heat transfer rates in the reattachment zone near the end of the cavity were quite high. The ratio of local heat transfer rate to the average rate, q/q is shown in Fig. 7-29 as a function of distance along the model. Larson also presents transition data for the separated flows. These data are necessary in order to determine whether separation will decrease or increase the heat transfer rates. The Reynolds number of transition Re_{tr} is plotted as a function of the free-stream Mach number on Fig. 7-30. The transition Reynolds number appears to be based on free-stream conditions and the length l' of the laminar separated region shown on Fig. 7-30. The value of l' is found by determining the cavity length for which transition will be just downstream of the reattachment point. Figure 7-30 displays two very interesting features. Firstly, it may be seen that the transition Reynolds number increases very rapidly with Mach number. This indicates that laminar separation is quite significant at high Mach numbers. Secondly, it may be noted that cooling the wall below the adiabatic temperature steadily decreases the transition Reynolds number. This is in contrast to the behavior for attached flows where, at least for some range of wall temperatures, the trend is the opposite.

The reduction in heat transfer with turbulent separation has also been noted in free flight at Mach numbers up to 8.5 (see Ref. 168). The increase in heat transfer at reattachment has also been detected by a number of investigators. In fact, the use of cavities to promote separation has in some cases been found to increase the total heat transfer even when the flow remained laminar. This is due to the high local rates in the reattachment region. Figure 7-31 from Ref. 169 shows the effect of separated flow on a cavitated conical nose. At the lowest wall temperature the boundary layer was attached to the cavity and the total heat transfer was approximately equal to that on the straight cone. At the higher wall temperatures, the flow separated and the heat transfer rates were very high at the reattachment point just ahead of the shoulder. High local heating rates at reattachment are also reported in Ref. 170 which states that streamwise pressure and heating rate gradients are extremely large just prior to reattachment and lead to exceptionally high pressures and heating rates downstream of attachment on trailing edge flaps in hypersonic flow.

Holloway, Sterrett, and Creekmore (Ref. 175) investigated at a Mach number of 6 the heat transfer associated with separated regions caused by wedges (10, 20, 30, and 40 deg) as well as forward and rearward facing steps on a flat plate. The trends of their heating rates in the laminar, transitional, and turbulent regions of separation substantiate those already discussed.

In discussing heating rates in separated regions, mention should be made of the pressure rise or pressure gradient required to induce separation. This information is required in order to determine whether an attached or separated condition is to be dealt with. Data on this subject are given in Refs. 171 to 173. A very comprehensive review of the information available at that time is given in Ref. 174.

7.7 Turbulent Heat Transfer Near Protuberances

A protuberance causes changes in the local static pressure, the recovery temperature, and the heat transfer rate. The temperature recovery factor near a single cylindrical protuberance is shown on Fig. 7-32. These data are wind-tunnel test results reported by Wisniewski in Ref. 176. The protuberance was mounted 14 in. from the conical tip (20 deg total angle) of a cone-cylinder model 1.75 in. in diameter and 18 in. in length. For these tests transition was fixed between 2 and 4 in. from the tip of the cone by means of sand blasting. At a Mach number of 3.12 and the test Reynolds numbers of 4.5×10^6 and 8×10^6 per foot, the protuberance shown on Fig. 7-32 was immersed in the boundary layer. Without the protuberance, the recovery factor would be approximately 0.89. The data show that the recovery factor is increased for several protuberance diameters upstream of the protuberance location and decreased for several diameters downstream. Data for recovery factors near two-dimensional protuberances are given by Brinich in Refs. 124 and 177, and data on 20 different protuberance configurations (listed in Table 7-2) are given by Burbank, et al in Ref. 178.

The effect on the heat transfer rate of the single cylindrical protuberance discussed above is shown on Fig. 7-33. The ratio of the film coefficient with and without the protuberance is plotted. The data show that for a protuberance immersed in the boundary layer, the heat transfer data is increased by a factor of up to 1.5. The effect of the protuberance on the heat transfer, like its effect on the recovery factor, extends for several diameters upstream and downstream of the protuberance. It is interesting to note that the heat transfer rate is increased at all measuring stations along the 0 deg generator on which the protuberance is located. The 22.5 deg generator also shows increased heating rates, but on the 45 deg generator there is no appreciable change.

Figure 7-33 should be compared with Fig. 7-34 which gives the heat-transfer ratio for a protuberance whose height is greater than the boundary-layer thickness. The data in Fig. 7-34 were taken from the wind-tunnel tests of Burbank, et al (Ref. 178). The protuberance in these tests was a cylinder 12.5 in. high, mounted on a flat plate. The measurements were made for three nominal boundary-layer thicknesses, 0.7, 1.5, and 6.0 in. The two smaller thicknesses were achieved by mounting the plate at two different places in a supporting structure and, for the 6 in. boundary layer, the plate was mounted on the wind-tunnel wall. Figure 7-34 shows that the heat transfer rate just in front of the protuberance can be increased by a factor of 7 or 8 at the test Mach number of 3.51. Downstream of the cylinder it is increased by a factor of two. Figure 7-35 gives more information on the effect of the cylinder in the 6 in. boundary layer. It shows:

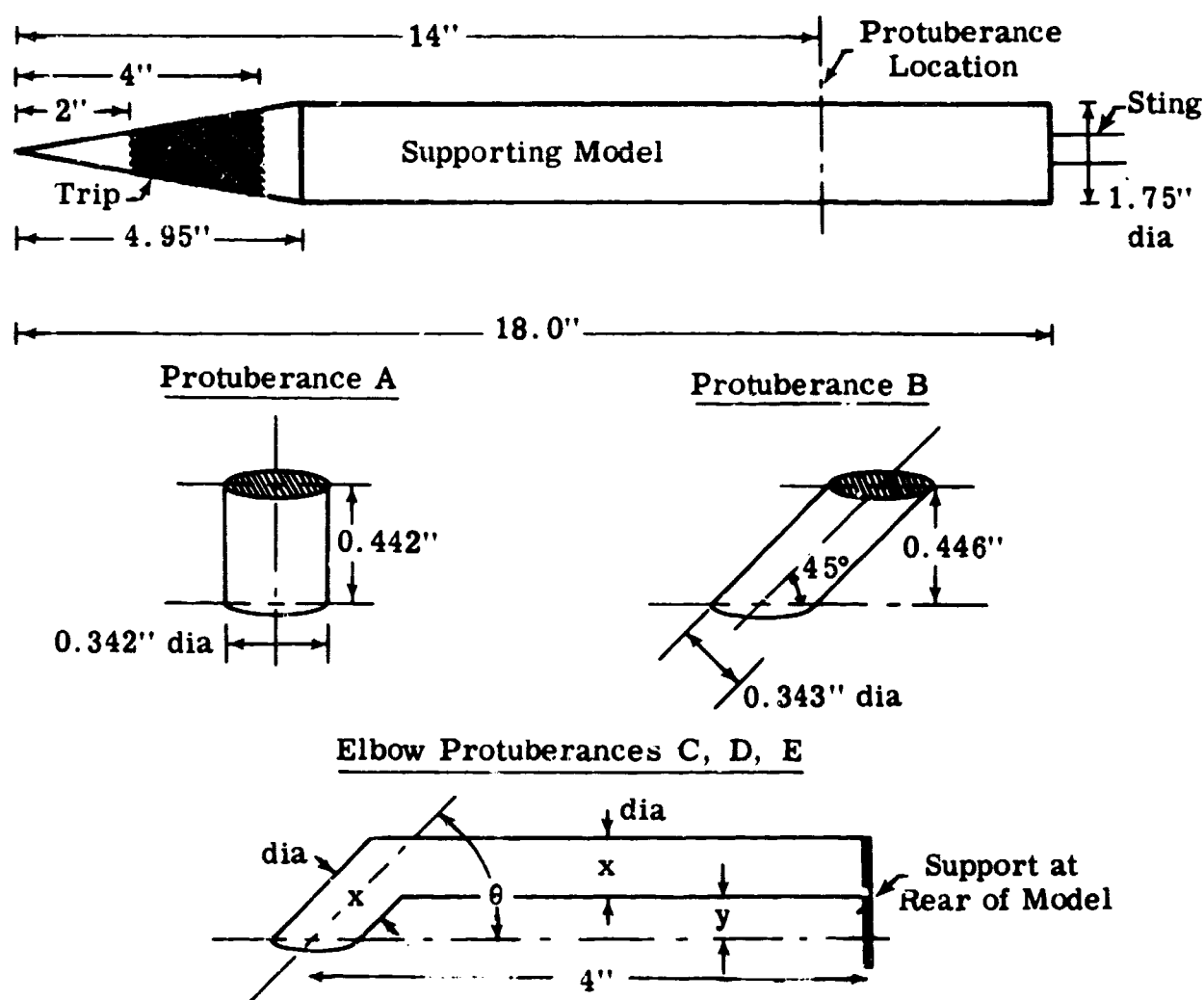
1. Contours of constant h/h_0 on the plate in the vicinity of the protuberance for $M = 3.51$ and $Re/ft = 2.76 \times 10^6$.
2. The effect of unit Reynolds number (1.6×10^6 , 2.76×10^6 , and 3.96×10^6) along the center line of the plate in the direction of the flow at $M = 3.51$.
3. The effect of Mach number (2.65, 3.51, and 4.44) at a Reynolds number of 2.76×10^6 per foot.

Figures 7-36 and 7-37 give similar information on the effect of sweeping the protuberance forward and aft, respectively. With a 45 deg forward sweep, the heat transfer rate in front of the cylinder is increased. At the highest test Mach number the heat transfer rate is twice the rate for the unswept cylinder. When the cylinder is swept aft, the heat transfer rates are greatly decreased. Figures 7-38 and 7-39 from Burbank, et al show heat transfer ratios in the neighborhood of simulated stiffeners, 2 and 4 in. in height, mounted transverse to the flow. Both the stiffeners have finite spans of 24 in. and were tested in boundary layers with a nominal thickness of 6 in. Both stiffeners were immersed in the boundary layer. It can be seen in Fig. 7-39 that the stiffener with the greatest height causes the largest increase in the heat transfer rate. This is consistent with the effect of the cylindrical protuberances.

The results of tests on several protuberance configurations are reported by Wisniewski in Ref. 176 and a large number by Burbank, et al in Ref. 178. In addition to these, heat transfer data are given by Bloom and Pallone in Ref. 179. These configurations and the conditions under which they were investigated are listed in Tables 7-1, 7-2, and 7-3.

Table 7-1

Protuberance Configurations Tested by Wisniewski (Ref. 176)



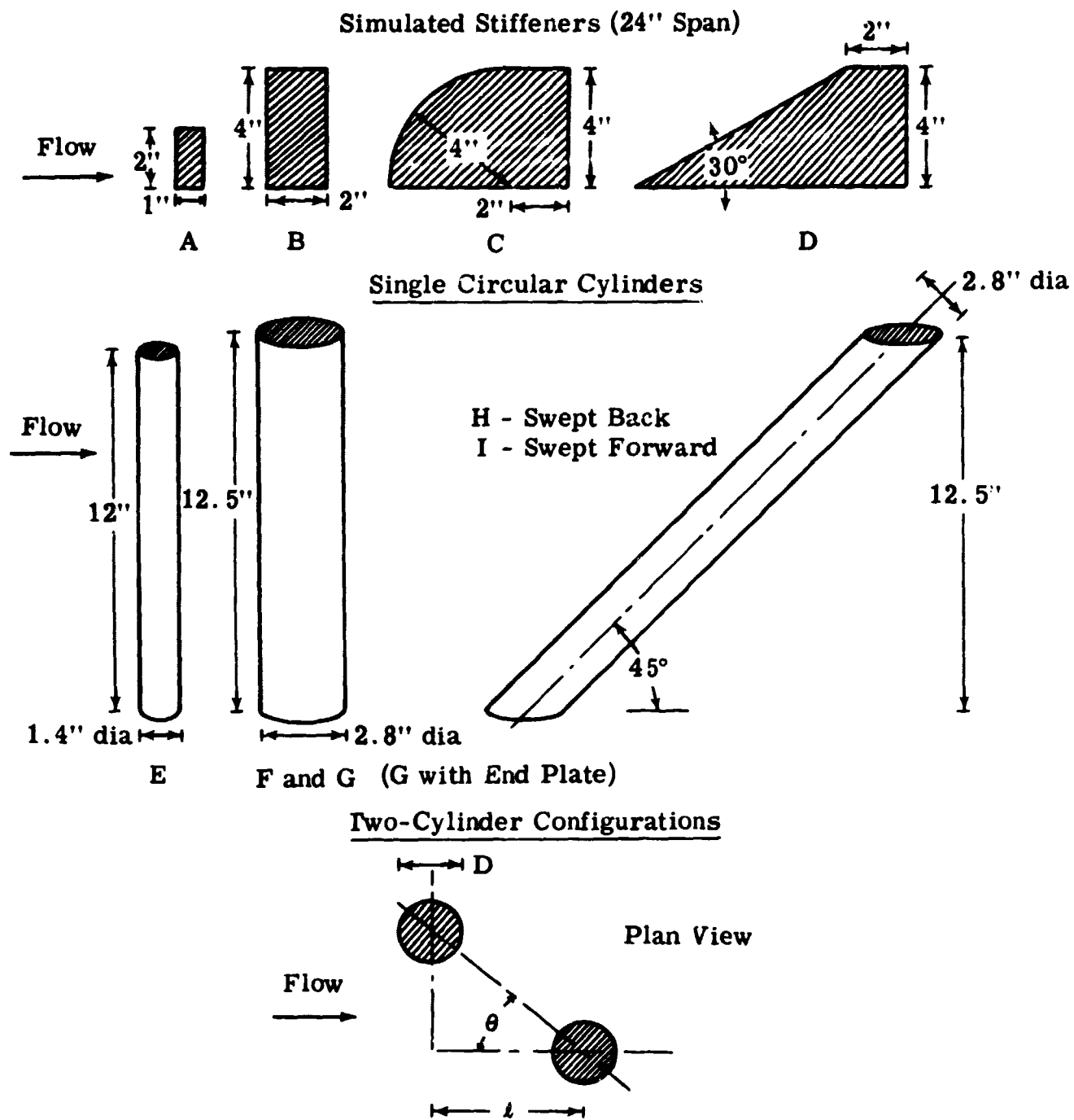
Model	x, in.	y, in.	θ , deg
C	0.345	0.096	90
D	0.498	0.091	90
E	0.342	0.090	45

Test Conditions and Measurements

Model	M_∞	$Re_\infty/\text{ft} \times 10^{-6}$	Recovery Factor	Heat Transfer
A	3.12	4.5, 8	Yes	Yes
B, C, D, E	3.12	8	No	Yes

Table 7-2

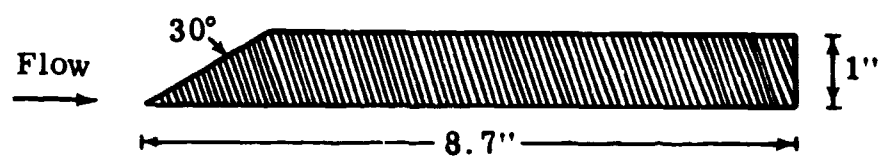
Protuberance Configurations Tested by Burbank, Newlander, and Collins
(Ref. 178)



Model	Ht, in.	D, in.	θ , deg	l
J	12.0	1.4	0	6.4D
K	12.0	1.4	26.5	6.4D
L	12.5	2.8	0	3.2D
M	12.5	2.8	0	6.4D
N	12.5	2.8	26.5	3.2D
O	12.5	2.8	45	3.2D

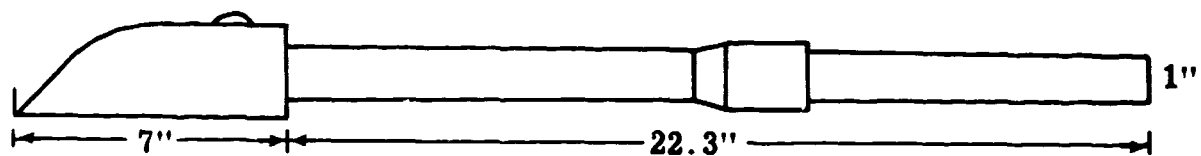
Table 7-2 (Cont.)

Simulated Cableway (24" Span)

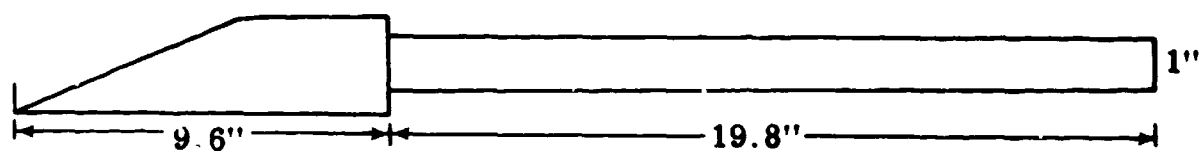


P

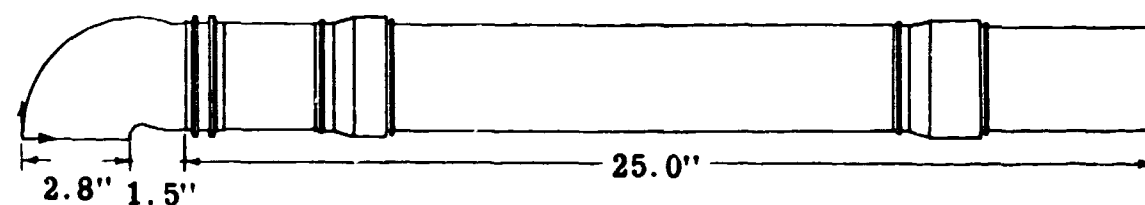
Simulated External Piping



Q (45° Fairing)



R (26° Fairing)



S (Lox Line)

Table 7-2 (Cont.)

Test conditions were:

1. $M_1 = 2.65$, $M_2 = 3.51$, and $M_3 = 4.44$.
2. $\delta_1 = 0.7$, $\delta_2 = 1.5$, and $\delta_3 = 6.0$ in.
3. At each M and δ , three Reynolds numbers were used between 1.25 and 4.7 millions per foot.
4. Pressures were measured on the supporting plate.
5. Heat transfer rates were measured on both the plate and the protuberance.

The table below itemizes the Mach numbers and boundary layer thickness used for each model. Exceptions to the general condition of three Reynolds numbers at each setting are noted in the end column.

Protuberance	M_∞	δ	Exceptions
A	M_1, M_2, M_3	all δ δ_1, δ_2	2 Re at δ_3 none
B*, C, D	all M	δ_3	*pressure at 1 Re only
E, K*	all M	δ_1, δ_2	*2 Re at δ_1
F*, I	all M	all δ	2 Re at δ_1 ; *no h at M_2, δ_2
G	all M	δ_1, δ_2	1 Re at δ_2, M_1 and M_3 ; 2 Re all others
H	all M	all δ	2 Re at δ_1, M_1 and M_2 ; at δ_2 , all M
J, Q, S*	all M	δ_2	*no h on model
L*, N*, P	all M	δ_2, δ_3	*2 Re at δ_2, M_2
M	all M	δ_2, δ_3	2 Re at δ_2, M_1 and M_3 ; 1 Re at δ_2, M_2
O	all M	δ_2, δ_3	2 Re at δ_2, M_1 ; 1 Re at δ_2, M_2 and M_3 ; no pressure at δ_2, M_3
R	M_1, M_2	δ_2	2 Re

Table 7-3

Protuberance Configurations Tested by Bloom and Pallone (Ref. 179)

All Models are Circular Cylinders of Stainless Steel

Group	Height (in.)	Diameter (in.)	Wall Thickness (in.)	Orientation to Surface (deg)
A	2, 1, $\frac{3}{4}$, $\frac{1}{2}$	3/8	0.05	90
B	2, 1	1	0.05	90
C	1	3/8	0.01	+45° and -45°

Test Conditions

$$\begin{aligned}
 M_{\infty} &= 6 \\
 Re/ft &= 4.4 \text{ to } 5.2 \text{ million} \\
 \delta &\sim 1.4 \text{ in.} \\
 p_t &= 600 \text{ psia} \\
 T_t &= 1460 - 1660^{\circ}\text{R}
 \end{aligned}$$

Heat transfer measurements made on the supporting
surface downstream of the protuberances

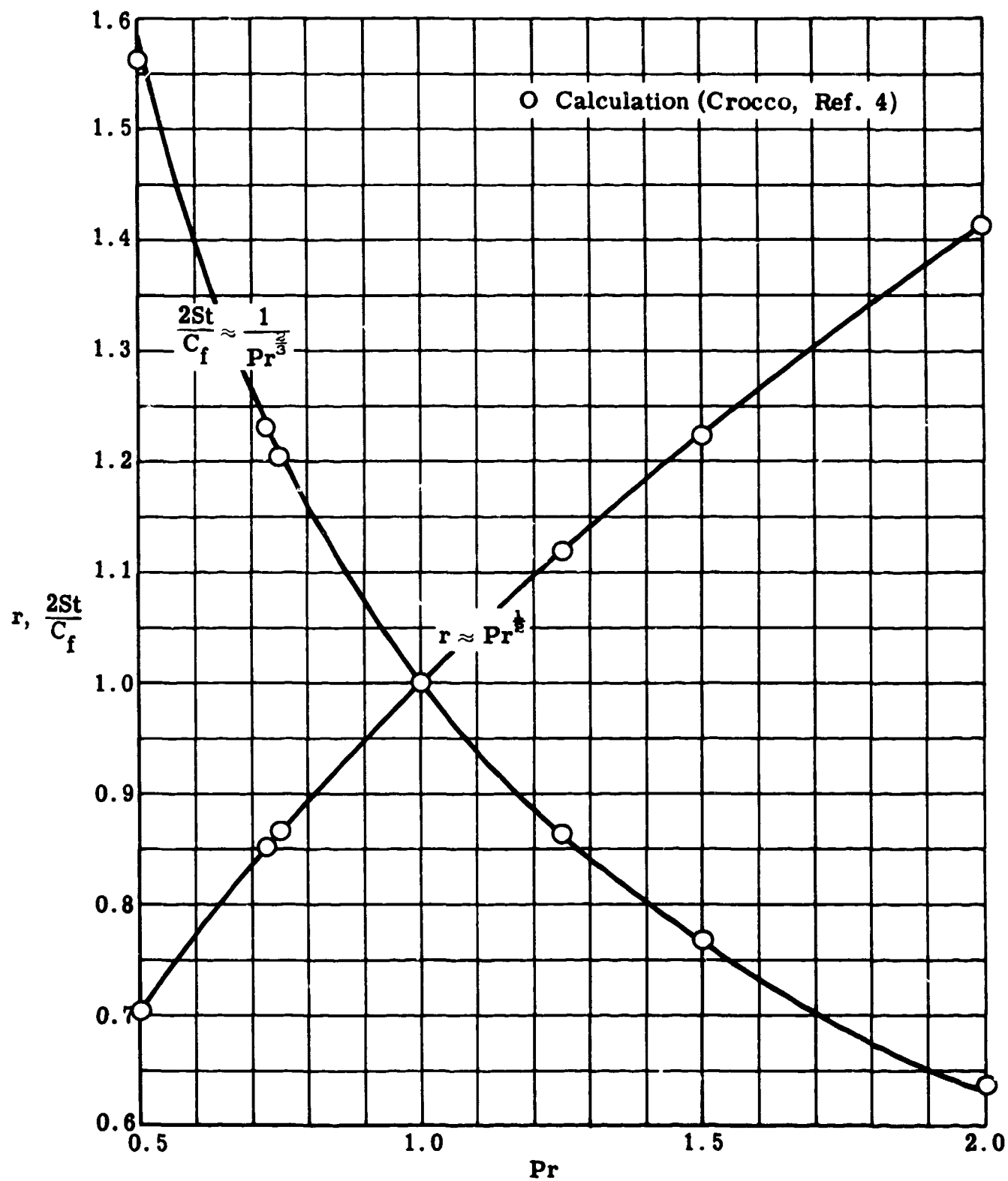


Fig. 7-1. Recovery factor and Reynolds analogy factor as a function of Prandtl number; flat plate, laminar flow, perfect gas.

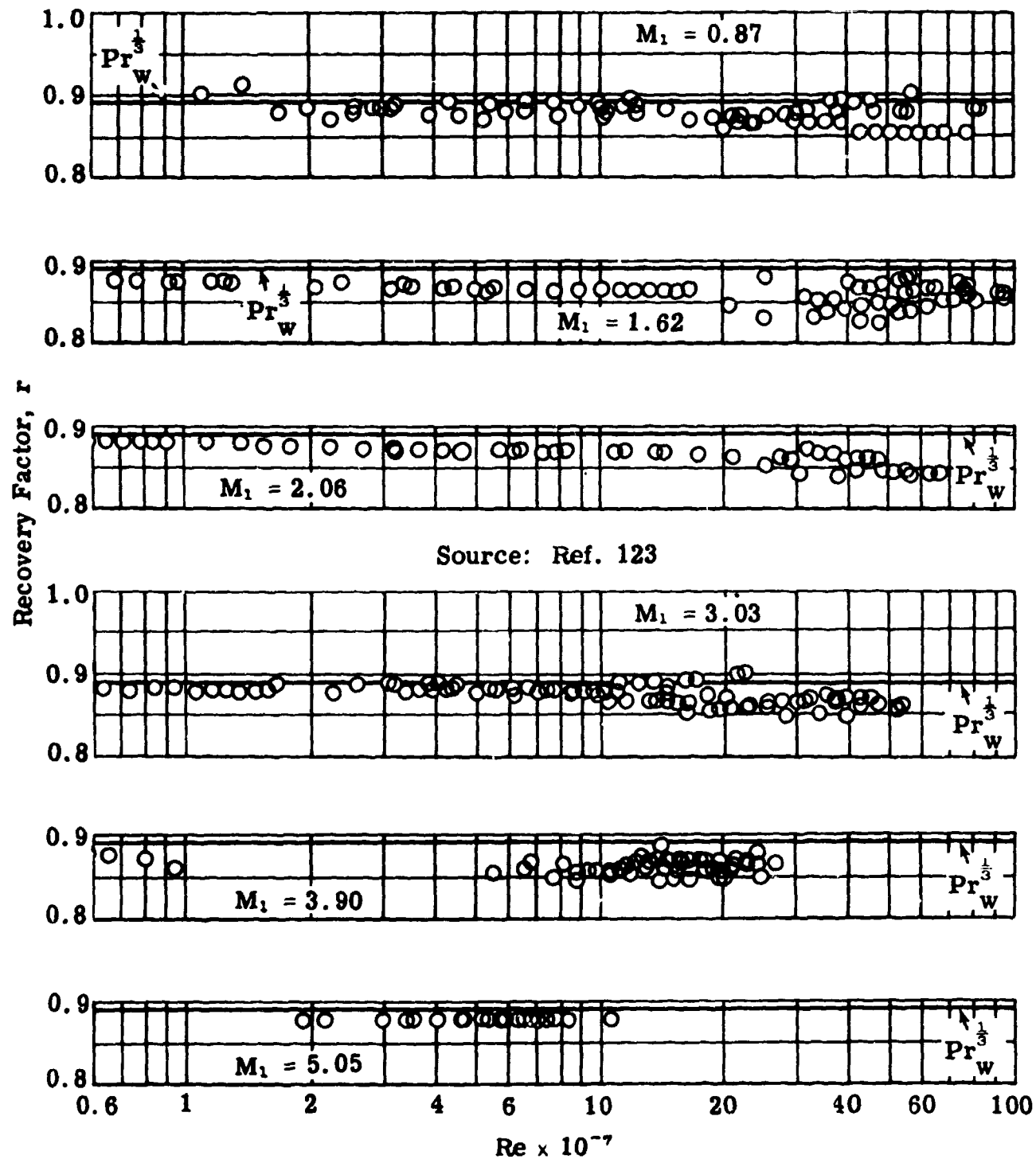


Fig. 7-2. Recovery factor vs Reynolds number; flat plate, turbulent flow, perfect gas; $M_1 = 0.87, 1.62, 2.06, 3.03, 3.90$, and 5.05 .

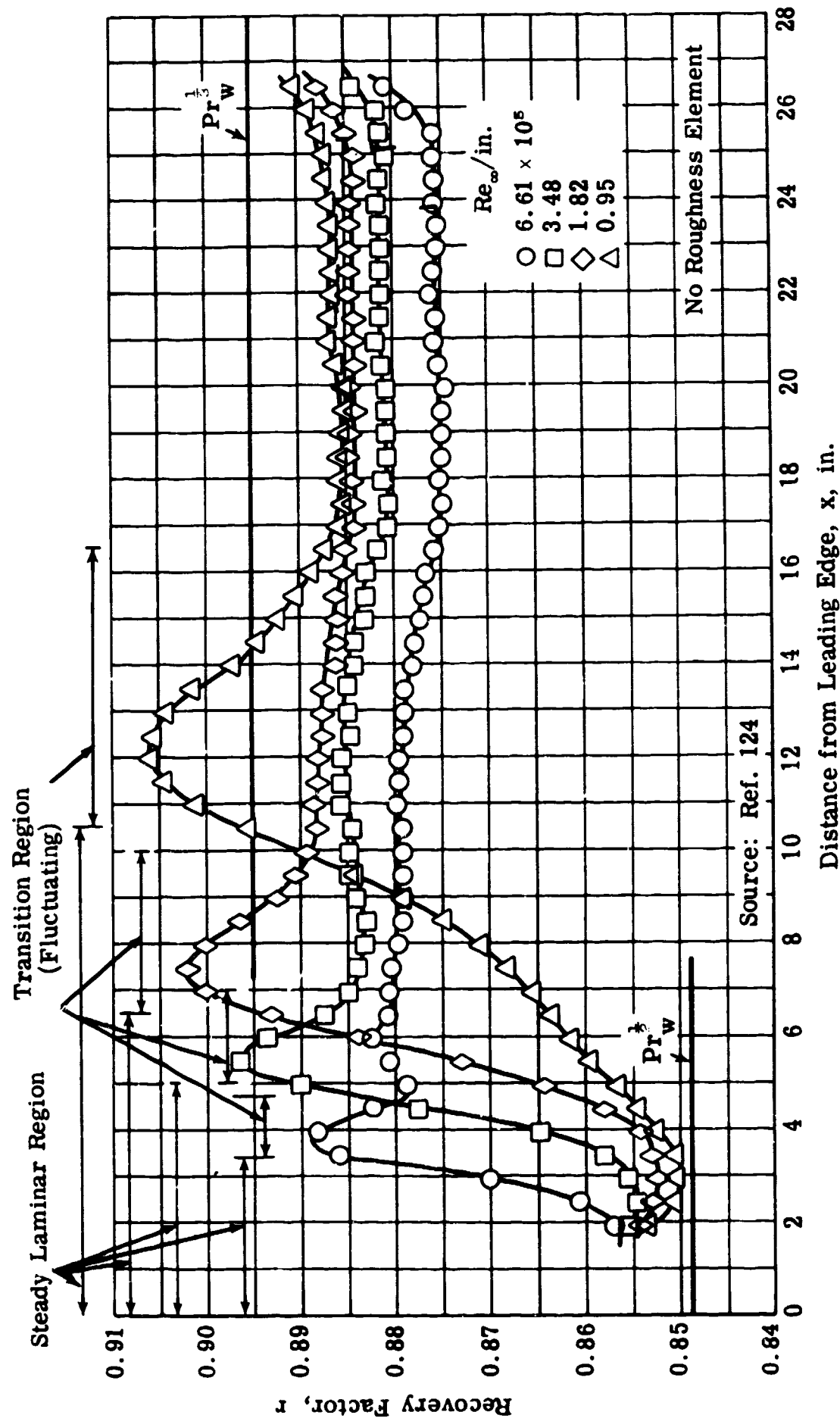


Fig. 7-3. Recovery factor as a function of distance from leading edge; transitional flow, perfect gas; $M_1 = 3.12$.

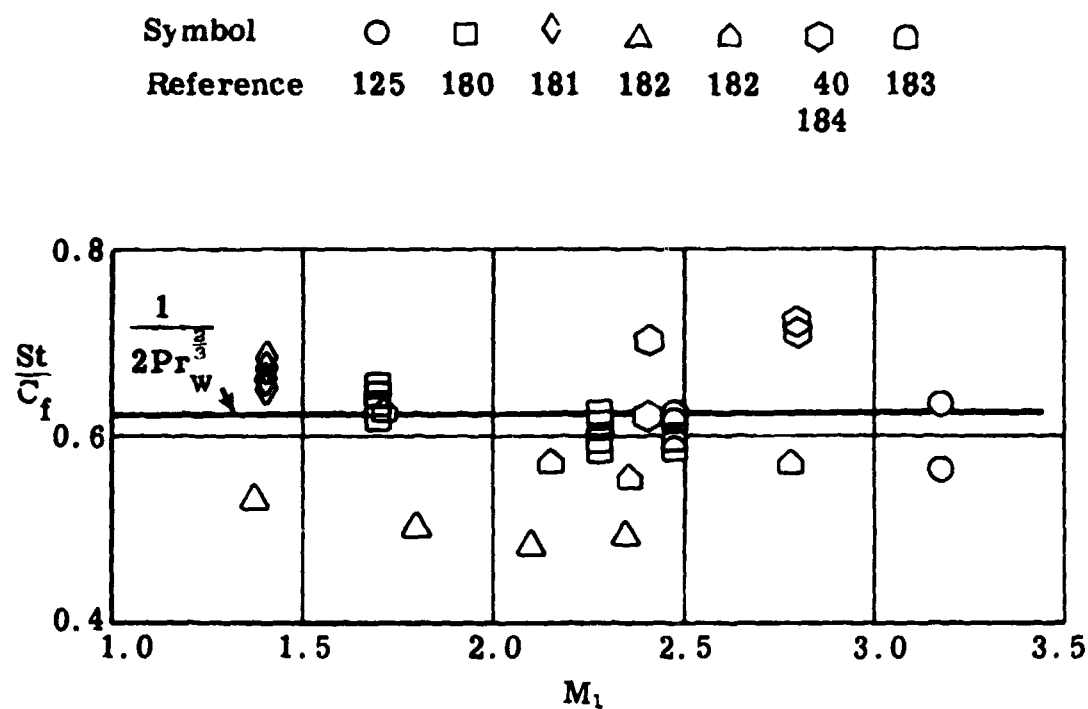


Fig. 7-4. St/C_f vs M_1 ; theoretical and experimental turbulent flow, flat plate, perfect gas.

Source: Ref. 125

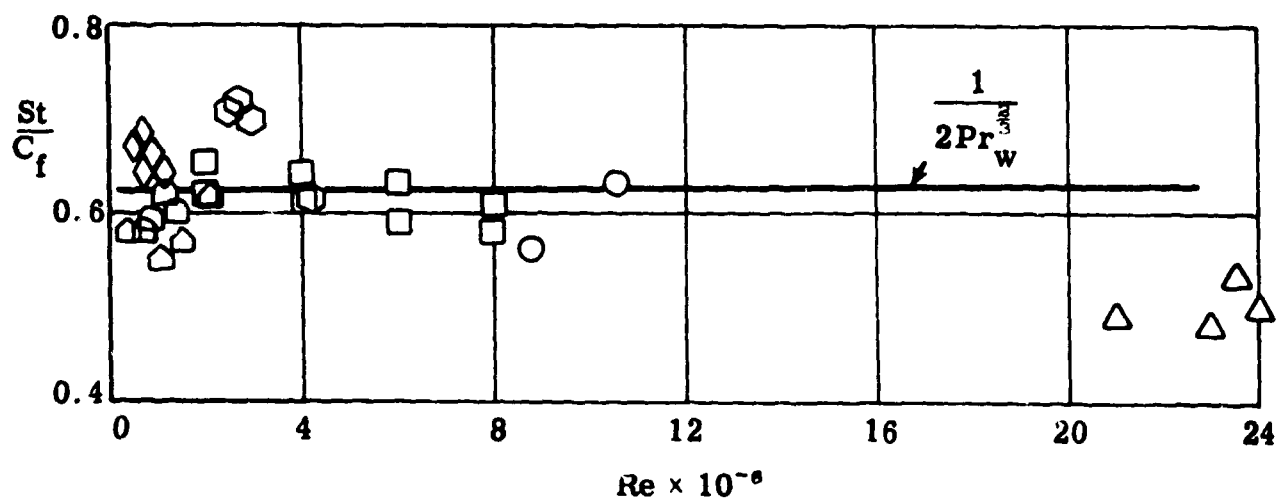


Fig. 7-5. St/C_f vs Re ; theoretical and experimental turbulent flow, flat plate, perfect gas.

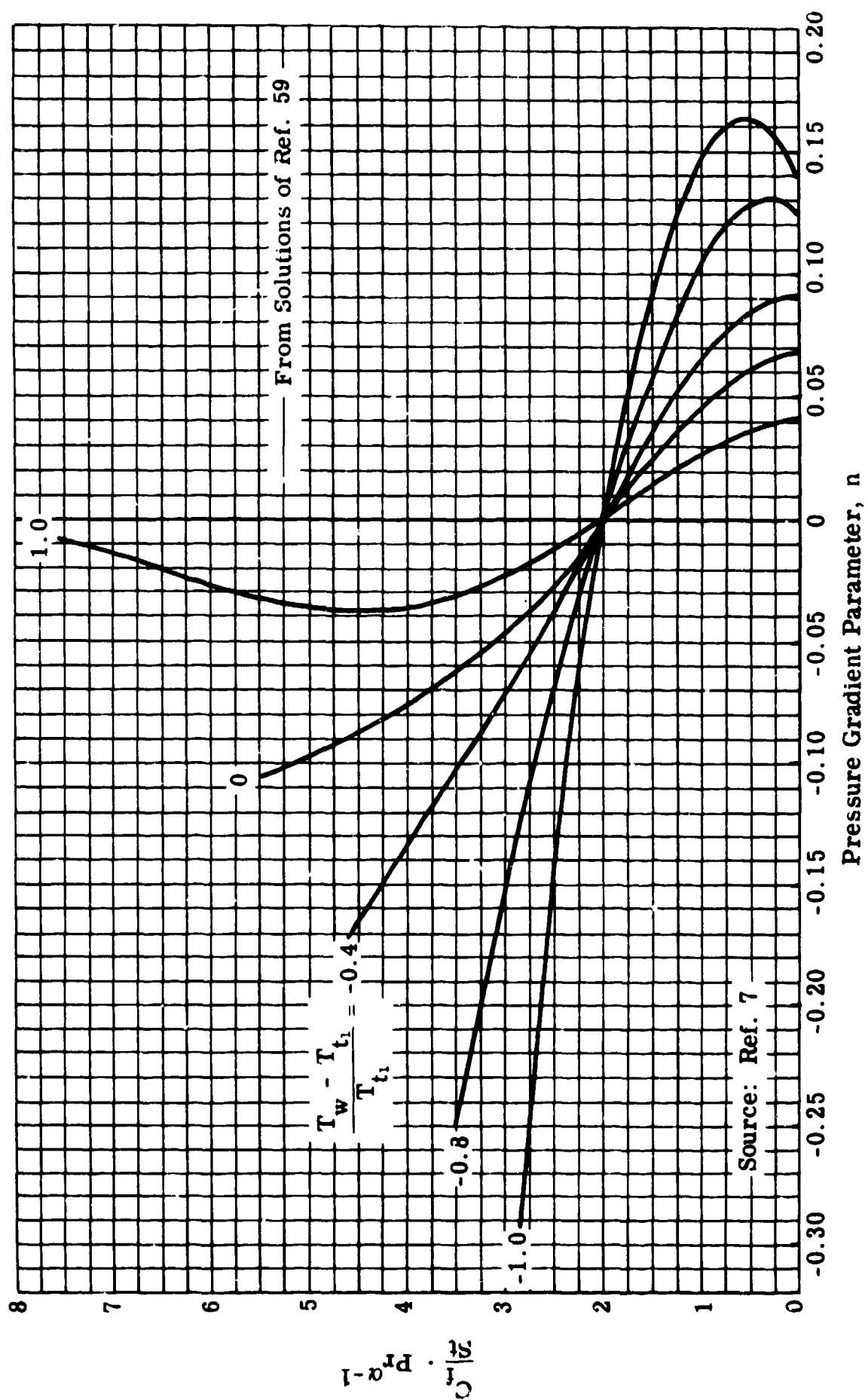


Fig. 7-6. Correlation of C_f/St with pressure gradient parameter, n , for $(T_w - T_{t1})/T_{t1} = -1.0, -0.8, -0.4, 0$, and 1.0 ; laminar flow, perfect gas.

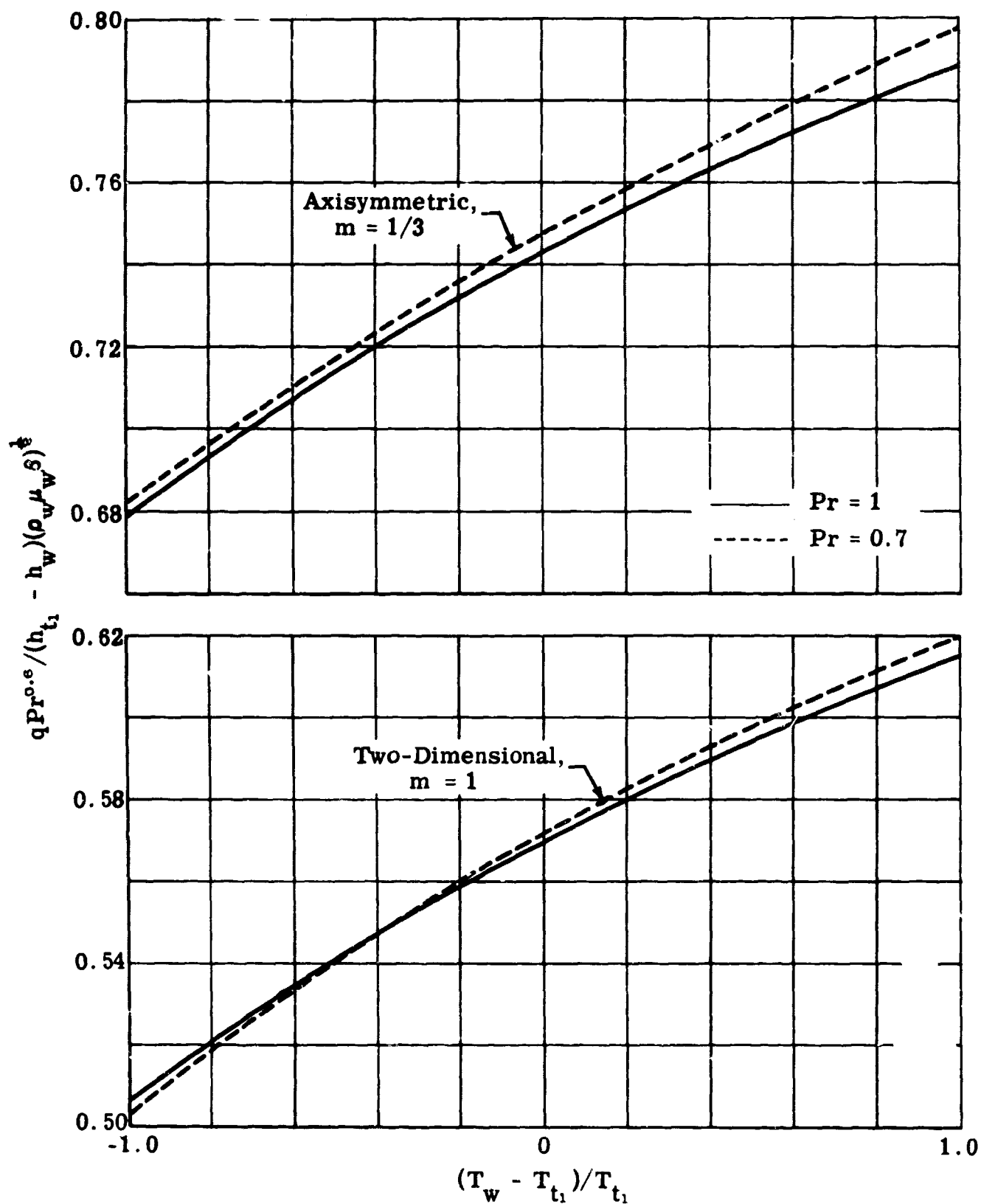


Fig. 7-7. Stagnation point heat transfer; laminar flow, perfect gas.

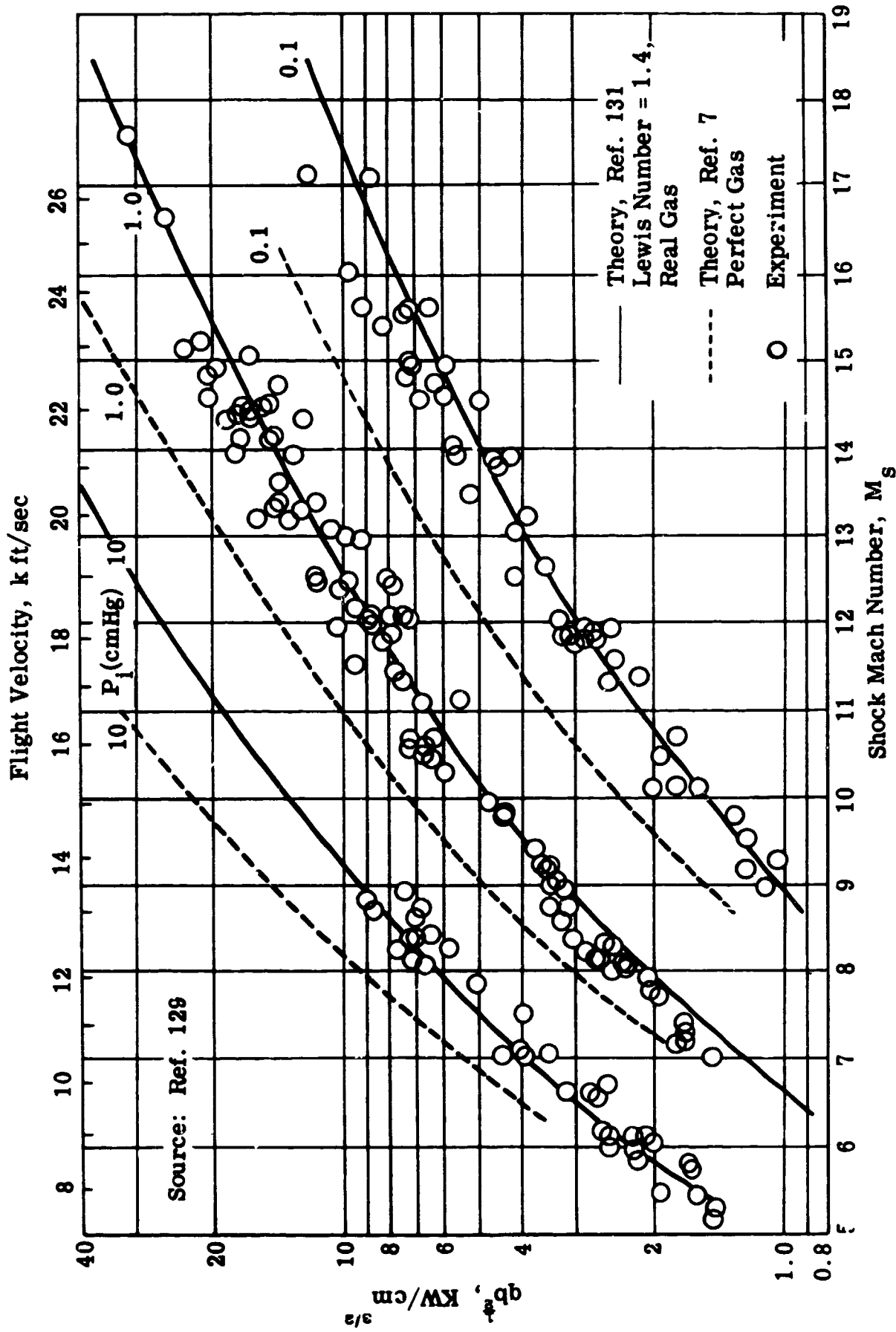


Fig. 7-8. Stagnation point heat transfer rate at suborbital velocities; theory and experiment, laminar flow.

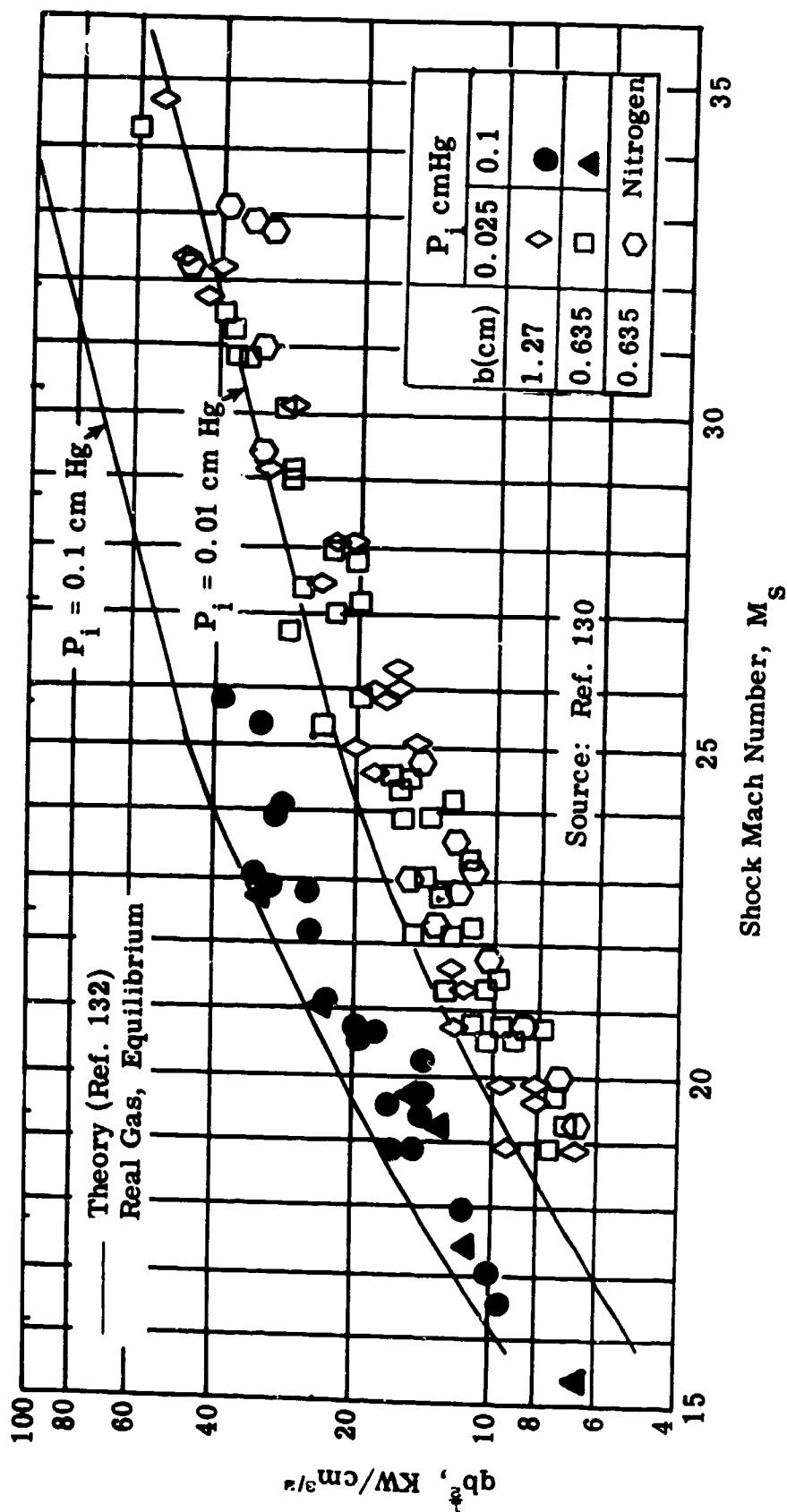


Fig. 7-9. Stagnation point heat transfer rate at super-orbital velocities; theory and experiment, laminar flow.

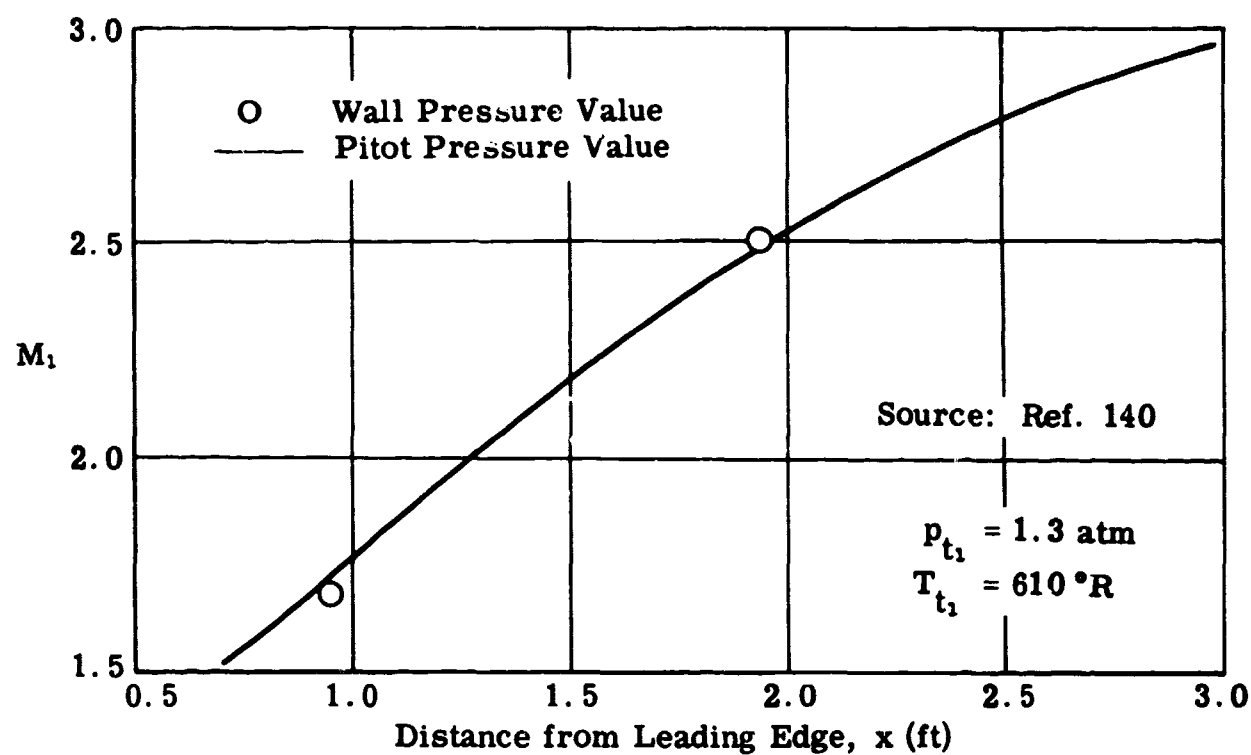


Fig. 7-10. Mach number distribution at outer edge of boundary layer; flat plate with pressure gradient; turbulent flow.

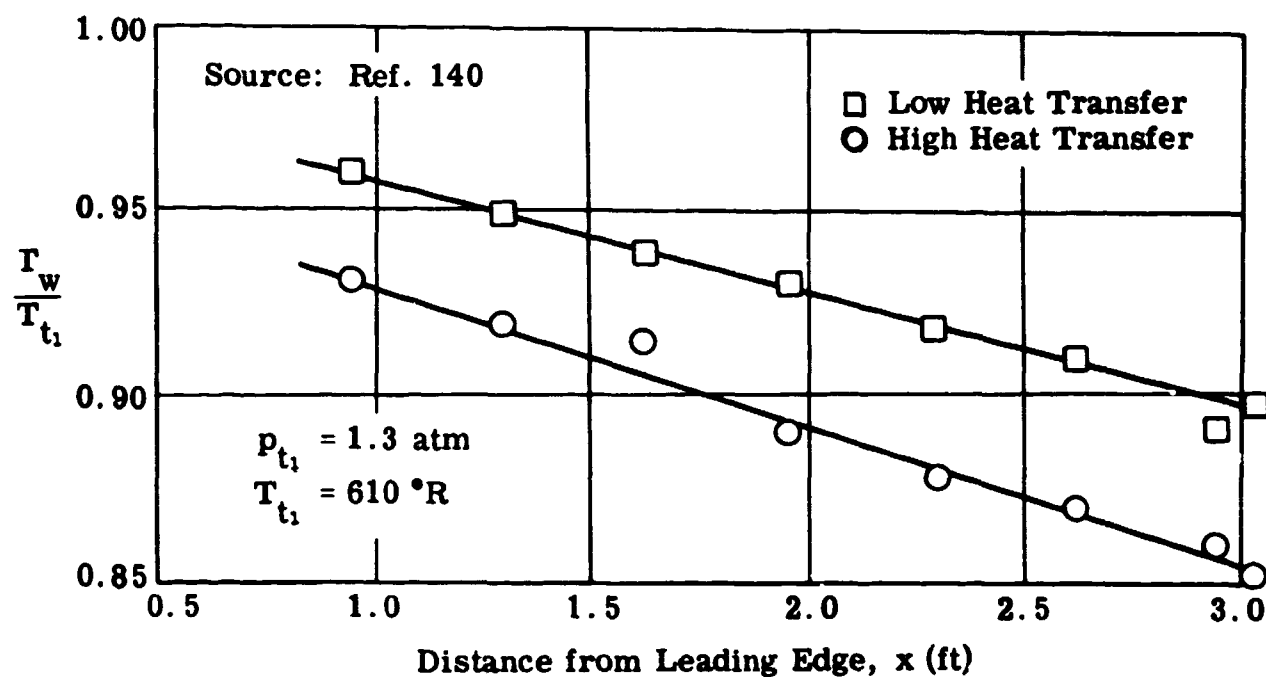


Fig. 7-11. Wall temperature distributions along a flat plate with pressure gradient; turbulent flow.

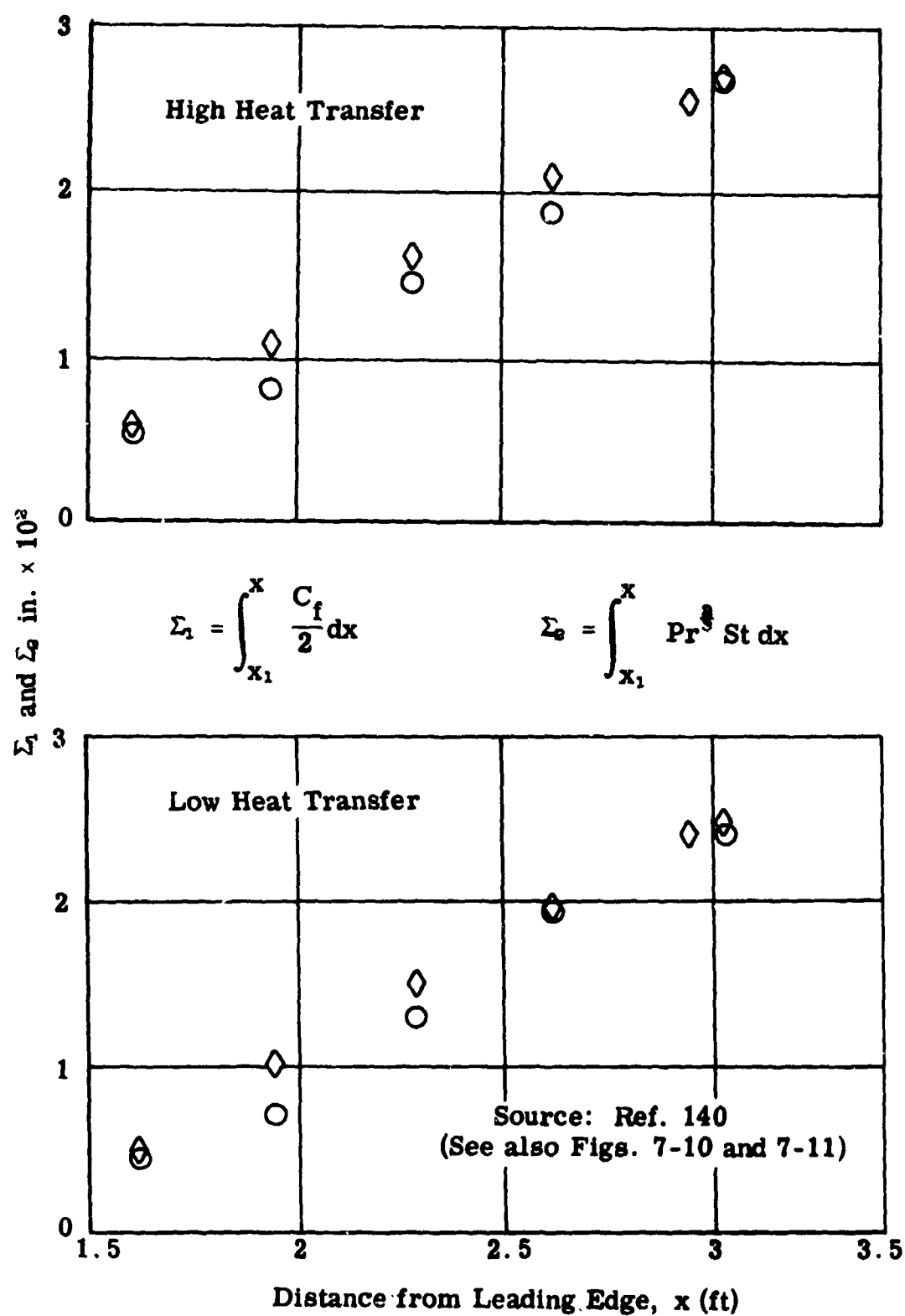


Fig. 7-12. Reynolds analogy factor along a plate with pressure gradient; turbulent flow.

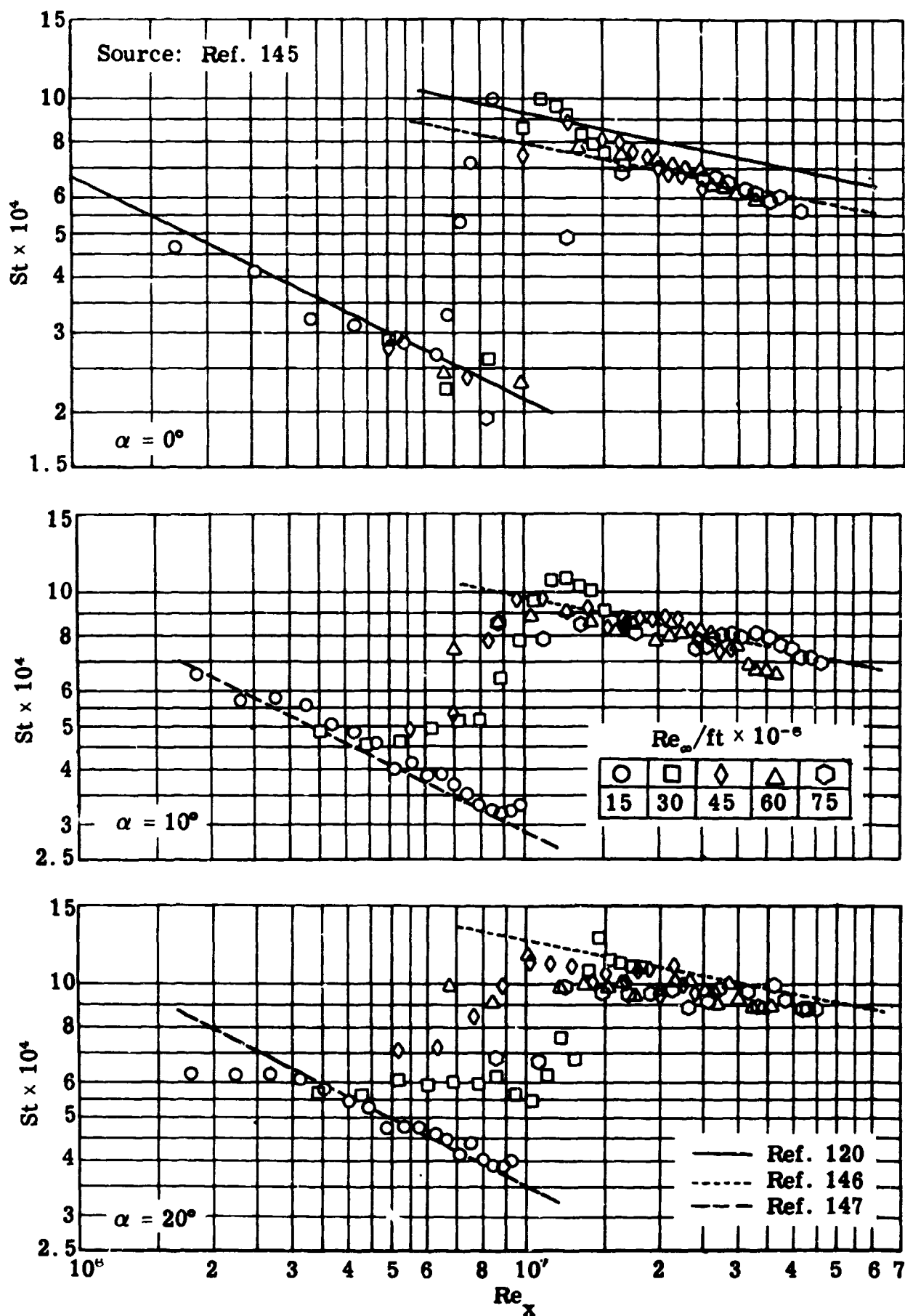


Fig. 7-13. Stanton number as a function of Reynolds number; theory and experiment; flow with transition on a 20° cone; $M_\infty = 4.95$; $\varphi = 0$; $\alpha = 0, 10$, and 20° .

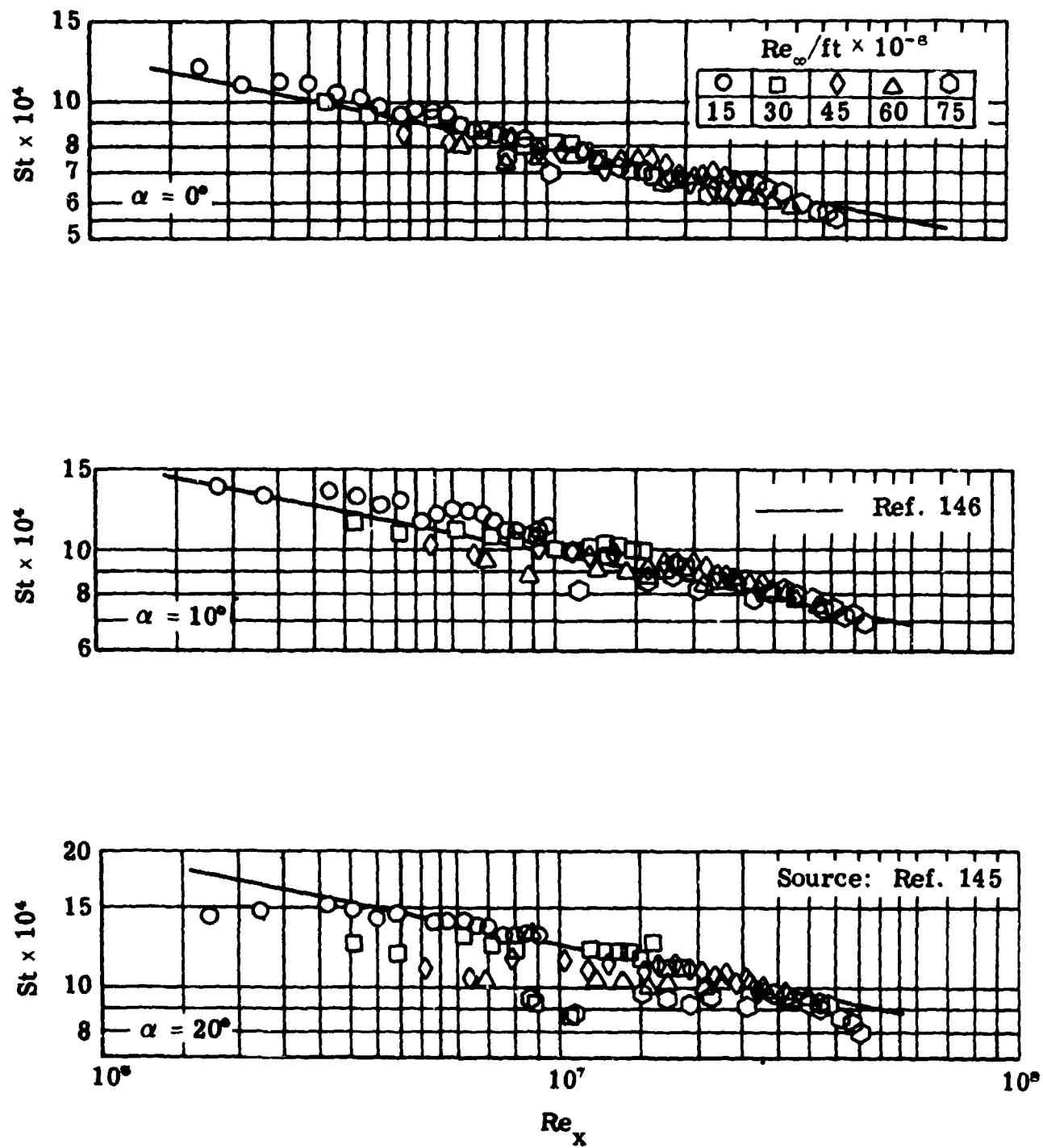


Fig. 7-14. Stanton number as a function of Reynolds number; theory and experiment; turbulent flow on a 20° cone; $M_\infty = 4.95$; $\phi = 0$; $\alpha = 0, 10, \text{ and } 20^\circ$.

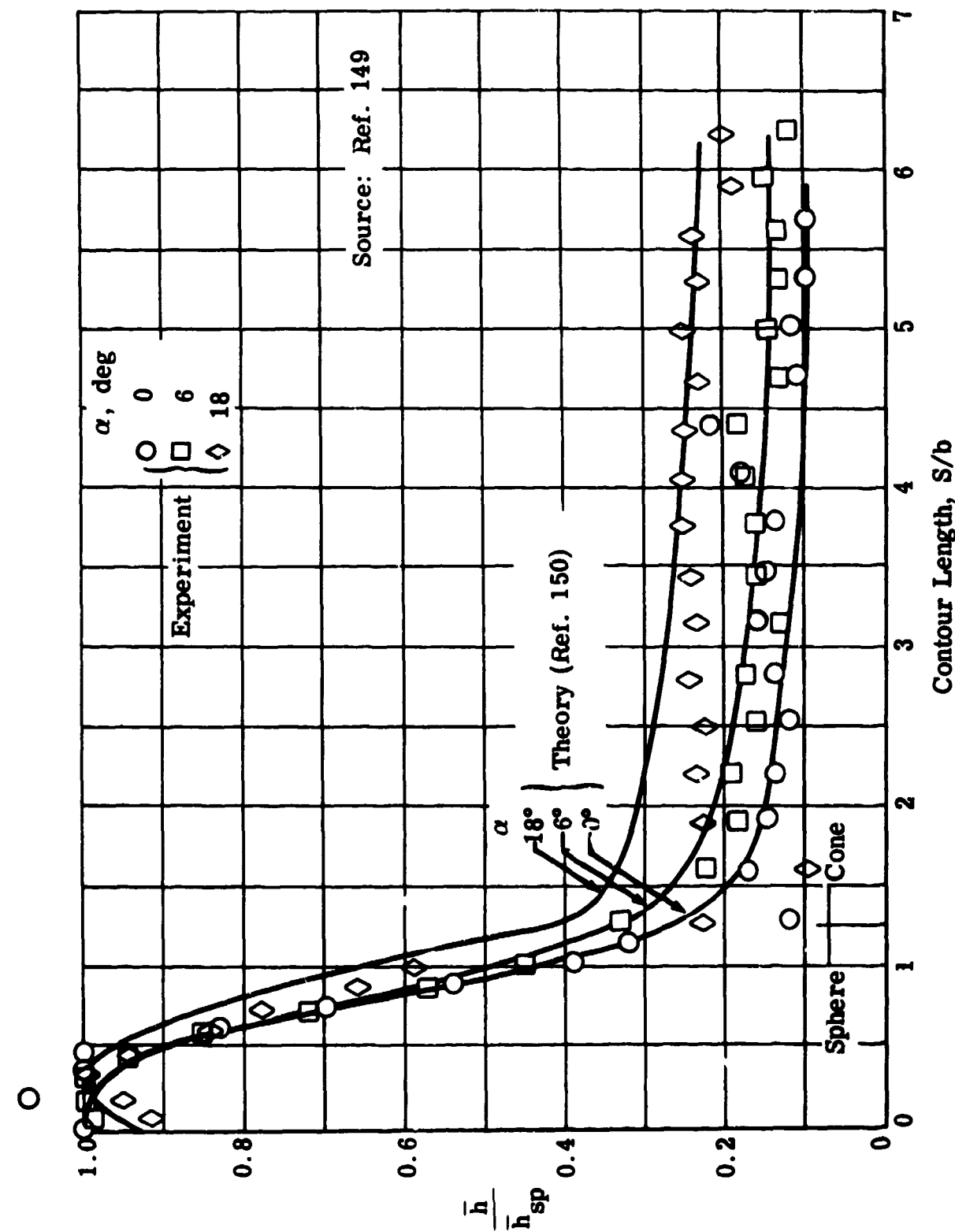


Fig. 7-15. Laminar heat transfer on a sphere-cone most windward generator:
 $M_\infty = 3.2$, $\sigma = 13.3^\circ$, $b = 0.78$ in., $p_{t_\infty} = 980$ -1210 mm Hg, $T_{t_\infty} = 318$ -335°K.

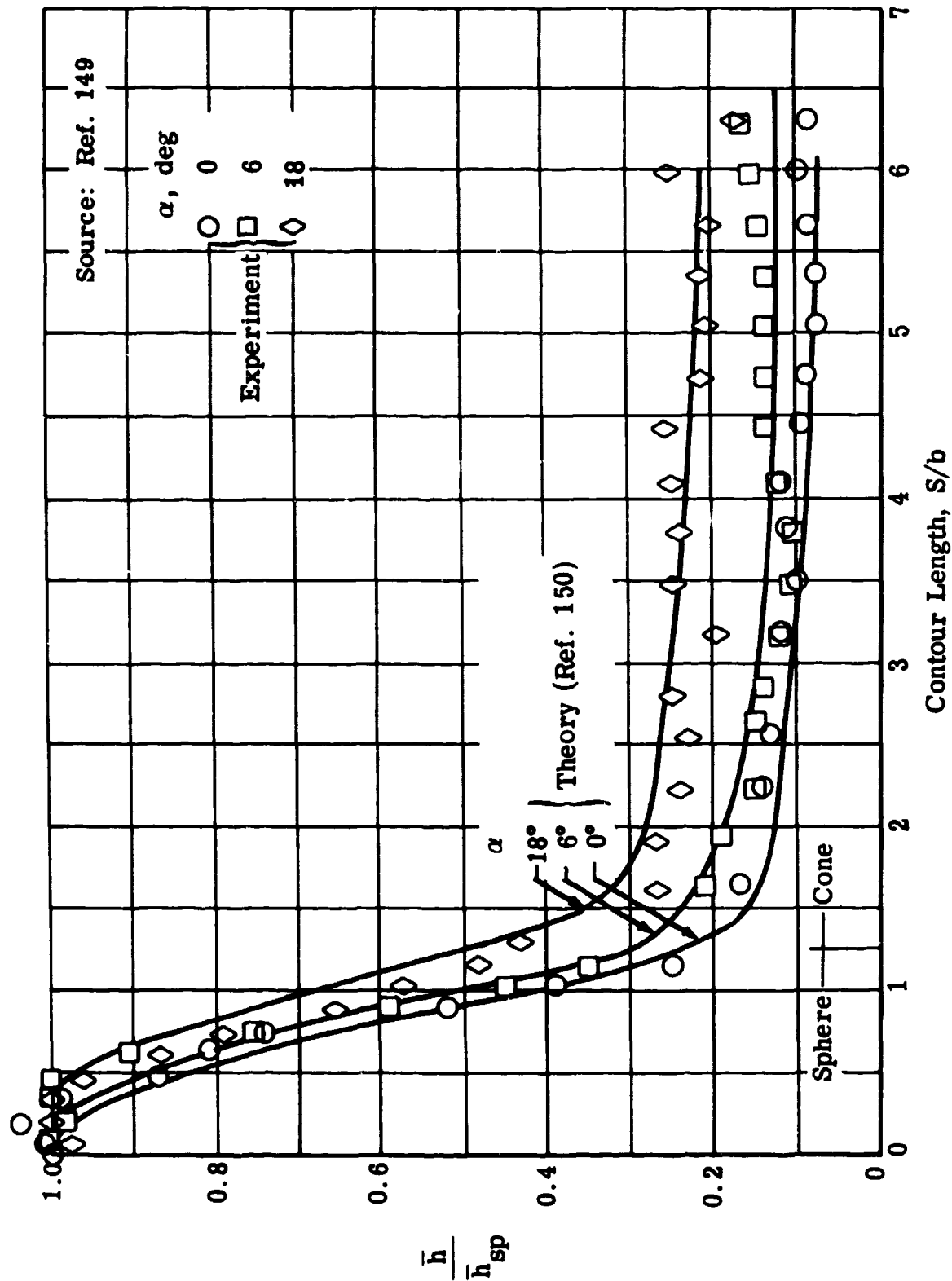


Fig. 7-16. Laminar heat transfer on a sphere-cone most windward generator; $M_\infty = 4.8$, $\sigma = 13.3^\circ$, $b = 0.78$ in., $p_{t_\infty} = 2090$ -2220 mm Hg, $T_{t_\infty} = 320^\circ\text{K}$.

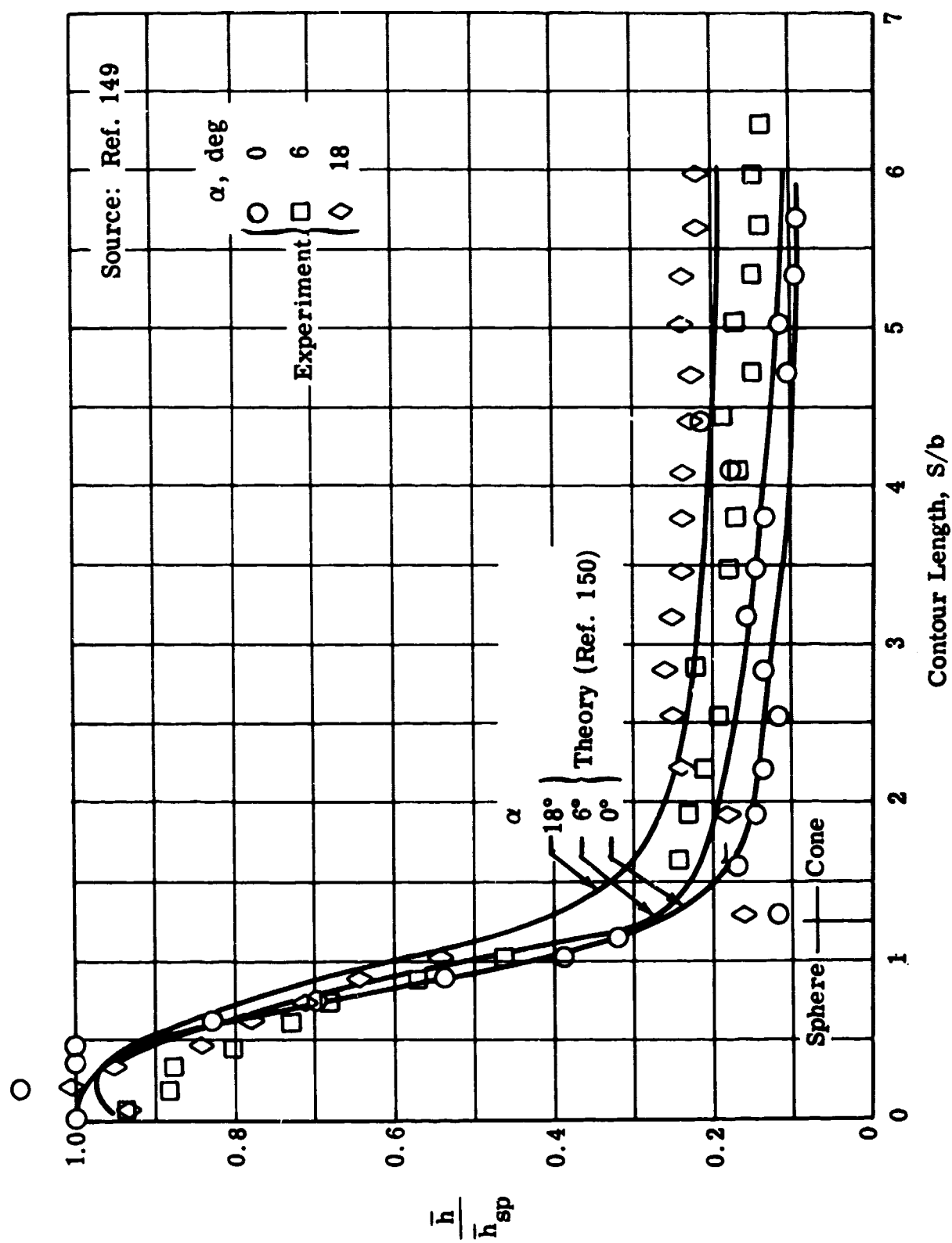


Fig. 7-17. Laminar heat transfer on a sphere-cone, $\phi = 45^\circ$; $M_\infty = 3.2$, $\sigma = 13.3^\circ$,
 $b = 0.78$ in., $P_{t_\infty} = 980$ -1210 mm Hg, $T_{t_\infty} = 318^\circ\text{K}$.

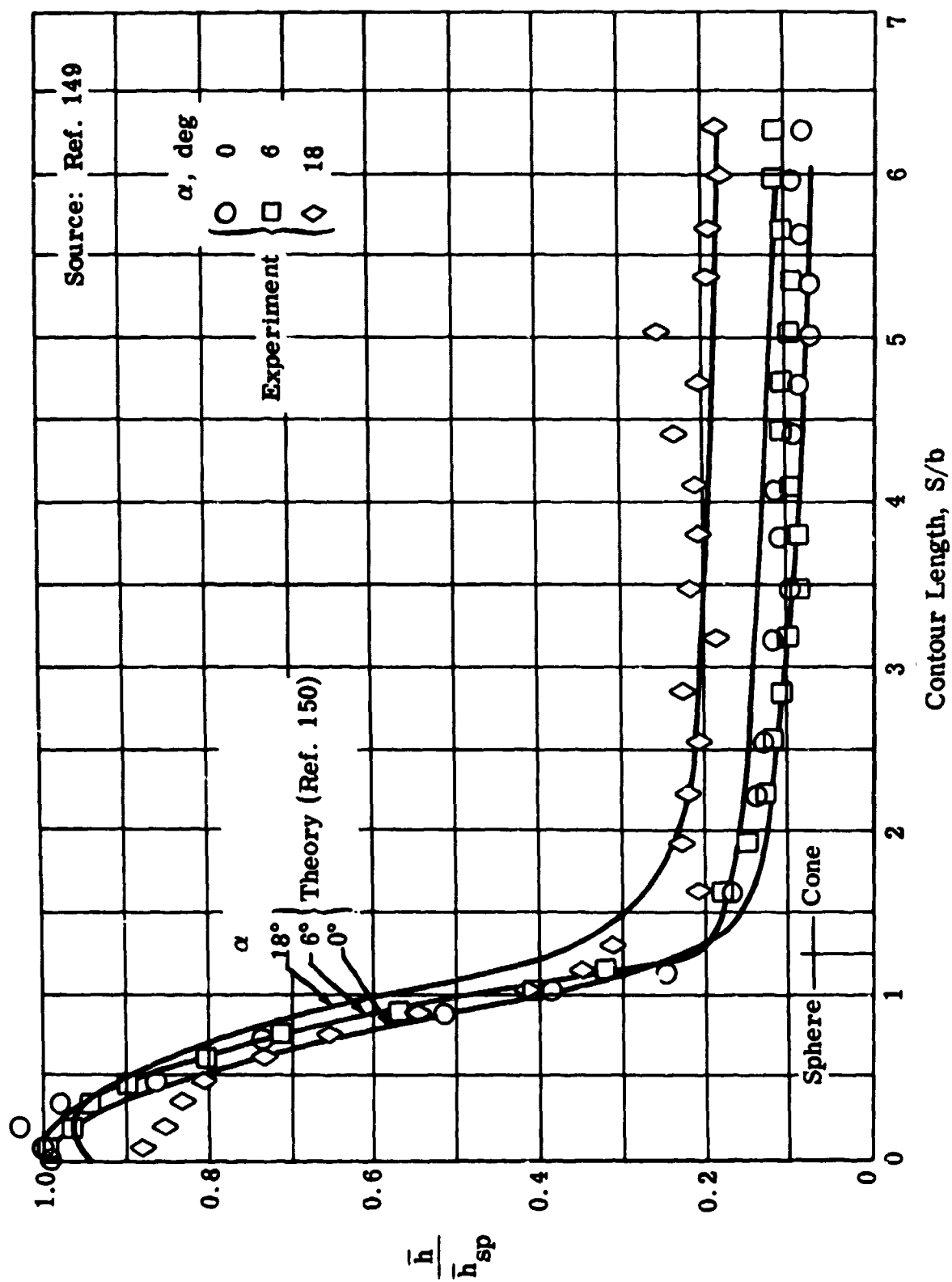


Fig. 7-18. Laminar heat transfer on a sphere-cone, $\phi = 45^\circ$; $M_\infty = 4.8$, $\sigma = 13.3^\circ$,
 $b = 0.78$ in., $p_{t_\infty} = 2090$ -2220 mm Hg, $T_{t_\infty} = 320^\circ\text{K}$.

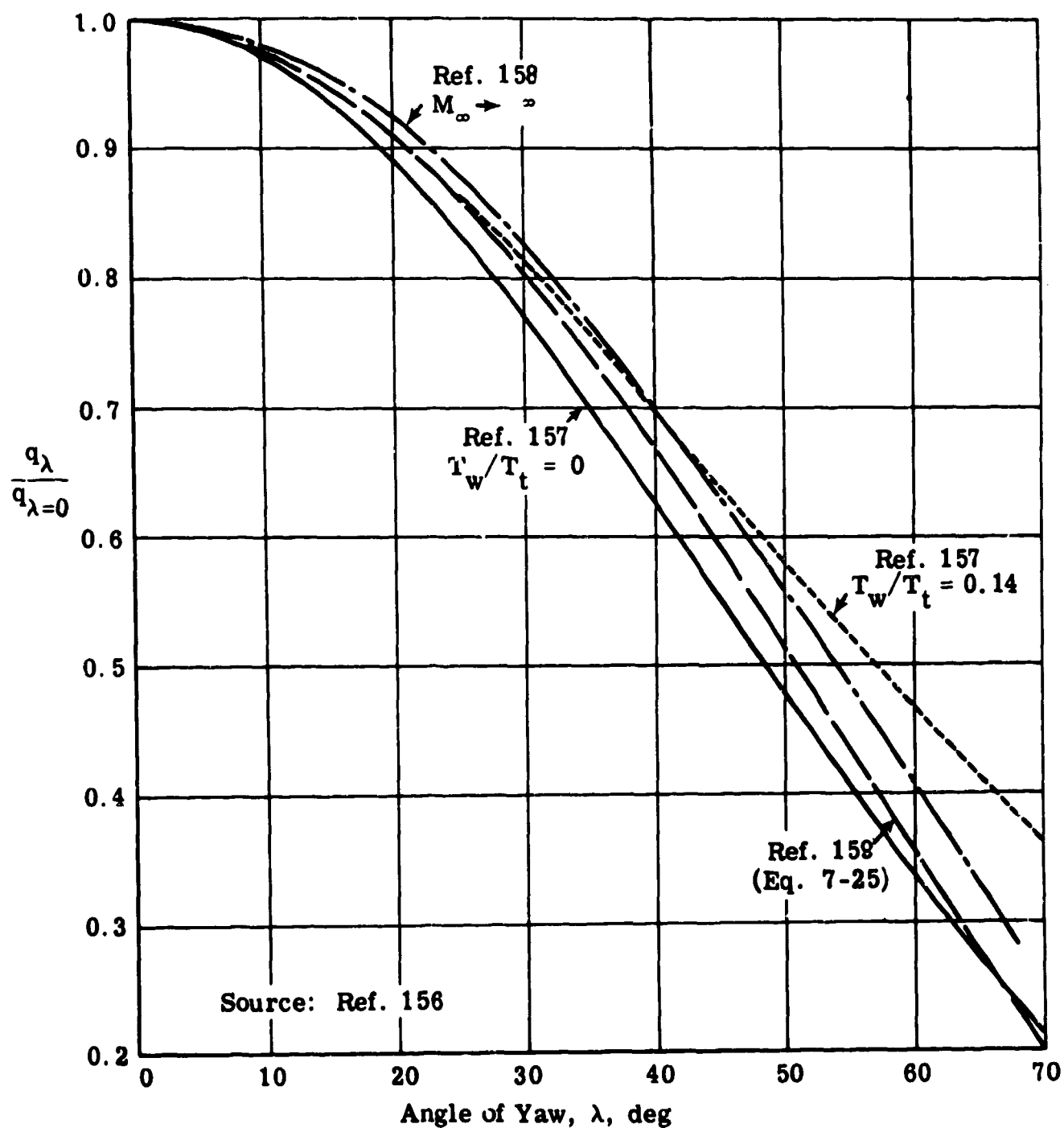


Fig. 7-19. Effect of angle of yaw on heat transfer rate on stagnation line of a cylinder; theory; laminar flow.

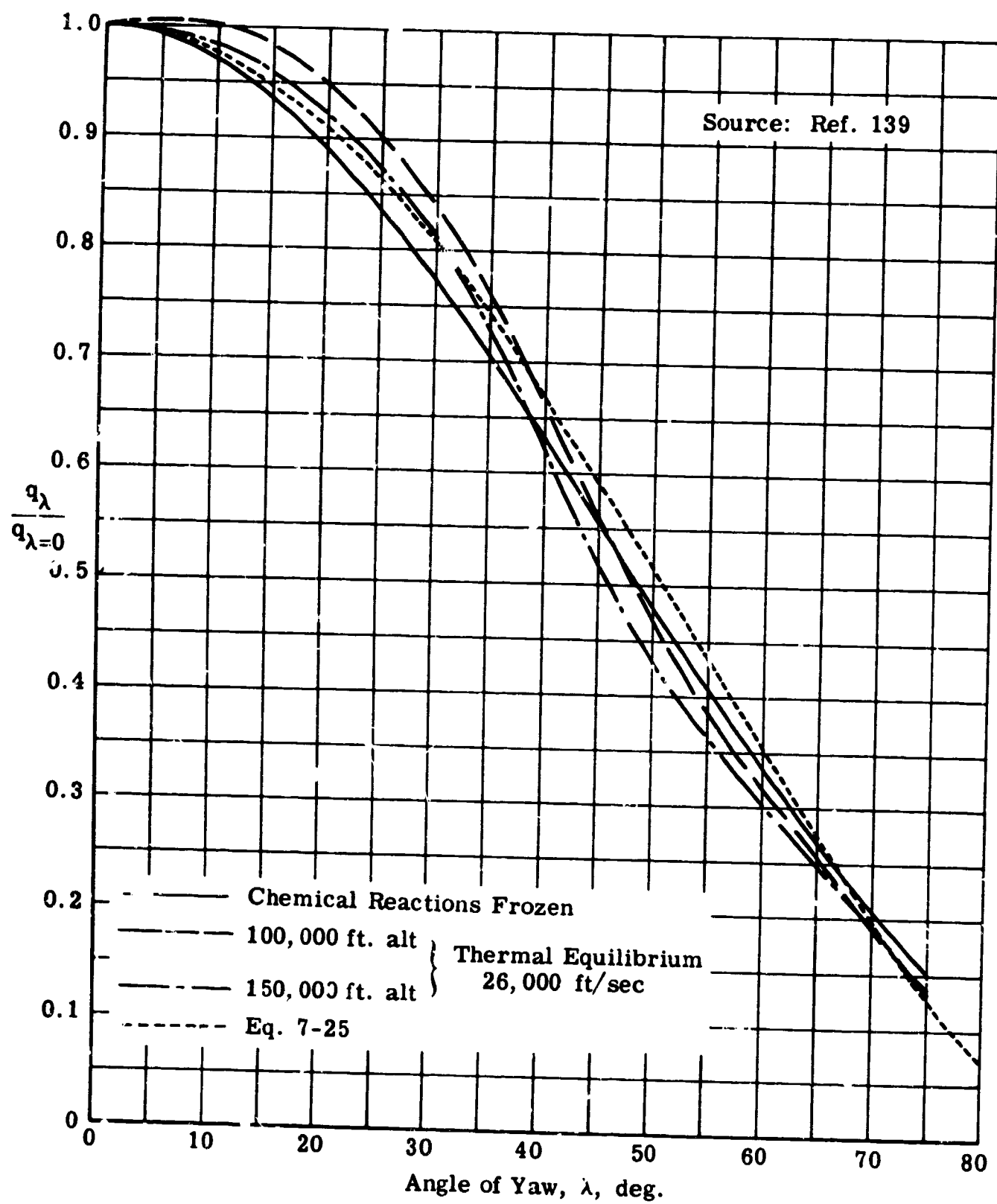


Fig. 7-20. Effect of angle of yaw on heat transfer rate on stagnation line of a cylinder; cool wall; laminar flow theory with real gas effects.

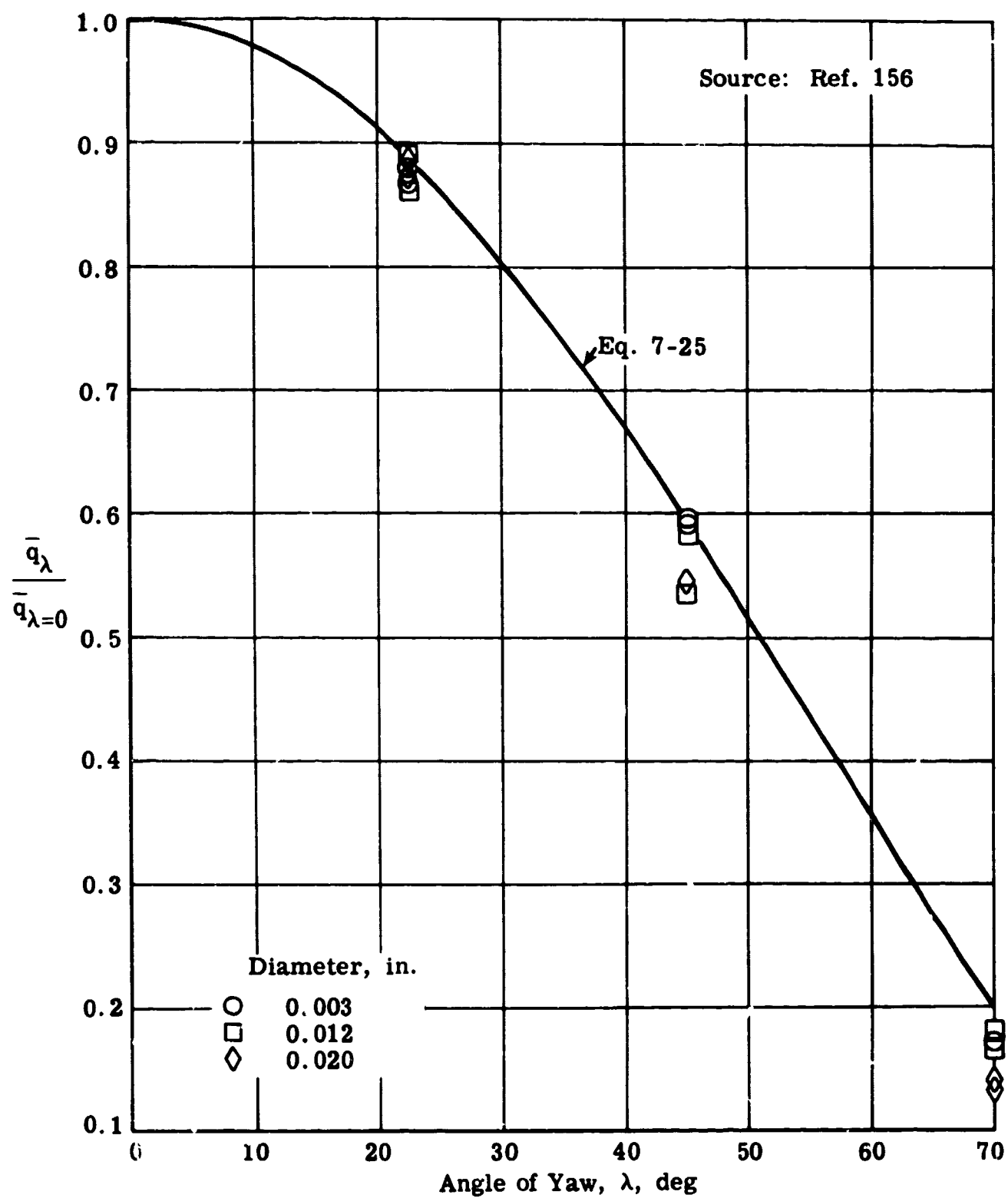


Fig. 7-21. Effect of angle of yaw on mean heat transfer rate to a cylinder; $M_\infty = 11$, $\rho_\infty u_\infty / \mu_t = 4.0 \times 10^4 / \text{ft}$, $T_t = 3660^\circ\text{R}$.

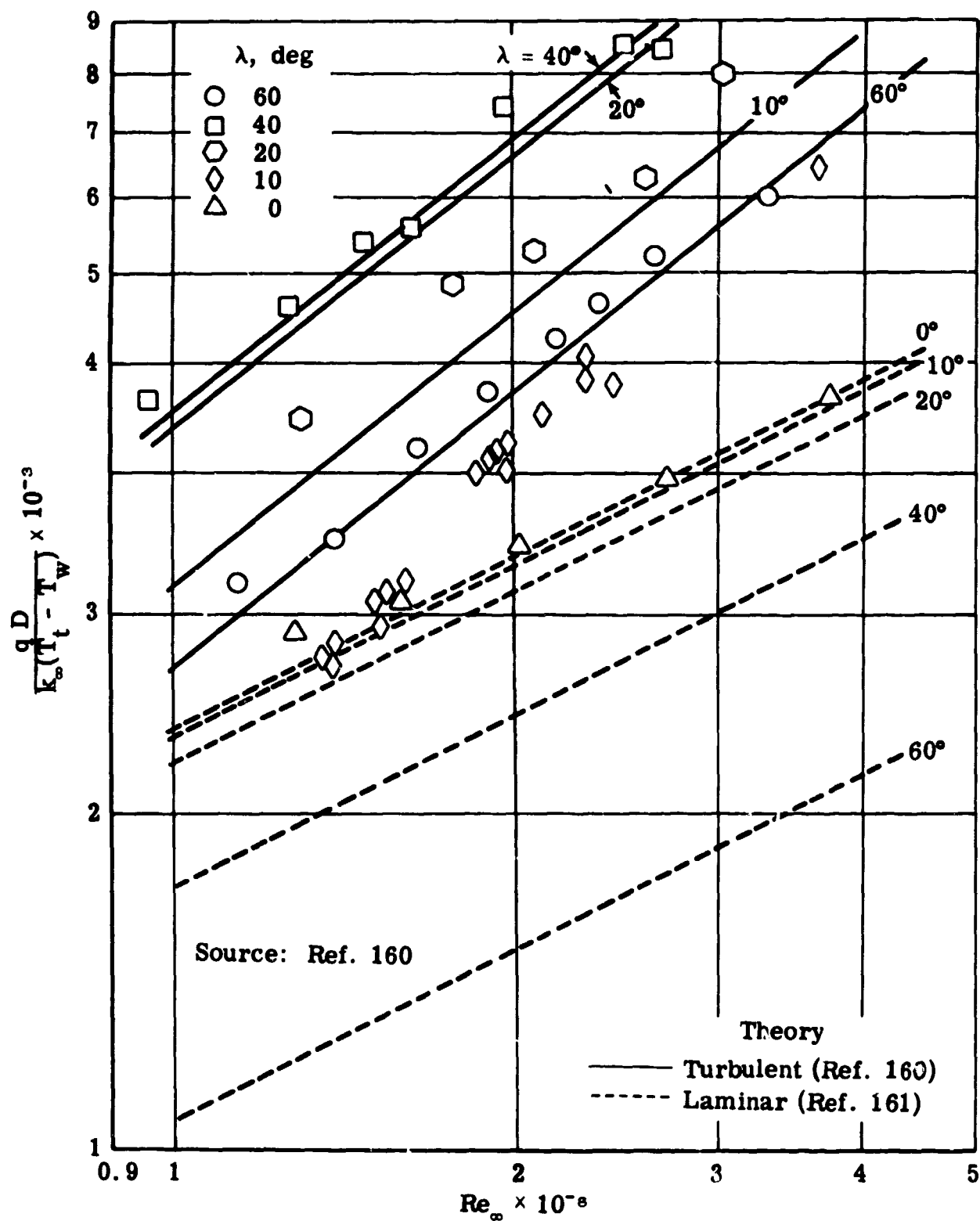


Fig. 7-22. Effect of angle of yaw on heat transfer rate along the stagnation line of a cylinder; theory and experiment; $M_{\infty} = 4.15$; $Re_{\infty} = \rho_{\infty} u_{\infty} D / \mu_{\infty}$.

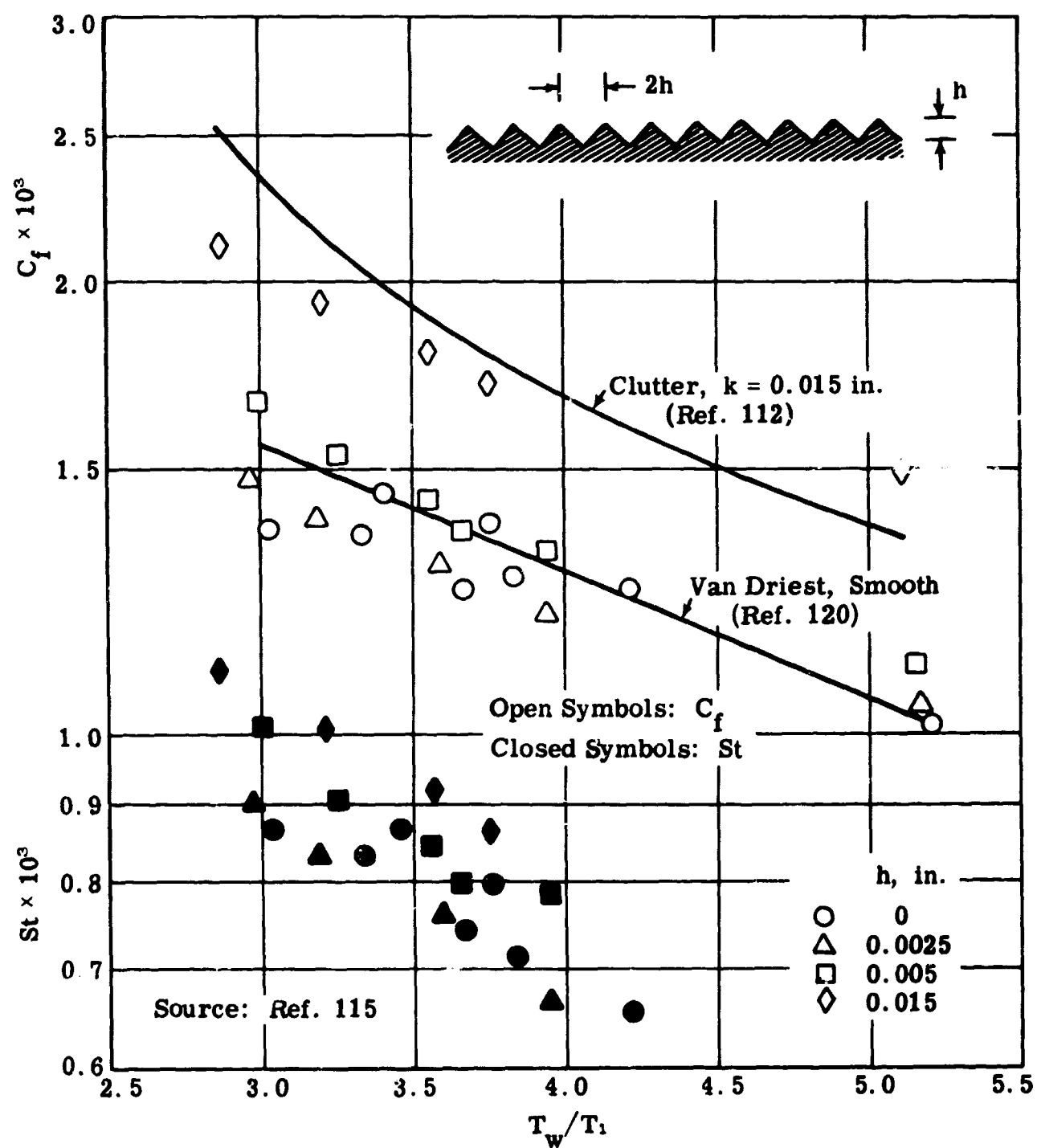


Fig. 7-23. Local skin friction and heat transfer data for two-dimensional V-groove roughness; flat plate; turbulent boundary layer; $M_1 = 4.93$, $p_t = 255$ psia, $T_w = 555^\circ\text{R}$, $x = 12.5$ in. (11 in. from start of roughness).

Sym.	T_w/T_1	$Re_x \times 10^{-7}$
○	3.75-3.94	0.76-1.01
△	3.55-3.67	0.74-0.84
□	3.18-3.33	0.60-0.67
◇	2.87-3.03	0.45-0.56

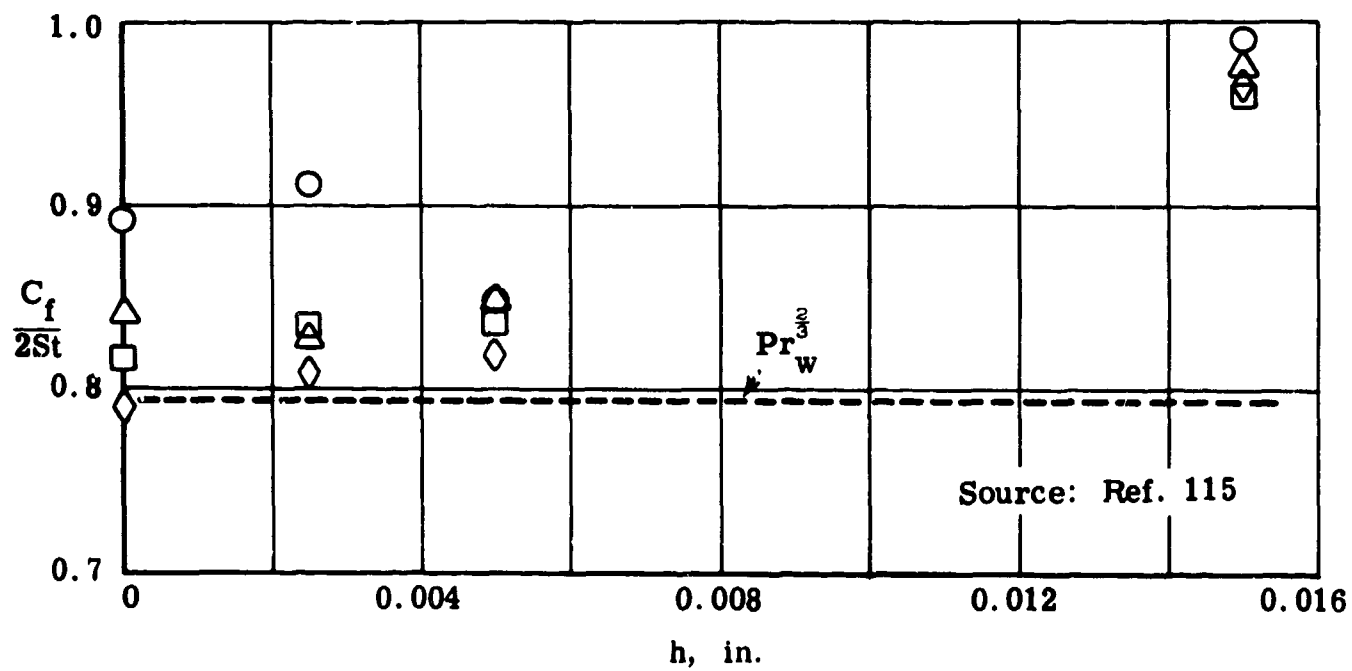


Fig. 7-24. Effect of two-dimensional V-groove roughness on Reynolds analogy factor; flat plate; turbulent boundary layer; $M_1 = 4.93$.

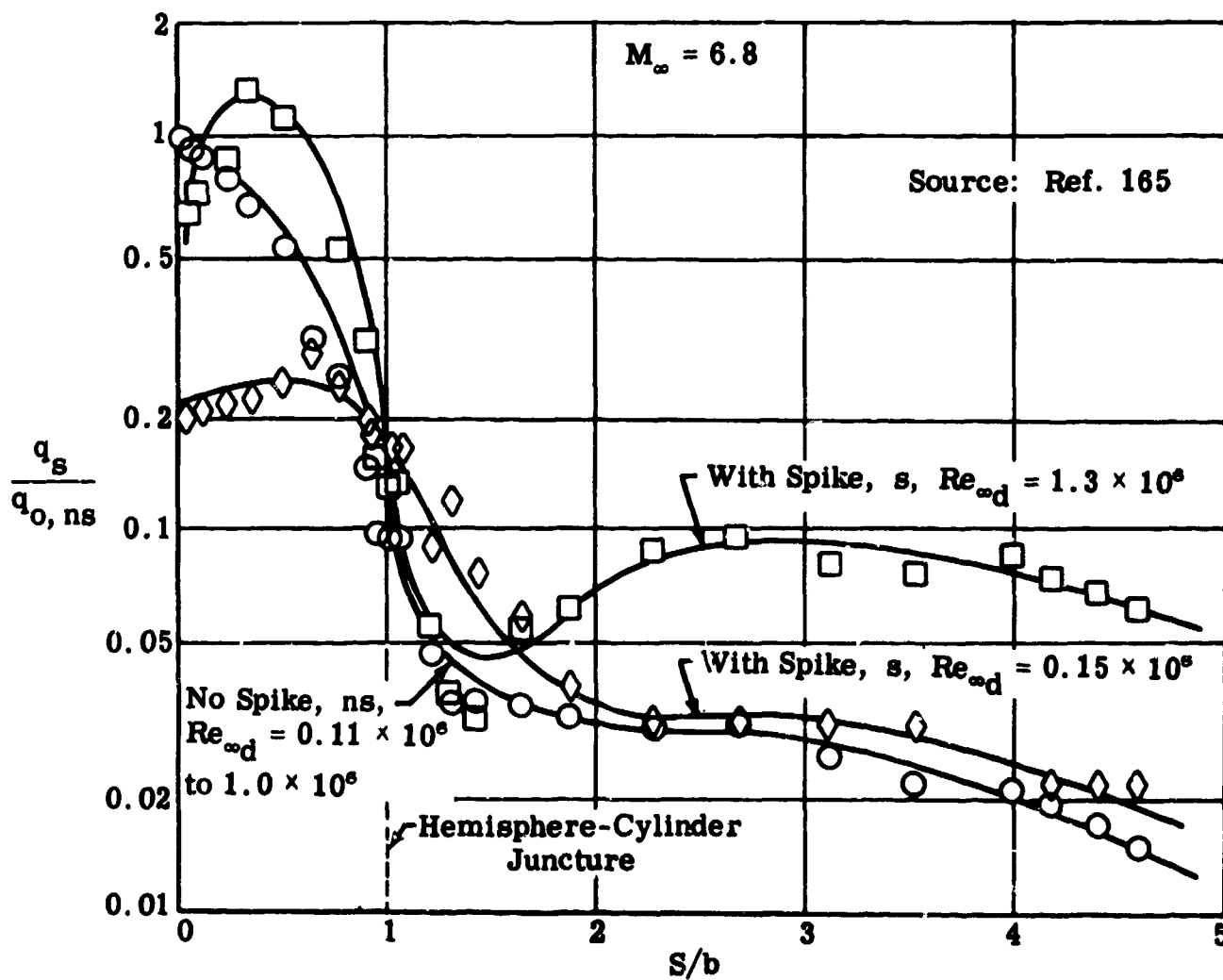
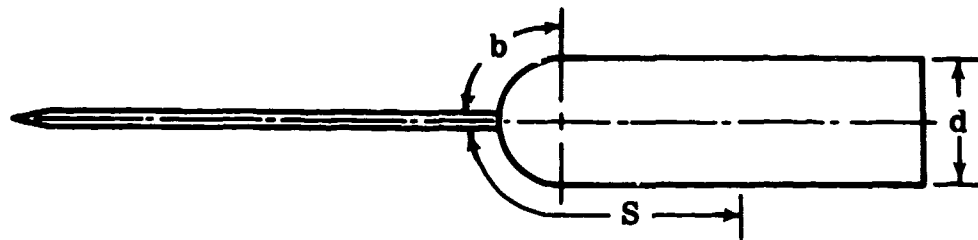


Fig. 7-25. Effect of spike on heat transfer rate; hemisphere-cylinder;
 $M_\infty = 6.8$.

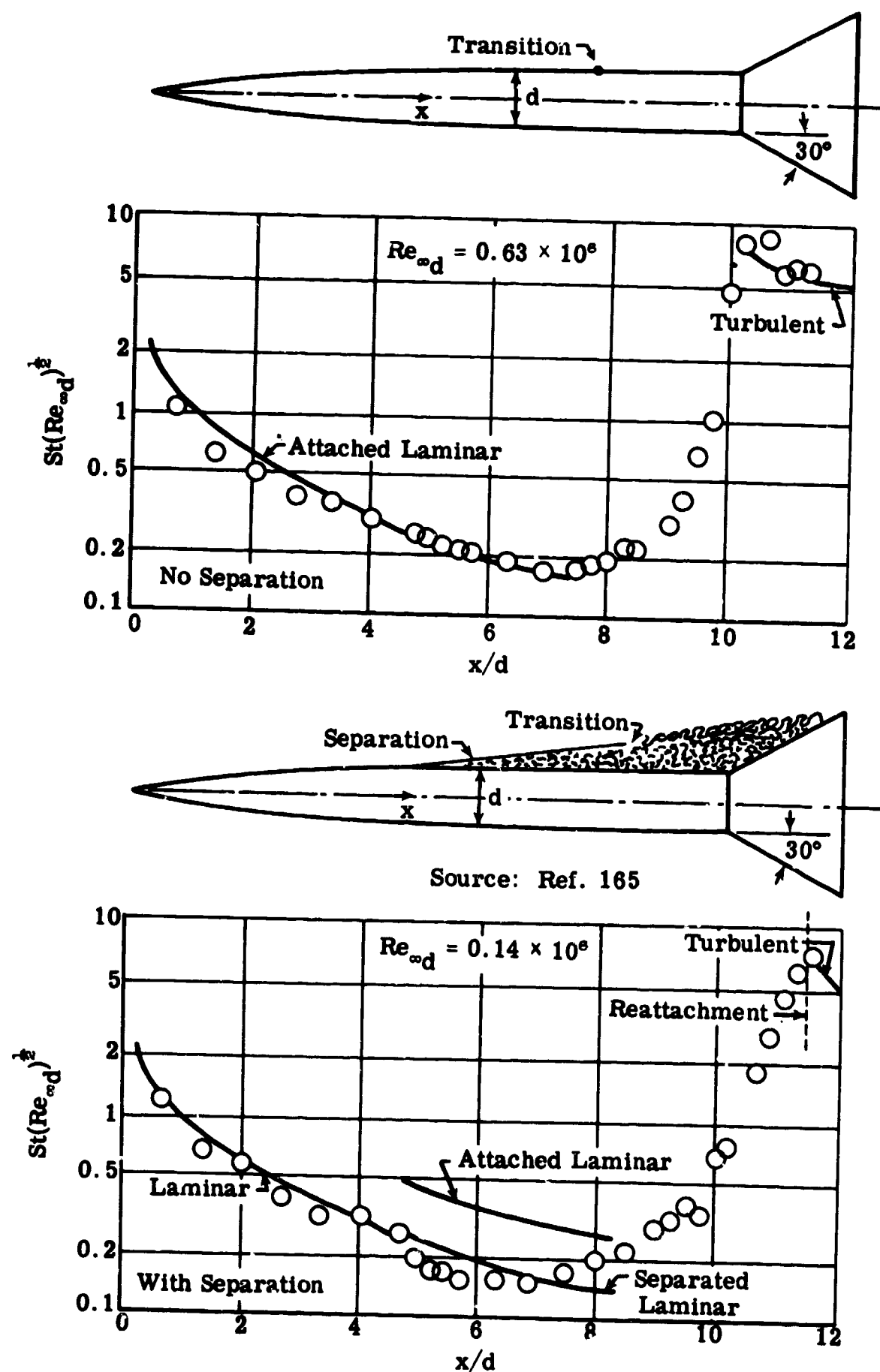


Fig. 7-26. Comparison of experimental and predicted heat transfer with and without separation; $M_\infty = 6.8$.

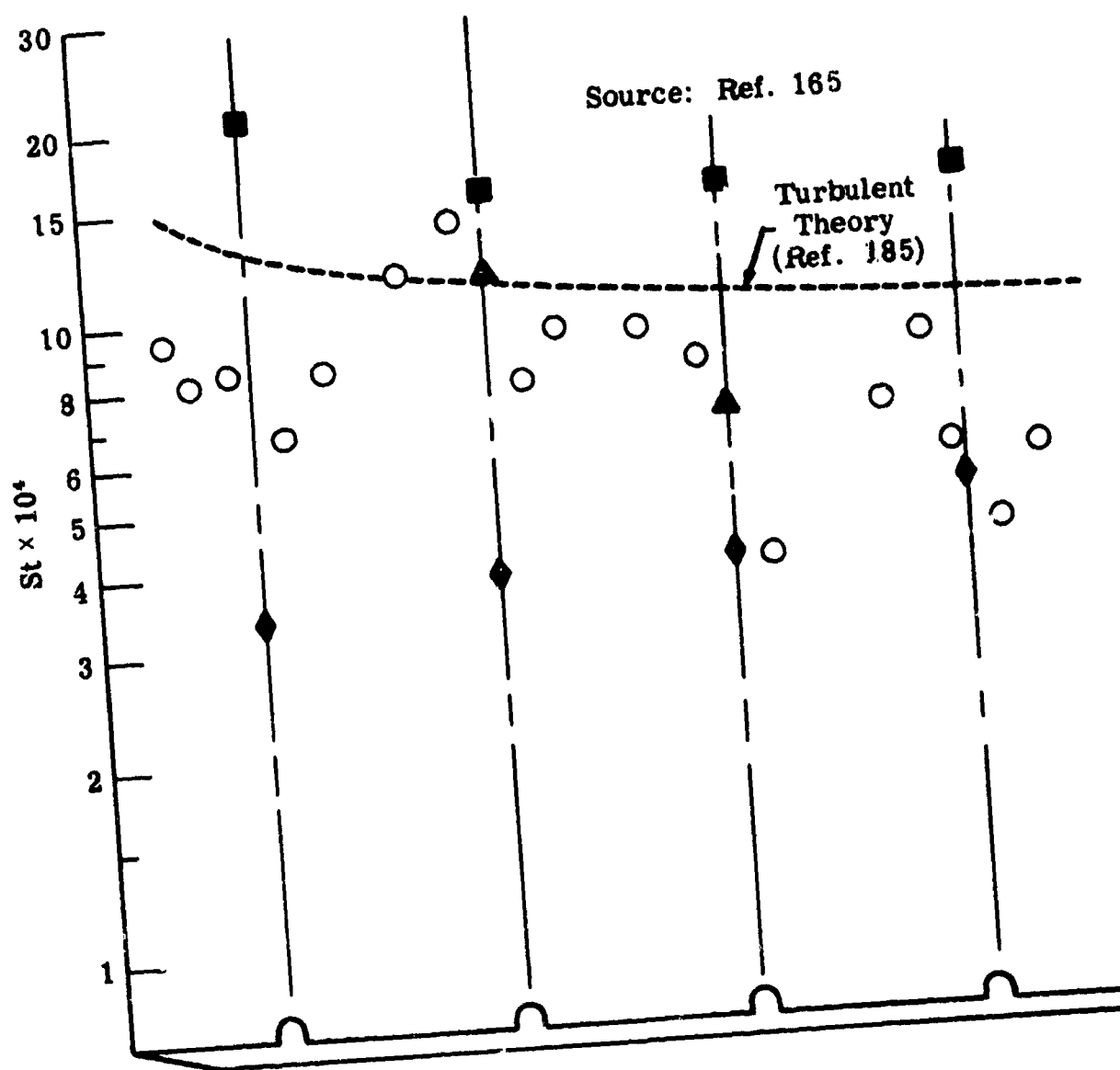
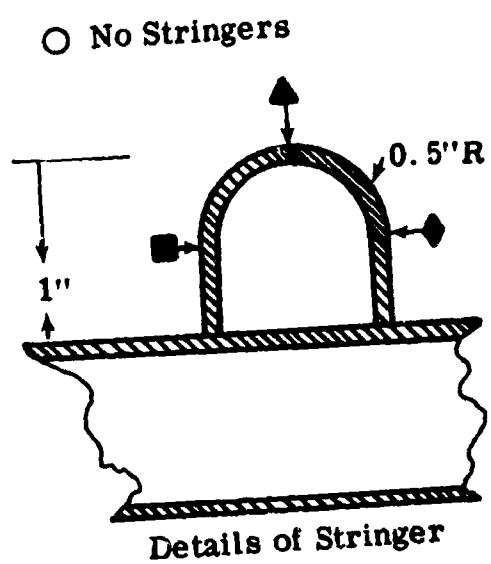


Fig. 7-27. Heat transfer on a flat plate with stringers;
 $M_\infty = 2$; $Re_\infty/ft = 15.2 \times 10^6$

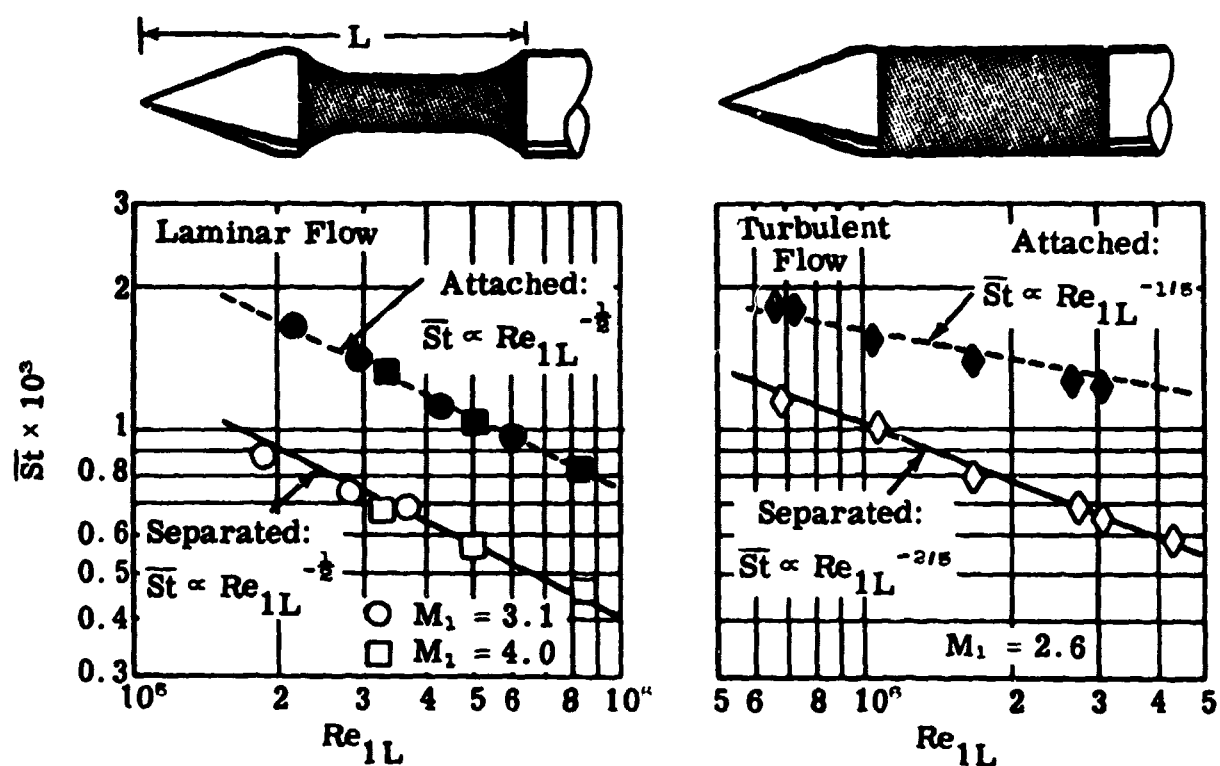


Fig. 7-28. Average values of the Stanton number; attached and separated flows; $M_1 = 2.6, 3.1$, and 4.0 .

Source: Ref. 167

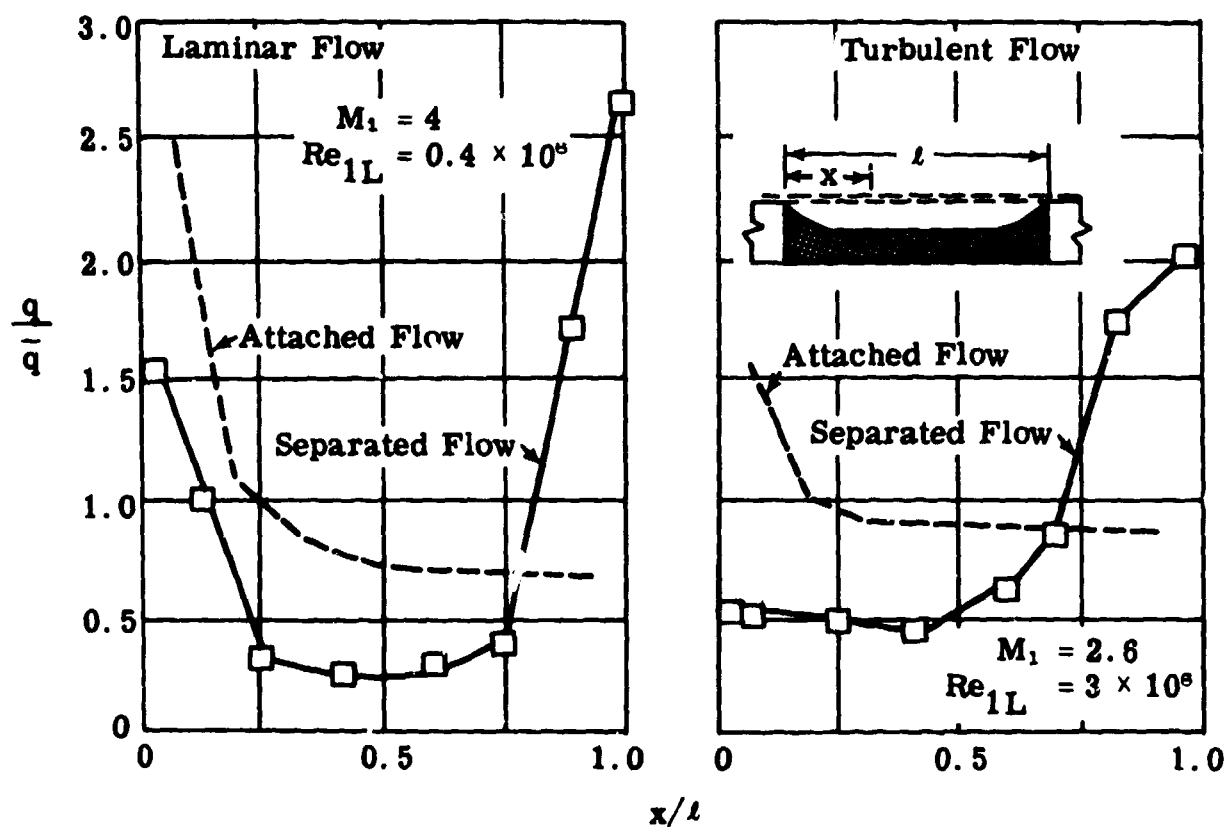


Fig. 7-29. Comparison of local heat transfer rates for attached and separated flows.

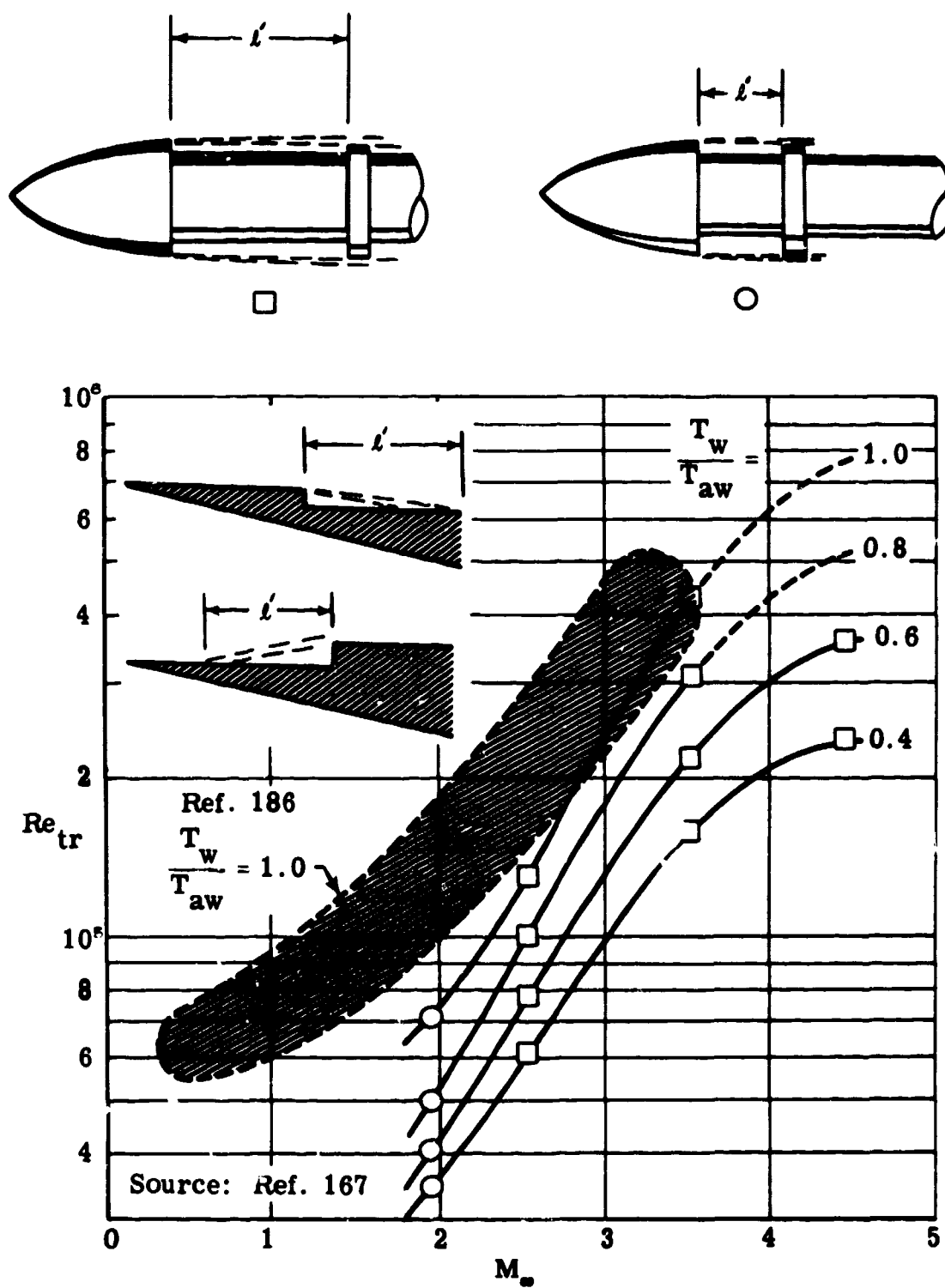


Fig. 7-30. Experimental data on the transition of separated laminar boundary layers; $0 < M_\infty < 5$.

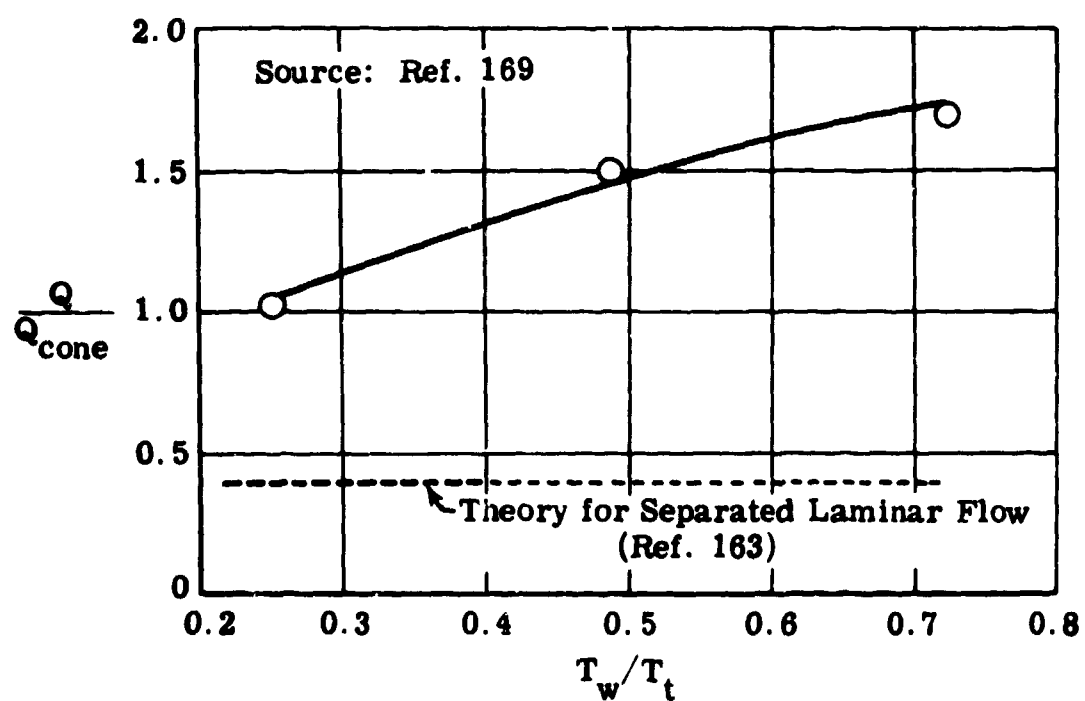
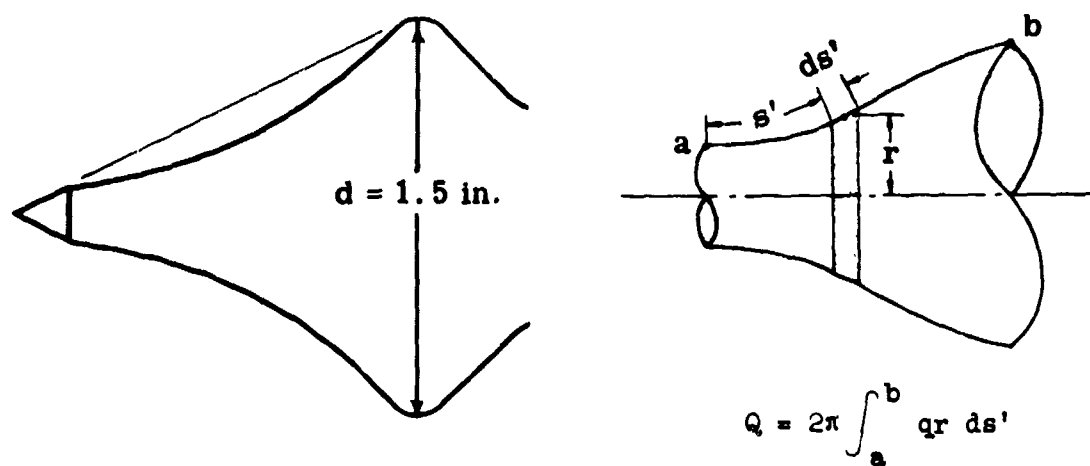


Fig. 7-31. Effect on the total heat transfer of a cavity on a sharp cone; $M_\infty = 5.09$, $Re_\infty/ft = 1.2 \times 10^6$; $T_w/T_t = 0.25$, 0.49 , and 0.72 .

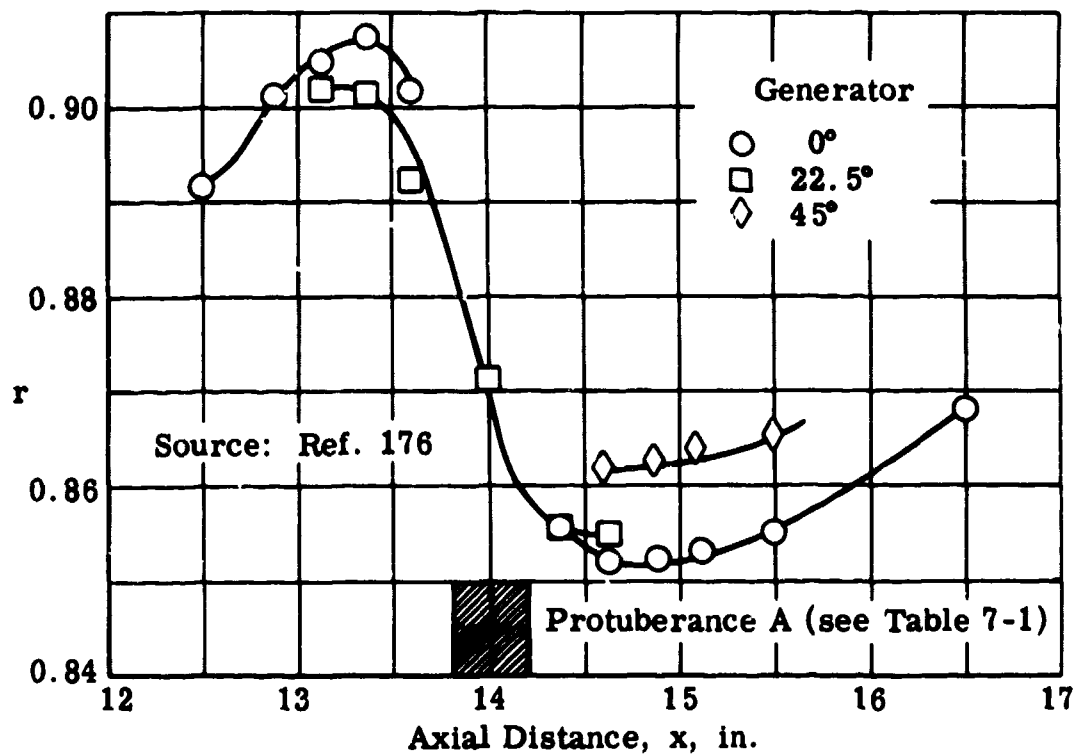


Fig. 7-32. Turbulent recovery factor distribution in the vicinity of a 90° cylindrical protuberance mounted on a cone-cylinder; $M_\infty = 3.12$.

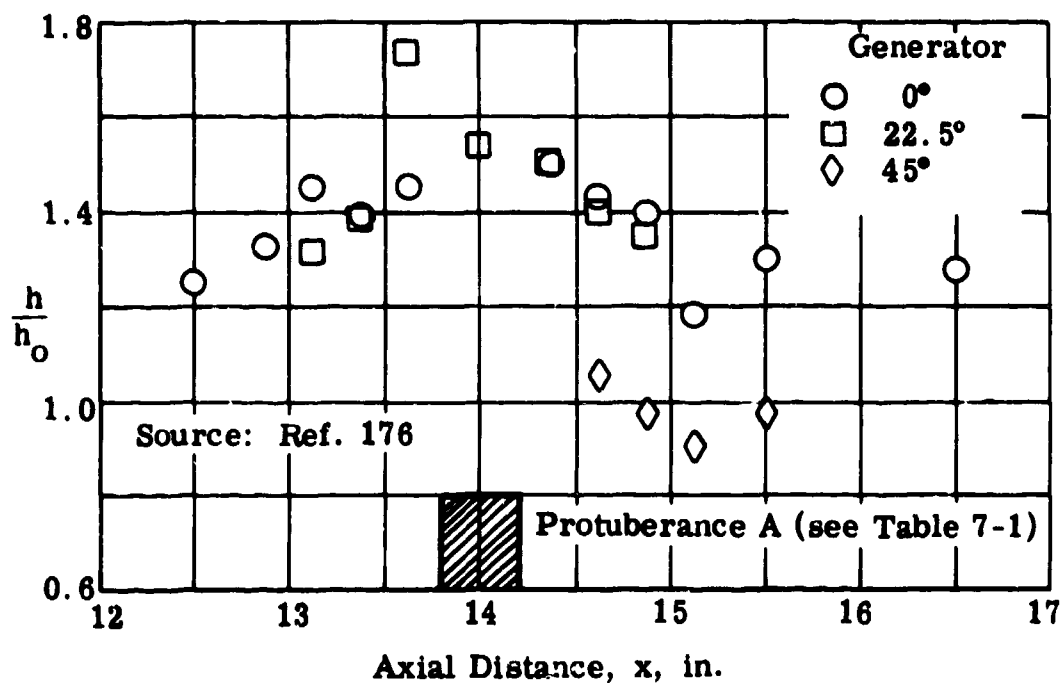


Fig. 7-33. Local turbulent film coefficients in the vicinity of a 90° cylindrical protuberance mounted on a cone-cylinder; $M_\infty = 3.12$; $Re_\infty = 8 \times 10^6/\text{ft}$.

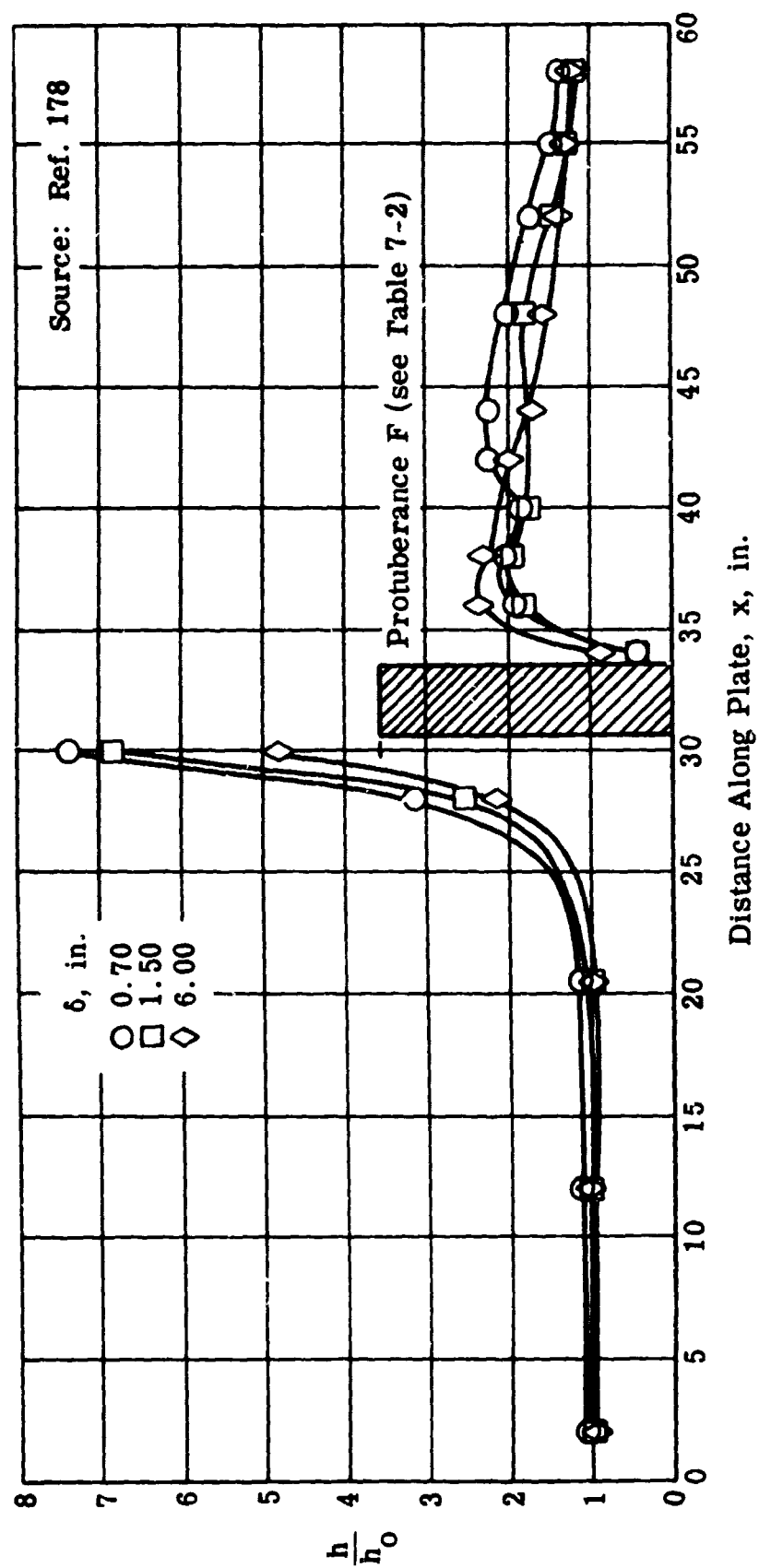
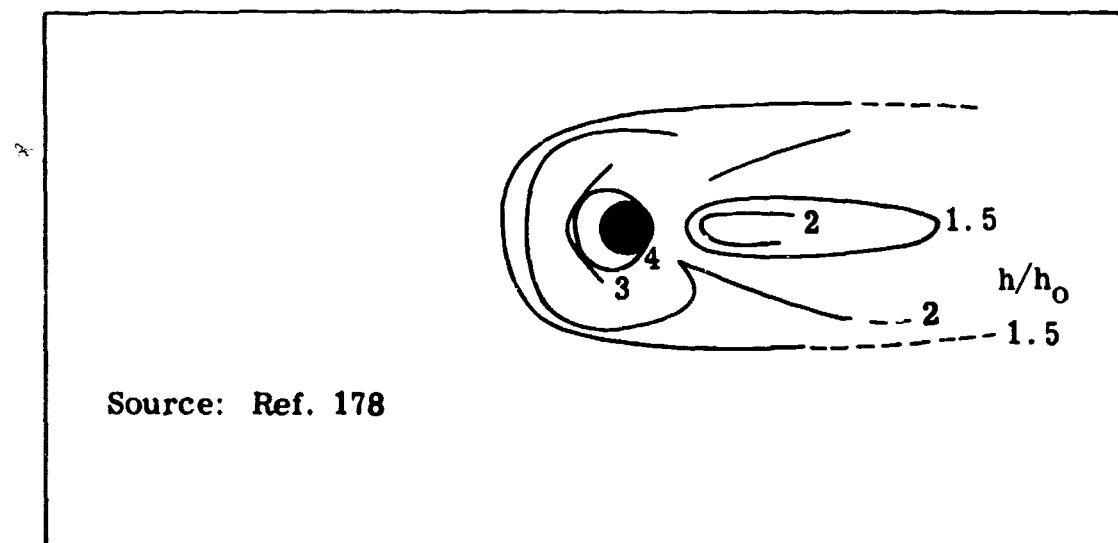
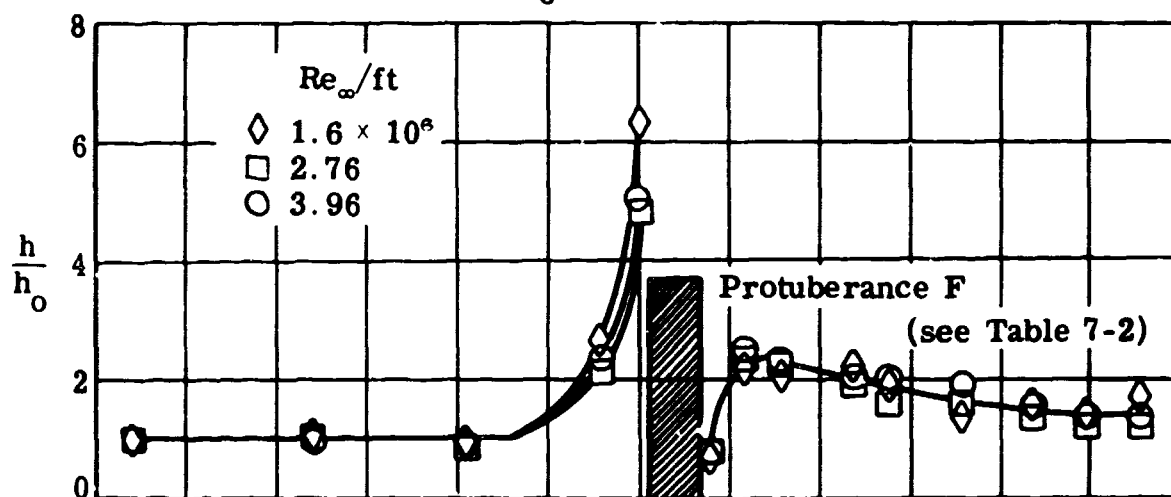


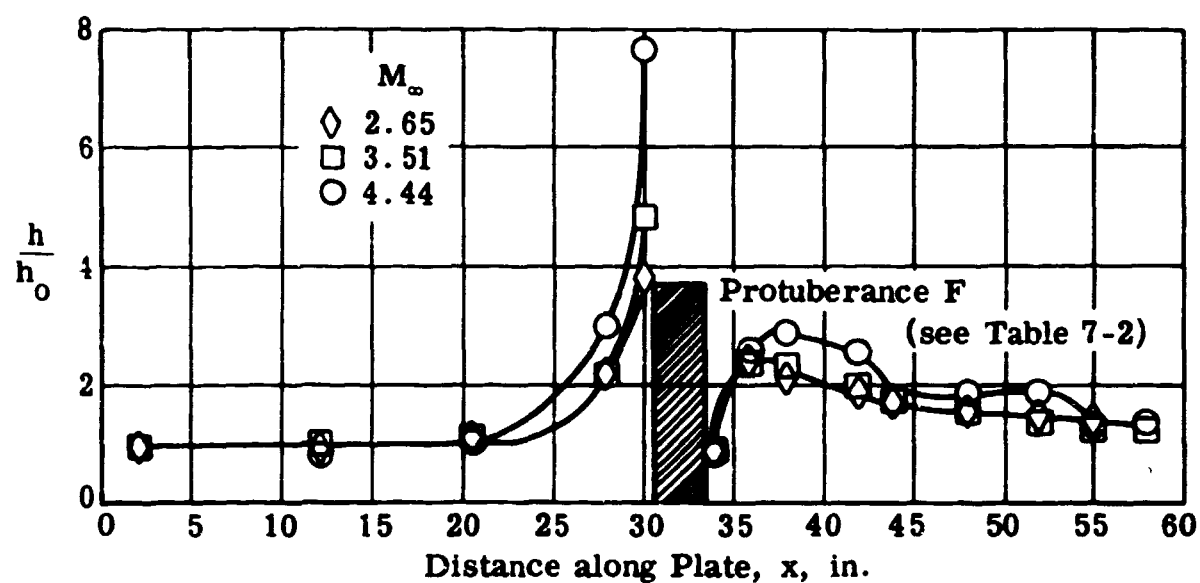
Fig. 7-34. Effect of boundary layer thickness on local film coefficients measured on the center line of a flat plate on which a cylindrical protuberance is mounted; turbulent flow; $M_\infty = 3.5$, $Re_\infty/ft = 2.9 \times 10^6$.



Lines of Constant h/h_0 , $M_\infty = 3.51$, $Re_\infty = 2.76 \times 10^6$ /ft



Effect of Reynolds Number on Center Line Values of h/h_0 , $M_\infty = 3.51$



Effect of Mach Number on Center Line Values of h/h_0 , $Re_\infty = 3.0 \times 10^6$ /ft

Fig. 7-35. Local turbulent film coefficients on a mounting plate in the vicinity of a 90° cylindrical protuberance; $\delta = 6.0$ in.

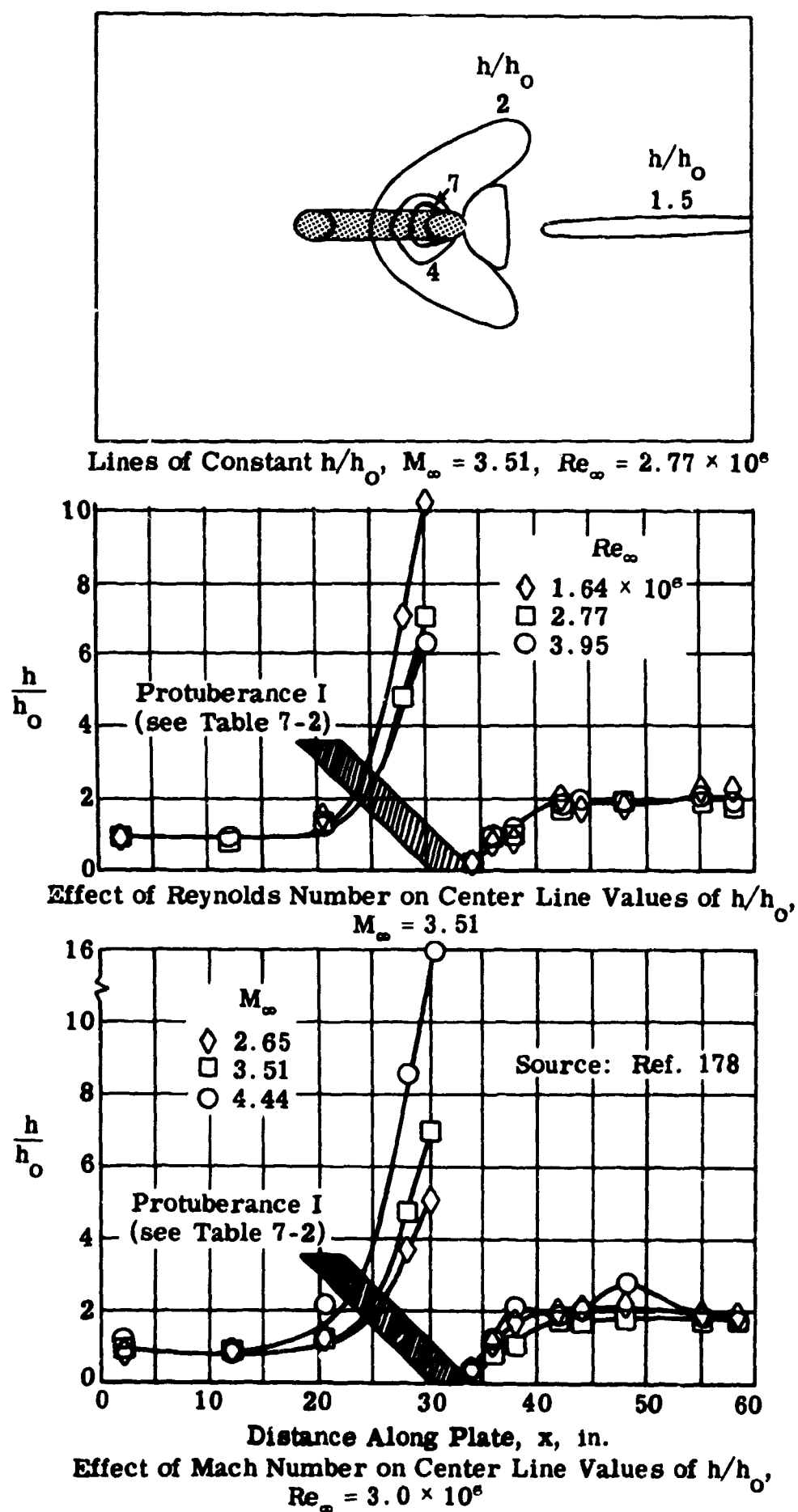
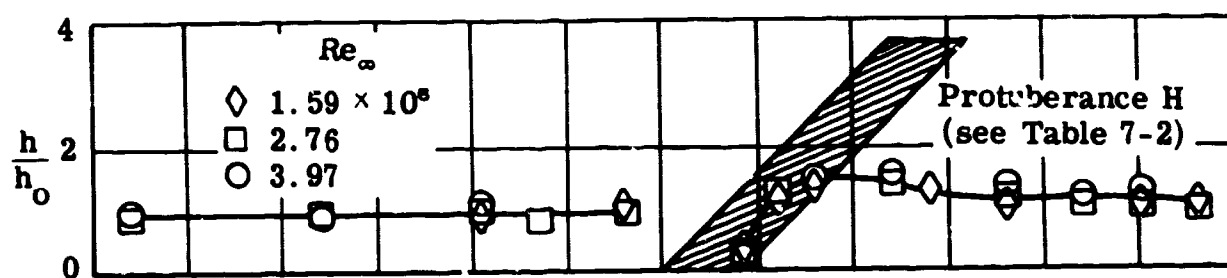
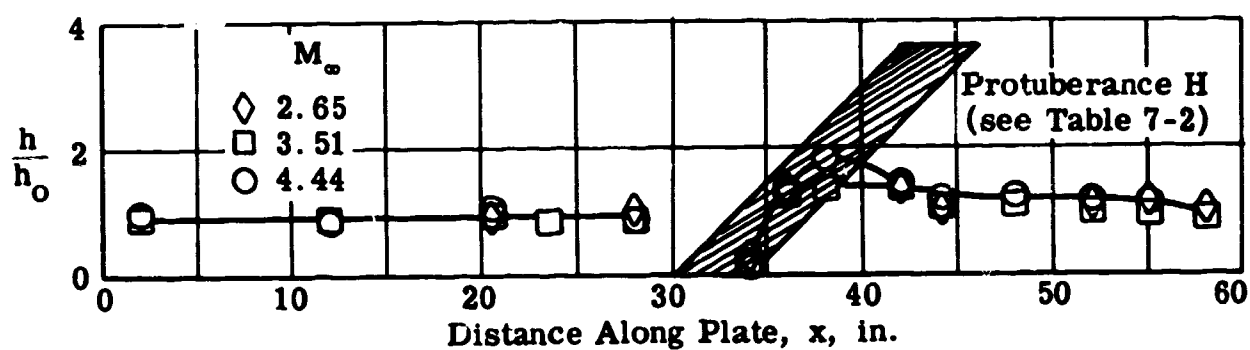


Fig. 7-36. Local turbulent film coefficients on a mounting plate in the vicinity of a cylinder swept forward 45° ; $\delta = 6$ in.



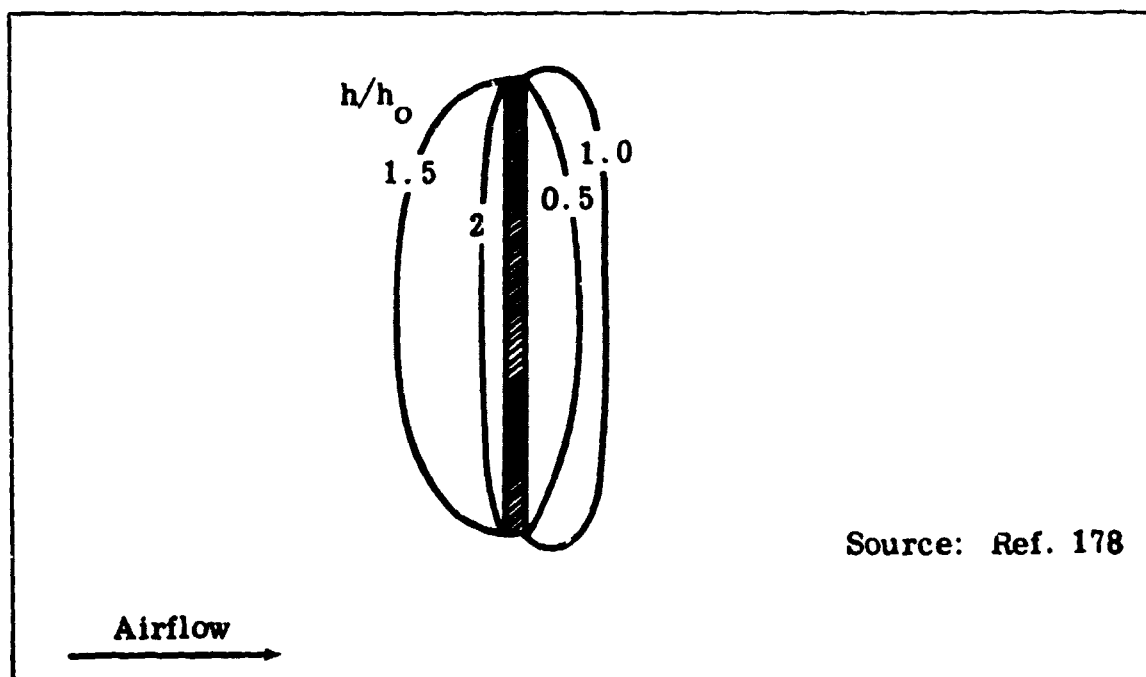
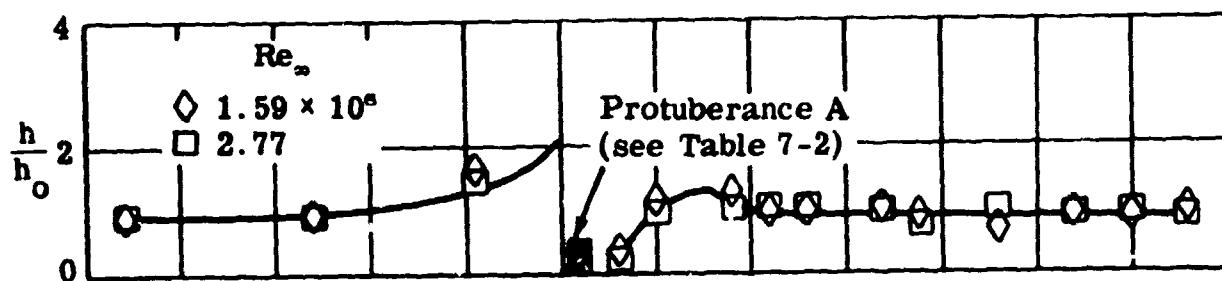
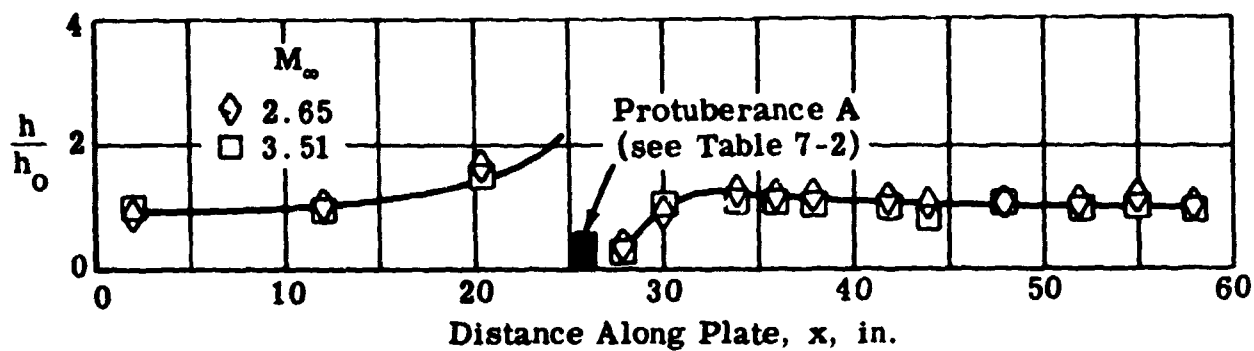
Effect of Reynolds Number on Center Line Values of h/h_0 , $M_\infty = 3.51$

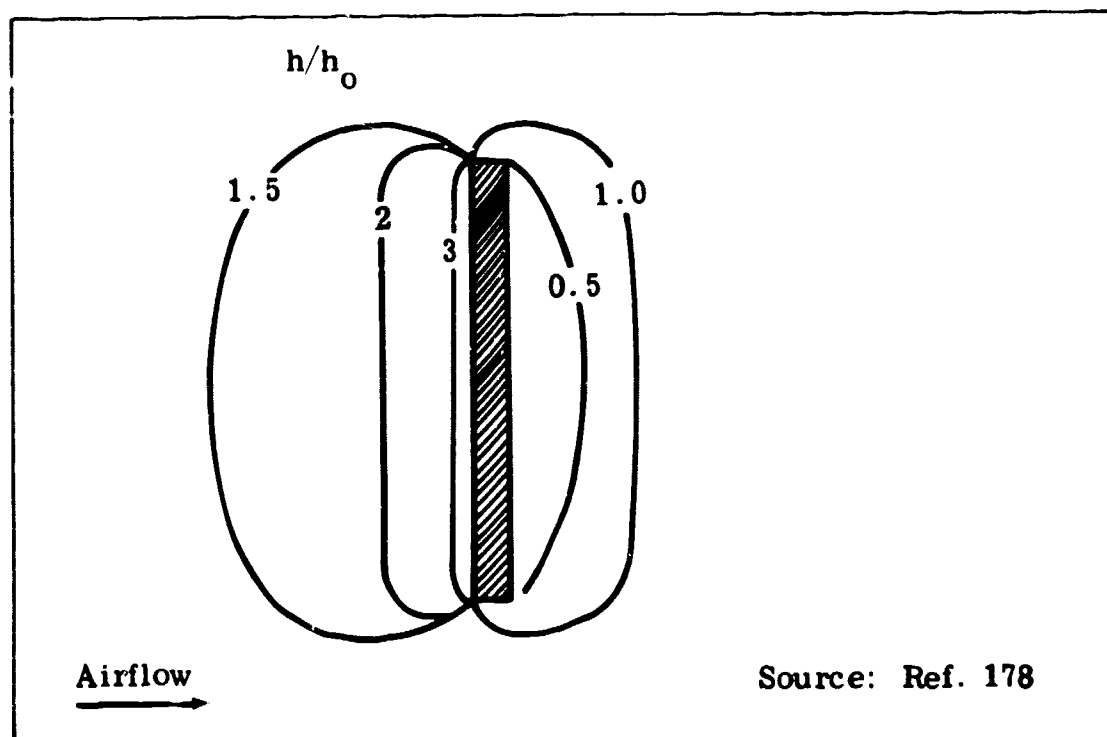
Source: Ref. 178



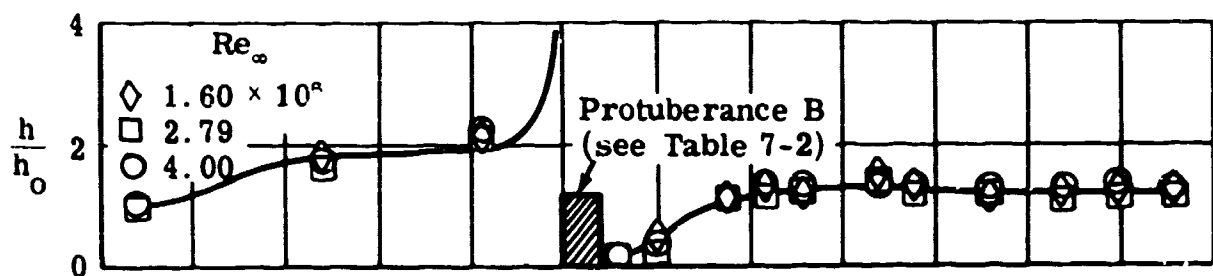
Effect of Mach Number on Center Line Values of h/h_0 , $Re_\infty = 3.0 \times 10^5$

Fig. 7-37. Local turbulent film coefficients on a mounting plate in the vicinity of a cylinder swept back 45° ; $\delta = 6$ in.

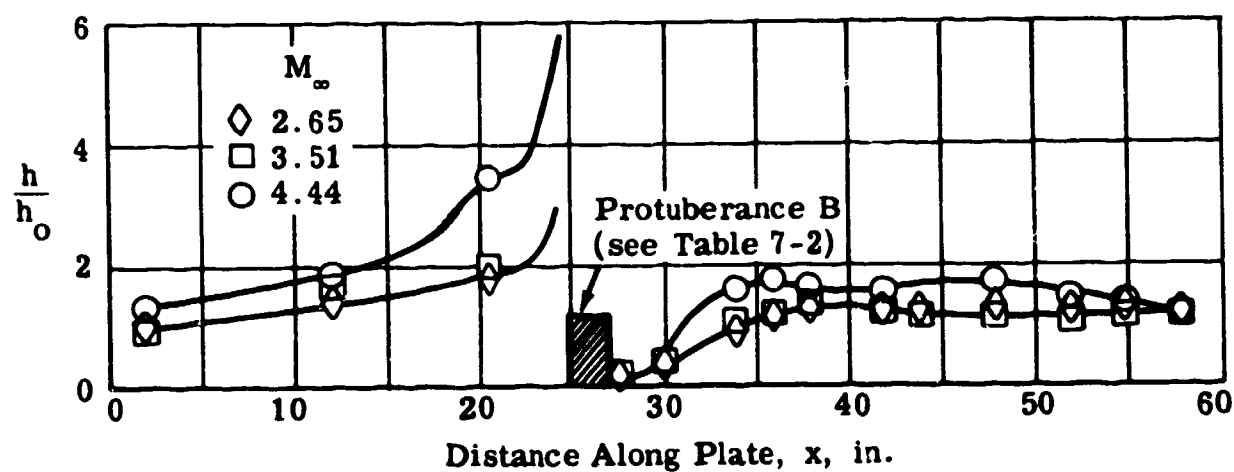
Lines of Constant h/h_0 , $M_\infty = 3.51$, $Re_\infty = 2.77 \times 10^6$ Effect of Reynolds Number on Center Line Values of h/h_0 , $M_\infty = 3.51$ Effect of Mach Number on Center Line Values of h/h_0 , $Re_\infty = 3.0 \times 10^6$ Fig. 7-38. Local turbulent film coefficients on a mounting plate in the vicinity of a rectangular stiffener $1 \times 2 \times 24$ in.; $\delta = 6$ in.



Lines of Constant h/h_0 , $M_\infty = 3.51$, $Re_\infty = 2.79 \times 10^6$



Effect of Reynolds Number on Center Line Values of h/h_0 , $M_\infty = 3.51$



Effect of Mach Number on Center Line Values of h/h_0 , $Re_\infty = 3.0 \times 10^6$

Fig. 7-39. Local turbulent film coefficients on a mounting plate in the vicinity of a stiffener $2 \times 4 \times 24$ in.; $\delta = 6$ in.

A. Gas Properties

It is evident that any solution of the equations derived in Subsec. 2 will require a knowledge of the physical properties of the fluid concerned. At the high Mach numbers and wide pressure ranges encountered today in free-flight, wind-tunnel, and shock-tube applications, many of the fluid properties change very rapidly in the boundary layer. Approximate solutions to the boundary layer equations have been obtained by assuming that at least one of the gas properties remains constant through the boundary layer. Even under these circumstances it is necessary to have an accurate knowledge of the properties in order to choose the constant value most appropriate to the given range of the variables and also to be able to estimate the extent of the error involved in the assumption of constancy.

The fluid properties usually are divided into two groups. The thermodynamic properties of the gas under equilibrium conditions include the entropy, enthalpy, internal energy, specific heat at constant pressure and at constant volume, the compressibility, and the speed of sound. The transport properties express the ability of the gas to transmit energy, momentum, and mass where there are small departures from equilibrium; they include the coefficients of viscosity, thermal conductivity, and diffusion.

At moderate temperatures and pressures, both the thermodynamic and the transport properties may be determined with accuracy by theoretical means and verified by experiment. Tabulated values of the gas properties for air together with the methods by which they are obtained have been given in Section 15 of the Handbook (Ref. 39). As the temperature is increased the gas may no longer be regarded as an ideal gas; however, the thermodynamic properties at high temperatures may still be calculated with confidence provided the energy levels of the gas particles are known at each stage of degeneracy. Most early investigators, including Hirschfelder on whose work many of the tables of Ref. 39 were based, used a low value (7.37 ev) for the energy of dissociation while recent evidence points to a much higher value (9.759 ev). In consequence these tables are invalid above about 3000°R.

A.1 Thermodynamic Properties

There are many reliable sources from which the thermodynamic properties of air (usually considered to be dry and free of argon) may be obtained. Table A-1 lists some of these sources and gives the ranges of the variables included in them. Table A-2 gives the compressibility, Z , the enthalpy, h/RT , and the pressure in terms of the density ratio, ρ/ρ_0 , for values of T from 2000 to 15,000 °K. This table is reproduced from Ref. 187 by Hilsenrath and Klein. Figures A-1, A-2, and A-3 present ρ , Z , and h vs T for various pressures. The data on these figures were taken from Ref. 187. Figure A-4 gives the relationship between $\log \rho$ and $\log h$ for several pressures.

A.2 Transport Properties

The transport properties of air at high temperatures cannot be calculated with the same degree of certainty as can the thermodynamic properties.

Too little is known of the effective intermolecular potentials in the relevant temperature or energy range. Many calculations have been made, based on several different theories, but because of the difficulty in making direct experimental observations at high temperatures it has been impossible to establish any norms by which the validity of the various theories may be checked. A continuing study of transport properties is being made by Liley at the Thermophysical Properties Research Center. References 188 and 189 review work which has been and is being done in this field and give a comprehensive bibliography.

Reference 190 includes a critical review of the status (1962) of the knowledge of the high-temperature transport properties of air and its constituents. The theoretical bases of the computations are described, the limitations indicated, and preferred values recommended. Table A-3 gives some of the readily available sources from which the transport properties may be obtained together with the range of the relevant variables. Values of these transport properties are tabulated in Ref. 17 (for relatively low temperatures) and in Ref. 191 (which contains the values recommended in Ref. 190 in the temperature range above 14,000 °R).

Figures A-5 to A-12 (taken from Ref. 190) give the coefficient of viscosity as a function of temperature for density ratios of 10^n ($n = +1$ to -6). The authors of Ref. 190 recommend using the viscosity curves of Bade, Mason, and Yun (Ref. 192), Bauer and Zlotnick (Ref. 193), and Stupechenko, et al (Ref. 194) for $T < 14,000$ °R. At temperatures above 14,000 °R they recommend using Hansen's results (Ref. 191). Liley suggests using the results of Green (unpublished), Hansen (Ref. 191), and Baulknight (Ref. 195).

Figures A-13 to A-19 give the variation of the thermal conductivity of air with temperature for the same density ratios as before. These values represent the total coefficient, i.e., they are the monatomic values with the Eucken correction plus the reaction conductivity. The values recommended by Ragert and Noble in Ref. 190 are those of Bauer and Zlotnick (Ref. 193) for temperatures below 14,000 °R and at higher temperatures, those of Hansen (Ref. 191). The partial Prandtl number is plotted in Fig. A-20 and the total Prandtl number is shown in Fig. A-21.

Hochstim's values of c_p/R (taken from Ref. 16) are given in Table A-4 as a function of T and $\log \rho/\rho_0$ ($\log \rho/\rho_0 = +1.6$ to -5.6 with $\Delta \log \rho/\rho_0 = +0.2$). Figure A-22 gives selected values of c_p/R vs T in order to show the trend of the data.

Table A-1

Some Sources of Thermodynamic Data*

Ref.	Independent Variables			Dependent Variable	Remarks
	Variable	Range	Δ Ver.		
39	T°K	50-800	10	ρ , h - E _o	T also given in °R Inaccurate at T > 3000 °R
		800-3000	50		
		3000-5000	100		
	p atm	0.01, 0.1, 0.4, 0.7, 1, 4, 7, 10, 40, 70, 100			
187	T°K	1500-15,000	100	Z, h/RT, log p	A new and extended version of AEDC- TDR 63-161
	log ρ/ρ_o	-7.0+2.2	0.2		
17	T°K	50-800	10	Z, ρ/ρ_o	
		800-3000	50		
		0.01, 0.1, 0.4, 0.7, 1, 4, 7, 10, 40, 70, 100			
	p atm				
15	T°K	2000-5000	200	Z, h/RT, p atm	
		5000-10,000	500		
		10,000-15,000	1000		
	ρ/ρ_o	2 to -6	-0.2		
16	T°K	as above	0.02	Z, h/E	Also many deriva- tives with respect to p, ρ and T
	ρ/ρ_o	1.6 to -5.6			
18	h/RT	20-500	10		All these are dis- played on a large Mollier diagram
	T°K	2000-5000	200		
		5000-10,000	500		
		10,000-13,000	1000		
	Z	1-1.9	0.05		
	log ρ/ρ_o	2 to -6	0.1		
191	T°K	500-15,000	500	Z, Zh/RT,	
	p	10 ⁿ , n = 2 to -4	$\Delta n = 1$		
197	T°K	1000-8000	1000	p atm	Some graphs also. A few values of p at $\rho/\rho_o = 10^{-1/2}$, 10 ^{-3/2} , 10 ^{5/2}
		12,000-24,000	6000		
	ρ/ρ_o	10 ⁿ , n = 1 to -6	$\Delta n = 1$		

*Only the variables used in this section of the Handbook have been included. The listed references do not represent a comprehensive survey of the field.

Table A-2
Thermodynamic Properties of Air*

T = 2000° K

$\log p/p_0$	Z	h/RT	$\log (p \text{ atm})$
-7.0	1.11662	7.53433	-6.08721
-6.8	1.10047	7.04084	-5.89354
-6.6	1.08526	6.57597	-5.69958
-6.4	1.07144	6.15343	-5.50515
-6.2	1.05923	5.78019	-5.31012
-6.0	1.04869	5.45787	-5.11447
-5.8	1.03975	5.18443	-4.91819
-5.6	1.03228	4.95566	-4.72132
-5.4	1.02609	4.76635	-4.52393
-5.2	1.02101	4.61104	-4.32609
-5.0	1.01688	4.48448	-4.12785
-4.8	1.01352	4.38189	-3.92928
-4.6	1.01082	4.29908	-3.73044
-4.4	1.00864	4.23247	-3.53138
-4.2	1.00689	4.17902	-3.33213
-4.0	1.00549	4.13622	-3.13274
-3.8	1.00438	4.10200	-2.93322
-3.6	1.00348	4.07469	-2.73361
-3.4	1.00277	4.05291	-2.53391
-3.2	1.00221	4.03555	-2.33416
-3.0	1.00175	4.02173	-2.13435
-2.8	1.00140	4.01073	-1.93451
-2.6	1.00111	4.00198	-1.73463
-2.4	1.00089	3.99502	-1.53473
-2.2	1.00071	3.98948	-1.33481
-2.0	1.00057	3.98509	-1.13487
-1.8	1.00046	3.98160	-0.93492
-1.6	1.00038	3.97884	-0.73495
-1.4	1.00033	3.97665	-0.53497
-1.2	1.00031	3.97493	-0.33498
-1.0	1.00031	3.97360	-0.13498
-0.8	1.00036	3.97257	+0.06504
-0.6	1.00046	3.97183	0.26508
-0.4	1.00065	3.97134	0.46516
-0.2	1.00096	3.97111	0.66530
0	1.00147	3.97119	0.86552
0.2	1.00229	3.97165	1.06588
0.4	1.00360	3.97266	1.26644
0.6	1.00569	3.97446	1.46735
0.8	1.00901	3.97748	1.66878
1.0	1.01428	3.98239	1.87104
1.2	1.02263	3.99028	2.07460
1.4	1.03587	4.00284	2.28019
1.6	1.05686	4.02279	2.48890
1.8	1.09012	4.05444	2.70236
2.0	1.14276	4.10462	2.92284
2.2	1.22601	4.18414	3.15338
2.4	1.35720	4.31010	3.39753

* Source: Ref. 187

Table A-2 (cont'd)

T = 2200° K

$\log \rho/\rho_0$	Z	h/RT	$\log (p \text{ atm})$
-7.0	1.19147	9.33625	-6.01764
-6.8	1.18357	9.11939	-5.82053
-6.6	1.17328	8.83597	-5.62432
-6.4	1.16061	8.48634	-5.42904
-6.2	1.14596	8.08117	-5.23456
-6.0	1.13002	7.63997	-5.04064
-5.8	1.11365	7.18653	-4.84697
-5.6	1.09768	6.74348	-4.65325
-5.4	1.08272	6.32856	-4.45921
-5.2	1.06920	5.95316	-4.26467
-5.0	1.05730	5.62276	-4.06953
-4.8	1.04705	5.33824	-3.87378
-4.6	1.03838	5.09738	-3.67737
-4.4	1.03114	4.89621	-3.48041
-4.2	1.02516	4.72995	-3.28293
-4.0	1.02025	4.59369	-3.08502
-3.8	1.01626	4.48274	-2.88672
-3.6	1.01303	4.39286	-2.68810
-3.4	1.01042	4.32035	-2.48922
-3.2	1.00832	4.26203	-2.29013
-3.0	1.00664	4.21525	-2.09085
-2.8	1.00529	4.17781	-1.89143
-2.6	1.00422	4.14788	-1.69190
-2.4	1.00336	4.12399	-1.49227
-2.2	1.00268	4.10494	-1.29256
-2.0	1.00213	4.08977	-1.09280
-1.8	1.00171	4.07769	-0.89298
-1.6	1.00137	4.06809	-0.69313
-1.4	1.00112	4.06046	-0.49324
-1.2	1.00093	4.05441	-0.29332
-1.0	1.00081	4.04963	-0.09337
-0.8	1.00075	4.04587	+0.10660
-0.6	1.00077	4.04295	0.30661
-0.4	1.00089	4.04074	0.50666
-0.2	1.00116	4.03914	0.70678
0	1.00163	4.03814	0.90698
0.2	1.00242	4.03776	1.10732
0.4	1.00371	4.03811	1.30788
0.6	1.00578	4.03943	1.50878
0.8	1.00909	4.04211	1.71021
1.0	1.01437	4.04682	1.91247
1.2	1.02274	4.05467	2.11604
1.4	1.03602	4.06738	2.32164
1.6	1.05707	4.08774	2.53038
1.8	1.09043	4.12017	2.74387
2.0	1.14323	4.17168	2.96441
2.2	1.22667	4.25338	3.19500
2.4	1.35798	4.38272	3.43917

Table A-2 (cont'd)

T = 2420° K

$\log \rho/\rho_0$	Z	h/RT	$\log (p \text{ atm})$
-7.0	1.20680	9.31789	-5.97430
-6.8	1.20539	9.28380	-5.77481
-6.6	1.20331	9.23314	-5.57556
-6.4	1.20028	9.15846	-5.37665
-6.2	1.19590	9.05018	-5.17824
-6.0	1.18977	8.89745	-4.98047
-5.8	1.18148	8.69012	-4.78351
-5.6	1.17081	8.42222	-4.58745
-5.4	1.15784	8.09542	-4.39229
-5.2	1.14299	7.72069	-4.19789
-5.0	1.12701	7.31649	-4.00401
-4.8	1.11074	6.90440	-3.81032
-4.6	1.09496	6.50440	-3.61654
-4.4	1.08028	6.13177	-3.42240
-4.2	1.06705	5.79601	-3.22775
-4.0	1.05545	5.50144	-3.03250
-3.8	1.04549	5.24840	-2.83661
-3.6	1.03708	5.03460	-2.64012
-3.4	1.03007	4.85629	-2.44307
-3.2	1.02428	4.70910	-2.24552
-3.0	1.01954	4.58857	-2.04753
-2.8	1.01568	4.49050	-1.84918
-2.6	1.01256	4.41109	-1.65051
-2.4	1.01005	4.34705	-1.45159
-2.2	1.00803	4.29557	-1.25246
-2.0	1.00641	4.25429	-1.05316
-1.8	1.00512	4.22125	-0.85372
-1.6	1.00409	4.19486	-0.65416
-1.4	1.00328	4.17381	-0.45451
-1.2	1.00265	4.15704	-0.25478
-1.0	1.00218	4.14371	-0.05499
-0.8	1.00184	4.13314	+0.14486
-0.6	1.00164	4.12479	0.34478
-0.4	1.00158	4.11826	0.54475
-0.2	1.00170	4.11324	0.74480
0	1.00206	4.10951	0.94496
0.2	1.00276	4.10698	1.14526
0.4	1.00398	4.10563	1.34579
0.6	1.00600	4.10561	1.54666
0.8	1.00927	4.10727	1.74807
1.0	1.01451	4.11122	1.95032
1.2	1.02287	4.11855	2.15388
1.4	1.03614	4.13098	2.35948
1.6	1.05720	4.15134	2.56822
1.8	1.09058	4.18410	2.78172
2.0	1.14341	4.23641	3.00227
2.2	1.22686	4.31954	3.23286
2.4	1.35799	4.45119	3.47696

Table A-2 (cont'd)

T = 2600° K

$\log p/p_0$	Z	h/RT	$\log (p \text{ atm})$
-7.0	1.20924	9.00839	-5.93866
-6.8	1.20885	8.99894	-5.73880
-6.6	1.20833	8.98707	-5.53899
-6.4	1.20761	8.97115	-5.33924
-6.2	1.20660	8.94881	-5.13961
-6.0	1.20515	8.91663	-4.94013
-5.8	1.20304	8.86974	-4.74089
-5.6	1.19999	8.80152	-4.54199
-5.4	1.19565	8.70346	-4.34357
-5.2	1.18960	8.56582	-4.14577
-5.0	1.18146	8.37936	-3.94876
-4.8	1.17098	8.13828	-3.75262
-4.6	1.15822	7.84347	-3.55738
-4.4	1.14357	7.50410	-3.36291
-4.2	1.12775	7.13637	-3.16896
-4.0	1.11157	6.75973	-2.97524
-3.8	1.09582	6.39258	-2.78143
-3.6	1.08111	6.04927	-2.58730
-3.4	1.06782	5.73897	-2.39267
-3.2	1.05615	5.46603	-2.19745
-3.0	1.04610	5.23108	-2.00160
-2.8	1.03760	5.03224	-1.80514
-2.6	1.03051	4.86618	-1.60812
-2.4	1.02465	4.72896	-1.41060
-2.2	1.01985	4.61649	-1.21264
-2.0	1.01594	4.52491	-1.01430
-1.8	1.01278	4.45073	-0.81566
-1.6	1.01024	4.39089	-0.61675
-1.4	1.00820	4.34277	-0.41763
-1.2	1.00658	4.30418	-0.21832
-1.0	1.00532	4.27332	-0.01887
-0.8	1.00434	4.24870	+0.18071
-0.6	1.00363	4.22912	0.38040
-0.4	1.00317	4.21361	0.58020
-0.2	1.00296	4.20142	0.78011
0	1.00306	4.19199	0.98015
0.2	1.00355	4.18491	1.18037
0.4	1.00461	4.17995	1.38082
0.6	1.00650	4.17708	1.58164
0.8	1.00967	4.17649	1.78300
1.0	1.01482	4.17870	1.98522
1.2	1.02311	4.18469	2.18875
1.4	1.03633	4.19617	2.39432
1.6	1.05734	4.21592	2.60304
1.8	1.09067	4.24844	2.81652
2.0	1.14344	4.30094	3.03704
2.2	1.22675	4.38480	3.26758
2.4	1.35752	4.51782	3.51157

Table A-2 (cont'd)

T = 2800° K

$\log \rho/\rho_0$	Z	h/RT	$\log (p \text{ atm})$
-7.0	1.21091	8.74718	-5.90588
-6.8	1.21047	8.73222	-5.70603
-6.6	1.21006	8.71914	-5.50618
-6.4	1.20963	8.70703	-5.30633
-6.2	1.20916	8.69495	-5.10650
-6.0	1.20860	8.68177	-4.90671
-5.8	1.20788	8.66604	-4.70696
-5.6	1.20691	8.64582	-4.50731
-5.4	1.20558	8.61836	-4.30779
-5.2	1.20369	8.57981	-4.10847
-5.0	1.20101	8.52487	-3.90944
-4.8	1.19722	8.44657	-3.71081
-4.6	1.19194	8.33651	-3.51273
-4.4	1.18476	8.18589	-3.31536
-4.2	1.17538	7.98765	-3.11881
-4.0	1.16370	7.73940	-2.92315
-3.8	1.14995	7.44581	-2.72831
-3.6	1.13468	7.11875	-2.53411
-3.4	1.11867	6.77490	-2.34028
-3.2	1.10274	6.43188	-2.14651
-3.0	1.08758	6.10478	-1.95253
-2.8	1.07366	5.80433	-1.75812
-2.6	1.06128	5.53661	-1.56316
-2.4	1.05051	5.30375	-1.36759
-2.2	1.04134	5.10506	-1.17140
-2.0	1.03363	4.93806	-0.97462
-1.8	1.02723	4.79934	-0.77732
-1.6	1.02198	4.68520	-0.57955
-1.4	1.01769	4.59197	-0.38137
-1.2	1.01423	4.51626	-0.18285
-1.0	1.01146	4.45509	+0.01596
-0.8	1.00927	4.40585	0.21502
-0.6	1.00757	4.36637	0.41429
-0.4	1.00631	4.33484	0.61374
-0.2	1.00547	4.30979	0.81338
0	1.00506	4.29005	1.01320
0.2	1.00514	4.27472	1.21324
0.4	1.00587	4.26319	1.41355
0.6	1.00750	4.25508	1.61426
0.8	1.01045	4.25033	1.81553
1.0	1.01544	4.24925	2.01767
1.2	1.02358	4.25266	2.22113
1.4	1.03668	4.26215	2.42666
1.6	1.05758	4.28043	2.63533
1.8	1.09080	4.31197	2.84876
2.0	1.14342	4.36394	3.06922
2.2	1.22652	4.44779	3.29969
2.4	1.35679	4.58129	3.54353

Table A-2 (cont'd)

T = 3000° K

$\log \rho/\rho_0$	Z	h/RT	$\log (p \text{ atm})$
-7.0	1.21537	8.63589	-5.87432
-6.8	1.21411	8.58884	-5.67477
-6.6	1.21308	8.55093	-5.47513
-6.4	1.21222	8.52011	-5.27544
-6.2	1.21147	8.49470	-5.07571
-6.0	1.21080	8.47324	-4.87595
-5.8	1.21016	8.45442	-4.67618
-5.6	1.20950	8.43696	-4.47642
-5.4	1.20876	8.41951	-4.27668
-5.2	1.20789	8.40046	-4.07700
-5.0	1.20677	8.37780	-3.87740
-4.8	1.20528	8.34885	-3.67794
-4.6	1.20325	8.30994	-3.47867
-4.4	1.20042	8.25612	-3.27969
-4.2	1.19649	8.18101	-3.08112
-4.0	1.19108	8.07697	-2.88308
-3.8	1.18381	7.93605	-2.68574
-3.6	1.17438	7.75192	-2.48922
-3.4	1.16271	7.52245	-2.29355
-3.2	1.14901	7.25185	-2.09870
-3.0	1.13385	6.95081	-1.90447
-2.8	1.11796	6.63443	-1.71060
-2.6	1.10215	6.31872	-1.51678
-2.4	1.08710	6.01748	-1.32276
-2.2	1.07329	5.74057	-1.12831
-2.0	1.06099	5.49365	-0.93331
-1.8	1.05030	5.27874	-0.73771
-1.6	1.04118	5.09525	-0.54150
-1.4	1.03353	4.94095	-0.34470
-1.2	1.02719	4.81275	-0.14738
-1.0	1.02199	4.70724	+0.05042
-0.8	1.01779	4.62106	0.24863
-0.6	1.01444	4.55111	0.44720
-0.4	1.01183	4.49466	0.64608
-0.2	1.00990	4.44934	0.84525
0	1.00860	4.41321	1.04469
0.2	1.00797	4.38467	1.24442
0.4	1.00812	4.36252	1.44449
0.6	1.00929	4.34590	1.64496
0.8	1.01187	4.33434	1.84610
1.0	1.01655	4.32783	2.04811
1.2	1.02445	4.32694	2.25147
1.4	1.03734	4.33304	2.45689
1.6	1.05805	4.34869	2.66548
1.8	1.09108	4.37823	2.87883
2.0	1.14349	4.42881	3.09921
2.2	1.22627	4.51178	3.32956
2.4	1.35596	4.64486	3.57322

Table A-2 (cont'd)

T = 3200°K

$\log \rho/\rho_0$	Z	h/RT	$\log (p \text{ atm})$
-7.0	1.22835	8.85130	-5.84167
-6.8	1.22450	8.71239	-5.64304
-6.6	1.22140	8.60130	-5.44414
-6.4	1.21891	8.51240	-5.24502
-6.2	1.21690	8.44113	-5.04574
-6.0	1.21525	8.38379	-4.84633
-5.8	1.21388	8.33736	-4.64682
-5.6	1.21272	8.29933	-4.44724
-5.4	1.21169	8.26759	-4.24761
-5.2	1.21073	8.24027	-4.04795
-5.0	1.20979	8.21564	-3.84829
-4.8	1.20877	8.19193	-3.64865
-4.6	1.20760	8.16717	-3.44907
-4.4	1.20616	8.13900	-3.24959
-4.2	1.20429	8.10440	-3.05026
-4.0	1.20180	8.05938	-2.85117
-3.8	1.19840	7.99881	-2.65239
-3.6	1.19377	7.91626	-2.45407
-3.4	1.18754	7.80452	-2.25635
-3.2	1.17936	7.65672	-2.05935
-3.0	1.16901	7.46836	-1.86318
-2.8	1.15652	7.23962	-1.66784
-2.6	1.14225	6.97667	-1.47324
-2.4	1.12681	6.69109	-1.27914
-2.2	1.11100	6.39728	-1.08528
-2.0	1.09555	6.10936	-0.89137
-1.8	1.08105	5.83869	-0.69715
-1.6	1.06792	5.59284	-0.50246
-1.4	1.05634	5.37568	-0.30719
-1.2	1.04636	5.18807	-0.11131
-1.0	1.03793	5.02883	+0.08517
-0.8	1.03090	4.89556	0.28222
-0.6	1.02515	4.78527	0.47979
-0.4	1.02054	4.69482	0.67783
-0.2	1.01693	4.62124	0.87630
0	1.01427	4.56182	1.07516
0.2	1.01252	4.51426	1.27441
0.4	1.01177	4.47665	1.47408
0.6	1.01220	4.44752	1.67427
0.8	1.01418	4.42589	1.87512
1.0	1.01839	4.41129	2.07692
1.2	1.02589	4.40392	2.28010
1.4	1.03844	4.40486	2.48539
1.6	1.05886	4.41641	2.69384
1.8	1.09162	4.44276	2.90707
2.0	1.14373	4.49088	3.12733
2.2	1.22612	4.57205	3.35754

Table A-2 (cont'd)

T = 3400° K

$\log \rho/\rho_0$	Z	h/RT	$\log (p \text{ atm})$
-7.0	1.26139	9.73073	-5.80382
-6.8	1.25102	9.37651	-5.60740
-6.6	1.24266	9.09135	-5.41031
-6.4	1.23594	8.86232	-5.21267
-6.2	1.23053	8.67865	-5.01457
-6.0	1.22619	8.53148	-4.81611
-5.8	1.22268	8.41354	-4.61735
-5.6	1.21984	8.31887	-4.41837
-5.4	1.21751	8.24265	-4.21919
-5.2	1.21558	8.18089	-4.01988
-5.0	1.21394	8.13031	-3.82047
-4.8	1.21249	8.08810	-3.62099
-4.6	1.21114	8.05184	-3.42147
-4.4	1.20982	8.01923	-3.22195
-4.2	1.20840	7.98800	-3.02245
-4.0	1.20679	7.95565	-2.82304
-3.8	1.20482	7.91924	-2.62375
-3.6	1.20229	7.87511	-2.42466
-3.4	1.19897	7.81865	-2.22586
-3.2	1.19453	7.74416	-2.02747
-3.0	1.18862	7.64514	-1.82962
-2.8	1.18090	7.51505	-1.63245
-2.6	1.17111	7.34900	-1.43607
-2.4	1.15920	7.14575	-1.24051
-2.2	1.14544	6.90932	-1.04570
-2.0	1.13037	6.64895	-0.85145
-1.8	1.11471	6.37727	-0.65750
-1.6	1.09923	6.10750	-0.46358
-1.4	1.08455	5.85096	-0.26942
-1.2	1.07113	5.61566	-0.07483
-1.0	1.05922	5.40615	+0.12032
-0.8	1.04892	5.22399	0.31607
-0.6	1.04020	5.06861	0.51245
-0.4	1.03297	4.93808	0.70942
-0.2	1.02712	4.82979	0.90695
0	1.02256	4.74090	1.10502
0.2	1.01924	4.66868	1.30361
0.4	1.01719	4.61066	1.50273
0.6	1.01655	4.56479	1.70246
0.8	1.01767	4.52952	1.90294
1.0	1.02116	4.50385	2.10443
1.2	1.02808	4.48754	2.30736
1.4	1.04015	4.48128	2.51243
1.6	1.06016	4.48707	2.72070
1.8	1.09253	4.50882	2.93377
2.0	1.14425	4.55331	3.15386
2.2	1.22618	4.63162	3.38389

Table A-2 (cont'd)

T = 3600° K

$\log \rho/\rho_0$	Z	h/RT	$\log (p \text{ atm})$
-7.0	1.33319	11.7686	-5.75495
-6.8	1.30952	11.0035	-5.56273
-6.6	1.29009	10.3754	-5.36922
-6.4	1.27423	9.86328	-5.17459
-6.2	1.26136	9.44788	-4.97900
-6.0	1.25096	9.11230	-4.78260
-5.8	1.24256	8.84201	-4.58553
-5.6	1.23579	8.62474	-4.38790
-5.4	1.23032	8.45028	-4.18982
-5.2	1.22591	8.31017	-3.99139
-5.0	1.22231	8.19748	-3.79266
-4.8	1.21935	8.10650	-3.59371
-4.6	1.21688	8.03252	-3.39460
-4.4	1.21475	7.97160	-3.19536
-4.2	1.21285	7.92037	-2.99604
-4.0	1.21106	7.87583	-2.79668
-3.8	1.20925	7.83514	-2.59733
-3.6	1.20729	7.79542	-2.39803
-3.4	1.20502	7.75348	-2.19885
-3.2	1.20222	7.70559	-1.99986
-3.0	1.19866	7.64724	-1.80115
-2.8	1.19401	7.57302	-1.60284
-2.6	1.18793	7.47686	-1.40505
-2.4	1.18010	7.35274	-1.20793
-2.2	1.17025	7.19614	-1.01156
-2.0	1.15837	7.00586	-0.81600
-1.8	1.14469	6.78542	-0.62116
-1.6	1.12973	6.54309	-0.42687
-1.4	1.11422	6.29031	-0.23287
-1.2	1.09888	6.03917	-0.03890
-1.0	1.08433	5.80010	+0.15532
-0.8	1.07105	5.58059	0.34997
-0.6	1.05928	5.38494	0.54517
-0.4	1.04915	5.21471	0.74099
-0.2	1.04066	5.06946	0.93747
0	1.03377	4.94750	1.13458
0.2	1.02844	4.84649	1.33233
0.4	1.02468	4.76394	1.53075
0.6	1.02263	4.69747	1.72987
0.8	1.02257	4.64511	1.92985
1.0	1.02509	4.60538	2.13092
1.2	1.03121	4.57759	2.33350
1.4	1.04262	4.56199	2.53828
1.6	1.06206	4.56021	2.74631
1.8	1.09393	4.57586	2.95915
2.0	1.14517	4.61543	3.17902
2.2	1.22654	4.68978	3.40884

Table A-2 (cont'd)

T = 3800°K

$\log p/p_0$	Z	h/RT	$\log (p \text{ atm})$
-7.0	1.46217	15.3529	-5.69136
-6.8	1.41838	14.0096	-5.50457
-6.6	1.38079	12.8571	-5.31623
-6.4	1.34907	11.8843	-5.12633
-6.2	1.32263	11.0736	-4.93493
-6.0	1.30080	10.4049	-4.74215
-5.8	1.28293	9.85742	-4.54816
-5.6	1.26837	9.41201	-4.35312
-5.4	1.25656	9.05125	-4.15718
-5.2	1.24700	8.76004	-3.96050
-5.0	1.23927	8.52546	-3.76320
-4.8	1.23302	8.33669	-3.56539
-4.6	1.22793	8.18472	-3.36719
-4.4	1.22376	8.06208	-3.16867
-4.2	1.22029	7.96257	-2.96990
-4.0	1.21735	7.88104	-2.77095
-3.8	1.21476	7.81311	-2.57187
-3.6	1.21238	7.75496	-2.37272
-3.4	1.21005	7.70306	-2.17356
-3.2	1.20761	7.65398	-1.97444
-3.0	1.20486	7.60411	-1.77543
-2.8	1.20159	7.54939	-1.57661
-2.6	1.19752	7.48515	-1.37808
-2.4	1.19234	7.40601	-1.17996
-2.2	1.18571	7.30617	-0.98239
-2.0	1.17730	7.18021	-0.78547
-1.8	1.16694	7.02445	-0.58931
-1.6	1.15463	6.83857	-0.39392
-1.4	1.14069	6.62668	-0.19919
-1.2	1.12567	6.39701	-0.00495
-1.0	1.11028	6.16032	+0.18907
-0.8	1.09523	5.92747	0.38314
-0.6	1.08112	5.70757	0.57751
-0.4	1.06835	5.50697	0.77235
-0.2	1.05720	5.32911	0.96779
0	1.04778	5.17507	1.16391
0.2	1.04015	5.04426	1.35073
0.4	1.03437	4.93505	1.53831
0.6	1.03057	4.84540	1.72671
0.8	1.02904	4.77326	1.91607
1.0	1.03032	4.71694	2.10661
1.2	1.03542	4.67536	2.29875
1.4	1.04597	4.64840	2.49315
1.6	1.06468	4.63731	2.68986
1.8	1.09592	4.64535	2.88841
2.0	1.14655	4.67372	3.08903
2.2	1.22729	4.74799	3.29258

Table A-2 (cont'd)

T = 4000° K

$\log \rho/\rho_0$	Z	h/RT	$\log (p \text{ atm})$
-7.0	1.64086	20.0395	-5.61901
-6.8	1.58052	18.2787	-5.43529
-6.6	1.52390	16.6267	-5.25113
-6.4	1.47261	15.1303	-5.06600
-6.2	1.42742	13.8122	-4.87953
-6.0	1.38848	12.6764	-4.69154
-5.8	1.35550	11.7146	-4.50199
-5.6	1.32793	10.9110	-4.31091
-5.4	1.30513	10.2466	-4.11843
-5.2	1.28641	9.70182	-3.92471
-5.0	1.27113	9.25788	-3.72990
-4.8	1.25871	8.89779	-3.53416
-4.6	1.24863	8.60667	-3.33765
-4.4	1.24045	8.37175	-3.14051
-4.2	1.23380	8.18225	-2.94284
-4.0	1.22834	8.02914	-2.74477
-3.8	1.22381	7.90488	-2.54637
-3.6	1.21997	7.80317	-2.34774
-3.4	1.21662	7.71866	-2.14893
-3.2	1.21356	7.64669	-1.95003
-3.0	1.21060	7.58303	-1.75108
-2.8	1.20755	7.52363	-1.55218
-2.6	1.20419	7.46434	-1.35339
-2.4	1.20024	7.40068	-1.15492
-2.2	1.19544	7.32767	-0.95656
-2.0	1.18943	7.23985	-0.75875
-1.8	1.18189	7.13174	-0.56151
-1.6	1.17257	6.99871	-0.36495
-1.4	1.16133	6.83839	-0.16913
-1.2	1.14833	6.65196	+0.02598
-1.0	1.13396	6.44471	0.22051
-0.8	1.11884	6.22526	0.41468
-0.6	1.10369	6.00369	0.60876
-0.4	1.08918	5.78952	0.80301
-0.2	1.07585	5.59022	0.99766
0	1.06407	5.41062	1.19288
0.2	1.05411	5.25305	1.38880
0.4	1.04615	5.11795	1.58551
0.6	1.04038	5.00448	1.78311
0.8	1.03713	4.91120	1.98175
1.0	1.03695	4.83656	2.18167
1.2	1.04079	4.77940	2.38328
1.4	1.05028	4.73936	2.58722
1.6	1.06811	4.71741	2.79453
1.8	1.09856	4.71646	3.00674
2.0	1.14848	4.74241	3.22604
2.2	1.22849	4.80554	3.45528

Table A-2 (cont'd)

T = 4200° K

$\log \rho/\rho_0$	Z	h/RT	$\log (p \text{ atm})$
-7.0	1.81225	24.0917	-5.55468
-6.8	1.75713	22.5574	-5.36809
-6.6	1.69711	20.8873	-5.18319
-6.4	1.63550	19.1727	-4.99925
-6.2	1.57538	17.5000	-4.81551
-6.0	1.51916	15.9360	-4.63129
-5.8	1.46837	14.5230	-4.44606
-5.6	1.42372	13.2810	-4.25947
-5.4	1.38530	12.2126	-4.07135
-5.2	1.35279	11.3090	-3.88167
-5.0	1.32563	10.5546	-3.69047
-4.8	1.30317	9.93137	-3.49790
-4.6	1.28473	9.42044	-3.30408
-4.4	1.26967	9.00406	-3.10921
-4.2	1.25740	8.66616	-2.91342
-4.0	1.24740	8.39267	-2.71689
-3.8	1.23925	8.17150	-2.51974
-3.6	1.23254	7.99243	-2.32209
-3.4	1.22697	7.84684	-2.12406
-3.2	1.22224	7.72748	-1.92574
-3.0	1.21809	7.62815	-1.72722
-2.8	1.21431	7.54344	-1.52857
-2.6	1.21065	7.46845	-1.32988
-2.4	1.20687	7.39851	-1.13124
-2.2	1.20272	7.32892	-0.93273
-2.0	1.19791	7.25469	-0.73447
-1.8	1.19211	7.17056	-0.53658
-1.6	1.18499	7.07109	-0.33918
-1.4	1.17625	6.95135	-0.14240
-1.2	1.16572	6.80796	+0.05370
-1.0	1.15342	6.64034	0.24909
-0.8	1.13963	6.45161	0.44387
-0.6	1.12488	6.24839	0.63821
-0.4	1.10986	6.03951	0.83237
-0.2	1.09526	5.83412	1.02662
0	1.08172	5.64008	1.22122
0.2	1.06972	5.46300	1.41637
0.4	1.05966	5.30611	1.61227
0.6	1.05188	5.17069	1.80907
0.8	1.04677	5.05664	2.00696
1.0	1.04494	4.96320	2.20619
1.2	1.04735	4.88951	2.40719
1.4	1.05561	4.83525	2.61061
1.6	1.07238	4.80122	2.81745
1.8	1.10192	4.79014	3.02925
2.0	1.15100	4.80761	3.24818
2.2	1.23018	4.86363	3.47707

Table A-2 (cont'd)

T = 4400° K

$\log \rho/\rho_0$	Z	h/RT	$\log (p \text{ atm})$
-7.0	1.91821	26.0505	-5.50980
-6.8	1.88579	25.1875	-5.31720
-6.6	1.84408	24.0775	-5.12691
-6.4	1.79362	22.7351	-4.93896
-6.2	1.73640	21.2130	-4.75304
-6.0	1.67543	19.5912	-4.56857
-5.8	1.61401	17.9575	-4.38479
-5.6	1.55502	16.3888	-4.20096
-5.4	1.50056	14.9409	-4.01644
-5.2	1.45187	13.6463	-3.83077
-5.0	1.40940	12.5176	-3.64366
-4.8	1.37308	11.5529	-3.45500
-4.6	1.34249	10.7408	-3.26478
-4.4	1.31702	10.0655	-3.07310
-4.2	1.29600	9.50895	-2.88009
-4.0	1.27874	9.05352	-2.68591
-3.8	1.26464	8.68267	-2.49073
-3.6	1.25311	8.38162	-2.29471
-3.4	1.24366	8.13751	-2.09799
-3.2	1.23586	7.93933	-1.90072
-3.0	1.22934	7.77771	-1.70302
-2.8	1.22376	7.64470	-1.50500
-2.6	1.21884	7.53343	-1.30675
-2.4	1.21430	7.43788	-1.10837
-2.2	1.20985	7.35257	-0.90996
-2.0	1.20523	7.27222	-0.71162
-1.8	1.20012	7.19160	-0.51347
-1.6	1.19421	7.10533	-0.31561
-1.4	1.18715	7.00798	-0.11819
-1.2	1.17865	6.89447	+0.07869
-1.0	1.16847	6.76094	0.27493
-0.8	1.15660	6.60585	0.47049
-0.6	1.14322	6.43087	0.66544
-0.4	1.12881	6.24110	0.85993
-0.2	1.11402	6.04414	1.05420
0	1.09956	5.84846	1.24853
0.2	1.08612	5.66179	1.44318
0.4	1.07431	5.49004	1.63844
0.6	1.06466	5.33699	1.83452
0.8	1.05771	5.20454	2.03167
1.0	1.05416	5.09327	2.23021
1.2	1.05502	5.00316	2.43057
1.4	1.06192	4.93426	2.63340
1.6	1.07750	4.88749	2.83973
1.8	1.10600	4.86548	3.05106
2.0	1.15414	4.87367	3.26956
2.2	1.23241	4.92179	3.49806

Table A-2 (cont'd)

T = 4600° K

$\log \rho/\rho_0$	Z	h/RT	$\log (p \text{ atm})$
-7.0	1.96438	26.3283	-5.48016
-6.8	1.94997	25.9595	-5.28336
-6.6	1.92923	25.4299	-5.08801
-6.4	1.90050	24.6971	-4.89452
-6.2	1.86267	23.7324	-4.70325
-6.0	1.81568	22.5348	-4.51435
-5.8	1.76095	21.1399	-4.32764
-5.6	1.70113	19.6155	-4.14265
-5.4	1.63949	18.0450	-3.95868
-5.2	1.57916	16.5081	-3.77496
-5.0	1.52259	15.0674	-3.59080
-4.8	1.47137	13.7631	-3.40567
-4.6	1.42626	12.6148	-3.21919
-4.4	1.38737	11.6255	-3.03120
-4.2	1.35441	10.7877	-2.84164
-4.0	1.32683	10.0876	-2.65057
-3.8	1.30396	9.50834	-2.45812
-3.6	1.28513	9.03278	-2.26444
-3.4	1.26966	8.64443	-2.06970
-3.2	1.25698	8.32833	-1.87406
-3.0	1.24653	8.07130	-1.67768
-2.8	1.23786	7.86193	-1.48072
-2.6	1.23054	7.69044	-1.28329
-2.4	1.22421	7.54841	-1.08553
-2.2	1.21854	7.42853	-0.88755
-2.0	1.21320	7.32431	-0.68946
-1.8	1.20788	7.22974	-0.49136
-1.6	1.20226	7.13909	-0.29339
-1.4	1.19599	7.04668	-0.09566
-1.2	1.18873	6.94693	+0.10169
-1.0	1.18017	6.83467	0.29856
-0.8	1.17007	6.70578	0.49482
-0.6	1.15838	6.55818	0.69046
-0.4	1.14525	6.39269	0.88551
-0.2	1.13112	6.21333	1.08012
0	1.11661	6.02669	1.27451
0.2	1.10246	5.84049	1.46898
0.4	1.08944	5.66210	1.66381
0.6	1.07826	5.49742	1.85933
0.8	1.06964	5.35051	2.05585
1.0	1.06442	5.22372	2.25372
1.2	1.06370	5.11829	2.45343
1.4	1.06916	5.03509	2.65565
1.6	1.08345	4.97543	2.86142
1.8	1.11080	4.94207	3.07225
2.0	1.15790	4.94042	3.29028
2.2	1.23518	4.98004	3.51834

Table A-2 (cont'd)

T = 4800° K

$\log \rho/\rho_0$	Z	h/RT	$\log (p \text{ atm})$
-7.0	1.98204	25.8965	-5.45779
-6.8	1.97600	25.7457	-5.25912
-6.6	1.96700	25.5228	-5.06110
-6.4	1.95367	25.1950	-4.86405
-6.2	1.93440	24.7220	-4.66836
-6.0	1.90749	24.0625	-4.47444
-5.8	1.87163	23.1846	-4.28269
-5.6	1.82651	22.0806	-4.09328
-5.4	1.77323	20.7771	-3.90814
-5.2	1.71422	19.3335	-3.72084
-5.0	1.65267	17.8282	-3.53672
-4.8	1.59180	16.3398	-3.35302
-4.6	1.53423	14.9327	-3.16901
-4.4	1.48175	13.6500	-2.98413
-4.2	1.43526	12.5145	-2.79797
-4.0	1.39501	11.5320	-2.61033
-3.8	1.36076	10.6971	-2.42112
-3.6	1.33201	9.99729	-2.23040
-3.4	1.30810	9.41699	-2.03826
-3.2	1.28835	8.93951	-1.84487
-3.0	1.27208	8.54874	-1.65039
-2.8	1.25867	8.22991	-1.45499
-2.6	1.24755	7.96985	-1.25885
-2.4	1.23824	7.75710	-1.06210
-2.2	1.23028	7.58174	-0.86490
-2.0	1.22328	7.43514	-0.66738
-1.8	1.21687	7.30971	-0.46966
-1.6	1.21067	7.19860	-0.27188
-1.4	1.20435	7.09543	-0.07415
-1.2	1.19753	6.99413	+0.12338
-1.0	1.18986	6.88886	0.32059
-0.8	1.18102	6.77431	0.51735
-0.6	1.17078	6.64621	0.71357
-0.4	1.15907	6.50221	0.90920
-0.2	1.14605	6.34268	1.10430
0	1.13214	6.17097	1.29900
0.2	1.11798	5.99290	1.49353
0.4	1.10436	5.81553	1.68821
0.6	1.09212	5.64577	1.88336
0.8	1.08214	5.48936	2.07938
1.0	1.07542	5.35045	2.27667
1.2	1.07318	5.23182	2.47577
1.4	1.07719	5.13543	2.67739
1.6	1.09015	5.06334	2.88258
1.8	1.11628	5.01867	3.09287
2.0	1.16227	5.00696	3.31040
2.2	1.23849	5.03773	3.53799

Table A-2 (cont'd)

T = 5000° K

$\log \rho/\rho_0$	Z	h/RT	$\log (p \text{ atm})$
-7.0	1.98961	25.2744	-5.43841
-6.8	1.98671	25.1996	-5.23904
-6.6	1.98260	25.0979	-5.03994
-6.4	1.97659	24.9525	-4.84126
-6.2	1.96767	24.7395	-4.64322
-6.0	1.95451	24.4275	-4.44614
-5.8	1.93547	23.9781	-4.25039
-5.6	1.90887	23.3511	-4.05640
-5.4	1.87337	22.5154	-3.86455
-5.2	1.82860	21.4621	-3.67506
-5.0	1.77559	20.2155	-3.48783
-4.8	1.71672	18.8314	-3.30248
-4.6	1.65518	17.3849	-3.11833
-4.4	1.59420	15.9517	-2.93463
-4.2	1.53642	14.5944	-2.75067
-4.0	1.48366	13.3555	-2.56584
-3.8	1.43687	12.2574	-2.37976
-3.6	1.39630	11.3064	-2.19220
-3.4	1.36174	10.4974	-2.00308
-3.2	1.33268	9.81885	-1.81245
-3.0	1.30848	9.25557	-1.62041
-2.8	1.28842	8.79152	-1.42712
-2.6	1.27183	8.41110	-1.23275
-2.4	1.25808	8.09990	-1.03747
-2.2	1.24658	7.84509	-0.84146
-2.0	1.23681	7.63537	-0.64487
-1.8	1.22832	7.46088	-0.44787
-1.6	1.22066	7.31295	-0.25058
-1.4	1.21342	7.18387	-0.05316
-1.2	1.20623	7.06657	+0.14425
-1.0	1.19868	6.95449	0.34153
-0.8	1.19041	6.84150	0.53852
-0.6	1.18110	6.72215	0.73511
-0.4	1.17053	6.59214	0.93121
-0.2	1.15865	6.44906	1.12678
0	1.14565	6.29310	1.32187
0.2	1.13197	6.12723	1.51666
0.4	1.11831	5.95673	1.71139
0.6	1.10553	5.78809	1.90639
0.8	1.09460	5.62773	2.10208
1.0	1.08667	5.48113	2.29892
1.2	1.08309	5.35252	2.49749
1.4	1.08574	5.24514	2.69855
1.6	1.09739	5.16197	2.90318
1.8	1.12230	5.10676	3.11293
2.0	1.16715	5.08535	3.32995
2.2	1.24228	5.10736	3.55704

Table A-2 (cont'd)

T = 5500° K

$\log \rho/\rho_0$	Z	h/RT	$\log (p \text{ atm})$
-7.0	2.00340	23.8997	-5.39402
-6.8	2.00044	23.8067	-5.19466
-6.6	1.99783	23.7275	-4.99522
-6.4	1.99538	23.6561	-4.79576
-6.2	1.99281	23.5864	-4.59632
-6.0	1.98983	23.5105	-4.39697
-5.8	1.98597	23.4183	-4.19781
-5.6	1.98062	23.2961	-3.99898
-5.4	1.97290	23.1244	-3.80068
-5.2	1.96161	22.8774	-3.60317
-5.0	1.94523	22.5220	-3.40681
-4.8	1.92204	22.0212	-3.21202
-4.6	1.89047	21.3412	-3.01921
-4.4	1.84966	20.4632	-2.82869
-4.2	1.79998	19.3952	-2.64052
-4.0	1.74325	18.1764	-2.45442
-3.8	1.68238	16.8694	-2.26986
-3.6	1.62068	15.5450	-2.08609
-3.4	1.56110	14.2668	-1.90235
-3.2	1.50582	13.0820	-1.71801
-3.0	1.45617	12.0188	-1.53257
-2.8	1.41266	11.0887	-1.34575
-2.6	1.37526	10.2912	-1.15740
-2.4	1.34355	9.61766	-0.96753
-2.2	1.31692	9.05516	-0.77622
-2.0	1.29465	8.58905	-0.58363
-1.8	1.27602	8.20451	-0.38992
-1.6	1.26035	7.88753	-0.19529
-1.4	1.24698	7.62531	+0.00008
-1.2	1.23532	7.40638	0.19600
-1.0	1.22483	7.22055	0.39229
-0.8	1.21500	7.05871	0.58879
-0.6	1.20536	6.91271	0.78533
-0.4	1.19549	6.77525	0.98176
-0.2	1.18504	6.64003	1.17795
0	1.17381	6.50207	1.37381
0.2	1.16177	6.35822	1.56934
0.4	1.14915	6.20767	1.76459
0.6	1.13652	6.05217	1.95979
0.8	1.12476	5.89564	2.15527
1.0	1.11508	5.74343	2.35152
1.2	1.10909	5.60135	2.54919
1.4	1.10894	5.47502	2.74912
1.6	1.11761	5.36988	2.95251
1.8	1.13954	5.29166	3.16095
2.0	1.18149	5.24763	3.37665
2.2	1.25378	5.24819	3.60244

Table A-2 (cont'd)

T = 6000° K

$\log \rho/\rho_0$	Z	h/RT	$\log (p \text{ atm})$
-7.0	2.03876	23.4575	-5.34863
-6.8	2.02897	23.1631	-5.15072
-6.6	2.02111	22.9272	-4.95241
-6.4	2.01477	22.7377	-4.75377
-6.2	2.00960	22.5845	-4.55488
-6.0	2.00531	22.4590	-4.35581
-5.8	2.00161	22.3536	-4.15561
-5.6	1.99823	22.2610	-3.95735
-5.4	1.99485	22.1736	-3.75809
-5.2	1.99107	22.0827	-3.55891
-5.0	1.98639	21.9771	-3.35993
-4.8	1.98008	21.8420	-3.16131
-4.6	1.97116	21.6573	-2.96327
-4.4	1.95832	21.3967	-2.76611
-4.2	1.93995	21.0279	-2.57021
-4.0	1.91430	20.5163	-2.37599
-3.8	1.87994	19.8332	-2.18385
-3.6	1.83631	18.9675	-1.99405
-3.4	1.78420	17.9348	-1.80655
-3.2	1.72580	16.7783	-1.62100
-3.0	1.66421	15.5596	-1.43679
-2.8	1.60268	14.3433	-1.25315
-2.6	1.54398	13.1839	-1.06935
-2.4	1.49003	12.1199	-0.88480
-2.2	1.44187	11.1723	-0.69907
-2.0	1.39984	10.3480	-0.51192
-1.8	1.36376	9.64372	-0.32326
-1.6	1.33312	9.04989	-0.13313
-1.4	1.30722	8.55371	+0.05835
-1.2	1.28534	8.14122	0.25102
-1.0	1.26671	7.79857	0.44468
-0.8	1.25062	7.51271	0.63913
-0.6	1.23641	7.27172	0.83417
-0.4	1.22347	7.06490	1.02960
-0.2	1.21125	6.88270	1.22524
0	1.19932	6.71682	1.42094
0.2	1.18737	6.56032	1.61659
0.4	1.17526	6.40787	1.81214
0.6	1.16316	6.25624	2.00765
0.8	1.15159	6.10456	2.20330
1.0	1.14152	5.95440	2.39949
1.2	1.13447	5.80944	2.59680
1.4	1.13262	5.67485	2.79609
1.6	1.13913	5.55681	2.99858
1.8	1.15861	5.46243	3.20594
2.0	1.19794	5.40041	3.42044
2.2	1.26752	5.38234	3.64496

Table A-2 (cont'd)

T = 6500° K

$\log \rho/\rho_0$	Z	h/RT	$\log (p \text{ atm})$
-7.0	2.13429	24.8043	-5.29398
-6.8	2.10570	24.0032	-5.09984
-6.6	2.08266	23.3576	-4.90462
-6.4	2.06413	22.8388	-4.70850
-6.2	2.04925	22.4225	-4.51164
-6.0	2.03731	22.0887	-4.31418
-5.8	2.02770	21.8209	-4.11623
-5.6	2.01993	21.6052	-3.91790
-5.4	2.01356	21.4302	-3.71927
-5.2	2.00823	21.2859	-3.52042
-5.0	2.00357	21.1635	-3.32143
-4.8	1.99921	21.0541	-3.12237
-4.6	1.99473	20.9484	-2.92335
-4.4	1.98958	20.8352	-2.72447
-4.2	1.98306	20.7005	-2.52590
-4.0	1.97418	20.5256	-2.32785
-3.8	1.96167	20.2864	-2.13061
-3.6	1.94393	19.9528	-1.93455
-3.4	1.91921	19.4925	-1.74011
-3.2	1.88596	18.8769	-1.54770
-3.0	1.84347	18.0925	-1.35760
-2.8	1.79230	17.1496	-1.16982
-2.6	1.73444	16.0850	-0.98407
-2.4	1.67290	14.9540	-0.79976
-2.2	1.61095	13.8170	-0.61615
-2.0	1.55145	12.7266	-0.43250
-1.8	1.49642	11.7205	-0.24818
-1.6	1.44704	10.8204	-0.06275
-1.4	1.40370	10.0342	+0.12404
-1.2	1.36626	9.35988	0.31230
-1.0	1.33423	8.78890	0.50200
-0.8	1.30692	8.30942	0.69302
-0.6	1.28357	7.90823	0.88519
-0.4	1.26341	7.57205	1.07831
-0.2	1.24571	7.28829	1.27218
0	1.22982	7.04545	1.46661
0.2	1.21521	6.83331	1.66142
0.4	1.20150	5.64312	1.85649
0.6	1.18854	6.46785	2.05178
0.8	1.17652	6.30251	2.24737
1.0	1.16607	6.14445	2.44349
1.2	1.15841	5.99359	2.64063
1.4	1.15557	5.85233	2.83956
1.6	1.16065	5.72533	3.04147
1.8	1.17830	5.61932	3.24802
2.0	1.21550	5.54340	3.46152
2.2	1.28268	5.50986	3.68489

Table A-2 (cont'd)

T = 7000° K

log ρ/ρ_0	Z	h/RT	log (p atm)
-7.0	2.34554	29.0378	-5.22080
-6.8	2.27838	27.2784	-5.03342
-6.6	2.22298	25.8272	-4.84411
-6.4	2.17764	24.6396	-4.65306
-6.2	2.14076	23.6737	-4.46048
-6.0	2.11090	22.8918	-4.26658
-5.8	2.08682	22.2611	-4.07156
-5.6	2.06743	21.7538	-3.87562
-5.4	2.05183	21.3461	-3.67891
-5.2	2.03928	21.0186	-3.48157
-5.0	2.02912	20.7548	-3.28374
-4.8	2.02083	20.5410	-3.08552
-4.6	2.01392	20.3654	-2.88701
-4.4	2.00793	20.2173	-2.68830
-4.2	2.00243	20.0866	-2.48949
-4.0	1.99689	19.9627	-2.29069
-3.8	1.99068	19.8331	-2.09205
-3.6	1.98298	19.6826	-1.89373
-3.4	1.97270	19.4915	-1.69599
-3.2	1.95843	19.2348	-1.49914
-3.0	1.93848	18.8828	-1.30359
-2.8	1.91109	18.4049	-1.10977
-2.6	1.87489	17.7771	-0.91807
-2.4	1.82946	16.9924	-0.72872
-2.2	1.77580	16.0678	-0.54165
-2.0	1.71626	15.0437	-0.35646
-1.8	1.65400	13.9745	-0.17251
-1.6	1.59220	12.9156	+0.01095
-1.4	1.53350	11.9122	0.19464
-1.2	1.47965	10.9951	0.37911
-1.0	1.43156	10.1802	0.56476
-0.8	1.38944	9.47162	0.75179
-0.6	1.35300	8.86499	0.94025
-0.4	1.32167	8.35102	1.13007
-0.2	1.29473	7.91784	1.32113
0	1.27142	7.55272	1.51324
0.2	1.25106	7.24324	1.70623
0.4	1.23306	6.97789	1.89994
0.6	1.21704	6.74659	2.09426
0.8	1.20290	6.54095	2.28918
1.0	1.19097	6.35473	2.48485
1.2	1.18217	6.18413	2.68163
1.4	1.17824	6.02811	2.88019
1.6	1.18209	5.88850	3.08160
1.8	1.19826	5.77013	3.28750
2.0	1.23367	5.68111	3.50015
2.2	1.29879	5.63348	3.72249

Table A-2 (cont'd)

T = 7500° K

$\log p/p_0$	Z	h/RT	$\log (p \text{ atm})$
-7.0	2.71419	36.6516	-5.12744
-6.8	2.59253	33.6600	-4.94736
-6.6	2.48678	31.0591	-4.76545
-6.4	2.39659	28.8409	-4.58149
-6.2	2.32083	26.9774	-4.39544
-6.0	2.25795	25.4304	-4.20737
-5.8	2.20622	24.1579	-4.01744
-5.6	2.16398	23.1187	-3.82583
-5.4	2.12967	22.2748	-3.63277
-5.2	2.10192	21.5924	-3.43847
-5.0	2.07953	21.0422	-3.24312
-4.8	2.06149	20.5993	-3.04690
-4.6	2.04693	20.2427	-2.84998
-4.4	2.03512	19.9549	-2.65249
-4.2	2.02544	19.7209	-2.45457
-4.0	2.01731	19.5277	-2.25631
-3.8	2.01019	19.3634	-2.05785
-3.6	2.00353	19.2164	-1.85929
-3.4	1.99668	19.0744	-1.66078
-3.2	1.98885	18.9229	-1.46248
-3.0	1.97900	18.7440	-1.26464
-2.8	1.96581	18.5151	-1.06754
-2.6	1.94765	18.2089	-0.87157
-2.4	1.92270	17.7959	-0.67717
-2.2	1.88938	17.2499	-0.48476
-2.0	1.84686	16.5570	-0.29465
-1.8	1.79559	15.7248	-0.10688
-1.6	1.73748	14.7839	+0.07883
-1.4	1.67546	13.7823	0.26305
-1.2	1.61280	12.7729	0.44650
-1.0	1.55236	11.8022	0.62991
-0.8	1.49621	10.9041	0.81391
-0.6	1.44553	10.0980	0.99894
-0.4	1.40074	9.39115	1.18527
-0.2	1.36171	8.78167	1.37300
0	1.32798	8.26196	1.56211
0.2	1.29892	7.82132	1.75250
0.4	1.27387	7.44787	1.94404
0.6	1.25232	7.12986	2.13663
0.8	1.23396	6.85654	2.33022
1.0	1.21888	6.61880	2.52487
1.2	1.20771	6.40970	2.72088
1.4	1.20192	6.22491	2.91879
1.6	1.20415	6.06317	3.11960
1.8	1.21873	5.92666	3.32482
2.0	1.25244	5.82150	3.53667
2.2	1.31566	5.75852	3.75806

Table A-2 (cont'd)

T = 8000° K

$\log \rho/\rho_0$	Z	h/RT	$\log (p \text{ atm})$
-7.0	3.18722	45.8320	-5.02964
-6.8	3.03096	42.2123	-4.85148
-6.6	2.88046	38.7252	-4.67359
-6.4	2.74120	35.4973	-4.49512
-6.2	2.61640	32.6041	-4.31535
-6.0	2.50740	30.0766	-4.13383
-5.8	2.41410	27.9126	-3.95030
-5.6	2.33549	26.0892	-3.76468
-5.4	2.27008	24.5717	-3.57702
-5.2	2.21617	23.3210	-3.38745
-5.0	2.17208	22.2979	-3.19618
-4.8	2.13622	21.4660	-3.00341
-4.6	2.10717	20.7924	-2.80936
-4.4	2.08370	20.2486	-2.61422
-4.2	2.06474	19.8101	-2.41819
-4.0	2.04939	19.4561	-2.22143
-3.8	2.03685	19.1691	-2.02410
-3.6	2.02645	18.9338	-1.82632
-3.4	2.01753	18.7366	-1.62824
-3.2	2.00945	18.5646	-1.42998
-3.0	2.00151	18.4045	-1.23170
-2.8	1.99288	18.2417	-1.03358
-2.6	1.98248	18.0582	-0.83585
-2.4	1.96897	17.8323	-0.63882
-2.2	1.95069	17.5377	-0.44287
-2.0	1.92584	17.1459	-0.24844
-1.8	1.89274	16.6310	-0.05597
-1.6	1.85048	15.9787	+0.13423
-1.4	1.79940	15.1940	0.32207
-1.2	1.74129	14.3047	0.50782
-1.0	1.67906	13.3549	0.69201
-0.8	1.61594	12.3947	0.87537
-0.6	1.55484	11.4685	1.05863
-0.4	1.49788	10.6092	1.24242
-0.2	1.44632	9.83575	1.42721
0	1.40063	9.15555	1.61327
0.2	1.36078	8.56717	1.80073
0.4	1.32640	8.06362	1.98962
0.6	1.29703	7.63497	2.17989
0.8	1.27233	7.27029	2.37154
1.0	1.25222	6.95900	2.56462
1.2	1.23714	6.69197	2.75936
1.4	1.22829	6.46222	2.95625
1.6	1.22807	6.26565	3.15617
1.8	1.24054	6.10169	3.36056
2.0	1.27229	5.97408	3.57153
2.2	1.33349	5.89179	3.79194

Table A-2 (cont'd)

T = 8500° K

$\log \rho/\rho_0$	Z	h/RT	$\log (p \text{ atm})$
-7.0	3.59359	52.5778	-4.95120
-6.8	3.46326	49.7246	-4.76724
-6.6	3.31657	46.5120	-4.58604
-6.4	3.16129	43.1096	-4.40686
-6.2	3.00567	39.6987	-4.22879
-6.0	2.85684	36.4354	-4.05084
-5.8	2.71989	33.4312	-3.87218
-5.6	2.59770	30.7502	-3.69214
-5.4	2.49134	28.4158	-3.51029
-5.2	2.40054	26.4224	-3.32642
-5.0	2.32418	24.7458	-3.14046
-4.8	2.26075	23.3526	-2.95248
-4.6	2.20852	22.2056	-2.76263
-4.4	2.16583	21.2681	-2.57110
-4.2	2.13112	20.5059	-2.37812
-4.0	2.10299	19.8887	-2.18389
-3.8	2.08022	19.3899	-1.98862
-3.6	2.06176	18.9867	-1.79249
-3.4	2.04670	18.6596	-1.59567
-3.2	2.03424	18.3918	-1.39833
-3.0	2.02361	18.1682	-1.20060
-2.8	2.01409	17.9747	-1.00265
-2.6	2.00488	17.7968	-0.80464
-2.4	1.99505	17.6190	-0.60677
-2.2	1.98344	17.4226	-0.40931
-2.0	1.96861	17.1852	-0.21257
-1.8	1.94883	16.8808	-0.01695
-1.6	1.92223	16.4814	+0.17708
-1.4	1.88722	15.9633	0.36909
-1.2	1.84302	15.3151	0.55880
-1.0	1.79021	14.5450	0.74618
-0.8	1.73080	13.6820	0.93152
-0.6	1.66777	12.7698	1.11541
-0.4	1.60439	11.8555	1.29858
-0.2	1.54343	10.9797	1.48176
0	1.48691	10.1711	1.66556
0.2	1.43597	9.44572	1.85042
0.4	1.39110	8.80887	2.03663
0.6	1.35232	8.25810	2.22435
0.8	1.31950	7.78633	2.41368
1.0	1.29262	7.38429	2.60474
1.2	1.27202	7.04238	2.79777
1.4	1.25875	6.75215	2.99321
1.6	1.25497	6.50739	3.19191
1.8	1.26454	6.30516	3.39520
2.0	1.29377	6.14682	3.60513
2.2	1.35262	6.03931	3.82445

Table A-2 (cont'd)

T = 9000° K

$\log \rho/\rho_0$	Z	h/RT	$\log (p \text{ atm})$
-7.0	3.82248	54.9668	-4.89956
-6.8	3.74938	53.4498	-4.70794
-6.6	3.65318	51.4526	-4.51923
-6.4	3.53388	48.9747	-4.33365
-6.2	3.39507	46.0899	-4.15105
-6.0	3.24345	42.9371	-3.97090
-5.8	3.08720	39.6866	-3.79234
-5.6	2.93420	36.5020	-3.61441
-5.4	2.79062	33.5123	-3.43620
-5.2	2.66049	30.8017	-3.25694
-5.0	2.54580	28.4114	-3.07608
-4.8	2.44690	26.3498	-2.89329
-4.6	2.36309	24.6021	-2.70842
-4.4	2.29301	23.1405	-2.52150
-4.2	2.23504	21.9313	-2.33262
-4.0	2.18747	20.9390	-2.14196
-3.8	2.14867	20.1297	-1.94973
-3.6	2.11714	19.4726	-1.75615
-3.4	2.09157	18.9404	-1.56143
-3.2	2.07080	18.5094	-1.36577
-3.0	2.05382	18.1591	-1.16934
-2.8	2.03972	17.8717	-0.97233
-2.6	2.02767	17.6310	-0.77491
-2.4	2.01681	17.4218	-0.57724
-2.2	2.00626	17.2286	-0.37952
-2.0	1.99492	17.0343	-0.18198
-1.8	1.98151	16.8191	+0.01509
-1.6	1.96442	16.5592	0.21133
-1.4	1.94181	16.2282	0.40630
-1.2	1.91181	15.7993	0.59954
-1.0	1.87303	15.2529	0.79064
-0.8	1.82513	14.5839	0.97939
-0.6	1.76920	13.8072	1.16587
-0.4	1.70769	12.9565	1.35050
-0.2	1.64378	12.0758	1.53394
0	1.58064	11.2084	1.71693
0.2	1.52085	10.3891	1.90018
0.4	1.46617	9.64070	2.08428
0.6	1.41763	8.97450	2.26966
0.8	1.37574	8.39258	2.45663
1.0	1.34081	7.89101	2.64546
1.2	1.31334	7.46271	2.83647
1.4	1.29436	7.09968	3.03015
1.6	1.28590	6.79491	3.22730
1.8	1.29161	6.54386	3.42923
2.0	1.31760	6.34600	3.63788
2.2	1.37354	6.20636	3.85594

Table A-2 (cont'd)

T = 9500° K

$\log \rho/\rho_0$	Z	h/RT	$\log (p \text{ atm})$
-7.0	3.91915	54.5340	-1.86523
-6.8	3.88604	53.8814	-4.66891
-6.6	3.83791	52.9318	-4.47453
-6.4	3.77051	51.6011	-4.28202
-6.2	3.68059	49.8246	-4.09251
-6.0	3.56729	47.5850	-3.90608
-5.8	3.43326	44.9336	-3.72272
-5.6	3.28446	41.9883	-3.54196
-5.4	3.12884	38.9060	-3.36304
-5.2	2.97447	35.8468	-3.18501
-5.0	2.82804	32.9434	-3.00694
-4.8	2.69416	30.2874	-2.82800
-4.6	2.57531	27.9285	-2.64759
-4.4	2.47224	25.8820	-2.46533
-4.2	2.38450	24.1392	-2.28103
-4.0	2.31087	22.6764	-2.09465
-3.8	2.24978	21.4624	-1.90628
-3.6	2.19953	20.4638	-1.71609
-3.4	2.15846	19.6476	-1.52428
-3.2	2.12502	18.9838	-1.33106
-3.0	2.09784	18.4450	-1.13665
-2.8	2.07570	18.0077	-0.94126
-2.6	2.05753	17.6511	-0.74508
-2.4	2.04233	17.3569	-0.54830
-2.2	2.02917	17.1084	-0.35110
-2.0	2.01711	16.8893	-0.15369
-1.8	2.00510	16.6828	+0.04371
-1.6	1.99189	16.4702	0.24084
-1.4	1.97596	16.2297	0.43736
-1.2	1.95554	15.9362	0.63284
-1.0	1.92869	15.5630	0.82684
-0.8	1.89369	15.0867	1.01889
-0.6	1.84961	14.4943	1.20866
-0.4	1.79683	13.7905	1.39608
-0.2	1.73721	12.9995	1.58143
0	1.67369	12.1597	1.76525
0.2	1.60959	11.3139	1.94829
0.4	1.54789	10.4998	2.13132
0.6	1.49088	9.74497	2.31502
0.8	1.44011	9.06507	2.49997
1.0	1.39667	8.46617	2.68667
1.2	1.36146	7.94744	2.87558
1.4	1.33573	7.50418	3.06730
1.6	1.32155	7.13053	3.26266
1.8	1.32247	6.82171	3.46296
2.0	1.34441	6.57608	3.67011
2.2	1.39677	6.39731	3.88670

Table A-2 (cont'd)

T = 10000° K

$\log \rho/\rho_0$	Z	h/RT	$\log (p \text{ atm})$
-7.0	3.95613	53.0375	-4.83888
-6.8	3.94182	52.7691	-4.64045
-6.6	3.92001	52.3597	-4.44286
-6.4	3.88740	51.7467	-4.24649
-6.2	3.83995	50.8538	-4.05182
-6.0	3.77344	49.6011	-3.85941
-5.8	3.68455	47.9255	-3.66976
-5.6	3.57234	45.8085	-3.48319
-5.4	3.43927	43.2960	-3.29368
-5.2	3.29117	40.4975	-3.11880
-5.0	3.13590	37.5613	-2.93978
-4.8	2.98152	34.6400	-2.76171
-4.6	2.83477	31.8616	-2.58363
-4.4	2.70036	29.3151	-2.40472
-4.2	2.58086	27.0497	-2.22438
-4.0	2.47709	25.0818	-2.04220
-3.8	2.38866	23.4039	-1.85799
-3.6	2.31438	21.9941	-1.67171
-3.4	2.25270	20.8232	-1.48344
-3.2	2.20192	19.8590	-1.29335
-3.0	2.16037	19.0704	-1.10162
-2.8	2.12649	18.4280	-0.90848
-2.6	2.09889	17.9058	-0.71416
-2.4	2.07632	17.4806	-0.51885
-2.2	2.05764	17.1319	-0.32278
-2.0	2.04181	16.8415	-0.12613
-1.8	2.02780	16.5920	+0.07088
-1.6	2.01453	16.3663	0.26803
-1.4	2.00076	16.1459	0.46505
-1.2	1.98502	15.9099	0.66162
-1.0	1.96556	15.6345	0.85734
-0.8	1.94043	15.2934	1.05175
-0.6	1.90775	14.8620	1.24437
-0.4	1.86624	14.3231	1.43482
-0.2	1.81580	13.6748	1.62292
0	1.75782	12.9339	1.80883
0.2	1.69501	12.1335	1.99303
0.4	1.63071	11.3144	2.17623
0.6	1.56819	10.5150	2.35925
0.8	1.51018	9.76525	2.54288
1.0	1.45879	9.08407	2.72785
1.2	1.41573	8.48053	2.91484
1.4	1.38272	7.95649	3.10459
1.6	1.36208	7.50979	3.29806
1.8	1.35741	7.13726	3.49657
2.0	1.37455	6.83744	3.70201
2.2	1.42261	6.61347	3.91694

Table A-2 (cont'd)

T = 11000°K

$\log \rho/\rho_0$	Z	h/RT	$\log (p \text{ atm})$
-7.0	3.97645	49.5483	-4.79526
-6.8	3.97338	49.4965	-4.59559
-6.6	3.96861	49.4156	-4.39611
-6.4	3.96121	49.2895	-4.19693
-6.2	3.94976	49.0939	-3.99818
-6.0	3.93223	48.7935	-3.80011
-5.8	3.90579	48.3392	-3.60304
-5.6	3.86678	47.6676	-3.40740
-5.4	3.81100	46.7057	-3.21371
-5.2	3.73454	45.3851	-3.02252
-5.0	3.63504	43.6642	-2.83424
-4.8	3.51304	41.5518	-2.64907
-4.6	3.37263	39.1179	-2.46678
-4.4	3.22070	36.4815	-2.28680
-4.2	3.06536	33.7833	-2.10827
-4.0	2.91411	31.1543	-1.93025
-3.8	2.77283	28.6961	-1.75183
-3.6	2.64518	26.4734	-1.57230
-3.4	2.53290	24.5169	-1.39114
-3.2	2.43620	22.8310	-1.20804
-3.0	2.35432	21.4025	-1.02289
-2.8	2.28586	20.2076	-0.83570
-2.6	2.22920	19.2183	-0.64661
-2.4	2.18261	18.4050	-0.45578
-2.2	2.14447	17.7398	-0.26343
-2.0	2.11326	17.1967	-0.06980
-1.8	2.08759	16.7524	+0.12489
-1.6	2.06619	16.3857	0.32042
-1.4	2.04785	16.0775	0.51654
-1.2	2.03134	15.8090	0.71303
-1.0	2.01534	15.5614	0.90960
-0.8	1.99836	15.3142	1.10592
-0.6	1.97863	15.0443	1.30161
-0.4	1.95417	14.7267	1.49021
-0.2	1.92297	14.3361	1.68922
0	1.88348	13.8529	1.88021
0.2	1.83518	13.2692	2.06892
0.4	1.77905	12.5946	2.25544
0.6	1.71760	11.8553	2.44017
0.8	1.65432	11.0875	2.62387
1.0	1.59302	10.3284	2.80747
1.2	1.53735	9.60913	2.99202
1.4	1.49073	8.95135	3.17865
1.6	1.45670	8.36794	3.36862
1.8	1.43956	7.86557	3.56348
2.0	1.44537	7.44842	3.76522
2.2	1.48283	7.12262	3.97634

Table A-2 (cont'd)

T = 12000°K

$\log \rho/\rho_0$	Z	h/RT	$\log (p \text{ atm})$
-7.0	3.98071	46.4014	-4.75700
-6.8	3.97968	46.3835	-4.55712
-6.6	3.97824	46.3603	-4.35727
-6.4	3.97612	46.3271	-4.15751
-6.2	3.97289	46.2771	-3.95786
-6.0	3.96793	46.1999	-3.75840
-5.8	3.96027	46.0804	-3.55924
-5.6	3.94850	45.8958	-3.36053
-5.4	3.93055	45.6130	-3.16251
-5.2	3.90358	45.1862	-2.96550
-5.0	3.86391	44.5567	-2.76994
-4.8	3.80741	43.6573	-2.57633
-4.6	3.73023	42.4259	-2.38523
-4.4	3.63012	40.8257	-2.19704
-4.2	3.50778	38.8667	-2.01193
-4.0	3.36735	36.6146	-1.82968
-3.8	3.21572	34.1795	-1.64969
-3.6	3.06089	31.6902	-1.47112
-3.4	2.91034	29.2665	-1.29302
-3.2	2.76976	27.0007	-1.11452
-3.0	2.64278	24.9519	-0.93490
-2.8	2.53107	23.1478	-0.75366
-2.6	2.43486	21.5925	-0.57049
-2.4	2.35334	20.2737	-0.38528
-2.2	2.28514	19.1696	-0.19805
-2.0	2.22862	18.2541	-0.00893
-1.8	2.18207	17.5003	+0.18190
-1.6	2.14383	16.8818	0.37422
-1.4	2.11234	16.3743	0.56780
-1.2	2.08614	15.9556	0.76238
-1.0	2.06387	15.6049	0.95772
-0.8	2.04413	15.3024	1.15354
-0.6	2.02548	15.0284	1.34956
-0.4	2.00628	14.7617	1.54543
-0.2	1.98469	14.4792	1.74073
0	1.95864	14.1559	1.93499
0.2	1.92615	13.7674	2.12773
0.4	1.88572	13.2948	2.31851
0.6	1.83703	12.7310	2.50715
0.8	1.78138	12.0852	2.69379
1.0	1.72172	11.3824	2.87900
1.2	1.66222	10.6568	3.06372
1.4	1.60767	9.94374	3.24923
1.6	1.56321	9.27314	3.43705
1.8	1.53453	8.66764	3.62901
2.0	1.52846	8.14406	3.82729
2.2	1.55336	7.71854	4.03431

Table A-2 (cont'd)

T = 13000°K

$\log \rho/\rho_0$	Z	h/RT	$\log (p \text{ atm})$
-7.0	3.98581	43.8076	-4.72169
-6.8	3.98378	43.7550	-4.52191
-6.6	3.98221	43.7181	-4.32208
-6.4	3.98079	43.6890	-4.12223
-6.2	3.97924	43.6618	-3.92240
-6.0	3.97725	43.6308	-3.72262
-5.8	3.97444	43.5895	-3.52293
-5.6	3.97029	43.5296	-3.32338
-5.4	3.96399	43.4390	-3.12407
-5.2	3.95437	43.3003	-2.92513
-5.0	3.93974	43.0878	-2.72674
-4.8	3.91766	42.7655	-2.52918
-4.6	3.88492	42.2848	-2.33282
-4.4	3.83759	41.5869	-2.13814
-4.2	3.77157	40.6099	-1.94568
-4.0	3.68368	39.3051	-1.75592
-3.8	3.57297	37.6571	-1.56917
-3.6	3.44176	35.6997	-1.38542
-3.4	3.29560	33.5150	-1.20427
-3.2	3.14207	31.2159	-1.02499
-3.0	2.98899	28.9200	-0.84668
-2.8	2.84305	26.7275	-0.66842
-2.6	2.70892	24.7096	-0.48941
-2.4	2.58928	22.9072	-0.30902
-2.2	2.48507	21.3349	-0.12686
-2.0	2.39596	19.9890	+0.05728
-1.8	2.32087	18.8534	0.24345
-1.6	2.25826	17.9058	0.43157
-1.4	2.20644	17.1212	0.62149
-1.2	2.16369	16.4745	0.81299
-1.0	2.12836	15.9417	1.00584
-0.8	2.09889	15.5002	1.19979
-0.6	2.07375	15.1290	1.39455
-0.4	2.05142	14.8075	1.58985
-0.2	2.03030	14.5151	1.78536
0	2.00861	14.2297	1.98069
0.2	1.98438	13.9275	2.17542
0.4	1.95555	13.5839	2.36907
0.6	1.92030	13.1760	2.56117
0.8	1.87766	12.6885	2.75141
1.0	1.82814	12.1191	2.93981
1.2	1.77417	11.4819	3.12679
1.4	1.72004	10.8045	3.31333
1.6	1.67144	10.1214	3.50089
1.8	1.63518	9.46729	3.69136
2.0	1.61893	8.87393	3.88702
2.2	1.62994	8.37461	4.08997

Table A-2 (cont'd)

T = 14000°K

$\log \rho/\rho_0$	Z	h/RT	$\log (p \text{ atm})$
-7.0	4.01350	42.2242	-4.68649
-6.8	4.00189	41.9153	-4.48775
-6.6	3.99421	41.7134	-4.28859
-6.4	3.98908	41.5815	-4.08915
-6.2	3.98551	41.4939	-3.88953
-6.0	3.98282	41.4332	-3.68983
-5.8	3.98046	41.3869	-3.49009
-5.6	3.97798	41.3453	-3.29036
-5.4	3.97492	41.2999	-3.09069
-5.2	3.97070	41.2416	-2.89115
-5.0	3.96453	41.1586	-2.69183
-4.8	3.95531	41.0349	-2.49284
-4.6	3.94140	40.8476	-2.29437
-4.4	3.92053	40.5646	-2.09667
-4.2	3.88963	40.1427	-1.90011
-4.0	3.84491	39.5284	-1.70513
-3.8	3.78231	38.6638	-1.51226
-3.6	3.69844	37.5005	-1.32200
-3.4	3.59192	36.0174	-1.13469
-3.2	3.46445	34.2372	-0.95038
-3.0	3.32103	32.2288	-0.76874
-2.8	3.16891	30.0933	-0.58911
-2.6	3.01587	27.9406	-0.41061
-2.4	2.86883	25.8678	-0.23231
-2.2	2.73281	23.9464	-0.05341
-2.0	2.61079	22.2197	+0.12675
-1.8	2.50400	20.7057	0.30862
-1.6	2.41233	19.4038	0.49242
-1.4	2.33481	18.3011	0.67823
-1.2	2.26997	17.3775	0.86600
-1.0	2.21612	16.6101	1.05558
-0.8	2.17154	15.9750	1.24675
-0.6	2.13453	15.4491	1.43928
-0.4	2.10343	15.0105	1.63291
-0.2	2.07663	14.6378	1.82734
0	2.05249	14.3103	2.02226
0.2	2.02925	14.0062	2.21732
0.4	2.00501	13.7027	2.41210
0.6	1.97779	13.3755	2.60616
0.8	1.94576	13.0010	2.79907
1.0	1.90776	12.5602	2.99050
1.2	1.86404	12.0450	3.18044
1.4	1.81692	11.4622	3.36932
1.6	1.77093	10.8342	3.55818
1.8	1.73261	10.1949	3.74868
2.0	1.70947	9.58577	3.94284
2.2	1.70383	9.06550	4.14141

Table A-2 (cont'd)*

T = 15000°K

$\log \rho/\rho_0$	Z	h/RT	$\log (p \text{ atm})$
-7.0	4.13453	43.1875	-4.64363
-6.8	4.08444	41.9232	-4.44892
-6.6	4.04942	41.0412	-4.25266
-6.4	4.02554	40.4420	-4.05523
-6.2	4.00952	40.0424	-3.85696
-6.0	3.99881	39.7789	-3.65812
-5.8	3.99155	39.6052	-3.45891
-5.6	3.98641	39.4886	-3.25947
-5.4	3.98241	39.4063	-3.05991
-5.2	3.97878	39.3418	-2.86030
-5.0	3.97484	39.2817	-2.66073
-4.8	3.96987	39.2141	-2.46128
-4.6	3.96297	39.1254	-2.26203
-4.4	3.95291	38.9988	-2.06314
-4.2	3.93798	38.8111	-1.86478
-4.0	3.91583	38.5307	-1.66723
-3.8	3.88330	38.1159	-1.47085
-3.6	3.83661	37.5159	-1.27611
-3.4	3.77177	36.6771	-1.08351
-3.2	3.68560	35.5562	-0.89355
-3.0	3.57705	34.1374	-0.70653
-2.8	3.44818	32.4462	-0.52246
-2.6	3.30420	30.5502	-0.34099
-2.4	3.15240	28.5451	-0.16141
-2.2	3.00044	26.5324	+0.01713
-2.0	2.85498	24.6006	0.19555
-1.8	2.72079	22.8140	0.37464
-1.6	2.60065	21.2107	0.55503
-1.4	2.49564	19.8059	0.73713
-1.2	2.40555	18.5981	0.92116
-1.0	2.32936	17.5744	1.10718
-0.8	2.26558	16.7160	1.29512
-0.6	2.21252	16.0011	1.48483
-0.4	2.16843	15.4073	1.67609
-0.2	2.13158	14.9125	1.86865
0	2.10029	14.4952	2.06223
0.2	2.07287	14.1346	2.25652
0.4	2.04758	13.8090	2.45119
0.6	2.02260	13.4962	2.64586
0.8	1.99606	13.1725	2.84012
1.0	1.96628	12.8145	3.03359
1.2	1.93225	12.4025	3.22601
1.4	1.89438	11.9261	3.41741
1.6	1.85515	11.3895	3.60832
1.8	1.81924	10.8151	3.79983
2.0	1.79155	10.2461	3.99317
2.2	1.75269	9.79390	4.18365

*Source: Ref. 187

Table A-3

Transport Properties of Air*

Ref.	Independent Variable			Dependent Variable	Remarks
	Variable	Range	Δ Var		
190	$T^\circ R$ ρ/ρ_0	0-28,000 10^1 to 10^{-8}	Graph	μ , k , Pr	Gives an analysis of data from many sources
193	$T^\circ R$ $T^\circ K$ ρ/ρ_0	5400-14,400 3000-8000 10^1 to 10^{-8}	Graphs	μ , k , Pr (frozen re-action)	Recommended especially good up to 8,000 +K, may be weak after that.
191	$T^\circ K$ p	500-15,000 10^{-4} to 10^2	500 by 10 's	μ/μ_0 , k/k_0 Pr	Recommended for $T > 14,000$
17	$T^\circ K$ p	50-800 800-3000 0.01, 0.1, 0.4, 0.7, 1, 4, 7, 10, 40, 70, 100	10 50	c_p/R , γ , μ (to 1900°K) k (to 1000°K) Pr (to 1000°K)	μ and Pr at 1 atm pressure
16	$T^\circ K$ $\log \rho/\rho_0$	2000-5000 5000-10,000 10,000-15,000 1.6-5.6	200 500 1000 0.2	c_p/R , ρ_v/R , γ	
196	Nomographs for μ , k ; low density				
39	$T^\circ K$ (also in $^\circ R$) p atm	50-800 800-3000 3000-5000 0.01, 0.4, 0.7, 1, 4, 7, 10, 40, 70, 100	10 50 100	c_v , c_p , γ , μ , k , Pr	μ and Pr only at $p = 1$ atm. Also gives $Pr^{1/2}$, $Pr^{1/3}$, $Pr^{2/3}$

* Only the variables used in this section of the Handbook have been included. The listed references do not represent a comprehensive survey of the field.

Table A-4

 c_p/R vs T for Various Values of $\log \rho/\rho_0$ $\log \rho/\rho_0$

T°K	1.6	1.4	1.2	1.0	0.8	0.6	0.4	0.2	0.	-0.2
2000	4.6617	4.6402	4.6267	4.6109	4.6059	4.6494	4.6574	4.6202	4.6567	4.6625
2200	4.6838	4.7105	4.7278	4.7542	4.7595	4.7284	4.7562	4.8087	4.7931	4.7991
2400	4.8853	4.3948	4.9074	4.9196	4.9382	4.9576	4.9788	5.0198	5.0578	5.1194
2600	5.0264	5.0333	5.0562	5.0851	5.1247	5.1760	5.2351	5.3054	5.4073	5.5196
2800	5.1369	5.1718	5.2173	5.2753	5.3419	5.4357	5.5525	5.6889	5.8582	6.0671
3000	5.3054	5.3670	5.4430	5.5345	5.6562	5.8088	5.9904	6.2245	6.5072	6.8683
3200	5.4954	5.5939	5.7182	5.8591	6.0547	6.2699	6.5577	6.9085	7.3467	7.8708
3400	5.7008	5.8435	6.0082	6.2299	6.4849	6.8095	7.2054	7.6836	8.2741	8.9603
3600	6.0100	6.1978	6.4413	6.7335	7.0859	7.5324	8.0548	8.6758	9.3865	1.0213
3800	6.2034	6.4524	6.7542	7.0995	7.5453	8.0641	8.6608	9.3508	1.0118	1.0940
4000	6.3858	6.6830	7.0229	7.4461	7.9502	8.5077	9.1432	9.8380	1.0543	1.1187
4200	6.7154	7.0588	7.4779	7.9594	8.5021	9.1083	9.7506	1.0378	1.0944	1.1366
4400	6.9651	7.3588	7.8043	8.3117	8.8519	9.4329	9.9794	1.0450	1.0783	1.0893
4600	7.2110	7.6224	8.0792	8.5752	9.1024	9.5806	1.0009	1.0272	1.0353	1.0226
4800	7.4288	7.7696	8.3011	8.7270	9.1541	9.6029	9.7867	9.8709	9.8583	9.6861
5000	7.5662	8.0487	8.3910	8.8947	9.1937	9.4525	9.5530	9.5489	9.3187	9.0179
5500	7.8547	8.2366	8.5366	8.8053	8.9463	8.9948	8.9801	8.9508	9.0199	9.1855
6000	8.0044	8.2990	8.5413	8.7367	8.9016	9.0757	9.3239	9.7045	1.0296	1.1133
6500	8.2267	8.5225	8.6176	9.1425	9.5502	1.0082	1.0813	1.1809	1.3128	1.4825
7000	8.6463	9.0663	9.5611	1.0189	1.0990	1.2030	1.3394	1.5126	1.7298	1.9959
7500	9.3400	9.9896	1.0812	1.1834	1.3131	1.4789	1.6839	1.9349	2.2332	2.5803
8000	1.0403	1.1379	1.2580	1.4072	1.5936	1.8199	2.0892	2.4034	2.7534	3.1275
8500	1.1865	1.3185	1.4815	1.6801	1.9161	2.1928	2.5060	2.8415	3.1803	3.4837
9000	1.3530	1.5221	1.7253	1.9630	2.2375	2.5386	2.8482	3.1438	3.3818	3.5186
9500	1.5311	1.7354	1.9643	2.2260	2.5211	2.7924	3.0422	3.2275	3.2886	3.2128
10000	1.7261	1.9575	2.2146	2.4891	2.7348	2.9614	3.1057	3.1196	3.0145	2.7335
11000	2.0700	2.2936	2.5117	2.6823	2.7787	2.7731	2.6601	2.4555	2.1993	1.9412
12000	2.2772	2.4300	2.5197	2.5251	2.4341	2.2633	2.0497	1.8343	1.6586	1.5473
13000	2.2926	2.3265	2.2802	2.1573	1.9828	1.8000	1.6432	1.5397	1.5027	1.5324
14000	2.1330	2.0771	1.9549	1.8137	1.6892	1.5975	1.5480	1.5416	1.5858	1.6929
15000	1.9412	1.8272	1.7087	1.6045	1.5354	1.5054	1.5399	1.6107	1.7609	1.9812

Table A-4 (cont'd)

 $\log \rho/\rho_0$

T°K	-0.4	-0.6	-0.8	-1.0	-1.2	-1.4	-1.6	-1.8	-2.0	-2.2
2000	4.6728	4.6650	4.6863	4.7150	4.7603	4.7937	4.8106	4.8480	4.9410	5.0172
2200	4.8129	4.8901	4.9273	4.9863	5.0510	5.1420	5.2666	5.4297	5.5972	5.8475
2400	5.1887	5.2757	5.3812	5.5091	5.6781	5.8905	6.1658	6.4941	6.9131	7.4260
2600	5.6623	5.8460	6.0745	6.3592	6.7185	7.1663	7.7005	8.3784	9.1991	1.0194
2800	6.3442	6.6805	7.0928	7.6176	8.2460	9.0021	9.9191	1.1023	1.2297	1.3759
3000	7.3076	7.8450	8.4996	9.2896	1.0219	1.1308	1.2570	1.3937	1.5371	1.6764
3200	8.5003	9.2594	1.0147	1.1163	1.2313	1.3548	1.4776	1.5889	1.6769	1.7218
3400	9.7713	1.0678	1.1700	1.2771	1.3818	1.4741	1.5402	1.5864	1.5423	1.4656
3600	1.1110	1.2061	1.2977	1.3776	1.4319	1.4519	1.4275	1.3563	1.2487	1.1205
3800	1.1733	1.2471	1.3003	1.3254	1.3136	1.2628	1.1765	1.0721	0.96397	0.86509
4000	1.1737	1.2051	1.2084	1.1776	1.1171	1.0357	0.94685	0.86538	0.79691	0.75308
4200	1.1563	1.1463	1.1101	1.0486	0.97497	0.90104	0.83685	0.79108	0.76796	0.76815
4400	1.0758	1.0394	0.98410	0.92381	0.86742	0.82368	0.79934	0.79600	0.81707	0.85972
4600	0.9087	0.94597	0.96837	0.95579	0.82917	0.82202	0.83931	0.87788	0.94165	0.10302
4800	0.2038	0.8661	0.86618	0.84702	0.85590	0.8745	0.93500	1.0265	1.1424	1.2904
5000	0.8401	0.86880	0.86978	0.89596	0.93966	0.10118	1.1110	1.2437	1.4184	1.6472
5500	0.5902	0.10171	1.1048	1.2217	1.3791	1.5766	1.8087	2.0841	2.4042	2.7758
6000	1.2289	1.3815	1.5779	1.8244	2.1289	2.4963	2.9326	3.4368	4.0011	4.6016
6500	1.6987	1.9656	2.2892	2.6737	3.1195	3.6151	4.1413	4.6594	5.1130	5.4279
7000	2.3157	2.6890	3.1123	3.5713	4.0386	4.4650	4.7919	4.9555	4.8981	4.6084
7500	2.9696	3.3849	3.7954	4.1568	4.4072	4.4917	4.3725	4.0479	3.5665	3.0150
8000	3.4966	3.8189	4.0409	4.1107	3.9928	3.6944	3.2590	2.7661	2.2965	1.9074
8500	3.7078	3.7995	3.7267	3.4847	3.1100	2.6723	2.2479	1.8935	1.6366	1.4800
9000	3.5134	3.3499	3.0511	2.6693	2.2794	1.9384	1.6837	1.5227	1.4498	1.4561
9500	3.0007	2.7003	2.3616	2.0602	1.8288	1.6537	1.5363	1.4904	1.5180	1.6266
10000	2.4849	2.1753	1.9174	1.7165	1.5686	1.5037	1.5095	1.5916	1.7519	1.9738
11000	1.7238	1.5746	1.5047	1.5131	1.5928	1.7383	1.9508	2.2337	2.5952	3.0489
12000	1.5074	1.5387	1.6371	1.8004	2.0301	2.3310	2.7127	3.1873	3.7666	4.4610
13000	1.6264	1.7842	2.0061	2.2980	2.6679	3.1243	3.6804	4.3416	5.1105	5.9719
14000	1.8731	2.1350	2.4749	2.9041	3.4091	4.0201	4.7191	5.4984	6.3197	7.1283
15000	2.2723	2.6345	3.0780	3.6043	4.2202	4.9027	5.6344	6.3837	7.0018	7.4503

Table A-4

NAWEPs Report 1488 (Vol. 5, Secs. 13 and 14)

Table A-4 (cont'd)

 $\log \rho/\rho_0$

T°K	-2.4	-2.6	-2.8	-3.0	-3.2	-3.4	-3.6	-3.8	-4.0	-4.2
2000	5.1047	5.2356	5.4540	5.7183	5.9827	6.3863	6.7432	7.1543	7.5017	7.7183
2200	6.1806	6.5509	6.9644	7.4418	7.9760	8.4855	9.0270	9.5280	1.0151	1.1175
2400	8.0665	8.8515	9.8141	1.0986	1.2395	1.4040	1.5944	1.8057	2.0300	2.2546
2600	1.1383	1.2778	1.4407	1.6215	1.8135	2.0072	2.1846	2.3232	2.4020	2.4036
2800	1.5353	1.7032	1.8667	2.0065	2.1044	2.1426	2.1035	1.9887	1.8082	1.5826
3000	1.7971	1.8838	1.9139	1.8772	1.7741	1.6117	1.4136	1.2065	1.0140	0.85320
3200	1.7134	1.6432	1.5176	1.3540	1.1763	1.0062	0.86197	0.75034	0.67362	0.62575
3400	1.3459	1.1983	1.0470	0.9062	0.7935	0.71785	0.6435	0.63636	0.62589	0.63057
3600	9.8934	8.7487	7.8240	7.1990	6.8107	6.6256	6.6533	6.8282	7.1579	7.6477
3800	7.8884	7.3585	7.0590	6.9872	7.0805	7.3818	7.8510	8.5002	9.3788	1.0498
4000	7.3128	7.2912	7.4897	7.8512	8.4332	9.2470	1.0287	1.1629	1.3340	1.5490
4200	7.8705	8.2951	8.9312	9.8078	1.0978	1.2472	1.4374	1.6765	1.9752	2.3450
4400	9.2550	1.0165	1.1392	1.2975	1.4968	1.7481	2.0609	2.4478	2.9203	3.4957
4600	1.1523	1.3095	1.5102	1.7603	2.0743	2.4598	2.9290	3.4987	4.1769	4.9711
4800	1.4813	1.7312	2.0251	2.3936	2.8524	3.3946	4.0429	4.7972	5.6610	6.5831
5000	1.9241	2.2597	2.6876	3.2017	3.7969	4.5014	5.3003	6.1613	7.0170	7.8070
5500	3.2499	3.8194	4.6092	5.5631	6.5763	7.4642	7.9858	7.9815	7.4167	6.4341
6000	5.1952	5.7106	6.0945	6.2464	6.1229	5.7229	5.0954	4.3300	3.5221	2.7643
6500	5.5345	5.3902	4.9944	4.4023	3.7050	2.9989	2.3660	1.8586	1.4955	1.2691
7000	4.1233	3.5199	2.8925	2.3241	1.8674	1.5414	1.3405	1.2420	1.2253	1.2714
7500	2.4772	2.0200	1.6763	1.4520	1.3315	1.2970	1.3317	1.4220	1.5684	1.7711
8000	1.6248	1.4499	1.3697	1.3664	1.4294	1.5520	1.7302	1.9735	2.2874	2.6872
8500	1.4128	1.4222	1.4967	1.6330	1.8309	2.0938	2.4341	2.8656	3.4043	4.0717
9000	1.5287	1.6637	1.8622	2.1276	2.4716	2.9051	3.4494	4.1214	4.9446	5.9443
9500	1.8058	2.0606	2.4055	2.8290	3.3537	4.0067	4.7919	5.7603	6.8936	8.2293
10000	2.2822	2.6691	3.1452	3.7458	4.4733	5.3508	6.4016	7.6065	8.9789	1.0444
11000	3.6065	4.2878	5.1014	6.0560	7.1447	8.3372	9.5679	1.0728	1.1674	1.2232
12000	5.2792	6.2135	7.2408	8.3075	9.3214	1.0158	1.0665	2.10716	2.10242	2.92826
13000	6.8971	7.8200	8.6480	9.2503	9.4972	9.2996	8.6401	7.6149	6.3719	5.1116
14000	7.3217	8.2881	8.3948	8.0645	7.3056	6.2680	5.1957	4.3159	3.7316	3.3999
15000	7.6058	7.3793	6.7884	5.9269	4.9943	4.1792	3.5427	3.0593	2.6441	2.1605

Table A-4 (cont'd)

 $\log \rho/\rho_0$

T°K	-4.4	-4.6	-4.8	-5.0	-5.2	-5.4	-5.6
2000	7.6967 0	7.4901 0	7.2491 0	7.3406 0	8.4323 0	1.0994 1	1.5397 1
2200	1.3020 1	1.6044 1	2.0299 1	2.5509 1	3.0789 1	3.5202 1	3.7812 1
2400	2.4538 1	2.6177 1	2.7112 1	2.7217 1	2.6406 1	2.4738 1	2.2360 1
2600	2.3179 1	2.1528 1	1.9260 1	1.6606 1	1.3872 1	1.1317 1	9.1536 0
2800	1.3427 1	1.1149 1	9.1982 0	7.6563 0	6.5723 0	5.8829 0	5.4739 0
3000	7.3226 0	6.4829 0	5.9573 0	5.6683 0	5.5586 0	5.5449 0	5.6204 0
3200	5.9937 0	5.9134 0	5.9427 0	6.0976 0	6.3395 0	6.6879 0	7.1827 0
3400	6.4969 0	6.8081 0	7.2532 0	7.8542 0	8.6326 0	9.6298 0	1.0899 1
3600	8.3136 0	9.1701 0	1.0287 1	1.1702 1	1.3474 1	1.5715 1	1.8501 1
3800	1.1940 1	1.3750 1	1.6029 1	1.8866 1	2.2410 1	2.6810 1	3.2205 1
4000	1.8183 1	2.1545 1	2.5692 1	3.0796 1	3.7041 1	4.4561 1	5.3523 1
4200	2.7992 1	3.3566 1	4.0296 1	4.8311 1	5.7682 1	6.8330 1	7.9951 1
4400	4.1856 1	4.9963 1	5.9299 1	6.9668 1	8.0623 1	9.1313 1	1.0051 2
4600	5.8714 1	6.8529 1	7.8607 1	8.8082 1	9.5623 1	9.9747 1	9.9196 1
4800	7.5202 1	8.3836 1	9.0300 1	9.3084 1	9.0841 1	8.3142 1	7.0983 1
5000	8.3966 1	8.6423 1	8.4416 1	7.7403 1	6.6567 1	5.4174 1	4.3006 1
5500	5.2475 1	4.0864 1	3.0978 1	2.3311 1	1.7864 1	1.4257 1	1.1980 1
6000	2.1211 1	1.6290 1	1.2925 1	1.0966 1	1.0117 1	1.0066 1	1.0592 1
6500	1.1552 1	1.1262 1	1.1615 1	1.2476 1	1.3792 1	1.5573 1	1.7894 1
7000	1.3708 1	1.5207 1	1.7241 1	1.9879 1	2.3244 1	2.7500 1	3.2824 1
7500	2.0383 1	2.3778 1	2.8085 1	3.3490 1	4.0212 1	4.8535 1	5.8781 1
8000	3.1870 1	3.8120 1	4.5865 1	5.5362 1	6.6933 1	8.0838 1	9.7263 1
8500	4.8953 1	5.9011 1	7.1108 1	8.5442 1	1.0202 2	1.2058 2	1.4028 2
9000	7.1399 1	8.5384 1	1.0131 2	1.1868 2	1.3655 2	1.5325 2	1.6647 2
9500	9.7233 1	1.1347 2	1.2973 2	1.4433 2	1.5514 2	1.5925 2	1.5473 2
10000	1.1918 2	1.3230 2	1.4185 2	1.4550 2	1.4095 2	1.2864 2	1.1013 2
11000	1.2269 2	1.1723 2	1.0645 2	9.1854 1	7.5525 1	5.9366 1	4.4933 1
12000	7.9918 1	6.5478 1	5.1457 1	3.9276 1	2.9657 1	2.2706 1	1.8053 1
13000	3.9786 1	3.0580 1	2.3777 1	1.9102 1	1.6060 1	1.4156 1	1.3028 1
14000	3.1157 1	2.7242 1	2.1863 1	1.6156 1	1.1406 1	8.4700 0	7.4402 0
15000	1.7125 1	1.3453 1	1.1184 1	1.0281 1	1.0582 1	1.1800 1	1.3715 2

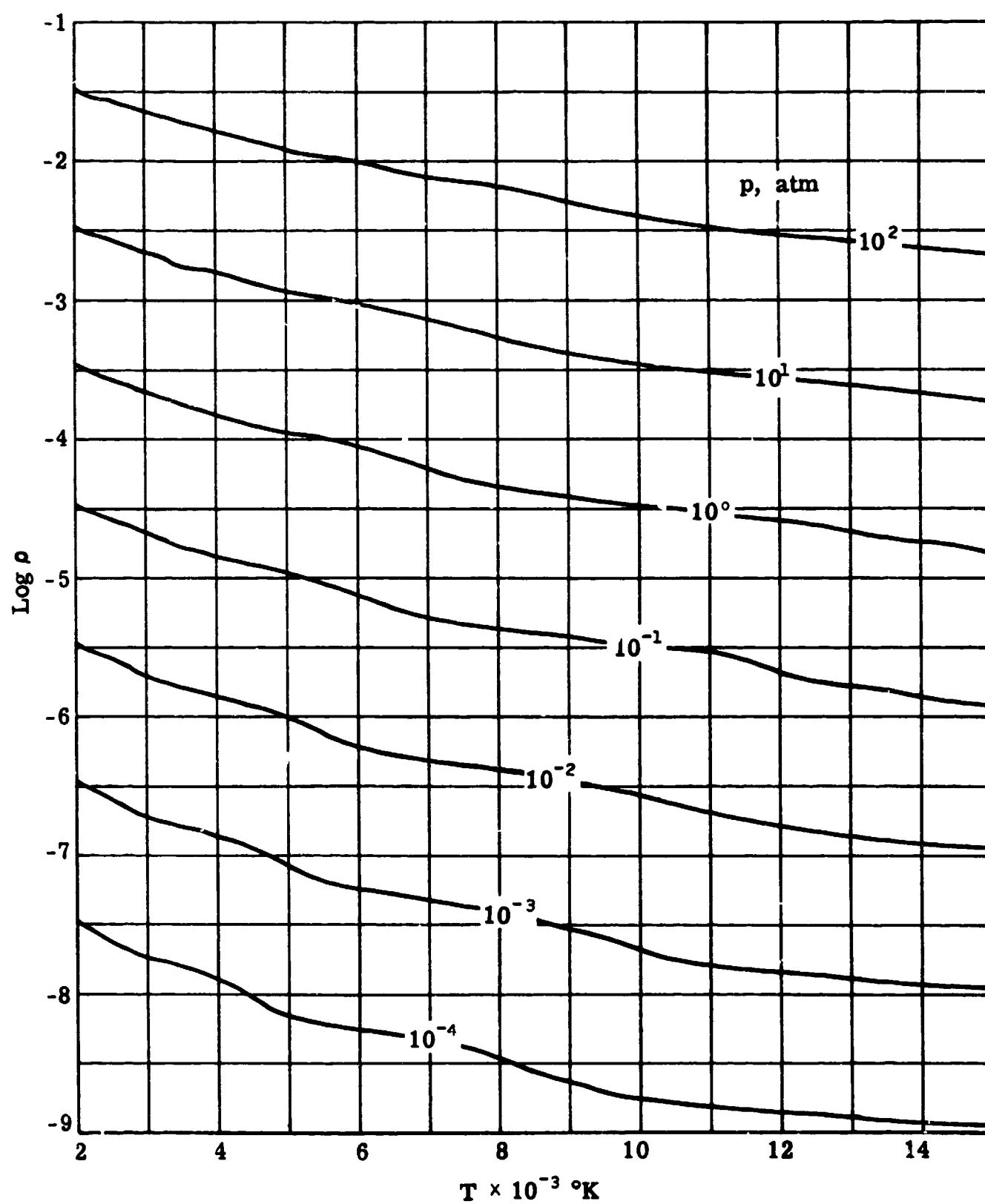


Fig. A-1. $\text{Log } \rho$ as a function of T ; p (atm) = 10^2 , 10^1 , 10^0 , 10^{-1} , 10^{-2} , 10^{-3} , and 10^{-4} ; cross-plot of data from Ref. 187.

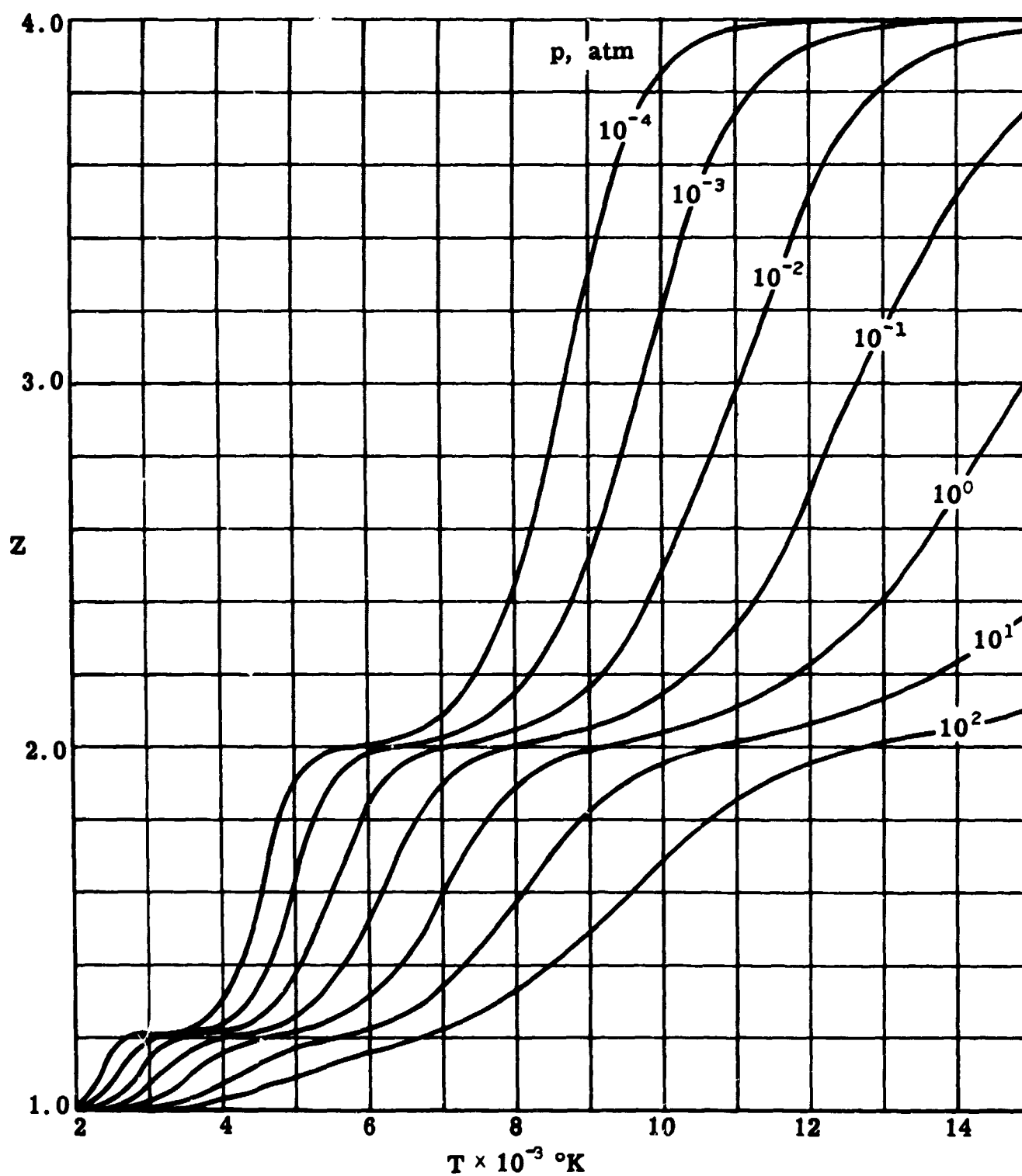


Fig. A-2. Z as a function of T ; p (atm) = 10^2 , 10^1 , 10^0 , 10^{-1} , 10^{-2} , 10^{-3} , and 10^{-4} ; cross-plot of data from Ref. 187.

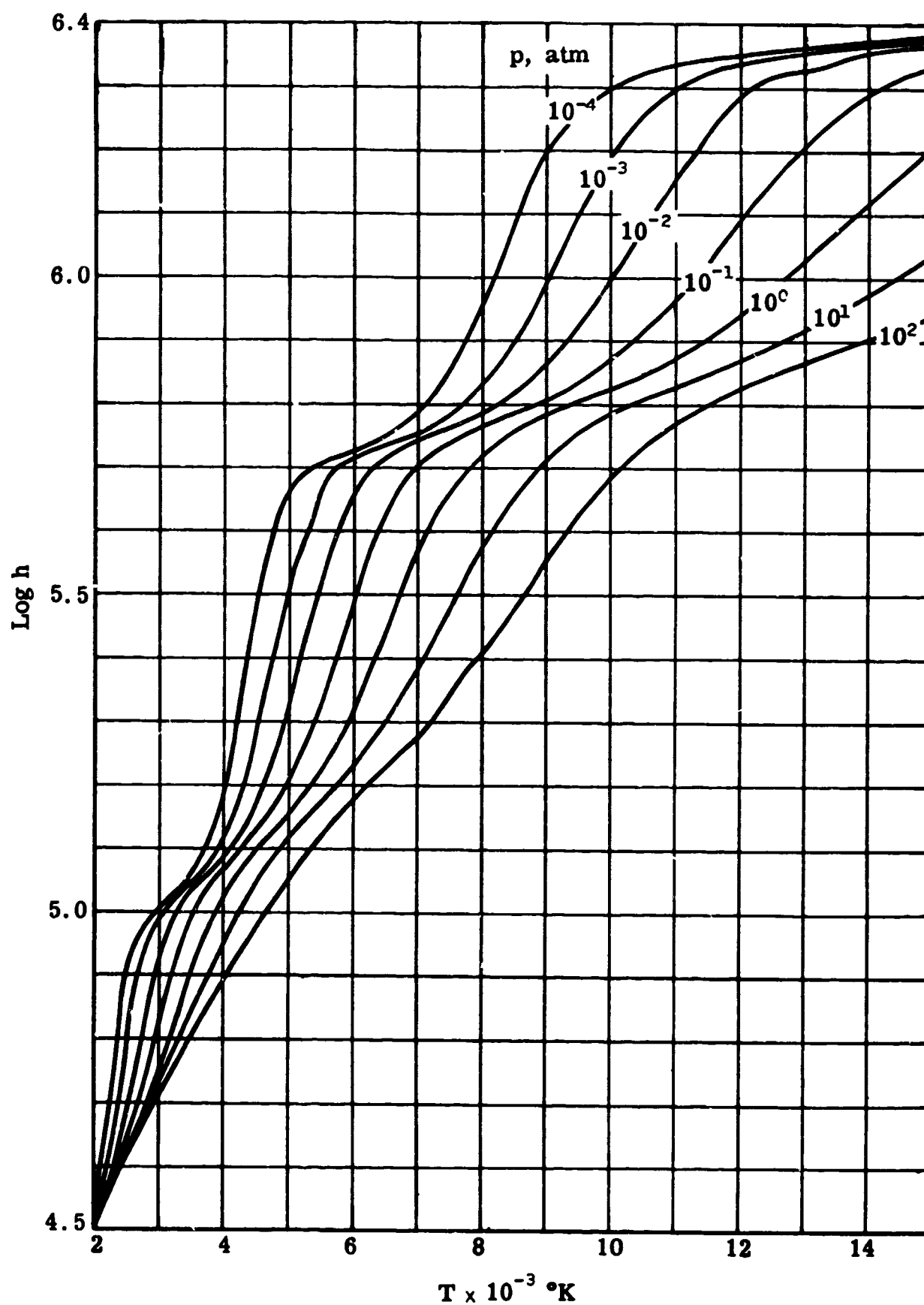


Fig. A-3. $\text{Log } h$ as a function of T ; p (atm) = 10^2 , 10^1 , 10^0 , 10^{-1} , 10^{-2} , 10^{-3} , and 10^{-4} ; cross-plot of data from Ref. 187.

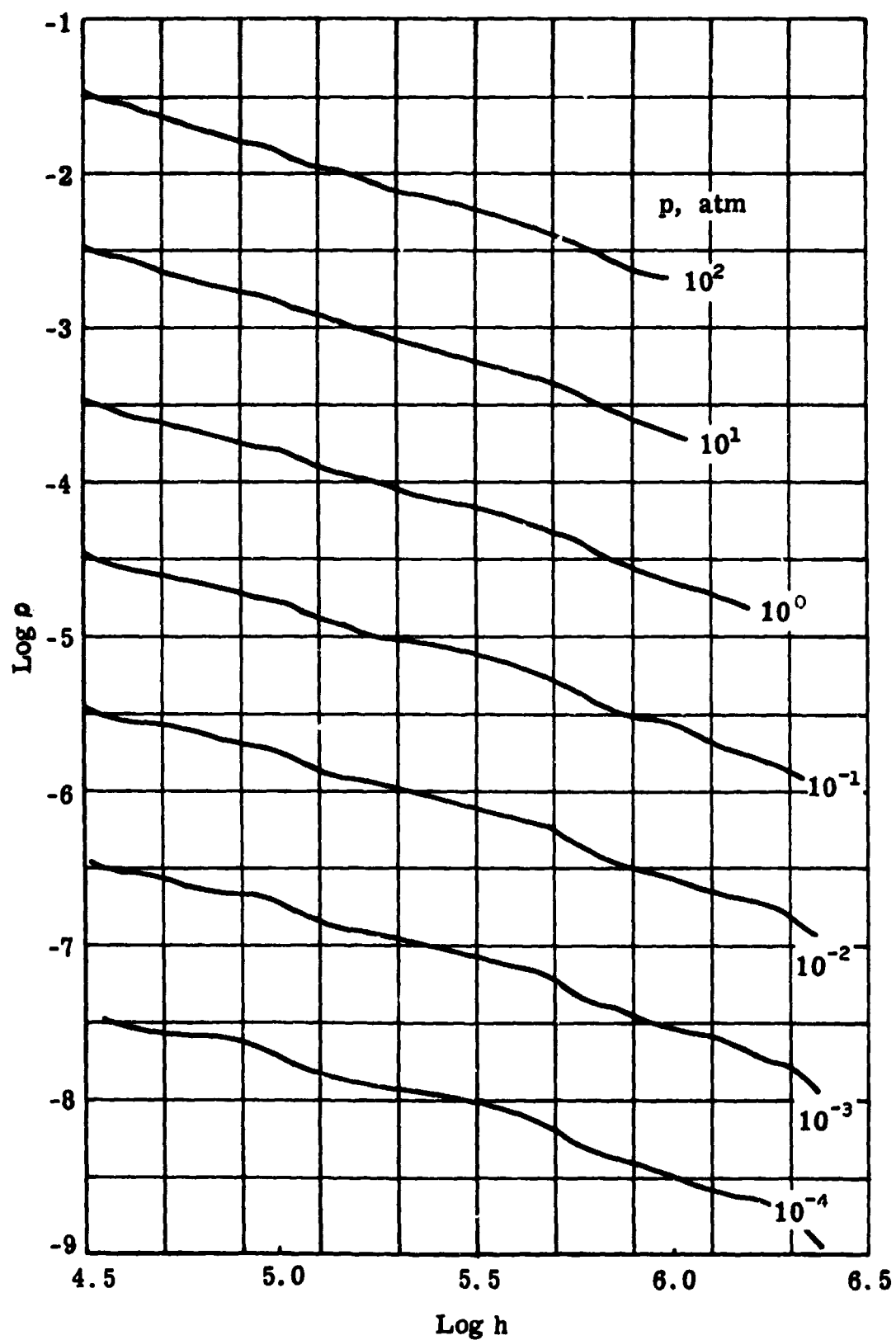


Fig. A-4. Log ρ as a function of log h ; p (atm) = 10^2 , 10^1 , 10^0 , 10^{-1} , 10^{-2} , 10^{-3} , and 10^{-4} ; cross-plot of data from Ref. 187.

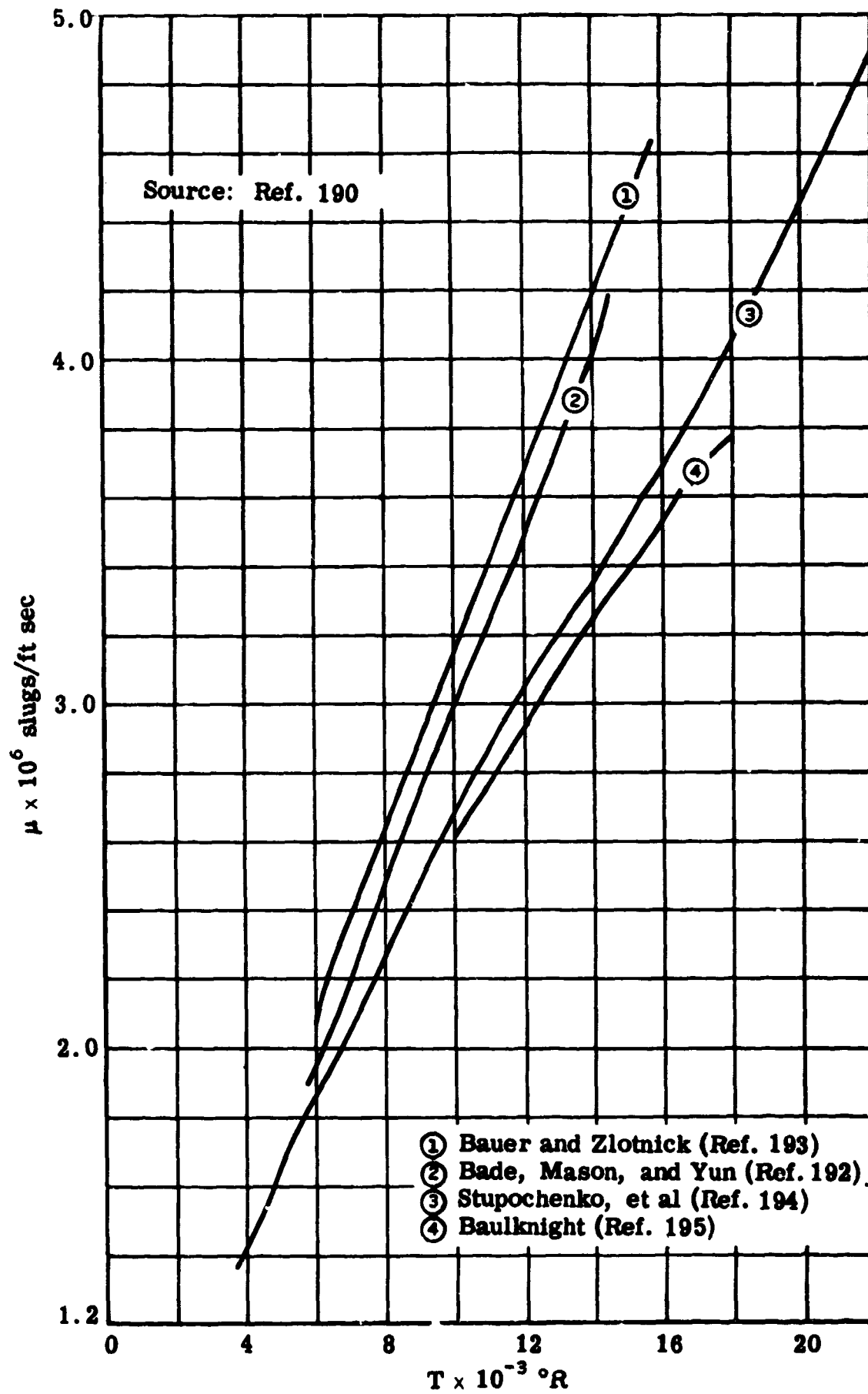
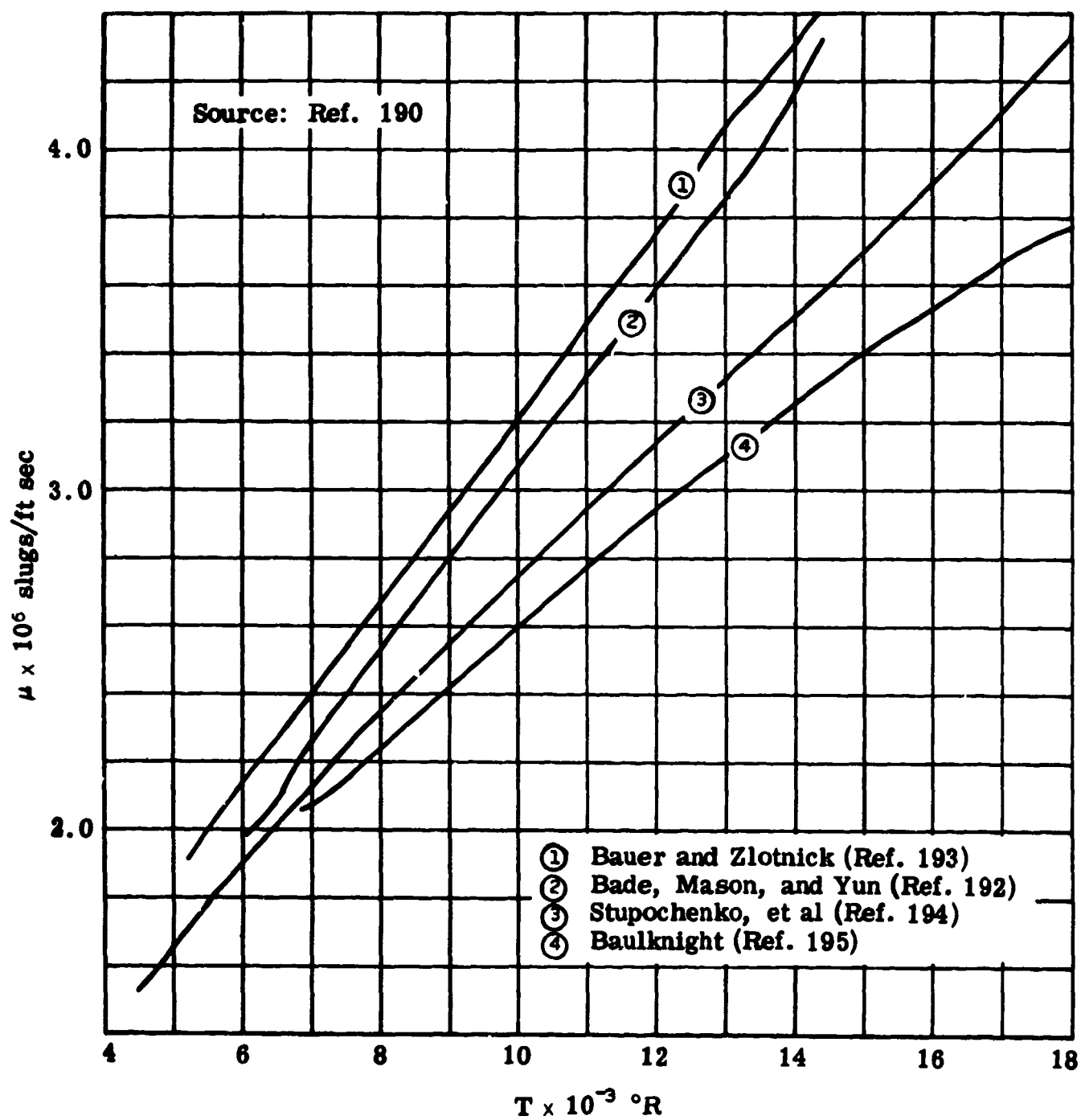


Fig. A-5. Coefficient of viscosity of air; $\rho/\rho_0 = 10^{+1}$.

Fig. A-6. Coefficient of viscosity of air; $\rho/\rho_0 = 1$.

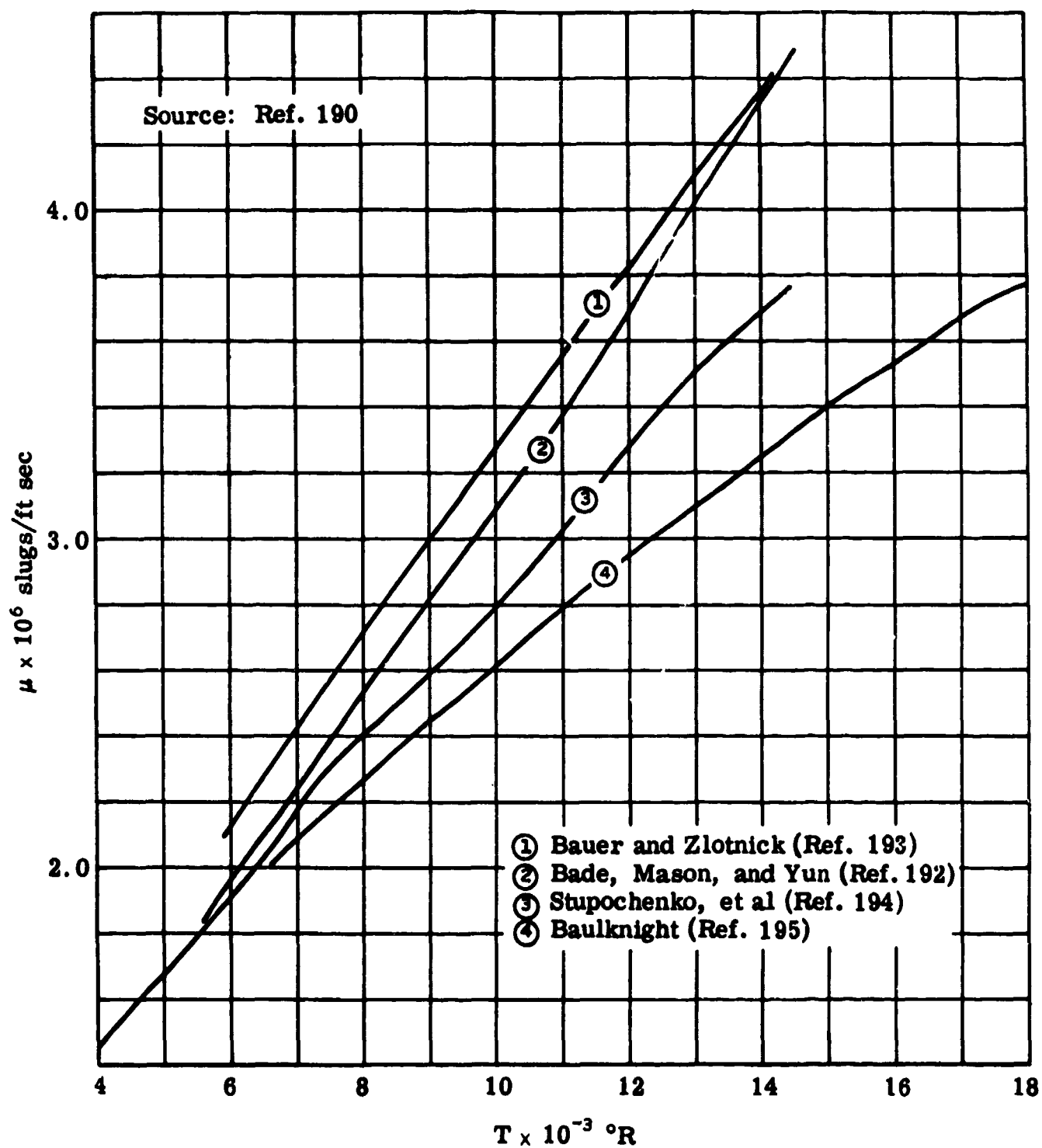


Fig. A-7. Coefficient of viscosity of air; $\rho/\rho_0 = 10^{-1}$.

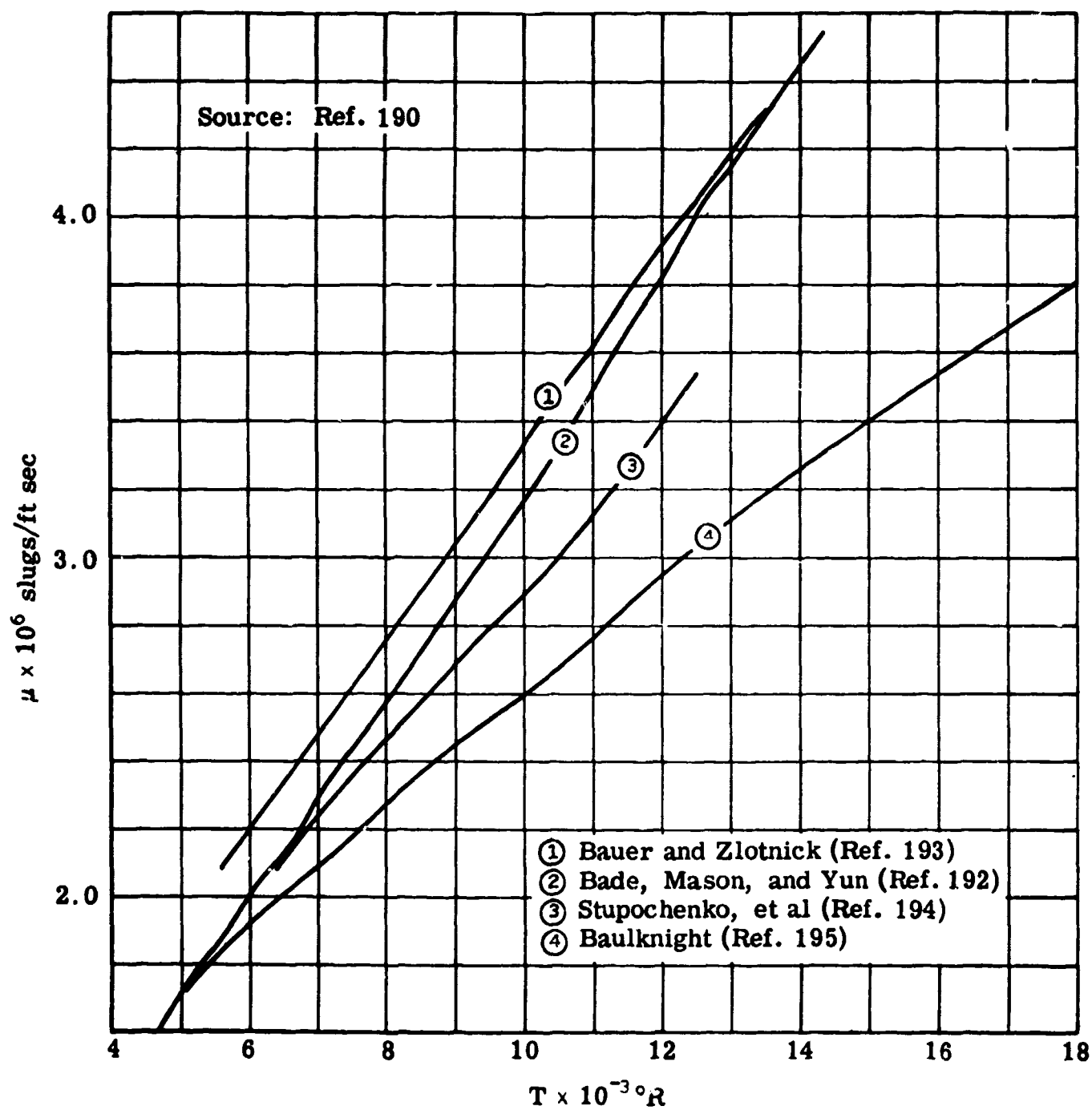


Fig. A-8. Coefficient of viscosity of air; $\rho/\rho_0 = 10^{-2}$.

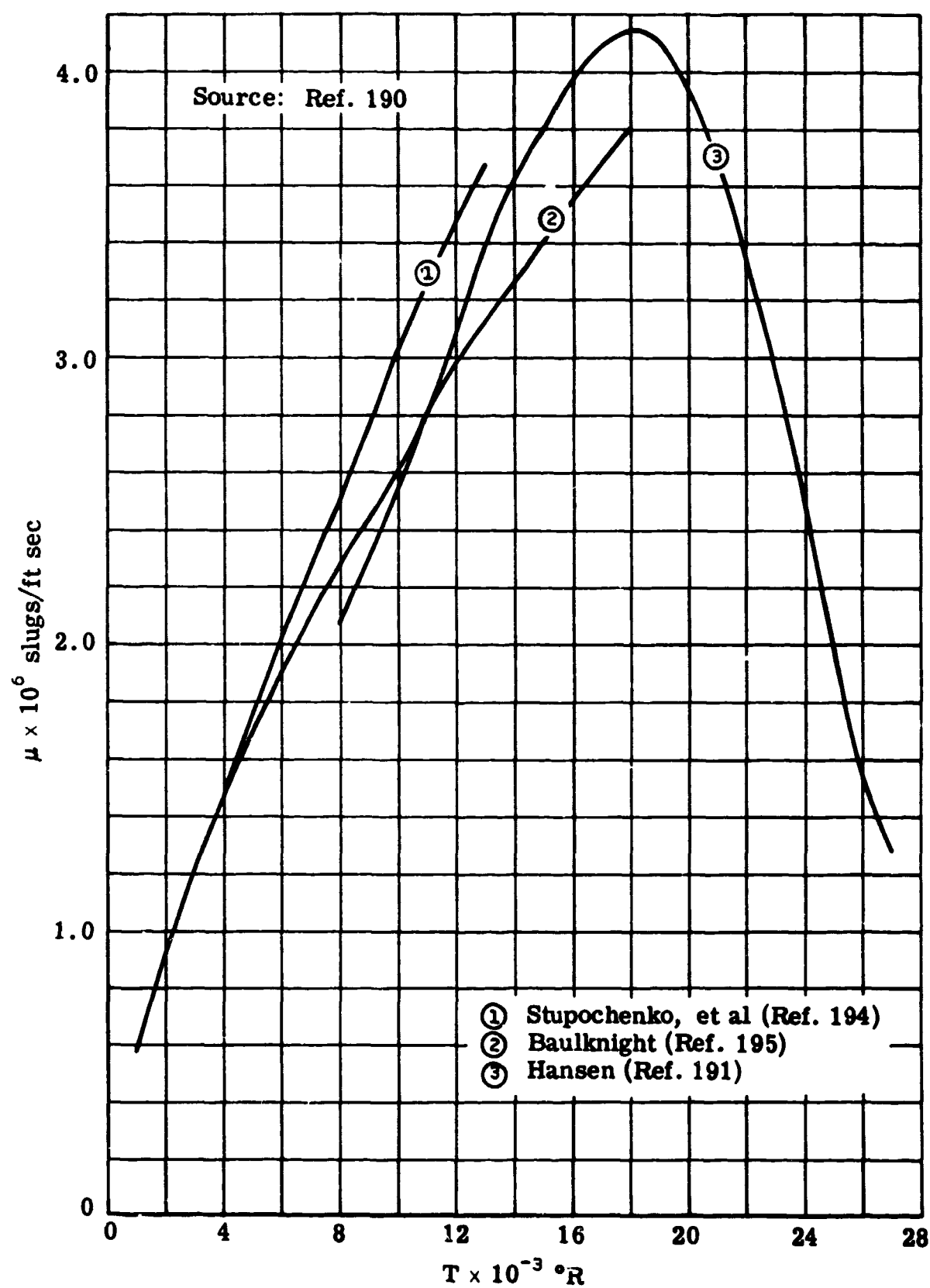


Fig. A-9. Coefficient of viscosity of air; $\rho/\rho_0 = 10^{-3}$.

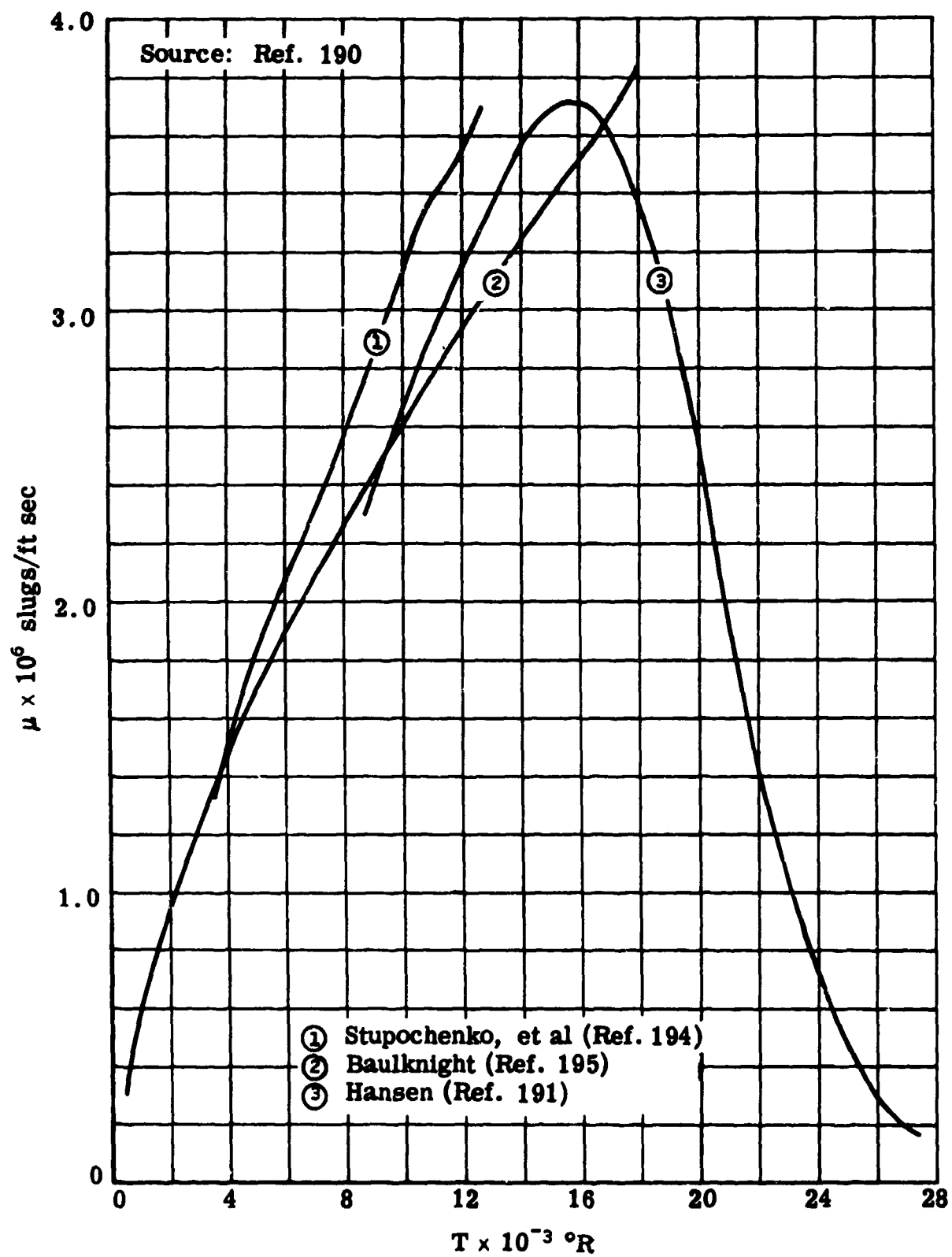


Fig. A-10. Coefficient of viscosity of air; $\rho/\rho_0 = 10^{-4}$.

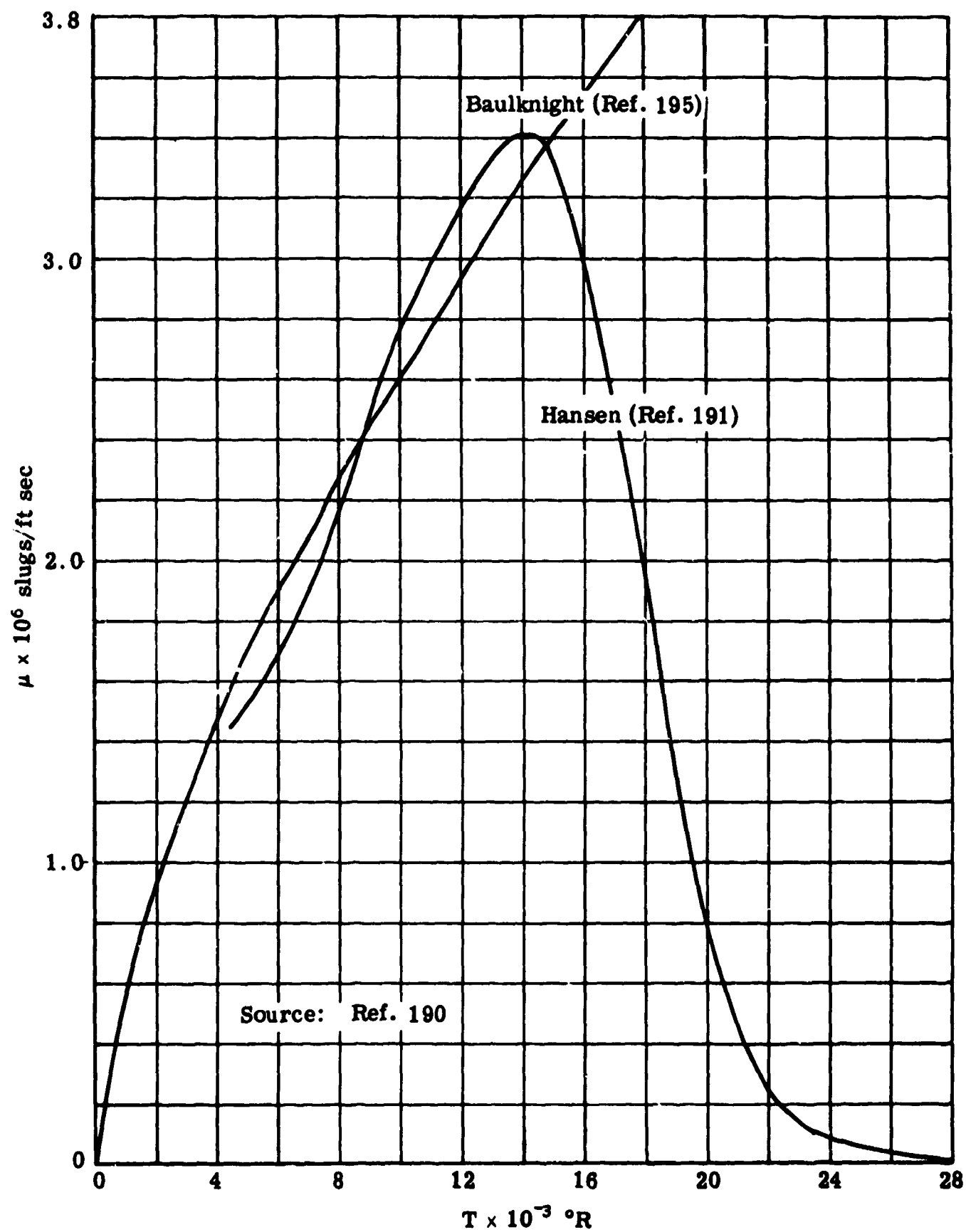
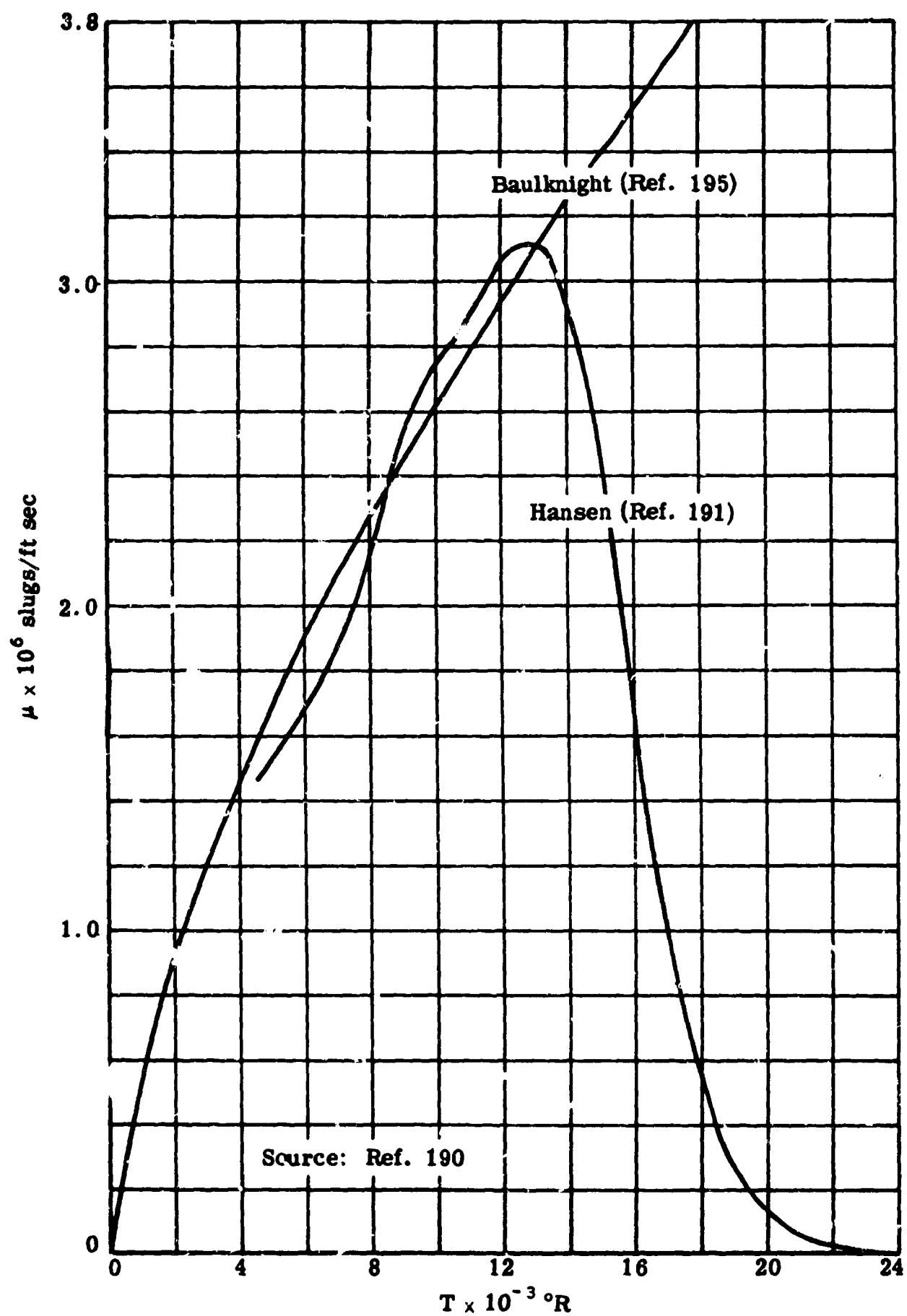


Fig. A-11. Coefficient of viscosity of air; $\rho/\rho_0 = 10^{-5}$.

Fig. A-12. Coefficient of viscosity of air; $\rho/\rho_0 = 10^{-6}$.

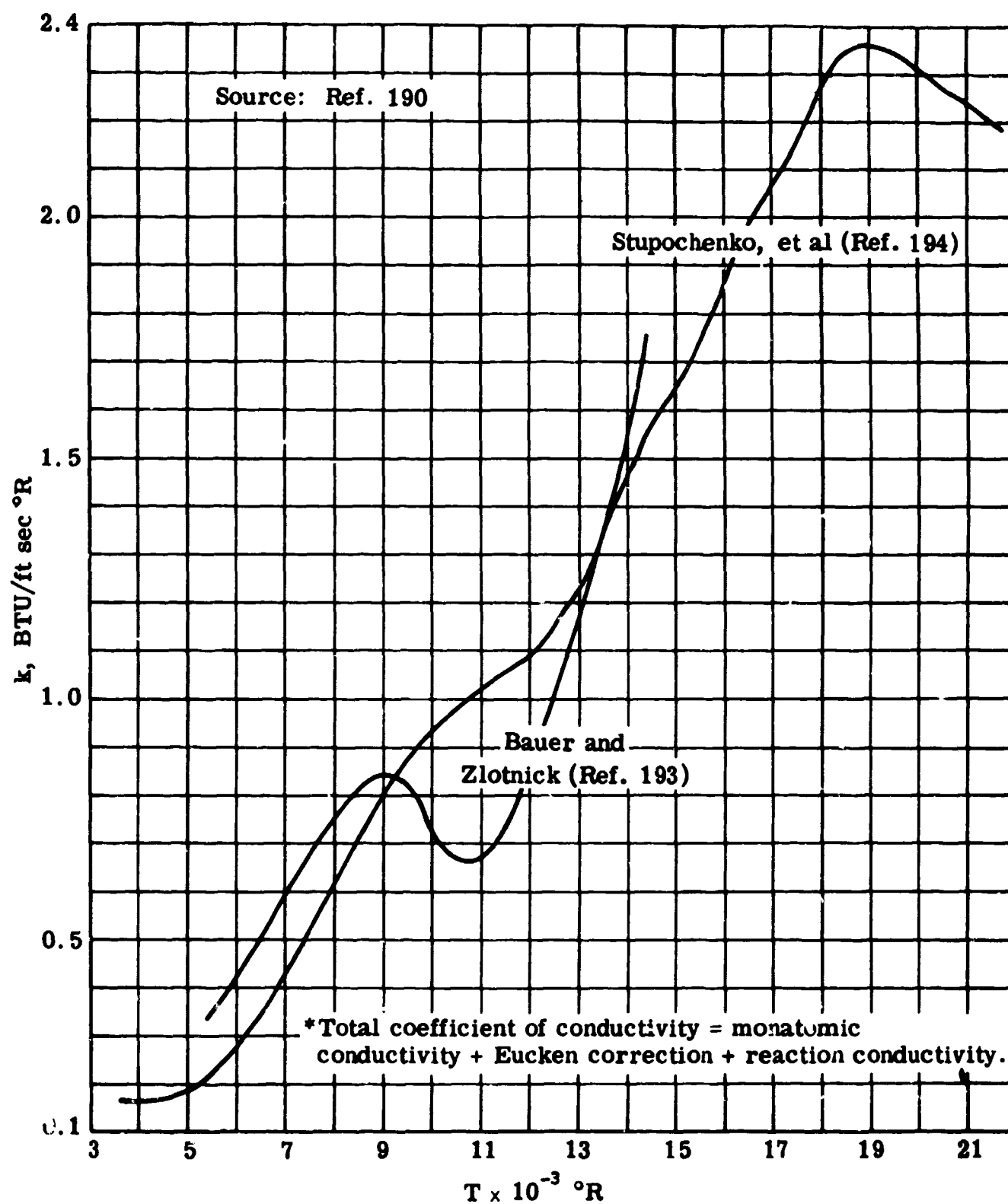


Fig. A-13. Total* coefficient of thermal conductivity of air; $\rho/\rho_0 = 10^{+1}$.

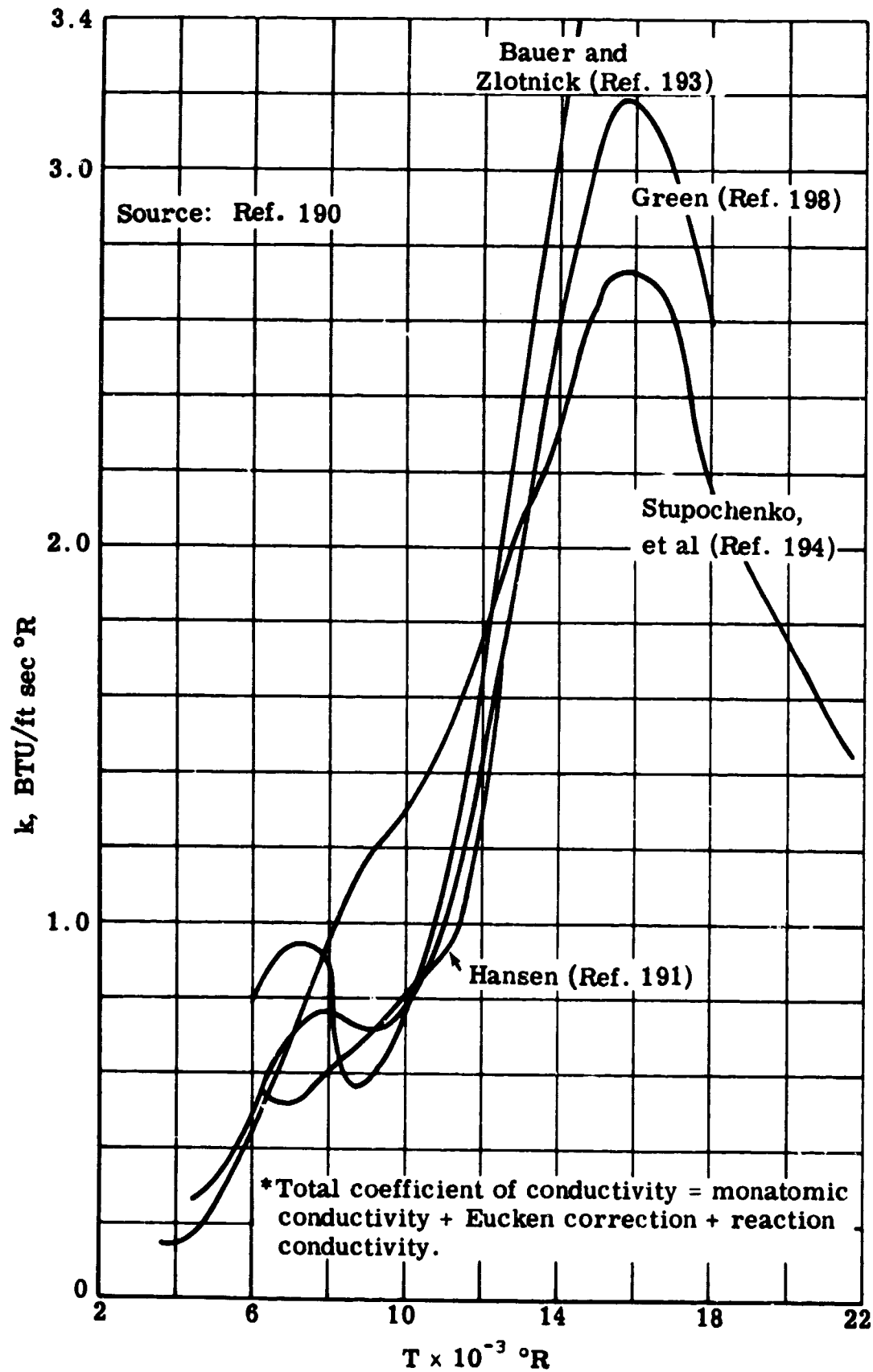


Fig. A-14. Total* coefficient of thermal conductivity of air; $\rho/\rho_0 = 10^{\circ}$.

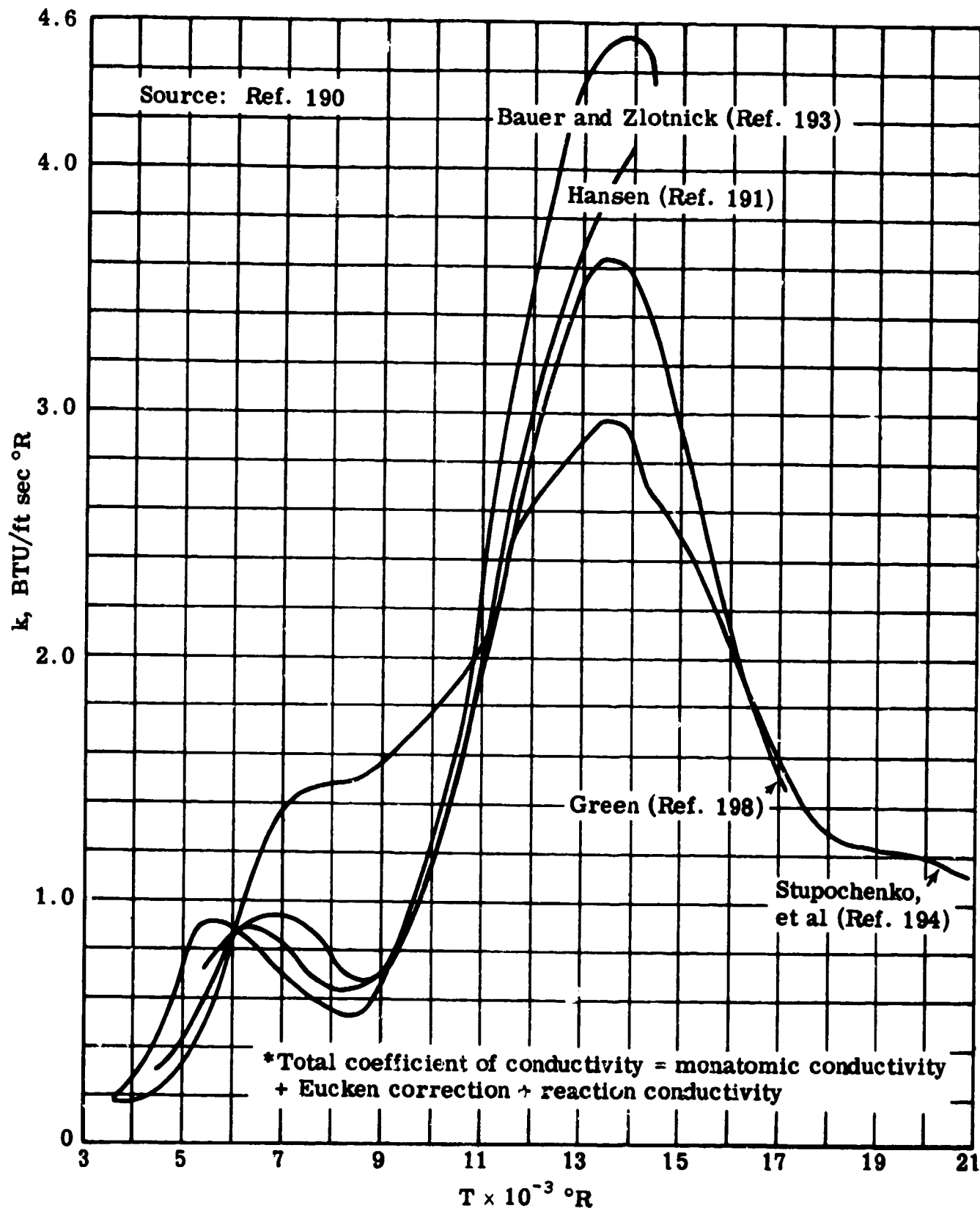


Fig. A-15. Total* coefficient of thermal conductivity of air; $\rho/\rho_0 = 10^{-1}$

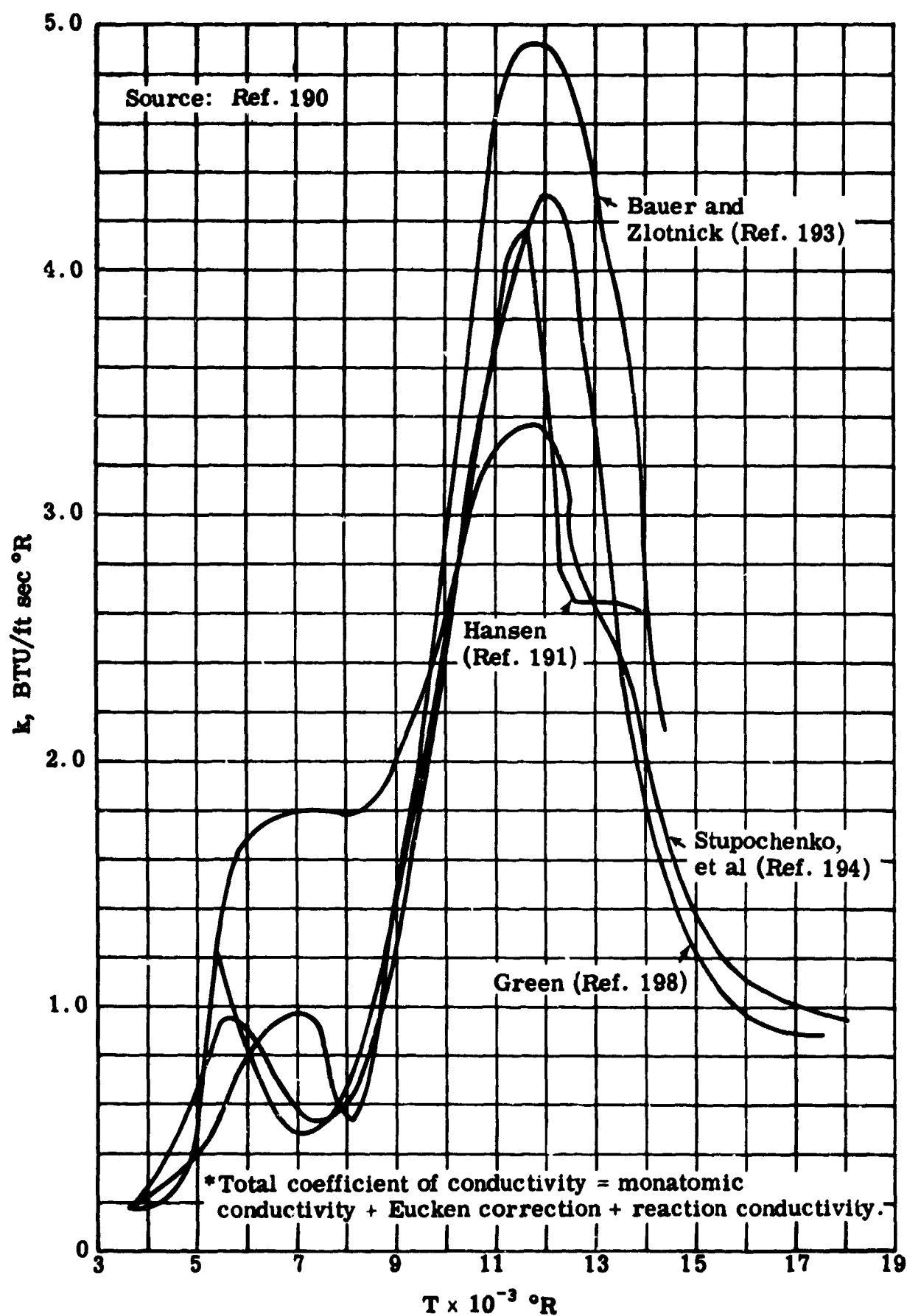


Fig. A-16. Total* coefficient of thermal conductivity of air; $\rho/\rho_0 = 10^{-2}$.

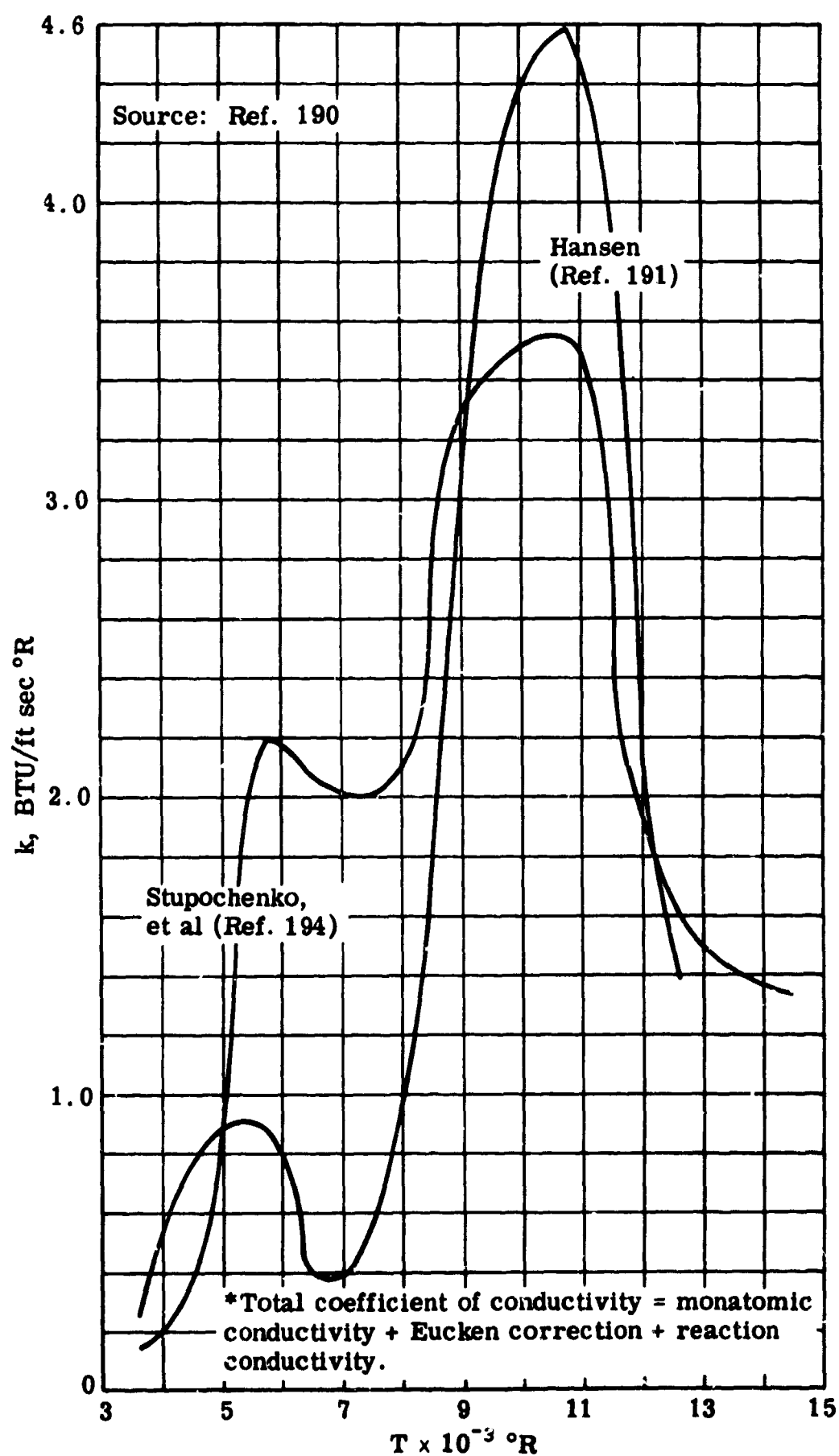


Fig. A-17. Total* coefficient of thermal conductivity of air;
 $\rho/\rho_0 = 10^{-3}$.

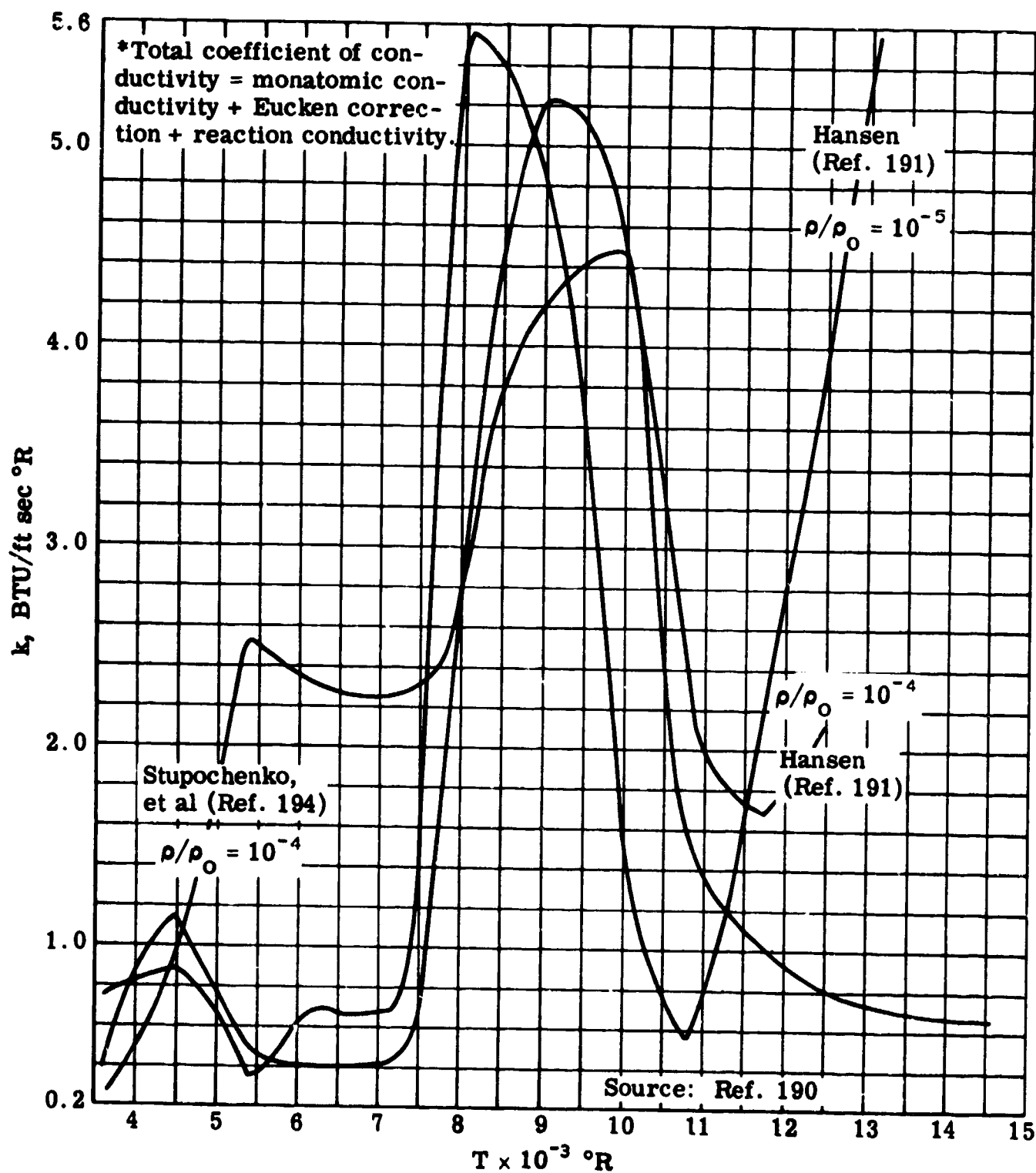


Fig. A-18. Total* coefficient of thermal conductivity of air;
 $\rho/\rho_0 = 10^{-4}$ and 10^{-5} .

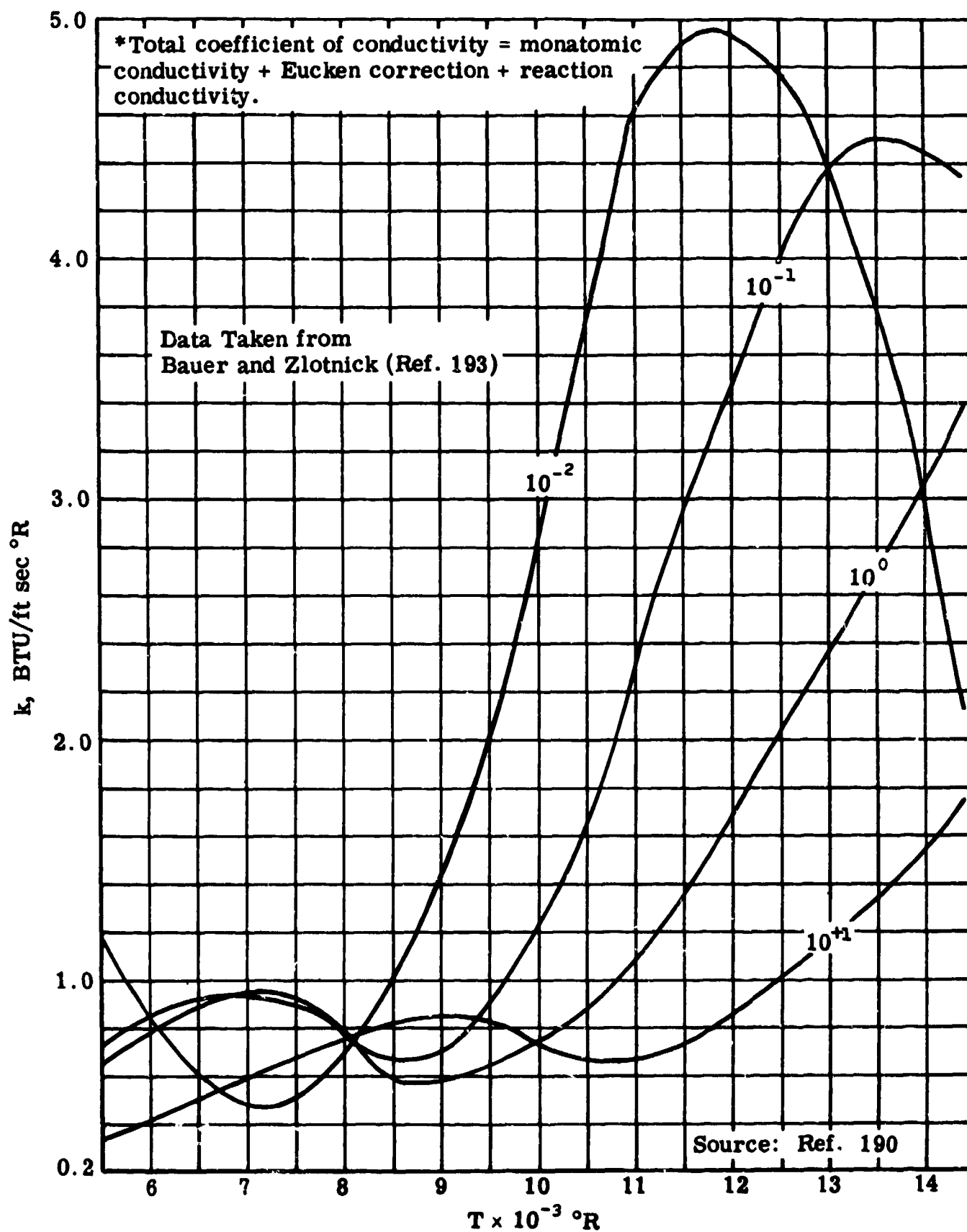


Fig. A-19. Total* coefficient of thermal conductivity of air;
 $\rho/\rho_0 = 10^{+1}, 10^0, 10^{-1}, \text{ and } 10^{-2}$.

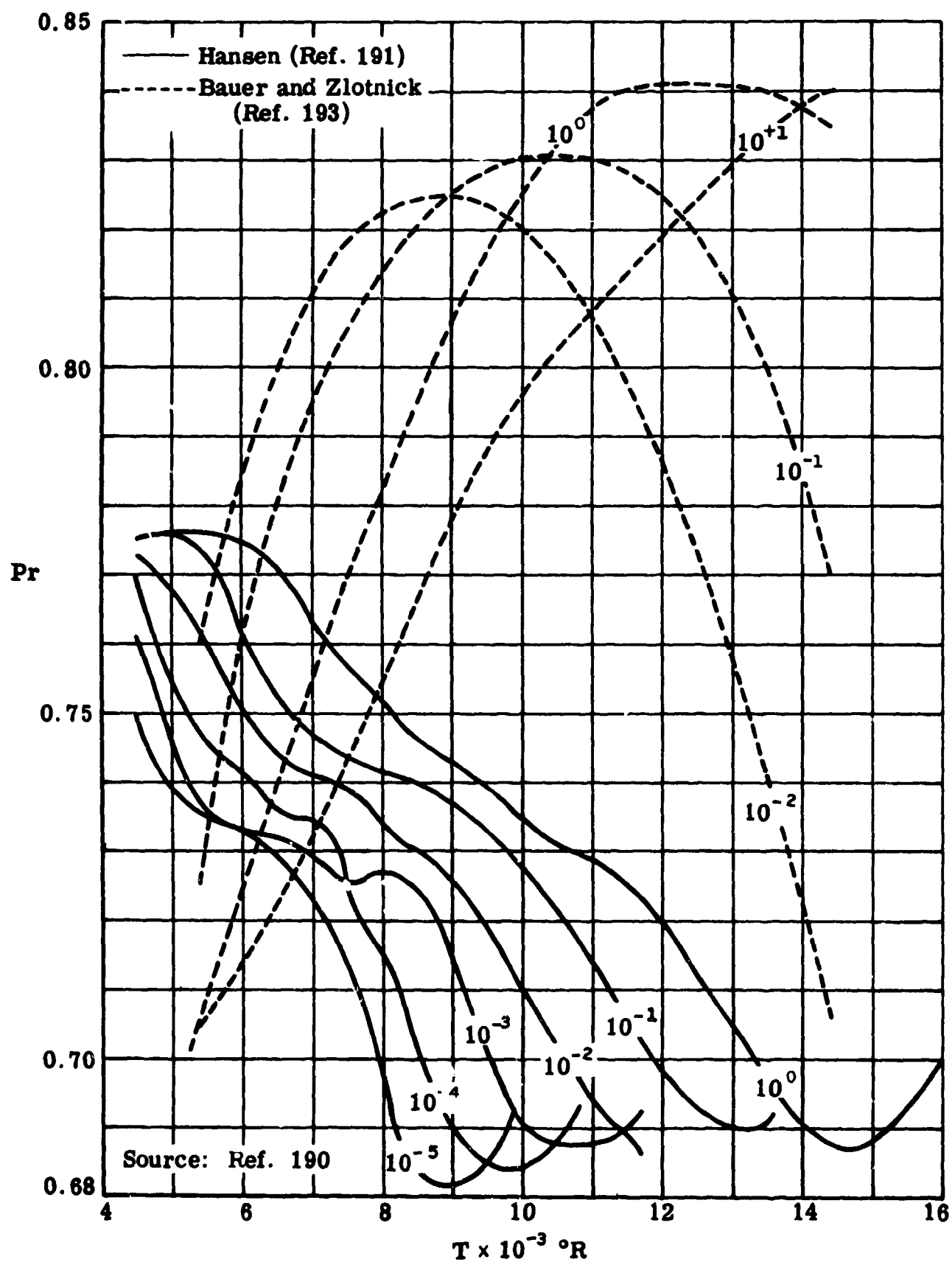


Fig. A-20. Prandtl number of air; effects of chemical reaction not included; $\rho/\rho_0 = 10^{+1}$, 10^0 , 10^{-1} , 10^{-2} , 10^{-3} , 10^{-4} , and 10^{-5} .

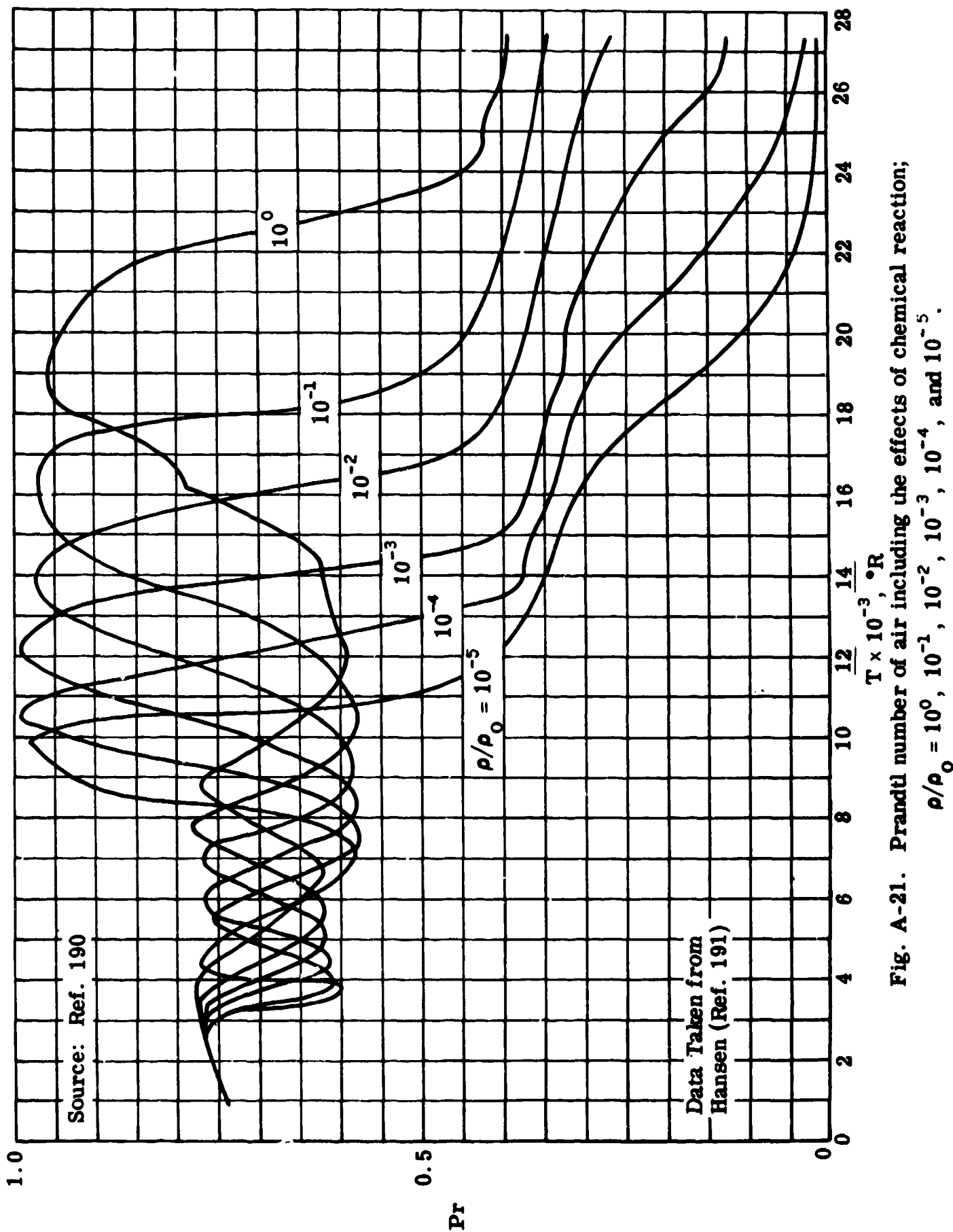


Fig. A-21. Prandtl number of air including the effects of chemical reaction;
 $\rho/\rho_0 = 10^0, 10^{-1}, 10^{-2}, 10^{-3}, 10^{-4},$ and 10^{-5} .

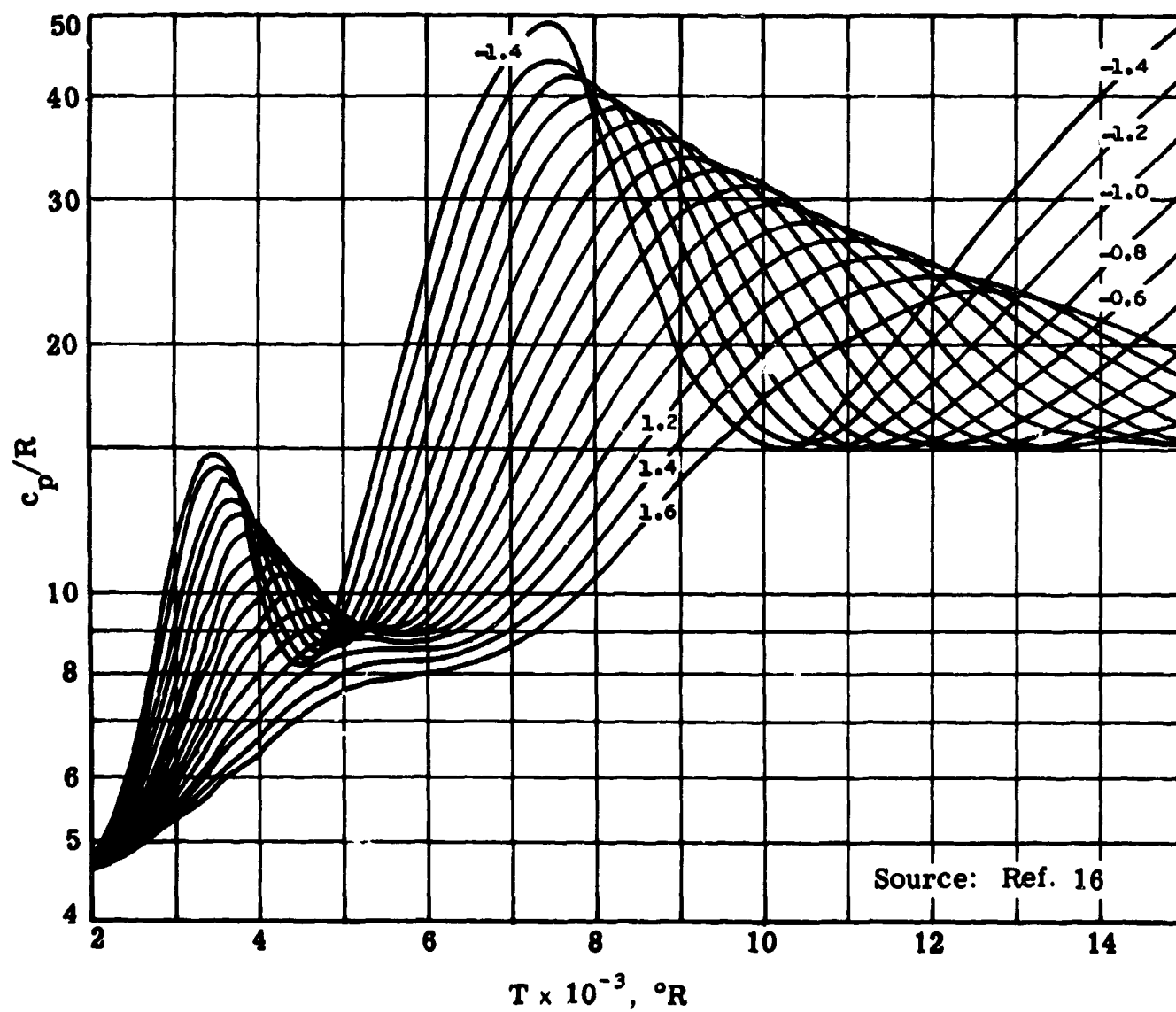


Fig. A-22. c_p/R as a function of $T^{\circ}R$ and $\log p/p_0$; $\log p/p_0 = -1.4$ to $+1.6$; $\Delta \log p/p_0 = +0.2$.

REFERENCES

1. Schlichting, H. Boundary Layer Theory. New York: McGraw-Hill Book Co., Inc., 1955.
2. Howarth, L. Modern Developments in Fluid Dynamics - High Speed Flow, Vol. I. London: Oxford University Press, 1953.
3. Mangler, W. Compressible Boundary Layers on Bodies of Revolution. British ARC Report 9740, 1946.
4. Crocco, L. The Laminar Boundary Layer in Gases. APL/NAA/CF-1038, North American Aviation, Inc., July 1948.
5. Shapiro, A. H. The Dynamics and Thermodynamics of Compressible Fluid Flow (Vol. I and II). New York: The Ronald Press Company, 1954.
6. Stewartson, K. "Correlated Incompressible and Compressible Boundary Layers," Proc. Roy. Soc., Ser. A, Vol. 200, No. A1060 (June 1949), pp. 84-100.
7. Cohen, C. B. and Reshotko, E. The Compressible Laminar Boundary Layer with Heat Transfer and Arbitrary Pressure Gradient, NACA Report 1294, 1956.
8. Blasius, H. The Boundary Layers in Fluids with Little Friction. NACA TM 1256, February 1950. (Translation of "Grenzschichten in Flüssigkeiten mit kleiner Reibung" Zeitschrift für Mathematik und Physik, Band 56, Heft 1, 1908, pp. 1-37.)
9. Van Driest, E. R. Investigation of Laminar Boundary Layer in Compressible Fluids Using the Crocco Method. NACA TN 2597, January 1952.
10. Rubesin, M. W. and Johnson, H. A. "A Critical Review of Skin-Friction and Heat-Transfer Solutions of the Laminar Boundary Layer of a Flat Plate," Trans. ASME (May 1949), pp. 383-388.
11. Monaghan, R. J. On the Behavior of Boundary Layers at Supersonic Speeds. Proceedings of the Fifth International Aeronautical Conference, June 1955, p. 286.
12. Wilson, R. E. "Real-Gas Laminar-Boundary-Layer Skin Friction and Heat Transfer," J. Aerospace Sci., Vol. 29, No. 6 (June 1962), pp. 640-647.
13. Wilson, R. E. "Laminar Boundary Layer Growth on Slightly Blunted Cones at Hypersonic Speeds," J. Spacecraft, Vol. 2, No. 4 (1965), pp. 490-496.
14. Romig, M. F. and Dore, F. J. Solutions of the Compressible Laminar Boundary Layer Including the Case of a Dissociated Free Stream. Report No. ZA-7-012, Convair, August 1954.

15. Hilsenrath, J. and Beckett, C. W. Tables of Thermodynamic Properties of Argon-Free Air to 15,000°K. AEDC-TN-56-12 (ASTIA Document No: AD-98974), September 1956.
16. Hochstim, A. R. Gas Properties Behind Shocks at Hypersonic Velocities. III. Tables of Thermodynamic Properties of Air. Report No. ZPh-004, Convair, August 1958.
17. Hilsenrath, J., et al. Tables of Thermal Properties of Gases. NBS Circular 564, November 1955.
18. Feldman, S. Hypersonic Gas Dynamic Charts for Equilibrium Air. Research Report 40, AVCO Research Laboratory, 1957.
19. Durand, W. F. Aerodynamic Theory, Vol. III, 1934.
20. von Kármán, T. Mechanical Similitude and Turbulence. NACA TM 611, 1931.
21. Frankl, F. and Voishel, V. Turbulent Friction in the Boundary Layer of a Flat Plate in a Two-Dimensional Compressible Flow at High Speeds. NACA TM 1053, December 1943.
22. Lin, C. C. and Shen, S. F. Studies of von Kármán's Similarity Theory and its Extension to Compressible Flows. A Similarity Theory for Turbulent Boundary Layer over a Flat Plate in Compressible Flow. NACA TN 2542, November 1951.
23. Li, T. Y. and Nagamatsu, H. T. Effects of Density Fluctuations on the Turbulent Skin Friction of an Insulated Flat Plate at High Supersonic Speeds. GALCIT Memo No. 5, May 1951.
24. Wilson, R. E. "Turbulent Boundary-Layer Characteristics at Supersonic Speeds - Theory and Experiment," J. Aeronaut. Sci., Vol. 17, No. 9 (September 1950), pp. 585-594.
25. Harkness, J. L. The Effect of Heat Transfer on Turbulent Boundary Layer Skin Friction. DRL Report 436, CM-940, Defense Research Laboratory, University of Texas, June 1959.
26. Schoenherr, K. E. "Resistance of Flat Surfaces Moving Through a Fluid," Trans. Soc. Naval Arch. and Marine Eng., Vol. 40 (1932), pp. 279-313.
27. Sommer, S. C. and Short, B. J. Free-Flight Measurements of Turbulent-Boundary-Layer Skin Friction in the Presence of Severe Aerodynamic Heating at Mach Numbers from 2.8 to 7.0. NACA TN 3391, March 1955.
28. Dhawan, S. Direct Measurements of Skin Friction. NACA Report 1121, 1953 (supercedes NACA TN 2567).
29. Smith, D. W. and Walker, J. H. Skin-Friction Measurements in Incompressible Flow. NACA TN 4231, March 1958.
30. von Kármán, T. "Turbulence and Skin Friction," J. Aeronaut. Sci., Vol. 1 (1934), pp. 20-48.

31. Kozlov, L. V. Experimental Study of Surface Friction on a Plane Plate in a Supersonic Flow with Heat Exchange. APL Translation 945, Applied Physics Laboratory, The Johns Hopkins University, February 1964. (Translated from Akad, Nauk SSSR. Izv. OTN. Mekhanika i Mashinostroenie, No. 2, pp. 11-19, March-April 1963.)
32. Coles, D. Measurements in the Boundary Layer on a Smooth Flat Plate in Supersonic Flow. III. Measurements in a Flat-Plate Boundary Layer at the Jet Propulsion Laboratory. ORDCIT Report No. 20-71, Jet Propulsion Laboratory, June 1953.
33. Korkegi, R. H. "Transition Studies and Skin-Friction Measurements on an Insulated Flat Plate at a Mach Number of 5.8," J. Aeronaut. Sci., Vol. 23, No. 2 (February 1956), pp. 97-107.
34. Matting, F. W., et al. Turbulent Skin Friction at High Mach Numbers and Reynolds Numbers in Air and Helium. NASA TR R-82, 1960.
35. Winkler, E. M. and Cha, M. H. Investigation of Flat Plate Hypersonic Turbulent Boundary Layers with Heat Transfer at a Mach Number of 5.2. NAVORD Report 6631, U.S. Naval Ordnance Laboratory, September 1959.
36. Tucker, M. Approximate Turbulent Boundary-Layer Development in Plane Compressible Flow Along Thermally Insulated Surfaces with Application to Supersonic-Tunnel Contour Correction. NACA TN 2045, March 1950.
37. Wilson, R. E. Characteristics of Turbulent Boundary Layer Flow Over a Smooth, Thermally Insulated Flat Plate at Supersonic Speeds. CM-712, DRL Report 301, Defense Research Laboratory, The University of Texas, June 1952.
38. Winter, K. G., Smith, K. G., and Gaudet, L. Measurements of Turbulent Skin Friction at High Reynolds Numbers at Mach Numbers of 0.2 and 2.2. Paper Presented at the AGARD Specialists' Meeting (AGARDograph 97, Part I, pp. 97-123), Naples, Italy, May 1965.
39. Applied Physics Laboratory, The Johns Hopkins University. Handbook of Supersonic Aerodynamics, NAVORD Report 1488, Vol. 5, Sec. 15, "Properties of Gases," August 1953.
40. Monaghan, R. J. and Cooke, J. R. The Measurement of Heat Transfer and Skin Friction at Supersonic Speeds. Part III: Measurements of Overall Heat Transfer and of the Associated Boundary Layers on a Flat Plate at $M = 2.43$. RAE Tech. Note Aero 2129. Royal Aircraft Establishment, Farnborough, Hants, England, December 1951.
41. Lobb, R. K., Winkler, E. M., and Persh, J. NOJ. Hypersonic Tunnel No. 4 Results. VII: Experimental Investigation of Turbulent Boundary Layers in Hypersonic Flow. NAVORD Report 3880, U.S. Naval Ordnance Laboratory, March 1955.
42. Kempf, G. "Hydromechanische Probleme des Schiffsantriebs," Proc. III Intern. Cong. Appl. Mech., Stockholm (1930), pp. 74-82.

43. Persh, J. A Theoretical Investigation of Turbulent Boundary Layer Flow with Heat Transfer at Supersonic and Hypersonic Speeds. NAVORD Report 3854, U.S. Naval Ordnance Laboratory, May 1955.
44. Applied Physics Laboratory, The Johns Hopkins University. Handbook of Supersonic Aerodynamics, NAVORD Report 1488, Vol. 6, Sec. 17, "Ducts, Nozzles and Diffusers," January 1964.
45. Van Driest, E. R. "Turbulent Boundary Layer in Compressible Fluids," J. Aeronaut. Sci., Vol. 18, No. 3 (March 1951), pp. 145-160.
46. Jackson, M. W., Czarnecki, K. R., and Monta, W. J. Turbulent Skin Friction at High Reynolds Numbers and Low Supersonic Velocities. NASA TN D-2687, March 1965.
- 47a. Smith, A. M. O. and Clutter, D. W. Solution of the Incompressible Laminar Boundary Layer Equations. Report No. ES 40446, Douglas Aircraft Co. Inc., Santa Monica, Calif., July 1961.
- 47b. Smith, A. M. O. and Clutter, D. W. "Solution of the Incompressible Laminar Boundary-Layer Equations," AIAA Journal, Vol. 1, No. 9 (September 1963), pp. 2062-2071.
- 47c. Clutter, D. W. and Smith, A. M. O. Solution of the General Boundary-Layer Equations for Compressible Laminar Flow, Including Transverse Curvature. Report No. LB 31088, Douglas Aircraft Co., Inc., Long Beach, California, February 1963.
48. Smith, A. M. O. and Jaffe, N. A. General Method for Solving the Nonequilibrium Boundary-Layer Equations of a Dissociating Gas. AIAA Paper No. 65-129, Presented at the AIAA Second Aerospace Sciences Meeting in New York, January 1965.
49. Wu, J. C. The Solution of the Laminar Boundary Layer Equations by the Finite Difference Method. Report SM-37484, Douglas Aircraft Co., Inc., June 1960.
50. Görtler, H. "A New Series for the Calculation of Steady Laminar Boundary Layer Flows," J. Math. and Mech., Vol. 6, No. 1 (1957).
- 51a. Hartree, D. R. A Solution of the Laminar Boundary-Layer Equation for Retarded Flow. British R and M No. 2426, 1949.
- 51b. Hartree, D. R. The Solution of the Equations of the Laminar Boundary Layer for Schubauer's Observed Pressure Distribution for an Elliptic Cylinder. British R and M No. 2427, 1949.
52. Hartree, D. R. and Womersley, J. R. "A Method for the Numerical or Mechanical Solution of Certain Types of Partial Differential Equations," Proc. Roy. Soc., Series A, Vol. 161, No. 906 (August 1937), pp. 353-366.
53. Raetz, G. S. A Method of Calculating the Incompressible Laminar Boundary Layer on Infinitely-long Swept Suction Wings, Adaptable to Small-capacity, Automatic Digital Computers. Report BLC-11, Northrop Aircraft Co., September 1953.

54. Baxter, D. C. and Flügge-Lotz, I. The Solution of Compressible Laminar Boundary Layer Problems by a Finite Difference Method. Part 2. Further Discussion of the Method and Computation of Examples. TR No. 110 (ASTIA AD148 040), Division of Engineering Mechanics, Stanford University, October 1957.
55. Kramer, R. F. and Lieberstein, H. M. "Numerical Solution of the Boundary-Layer Equations without Similarity Assumptions," J. Aero Space Sciences, Vol. 26, No. 8 (August 1959), pp. 508-514.
56. Blottner, F. G. and Flügge-Lotz, I. "Finite-Difference Computation of the Boundary Layer with Displacement Thickness Interaction," J. Mech., Vol. II, No. 4 (December 1963), pp. 397-423.
57. Parr, W. Laminar Boundary Layer Calculations by Finite Differences. NOL TR 63-261, U.S. Naval Ordnance Laboratory, December 1963.
58. Lewis, C. H. and Whitfield, J. D. Theoretical and Experimental Studies of Hypersonic Viscous Effects. Paper Presented at the AGARD Specialists' Meeting (AGARDograph 97, Part III), Naples, Italy, May 1965.
59. Cohen, C. B. and Reshotko, E. Similar Solutions for the Compressible Laminar Boundary Layer with Heat Transfer and Pressure Gradient. NACA Report 1293 (Supersedes NACA TN 3325), 1956.
60. Van Driest, E. R. "Turbulent Boundary Layer on a Cone in a Supersonic Flow at Zero Angle of Attack," J. Aeronaut. Sci., Vol. 19, No. 1 (1952), pp. 55-57.
61. Lewis, C. H. Pressure Distribution and Shock Shape over Blunted Slender Cones at Mach Numbers from 16 to 19. AEDC-TN-61-81, August 1961.
62. Ferri, A. "Some Heat Transfer Problems in Hypersonic Flow," Aeronautics and Astronautics. New York: Pergamon Press, 1960.
63. Moeckel, W. E. Approximate Method for Predicting Form and Location of Detached Shock Waves Ahead of Plane or Axially Symmetric Bodies. NACA TN 1921, July 1949.
64. Heybey, W. H. Shock Distances in Front of Symmetrical Bodies. NAVORD Report 3594, U.S. Naval Ordnance Laboratory, December 1953.
65. Zakkay, V. and Krause, E. "Boundary Conditions at the Outer Edge of the Boundary Layer on Blunted Conical Bodies," AIAA Journal, Vol. 1, No. 7 (July 1963), pp. 1671-1672.
66. Lees, L. "Laminar Heat Transfer over Blunt-Nosed Bodies at Hypersonic Speeds," Jet Propulsion, Vol. 26 (April 1956), pp. 259-269 and 274.
67. Dailey, C. L. and Wood, F. C. Computation Curves for Compressible Fluid Problems. New York: John Wiley and Sons, Inc., 1949.

68. Kopal, Z., et al. Tables of Supersonic Flow Around Cones. TR 1, Massachusetts Institute of Technology, 1947.
69. Kennedy, E. C. Tables of Supersonic Conical Flow. OAL Memo. 143 (CM-973), May 1960.
70. Lyons, W. C., Jr., Brady, J. J., and Levensteins, Z. J. Hypersonic Drag, Stability, and Wake Data for Cones and Spheres. Paper Presented at January 1964 AIAA Meeting (Preprint No. 64-44).
71. Rubin, I. "Shock Curvature Effect on the Outer Edge Conditions of a Laminar Boundary Layer," AIAA Journal, Vol. 1, No. 12 (December 1963), pp. 2850-2852.
72. Brinich, P. F. and Sands, N. Effect of Bluntness on Transition for a Cone and a Hollow Cylinder at Mach 3.1 NACA TN 3979, May 1957.
73. Potter, J. L. and Whitfield, J. D. "Effects of Slight Nose Bluntness and Roughness on Boundary-Layer Transition in Supersonic Flows," J. Fluid Mech., Vol. 12 (November 1962), pp. 501-535.
74. Applied Physics Laboratory, The Johns Hopkins University. Handbook of Supersonic Aerodynamics, NAVORD Report 1488, Vol. 6, Sec. 20, "Wind Tunnel Instrumentation and Operation," January 1961.
75. Van Driest, E. R. and Boison, J. C. "Experiments on Boundary Layer Transition at Supersonic Speeds," J. Aeronaut. Sci., Vol. 24 (December 1957), pp. 885-899.
76. Jack, J. R., Wisniewski, R. J., and Diaconis, N. S. Effects of Extreme Surface Cooling on Boundary-Layer Transition. NACA TN 4094, October 1957.
77. Lyons, W. C., Jr., and Sheetz, N. W., Jr. Free Flight Experimental Investigations of the Effect of Boundary Layer Cooling on Transition. NOL TR 61-83, U.S. Naval Ordnance Laboratory, September 1961.
78. Sheetz, N. W., Jr. Free-Flight Boundary Layer Transition Investigations at Hypersonic Speeds. AIAA Paper No. 65-127, Presented at AIAA Second Aerospace Sciences Meeting in New York City, January 1965.
79. Witt, W. R., Jr. "Free Flight Boundary Layer Transition Studies on Cones." Proceedings of the Fourth Midwestern Conference on Fluid Mechanics, Purdue University Engineering Experiment Station. Research Series No. 128, September 1955.
80. Rumsey, C. B. and Lee, D. B. Measurements of Aerodynamic Heat Transfer and Boundary-Layer Transition on a 10° Cone in Free Flight at Supersonic Mach Numbers up to 5.9. NASA TN D-745, May 1961.
81. Brinich, P. F. Recovery Temperature, Transition, and Heat-Transfer Measurements at Mach 5. NASA TN D-1047, August 1961.

-
82. Deem, R. E. and Murphy, J. S. Flat Plate Boundary Layer Transition at Hypersonic Speeds. AIAA Paper No. 65-128, Presented at AIAA Second Aerospace Sciences Meeting in New York City, January 1965.
83. Richards, B. E. and Stollery, J. L. "Transition Reversal on a Flat Plate at Hypersonic Speeds." AGARDograph 97 on Recent Developments in Boundary Layer Research, Part 1 (May 1965), pp. 477-501.
84. James, C. S. Boundary-Layer Transition on Hollow Cylinders in Supersonic Free Flight as Affected by Mach Number and a Screwthread Type of Surface Roughness. NASA Memo 1-20-59A, February 1959.
85. Czarnecki, K. R. and Sinclair, A. R. Preliminary Investigation of the Effects of Heat Transfer on Boundary-Layer Transition on a Parabolic Body of Revolution (NACA RM-10) at a Mach Number of 1.61. NACA TN3165, April 1954.
86. Czarnecki, K. R. and Sinclair, A. R. An Extension of the Investigation of the Effects of Heat Transfer on Boundary-Layer Transition on a Parabolic Body of Revolution (NACA RM-10) at a Mach Number of 1.61. NACA TN 3166, April 1954.
87. Sinclair, A. R. and Czarnecki, K. R. Investigation of Boundary-Layer Transition on 10° Cone in Langley 4- by 4-Foot Supersonic Pressure Tunnel at Mach Numbers of 1.41, 1.61, and 2.01. NACA TN 3648, May 1956.
88. Czarnecki, K. R. and Jackson, M. W. Effects of Nose Angle and Mach Number on Transition on Cones at Supersonic Speeds. NACA TN4388, September 1958.
89. Lange, A. H., Gieseler, L. P., and Lee, R. E. "Variation of Transition Reynolds Number with Mach Number," J. Aeronaut. Sci., Vol. 20, No. 10 (October 1953), pp. 718-719.
90. Ross, A. O. Determination of Boundary-Layer Transition Reynolds Numbers by Surface-Temperature Measurement of a 10° Cone in Various NACA Supersonic Wind Tunnels. NACA TN 3020, October 1953.
91. Lee, R. E. Measurements of Pressure Distribution and Boundary-Layer Transition on a Hollow-Cylinder Model. NAVORD Report 2823, U.S. Naval Ordnance Laboratory, April 1953.
92. Jillie, D. W. and Hopkins, E. J. Effects of Mach Number, Leading-Edge Bluntness, and Sweep on Boundary-Layer Transition on a Flat Plate, NASA TN D-1071, September 1961.
93. Coles, D. Measurements in the Boundary Layer on a Smooth Flat Plate in Supersonic Flow. GALCIT, Ph. D. Thesis, June 1953.
- 94a. Coles, D. Measurements in the Boundary Layer on a Smooth Flat Plate in Supersonic Flow. 1. The Problem of the Turbulent Boundary Layer. Report No. 20-69, Jet Propulsion Laboratory, June 1953.

- 94b. Coles, D. Measurements in the Boundary Layer on a Smooth Flat Plate in Supersonic Flow. II. Instrumentation and Experimental Techniques at the Jet Propulsion Laboratory. Report No. 20-70, Jet Propulsion Laboratory, June 1953.
95. Hilton, J. H., Jr., and Czarnecki, K. R. An Exploratory Investigation of Skin Friction and Transition on Three Bodies of Revolution at a Mach Number of 1.61. NACA TN 3193, June 1954.
96. Jack, J. R. Effect of Favorable Pressure Gradients on Transition for Several Bodies of Revolution at Mach 3.12. NACA TN 4313, July 1958.
97. Jedlicka, J. R., Wilkins, M. E. and Seiff, A. Experimental Determination of Boundary-Layer Transition on a Body of Revolution at $M = 3.5$. NACA TN 3342, October 1954.
98. Czarnecki, K. R. and Jackson, M. W. Effects of Cone Angle, Mach Number, and Nose Blunting on Transition at Supersonic Speeds. NASA TN D-634, January 1961.
99. Witt, W. R., Jr. and Persh, J. A Correlation of Free-Flight Transition Measurements on Various Blunt Nose Shapes by use of the Momentum Thickness Reynolds Number. NAVORD Report 4400, U.S. Naval Ordnance Laboratory, December 1956.
100. Buglia, J. J. Heat Transfer and Boundary-Layer Transition on a Highly Polished Hemisphere-Cone in Free Flight at Mach Numbers up to 3.14 and Reynolds Numbers up to 24×10^6 . NASA TN D-955, September 1961.
101. Dunning, R. W. and Ulmann, E. F. Effects of Sweep and Angle of Attack on Boundary-Layer Transition on Wings at Mach Number 4.04. NACA TN 3473, August 1955.
102. Chapman, G. T. Some Effects of Leading-Edge Sweep on Boundary-Layer Transition at Supersonic Speeds. NASA TN D-1075, September 1961.
103. Van Driest, E. R. and Blumer, C. B. "Boundary-Layer Transition at Supersonic Speeds -- Three-Dimensional Roughness Effects (Spheres)," J. Aerospace Sci., Vol. 29, No. 8 (August 1962), pp. 909-916.
104. Van Driest, E. R. and McCauley, W. D. "The Effect of Controlled Three-Dimensional Roughness on Boundary-Layer Transition at Supersonic Speeds," J. Aerospace Sci., Vol. 27, No. 4 (April 1960), pp. 261-271 and 303.
105. Klebanoff, P. S., Schubauer, G. B., and Tidstrom, K. D. "Measurements of the Effect of Two-Dimensional and Three-Dimensional Roughness Elements on Boundary-Layer Transition," J. Aeronaut. Sci., Vol. 22, No. 11 (November 1955), pp. 803-804.
106. Braslow, A. L., Knox, E. C., and Horton, E. A. Effect of Distributed Three-Dimensional Roughness and Surface Cooling on Boundary Layer Transition and Lateral Spread of Turbulence at Supersonic Speeds. NASA TN D-53, October 1959.

107. Lyons, W. C., Jr., and Levensteins, Z. J. The Determination of Critical Roughness Height for Boundary Layer Transition. NOLTR 61-87, U.S. Naval Ordnance Laboratory, October 1962.
108. Liepmann, H. W., Roshko, A., and Dhawan, S. On Reflection of Shock Waves from Boundary Layers. NACA TN 2334, April 1951.
109. Charters, A. C., Jr. Transition Between Laminar and Turbulent Flow by Transverse Contamination. NACA TN 891, March 1943.
110. Fenter, F. W. A Theoretical Analysis of the Effects of Surface Roughness on the Turbulent Boundary Layer in Compressible Flow with Zero Heat Transfer. DRL Report 365, CM-824, Defense Research Laboratory, The University of Texas, April 1955.
111. Goddard, F. E., Jr. "Effect of Uniformly Distributed Roughness on Turbulent Skin-Friction Drag at Supersonic Speeds," J. Aero-Space Sci., Vol. 26, No. 1 (January 1959), pp. 1-15.
112. Clutter, D. W. Charts for Determining Skin-Friction Coefficients on Smooth and on Rough Flat Plates at Mach Numbers up to 5.0 with and without Heat Transfer. Report No. ES 29074, Douglas Aircraft Co., Inc., El Segundo, California, April 1959.
113. Fenter, F. W. The Turbulent Boundary Layer on Uniformly Rough Surfaces at Supersonic Speeds. DRL Report 437, CM-941, Defense Research Laboratory, The University of Texas, January 1960.
114. Wade, J. H. T. An Experimental Investigation of the Effect of Surface Roughness on the Drag of a Cone-Cylinder Model at a Mach Number of 2.48. UTIA Report No. 34, University of Toronto, Canada, September 1955.
115. Young, F. L. Experimental Investigation of the Effects of Surface Roughness on Compressible Turbulent Boundary Layer Skin Friction and Heat Transfer. DRL Report 532, CR-21, Defense Research Laboratory, The University of Texas, May 1965.
116. Prandtl, L. and Schlichting, H. Das Widerstandsgesetz rauher Platten Werft Reederei Hafen, Jahrg. 15, Heft 1, January 1934, pp. 1-4. (The Resistance Law for Rough Plates. DTMB Translation 258, September 1955.)
117. Lobb, R. K., Winkler, E. M., and Persh, J. "Experimental Investigation of Turbulent Boundary Layers in Hypersonic Flow," J. Aeronaut. Sci., Vol. 22, No. 1 (January 1955), pp. 1-9.
- 118a. Coles, D. Measurements in the Boundary Layer on a Smooth Flat Plate in Supersonic Flow. III. Measurements in a Flat-Plate Boundary Layer at the Jet Propulsion Laboratory. Report No. 20-71, Jet Propulsion Laboratory, June 1953.
- 118b. Coles, D. "Measurements of Turbulent Friction on a Smooth Flat Plate in Supersonic Flow," J. Aeronaut. Sci., Vol. 21, No. 7 (July 1954), pp. 433-448.

119. Liepmann, H. W. and Goddard, F. E., Jr. "Note on the Mach Number Effect Upon the Skin Friction of Rough Surfaces," J. Aeronaut. Sci., Vol. 24, No. 10 (October 1957), p. 784.
120. Van Driest, E. R. "The Problem of Aerodynamic Heating," Aeronautical Engineering Review, Vol. 15, No. 10 (October 1956), pp. 26-41.
121. Squire, H. B. Heat Transfer Calculations for Aerofoils. British R and M No. 1986, November 1942.
122. Van Driest, E. R. "Turbulent Flows and Heat Transfer." High-Speed Aerodynamics and Jet Propulsion, Vol. V (edited by C. C. Lin). Princeton: Princeton University Press, 1959, pp. 372-388.
123. Brevoort, M. J. and Arabian, B. D. Summary of Experimental Heat-Transfer Measurements in Turbulent Flow for a Mach Number Range from 0.87 to 5.05. NACA TN 4248, May 1958.
124. Brinich, P. F. A Study of Boundary-Layer Transition and Surface Temperature Distributions at Mach 3.12. NACA TN 3509, July 1955.
125. Seiff, A. Examination of the Existing Data on the Heat Transfer of Turbulent Boundary Layers at Supersonic Speeds from the Point of View of Reynolds Analogy. NACA TN 3284, August 1954.
126. Tifford, A. N. and Chu, S. T. Heat Transfer in Laminar Boundary Layers Subject to Surface Pressure and Temperature Distributions. Proceedings of the Second Midwestern Conference on Fluid Mechanics, Ohio State University, March 1952, pp. 363-377.
127. Goldstein, S. Modern Developments in Fluid Dynamics, Vol. 2. Oxford: Clarendon Press, 1938, pp. 631-632.
128. Korobkin, I. Laminar Heat Transfer Characteristics of a Hemisphere for the Mach Number Range 1.9 to 4.9. NAVORD Report 3841, U.S. Naval Ordnance Laboratory, October 1954.
129. Rose, P. H. and Stark, W. I. "Stagnation Point Heat-Transfer Measurements in Dissociated Air," J. Aeronaut. Sci., Vol. 25, No. 2 (February 1958), pp. 86-97.
130. Rose, P. H. and Stankevics, J. O. "Stagnation-Point Heat-Transfer Measurements in Partially Ionized Air," AIAA Journal, Vol. 1, No. 12 (December 1963), pp. 2752-2763.
131. Fay, J. A. and Riddell, F. R. "Theory of Stagnation Point Heat Transfer in Dissociated Air," J. Aeronaut. Sci., Vol. 25, No. 2 (February 1958), pp. 73-85.
132. Fay, J. A. and Kemp, N. H. Theory of Stagnation Point Heat Transfer in a Partially Ionized Diatomic Gas. IAS Preprint 63-60, January 1963.

-
133. Lees, L. "Laminar Heat Transfer over Blunt-Nosed Bodies at Hypersonic Flight Speeds," Jet Propulsion, Vol. 26, No. 4 (April 1956), pp. 259-269.
 134. Probst, R. F. "Method of Calculating the Equilibrium Laminar Heat Transfer Rate at Hypersonic Flight Speeds," Jet Propulsion, Vol. 26, No. 6 (June 1956), pp. 497-499.
 135. Eckert, E. R. G. and Tewfik, O. E. "Use of Reference Enthalpy in Specifying the Laminar Heat-Transfer Distribution Around Blunt Bodies in Dissociated Air," J. Aero/Space Sci., Vol. 27, No. 6 (June 1960), pp. 464-466.
 136. Kemp, N. H., Rose, P. H., and Detra, R. W. "Laminar Heat Transfer Around Blunt Bodies in Dissociated Air," J. Aero/Space Sci., Vol. 26, No. 7 (July 1959), pp. 421-430.
 137. Solomon, J. M. The Calculation of Laminar Boundary Layers in Equilibrium Dissociated Air by an Extension of the Cohen and Reshotko Method. NOLTR 61-143, U.S. Naval Ordnance Laboratory, February 1962.
 138. Eckert, E. R. G. "Engineering Relations for Friction and Heat Transfer to Surfaces in High Velocity Flow," J. Aeronaut. Sci., Vol. 22, No. 8 (August 1955), pp. 585-587.
 139. Eggers, A. J., Jr., Hansen, C. F., and Cunningham, B. E. Stagnation-Point Heat Transfer to Blunt Shapes in Hypersonic Flight, Including Effects of Yaw. NACA TN 4229, April 1958.
 140. Pasiuk, L., Hastings, S. M., and Chatham, R. Experimental Reynolds Analogy Factor for a Compressible Turbulent Boundary Layer with a Pressure Gradient. NOLTR 64-200, U.S. Naval Ordnance Laboratory, November 1964.
 141. Rubesin, M. W. A Modified Reynolds Analogy for the Compressible Turbulent Boundary Layer on a Flat Plate. NACA TN 2917, March 1953.
 142. Cohen, N. B. A Method for Computing Turbulent Heat Transfer in the Presence of a Streamwise Pressure Gradient for Bodies in High-Speed Flow. NASA Memo 1-2-59L, March 1959.
 143. Wilson, R. E. Recent Developments in Boundary-Layer Research. Paper Presented at the AGARD Specialists' Meeting (AGARDograph 97, Part I, pp. 1025-1048), Naples, Italy, May 1965.
 144. Harris, E. L. Determination of the Streamlines on a Sphere-Cone at Angle of Attack from the Measured Surface Pressure Distribution. NOLTR 63-37, U.S. Naval Ordnance Laboratory, February 1963.
 145. Julius, J. D. Measurements of Pressure and Local Heat Transfer on a 20° Cone at Angles of Attack up to 20° for a Mach Number of 4.95. NASA TN D-179, December 1959.

146. Braun, W. H. Turbulent Boundary Layer on a Yawed Cone in a Supersonic Stream. NACA TN 4208, January 1958.
147. Brunk, W. E. Approximate Method for Calculation of Laminar Boundary Layer with Heat Transfer on a Cone at Large Angles of Attack in Supersonic Flow. NACA TN 4380, September 1958.
148. Burbank, P. B. and Hodge, B. L. Distribution of Heat Transfer on a 10° Cone at Angles of Attack from 0° to 15° for Mach Numbers of 2.49 to 4.65 and a Solution to the Heat-Transfer Equation that Permits Complete Machine Calculations. NASA Memo 6-4-59L, June 1959.
149. Pasiuk, L. Comparisons of Experimental and Theoretical Heat Transfer to a Yawed Sphere-Cone Model at Supersonic Speeds. NOLTR 63-208, U.S. Naval Ordnance Laboratory, December 1963.
150. Beckwith, I. E. Similarity Solutions for Small Cross Flows in Laminar Compressible Boundary Layers. NASA TR R-107, 1961.
151. Van Camp, W. M. Aerodynamic Heating Characteristics of a Nose Cone at Angle of Attack. Report No. 5978, McDonnell Aircraft Corporation, Research Department, May 1958.
152. Aeillo, G. F. An Investigation of a Three-Dimensional Turbulent Boundary Layer in Hypersonic Flow. ARL 63-26, Aeronautical Research Laboratories, Wright-Patterson Air Force Base, Ohio, February 1963.
153. Ferri, A. and Libby, P. A. "A New Technique for Investigating Heat Transfer and Surface Phenomena Under Hypersonic Flow Conditions," J. Aeronaut. Sci., Vol. 24, No. 6 (June 1957), pp. 464-465.
154. Feller, W. V. Heat Transfer to Bodies at Angles of Attack. NACA RM L57D19c, June 1957.
155. Sands, N. and Jack, J. R. Preliminary Heat-Transfer Studies on Two Bodies of Revolution at Angle of Attack at a Mach Number of 3.12. NACA TN 4378, September 1958.
156. Cunningham, B. E. and Kraus, S. Experimental Investigation of the Effect of Yaw on Rates of Heat Transfer to Transverse Circular Cylinders in a 6500-Foot-Per-Second Hypersonic Air Stream. NACA RM A58E19, August 1958.
157. Eggers, A. J., Jr., Funsen, C. F., and Cunningham, B. E. Theoretical and Experimental Investigation of the Effect of Yaw on Heat Transfer to Circular Cylinders in Hypersonic Flow. NACA RM A55E02, 1955.
158. Reshotko, E. and Beckwith, I. E. Compressible Laminar Boundary Layer over a Yawed Infinite Cylinder with Heat Transfer and Arbitrary Prandtl Number. NACA TN 3986, June 1957.
159. Goodwin, G., Creager, M. O., and Winkler, E. L. Investigation of Local Heat-Transfer and Pressure Drag Characteristics of a Yawed Circular Cylinder at Supersonic Speeds. NACA RM A55H31, January 1956.

160. Beckwith, I. E. and Gallagher, J. J. Local Heat Transfer and Recovery Temperatures on a Yawed Cylinder at a Mach Number of 4.15 and High Reynolds Numbers. NASA TR R-104, 1961.
161. Beckwith, I. E. Similar Solutions for the Compressible Boundary Layer on a Yawed Cylinder with Transpiration Cooling. NASA TR R-42, 1959.
162. Jones, J. J. Experimental Investigation of the Heat-Transfer Rate to a Series of 20° Cones of Various Surface Finishes at a Mach Number of 4.95. NASA Memo 6-10-59L, June 1959.
163. Chapman, D. R. A Theoretical Analysis of Heat Transfer in Regions of Separated Flow. NACA TN 3792, October 1956.
164. Stalder, J. R. and Nielsen, H. V. Heat Transfer from a Hemisphere-Cylinder Equipped with Flow Separation Spikes. NACA TN 3287, 1954.
165. Crawford, D. H. and Rumsey, C. B. Heat Transfer in Regions of Separated and Reattached Flows. NACA RM L57D25b, June 1957.
166. Crawford, D. H. Investigation of the Flow over a Spiked-Nose Hemisphere-Cylinder at a Mach Number of 6.8. NASA TN D-118, December 1959.
167. Larson, H. K. "Heat Transfer in Separated Flows," J. Aero/Space Sci., Vol. 26, No. 11 (November 1959), pp. 731-738.
168. McConnell, D. G. Free Flight Observation of a Separated Turbulent Flow Including Heat Transfer up to Mach 8.5. NASA TN D-278, October 1961.
169. Centolanzi, F. J. Heat Transfer to Blunt Conical Bodies Having Cavities to Promote Separation. NASA TN D-1975, July 1963.
170. Kaufman, L. G., et al. An Investigation of Hypersonic Flow Separation and Control Characteristics. Report No. AFFDL-TR-64-174, Grumman Aircraft Engineering Corporation, Wright-Patterson Air Force Base, Ohio, January 1965.
171. Kuehn, D. M. Turbulent Boundary-Layer Separation Induced by Flares on Cylinders at Zero Angle of Attack. NASA TR R-117, 1961.
172. Kuehn, D. M. Laminar Boundary-Layer Separation Induced by Flares on Cylinders at Zero Angle of Attack. NASA TR R-146, 1962.
173. Sterrett, J. R. and Emery, J. C. Experimental Separation Studies for Two-Dimensional Wedges and Curved Surfaces at Mach Numbers of 4.8 to 6.2. NASA TN D-1014, February 1962.
174. Kaufman, L. G., et al. A Review of Hypersonic Flow Separation and Control Characteristics. ASD TDR 62-168, Grumman Aircraft Engineering Corporation, Wright-Patterson Air Force Base, Ohio, March 1962.
175. Holloway, P. F., Sterrett, J. R., and Creekmore, H. S. An Investigation of Heat Transfer within Regions of Separated Flow at a Mach Number of 6.0. NASA TN D-3074, November 1965.

176. Wisniewski, R. J. Turbulent Heat-Transfer Coefficients in the Vicinity of Surface Protuberances. NASA Memo 10-1-58E, October 1958.
177. Brinich, P. F. Recovery Temperatures and Heat Transfer Near Two-Dimensional Roughness Elements at Mach 3.1. NACA TN 4213, February 1958.
178. Burbank, P. B., Newlander, R. A., and Collins, I. K. Heat-Transfer and Pressure Measurements on a Flat-Plate Surface and Heat-Transfer Measurements on Attached Protuberances in a Supersonic Turbulent Boundary Layer at Mach Numbers of 2.65, 3.51, and 4.44. NASA TN D-1372, December 1962.
179. Bloom, M. H. and Pallone, A. Heat Transfer to Surfaces in the Neighborhood of Protuberances in Hypersonic Flow. WADC TN 57-95 (ASTIA Document No. AD 118138), August 1957.
180. Pappas, C. C. Measurement of Heat Transfer in the Turbulent Boundary Layer on a Flat Plate in Supersonic Flow and Comparison with Skin-Friction Results. NACA TN 3222, 1954.
181. Scherrer, R., Wimbrow, W. R., and Gowen, F. E. Heat-Transfer and Boundary-Layer Transition on a Heated 20° Cone at a Mach Number of 1.53. NACA RM A8L28, 1949. (See also NACA Rep. 1055).
182. Fischer, W. W. and Norris, R. H. "Supersonic Convective Heat-Transfer Correlation from Skin-Temperature Measurements on a V-2 Rocket in Flight," Trans. ASME, Vol. 71, No. 5 (July 1949), pp. 457-469.
183. Fallis, W. B. Heat Transfer in the Transitional and Turbulent Boundary Layers on a Flat Plate at Supersonic Speeds. Report No. 19, University of Toronto, Institute of Aerophysics, May 1952.
184. Monaghan, R. J. and Cooke, J. R. The Measurement of Heat Transfer and Skin Friction at Supersonic Speeds. Part IV: Tests on a Flat Plate at $M = 2.82$. RAE Tech. Note Aero. 2171, June 1952.
185. Van Driest, E. R. The Turbulent Boundary Layer with Variable Prandtl Number. Report No. AL-1914, North American Aviation, Inc., April 1954.
186. Chapman, D. R., Kuehn, D. M., and Larson, H. K. Investigation of Separated Flows in Supersonic and Subsonic Streams with Emphasis on the Effect of Transition. NACA TN 3869, March 1957, and Report 1356, 1958.
187. Hilsenrath, J. and Klein, M. Tables of Thermodynamic Properties of Air in Chemical Equilibrium Including Second Virial Corrections from 1500°K to 15,000°K. AEDC-TR-65-58, March 1965.
188. Liley, P. E. Review of Work on the Transport Properties of Gases and Gas Mixtures. TPRC Report 10, Purdue University, December 1959. (See also Supplement 1 to above, TPRC Report 12, April 1961).

189. Liley, P. E. Survey of Recent Work on the Viscosity, Thermal Conductivity, and Diffusion of Gases and Liquefied Gases Below 500°K. TPRC Report 13, Purdue University, June 1961.
190. Ragent, B. and Noble, C. E., Jr. High-Temperature Transport Coefficients of Selected Gases. ARL 62-328, Aeronautical Research Laboratories, April 1962.
191. Hansen, C. F. Approximations for the Thermodynamic and Transport Properties of High-Temperature Air. NASA TR R-50, 1959.
192. Bade, W. L., Mason, E. A., and Yun, K. S. Transport Properties of Dissociated Air. Unpublished Report AVCO RAD, Wilmington, Mass. and Institute for Molecular Physics, University of Maryland, College Park, Md.
193. Bauer, E. and Zlotnick, M. "Transport Coefficients of Air to 8000°K," ARS Journal, Vol. 29 (October 1959), pp. 721-728.
194. Stupochenko, E. V., et al. "Method of Calculation of the Transport Coefficients of Air at High Temperatures," ARS Journal, Vol. 30 (April 1960), pp. 394-402.
195. Scala, S. M. and Baulknight, C. W. "Transport and Thermodynamic Properties in a Hypersonic Laminar Boundary Layer. Part 1: Properties of the Pure Species," ARS Journal, Vol. 29 (January 1959), pp. 39-45. Part 2: "Application," ARS Journal, Vol. 30 (April 1960), pp. 329-336.
196. Brokaw, R. S. Alignment Charts for Transport Properties, Viscosity, Thermal Conductivity, and Diffusion Coefficients for Nonpolar Gases and Gas Mixtures at Low Density. NASA TR R-81, 1960.
197. Gilmore, F. R. Equilibrium Composition and Thermodynamic Properties of Air to 24,000°K. Project Rand, RM-1543 (ASTIA Document No. AD84052), August 1955.
198. Green, M. S. The Transport Properties of Air at Elevated Temperatures. NBS Reports 7C101, 7C102, 7C103, 9235-9, National Bureau of Standards, 1956.
199. Pai, Shih-I. Viscous Flow Theory. I-Laminar Flow. Princeton, N. J.: D. van Nostrand Co., Inc., 1956.
200. Rouse, H. Advanced Mechanics of Fluids. New York: John Wiley and Sons, Inc., 1959.
201. Dorrance, W. H. Viscous Hypersonic Flow. New York: McGraw-Hill Book Co., Inc., 1962.
202. Kutateladze, S. S. and Leont'ev, A. I. Turbulent Boundary Layer in Compressible Gases. (Originally published in Russia in 1962 by the Academy of Sciences of the U.S.S.R., Siberian Division.) New York: Academic Press, Inc., 1964.
203. Clarke, J. F. and McChesney, M. The Dynamics of Real Gases. London: Butterworth and Co., 1964.

INDEX

- angle of attack
 - boundary-layer transition, effect on, 124, 141
 - heat transfer, effect on, 200, 227, 228
- axisymmetric
 - bodies, 85ff, 200ff
 - flow, 7, 11, 77, 91ff, 98ff, 102, 195ff
- blunted cones, 12, 86, 88, 98ff, 101, 105, 118, 147, 150
- bluntness
 - boundary-layer transition, effect on, 125, 142
- bodies
 - axisymmetric, 85ff, 200ff
 - ducted, 35
 - two-dimensional, 83ff, 195ff
- boundary layer
 - displacement thickness, 11, 24, 28, 40-42, 61, 71, 88, 99, 116, 153
 - equations, derivations of, 3ff
 - axisymmetric flow, 11, 85
 - solutions, 17ff, 77ff
 - two-dimensional flow, 12, 83
 - laminar, on
 - bodies, 77
 - cones, 91
 - flat plate
 - perfect gas, 7, 189
 - real gas, 25, 191
 - sphere-cones, 98
 - spheres, 94
 - sublayer, 31, 43, 66, 73ff, 160
 - momentum thickness, 11, 24, 28, 34, 40, 61, 88, 96, 99
 - shape parameter, 11, 24, 28, 40, 59, 72, 88, 99, 116
 - thickness, 5, 28, 40, 60, 71, 99, 116
 - transition, 119ff, 193, 219
 - angle of attack, effect of, 124, 141
 - blunt bodies, effect on, 125, 142
 - cones, effect on, 93, 121, 147, 227
 - cooling, effect of, 121, 137
 - flat plate, effect on, 47ff, 119ff, 219
 - insulation, effect of, 123
 - Mach number, effect of, 121, 138, 139
 - Reynolds number, effect of, 121, 135
 - roughness, effect of, 127, 165, 204
 - stream turbulence, effect of, 132, 157
 - sweep, effect on, 127
 - turbulent, on
 - bodies, 89
 - cones, 92
- flat plate
 - perfect gas, 29, 193, 218
 - real gas, 45
- conductivity
 - coefficient of, 5, 26, 62
 - eddy, 15, 193
- cone
 - blunt, 12, 86, 88, 98ff, 101, 105, 118, 147, 148, 150
 - heat transfer, 202, 244
 - sharp, 90, 92, 147, 148, 153, 154, 200, 244
 - transition, 93, 121, 154, 227, 228
- continuity equation, 3, 6ff, 15, 77
- cooling
 - C_f , effect on, 32, 33, 57, 65, 66, 70
 - transition, effect on, 121, 137
- critical pressure rise coefficient, 124, 142
- Crocco transformation, 8, 15, 17, 53, 79, 83, 85
- cylinders, at yaw, 203, 233ff
- displacement thickness of boundary-layer, 11, 24, 28, 40, 42, 61, 71, 88, 99, 116, 153
- dissipation function, 5
- drag, friction 105, 119
- ducted bodies, 85, 87
- eddy
 - conductivity, 15, 193
 - viscosity, 14, 29, 193
- energy, equation of, 5, 6, 8, 15, 17, 78
- enthalpy, 8, 27, 45
 - gradient, 191
 - reference, 193
- entropy, variable, 98
- equilibrium temperature, 20
- Falkner-Skan flow, 80ff
- film coefficient, 202, 209
- finite difference method, 77ff, 111
- friction velocity, 30, 159
- heat, conduction rate, 5
 - flux, 15
- heat transfer
 - angle of attack effect, 200, 227, 228
 - laminar boundary layer
 - bodies, 195
 - cones, spheres, 200, 244

- flat plate
 - perfect gas, 189, 241
 - real gas, 191
- pressure gradient, effect on, 196, 225
- protuberance effect, 209ff, 245ff
- roughness, effect on, 155, 156, 164, 204, 237
- separated flow, effect of, 207, 242
- stagnation point, 223
- turbulent boundary layer
 - bodies, 199
 - flat plate
 - perfect gas, 193, 241
 - real gas, 195
- laminar sublayer, 31, 43, 66, 73ff, 160
- Mangler transformation, 7, 12, 91, 99, 129
- mixing length, 29
- momentum equation, 4, 6, 17, 77, 102
- momentum integral equation
 - axisymmetric, 11, 85ff
 - flat plate, 10, 31, 47
 - two-dimensional, 12, 83
- momentum parameter, 81, 113
- momentum thickness of boundary layer, 11, 24, 28, 34, 40, 61, 88, 96, 99
- motion, equation of, 4, 6, 8
- Navier Stokes equation, 4
- Newtonian flow, 95, 197, 202
- Prandtl number, 9, 16, 20, 23, 27, 38, 64, 189
- pressure, critical rise, 124, 142
 - gradient parameter, 80, 113ff, 221
 - heat transfer, effect on, 196, 225
 - transition, effect on, 140
- protuberances, effect on heat transfer, 209ff, 245ff
- real gas effects
 - blunt cone, 109
 - flat plate
 - laminar, 25-28, 191
 - turbulent, 45
- recovery factor, 20, 32, 119, 190, 199, 217
 - temperature, 20
- reference enthalpy, 193
- reference length, 7
- reference temperature, 21, 24, 27, 35, 59, 99
- Reynolds analogy factor, 194ff, 217, 226, 238
 - pressure gradient, effect of, 196
- Reynolds stress, 14, 30
- roughness
 - critical, 131
 - flat plate, 159ff, 165
 - heat transfer, effect on, 155, 164, 204, 237
 - three-dimensional, 128, 152, 154, 161
 - transition, effect on, 127, 165, 204
 - two-dimensional, 132, 237
 - roughness types, 166
 - rough plate, with heat transfer, 164
 - insulated, 159
 - transition on, 165
- separated flow
 - heat transfer, effect on, 207, 242
- shape parameter, 11, 24, 28, 40-42, 59, 72, 88, 99, 116
- shear parameter, 80, 115
 - stress, 3, 6, 29, 38, 88, 189
- shockwave shape, 101
- skin friction coefficient
 - axisymmetric bodies, 11
 - cones
 - blunt, 12, 103, 105, 118
 - sharp, 90, 92, 147, 153, 200, 244
 - laminar, 90
 - transition, with, 93
 - turbulent, 92
 - experimental, 37-39
 - flat plate
 - laminar, 21, 27, 57, 65
 - turbulent, 32ff, 46ff, 62ff
 - roughness effect, 162ff
 - sphere-cones, 99, 105
 - transition, with
 - cone, 93
 - flat plate, 48ff
 - sphere, boundary layer on, 94
 - heat transfer, 202
 - sphere-cone, boundary layer on, 98, 147, 148
 - heat transfer, 202, 229ff
 - spikes, nose, effect on heat transfer, 207, 239
 - spreading of boundary layer turbulence, 133
 - stagnation point flow, 197, 222, 224
 - Stanton number, 38, 189ff, 220ff, 227
 - stream turbulence
 - transition, effect on, 132, 157
 - surface pressure
 - transition, effect on, 123
 - Sutherland's viscosity law, 13, 18, 20, 99
 - sweep
 - heat transfer, effect on, 203
 - transition, effect on, 127, 151
 - temperature
 - equilibrium, 20
 - profile, 21, 56, 131
 - recovery, 20

- reference, 21, 24, 27, 35, 59, 99
- skin friction, effect on, 23
- transition boundary layer, 47, 119ff, 193, 219
 - angle of attack effect, 124, 141
 - bluntness effect, 125, 142
 - cones, 93, 121, 147ff, 227
 - flat plates, 47, 121, 123, 154
 - heat transfer effect, 204
 - insulated surfaces, 123
 - Mach number effect, 121, 136, 139
 - Reynolds number effect, 121, 135
 - roughness effect, 127, 165, 204
 - separated flows, effect of, 208
 - sweep effect, 127
- turbulence
 - boundary-layer transition, effect on, 132
 - lateral spreading, 133
- velocity
 - distribution, 21
 - friction, 30, 159
 - profile, 21, 41, 55, 159
- viscosity
 - coefficient of, 13, 18, 26, 62, 64, 99
 - eddy, 14, 29, 193
 - Sutherland's law, 13, 18, 20, 99
- yaw
 - heat transfer, effect on, 203, 233ff